



HAL
open science

Experimental and modelling studies of ether oxidation

Giorgia Cenedese

► **To cite this version:**

Giorgia Cenedese. Experimental and modelling studies of ether oxidation. Theoretical and/or physical chemistry. Université d'Orléans, 2024. English. NNT : 2024ORLE1053 . tel-04957491

HAL Id: tel-04957491

<https://theses.hal.science/tel-04957491v1>

Submitted on 19 Feb 2025

HAL is a multi-disciplinary open access archive for the deposit and dissemination of scientific research documents, whether they are published or not. The documents may come from teaching and research institutions in France or abroad, or from public or private research centers.

L'archive ouverte pluridisciplinaire **HAL**, est destinée au dépôt et à la diffusion de documents scientifiques de niveau recherche, publiés ou non, émanant des établissements d'enseignement et de recherche français ou étrangers, des laboratoires publics ou privés.

UNIVERSITÉ D'ORLÉANS

**ÉCOLE DOCTORALE ENERGIE, MATERIAUX, SCIENCES DE LA TERRE
ET DE L'UNIVERS**

*INSTITUT de COMBUSTION, AEROTHERMIQUE, REACTIVITE et
ENVIRONNEMENT*

THÈSE présentée par :

Giorgia CENEDESE

soutenue le : **23 février 2024**

pour obtenir le grade de : **Docteur de l'Université d'Orléans**

Discipline/ Spécialité : **Chimie**

Experimental and modelling studies of ether oxidation

THÈSE dirigée par :

Mme SERINYEL Zeynep
M. FOUCHER Fabrice

Maître de Conférences, HDR, Université d'Orléans
Professeur, Université d'Orléans

RAPPORTEURS :

M. HERBINET Olivier
M. VANHOVE Guillaume

Maître de Conférences, HDR, Université de Lorraine
Maître de Conférences, HDR, Université de Lille

JURY :

M. HERBINET Olivier
M. VANHOVE Guillaume
Mme ALZUETA Maria Uxue
M. CURRAN Henry
M. DAGAUT Philippe
M. GOLDSBOROUGH Scott
M. DAYMA Guillaume
Mme SERINYEL Zeynep
M. FOUCHER Fabrice

Maître de Conférences, HDR, Université de Lorraine
Maître de Conférences, HDR, Université de Lille
Professeur, University of Zaragoza
Professeur, University of Galway
Directeur de Recherche, CNRS, Orléans, **Président du jury**
Chercheur, Argonne National Laboratory
Professeur, Université d'Orléans
Maître de Conférences, HDR, Université d'Orléans
Professeur, Université d'Orléans

UNIVERSITÉ D'ORLÉANS

**ÉCOLE DOCTORALE ENERGIE, MATERIAUX, SCIENCES DE LA TERRE
ET DE L'UNIVERS**

*INSTITUT de COMBUSTION, AEROTHERMIQUE, REACTIVITE et
ENVIRONNEMENT*

THÈSE présentée par :

Giorgia CENEDESE

soutenue le : **23 février 2024**

pour obtenir le grade de : **Docteur de l'Université d'Orléans**

Discipline/ Spécialité : **Chimie**

**Études expérimentales et de modélisation de l'oxydation
des éthers**

THÈSE dirigée par :

Mme SERINYEL Zeynep
M. FOUCHER Fabrice

Maître de Conférences, HDR, Université d'Orléans
Professeur, Université d'Orléans

RAPPORTEURS :

M. HERBINET Olivier
M. VANHOVE Guillaume

Maître de Conférences, HDR, Université de Lorraine
Maître de Conférences, HDR, Université de Lille

JURY :

M. HERBINET Olivier
M. VANHOVE Guillaume
Mme ALZUETA Maria Uxue
M. CURRAN Henry
M. DAGAUT Philippe
M. GOLDSBOROUGH Scott
M. DAYMA Guillaume
Mme SERINYEL Zeynep
M. FOUCHER Fabrice

Maître de Conférences, HDR, Université de Lorraine
Maître de Conférences, HDR, Université de Lille
Professeur, University of Zaragoza
Professeur, University of Galway
Directeur de Recherche, CNRS, Orléans, **Président du jury**
Chercheur, Argonne National Laboratory
Professeur, Université d'Orléans
Maître de Conférences, HDR, Université d'Orléans
Professeur, Université d'Orléans

Giorgia CENEDESE

Études expérimentales et de modélisation de l'oxydation des éthers

Résumé :

Ces dernières années, l'augmentation des préoccupations liées aux émissions de polluants et à l'épuisement des ressources fossiles a incité l'étude et le développement de solutions alternatives pour le secteur des transports. Les biocarburants dérivés de la biomasse sont envisagés parmi ces solutions potentielles, et en particulier, les composés oxygénés ont démontré des caractéristiques intéressantes pour différentes applications. Cette thèse se concentre sur la famille des éthers, étudiant leur oxydation d'un point de vue expérimental et de modélisation cinétique. Certains combustibles de cette famille ont déjà fait l'objet de nombreuses études dans la littérature, mais une compréhension plus approfondie de leur oxydation complexe est nécessaire pour une éventuelle application dans la vie réelle. De plus, d'un point de vue fondamental de la combustion, l'analyse de l'influence de la structure sur la réactivité de ces combustibles est profondément intéressante et stimulante. À cette fin, une campagne expérimentale exhaustive a été menée au cours de cette thèse, grâce à deux installations complémentaires : un réacteur auto-agité par jets gazeux et une machine à compression rapide. Les résultats expérimentaux sont analysés et comparés entre différents éthers, afin de comprendre comment différentes caractéristiques structurales (comme la longueur de la chaîne, la ramification et l'asymétrie) peuvent influencer la réactivité. De plus, un mécanisme cinétique détaillé a été élaboré et comparé aux mesures expérimentales pour mieux comprendre les réactions qui contrôlent l'oxydation dans ces conditions.

Mots clés : oxydation, combustion, éthers, biocombustibles, réacteur auto-agité par jets gazeux, machine à compression rapide

Experimental and modelling studies of ether oxidation

Abstract:

In the latest years, increasing concerns regarding pollutant emissions and the depletion of fossil resources have prompted the investigation and development of alternative solutions for the transport sector. Biofuels derived from biomass are considered among these potential solutions and in particular, oxygenated compounds have been proven to have interesting characteristics for a wide range of applications. This thesis focuses on the family of ethers, studying their oxidation from both an experimental and modelling point of view. Some of the fuels of this group have already been studied in the past, but a deeper understanding of their complex oxidation chemistry is needed for possible real-life applications. Moreover, from a fundamental combustion perspective, studying the influence of the structure on the reactivity of these fuels is deeply interesting and challenging. To this end, a comprehensive experimental campaign was conducted during this thesis, thanks to two complementary set-ups: a jet-stirred reactor and a rapid compression machine. The experimental results are analysed and compared between different ethers, in order to understand how different structural features (such as chain length, branching, and asymmetry) can influence the reactivity. Furthermore, a detailed kinetic mechanism was developed and compared to experimental measurements to gain a better understanding of the reactions that control combustion under these conditions.

Keywords : oxidation, combustion, ethers, biofuels, jet-stirred reactor, rapid compression machine



Institut de Combustion, Aérothermique,
Réactivité et Environnement
1C, Avenue de la Recherche Scientifique
45071 Orléans, CEDEX 2



“Mon apprentissage n’a d’autre fruit que de me faire sentir combien il me reste à apprendre.”

Michel de Montaigne

“It’s just basic chemistry”

Bring Me The Horizon

Acknowledgements

This PhD has been an adventure of three years which is hard to summarise in one manuscript. This journey has been shared with so many people, some who stayed all along, others who stuck around only for a part of it, but all of them deserve my acknowledgements today, because they all contributed in some ways.

I would like to start by thanking all the members of the jury, who accepted to evaluate my work. Your questions and comments have been precious and have helped me to gain new insights and perspectives. I would like to thank in particular Dr Olivier Herbinet and Dr Guillaume Vanhove, who were designated as my “rapporteurs”: thank you for dedicating some time to my manuscript and for all your useful comments. I would also like to extend a special thanks to Dr Scott Goldsborough, who guided me through the complicated world of the heat release rate analysis: I learned so much thanks to you, and our discussions really allowed me to get another perspective on the rapid compression machine work. A huge acknowledgement also goes to Dr Henry Curran, who were part of the jury, but also welcomed me in his laboratory in order to perform experiments with their shock tube and rapid compression machine. Having the opportunity to join another team and enrich the experimental results using other facilities was invaluable.

This thesis wouldn't have been possible without the presence of my director, co-director and supervisor. The first person I want to thank is Dr Zeynep Serinyel, my director: thank you for giving me this opportunity, thank you for believing in me, even if my background was so far away as possible from chemistry, thank you for teaching me everything about chemical kinetics, experiments and so much more. Thank you to Dr Fabrice Foucher, my co-director: if the rapid compression machine and ignition delay times hold no more secrets (or almost) to me, it's thanks to you and all the scientific discussion we could share, it was nice to hear a little less about chemistry and a little more about engines and engineering from time to time. Finally, a big thank you to Dr Guillaume Dayma, my co-supervisor: your insights on every small issues or doubts have always been very useful and you made me feel very welcome from the first day in ICARE. Also, exchanging coins and sharing hints for Christmas riddles were small pleasures that added a plus to these three years.

Carrying out a thesis in two laboratories means meeting a lot of people and sharing facilities/offices/meals/everything with a lot of colleagues. It would be an exaggeration to say that everything is always perfect, but I am truly honest in saying that I wouldn't have wanted to share these three years with anybody else. I started this journey in ICARE, so I will start my acknowledge-

ments from this group of colleagues. Thanks to all the “French” crew of the lunch breaks: Nesrine, Valentin, Fanny, HugoN, Samuel, HugoK, Vincente, Dylan, Victor, Laura. You forced me to speak French, and now people think my accent is from the South of France and not from Italy (I don’t know if I should really thank you for that). The truth is, we shared much more than just lunch, and you made it much easier to deal with the everyday life of the lab. The list is obviously not complete, because some people deserve some special thanks. Starting from Antoine: you left ICARE too early after I arrived, but we had the opportunity to share so much more moments, in Canada and in Toulouse. I really think our friendship is precious and I look forward to our next adventure (Pyrénées!). Léo, it has taken some time for us to really get to know each other, but I’m happy of where we are now. I enjoy our little dinners and game nights and I would like to thank you for all the patience and the support. Thank you also to Jean-Noel, for being my neighbour at first, then a colleague and a very good friend. And last, but not least, thank you Maxence, my coffee partner from the very beginning: you made me feel like I could be at home in Orléans (and in France), you surely shared your knowledge of the lab and chemistry with me, as a good post-doc would do, but you added so much more to this journey and words are just not enough to thank you.

I spent a good deal of time also in PRISME, mainly in the RCM room, but I still got to meet amazing people, that become my friends also outside the lab. A special thanks to Seif, for all our talks, it’s always nice to get to see who has the most complicated and messed up life at the moment, in front of a good beer. Thank you to the “Gnocchi lunch” crew, for all the moments we spent together, cooking, talking and laughing, you helped me overcome the moments of stress. This includes, from the lab, Alfredo, Nicolas, Richard, Ronan, Caio, Joao, and from outside Augusto, Anthony, Alka, Leticia, Vinni.

Other PhD students and post-docs surely share the journey and make it nicer, but the people that really made this thesis possible are the permanents of the laboratories, who helped along the way in so many ways. So, a big thank to Dr Philippe Dagaut and Dr Azeddine Kourta for welcoming me in their labs. Then, a huge, huge thanks to the best PRISME technicians: Bruno and Yahia, all these experiments from the RCM wouldn’t have been possible if you weren’t there, sharing your knowledge and solving any issue.

Even if sometimes people think PhD students don’t have personal lives, it usually is the case, so I have some more people that deserve a word. First of all, my Italian friends: sometimes it is hard to maintain a friendship when you are 1000 km apart and living different moments of our lives. Nevertheless, it always felt nice to go back home and know that we could still share a pizza and a board game night and talk again as if time and space were not really separating us. So, thank you Michele, Danilo, Carlo, Arianna, Valentina, Ramona. And a special thanks to Marco, you’ve always been there to support me, even if not always in person, since high school. This kind of friendship is the most precious thing in the world. One of my biggest thanks also goes to Massimiliano, in the last ten years we’ve shared so many moments and talks and thoughts, that I feel like you are part of my family. Thank you also for being there in the day of the defense, it meant the world to me.

Finally, they say friends are the family we choose, but I have to say that I am also very happy with the one I got from the beginning. This final part will be in Italian, because they deserve to be able to read it. Ai miei genitori: non sarei qui a scrivere queste parole, se non fosse per voi. Non esiste un modo per ringraziarvi per tutto il supporto che mi avete dato in tutti questi anni, tra alti e bassi, se non condividere questo momento con voi. Grazie per avermi lasciata libera di spiegare le ali e per aver sempre creduto in me. Sapere di rendervi orgogliosi ha reso ancora più speciale questo traguardo.

Contents

1	Introduction	1
2	State of the art	6
2.1	Combustion of oxygenated compounds	6
2.1.1	Low-temperature oxidation	7
2.1.2	High-temperature oxidation	9
2.2	Ethers	10
2.2.1	Production processes	10
2.2.2	Diethyl ether (DEE)	10
2.2.3	Di- <i>n</i> -propyl ether (DPE)	13
2.2.4	Di- <i>iso</i> -propyl ether (DIPE)	15
2.2.5	Di- <i>n</i> -butyl ether (DBE)	17
2.2.6	Butyl ethyl ether (BEE), di- <i>n</i> -pentyl ether (DNPEE), di- <i>iso</i> -pentyl ether (DIPEE)	20
2.2.7	Ethyl lactate	21
2.3	Conclusions	22
3	Experimental facilities	23
3.1	Jet-Stirred Reactor	24
3.1.1	Fourier Transform InfraRed spectroscopy (FTIR)	26
3.1.2	Gas chromatography	26
3.2	Rapid Compression Machine	28
3.2.1	Preliminary study on the RCM configuration	34
3.3	University of Galway facilities	36
3.3.1	High Pressure Shock Tube	36
3.3.2	Rapid Compression Machine	37
3.4	Uncertainty of measurements	38
3.4.1	Jet-stirred reactor	38
3.4.2	Rapid compression machine	39
3.4.3	University of Galway facilities	40

4	Modelling, simulations and analysis	41
4.1	Construction of the model	42
4.1.1	DEE, DPE, DIPE, DBE	42
4.1.2	BEE	44
4.1.3	DIPEE	45
4.1.4	Ethyl lactate	46
4.2	Simulations	47
4.2.1	Chemkin files	47
4.2.2	Chemkin models	48
4.3	Further analysis	49
5	Results and discussion: DNPEE and DIPEE in the JSR	52
5.1	DIPEE	53
5.1.1	Reaction pathways	68
5.2	DNPEE	70
5.2.1	Expected reaction pathways	80
5.3	Comparison to the other ethers	81
5.4	Conclusions	83
6	Results and discussion: oxidation of ethers in the RCM	84
6.1	DEE	86
6.1.1	Reaction pathways	88
6.1.2	HRR	89
6.2	DPE	91
6.2.1	Reaction pathways	95
6.2.2	HRR	98
6.3	DIPE	99
6.3.1	Reaction pathways	102
6.3.2	HRR	105
6.4	BEE	107
6.4.1	Reaction pathways	109
6.4.2	HRR	111
6.5	DBE	113
6.5.1	Reaction pathways	116
6.5.2	HRR	118
6.6	DIPEE	120
6.6.1	Reaction pathways	123
6.6.2	HRR	126
6.7	DNPEE	128

6.7.1	HRR	130
6.8	Comparison	132
6.8.1	DPE vs DIPE	132
6.8.2	DNPEE vs DIPEE	135
6.8.3	BEE vs DEE/DBE/DPE	136
6.8.4	Final comparison	138
6.9	Ethyl lactate	142
6.9.1	Reaction pathways	143
6.9.2	Comparison to ethanol	145
6.9.3	Comparison to DIPE	146
6.10	Conclusion	147
7	Conclusions and perspectives	149
	Résumé	153
	Bibliography	173
A	JSR: additional results	187
A.1	DIPEE: additional species	188
A.2	DNPEE: additional species	193
A.3	BEE: further validation	198
B	RCM: pressure profiles and additional results	204
B.1	Pressure profiles	204
B.1.1	Diethyl ether	204
B.1.2	Di-n-propyl ether	211
B.1.3	Di-iso-propyl ether	216
B.1.4	Butyl ethyl ether	224
B.1.5	Dibutyl ether	230
B.1.6	Di-iso-pentyl ether	238
B.1.7	Di-n-pentyl ether	248
B.1.8	Ethyl lactate	254
B.2	HRR	259
C	Ethyl lactate: additional data	269
C.1	OPTIPRIME	269
C.2	Laminar flame speeds	270
C.2.1	Sensitivity analysis	272

List of Figures

1.1	Worldwide annual CO ₂ emissions from fossil fuels and industry, from 1900 to today.	2
1.2	Greenhouse gases emissions from the different sectors in France, from 1990 to 2021.	3
2.1	Example of different regimes of reactivity (JSR experiments, diethyl ether, $\phi = 0.5$, $p = 10$ atm, $\tau = 700$ ms).	8
2.2	Main reactions pathways happening during the oxidation of oxygenated compounds at low temperature.	8
2.3	Molecular structures of BEE, DNPEE and DIPEE.	20
2.4	The molecular structure of ethyl lactate.	21
3.1	Jet stirred reactor in ICARE laboratory.	24
3.2	Example of the chromatogram obtained through gas chromatography analysis from the GC Shimadzu QP2010-SE equipped with CP-SIL 5CB column (DIPEE, $\phi = 1$, 650 K, 10 atm, $\tau = 700$ ms).	27
3.3	Pressure and temperature conditions of engines and experimental devices.	28
3.4	Simplified scheme of the rapid compression machine in PRISME laboratory (University of Orléans).	29
3.5	Example of the data measured in the RCM: in black, pressure profiles for reactive (solid) and non reactive (dashed) mixtures, in blue, the position of the piston and in red, the first derivative of the pressure for the reactive test. Top dead center (TDC) and ignition delay times (IDTs) are also indicated. (DEE, $\phi = 1$, dilution = 10 (fuel initial mole fraction: 1.5%), $T_c = 596$ K, $p_c = 14.8$ bar).	31
3.6	Example of a test with a non reactive mixture: in black, the measured pressure profile, in red the computed normalised volume profile used in the simulations (DIPE, $\phi = 2$, dilution = 5 (fuel initial mole fraction: 3.6%), $T_c = 501$ K, $p_c = 14.8$ bar).	32
3.7	Photos of some of the wedges that were used in this work.	34
3.8	Influence of the different compression ratio on a) the ignition delay times, b) the pressure decrease in the tests with non-reactive mixture (DEE, $\phi = 1$, dilution in "air", $p_c = 3$ bar).	35
3.9	Simplified scheme of the RCM at the university of Galway (courtesy of C3 Galway).	37

3.10	Example of calibration curves of two of the flowmeters used in the jet-stirred reactor set-up (one for oxygen and one for nitrogen).	39
3.11	Example of repeated shot for a condition in the RCM (di- <i>n</i> -propyl ether, $\phi = 1$, $p_c = 15$ bar, $T_c = 587$ K).	40
4.1	Example of the resulting curves from the heat release rate analysis (BEE, $\phi = 1$, dilution = 10, inert gas: 50% CO ₂ + 50% N ₂ , $T_c = 583$ K, $p_c = 15$ bar).	51
5.1	Fuel conversion of di- <i>iso</i> -pentyl ether over the temperature range studied in the JSR for the four equivalence ratios at $p = 10$ atm, $\tau = 700$ ms, $\chi_{0,\text{fuel}} = 1000$ ppm (lines are only added to represent the trend).	54
5.2	Mole fraction of di- <i>iso</i> -pentyl ether over the temperature range studied in the JSR ($\phi = 2$, $p = 10$ atm, $\tau = 700$ ms, $\chi_{0,\text{fuel}} = 1000$ ppm).	54
5.3	(a) DIPEE mole fraction ($\phi = 2$); (b) Contributions to OH formation from different reactions: R1) formation (solid line, (a)) and decomposition (dashed line (b)) of dipee-1oohketa, R2) formation (solid, (a)) and decomposition (dashed, (b)) of dipee-toohketa and dipee-poohaldp, R3) formation (solid, (a)) and decomposition (dashed, (b)) of ic4toohcho, R4) formation+decomposition of khp derived from isopentanal, R5) H ₂ O ₂ decomposition; (c) Mole fractions of some of the molecules involved in the reactions producing OH.	57
5.4	Mole fractions of the fuel and the main products and intermediates during the oxidation of DIPEE in the JSR for $\phi = 1$ ($p = 10$ atm, $\tau = 700$ ms, $\chi_{0,\text{fuel}} = 1000$ ppm). . . .	59
5.5	Mole fractions of the fuel and the main products and intermediates during the oxidation of DIPEE in the JSR for $\phi = 2$ ($p = 10$ atm, $\tau = 700$ ms, $\chi_{0,\text{fuel}} = 1000$ ppm). . . .	60
5.6	Mole fractions of the fuel and the main products and intermediates during the oxidation of DIPEE in the JSR for $\phi = 4$ ($p = 10$ atm, $\tau = 700$ ms, $\chi_{0,\text{fuel}} = 1000$ ppm). . . .	61
5.7	Mole fractions of the fuel and the main products and intermediates during the oxidation of DIPEE in the JSR for $\phi = 0.5$ ($p = 10$ atm, $\tau = 700$ ms, $\chi_{0,\text{fuel}} = 1000$ ppm). . .	62
5.8	Main reaction pathways leading to the formation of isopentanal during the oxidation of DIPEE in the jet-stirred reactor.	64
5.9	Rate of production of isopentanal from the five most important reactions in its production path and isopentanal mole fractions (symbols: experiments, lines: simulations) for the all equivalence ratios. R1: decomposition of QOOH radical from the α -radical of the fuel; R2: β -scission of the α -radical of the fuel; R3: reaction of two RO ₂ radicals obtained from the isopentyl radical; R5: decomposition of the carbonylhydroperoxide obtained from the α -radical of the fuel. (All the reactions are summarised in Table 5.3).	66
5.10	Reaction pathways in di- <i>iso</i> -pentyl ether oxidation in the jet-stirred reactor ($\phi = 1$, $p = 10$ atm, 500 K, $\chi_{0,\text{fuel}} = 1000$ ppm).	69

5.11	Reaction pathways in di- <i>iso</i> -pentyl ether oxidation in the jet-stirred reactor ($\phi = 1$, $p = 10$ atm, 1000 K, $\chi_{0,\text{fuel}} = 1000$ ppm).	70
5.12	Fuel conversion of di- <i>n</i> -pentyl ether over the temperature range studied in the jet-stirred reactor for the four equivalence ratios at $p = 10$ atm, $\tau = 700$ ms, $\chi_{0,\text{fuel}} = 1000$ ppm (lines are only added to represent the trend).	71
5.13	Mole fraction of di- <i>n</i> -pentyl ether over the temperature range studied in the jet-stirred reactor ($\phi = 2$, $p = 10$ atm, $\tau = 700$ ms, $\chi_{0,\text{fuel}} = 1000$ ppm).	72
5.14	Mole fractions of the fuel and the main products and intermediates during the oxidation of DNPEE in the JSR for $\phi = 1$ ($p = 10$ atm, $\tau = 700$ ms, $\chi_{0,\text{fuel}} = 1000$ ppm). . .	73
5.15	Mole fractions of the fuel and the main products and intermediates during the oxidation of DNPEE in the JSR for $\phi = 2$ ($p = 10$ atm, $\tau = 700$ ms, $\chi_{0,\text{fuel}} = 1000$ ppm). . .	74
5.16	Mole fractions of the fuel and the main products and intermediates during the oxidation of DNPEE in the JSR for $\phi = 4$ ($p = 10$ atm, $\tau = 700$ ms, $\chi_{0,\text{fuel}} = 1000$ ppm). . .	75
5.17	Mole fractions of the fuel and the main products and intermediates during the oxidation of DNPEE in the JSR for $\phi = 0.5$ ($p = 10$ atm, $\tau = 700$ ms, $\chi_{0,\text{fuel}} = 1000$ ppm). .	76
5.18	a) Formaldehyde mole fractions for all conditions; b) Formaldehyde and DNPEE mole fractions at $\phi = 4$, $p = 10$ atm, $\tau = 700$ ms, $\chi_{0,\text{fuel}} = 1000$ ppm.	77
5.19	Mole fraction profiles of <i>n</i> -pentanal at all conditions during DNPEE oxidation. . . .	78
5.20	<i>N</i> -pentanal most probable formation pathways.	79
5.21	Most probable reaction pathways of the α -radical of DNPEE.	80
5.22	Comparison of fuel conversion for three different equivalence ratios (0.5, 1, 2) for seven different ethers (DEE, DPE, DIPE, BEE, DBE, DNPEE, DIPEE), $p = 10$ atm. . . .	82
6.1	Ignition delay times of diethyl ether in the RCM (points: experimental data, lines: simulations (solid: main IDT, dashed: first IDT)), $p_c = 15$ bar.	87
6.2	Experimental and simulated pressure profiles for diethyl ether mixtures at $\phi = 0.5$, $p_c = 15$ bar.	88
6.3	Reaction pathways in diethyl ether oxidation ($\phi = 1$, DEE = 1.5%, $p_c = 15$ bar, 549 K and 608 K (in parenthesis), at 20% fuel consumption).	89
6.4	Experiments (solid) vs simulations (dashed): a) HRR vs aHR, b) pressure profiles. Mixture: DEE, $\phi = 1$, dilution = 10 (inert gases: 50% CO ₂ / 50% N ₂), DEE = 1.5%, $p_c = 15$ bar.	90
6.5	Low-temperature heat release and maximum accumulated heat release (normalised by the mixture LHV): comparison between experiments (points) and simulations (lines). Mixture: DEE, $\phi = 1$, dilution = 10 (inert gases: 50% CO ₂ / 50% N ₂), DEE = 1.5%, $p_c = 15$ bar.	91
6.6	Ignition delay times of di- <i>n</i> -propyl ether in the RCM and ST (points: experimental data, lines: simulations (solid: main IDT, dashed: first IDT)), $p_c = 15$ bar.	93

6.7	Experimental and simulated pressure profiles for a mixture of DPE at $\phi = 1$, dilution = 10 (inert gas: 100% CO ₂), DPE = 1.0%, $p_c = 15$ bar, $T_c = 558$ K.	94
6.8	Experimental and simulated pressure profiles for a mixture of DPE at $\phi = 2$, dilution = 10 (inert gas: 100% CO ₂), DPE = 2.0%, $p_c = 15$ bar, $T_c = 529$ K (a), 608 K (b).	94
6.9	Reaction pathways in di- <i>n</i> -propyl ether oxidation ($\phi = 1$, DPE = 1.0%, $p_c = 15$ bar, 610 K and 789 K (in parenthesis), at 20% fuel consumption).	96
6.10	Reaction pathways in di- <i>n</i> -propyl ether oxidation in the HPST ($\phi = 1$, DPE = 1.0%, $p_c = 15$ bar, 1000 K and 1200 K (in parenthesis), at 20% fuel consumption).	97
6.11	Experiments (solid) vs simulations (dashed): a) HRR vs aHR, b) pressure profiles. Mixture: DPE, $\phi = 1$, dilution = 10 (inert gases: 50% CO ₂ + 50% N ₂), DPE = 1.0%, $p_c = 15$ bar.	98
6.12	Low-temperature heat release and maximum accumulated heat release (normalised by the mixture LHV): comparison between experiments (points) and simulations (lines). Mixture: DPE, $\phi = 1$, dilution = 10 (inert gases: 50% CO ₂ + 50% N ₂), DPE = 1.0%, $p_c = 15$ bar.	99
6.13	Ignition delay times of di- <i>iso</i> -propyl ether in the RCM (points: experimental data, lines: simulations (solid: main IDT, dashed: first IDT), $p_c = 15$ bar.	101
6.14	Experimental and simulated pressure profiles for a mixture of DIPE at $\phi = 1$, dilution = 5 (inert gas: 100% N ₂), DIPE = 1.8%, $p_c = 15$ bar, $T_c = 676$ K.	102
6.15	Reaction pathways in di- <i>iso</i> -propyl ether oxidation ($\phi = 1$, DIPE = 1.8%, $p_c = 15$ bar, 600 K and 792 K (in parenthesis), at 20% fuel consumption).	104
6.16	Reaction pathways in di- <i>iso</i> -propyl ether oxidation in the HPST ($\phi = 1$, DIPE = 1.8%, $p_c = 15$ bar, 1000 K and 1200 K (in parenthesis), at 20% fuel consumption).	105
6.17	Experiments (solid) vs simulations (dashed): a) HRR vs aHR, b) pressure profiles. Mixture: DIPE, $\phi = 1$, dilution = 5 (inert gases: 50% CO ₂ + 50% N ₂), DIPE = 1.8%, $p_c = 15$ bar.	106
6.18	Low-temperature heat release and maximum accumulated heat release (normalised by the mixture LHV): comparison between experiments (points) and simulations (lines). Mixture: DIPE, $\phi = 1$, dilution = 5 (inert gases: 50% CO ₂ + 50% N ₂), DIPE = 1.8%, $p_c = 15$ bar.	107
6.19	Ignition delay times of butyl ethyl ether in the RCM (points: experimental data, lines: simulations (solid: main IDT, dashed: first IDT), $p_c = 15$ bar.	108
6.20	Reaction pathways in butyl ethyl ether oxidation ($\phi = 1$, dilution = 5, BEE = 1.8%, $p_c = 15$ bar, 538 K, at 20% fuel consumption).	110
6.21	Experiments (solid) vs simulations (dashed): a) HRR vs aHR, b) pressure profiles. Mixture: BEE, $\phi = 1$, dilution = 10 (inert gases: 50% CO ₂ + 50% N ₂), BEE = 1.0%, $p_c = 15$ bar.	112

6.22	Low-temperature heat release and maximum accumulated heat release (normalised by the mixture LHV): comparison between experiments (points) and simulations (lines). Mixture: BEE, $\phi = 1$, dilution = 10 (inert gases: 50% CO ₂ + 50% N ₂), BEE = 1.0%, $p_c = 15$ bar.	113
6.23	Ignition delay times of dibutyl ether in the RCM (points: experimental data, lines: simulations (solid: main IDT, dashed: first IDT), $p_c = 15$ bar.	114
6.24	Ignition delay times of dibutyl ether in the RCM (points: experimental data, lines: simulations (solid: main IDT, dashed: first IDT)).	115
6.25	Reaction pathways in dibutyl ether oxidation in the rapid compression machine ($\phi = 1$, dilution = 5, DBE = 1.4%, $p_c = 15$ bar, 560 K, 20% fuel consumption).	117
6.26	Experiments (solid) vs simulations (dashed): a), c) HRR vs aHR, b), d) pressure profiles. Mixture: DBE, $\phi = 1$, dilution = 10 (inert gases: a)-b) : 50% CO ₂ + 50% N ₂ , c)-d) : 100% N ₂), DBE = 0.8%.	118
6.27	Low-temperature heat release and maximum accumulated heat release (normalised by the mixture LHV): comparison between experiments (points) and simulations (lines). Mixture: DBE, $\phi = 1$, dilution = 10 (inert gases: black 50% CO ₂ + 50% N ₂ , red 100% N ₂), DBE = 0.8%, $p_c = 15$ bar.	120
6.28	Ignition delay times of di- <i>iso</i> -pentyl ether in the RCM (points: experimental data, lines: simulations (solid: main IDT, dashed: first IDT), $p_c = 15$ bar.	121
6.29	Ignition delay times of di- <i>iso</i> -pentyl ether in the RCM, dilution = 10, $\phi = 1$ and 2 (points: experimental data, lines: simulations (solid: main IDT, dashed: first IDT)).	122
6.30	Reaction pathways in di- <i>iso</i> -pentyl ether oxidation in the RCM ($\phi = 1$, $p_c = 15$ bar, 560 K and 800 K (in parenthesis), dilution = 10, DIPEE = 0.6%, at 20% fuel consumption).	124
6.31	Isopentanal production during the ignition of DIPEE in the RCM: a) mole fraction of the fuel and of isopentanal over the test time (both normalised by the initial mole fraction of DIPEE), b) OH rate of production from the most important reactions during the first stage and the most important one during the main stage for comparison. Conditions: $\phi = 1$, dilution = 10, DIPEE = 0.6%, $p_c = 15$ bar, $T_c = 560$ K.	125
6.32	Experiments (solid) vs simulations (dashed): a) HRR vs aHR, b) pressure profiles. Mixture: DIPEE, $\phi = 1$, dilution = 10 (inert gases: 50% CO ₂ + 50% N ₂), DIPEE = 0.6%, $p_c = 15$ bar.	127
6.33	Low-temperature heat release and maximum accumulated heat release (normalised by the mixture LHV): comparison between experiments (points) and simulations (lines). Mixture: DIPEE, $\phi = 1$, dilution = 10 (inert gases: 50% CO ₂ + 50% N ₂), DIPEE = 0.6%, $p_c = 15$ bar.	128
6.34	Ignition delay times of di- <i>n</i> -pentyl ether in the RCM.	129
6.35	Comparison of the main ignition delay times of di- <i>n</i> -pentyl ether in the RCM for different equivalence ratios (0.5, 1 and 2), with dilution = 5 and $p_c = 15$ bar.	130

6.36	Experimental results for the heat release rate analysis: a) HRR vs aHR, b) pressure profiles. Mixture: DNPEE, $\phi = 1$, dilution = 10 (inert gases: 50% CO ₂ + 50% N ₂), DNPEE = 0.6%, $p_c = 15$ bar.	131
6.37	Experimental low-temperature heat release and maximum accumulated heat release (normalised by the mixture LHV). Mixture: DNPEE, $\phi = 1$, dilution = 10 (inert gases: 50% CO ₂ + 50% N ₂), DNPEE = 0.6%, $p_c = 15$ bar.	132
6.38	Comparison of the main ignition delay times of di- <i>n</i> -propyl and di- <i>iso</i> -propyl ethers at $\phi = 2$, dilution = 10, $p_c = 15$ bar, DPE = 2.0%, DIPE = 2.0%.	133
6.39	Comparison of the main ignition delay times of di- <i>n</i> -propyl, di- <i>iso</i> -propyl and diethyl ethers at low temperatures, with $\phi = 2$, dilution = 10 (DEE = 2.9%, DPE = 2.0%, DIPE = 2.0%), $p_c = 15$ bar.	134
6.40	Comparison of the experimental results of di- <i>n</i> -pentyl and di- <i>iso</i> -pentyl ethers, at $\phi = 1$, dilution = 5 (a)), 10 (b)), $p_c = 15$ bar.	135
6.41	Comparison of the main ignition delay times of di- <i>n</i> -pentyl, di- <i>iso</i> -pentyl and dibutyl ethers at low temperatures, with $\phi = 1$, dilution = 10 (DBE = 0.8%, DIPEE = 0.6%, DNPEE = 0.6%), $p_c = 15$ bar.	136
6.42	Comparison of the experimental results of butyl ethyl ether and diethyl and dibutyl ethers, at $\phi = 0.5$, dilution = 5, BEE = 0.9%, DEE = 1.37%, DBE = 0.7% (a)) and $\phi = 1$, dilution = 10, BEE = 1.0%, DEE = 1.5%, DBE = 0.8% (b)), $p_c = 15$ bar.	137
6.43	Comparison of the experimental results of butyl ethyl ether and diethyl and dibutyl ethers, at $\phi = 1$, dilution = 10, BEE = 1.0%, DPE = 1.0% (a)) and $\phi = 2$, dilution = 10, BEE = 1.98%, DPE = 2.0% (b)), $p_c = 15$ bar.	138
6.44	Comparison of the experimental results for all the ethers studied in the RCM, at $\phi = 1$, dilution = 10 (a)) and $\phi = 2$, dilution = 10 (b)), $p_c = 15$ bar.	139
6.45	Comparison of the experimental pressure traces for all the ethers studied in the RCM (except DIPE), with $\phi = 1$, dilution = 10, $T_c = 615$ K, $p_c = 15$ bar.	140
6.46	Comparison of the experimental results from the heat release analysis for all the ethers studied in the RCM (it must be noted that DIPE has a different dilution), with $\phi = 1$, dilution = 10 (except for DIPE, for which the dilution is 10), $p_c = 15$ bar, inert gases: 50% CO ₂ + 50% N ₂ (unless differently specified).	141
6.47	Ethyl lactate ignition delay times, for three different equivalence ratios at a compressed pressure of 20 bar (points: experiments, lines: simulations).	142
6.48	Ethyl lactate ignition delay times, for two different pressures at $\phi = 1$, EtLac = 3.38% (points: experiments, lines: simulations).	143
6.49	Reaction pathways in ethyl lactate oxidation ($\phi = 1$, EtLac = 3.38%, $p_c = 20$ bar, 830 K and 915 K (in parenthesis)).	144
6.50	Comparison between the ignition delay times of ethyl lactate and ethanol ($\phi = 1$, $p_c = 20$ bar, in "air", EtOH = 6.5%, EtLac = 3.38%).	146

6.51	Comparison between the ignition delay times of ethyl lactate and di- <i>iso</i> -propyl ether ($\phi = 0.5$, $p_c = 20$ bar (ethyl lactate), 15 bar (DIPE), in "air" (EtLac = 1.72%, DIPE = 1.15%)).	147
A.1	Mole fractions of some products and intermediates during the oxidation of DIPEE in the JSR $\phi = 1$, $p = 10$ atm, $\tau = 700$ ms, $\chi_{0,\text{fuel}} = 1000$ ppm (in addition to the ones included in chapter 5).	189
A.2	Mole fractions of some products and intermediates during the oxidation of DIPEE in the JSR $\phi = 2$, $p = 10$ atm, $\tau = 700$ ms, $\chi_{0,\text{fuel}} = 1000$ ppm (in addition to the ones included in chapter 5).	190
A.3	Mole fractions of some products and intermediates during the oxidation of DIPEE in the JSR $\phi = 4$, $p = 10$ atm, $\tau = 700$ ms, $\chi_{0,\text{fuel}} = 1000$ ppm (in addition to the ones included in chapter 5).	191
A.4	Mole fractions of some products and intermediates during the oxidation of DIPEE in the JSR $\phi = 0.5$, $p = 10$ atm, $\tau = 700$ ms, $\chi_{0,\text{fuel}} = 1000$ ppm (in addition to the ones included in chapter 5).	192
A.5	Mole fractions of some products and intermediates during the oxidation of DNPEE in the JSR $\phi = 1$, $p = 10$ atm, $\tau = 700$ ms, $\chi_{0,\text{fuel}} = 1000$ ppm (in addition to the ones included in chapter 5).	194
A.6	Mole fractions of some products and intermediates during the oxidation of DNPEE in the JSR $\phi = 2$, $p = 10$ atm, $\tau = 700$ ms, $\chi_{0,\text{fuel}} = 1000$ ppm (in addition to the ones included in chapter 5).	195
A.7	Mole fractions of some products and intermediates during the oxidation of DNPEE in the JSR $\phi = 4$, $p = 10$ atm, $\tau = 700$ ms, $\chi_{0,\text{fuel}} = 1000$ ppm (in addition to the ones included in chapter 5).	196
A.8	Mole fractions of some products and intermediates during the oxidation of DNPEE in the JSR $\phi = 0.5$, $p = 10$ atm, $\tau = 700$ ms, $\chi_{0,\text{fuel}} = 1000$ ppm (in addition to the ones included in chapter 5).	197
A.9	Mole fractions of some products and intermediates during the oxidation of BEE in the JSR $\phi = 1$, $p = 10$ atm, $\tau = 700$ ms, $\chi_{0,\text{fuel}} = 1000$ ppm.	200
A.10	Mole fractions of some products and intermediates during the oxidation of BEE in the JSR $\phi = 2$, $p = 10$ atm, $\tau = 700$ ms, $\chi_{0,\text{fuel}} = 1000$ ppm.	201
A.11	Mole fractions of some products and intermediates during the oxidation of BEE in the JSR $\phi = 4$, $p = 10$ atm, $\tau = 700$ ms, $\chi_{0,\text{fuel}} = 1000$ ppm.	202
A.12	Mole fractions of some products and intermediates during the oxidation of BEE in the JSR $\phi = 0.5$, $p = 10$ atm, $\tau = 700$ ms, $\chi_{0,\text{fuel}} = 1000$ ppm.	203
B.1	Diethyl ether: $\phi = 1$, dilution = 10 (inert gas: 100% CO ₂), $p_c = 15$ bar, DEE = 1.5%. . .	204
B.2	Diethyl ether: $\phi = 2$, dilution = 10 (inert gas: 100% CO ₂), $p_c = 15$ bar, DEE = 2.9%. . .	206

B.3 Diethyl ether: $\phi = 0.5$, dilution = 10 (inert gas: 100% CO ₂), $p_c = 15$ bar, DEE = 0.8%.	207
B.4 Diethyl ether: $\phi = 0.5$, dilution = 5 (inert gas: 100% CO ₂), $p_c = 15$ bar, DEE = 1.37%.	209
B.5 Di-n-propyl ether: $\phi = 1$, dilution = 10 (inert gas: 100% CO ₂), $p_c = 15$ bar, DPE = 1.0%.	211
B.6 Di-n-propyl ether: $\phi = 0.5$, dilution = 10 (inert gas: 100% CO ₂), $p_c = 15$ bar, DPE = 0.5%.	212
B.7 Di-n-propyl ether: $\phi = 2$, dilution = 10 (inert gas: 100% CO ₂), $p_c = 15$ bar, DPE = 2.0%.	214
B.8 Di-iso-propyl ether: $\phi = 1$, dilution = 5, $p_c = 15$ bar (a)-d) inert gases 50% CO ₂ + 50% N ₂), DIPE = 1.8%.	216
B.9 Di-iso-propyl ether: $\phi = 0.5$, dilution = 5 (inert gas: 100% Ar), $p_c = 15$ bar, DIPE = 0.9%.	219
B.10 Di-iso-propyl ether: $\phi = 2$, dilution = 5, $p_c = 15$ bar (a)-b) inert gases 50% CO ₂ + 50% N ₂), DIPE = 3.6%.	220
B.11 Di-iso-propyl ether: $\phi = 2$, dilution = 10, $p_c = 15$ bar (a)-b) inert gases 50% CO ₂ + 50% N ₂ , c) 50% N ₂ + 50% Ar), DIPE = 2.0%.	222
B.12 Butyl ethyl ether: $\phi = 1$, dilution = 5 (inert gases: 50% CO ₂ + 50% N ₂), $p_c = 15$ bar, BEE = 1.8%.	224
B.13 Butyl ethyl ether: $\phi = 0.5$, dilution = 5 (inert gases: 50% CO ₂ + 50% N ₂), $p_c = 15$ bar, BEE = 0.9%.	225
B.14 Butyl ethyl ether: $\phi = 2$, dilution = 5 (inert gases: 50% CO ₂ + 50% N ₂), $p_c = 15$ bar, BEE = 3.6%.	227
B.15 Butyl ethyl ether: $\phi = 2$, dilution = 10 (inert gases: 50% CO ₂ + 50% N ₂), $p_c = 15$ bar, BEE = 1.98%.	228
B.16 Dibutyl ether: $\phi = 1$, dilution = 5 (inert gases: 50% CO ₂ + 50% N ₂), $p_c = 15$ bar, DBE = 1.4%.	230
B.17 Dibutyl ether: $\phi = 0.5$, dilution = 5 (inert gases: 50% CO ₂ + 50% N ₂), $p_c = 15$ bar, DBE = 0.7%.	231
B.18 Dibutyl ether: $\phi = 2$, dilution = 5 (inert gases: 50% CO ₂ + 50% N ₂), $p_c = 15$ bar, DBE = 2.7%.	233
B.19 Dibutyl ether: $\phi = 2$, dilution = 10 (inert gases: 100% N ₂), $p_c = 15$ bar, DBE = 1.5%.	235
B.20 Dibutyl ether: $\phi = 1$, dilution = 10 (inert gases: 50% CO ₂ + 50% N ₂), $p_c = 20$ bar, DBE = 0.8%.	236
B.21 Di-iso-pentyl ether: $\phi = 1$, dilution = 5 (inert gas: 100% CO ₂), $p_c = 15$ bar, DIPEE = 1.1%.	238
B.22 Di-iso-pentyl ether: $\phi = 2$, dilution = 5 (inert gas: 100% CO ₂), $p_c = 15$ bar, DIPEE = 2.2%.	239
B.23 Di-iso-pentyl ether: $\phi = 0.5$, dilution = 5 (inert gas: 100% CO ₂), $p_c = 15$ bar, DIPEE = 0.5%.	240
B.24 Di-iso-pentyl ether: $\phi = 1$, dilution = 10 (inert gases: 50% CO ₂ + 50% N ₂), $p_c = 15$ bar, DIPEE = 0.6%.	242
B.25 Di-iso-pentyl ether: $\phi = 2$, dilution = 10 (inert gases: 50% CO ₂ + 50% N ₂), $p_c = 15$ bar, DIPEE = 1.2%.	244

B.26 Di-iso-pentyl ether: $\phi = 1$, dilution = 10 (inert gases: 50% CO ₂ + 50% N ₂), $p_c = 20$ bar, DIPEE = 0.6%.	246
B.27 Di-n-pentyl ether: $\phi = 1$, dilution = 5 (inert gas: 100% CO ₂), $p_c = 15$ bar, DNPEE = 1.1%.248	
B.28 Di-n-pentyl ether: $\phi = 2$, dilution = 5 (inert gas: 100% CO ₂), $p_c = 15$ bar, DNPEE = 2.2%.249	
B.29 Di-n-pentyl ether: $\phi = 0.5$, dilution = 5 (inert gas: 100% CO ₂), $p_c = 15$ bar, DNPEE = 0.5%.	250
B.30 Di-n-pentyl ether: $\phi = 1$, dilution = 10 (inert gases: 50% CO ₂ + 50% N ₂), $p_c = 15$ bar, DNPEE = 0.6%.	251
B.31 Di-n-pentyl ether: $\phi = 1$, dilution = 10 (inert gases: 50% CO ₂ + 50% N ₂), $p_c = 20$ bar, DNPEE = 0.6%.	252
B.32 Di-n-pentyl ether: $\phi = 2$, dilution = 10 (inert gases: 50% CO ₂ + 50% N ₂), $p_c = 15$ bar, DNPEE = 1.2%.	253
B.33 Ethyl lactate: $\phi = 1$, dilution: "air", $p_c = 20$ bar, EtLac = 3.38%.	254
B.34 Ethyl lactate: $\phi = 1$, dilution: "air", $p_c = 30$ bar, EtLac = 3.38%.	255
B.35 Ethyl lactate: $\phi = 0.5$, dilution: "air", $p_c = 20$ bar, EtLac = 1.72%.	257
B.36 Ethyl lactate: $\phi = 1.5$, dilution: "air", $p_c = 20$ bar, EtLac = 4.99%.	258
B.37 Heat release rate analysis for DEE: $\phi = 2$, $p_c = 15$ bar, dilution = 10 (50% CO ₂ + 50% N ₂), DEE = 2.9%.	260
B.38 Heat release rate analysis for DEE: comparison between stoichiometric and rich mixture, $T_c = 608$ K, $p_c = 15$ bar, dilution = 10 (50% CO ₂ + 50% N ₂).	261
B.39 Heat release rate analysis for DIPE: $\phi = 2$, $p_c = 15$ bar, dilution = 5 (50% CO ₂ + 50% N ₂), DIPE = 3.6%.	262
B.40 Heat release rate analysis for DIPE: comparison between stoichiometric and rich mixture, $T_c = 615$ K, $p_c = 15$ bar, dilution = 5 (50% CO ₂ + 50% N ₂).	263
B.41 Heat release rate analysis for BEE: $\phi = 2$, $p_c = 15$ bar, dilution = 10 (50% CO ₂ + 50% N ₂), BEE = 1.98%.	264
B.42 Heat release rate analysis for BEE: comparison between stoichiometric and rich mixture, $T_c = 610$ K, $p_c = 15$ bar, dilution = 10 (50% CO ₂ + 50% N ₂).	265
B.43 Heat release rate analysis for DIPEE: $\phi = 2$, $p_c = 15$ bar, dilution = 10 (a), b): 50% CO ₂ + 50% N ₂ , c), d): 100% N ₂), DIPEE = 1.2%.	267
B.44 Heat release rate analysis for DIPEE: comparison between stoichiometric and rich mixture, $T_c = 610$ K, $p_c = 15$ bar, dilution = 10 (50% CO ₂ + 50% N ₂).	268
C.1 Laminar flame speeds of ethyl lactate.	271
C.2 Laminar flame speed analysis for two conditions: left panel: $\phi = 1$, $p_0 = 1$ bar, right panel: $\phi = 0.7$, $p_0 = 3$ bar.	272

List of Tables

2.1	Summary of the literature on the oxidation of diethyl ether	12
2.2	Summary of the literature on the combustion of di- <i>n</i> -propyl ether	15
2.3	Summary of the literature on the combustion of di- <i>iso</i> -propyl ether	16
2.4	Summary of the literature on the combustion of dibutyl ether	19
3.1	The fuels tested and experimental conditions studied in the jet-stirred reactor.	25
3.2	Gas chromatographs used in this work, with coupled columns and detectors.	26
3.3	Characteristics of the rapid compression machine in PRISME laboratory.	30
3.4	Tested fuels and experimental conditions in the rapid compression machine in Or- léans (dilution is defined as the inert gases molar fraction over oxygen molar fraction)	33
3.5	Tested fuels and experimental conditions in the high-pressure shock tube.	37
3.6	Tested fuels and experimental conditions in the rapid compression machine in Galway.	38
5.1	Experimental conditions of the oxidation of pentyl ethers in the jet-stirred reactor.	53
5.2	Different reactions involved in the formation of OH radicals during the oxidation of DIPEE in the JSR.	56
5.3	Main reactions leading to the formation of isopentanal during the oxidation of DIPEE in the JSR.	65
6.1	Comparison of ethyl lactate characteristics with ethanol and gasoline.	145
B.1	Tested fuels and experimental conditions for the heat release rate analysis of rich mixtures	259
C.1	Experimental conditions for the measurements of laminar flame speeds of ethyl lac- tate in OPTIPRIME	270

Acronyms

aHR Accumulated heat release

CFD Computational fluid dynamics

ECN Effective carbon number

FID Flame ionization detector

FS Flame speed

FTIR Fourier transform infrared

GC Gas chromatography

GHG Greenhouse gas

HCCI Homogeneous charge compression ignition

HPST High-pressure shock tube

HRR Heat release rate

IDT Ignition delay time

JSR Jet-stirred reactor

LHV Lower heating value

LTHR Low-temperature heat release

MS Mass spectrometry

NTC Negative temperature coefficient

RCM Rapid compression machine

ROP Rate of production

SI Spark ignition

ST Shock tube

TCD Thermal conductivity detector

TDC Top dead center

Species

BEE Butyl ethyl ether

DBE Dibutyl ether

DEE Diethyl ether

DIPE Di-iso-propyl ether

DIPEE Di-iso-pentyl ether

DNPEE Di-n-pentyl ether

DPE Di-n-propyl ether

ETBE Ethyl tert-butyl ether

MTBE Methyl tert-butyl ether

TAME Tert-amyl methyl ether

Symbols

p Pressure (atm, bar, Pa: 1 atm = 101325 Pa, 1 bar = 10^5 Pa)

T Temperature (K, °C: $T(\text{K}) = T(^{\circ}\text{C}) + 273.15$)

τ Residence time (s)

V Volume (m^3)

γ Heat capacity ratio or adiabatic index ($\gamma = \frac{c_p}{c_v}$)

ϕ Equivalence ratio ($\phi = \frac{[fuel]/[O_2]}{([fuel]/[O_2])_{\text{stoich}}}$)

χ Mole fraction (ppm)

Chapter 1

Introduction

Context

Transportation is a central feature of modern life. The movement of people and goods has been increasing steadily, as a result of globalization [1]. In our days, almost the totality (99.8%) of transportation is powered by internal combustion engines and 95% of the energy required for transport comes from liquid fuels made from petroleum [2–4]. Although in the last few decades engines have become cleaner and more efficient, transport still accounts for around a quarter of the total greenhouse gas (GHG) emissions worldwide [1] and emissions are growing, even in the developed world, where generally other emissions tend to be flat. As an example, the GHG emissions from different sectors in France are shown in Figure 1.2, from 1990 to 2021. It can be seen that in 1990 the transport sector was already responsible for 23% of the GHG emissions, but this percentage increased to 31% by 2021. In general, worldwide, the annual emissions of CO₂ linked to industry and fossil fuels is still increasing. Figure 1.1 shows the evolution of CO₂ emissions from 1900 to today. If the Covid-19 pandemic slowed down the emissions by a small amount, since restrictions preventing traveling were in place, it also brought a huge economic crisis, showing how restricting the possibility of travelling cannot be a solution in reducing the emissions [4]. Internal combustion engines fuelled with petroleum-derived fuels are also responsible for the emissions of nitrogen oxides (NO_x), carbon monoxide, unburnt hydrocarbons and particulate matter. This adds concerns for human health, to the already present environmental problem.

One solution envisaged so far is the electrification of the transport fleet. Nevertheless, this technology has still some limitations. If this can actually be a solution for light-duty passenger vehicles, its feasibility for heavy duty vehicles can hardly be proven, since the long charging time is prohibitive. Another problem is the fact that the previsions suggest that in 2050 (year by which net-zero emissions should be reached to avert the worst impact of climate change [5]) many of today's new cars will still be on the road. Therefore, unless fleet renewal is globally founded at high levels, only low-carbon fuels compatible with the current technology, can help decarbonization [4]. As Powell et

al. suggested in their analysis [6], the fastest and most effective CO₂ reduction can be reached only through the coexistence of low-carbon fuels and an electrified fleet.

Biofuels are not strictly defined as low-carbon fuels. Nevertheless, in theory, a biofuel can be carbon-neutral, if any biomaterial used to create the fuel is then replanted. In practice, there can be other carbon emissions, linked for example to the production and transportation. However, the potential of biofuel to reduce CO₂ emissions is significant [7].

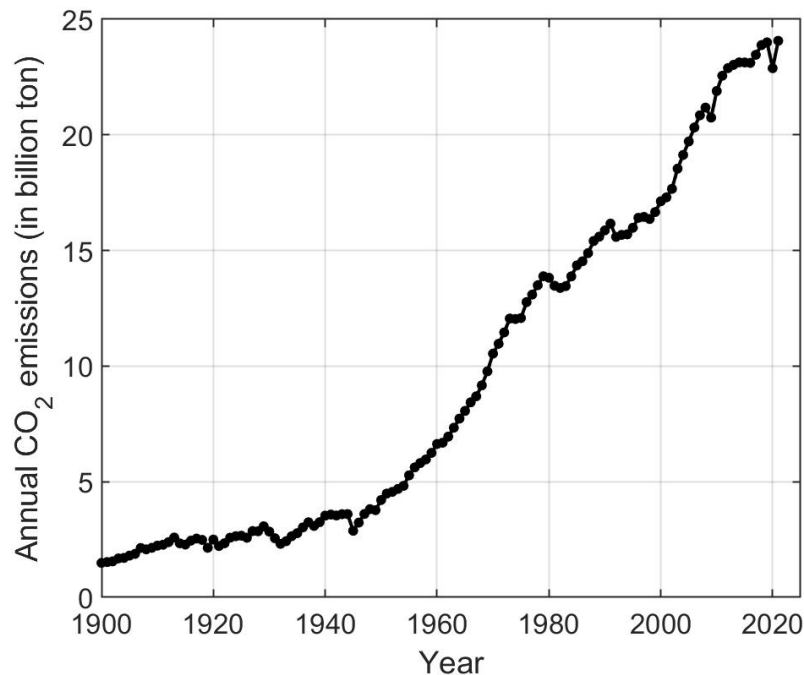


Figure 1.1: Worldwide annual CO₂ emissions from fossil fuels and industry, from 1900 to today (adapted from [8]).

In this context, the importance of the study of the combustion properties and the emissions of possible biofuels has largely grown. In fact, if the feasibility of this transition has to be studied from different points of view (economic, geo-politic, etc), the base for the application of new fuels issued from biomass is assessing the possibility to actually use them with the actual technology (or with small modifications to this). Also, if it has already been proven that oxygenated compounds, as biofuels, can have a positive effect on some emissions, it is important to assure that also no other harmful or toxic emissions (as for example aldehydes) are released.

To this aim, the fundamentals of combustion of potential interesting biofuels have to be studied, in order to understand which compounds can be formed and then released and also to be able to possibly predict their performance in the desired applications. This is why in the latest years the combustion community has been focusing on collecting experimental data and on developing kinetic mechanisms that can predict and help the understanding of the reactions involved in the oxidation and pyrolysis of several oxygenated compounds, including alcohols, esters and ethers.

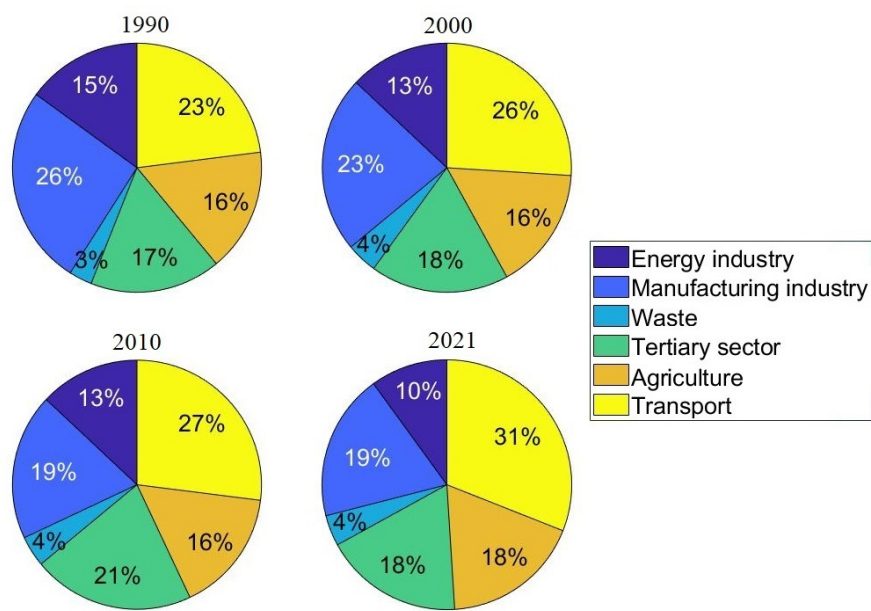


Figure 1.2: Greenhouse gases emissions from the different sectors in France, from 1990 to 2021 (from [9], based on Climate Analysis Indicators Tool (CAIT)).

Objectives

Smaller ethers, as dimethyl and diethyl ethers or methyl-tert-butyl and ethyl-tert-butyl ethers have been already largely studied, both from the point of view of the fundamentals of combustion and of real-life applications. Concerning longer chain ethers, dibutyl ether has also been studied and considered for some applications. A quite thorough review has also been published on oxygenated compounds by Rotavera [10], where an analysis on the influence of the different functional groups (among which the ether group can be found) on the low temperature reactivity was presented. Nevertheless, the literature lacks more experimental data, for example for longer-chained ethers. Also, even if the influence of the different functional groups has been explored, no indications are given on the influence of the structure of the molecules belonging to the same family.

This work therefore focuses on the influence of the structure of different fuels belonging to the same family and therefore showing the same functional group, the ether function. To this aim, different ethers have been considered, some of which have already been studied in our group. Two complementary set-ups are used to collect experimental data: one jet-stirred reactor, to measure the mole fractions of intermediates and products, and one rapid compression machine, to measure the ignition delay times and assess the global reactivity of the fuels.

The ethers that are included in this study were chosen in order to observe the maximum possible variations in the structure:

- *Length of the chain*: different symmetrical linear ethers were studied in order to assess the

influence of the length of the carbon chain. Some of these have already been studied in the JSR, while for all of them the experiments in the RCM were performed in this study. The selected ethers for this part were: diethyl ether, di-n-propyl ether, dibutyl ether, di-n-pentyl ether.

- *Branching*: two groups of comparison were considered, each made of three ethers: the first one regroups diethyl ether, di-n-propyl ether and di-iso propyl ether, the second one is formed by dibutyl ether, di-n-pentyl ether and di-iso-pentyl ether. In each group, either isomers or ethers with similar structure (with or without ramification) are included;
- *Asymmetry*: only one ether has been considered, which is butyl ethyl ether. As the name suggested, its structure is common on one side to dibutyl ether and on the other to diethyl ether. Nevertheless, it should be noted that butyl ethyl ether is also an isomer of di-n-propyl and di-iso-propyl ethers.
- *Other functional groups*: lastly, it can be interesting to assess the possible interactions of the ether group with other functional groups and to this aim, ethyl lactate was included in the study.

If collecting experimental data is of paramount importance in order to better understand the behaviour of these fuels, the development of the kinetic mechanism that can correctly predict and explain these characteristics is of equal interest. The second objective of this work is therefore the development of a kinetic mechanism that can represent the experimental results, with the aim of being able to predict the behaviour of any molecule in the ether family mainly based on the analysis of its structure.

Outline

The presentation of this work is divided into six chapters, following this introduction (**Chapter 1**). **Chapter 2** gives an overview on the combustion of oxygenated compounds, focusing on the low- and high-temperature reaction classes. This is followed by a small section on the possible processes leading to the production of ethers and by a review of the main literature results concerning the fuels that are presented in this work.

In **Chapter 3**, the experimental set-ups that were used in the experimental campaign are presented. The first part focuses on the set-ups in the two laboratories in Orléans (ICARE and PRISME), while a second part is dedicated to the presentation of the two set-ups that were used in the University of Galway. The final part of the chapter shortly discusses the uncertainty associated to the measures.

Chapter 4 presents the construction of the kinetic mechanism and the process linked to the simulations. A small discussion of the choice of the main reaction rates is given, as well as a general

description of the software used for the simulations. The final part of the chapter is used to explain the process linked to the heat release rate analysis in the RCM.

The following two chapters, **Chapters 5 & 6**, introduce the results. The first of these two chapters focuses on the results obtained in the jet-stirred reactor for di-iso-pentyl and di-n-pentyl ethers. The section on di-iso-pentyl ether is completed by the comparison to the simulations, while the one on di-n-pentyl ether focuses on the experimental results and the expected important products and reactions. A comparison is also provided on the reactivity of these two isomers and all the other ethers previously studied in the same conditions. The second chapter on the experimental results focuses on the measurements from the rapid compression machine. All of the ethers and ethyl lactate are included in this section and comparisons, both to the simulations and between different ethers, are provided.

This manuscript ends with **Chapter 7**, where general conclusions are drawn and some future perspectives are presented.

Chapter 2

State of the art

In this chapter, a general overview of the combustion process of oxygenated compounds is given, with specific sections for both low- and high-temperature reactivity. Thereafter, the second part of the chapter focuses on the state of art of each ether studied in this work, considering both the ways of production (when available in the literature) and the studies performed on the fundamentals of combustion and on possible real-life applications.

Contents

2.1 Combustion of oxygenated compounds	6
2.1.1 Low-temperature oxidation	7
2.1.2 High-temperature oxidation	9
2.2 Ethers	10
2.2.1 Production processes	10
2.2.2 Diethyl ether (DEE)	10
2.2.3 Di- <i>n</i> -propyl ether (DPE)	13
2.2.4 Di- <i>iso</i> -propyl ether (DIPE)	15
2.2.5 Di- <i>n</i> -butyl ether (DBE)	17
2.2.6 Butyl ethyl ether (BEE), di- <i>n</i> -pentyl ether (DNPEE), di- <i>iso</i> -pentyl ether (DIPEE)	20
2.2.7 Ethyl lactate	21
2.3 Conclusions	22

2.1 Combustion of oxygenated compounds

Biofuels are fuels that are produced from biomass, i.e. non-fossil organic matter, that can derive from vegetable, animal or microbial sources.

It is possible to distinguish between:

- First generation: derived from plant-related sources, they are usually in competition with food supplies;
- Second generation: derived from lignocellulosic biomass, in which the competition with the food sector can be avoided;
- Third generation: derived from micro-seaweed, they look interesting, but they are still quite unknown and undergoing investigation;
- Fourth generation: derived from genetically modified organisms, they pose issues related to risks to the environment and biodiversity.

Biofuels, unlike conventional fuels derived from petroleum, have an oxygen content of 10–45% [11]. Nevertheless, the combustion chemistry is quite similar to conventional fuels and it involves the same reaction classes. When looking at the reactivity of these kind of compounds over the temperature range where combustion is possible, it is possible to distinguish different regions, as shown in Figure 2.1. At low temperatures (600–800 K), reactions specific to the low-temperature regime can happen, especially peroxidation and isomerisation reactions. These reactions are generally quite slow and are characterised by a low exothermicity, which explains the denomination of this region as "cool flame". In the intermediate temperature zone, the so called "negative-temperature coefficient" (NTC) zone can be observed. In this zone, the shifting of the equilibrium of some reactions leads to the deceleration of the reactivity, it either reaches a plateau or decreases with the increase of temperature. After this zone, the high temperature reactivity zone is reached. Here the reactivity strongly increases with the temperature and typically β -scission reactions become dominant. These reactions are strongly exothermic and usually fast. In the following, a deeper insight in the reaction classes typical of low and high temperature regimes is given.

2.1.1 Low-temperature oxidation

The chemistry of low-temperature oxidation can be very complex and include a wide range of reaction classes. The main classes have been summarised already in 1981 by Benson [13] and several reviews [14–16] over the years. The scheme in Figure 2.2 summarises the main pathways at low temperatures.

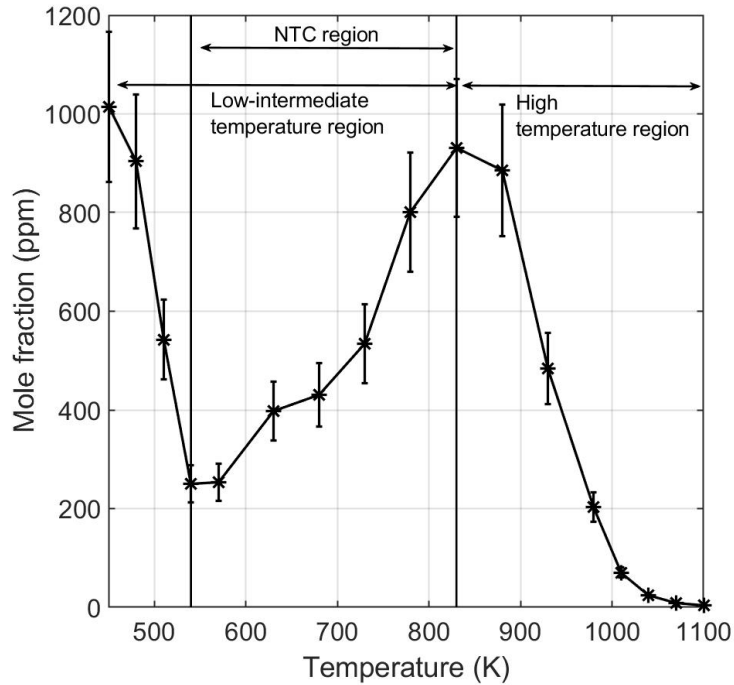


Figure 2.1: Example of different regimes of reactivity (JSR experiments, diethyl ether, $\phi = 0.5$, $p = 10$ atm, $\tau = 700$ ms, from [12]).

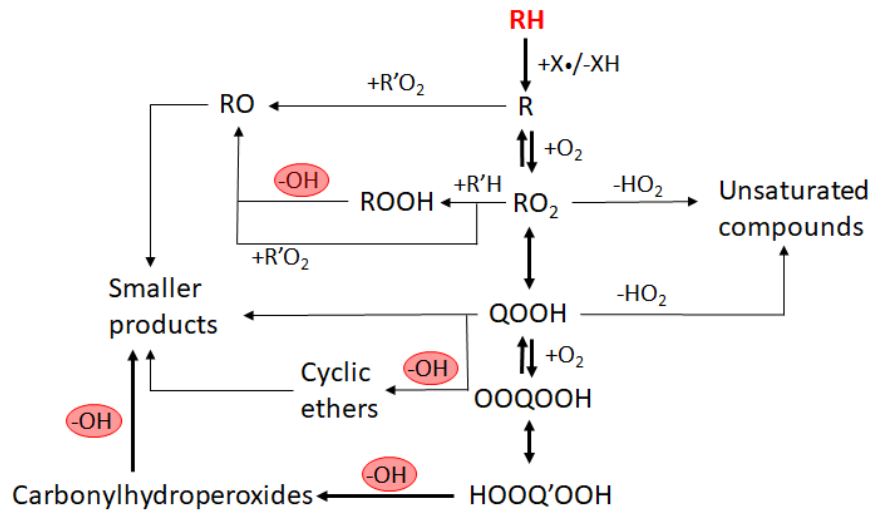


Figure 2.2: Main reactions pathways happening during the oxidation of oxygenated compounds at low temperature.

The primary radical R mainly undergoes addition to molecular oxygen at low temperature, forming the peroxyalkyl radical RO_2 . These RO_2 radicals can either react with radicals such as RO_2, HO_2, CH_3O_2 , leading to the formation of an alkoxy radical RO or eliminate an HO_2 radical to form an unsaturated compound or undergo isomerization to $QOOH$ by internal H-transfer. This

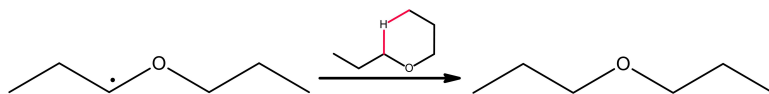
last one is usually the most common path and the most favourable cyclic transition state is the one with a ring formed by six atoms. The QOOH radical can then lead to the formation of cyclic ethers or eliminate an HO₂ radical forming an unsaturated compound (depending on its structure) or go through β -scission reactions (propagating pathways less common at low temperature). At low temperature, it can add to molecular oxygen, forming the OOQOOH radical. Another internal isomerization follows, with the formation of the HOOQ'OOH radical, which finally yields a carbonyl-hydroperoxide through the scission of the O–OH bond, then yielding chain branching agents and another OH radical.

The competition between the pathway leading to the formation of carbonylhydroperoxides and the propagating pathways is very important, since it affects the NTC behaviour. In fact, carbonylhydroperoxide formation is a chain-branching path, thus accelerating the reactivity, while the formation of the cyclic ether leads to the release of only one OH radical, thus being less favorable for the reactivity. These reactions are very important in order to understand what is happening in the NTC region. In fact, as temperature increases, the equilibrium of $\text{QOOH} + \text{O}_2 \rightleftharpoons \text{OOQOOH}$ tends to move towards the reactants, thus limiting the formation of ketohydroperoxides. After the NTC region within which reactivity decreases, high-temperature reactions become dominant, thus increasing the reactivity again.

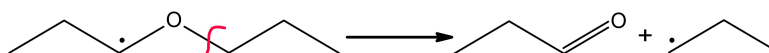
2.1.2 High-temperature oxidation

At high temperatures oxidation can also be initiated by unimolecular reactions forming radicals from the molecule, as for example the homolytic fissions. The rate constants of this kind of reactions strongly depend on the energy of the bond that has to be broken.

Concerning radicals, the most common reactions at high temperature are the isomerization and the β -scission reactions. The isomerization reactions allow for a re-organisation of the structure of the radical, through the displacement of a hydrogen atom, through a cyclic transition state. Here is an example:



The β -scission reactions allow the breaking of the bond in the β position with respect to the radical site and the formation of a double bond on the side of the radical site. This kind of reaction becomes more and more important at higher temperatures. An example of this reaction is shown below:



2.2 Ethers

Ethers can be produced through the dehydration and condensation of two molecules of alcohols. Since alcohols can be produced from biomass, it is also possible to obtain bio-ethers. It has been proven that oxygenated compounds can be very interesting for engine applications (both as fuels or as additives), enhancing the combustion efficiency and reducing the emissions [17]. Therefore bio-ethers are very interesting compounds to study as they can possibly be used for engine applications in the future.

2.2.1 Production processes

Concerning the production process of some of the ethers that have been studied in this work, it is possible to find some studies in the literature, especially for the ones that have been more widely studied in the past decade.

- Diethyl ether can be produced by the dehydration and etherification of two molecules of ethanol [18–22].
- Di-*iso*-propyl ether can be produced from the etherification reaction of isopropanol with propylene or from the dehydrative etherification of isopropanol [23–25].
- Similarly to diethyl ether, dibutyl ether can be obtained through a reaction of etherification from the corresponding alcohol, butanol [26–28].
- Di-*n*-pentyl ether has also been studied regarding its way of production, which is based on the etherification of 1-pentanol [29–32].

The other ethers included in this work can also be obtained from the etherification reaction of the corresponding alcohol, but no specific work could be found in the literature to the best of our knowledge. A general review on the processes of synthesis of ethers from biomass-derived platform chemicals has been presented by Rorrer et al. [33] in 2019.

2.2.2 Diethyl ether (DEE)

After dimethyl ether, diethyl ether is the smallest symmetrical linear ether. DME has been largely studied since the 90s. In fact, tests in Diesel engines showed encouraging results, leading to the wide interest in studying the fundamental combustion properties of this small oxygenated compound, which translated in a considerable number of publications (for example [34–41], ranging from 1996 to today). DEE, on the other hand, has also started to gather interest as a possible bio-fuel or additive in Diesel engines, as summarised in Sezer [42]. Already in 1959, Waddington [43] proposed the first study on the main products that could be observed during the gas-phase oxidation of diethyl ether. In 1965, Agnew [44] published another study on the species quantification in

a flat-flame burner. Starting from 2010 more recent works have been published on the oxidation and pyrolysis of this ether, as summarized below.

Concerning the studies in jet-stirred reactors, Vin et al. [45] performed the first study on DEE pyrolysis, considering different fuel concentrations, pressures and residence times. They nevertheless stated that the reactivity is mostly influenced by the temperature, while the effect of the pressure was limited. In 2019, Serinyel et al. [12] studied the oxidation of DEE in a jet-stirred reactor (JSR) at 1 atm and 10 atm, for lean, stoichiometric and rich conditions. At high pressure, a strong low temperature reactivity was recorded, while at atmospheric pressure that was limited and not detectable for the rich mixture. They also developed a new kinetic model, since the ones available in the literature were not capable of predicting this strong low-temperature reactivity. In 2019 and 2020, Tran et al. [46, 47] published two other studies on the oxidation of DEE, detecting two negative-temperature coefficient zones. A new model capable of representing this behaviour was also proposed. In 2021, Serinyel et al. [48] proposed a study on the pyrolysis of four symmetrical ethers, including DEE, in a JSR. They found that the four main products common to all four ethers are CO, CH₄, H₂ and C₂H₄, showing that the most important reactions are H-abstractions by H and CH₃ and the β -scissions of the primary radicals. They also found that all ethers produced the associated alcohol by molecular reaction to a lower extent. The latest JSR study on DEE, to our knowledge, was published in 2021 by Belhadj et al. [49], focusing on the elusive cool flame products, such as ketohydroperoxides and other highly oxygenated compounds, through the use of liquid chromatography and high resolution mass spectrometry.

Concerning the use of rapid compression machines and shock tubes several studies are also available. Already in 2010, Yasunaga et al. [50] studied both the oxidation and the pyrolysis of DEE in a shock tube. They measured both ignition delay times and species profiles and they assembled a mechanism in good agreement with these results. Thanks to the reaction pathway analysis, they showed that both for pyrolysis and oxidation, at the early stages of the reaction, the unimolecular decomposition and H-abstraction of DEE and the decomposition of the ethoxy radicals have the largest influence on the reactivity. Then, in 2015, Werler et al. [51] measured ignition delay times of DEE in an RCM and in a ST under a wide range of conditions. In the RCM, they recorded two-stage ignition between 500 and 665 K and they saw that between 590 and 800 K the ignition delay times showed little dependence on the temperature. In the ST, IDTs showed a strong dependence on both pressure and temperature in the studied conditions. They compared these results to simulations from the mechanism proposed by Yasunaga [50], with good agreement, and they stated the importance of the H-abstraction reactions from DEE by HO₂ radicals under these conditions. In 2018, the first study on the ignition delay times of undiluted DEE/air mixtures was presented by Uygun [52]. He also reported an NTC region in his data and he stated that in some conditions even a three-stage ignition was observed. The most recent publication on IDTs measured in a shock tube and RCM was published in 2020 by Issayev et al. [53]. At fuel lean conditions, they also recorded a three-stage ignition. In this study, also a blend of DEE and ethanol was studied and a

combined model was proposed, with an accent on the interplay between radicals originating from the two fuels.

Some studies are also available in the literature on the measurements of laminar flame speeds [54–56].

In the Table 2.1, the literature studies presented above are summarised, with the corresponding set-ups and experimental conditions.

Table 2.1: Summary of the literature on the oxidation of diethyl ether

Set-up	Conditions	Measurements	Year and reference
JSR	$T = 600\text{--}1100\text{ K}$ $p = 26.7\text{--}107.7\text{ kPa}$ Pyrolysis $\tau = 1\text{--}10\text{ s}$	Speciation	2016 Vin et al. [45]
JSR	$T = 450\text{--}1250\text{ K}$ $p = 1, 10\text{ atm}$ $\phi = 0.5, 1, 2$ $\tau = 0.07, 0.7\text{ s}$	Speciation	2018 Serinyel et al. [12]
2 JSR	$T = 400\text{--}1100\text{ K}$ $p = 1.06\text{ bar}$ $\phi = 1$ $\tau = 2\text{ s}$	Speciation	2019 Tran et al. [46]
JSR	$T = 400\text{--}1100\text{ K}$ $p = 5\text{ bar}$ $\phi = 1$ $\tau = 2\text{ s}$	Speciation	2020 Tran et al. [47]
JSR	$T = 720\text{--}1140\text{ K}$ $p = 10\text{ atm}$ Pyrolysis $\tau = 0.7\text{ s}$	Speciation	2021 Serinyel et al. [48]
JSR	$T = 440\text{--}740\text{ K}$ $p = 10\text{ atm}$ $\phi = 1$ $\tau = 1\text{ s}$	Cool flame products	2021 Belhadj et al. [49]
ST	$T = 900\text{--}1900\text{ K}$ $p = 1\text{--}4\text{ atm}$ $\phi = 0.5, 1, 2$ and pyrolysis	IDTs and speciation by GC	2010 Yasunaga et al. [50]

ST + RCM	$T = 500\text{--}1060$ K (RCM), 900–1300 K (ST) $p = 2.5\text{--}13$ bar (RCM), 10, 20, 40 bar (ST) $\phi = 0.5, 1, 2$	IDTs	2015 Werler et al. [51]
ST	$T = 622\text{--}1100$ K $p = 18, 40$ bar $\phi = 1$	IDTs	2018 Uygun [52]
ST + RCM	$T = 550\text{--}1000$ K $p = 20, 40$ bar $\phi = 0.5, 1$ (+ blend with ethanol)	IDTs	2020 Issayev et al. [53]
Flat-flame burner	$T = 127^\circ\text{C}$ (at burner-tube-exit) $\phi = 3.9$ $\tau = 0.07, 0.7$ s	Temperature profile + Intermediates mole fractions	1965 Agnew et al. [44]
Constant volume combustion vessel	$T_u = 323, 343, 363$ K Dilution = 0, 5, 10, 15, 20% $\phi = 0.8, 1, 1.2$	Laminar burning velocity, Markstein length and Zeldovich number	2009 Zhang et al. [54]
Flat-flame burner	$T_u = 298\text{--}398$ K $p = 1$ atm $\phi = 0.55\text{--}1.6$	Laminar burning velocity	2012 Gillespie et al. [55]
McKenna burner + constant-volume cylindrical chamber	$T_u = 333$ K (burner), 298 K (chamber) $\phi = 1.8$ (burner), 1.4 (chamber) $p = 4$ kPa (burner), 101, 203, 304, 405, 507 kPa (chamber)	Laminar burning velocity and species distribution	2017 Tran et al. [56]

2.2.3 Di-*n*-propyl ether (DPE)

Di-*n*-propyl ether, which stands between diethyl ether and dibutyl ether from a structural point of view, has only recently been considered for studies on its combustion properties. In fact, it has not been considered so far as a potential biofuel; nevertheless, it is of great interest in order to understand the behaviour of linear ethers with different chain lengths. To our knowledge, the first study published on the oxidation of DPE in a jet-stirred reactor was performed in 2020 by Serinyel et

al. [57]. This study was performed at high pressure (10 atm) for different equivalence ratios, ranging from fuel-lean to fuel-rich. This molecule showed a strong low-temperature chemistry and the carbon adjacent to the ether group proved to be the most favourable site for H-abstraction, forming the α -radical. A kinetic model was also developed, with good agreement with the experimental results, but the authors underlined the necessity of atmospheric pressure results. This gap was partially filled in early 2021 by Belhadj et al. [58], who performed a study on the oxidation of DPE at 1 and 10 atm in a JSR. The focus was on the characterization of cool flame products through the use of liquid chromatography and mass spectrometry. Stable species were quantified, but only at 10 atm. In agreement with Serinyel and al. [57], the carbon site adjacent to the ether group was found to be the most favourable for H-abstraction, but from the large pool of intermediates that was identified, it was shown that β - and γ -radicals were also formed. Also in 2021, Fan et al. [59] reported speciation data on the oxidation of DPE in a JSR at near-atmospheric conditions and low temperature. In these results, a double-NTC behaviour was identified and attributed to the competition of chain-branching and termination reactions of the fuel itself and specific decomposition products, respectively. The paper also underlines the requirements for a fuel to show a double-NTC behaviour. In the same year, Serinyel et al. [48] also published their work on the pyrolysis of four ethers in a JSR, already cited in the previous section. DPE was the second most reactive fuel at high temperature, following its isomer DIPE. Similarly to DEE, the reaction pathway analysis showed that the most important reactions consuming DPE were H-abstraction reactions by H and CH₃ radicals and then the β -scission reactions of the primary radicals. The most recent published work concerning the oxidation and pyrolysis of DPE was published in 2022 by Cheng et al. [60], following their first study on DPE in a flow reactor in 2021 [61]. This latest work [60] focused on the isomeric effect between DPE and DIPE, through experiments performed in two jet-stirred reactors for speciation and a constant volume cylindrical combustion vessel for the measurement of laminar flame speeds. On the other hand, this first study [61] dealt with the pyrolysis of DPE in a flow reactor, with the determination of its intermediate products and the development of a detailed kinetic model, which showed how the unimolecular decomposition reactions control the reactivity at the conditions studied. In Table 2.2, the studies presented above are summarised, together with the set-ups used and experimental conditions investigated.

Table 2.2: Summary of the literature on the combustion of di-*n*-propyl ether

Set-up	Conditions	Measurements	Year and reference
JSR	$T = 470\text{--}1160\text{ K}$ $p = 10\text{ atm}$ $\phi = 0.5, 1, 2, 4$ $\tau = 0.7\text{ s}$	Speciation	2020 Serinyel et al. [57]
JSR	$T = 720\text{--}1140\text{ K}$ $p = 10\text{ atm}$ Pyrolysis $\tau = 0.7\text{ s}$	Speciation	2021 Serinyel et al. [48]
JSR	$T = 450\text{--}950\text{ K}$ $p = 1, 10\text{ atm}$ $\phi = 0.5$ $\tau = 1, 0.7\text{ s}$	Cool flame products	2021 Belhadj et al. [58]
JSR	$T = 425\text{--}850\text{ K}$ $p = 1\text{ atm}$ $\phi = 1$ $\tau = 2\text{ s}$	Speciation	2021 Fan et al. [59]
2 JSR + constant volume cylindrical combustion vessel	JSR: $T = 780\text{--}1050\text{ K}$, $p = 1\text{ atm}$ FS: $T_u = 373\text{ K}$, $p_u = 1\text{--}10\text{ atm}$ pyrolysis (JSR), $\phi = 0.7\text{--}1.5$ (FS) $\tau = 1\text{ and }2\text{ s}$	Speciation and laminar flame speeds	2022 Cheng et al. [60]
Tubular flow reactor	$T = 850\text{--}1350\text{ K}$ $p = 0.04, 1\text{ atm}$ Pyrolysis	Speciation	2021 Cheng et al. [61]

2.2.4 Di-*iso*-propyl ether (DIPE)

Di-*iso*-propyl ether is the isomeric branched counterpart of di-*n*-propyl ether. If DPE has not been proven to be actually useable as a biofuel or additive, some studies have already been published on the use of DIPE as an additive in SI or HCCI engines [62–64]. Already in 1998, Goldaniga et al. [65] studied DIPE as an octane improver, along with other well known additives including MTBE, ETBE and TAME. In this study, the oxidation of these fuels was performed in a JSR, for fuel-lean to fuel-rich mixtures. They also added the sub-mechanism for these ethers to an oxidation reaction model for the primary reference fuels already available [66] and the agreement with the experimental re-

sults proved to be quite good. In 2021, Serinyel et al. [48] included DIPE among the four symmetrical ethers considered in their pyrolysis study. At high temperature, DIPE was shown to be the most reactive one among the ethers considered and its specific alcohol (isopropanol) appeared at lower temperature (product of the molecular reaction $\text{dipe} \rightleftharpoons \text{C}_3\text{H}_6 + \text{iC}_3\text{H}_7\text{OH}$) and reached the highest peak in mole fraction. In the same year, Fan et al. [67] performed a study on the oxidation of DIPE in a JSR at atmospheric pressure and stoichiometric conditions, with a residence time of 2 s. In these conditions, the consumption of DIPE only starts after 750 K. They explained this through their kinetic model, saying that the OOQOOH radicals dissociate back to QOOH + O₂, instead of undergoing intramolecular isomerization, thus inhibiting the reactivity at low temperature. Also Serinyel et al. in 2022 [68] stated that DIPE did not show any low temperature reactivity (T < 700 K) in their oxidation experiments in a JSR. The oxidation of the rich mixture ($\phi = 4$) was actually quite similar to the pyrolysis, with an important production of propene and isopropanol. They also underlined how DIPE showed a smaller fuel conversion when compared to the other ethers they studied at the same conditions.

Other measurements were performed for DIPE by Liu et al. [69] and Hashimoto et al. [70]. The first study focused on the comparison of five different ethers, by characterising the oxidation temperatures and pressures and some intermediates products in an accelerating rate calorimeter. The second also focused on a comparison, this time between three ethers that are considered potential octane improvers (ETBE, DIPE, TAME), by measuring the extinction limits and the flame structures in a counterflow burner. In the Table 2.3, the literature studies presented above are summarised, with the set-ups used and associated experimental conditions.

Table 2.3: Summary of the literature on the combustion of di-*iso*-propyl ether

Set-up	Conditions	Measurements	Year and reference
JSR	$T = 800\text{--}1150 \text{ K}$ $p = 10 \text{ atm}$ $\phi = 0.5\text{--}2$ $\tau = 0.5 \text{ s}$	Speciation	1998 Goldaniga et al. [65]
JSR	$T = 720\text{--}1140 \text{ K}$ $p = 10 \text{ atm}$ Pyrolysis $\tau = 0.7 \text{ s}$	Speciation	2021 Serinyel et al. [48]
JSR	$T = 525\text{--}900 \text{ K}$ $p = 1 \text{ atm}$ $\phi = 1$ $\tau = 2 \text{ s}$	Speciation	2021 Fan et al. [67]

JSR	$T = 500\text{--}1160\text{ K}$ $p = 10\text{ atm}$ $\phi = 0.5, 1, 2, 4$ $\tau = 0.7\text{ s}$	Speciation	2022 Serinyel et al. [68]
2 JSR + constant volume cylindrical combustion vessel	$T = 780\text{--}1050\text{ K}$ (JSR), $T_u = 373\text{ K}$ (FS) $p = 1\text{ atm}$ (JSR), $p_u = 1\text{--}10\text{ atm}$ (FS) pyrolysis (JSR), $\phi = 0.7\text{--}1.5$ (FS) $\tau = 1\text{ and }2\text{ s}$	Speciation and laminar flame speeds	2022 Cheng et al. [60]
Accelerating rate calorimeter	$T_0 = 323\text{ K}$ $P_0 = 1.0\text{ MPa}$	Oxidation temperatures and pressures + speciation	2016 Liu et al. [69]
Counterflow burner	$T = 333\text{ K}$ (fuel), 298 K (oxidizer) $p = 0.1\text{ MPa}$	Extinction limits + speciation	2017 Hashimoto et al. [70]

2.2.5 Di-n-butyl ether (DBE)

Recently, di-n-butyl ether has been identified as a potential biofuel for Diesel engine application, several studies [71–75] have shown how the addition of DBE to biodiesel or diesel can improve the performances and at the same time reduce the soot formation and the emissions. Considering the huge potential of this fuel, it is not surprising to see that many studies on the fundamental characteristics of DBE combustion are available in the literature.

Concerning speciation, the first study, to our knowledge, was published by Thion et al. in 2017 [76]. In this study, the oxidation of DBE at two different pressures (1 and 10 atm) and three equivalence ratios was considered. From the experimental results at 10 atm, a double-NTC zone was identified and attributed to the fact that the low-temperature reactivity of the fuel and of smaller species are triggered at different threshold temperatures. A detailed kinetic mechanism was also developed, allowing for an analysis on the reactivity, which showed how the carbon neighbouring the ether group was the most favourable site for H-atom abstraction and therefore the corresponding fuel radical chemistry was driving the overall reactivity. This double NTC behaviour was then confirmed also in the work of Tran et al. [77], who studied DBE oxidation at near atmospheric pressure and stoichiometric conditions, but with different residence times and initial fuel mole fraction. In their study, they found some traces of highly oxygenated peroxides, which suggested a third addi-

tion to molecular oxygen. They also compared their results to the models proposed by Thion et al. [76] and by Cai et al. [78], obtaining significant discrepancies, leading to the need to include more low-temperature intermediates. Two studies were then published by Belhadj et al. [79, 80], concerning the speciation of specific products in the cool flame and highly oxygenated products. The first study in 2020 compares the results obtained in a jet-stirred reactor and in a rapid compression machine, showing that similar oxidation pathways are followed in both set-ups. In both cases, the α C-H bond was found to be the most favourable site for hydrogen abstraction, however the results from speciation showed that other primary radicals could also be formed, resulting in a large pool of intermediates and products. In the second study in 2021, only jet-stirred reactor conditions were considered, again with speciation of cool-flame products and highly oxygenated molecules. In this case, the pressure was set at 10 bar and oxidation was performed in fuel-rich conditions. Authors found a strong similarity to atmospheric oxidation, considering the classes of products that were identified. In 2021, DBE pyrolysis was studied in the comparative study done by Serinyel et al. [48], together with DEE, DPE and DIPE. DBE was found to be the least reactive under these conditions at high temperature, feature that the kinetic model proposed was not completely able to capture. The main pathways followed by DBE in its pyrolysis were found to be similar to the other ethers, with a predominance of H-atom abstraction by H and CH_3 and then β -scissions of the primary radicals.

Several studies can also be found in the literature reporting ignition delay times, both in shock tubes and in rapid compression machines. A first study by Guan et al. [81] performed ignition delay times measurements at low pressures (1.2-4 bar) and high temperatures in a shock tube. They compared their data with the Cai et al. mechanism [78], showing good agreement. They noticed that the IDTs have a strong negative dependence upon the equivalence ratio at high temperature, while the ignition delays have similar values independently from the equivalence ratio at lower temperatures. They also noticed, through a reaction pathway analysis, that the unimolecular decomposition becomes more important as the temperature increases. Also in 2021 Hakimov et al. [82] measured DBE ignition delay times, using both an RCM and a ST. They also measured CO molar fractions in a shock tube during DBE pyrolysis. Interestingly, in the RCM at fuel-lean conditions, the pressure traces showed ignition happening in three or even four stages. They compared their results to the Thion et al. [76] and Cai et al. [78] mechanisms, showing important discrepancies, which made them conclude that the rate of decomposition of DBE should be revisited. The most recent study on IDTs was published by Zhong et al. [83], using a rapid compression machine. They observed an NTC behaviour for the total IDTs in the temperature range investigated (525–707 K). They also tested literature models against their data, with unsatisfactory performance, leading to the tuning of the Thion [76] mechanism, which was also validated against other literature data. Concerning other studies published for DBE combustion, laminar flame speeds and IDTs were measured by Cai et al. [78], together with the development of the first detailed kinetic model. Moreover, Fan et al. [84] performed a pyrolysis study in a flow reactor, leading to the identification

of around 30 intermediates and products and to the development of a new pyrolysis mechanism for DBE. In the Table 2.4, the literature studies presented above are summarised, with the set-ups used and associated experimental conditions.

Table 2.4: Summary of the literature on the combustion of dibutyl ether

Set-up	Conditions	Measurements	Year and reference
JSR	$T = 470\text{--}1250\text{ K}$ $p = 1, 10\text{ atm}$ $\phi = 0.5, 1, 2$ $\tau = 70, 700\text{ ms}$	Speciation	2017 Thion et al. [76]
2 JSR	$T = 440\text{--}1100\text{ K}$ $p = 106.7\text{ kPa}$ $\phi = 1$ $\tau = 2\text{ s}$	Speciation	2019 Tran et al. [77]
JSR + RCM	$T = 480\text{--}670\text{ K}$ (JSR), $550\text{--}630\text{ K}$ (RCM) $p = 1, 10\text{ atm}$ (JSR), 5 bar (RCM) $\phi = 0.5$ (JSR), 1 (RCM) $\tau = 1\text{ s}$	Cool flame products	2020 Belhadj et al. [79]
JSR	$T = 720\text{--}1140\text{ K}$ $p = 10\text{ atm}$ Pyrolysis $\tau = 0.7\text{ s}$	Speciation	2021 Serinyel et al. [48]
JSR	$T = 460\text{--}780\text{ K}$ $p = 10\text{ atm}$ $\phi = 2$ $\tau = 1\text{ s}$	Cool flame products	2021 Belhadj et al. [80]
ST	$T = 1100\text{--}1570\text{ K}$ $p = 1.2\text{--}4\text{ bar}$ $\phi = 0.5, 1, 1.5$	IDTs	2014 Guan et al. [81]
RCM + ST	$T = 550\text{--}650\text{ K}$ (RCM), $900\text{--}1300\text{ K}$ (ST) $p = 10, 20, 40\text{ bar}$ (RCM), $20, 40\text{ bar}$ (ST) $\phi = 0.5, 1$ (RCM + ST)	IDTs + CO speciation in ST (20 bar, 1100-1400 K)	2021 Hakimov et al. [82]

RCM	$T = 525\text{--}707\text{ K}$ $p = 7, 10\text{ bar (RCM)}$ $\phi = 0.7, 1, 1.4$	IDTs	2022 Zhong et al. [83]
Laminar flow reactor (IDTs) + stagnation flame configuration (FS)	$T = 485\text{--}525\text{ K (IDTs)}, T_u = 373\text{ K (FS)}$ $p = 1\text{ atm (IDTs and FS)}$ $\phi = 0.5, 0.7, 1\text{ (IDTs)}, 0.7\text{--}1.5\text{ (FS)}$	IDTs and laminar flame speeds	2014 Cai et al. [78]
Flow reactor	$T = 800\text{--}1250\text{ K}$ pyrolysis $p = 30, 760\text{ Torr}$	Speciation	2021 Fan et al. [84]

2.2.6 Butyl ethyl ether (BEE), di-*n*-pentyl ether (DNPEE), di-*iso*-pentyl ether (DIPEE)

Butyl ethyl ether and di-*iso*-pentyl ether have so far not been considered as potential biofuels or additives for engine applications. Di-*n*-pentyl ether, on the other hand, has been previously tested in engines, in mixtures with other components. In 2015, Koivisto et al. [85] tested several oxygenated compounds obtained from lignocellulosic biomass in mixtures with 30% wt of *n*-heptane. They focused on the effect of oxygen in the molecular structure and they saw that the ignition delay times of DNPEE were similar to the ones of the corresponding alkane. They explained this through the competing effect of the physical properties of the ether (increasing the IDT) and the ether function itself (decreasing the IDT by making H-atom abstraction and fuel peroxy radical isomerisation reactions easier). They also measured the emissions from the diesel engine fuelled with these mixtures, but no specific observation was provided on DNPEE. In 2020, Aakko-Saksa et al. [86] used DNPEE as an additive in their tests for a biomethanol fuelled engine. Nevertheless, only a small percentage of DNPEE was used in mixtures with other additives, and the focus was more on the feasibility of methanol mixtures in an ethanol-based engine.

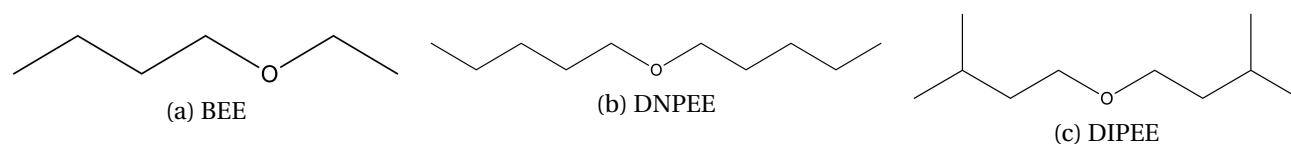


Figure 2.3: Molecular structures of BEE, DNPEE and DIPEE.

In the aim of understanding the reactivity of the molecules of this family and how molecular structure influences it, all of these ethers are very interesting to study in similar conditions as the other ethers previously presented. The molecular structure of these fuels is shown in Figure 2.3. In particular, BEE allows us to see how the lack of symmetry can change the reactivity when compared to DPE and DIPE (all three having six C-atoms). DNPEE and DIPEE, on the other hand, can give a deeper knowledge on the influence given by the length of the chain, but also by the branched structure. They also give another example of how two isomers can behave under similar conditions. To the best of our knowledge, there are no studies available in the literature on the fundamental combustion properties of these molecules, nor is there a kinetic mechanism available. Therefore, in order to have a complete overview of the reactivity of ethers, it is necessary to collect experimental data at similar conditions for all these molecules and develop a mechanism capable of predicting the combustion properties and possibly help to understand the effect of the molecular structure.

2.2.7 Ethyl lactate

Ethyl lactate is an oxygenated compound ($C_5H_{10}O_3$) whose molecular structure is shown in Figure 2.4. It is a very interesting molecule, since it presents different functional groups, among which an ether group is present. In the past, it has been used as a solvent and food additive [87, 88]. To the best of our knowledge, no studies were available in the literature about its fundamental combustion properties, except the one that has been derived from our recent work [89], where ignition delay times and laminar flame speeds were measured and a first kinetic model was proposed. Nevertheless, since ethyl lactate has promising characteristics as solvent, some studies have been published about the possible ways of its production. The most common process to produce ethyl lactate is the esterification of lactic acid with ethanol, using an acid as a catalyzer, as explained by Pereira et al. [87]. New pathways have been recently proposed by Koutinas et al. [90] and by Li et al. [91]. It is important to note that all these processes are based on renewable sources, which is one of the reasons why ethyl lactate has been considered as a promising biofuel, in particular as an octane enhancer.

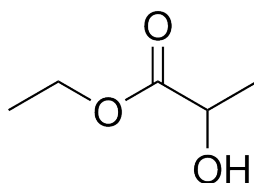


Figure 2.4: The molecular structure of ethyl lactate.

2.3 Conclusions

From this literature review, it can be concluded that experimental data are still missing, especially for longer chain ethers, including DNPEE and DIPEE. Moreover, available literature mechanisms are not able to reasonably simulate all the experimental data from the different experimental facilities. Moreover, studies comparing the relative reactivity of the different ethers are scarce and most of the collected experimental data are in different conditions and from different set-ups, which makes it hard to have a direct way of comparing. In the light of these findings, this study is trying to present a wide dataset for seven different ethers, allowing to compare them and possibly to understand the relation between the different structures and the reactivity.

Chapter 3

Experimental facilities

In this chapter, the experimental facilities used to carry out the experimental campaign are presented. First, a description of the jet-stirred reactor, as well as the analysis techniques used to identify and quantify intermediate products is included. Then, the three different experimental set-ups used for measuring the ignition delay times are described.

Contents

3.1 Jet-Stirred Reactor	24
3.1.1 Fourier Transform InfraRed spectroscopy (FTIR)	26
3.1.2 Gas chromatography	26
3.2 Rapid Compression Machine	28
3.2.1 Preliminary study on the RCM configuration	34
3.3 University of Galway facilities	36
3.3.1 High Pressure Shock Tube	36
3.3.2 Rapid Compression Machine	37
3.4 Uncertainty of measurements	38
3.4.1 Jet-stirred reactor	38
3.4.2 Rapid compression machine	39
3.4.3 University of Galway facilities	40

Introduction

The characterisation of the combustion of these molecules is of primary importance, both for the possible applications and from a fundamental point of view. The collection of experimental results allows the validation of the kinetic models, that in turn allow to predict the behaviour under

different conditions. Information on both global reactivity and specific products are therefore of interest for a better understanding of these molecules under combustion conditions. To this end, a jet-stirred reactor was used in order to measure the mole fractions of the reactants, products and intermediate species over a wide range of temperatures. On the other hand, in order to have an insight on the global reactivity, ignition delay times were measured using two rapid compression machines and one shock tube.

3.1 Jet-Stirred Reactor

Jet-stirred reactors (JSR) are widely used to study fuel oxidation or pyrolysis for gas-phase kinetic studies. Their main advantage is the possibility of decoupling the transport effects, thanks to the homogeneity of the chemical and physical properties inside the reactor, leading to a simplification in the modeling. The JSR used in this work is in ICARE laboratory (CNRS, France). It was built in the 80s by Dagaut, as described in [92] and shown in Figure 3.1. The interesting feature of this reactor, which was a novelty for that period, is the possibility of carrying out experiments at pressure up to around 10 atmospheres. This is done thanks to the pressure jacket where the reactor is placed and to the four holes at the bottom of the prolongation tube, which let the gases exiting the reactor to diffuse into the metallic vessel, so that they equilibrate the pressure inside the reactor itself.

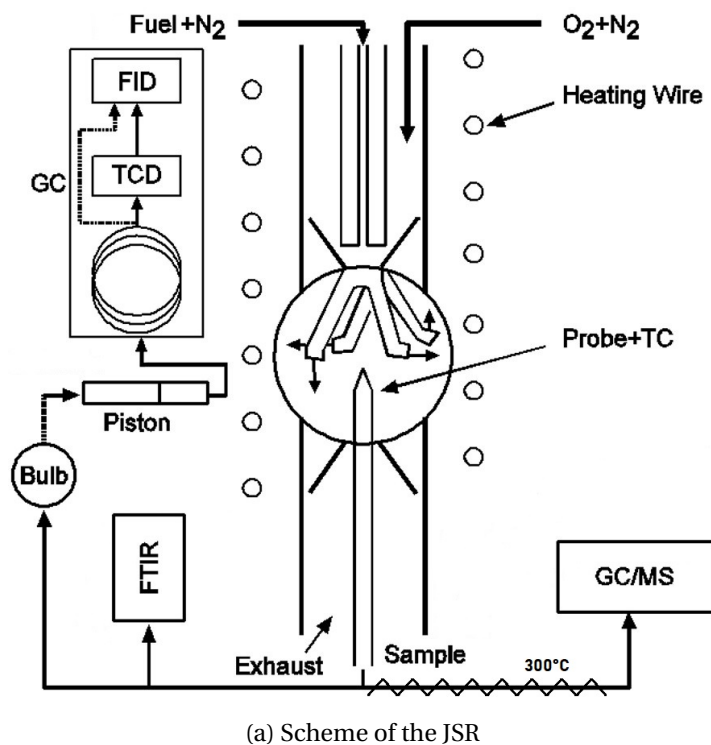


Figure 3.1: Jet stirred reactor in ICARE laboratory.

The reactor is made of fused silica in order to prevent any reaction at the walls. Its diameter is

40 mm, while the four nozzles which introduce the four turbulent flows have a diameter of 1 mm. The position of the nozzles allows the insertion of a sampling sonic quartz probe and a thermocouple in the reactor. These two can be moved along the axis of the reactor, thus allowing to both check the homogeneity and collect samples at any position of the reactant mixture. The reactor is heated by an electrical oven, up to 1280 K. As can be seen from Figure 3.1a, the flows of oxygen and vaporised fuel are brought separately to the reactor, in order to avoid any pre-reactions. Moreover, the mixture is highly diluted in nitrogen, in order to assure temperature stability avoiding high heat releases, which may damage the reactor. An HPLC pump is used to control the fuel flow rate and a vaporisation system ensures the vaporisation of the fuel before the reactor is reached. The flow rates of oxygen and nitrogen are controlled through different mass flow controllers, which are regularly calibrated. All the experiments are performed with a constant residence time, which depends in turn on the pressure, temperature and total flow rate in the reactor, as shown by equation 3.1

$$\tau = \frac{V_r}{Q_{tot}} \cdot \frac{T_0}{T} \cdot \frac{P}{P_0} \quad (3.1)$$

where T_0 and P_0 represent ambient temperature and pressure, Q_{tot} is the total flow rate (in cm^3/s) and V_r is the reactor volume (in cm^3). As this equation implies, in order to keep the residence time constant, it is necessary to adjust the mass flow rates of the reactants, as the reactor temperature is increased.

A low-pressure sonic probe is used to collect samples of the reacting mixture. Online analysis of the sample is performed through a FTIR, which is going to be described in more details in Section 3.1.1. The line leading the sample to the FTIR is heated up to 150°C, in order to avoid condensation. The same line also allows to store the sample in Pyrex bulbs, at ambient temperature and a pressure of around 80 mbar, in order to perform offline GC analyses, which will be detailed in Section 3.1.2. Two ethers have been studied in the JSR in this work, di-*iso*-pentyl and di-*n*-pentyl ethers. The conditions, similar to the ones used in previous works performed in this set-up, are reported in Table 3.1.

Table 3.1: The fuels tested and experimental conditions studied in the jet-stirred reactor.

Fuel	ϕ	P (atm)	T (K)	Initial fuel mole fraction	τ (ms)	Identified species
Di- <i>iso</i> -pentyl ether	0.5, 1.0, 2.0, 4.0	10	450-1210	1000 ppm	700	≈ 48
Di- <i>n</i> -pentyl ether	0.5, 1.0, 2.0, 4.0	10	450-1210	1000 ppm	700	≈ 52

3.1.1 Fourier Transform InfraRed spectroscopy (FTIR)

Fourier transform infrared spectroscopy (FTIR) is an analytical technique which allows the quantification of gaseous products, based on the interaction of light and matter. Its functioning is based on the Beer-Lambert law, which relates the absorbance to the concentration of a certain molecule. In order to quantify the products, it is necessary to calibrate in advance and create a method which will be able to determine if a certain molecule is present and with which mole fraction, based on the position of its absorption/emission peaks and taking into account possible interferences. The spectrometer used in this work is the Thermo Nexus 670. The optical path is 10 m and the number of scans per measure is 32, with a resolution of 0.5 cm^{-1} .

This technique is used in this work to quantify H_2O , CO , CO_2 , formaldehyde and methanol, plus possible organic acids. Moreover CH_4 , C_2H_6 , C_3H_6 , C_2H_8 and C_2H_2 can be quantified, but their profiles are usually obtained from the GC. Other products, like for example hydrocarbons, are quantified through gas chromatography (Section 3.1.2), since they would absorb in similar bands and would therefore have too many interferences.

3.1.2 Gas chromatography

Gas chromatography is an analytical process allowing the separation of different compounds contained in a mixture. A gas chromatograph (GC) is mainly composed of three elements: the injector, the column and the detector. Different columns and detectors were used in this work, as reported in Table 3.2. Each compound has a different interaction with the column and with the carrier gas. This allows to identify the different species based on the retention time, which is measured as the time required to travel inside the column. A typical resulting chromatogram from a GC analysis is shown in Figure 3.2, the area of the peaks being proportional to the mole fraction of each species. The conversion from the area to the mole fraction is done thanks to a conversion coefficient which can be directly obtained, if pure samples of that species are available in the laboratory, or estimated through the effective carbon number rule as described in [93].

Table 3.2: Gas chromatographs used in this work, with coupled columns and detectors.

GC	Column	Detector	Species	Carrier gas
Shimadzu QP2010-SE	CP-SIL 5CB, L = 25 m, $D_{\text{int}} = 0.32 \text{ mm}$, $D_{\text{f}} = 1.2 \mu\text{m}$ DB1, L = 30 m, $D_{\text{int}} = 0.53 \text{ mm}$, $D_{\text{f}} = 3 \mu\text{m}$	FID/MS	Hydrocarbons + oxygenated species	He: 0.7 mL/min
Shimadzu QP2010-SE	CP- $\text{Al}_2\text{O}_3/\text{KCl}$, L = 50 m, $D_{\text{int}} = 0.32 \text{ mm}$, $D_{\text{f}} = 5 \mu\text{m}$	FID/MS	Hydrocarbon species	He: 0.7 mL/min
Varian 3300	CP-Carboplot P7, L = 25 m, $D_{\text{int}} = 0.32 \text{ mm}$, $D_{\text{f}} = 1.2 \mu\text{m}$	TCD	H_2 and O_2	N_2 : 15 mL/min

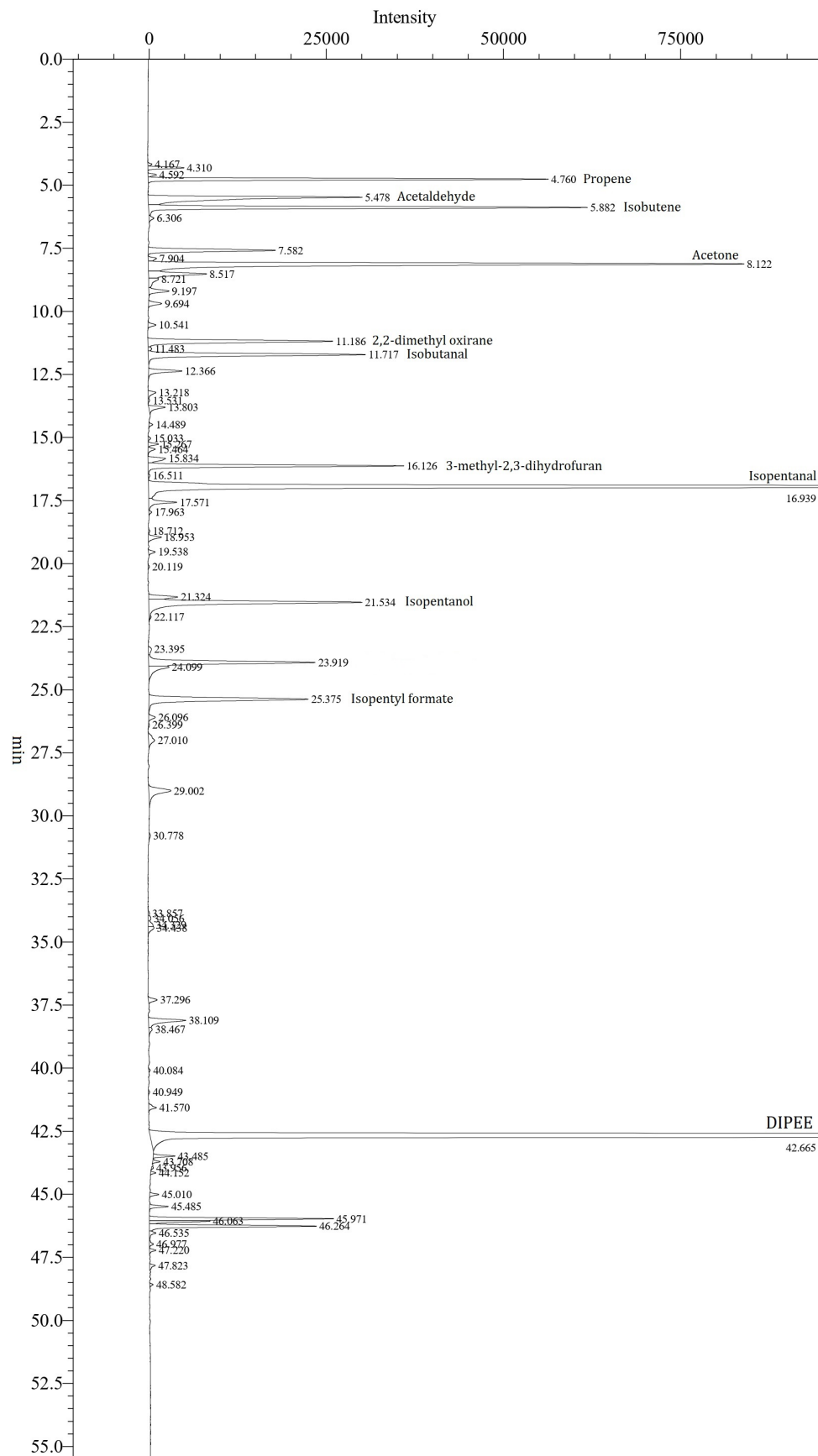


Figure 3.2: Example of the chromatogram obtained through gas chromatography analysis from the GC Shimadzu QP2010-SE equipped with CP-SIL 5CB column (DIPEE, $\phi = 1$, 650 K, 10 atm, $\tau = 700$ ms).

3.2 Rapid Compression Machine

Rapid compression machines (RCMs) are important facilities in gas-phase kinetics, providing experimental data on the global reactivity of fuel oxidation. A thorough review on the design and advances on RCM has been given in Goldsborough et al. [94], with a focus on the applications in the study of low- and intermediate-temperature phenomena.

The set-up of an RCM simplifies the design of a common engine: a cylindrical combustion chamber (similar to an engine cylinder) is filled with a mixture of vaporised fuel, oxygen and inert gases and a piston compresses the reactants over a short time. The pressure in the chamber is measured and is used to determine the ignition delay time, i.e. the time interval between the end of the compression (when the piston reaches its top-dead center) and the ignition. Rapid compression machines are particularly useful for low/intermediate temperature and high pressure conditions, which can be similar to what is experienced in engines, as can be seen in Figure 3.3.

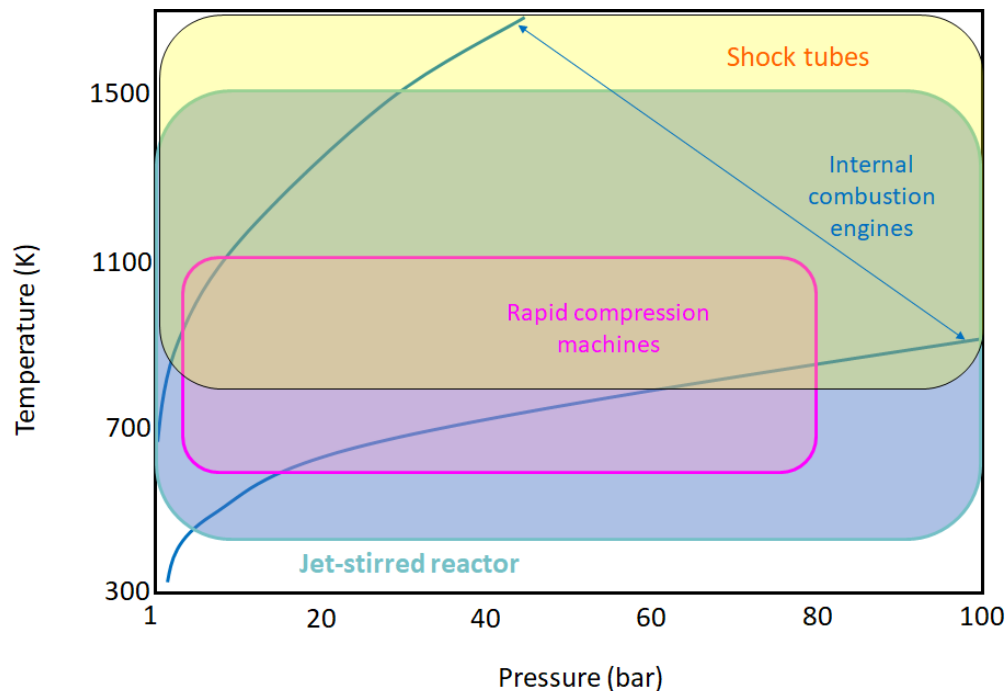


Figure 3.3: Pressure and temperature conditions of engines and experimental devices (adapted from [94]).

Over the years, different studies have been published, both based on experiments and CFD calculations, in order to prove the homogeneity of the reacting core in the combustion chamber and to improve the design of this kind of experimental device. In fact, since the simulations involving big kinetic mechanisms can become very time and resource consuming, it is necessary to be able to simulate the experimental results obtained through 0D models. In order to do so, the assumption of a homogeneous reacting core is necessary. In reality, the formation of a colder boundary

layer and related roll-up vortex might create a temperature gradient in the chamber and result in inhomogeneous ignition. This problem has been partially solved through the use of creviced piston heads, which capture the boundary layer and prevent its mixing with the hotter core. In this way, the core can be supposed homogeneous, 0D models can be used and the temperature at the end of the compression can be computed by assuming that the core is adiabatic:

$$\int_{T_0}^{T_c} \frac{\gamma}{\gamma-1} \frac{dT}{T} = \ln \frac{p_c}{p_0} \quad (3.2)$$

where $\gamma = c_p/c_v$, p_c and T_c are the pressure and temperature at the end of the combustion and p_0 and T_0 are the initial pressure and temperature.

Nevertheless, heat losses and facility effects are still present in each experimental set-up. In order to take this into account in the simulation, the hypothesis of an expanding adiabatic core is employed. For each condition tested (mixture, compressed temperature and pressure), a test with a non-reactive mixture where oxygen is replaced by nitrogen is performed. From the pressure profiles of these tests, volume-time histories are computed, allowing to consider the facility effects during the simulations. The validity of this simplification has been discussed by Mittal [95]. Although in the case of two-stage ignition the error of the simplified 0D model is bigger than in the case of single-stage ignition, the conclusion is that this simplification still leads to acceptable results, when considering the lowest overall cost.

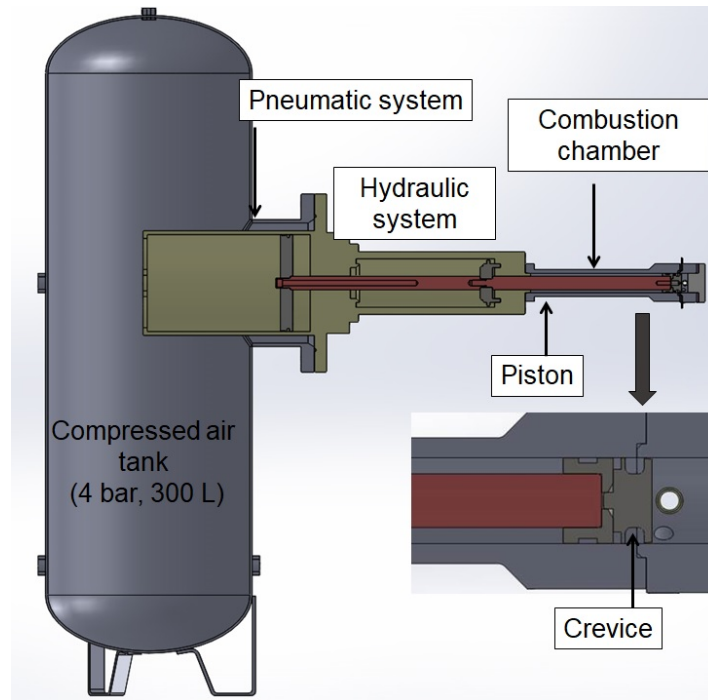


Figure 3.4: Simplified scheme of the rapid compression machine in PRISME laboratory (University of Orléans).

The rapid compression machine used in this work is located in PRISME laboratory, at University of Orléans. A simplified experimental set-up scheme is reported in Figure 3.4. This RCM is a single-piston machine, which is pneumatically driven and hydraulically controlled. Some of its characteristics are reported in Table 3.3, more can be found in a detailed description given by Pochet [96].

Table 3.3: Characteristics of the rapid compression machine in PRISME laboratory.

Stroke	200–250–300 mm
Piston diameter	50 mm
Compression ratio	4–14.5
Maximum piston velocity	11.5 m/s
Compression time	35 ms
Crevice volume	4.82 cm ³
Intake temperature	20–180°C

The mixture to be tested is prepared in a separate tank, which is heated in order to avoid condensation and mechanically mixed in order to ensure homogeneity. All the valves and connections between the mixing tank and the combustion chamber are also heated to a temperature higher than the saturation temperature, in order to avoid the condensation of the liquid fuel. The mass of liquid fuel is measured with a high-precision scientific scale (Phoenix instrument BTG-3030) and injected in the tank with a syringe. The different gases composing the mixture are introduced in the tank using a mass flow controller (CORIFLOW M13-Bronkhorst), which is in turn controlled with an in-house program developed through LabView. The initial temperature of the whole set-up can be controlled, giving the possibility to obtain different temperatures in the combustion chamber at the end of the compression without needing to change the compression ratio. For all the tests performed, the compression ratio has therefore been kept constant, even if the RCM was designed in such a way to allow a wide range of compression ratio. More details on this decision will be given in Section 3.2.1.

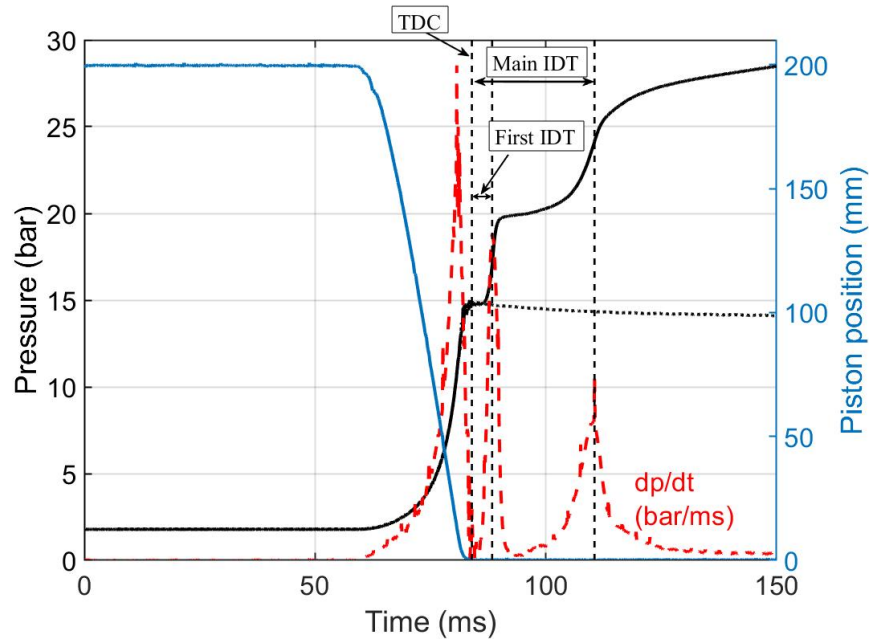


Figure 3.5: Example of the data measured in the RCM: in black, pressure profiles for reactive (solid) and non reactive (dashed) mixtures, in blue, the position of the piston and in red, the first derivative of the pressure for the reactive test. Top dead center (TDC) and ignition delay times (IDTs) are also indicated. (DEE, $\phi = 1$, dilution = 10 (fuel initial mole fraction: 1.5%), $T_c = 596$ K, $p_c = 14.8$ bar).

Concerning the diagnostics, the intake temperature is measured through a type K thermocouple (accuracy ± 1 K). A piezoresistive transducer, AVL QC34C, is used to measure the pressure inside the combustion chamber and the position of the piston is also recorded in order to identify the exact time of the end of the compression (piston at the top dead center). An example of the recorded pressure trace and piston position can be seen in Figure 3.5, along with the first derivative of the pressure, which is used in order to identify the ignition delay times. The data collected from the experimental runs are then post-processed through an in-house Matlab script developed in this study that detects the pressure at the TDC, computes the temperature using the adiabatic core assumption and determines the ignition delay time by computing the first derivative of the pressure. The volume profiles that are used to take into account the facility effects during the simulations are also computed through a Matlab script developed in this study, also by assuming an adiabatic expansion of the core gas. A typical pressure profile for a non reactive mixture and its computed volume profile are shown in Figure 3.6.

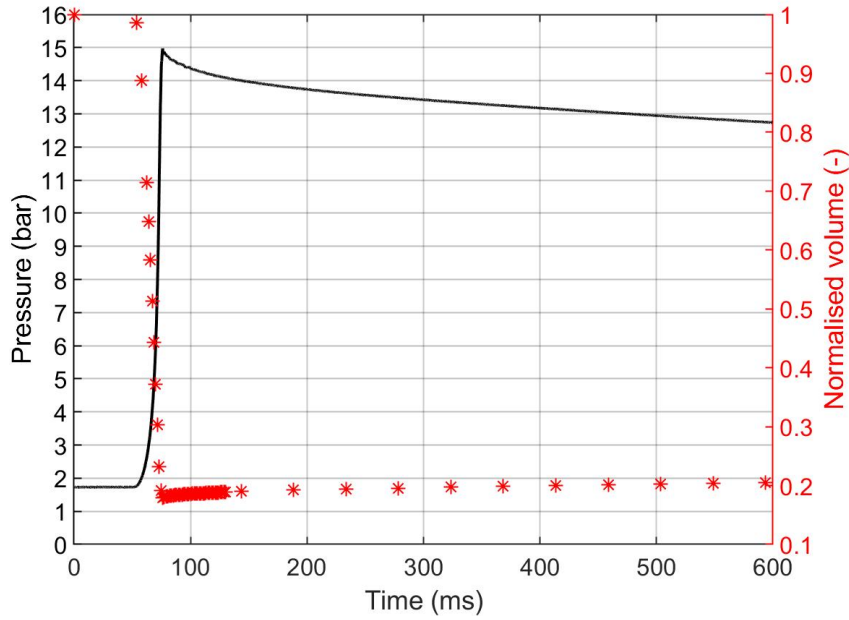


Figure 3.6: Example of a test with a non reactive mixture: in black, the measured pressure profile, in red the computed normalised volume profile used in the simulations (DIPE, $\phi = 2$, dilution = 5 (fuel initial mole fraction: 3.6%), $T_c = 501$ K, $p_c = 14.8$ bar).

Seven ethers were studied in the rapid compression machine (Table 3.4). Since it may be of interest to compare their relative reactivities, similar conditions were selected when possible. In addition, ethyl lactate, a molecule also presenting an ether function, has been studied in the RCM, but under different conditions due to its much lower reactivity. All of the conditions tested are reported in Table 3.4. An additional analysis on the heat release rate has been performed for some conditions. This required a different acquisition system that was implemented specifically for this kind of analysis. A separate computer was coupled with an acquisition card (PCi NI 6123, 16 bits, ± 10 V, 500 kSamples/second/channel), in order to obtain a better time resolution of the pressure signals (acquisition frequency of the previous system: 6.67 Hz). Following the theory explained by Goldsborough in [97], the heat release rate was computed with the following formula:

$$HRR = \frac{\gamma}{\gamma - 1} \frac{dV}{dt} [P - P_{nr}] + \frac{1}{\gamma - 1} V \left[\frac{dP}{dt} - \frac{dP}{dt} \Big|_{nr} \right] - \frac{PV}{(\gamma - 1)^2} \left[\frac{d\gamma}{dt} - \frac{d\gamma}{dt} \Big|_{nr} \right] \quad (3.3)$$

The analysis performed on the heat release will be further discussed in section 4.3.

Table 3.4: Tested fuels and experimental conditions in the rapid compression machine in Orléans (dilution is defined as the inert gases molar fraction over oxygen molar fraction)

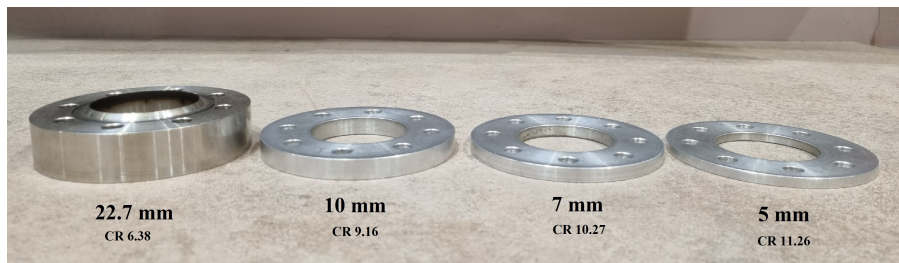
Fuel	Dilution	ϕ	% Fuel	p (bar)	T (K)
DEE	10	0.5	0.8	15	450–700
		1.0	1.5		500–750
		2.0	2.9		500–700
	5	0.5	1.37	15	530–605
DPE	10	0.5	0.5	15	450–700
		1.0	1.0		500–750
		2.0	2.0		500–700
DIPE	5	0.5	0.9	15	860–970
		1.0	1.8		535–870
		2.0	3.6		500–700
	10	2.0	2.0	15	500–900
	3.76	0.5	2.28	15	590–915
BEE	5	0.5	0.9	15	535–615
		1.0	1.8		530–640
		2.0	3.6		535–630
	10	1.0	1.0	15	540–640
2.0	1.98	540–720			
DBE	5	0.5	0.7	15	530–650
		1.0	1.4		530–650
		2.0	2.7		520–650
	10	1.0	0.8	15, 20	535–680
2.0	1.5	15			
DNPEE	5	0.5	0.5	15	530–630
		1.0	1.1		520–620
		2.0	2.2		530–600
	10	1.0	0.6	15, 20	570–760
2.0	1.2	15			
DIPEE	5	0.5	0.5	15	540–630
		1.0	1.1		530–620
		2.0	2.2		530–600
	10	1.0	0.6	15, 20	580–840
2.0	1.2	15			
Ethyl lactate	3.76	0.5	1.72	20	822–919
		1.0	3.38	20, 30	824–925
		1.5	4.99	20	788–885

3.2.1 Preliminary study on the RCM configuration

Ignition delay times measured in rapid compression machines can be sensitive to different parameters. As already stated before, facility effects (as for example heat losses) are usually taken into account through the use of volume profiles and with the assumption of the adiabatic core region. Nevertheless, in the beginning of this study it has been noticed that also the compression ratio could influence the ignition delay times. In particular, in this specific facility it is possible to change the compression ratio by changing a wedge at the end of the combustion chamber, which in turn changes the volume at the top and bottom dead centres. Some of the wedges used in this work are shown in Figure 3.7, with different thicknesses of 22.7 mm, 10 mm, 7 mm, 5 mm (included in the figure), 12.7 mm, 3 mm and 1 mm (not shown in the figure). Figure 3.8a shows the ignition delay times obtained for a mixture of DEE/air at a compressed pressure of 3 bar (in this preliminary part, the initial aim was to obtain results in comparable conditions as the ones used by Werler [51]). Four wedges have been used and Figure 3.8a shows that the measured ignition delay times are quite different. Taking for example a compressed temperature around 655 K, it is possible to see that the IDT is ranging from 66.8 ms (wedge of 7 mm) to 15.6 ms (wedge of 35.7 mm). This variation is not linear with the variation of the thickness of the wedge. In fact, we noticed that increasing the thickness of the wedge was leading to a convergence of the resulting ignition delay times. A trade-off between the thickness of the wedge (which implies the compression ratio) and the temperature range that was reachable was therefore necessary, leading to the decision of keeping the wedge constant, with a thickness of 27.7 mm.

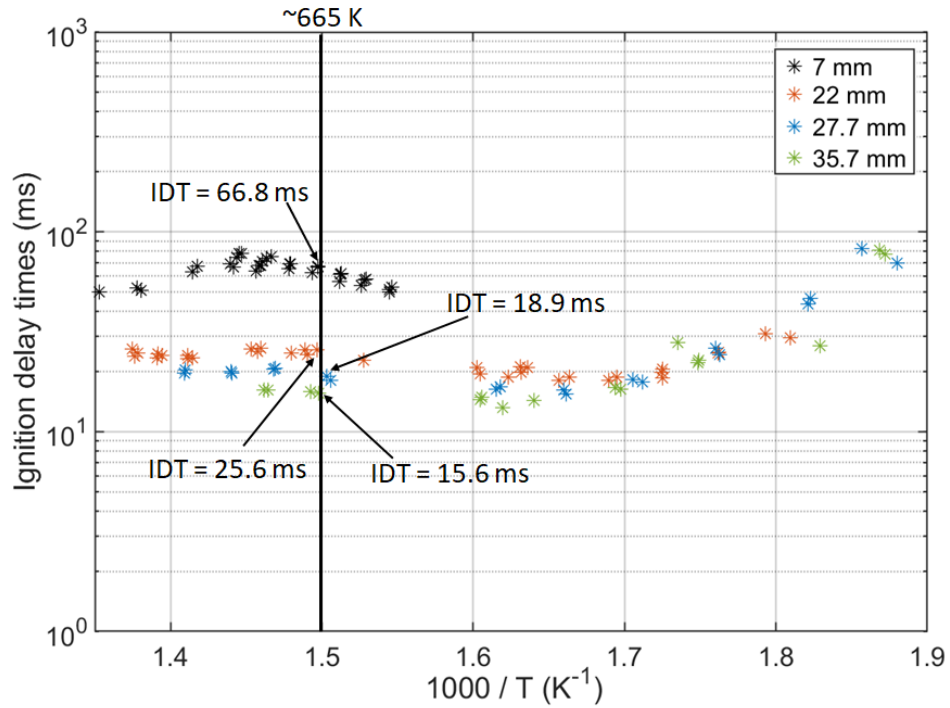


(a) Top view of the wedges (with thickness)

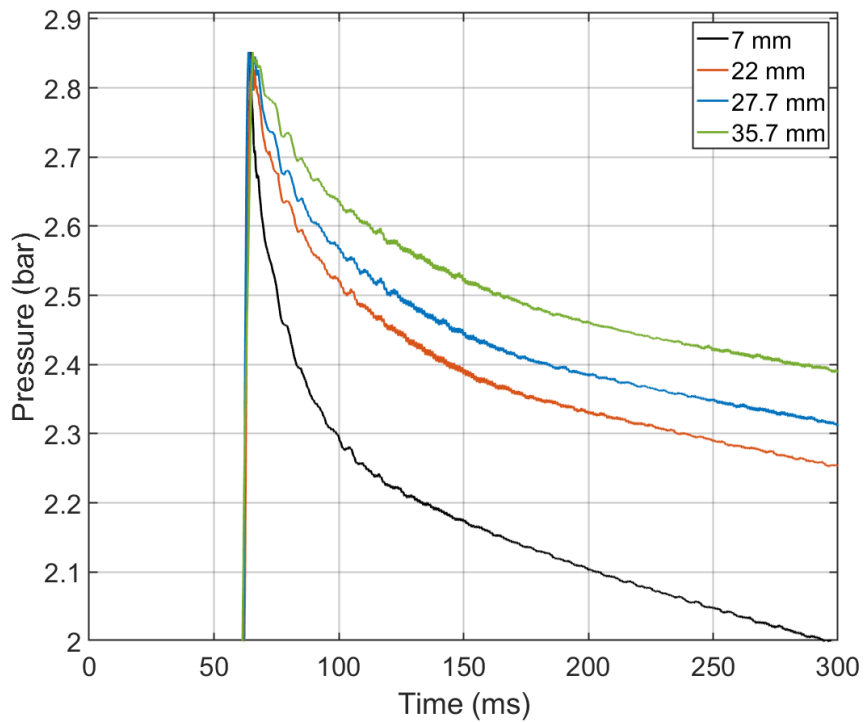


(b) Side view of the wedges (with thickness)

Figure 3.7: Photos of some of the wedges that were used in this work.



(a) IDTs obtained using different wedges for a mixture of DEE, $\phi = 1$, dilution in "air", $p_c = 3$ bar



(b) Tests with non-reactive mixture (DEE, $\phi = 1$, dilution in "air") at the same $T_c = 665$ K, using different wedges

Figure 3.8: Influence of the different compression ratio on a) the ignition delay times, b) the pressure decrease in the tests with non-reactive mixture (DEE, $\phi = 1$, dilution in "air", $p_c = 3$ bar).

It is interesting to have a deeper look at the effect that this parameter can have. In order to do that, a comparison of pressure profiles obtained for non-reactive mixtures was performed. Non-reactive mixtures have been selected for this analysis in order to rule out any effect on the pressure caused by combustion reactions that may happen even before the ignition. The resulting plot is shown in Figure 3.8b. It is possible to see that the lowest thickness of the wedge is leading to a greater and faster pressure decrease in the profile obtained for a non-reactive mixture, while the profiles obtained in the configurations with a wedge over 20 mm thickness show a slower pressure decay. The conclusion that can be obtained from this comparison is that the thinner wedge enhances the heat losses, probably imputable to a less effective capture of the vortices by the crevice. This effect was also shown by Mittal et al. in [98], where they performed CFD simulations in order to assess the effect of compressed pressure, stroke length and clearance on the vortex roll-up. They showed that increasing the clearance, as well as decreasing the stroke length, led to a smaller vortex formation. Therefore, the configuration chosen for this work was one with a shorter stroke (200 mm) and a sufficiently thick wedge (27.7 mm), while still being able to reach an interesting range of temperature for the studied fuels. Also, the compressed pressure of 3 bar was deemed as too low, both for vortex effect and for the noise on the pressure signal. The optimal conditions for this RCM were evaluated to be over 10 bar, all the tests were therefore performed at 15 bar, with some fuels tested also at 20 bar under some conditions.

3.3 University of Galway facilities

In complement, ignition delay times for two of the above mentioned ethers (DPE and DIPE) have been measured in the facilities of the Combustion Chemistry Centre at the University of Galway. A high pressure shock tube, presented in Section 3.3.1, was used for the high temperature range, while a twin-piston rapid compression machine (Section 3.3.2) was used to fill the intermediate temperatures between the maximum obtainable temperature in the RCM in Orléans and the minimum temperature achievable in the shock tube.

3.3.1 High Pressure Shock Tube

The high pressure shock tube in the Combustion Chemistry Centre of the University of Galway has been employed in order to measure ignition delay times at high temperatures. A comprehensive description can be found in previous publications of the Galway team [99, 100].

The driver section is 3 m long, while the driven section is 5.7 m long, and both have an internal diameter of 63.5 mm. The two sections are separated by a 3 cm diaphragm section, which employs two pre-scored aluminium diaphragms, with a thickness varying from 0.8 to 2 mm, depending on the pressures used in the system. Helium is used as a driver gas, while the tested mixtures are diluted in nitrogen. Six pressure transducers (PCB; 113A24) on the sidewall and one at the endwall

(Kistler; 603B) were used to determine the velocity of the incident shock wave. This velocity is then used in the program Gaseq [101] in order to determine the temperature of the mixture behind the reflected shock, while the pressure was measured thanks to the sensor on the endwall. A heating system is employed on the shock tube, in order to avoid condensation of the fuel in the tested mixture. The ignition delay times were computed as the interval between the rise in the pressure due to the shock wave and the maximum rate of rise of OH*. The OH* concentration was determined thanks to a photomultiplier placed on the endwall and equipped with the OH* filter FBH300-10 (CWL: 300 nm ± 10 FWHM) by Thorlabs. The mixtures that have been tested in the high-pressure shock tube and the considered conditions are summarised in Table 3.5

Table 3.5: Tested fuels and experimental conditions in the high-pressure shock tube.

Fuel	Dilution	ϕ	% Fuel	P (bar)	T (K)
DPE	10	0.5	0.5	15	1050–1415
		1.0	1.0		1000–1450
		2.0	2.0		960–1510
DIPE	5	0.5	0.5	15	1005–1475
		1.0	1.0		1000–1510
		2.0	2.0		1010–1510
	10	2.0	2.0	15	1110–1510

3.3.2 Rapid Compression Machine

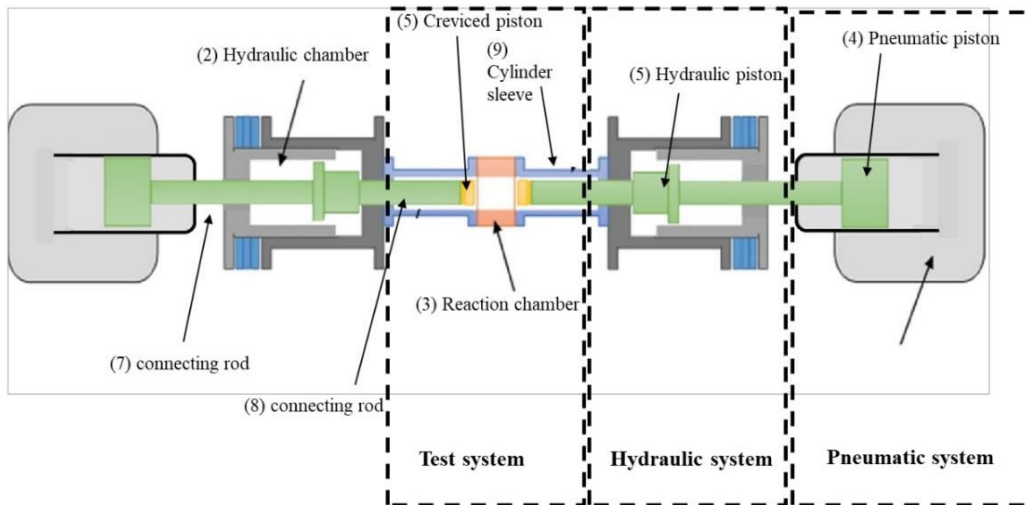


Figure 3.9: Simplified scheme of the RCM at the university of Galway (courtesy of C3 Galway).

The rapid compression machine at the university of Galway has a very different design compared to the one in PRISME laboratory, as it employs two synchronised pistons to compress the tested gaseous mixtures. This set-up has been previously described in [102, 103] and a simplified scheme

is shown in Figure 3.9. The movement of the two pistons allows for a shorter compression time (around 16 ms) compared to the time of the single piston RCM in Orléans (around 35 ms). Both pistons have a creviced head, in order to avoid inhomogeneity caused by the vortex roll-up during compression. Similar to the other RCM, the set-up is heated, in order to avoid fuel condensation. Moreover, the temperature can be controlled in order to achieve different compressed temperatures without the need of changing the composition of the inert gases in the mixture. The pressure signal in the cylinder is recorded through a pressure transducer (Kistler 603B) and the ignition delay times were computed as the interval between the end of the compression and the maximum rate of the pressure rise, as already explained for the other RCM. The compressed temperature is computed using the adiabatic core assumption. Similarly to what is already explained in Section 3.2, tests with a non reactive mixture where oxygen is replaced with nitrogen are performed, in order to obtain volume profiles that can be used to take into account the facility effects when the simulations are performed. Table 3.6 reports the mixtures and conditions that were studied in this rapid compression machine, allowing to represent ignition delay times over a wide range of temperatures.

Table 3.6: Tested fuels and experimental conditions in the rapid compression machine in Galway.

Fuel	Dilution	ϕ	% Fuel	P (bar)	T (K)
DPE	10	0.5	0.5	15	770–940
		1.0	1.0		750–930
		2.0	2.0		660–850
DIPE	5	2.0	2.0	15	715–925

3.4 Uncertainty of measurements

The experimental data collected from the different set-ups presented in the sections above are used in order to validate and improve the kinetic model for the combustion of these fuels. It is therefore important to have an estimate of the possible uncertainties in the measurements.

3.4.1 Jet-stirred reactor

Different sources of uncertainty are possible in the jet-stirred reactor. First of all, the temperature, measured using a thermocouple, can have an uncertainty of around ± 5 K, which is linked to both the precision of the thermocouple itself and to the actual homogeneity inside the reactor.

Another factor that must be considered is the real composition of the mixture which is oxidized inside the reactor. All mass flow meters are regularly calibrated, with a R^2 coefficient of the calibration curve always greater than 0.995 (as can be seen in Figure 3.10). Nevertheless, some small errors are possible, linked mainly to the conversion of the voltage which controls the flow.

Considering the quantification of the intermediate species, the conversion of the areas of the peaks to mole fractions can also lead to some uncertainty. In fact, for some species it is possible to have a direct calibration, which leads to a small possible error, but for other species, it is necessary to estimate a conversion coefficient through the rule of the effective carbon number (ECN) [93], which is less accurate. In order to take into account all of these possible uncertainties, it has been estimated that an overall uncertainty of 15% should be applied.

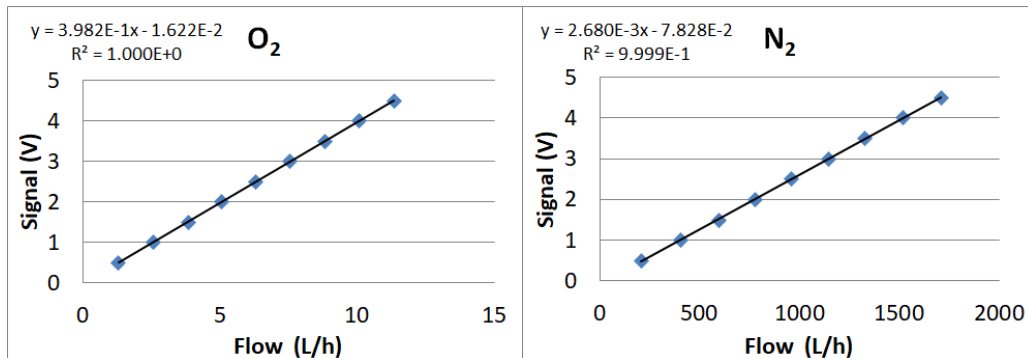


Figure 3.10: Example of calibration curves of two of the flowmeters used in the jet-stirred reactor set-up (one for oxygen and one for nitrogen).

3.4.2 Rapid compression machine

Similar to the jet-stirred reactor, some source of uncertainties can be identified for the rapid compression machine. First of all, the initial temperature imposed to the mixture through the heating of the machine is measured in different points of the cylinder itself, leading to a quite good accuracy. The accuracy of the thermocouple is ± 1 K, but small differences (± 0.5 K) can be found between the different locations, therefore the uncertainty on the initial temperature is estimated to be around ± 2 K. This leads to an uncertainty on the compressed temperature of less than 1%. Concerning the mixture composition, the digital flow meter has a good precision, while the fuel is injected through a syringe, leading to a bigger uncertainty. The quantity of fuel which is injected is recorded every time and compared to the desired value; the effective equivalence ratio is also checked and the maximum difference from the desired value has been found to be 2%. The repeatability of the tests has been checked thanks to at least three shots for each condition. In general, when the tests are performed from ignition delay times in the reliable operational zone (2–200 ms), the maximum uncertainty found is around 10% (but in general lower, as shown in Figure 3.11 for example). In some cases, tests have been performed for the same conditions at different times (after several months) and the repeatability is proven to be very good.

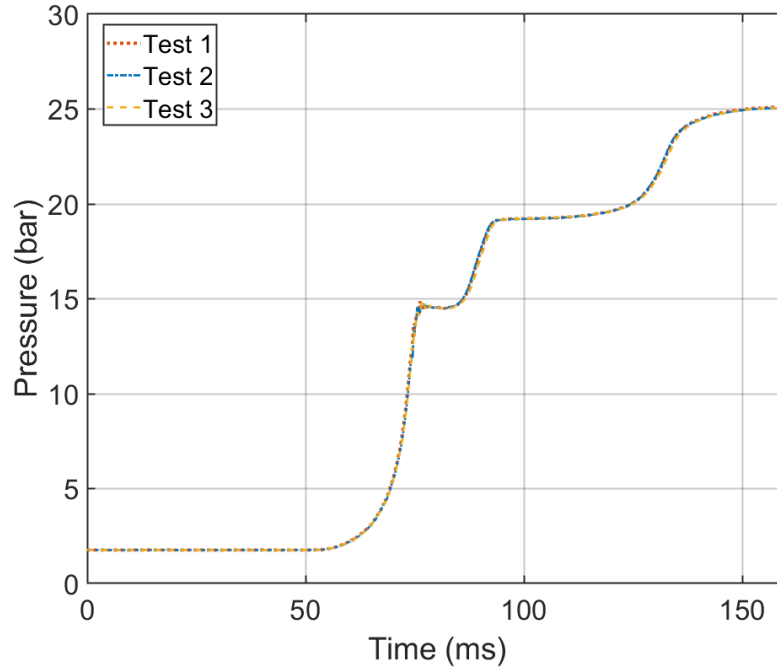


Figure 3.11: Example of repeated shot for a condition in the RCM (di-*n*-propyl ether, $\phi = 1$, $p_c = 15$ bar, $T_c = 587$ K).

3.4.3 University of Galway facilities

Concerning the experimental facilities provided by the University of Galway, the uncertainties in the measurements can be found in the literature, as provided by their team.

The ignition delay times measured in the rapid compression machine of the University of Galway are estimated to have an uncertainty of around 15% [102, 103], quite similar to the RCM in PRISME. Considering the shock tube, different uncertainties are described in previous works [99, 100]: the IDTs are estimated to have an uncertainty of around 20%, while the temperatures after the shock are expected to be in a range of $\pm 0.5\%$. Finally, the mixture composition shows an uncertainty of 0.5%, which can be expected also in the case of the RCM, since the preparation of the mixture follows the same procedure in the two facilities.

Chapter 4

Modelling, simulations and analysis

In this chapter, the construction of the detailed kinetic model for each fuel is discussed. For some of them, already available mechanisms have been updated and improved, while others had to be developed from scratch. In the second section, the simulations performed through ChemkinPRO are discussed, with some details on each model used. In the third part, the analysis on the heat release rate in the RCM is further discussed and some other information are added on the post-processing of the data.

Contents

4.1 Construction of the model	42
4.1.1 DEE, DPE, DIPE, DBE	42
4.1.2 BEE	44
4.1.3 DIPEE	45
4.1.4 Ethyl lactate	46
4.2 Simulations	47
4.2.1 Chemkin files	47
4.2.2 Chemkin models	48
4.3 Further analysis	49

Introduction

Interest in oxygenated compounds applications has been growing in the latest decades. Both experiments and kinetic modelling studies have therefore become of paramount importance towards the understanding of the mechanism governing the combustion of these fuels. In the past few years, our team has focused on the kinetic modelling of several fuels of the ether family, together with the collection of experimental data allowing to develop and improve the mechanisms.

The following section will present the construction and improvement of this kinetic model, which aims to capture the behaviour of all of the molecules in this family and to relate their behaviour to their structure. Direct calculations to obtain the reaction rates and thermochemistry of the species would be the most accurate way of predicting the reactivity; nevertheless, it is expensive and time consuming. Most of the reaction rate constants will therefore be taken by analogy, given that ethers have been little studied in the literature for one to be able to have specific rates computed for each reaction.

The process of simulating the results is also explained, showing how the physics of the real set-ups can be simplified to 0D models, which allow to have reasonably good results, without the overcomplication of CFD modelling. A final section discusses the heat release rate in the rapid compression machine. This is a very interesting part, since very few studies in the literature have dealt with this kind of analysis, especially concerning the comparison of the experiments with the simulations. Nevertheless, it requires a certain attention in the post-processing of the measured pressure traces in order to have meaningful results, which is why a further section is devoted to this analysis in this chapter.

4.1 Construction of the model

Detailed kinetic mechanisms of some of the ethers were already available from the previous studies of our group. In these cases, the mechanisms were tested against the new experimental data and improvements were made, when necessary. For other ethers, i.e. butyl ethyl and di-*iso*-pentyl ethers, and for ethyl lactate no mechanism is available in the literature, therefore they have had to be developed from scratch. The next section will resume some of the most important reactions in the mechanisms already available and will discuss the modifications done. Then, a specific section for each newly developed sub-mechanism will include the main reactions and the choice of their rate constants for BEE, DIPEE and ethyl lactate. The core mechanism was the same for all these molecules, i.e. a sub-mechanism for ethanol and other smaller species (C_0 – C_2) that was developed in ICARE.

4.1.1 DEE, DPE, DIPE, DBE

As explained above, for these four ethers the mechanisms available in the previous studies of our team [12, 57, 68, 76] were used as a starting point. In particular, for diethyl and dibutyl ether no major modifications were applied, since the mechanism performed reasonably well when compared to the new experimental data, which were therefore used as a further validation. On the other hand, the next sections will present the modifications that were applied to di-*n*-propyl and di-*iso*-propyl ether mechanisms.

DPE

As a starting point, the mechanism presented by Serinyel in [57] was considered. The mechanism was performing already quite well, but some small modifications are brought, as follows:

- hydrogen abstraction from the fuel by OH at the α -site is no longer taken from Zhou et al. [104], but is estimated by analogy with DEE. For the α -site of DEE the rate constant is evaluated using the total (α - and β -sites) rate constant measurements from the literature and is fit to a modified Arrhenius expression for the α -site while considering the β -site to be analogous to an n -alkane;
- unimolecular decompositions of the fuel are taken by analogy to Cook et al. [105] and Lizardo-Huerta [106] for alcohol elimination;
- it should also be noted that after the work of Belhadj et al. [58], more possible low-temperature reactions have been included, since the analysis of low-temperature products showed that all of the possible radicals were actually formed.

DIPE

The mechanism for di-*iso*-propyl ether is a little different from the other ethers of this section. In fact, a mechanism was already available from a previous work published in 2022 [68]. Nevertheless, in the experiment performed in the JSR under those specific conditions ($p = 10$ atm, $\tau = 700$ ms, initial fuel fraction: 1000 ppm), DIPE showed no low-temperature reactivity, therefore in that mechanism no reactions specific to that oxidation regime were included. In the experimental tests performed in the RCM in this study, DIPE shows low-temperature reactivity, implying the necessity to include the specific reaction classes in the mechanism. The rate constants for the reactions specific to the low-temperature regime are determined as follows:

- the first fuel radical addition to oxygen is taken from Goldsmith [107] and the second oxygen addition is taken as half of the first addition, similarly to that used for the other ethers;
- the reaction rates of the β -scissions of the QOOH radicals are taken either by similarity to what was assumed for DEE from Sakai [108];
- the rates for the formation of cyclic ethers from the QOOH radicals are also taken from the calculations of Villano et al. [109];
- the decomposition of the carbonyl-hydroperoxides are taken by similarities to the ethers previously studied [12, 57, 76];
- all of the others low-temperature reaction rates are also taken by analogy with the other ethers previously studied by our team [12, 57, 76].

Some reactions that were already included in the original mechanism are also worth mentioning:

- the unimolecular decompositions of the fuel are taken by analogy with MTBE as proposed by Benson [110] and to DME, increasing the activation energy by 1 kcal/mol, since the bond energy is expected to be higher;
- hydrogen abstraction by OH radicals was taken by similarity to isopropyl methyl ether for the α -site, as calculated by Zhou et al. [104];
- the same reaction for the β -site was taken by a fit based on the calculations of Zador [111], Zhou [112], Truhlar [113] for 1-butanol and of Droege et al. [114] for *n*-butane, but slowed down by a factor of two, since this C–H bond is expected to be slightly stronger;
- hydrogen abstraction by HO₂ radicals were estimated from Mendes [115] by analogy to isopropyl methyl ether.

No major modifications were made to the reaction rate constants already present in the mechanism proposed by Serinyel et al. in [68]. The major difference was therefore the inclusion of the low-temperature reaction classes.

4.1.2 BEE

The butyl ethyl ether sub-mechanism was developed and added to the ethanol core mechanism, similar to the other ethers previously studied. Both low- and high-temperature reaction classes were included. Since BEE shares a side chain with DEE and one with DBE, most of the reaction rate constants have been taken by analogy to these two other ethers previously studied by our team. The following list presents some of the choices made for the important reactions:

- hydrogen abstractions by OH and CH₃ radicals were estimated by analogy to DEE and DBE in the previous work by our team [12, 76];
- hydrogen abstractions by HO₂ radicals were estimated by analogy to butyl methyl and ethyl methyl ethers in the work of Mendes [115];
- β -scission reactions of the radicals of the fuel were also estimated by analogy to either DEE or DBE;
- the first fuel radical addition to oxygen is taken from Goldsmith [107] and the second oxygen addition rates were taken as half of the first addition rates, similarly to what was used for the other ethers;

- the isomerisation of RO₂ radicals to QOOH are taken from the computations of Villano et al. [109];
- the decomposition of the carbonyl-hydroperoxides are taken to be similar to the ethers previously studied [12, 76];
- the unimolecular decomposition reactions of the fuel are taken by analogy from the studies of Lizardo-Huerta [106] for alcohol elimination and from Cook et al. [105] or from similarity to the other ethers concerning the other decomposition reactions.

4.1.3 DIPEE

The sub-mechanism for DIPEE was developed mainly by analogies with the other ethers or to similar molecules, since no direct calculations were available on the most important reactions. The rate constants adopted from the literature for some of the most important reactions were chosen as follows:

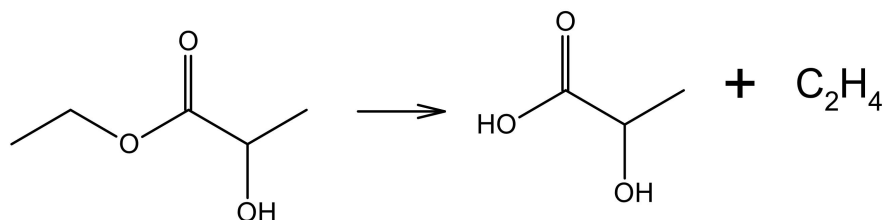
- hydrogen abstraction by OH on the β C-H site of the fuel is taken from the calculations performed for *n*-butanol in [112, 116], while for the α -site the rate constant is taken by similarity to di-*n*-propyl ether in [57];
- the hydrogen abstractions by OH on the γ - and δ -sites are both taken from Cohen [117], in analogy to respectively the tertiary and the primary carbons in an alkane;
- similar consideration are made for the hydrogen abstractions by H atoms on the γ - and δ -sites;
- H-abstraction reaction by H atoms on the α - and β -sites are taken similarly to DPE, from Ogura [118] and by analogy to alkanes;
- similar considerations were made for the H-atom abstractions by HO₂ and by CH₃ radicals, for which the rate constants were taken respectively from Mendes [115] and Aguilera [119] and from Xu [120];
- in accordance with the rate constants adopted for the other ethers, the rate constants for the first oxygen addition ($R+O_2 \rightleftharpoons RO_2$) are taken from Goldsmith [107], while for the second addition to oxygen, the rate constants were taken as half the ones for first addition;
- rate constants for the β -scission reactions of the fuel radicals are taken as similar to DBE in [76];
- rate constants for the β -scission reactions of QOOH radicals are adopted from the theoretical calculations performed by Villano et al. [109];

- other reactions that might be important in the low-temperature reactivity are estimated by analogy to the other ethers already presented [12, 57, 68, 76];
- the unimolecular decompositions of the fuel are taken by analogy from the studies of Cook et al. [105] and Lizardo-Huerta [106] for alcohol elimination.

4.1.4 Ethyl lactate

Similar to the other ethers, for which no mechanism was available in the literature, the ethyl lactate kinetic model has been developed and joined to the ethanol sub-mechanism. The specific reactions for ethyl lactate, its radicals and the main products were added. When possible, rate parameters have been taken from direct calculations; in the other cases, analogies were used to estimate the rate constants of the reactions. It should be noted that, based on the experiments performed in this work and therefore in these specific conditions, no low-temperature reactivity was detected. Therefore, only the high-temperature reactions classes are included in the model. Here is a list of the most important reactions that are in the mechanism and from where their reaction rates were taken:

- H-atom abstraction reactions by H atoms and CH₃ radicals have been taken from the calculations of Würmel et al. [88];
- H-abstraction by HO₂ radicals on the tertiary side (neighbouring the carbonyl and the OH groups) has been considered similar to isopropanol in [121], but multiplied by a factor of four to take into account the proximity of the carbonyl group;
- the same previous H-atom abstraction, but performed by H atoms, has been taken from the calculations proposed by Mendes et al. [122], this time by analogy to iso-butanal;
- the rate constants for the H-atom abstraction reactions on the α -site neighbouring the ether group by HO₂ radicals were taken by comparison to the ones for *n*-butanol used by Zhou et al. [112] and multiplied by a factor of two;
- the rate constants for the same previous reaction performed by OH radicals were taken by analogy with DEE [12];
- the rate constant for the molecular elimination of ethylene producing lactic acid:



was taken as that of propyl acetate proposed by Dayma et al. [123]. The same rate constant was also used for the unimolecular reactions of some of the main products of ethyl lactate (ethyl pyruvate, ethyl glycolate);

- β -scission reactions of the primary fuel radicals were all estimated by analogy with similar radicals: 1-pentanol radicals [124], ethyl acetate radicals [125] and butyl formate radicals [126].

The thermochemistry of the species involved (fuel, radicals, products) is also very important and can have a deep impact on the resulting simulations. When calculations were available in the literature, the specific thermochemistry of the species has been used. In the other cases, the thermochemistry has been estimated by the group additivity method proposed by Benson [127].

4.2 Simulations

All of the simulations presented in this work were performed using the ChemkinPRO software by Ansys [128]. Two different models were used to simulate the jet-stirred reactor and the rapid compression machine, but both rely on the same files for the description of the mechanism, one for the reactions and their rate constants and one for the thermodynamic properties of the species involved. These two input files will be discussed in the next section, while the models for the JSR and the RCM are presented in Section 4.2.2.

4.2.1 Chemkin files

One of the files required in Chemkin is the mechanism file. The first part of this file (extension .inp) is used to declare the elements that will be involved in the reactions (usually H, C, O, N, Ar, He) and the species that will interact. Following this, the reactions considered in the mechanism are listed, with their rate constants expressed through modified Arrhenius law:

$$k = A \times T^n \times \exp\left(-\frac{E_a}{RT}\right) \quad (4.1)$$

where T represents the temperature (in Kelvin) and R is the ideal gas constant ($1.987 \text{ cal} \times \text{K}^{-1} \times \text{mol}^{-1}$). The other parameters should be included in the file and are defined as follow:

- A : pre-exponential factor or frequency factor, it is expressed in $\text{mol} \times \text{cm}^{-3} \times \text{s}^{-1}$;
- n : exponential factor, it has been added in the modified form of Arrhenius law for bimolecular reactions in order to represent the dependence of the pre-exponential factor on temperature. It has no units;

- E_a : activation energy, it represents the energy barrier that must be overcome for the reaction to occur. It is expressed in $\text{cal} \times \text{mol}^{-1}$.

In some cases, a dependence on pressure is required for the rate of some reactions. This can be included through a formulation called "plog", where the Arrhenius parameters of the rate constant are provided at different selected pressures. Another way to express the pressure dependence is Troe's formula [129], which requires some additional parameters. More information can be found in the theory manual [130].

The second file (extension .dat) collects the thermodynamic properties of all the species that have been declared in the mechanism file. These properties are expressed in polynomial form, through NASA formalism [131]. Two sets of seven coefficients ($a_{i,k}$, with $i = 1, \dots, 7$ and k identifying the species) are used, the first set to express the properties in the higher temperature range (usually from 1000 to 5000 K) and the second set for the lower temperature range (usually from 300 to 1000 K). Thanks to these coefficients, the thermodynamic properties of species k can be expressed as:

$$\begin{aligned}
 c_{p,k}/R &= a_{1,k} + a_{2,k}T + a_{3,k}T^2 + a_{4,k}T^3 + a_{5,k}T^4 \\
 H_k^0/(RT) &= a_{1,k} + a_{2,k}\frac{T}{2} + a_{3,k}\frac{T^2}{3} + a_{4,k}\frac{T^3}{4} + a_{5,k}\frac{T^4}{5} + a_{6,k}\frac{1}{T} \\
 S_k^0/R &= a_{1,k} \ln T + a_{2,k}T + a_{3,k}\frac{T^2}{2} + a_{4,k}\frac{T^3}{3} + a_{5,k}\frac{T^4}{4} + a_{7,k}
 \end{aligned} \tag{4.2}$$

Thanks to the thermodynamic properties and the rate constant of the reaction in forward direction, the software can calculate the rate of the reverse reaction.

4.2.2 Chemkin models

As previously stated, two different models were used for the simulations, depending on the physical configuration of the set-ups.

The jet-stirred reactor is simulated through the use of the Perfectly Stirred Reactor (PSR) model. This model allows to simulate an adiabatic, constant volume open reactor where a stationary flow is introduced and allowed to react for a well defined amount of time (residence time). The parameters that have to be provided are the following:

- residence time (s);
- temperature (K): since in our experiments the temperature is varied from 450 to 1210 K, a series of continuations is added to the model, in order to compute the species mole fractions at different fixed temperatures;
- pressure (atm);
- volume of the reactor (cm^3).

In addition, the mole fractions of the reactants have to be provided in the section devoted to the inlet properties. Once these parameters are given, thanks to the equations of mass and energy conservation, the software can compute the mole fractions of all of the species that are included in the mechanism.

The second model that was used in order to simulate the rapid compression machine and the shock tube is the Closed Homogeneous Reactor. This model allows for different kind of settings and in the case of RCM and ST, the chosen problem type is the one constraining the volume and solving the energy equation. The difference between RCM and ST is mainly given by the volume constraint. In the case of the shock tube simulation, the volume is fixed as constant and the initial conditions provided (temperature and pressure) are going to be the one of the reflected shock. Considering that the maximum ignition delay time that is considered to be acceptable in the shock tube is around 1–2 ms, the end time of the simulations can be fixed at 10 ms, thus avoiding the calculations to go on for longer than needed and reducing the computational cost. The case of the rapid compression machine is slightly more complicated, since the volume should be constrained as the volume computed from the test with the non reactive mixture, as explained in Section 3.2. The volume can be computed in every point recorded by the pressure sensor, but results in a volume profile composed of thousands of points, causing a very long computational time. In order to avoid this, in the in-house script developed for this work some points were selected, with a higher concentration close to the TDC, in order to maintain the same accuracy, but reducing the simulation time. Our volume histories are therefore made of around 60 points over the 600 ms of the pressure trace recorded. Once the volume profile is given to the model, it is necessary to specify the initial conditions (T_0 and p_0) as the conditions set before compression.

The mixture composition should be also set, giving the molar fractions of the reactants under the “Reactant Species” section. Using the given initial conditions and constraints, the software will then solve the energy and mass conservation equations. In this case, the desired output will be the pressure profile (even if also the mole fractions of the reactants and the products will be available). From the pressure profiles, similarly to what was done for the experimental traces, it is possible to compute the first derivative and identify the ignition delay time (either from the time zero of the simulation for the ST or from the end of the compression for the RCM).

4.3 Further analysis

As anticipated in Section 3.2, a more detailed analysis was performed for some conditions concerning the heat release rate (HRR) in the rapid compression machine. Most of the results obtained from RCMs usually focus on the ignition delay times and when assessing the performance of the kinetic models, the comparison between experiments and simulations does not go further than the typical IDTs versus temperature plots. Nevertheless, it is interesting to explore the available data from the heat release point of view. To this aim, a secondary acquisition system was imple-

mented for a small part of the experimental campaign, allowing pressure profiles with a higher acquisition rate to be obtained (500 kSamples/s versus the previous acquisition frequency of 6.67 Hz). This was necessary for the HRR analysis, since, as shown in equation 3.3 (and shown again as equation 4.3), the heat release rate depends on the first derivative of the pressure and in order to avoid propagation of the noise distorting the results, it was necessary to filter the signal in an appropriate way. It has to be noted that the noise level does not affect the ignition delay time computation, but it can have a huge impact on the heat release.

The first step of the analysis, also performed through a Matlab script developed for this work, was therefore the filtering of the signal. Thanks to an in-built Matlab function, Savitzky-Golay finite impulse response smoothing filter was applied to the pressure signal. Different orders and frame length for this function were tested, in order to determine the best parameters for this specific case. For each condition, both tests with reactive and with non reactive mixtures were filtered with this method. Then, all the quantities required in the formula (reported here again for clarity and derived by Goldsborough in [97]) were computed. The subscripts r and nr identify the quantities related to the reactive and non reactive mixture tests, respectively.

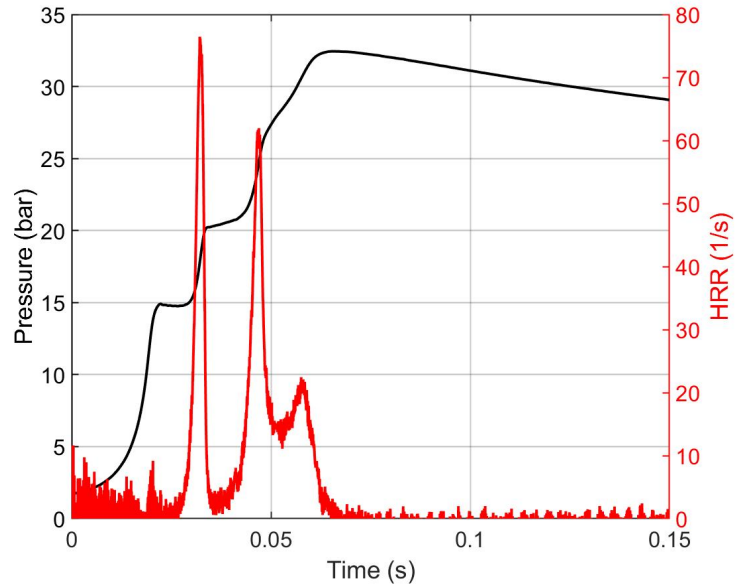
$$HRR = \frac{\gamma}{\gamma-1} \frac{dV}{dt} [P - P_{nr}] + \frac{1}{\gamma-1} V \left[\frac{dP}{dt} - \frac{dP}{dt} \Big|_{nr} \right] - \frac{PV}{(\gamma-1)^2} \left[\frac{d\gamma}{dt} - \frac{d\gamma}{dt} \Big|_{nr} \right] \quad (4.3)$$

Once the HRR is computed, the accumulated heat release (aHR) can also be computed, as:

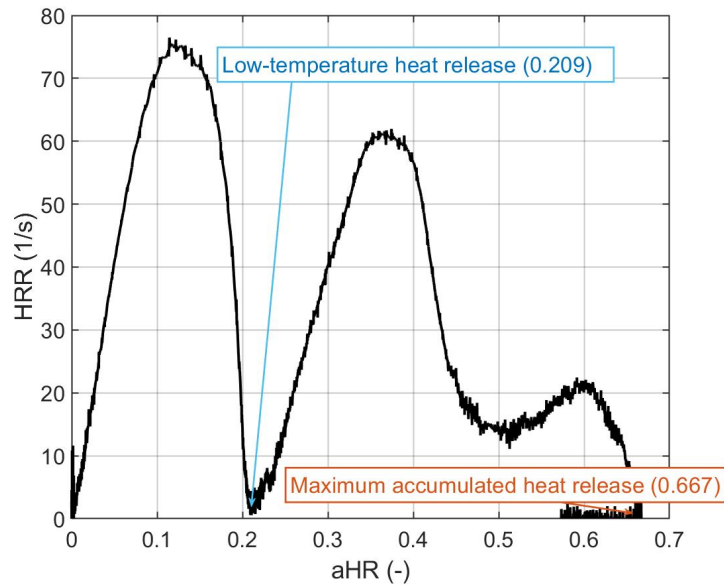
$$aHR = \int (HRR) dt \quad (4.4)$$

Both the HRR and the aHR are usually normalised by the lower heating value (LHV) of the mixture. An example of the computed heat release rate, together with the pressure profile from which it was computed, is shown in Figure 4.1a. From the plot of aHR vs HRR, as shown in Figure 4.1b, it is then possible to determine the low-temperature heat release (LTHR), which is identified as the abscissa of the first inflection point in the curve and the maximum heat release, which is defined as the peak accumulated heat release.

The same analysis can be performed on the simulated pressure traces (paying attention to the time-steps, that need to be imposed as the same that were obtained in the experiments) and this allows to have more information that could help in the development and improvement of the mechanism.



(a) Pressure profile and computed heat release rate



(b) Normalised heat release rate vs normalised accumulated heat release

Figure 4.1: Example of the resulting curves from the heat release rate analysis (BEE, $\phi = 1$, dilution = 10, inert gas: 50% CO_2 + 50% N_2 , $T_c = 583$ K, $p_c = 15$ bar).

Chapter 5

Results and discussion: DNPEE and DIPEE in the JSR

*In this chapter, the main results for the oxidation of di-*n*-pentyl and di-iso-pentyl ethers in the jet-stirred reactor are presented. The performance of the simulations against the experimental mole fraction profiles for the main intermediates and products are presented and a reaction pathway analysis is performed at low and high temperatures for DIPEE. The experimental results for DNPEE are presented and commented, with a particular focus on the specific products that are expected to have an influence on the overall reactivity. The two fuels will then be compared to each other, as well as to the other ethers that were previously studied in the same set-up under the same conditions.*

Contents

5.1	DIPEE	53
5.1.1	Reaction pathways	68
5.2	DNPEE	70
5.2.1	Expected reaction pathways	80
5.3	Comparison to the other ethers	81
5.4	Conclusions	83

Introduction

Several ethers have already been studied in this jet-stirred reactor (presented in Section 3.1), both considering their oxidation and their pyrolysis. In this work, two more symmetrical ethers, di-*iso*-pentyl and di-*n*-pentyl ethers, have been studied for oxidation under the same conditions as the rest of the fuels. Several intermediates and products have been identified; for DIPEE, the experimental results have also been compared to the simulations obtained with the developed kinetic

mechanism. As a recall, the studied conditions are reported in Table 5.1. The measured mole fractions of the species that are only found in trace amounts and are therefore not included in the next sections can be found in the appendices A.1 and A.2.

Table 5.1: Experimental conditions of the oxidation of pentyl ethers in the jet-stirred reactor.

Fuel	ϕ	p (atm)	T (K)	Initial fuel mole fraction	τ (ms)	Identified species
Di- <i>iso</i> -pentyl ether	0.5, 1.0, 2.0, 4.0	10	450–1210	1000 ppm	700	≈ 48
Di- <i>n</i> -pentyl ether	0.5, 1.0, 2.0, 4.0	10	450–1210	1000 ppm	700	≈ 52

5.1 DIPEE

The oxidation of di-*iso*-pentyl ether has been studied in the jet-stirred reactor for four different equivalence ratios (0.5, 1, 2, 4), at a pressure of 10 atm and with a constant residence time of 700 ms. The fuel conversion for all conditions is reported in Figure 5.1. Before considering the performance of the mechanism and analysing the identified products, it is interesting to take a deeper look at the experimental results for the fuel mole fraction.

Figure 5.2 shows the mole fractions of DIPEE for a rich mixture ($\phi = 2$). Five different zones of reactivity can be identified under these conditions: DIPEE consumption starts at very low temperature, with a conversion of already 12% at 470 K. The first zone, where the reactivity is increasing with the temperature and therefore the fuel mole fraction is decreasing, goes up to 530 K, where the first NTC region is reached and the mole fraction reaches a plateau within a small temperature window of around 50 K. Then, the reactivity starts increasing again up to around 640 K, where the second NTC zone begins. In this interval (of around 100 K), the reactivity is strongly decreasing when the temperature is increased, with the fuel conversion going as low as 38% (similar to the plateau value of the first NTC). After this point is reached (740 K), the reactivity starts increasing again in the fifth zone, up to around 1100 K, where all the fuel is converted.

As can be seen from the fuel conversion in Figure 5.1, the double-cool flame behaviour is even more pronounced for the richest mixture ($\phi = 4$), while it is almost impossible to clearly identify the first NTC zone for the lean mixture. This double-cool flame regime is caused by the long chain of this fuel, which allows the formation of products and radicals that have their own low-temperature reactivity in a different range of temperature compared to DIPEE itself. This is in line with the factors determining this behavior identified by Fan [59]: the first one is that both the fuel and its oxidation intermediates can undergo low-temperature chain branching reactions and the second is that the temperature windows of low-temperature reactivities are separated. This will be better discussed in the next paragraphs and in Section 5.3.

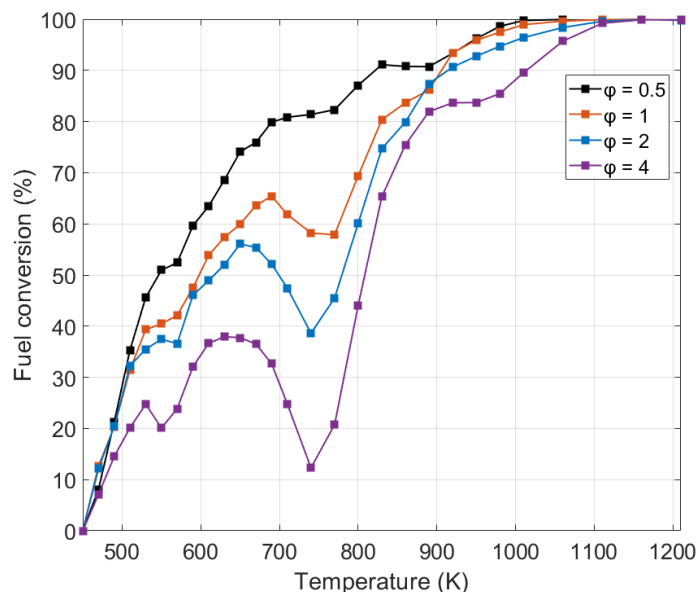


Figure 5.1: Fuel conversion of di-*iso*-pentyl ether over the temperature range studied in the JSR for the four equivalence ratios at $p = 10$ atm, $\tau = 700$ ms, $\chi_{0,\text{fuel}} = 1000$ ppm (lines are only added to represent the trend).

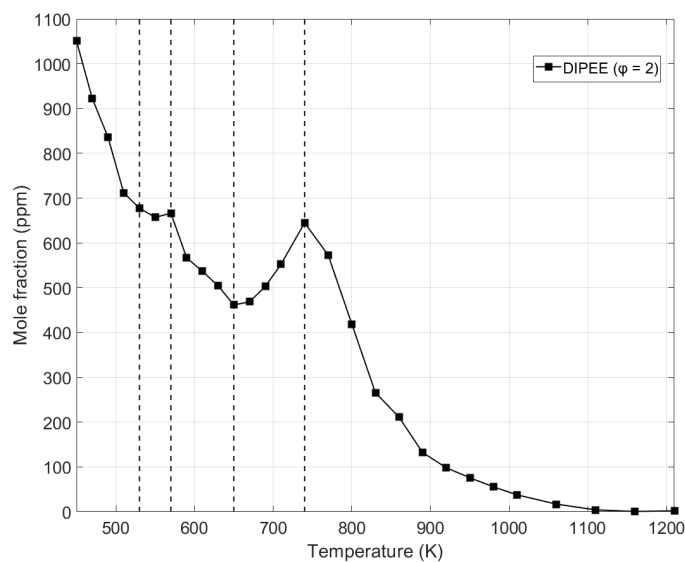


Figure 5.2: Mole fraction of di-*iso*-pentyl ether over the temperature range studied in the JSR ($\phi = 2$, $p = 10$ atm, $\tau = 700$ ms, $\chi_{0,\text{fuel}} = 1000$ ppm).

In order to better understand the different molecules and reactions that are involved in this double cool flame behaviour, it is interesting to have a look at the predictions of the mechanism and analyse the reaction pathways leading to the formation of OH radicals. First of all, in Figure 5.3a, the comparison of the measured and predicted mole fractions of DIPEE for $\phi = 2$ is shown.

It is important to start the analysis from this comparison, in order to verify if the model predicts the same double cool flame regime and in the same temperature zones. The mechanism predicts reasonably well the fuel profile. It slightly underpredicts the temperature range of the first cool flame (530–550 K, instead of 530–570 K), while it anticipates the second cool flame zone (630–730 K, instead of 650–740 K). Nevertheless, the accuracy of this prediction is quite good. Therefore, in the plots included in Figure 5.3, the black vertical lines define the temperature zones as identified from the experimental results.

The reactions which lead to the biggest production of OH can be quite different in the different temperature zones. At low temperature, the pathways leading to the formation of carbonyl-hydroperoxides and their following decomposition are very important for the reactivity. At intermediate temperature, the β -scission of the primary fuel radicals lead to the formation of other products and radicals that have their own low-temperature reactions, as for example isopentanal and isopentyl radical, which also lead to the formation and then decomposition of carbonyl-hydroperoxides (as the ones included in Figure 5.3c, shown in the Table 5.2 and identified as butal3m-4o2ooh and ic4toohcho, respectively).

Figures 5.3b and 5.3c show respectively the rate of production of OH over the low-intermediate temperature range for the main reactions responsible for OH formation and the mole fraction of the main radicals and molecules involved. These main reactions are shown in Table 5.2. It is interesting to note how the ROP of the main reactions involved in OH formation peaks in different zones of DIPEE reactivity. In fact, it is possible to see that in the first zone, where DIPEE is already very reactive, the OH production is mainly due to the formation and decomposition of the carbonyl-hydroperoxide derived from the α -radical of the fuel. The ROP of OH radicals from these reactions is rapidly decreasing when the second zone (the first cool flame) is reached, but it is counter-balanced by the rapid growth of the ROP related to the formation of ic4toohcho from the isopentyl radical, thus creating an actual plateau in the reactivity. In the third zone, where the reactivity is increasing again, the reactions related to ic4toohcho and butal3m-4o2ooh formation and decomposition reach their peak. The second cool flame zone is reached when the ROP of OH due to the reactions involving ic4toohcho and butal3m-4o2ooh start decreasing and it is not being counterbalanced fast enough by the high temperature decomposition reaction of H_2O_2 , thus determining the decrease in reactivity in this second NTC zone. Finally, at high temperature the H_2O_2 decomposition becomes the driver of the production of OH, increasing the reactivity again, until complete conversion of the fuel.

A final remark should be made on the mole fraction of the species and radicals involved in these reactions. As it can be seen in Figure 5.3c, the peak mole fraction of ic4toohcho is much higher than the other considered species, which might seem illogical only considering the reactions presented in Table 5.2. In reality, this is not the only way of formation of this species and if the rate of production is analysed at the temperature of the peak of the mole fractions, it is possible to see that another very important pathway leading to its formation is derived from the tertiary radical

of the fuel, as follows:

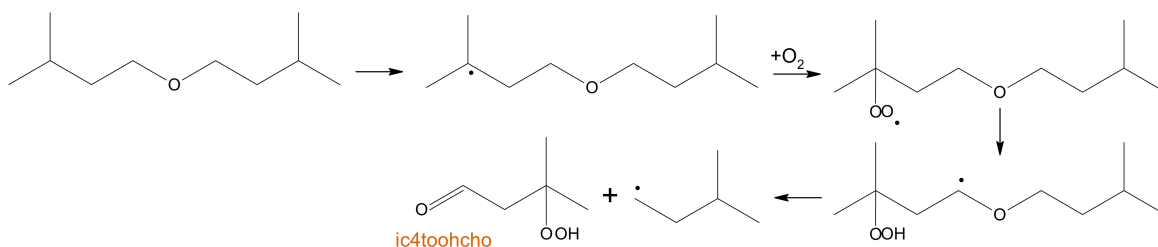
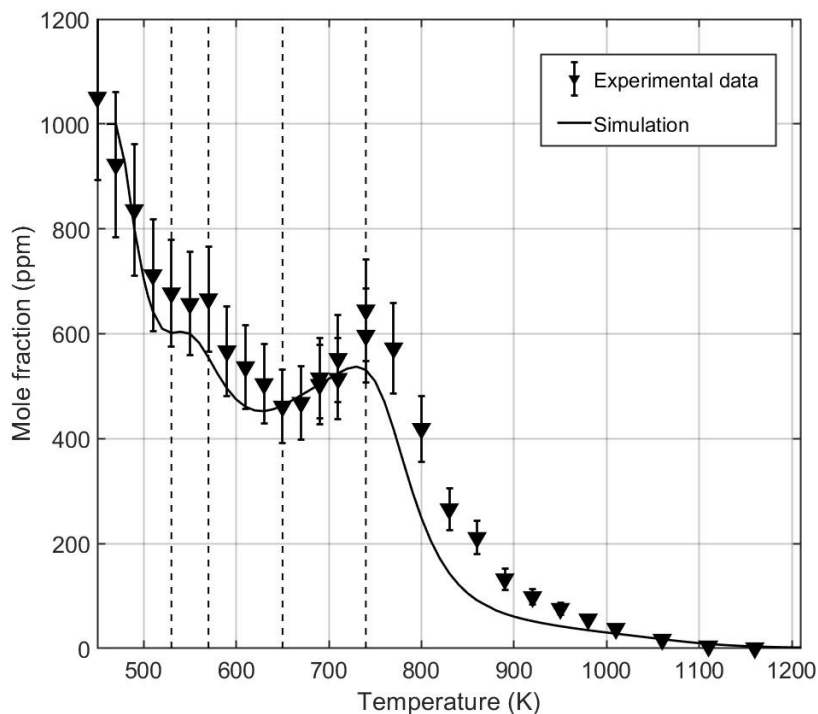
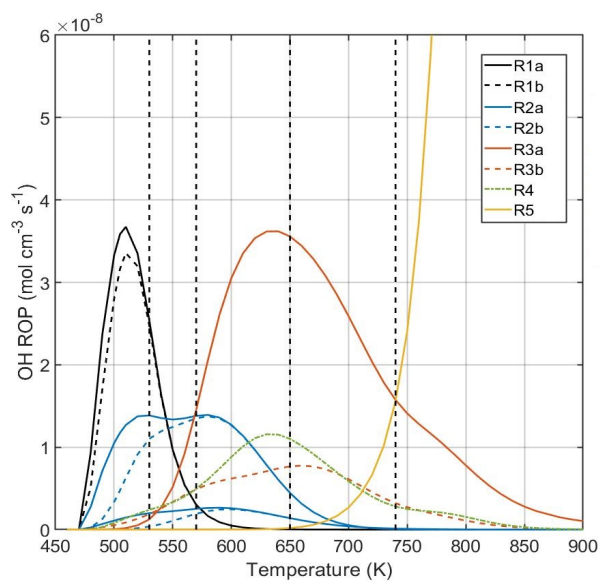


Table 5.2: Different reactions involved in the formation of OH radicals during the oxidation of DIPEE in the JSR.

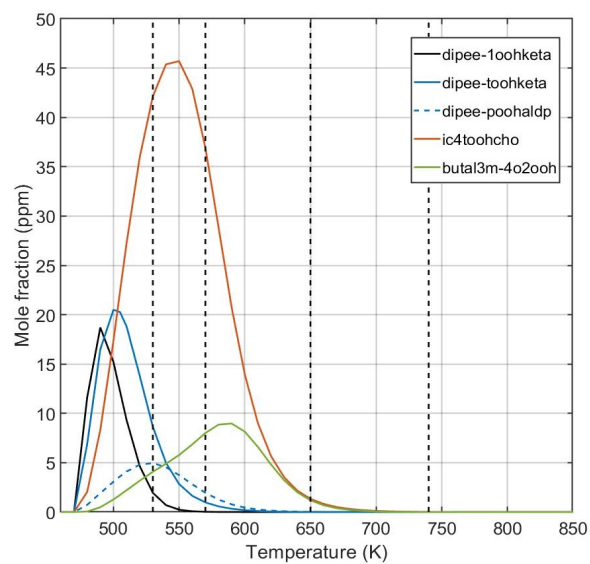
Label	Reaction scheme	Mechanism expression
R1a		$\text{dipee-aoo1oo} \rightleftharpoons \text{dipee-1oohketa} + \text{oh}$
R1b		$\text{dipee-1oohketa} \Rightarrow \text{butal3m} + \text{ic4h9co2} + \text{oh}$ $\text{dipee-1oohketa} \Rightarrow \text{ic5cooh} + \text{ic4h9co} + \text{oh}$
R2a		$\text{dipee-aoohtoo} \rightleftharpoons \text{dipee-toohketa} + \text{oh}$ $\text{dipee-poohpoo} \rightleftharpoons \text{dipee-pooaldp} + \text{oh}$
R2b		$\text{dipee-toohketa} \Rightarrow \text{ch3coch3} + \text{buto3m} + \text{ch2co} + \text{oh}$ $\text{dipee-pooaldp} \Rightarrow \text{cjoic5} + \text{c2h3cho} + \text{ch2o} + \text{oh}$
R3a		$\text{but2m-4oohtoo} \rightleftharpoons \text{ic4toohcho} + \text{oh}$
R3b		$\text{ic4toohcho} \Rightarrow \text{ch3coch3} + \text{ch2cho} + \text{oh}$
R4		$\text{butal3m-4o2h2o2} \rightleftharpoons \text{butal3m-4o2ooh} + \text{oh}$ $\text{butal3m-4o2ooh} \Rightarrow \text{metchocho} + \text{hco} + \text{oh}$
R5		$\text{h2o2} (+\text{M}) \rightleftharpoons \text{oh} + \text{oh} (+\text{M})$



(a)



(b)



(c)

Figure 5.3: **(a)** DIPEE mole fraction ($\phi = 2$); **(b)** Contributions to OH formation from different reactions: R1) formation (solid line, (a)) and decomposition (dashed line (b)) of dipee-1oohketa, R2) formation (solid, (a)) and decomposition (dashed, (b)) of dipee-toohketa and dipee-pooahdp, R3) formation (solid, (a)) and decomposition (dashed, (b)) of ic4toohcho, R4) formation+decomposition of khp derived from isopentanal, R5) H_2O_2 decomposition; **(c)** Mole fractions of some of the molecules involved in the reactions producing OH.

Figures 5.4–5.7 show the measured and simulated mole fractions for di-*iso*-pentyl ether and its products for the four studied equivalence ratios. First of all, it is possible to note that in general the mechanism is capable of predicting reasonably well the mole fractions of the fuel and of its main products. Nevertheless, some discrepancies can still be found, generally more in the absolute values, while the trends are usually well predicted.

A small remark has to be made about the profile labeled "acetone+propanal". The peaks of these two species in the GC analysis were coeluted, therefore it was impossible to distinguish one from the other. In order to be coherent, for the simulation the line plotted represents the sum of the mole fractions of these two species.

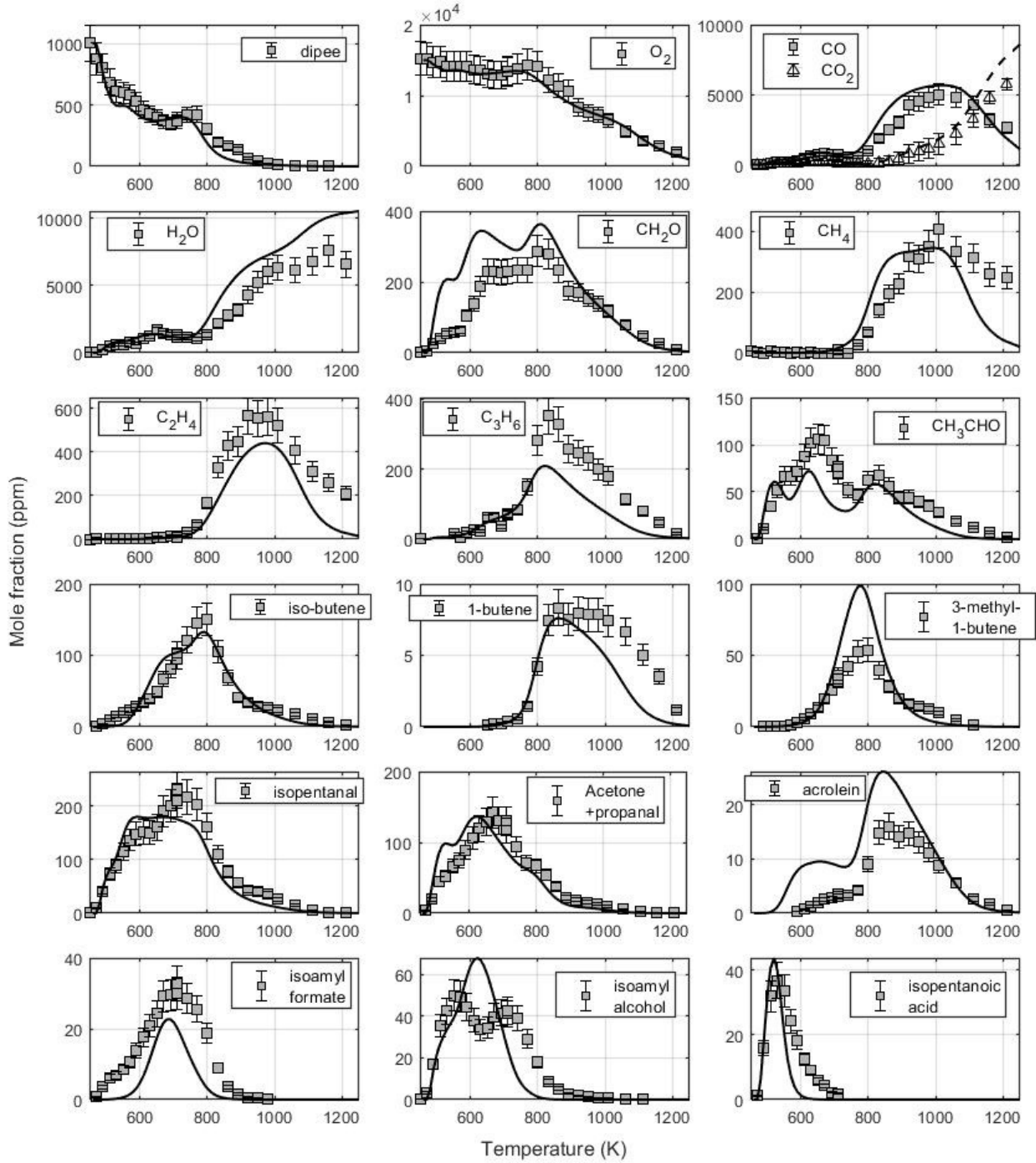


Figure 5.4: Mole fractions of the fuel and the main products and intermediates during the oxidation of DIPEE in the JSR for $\phi = 1$ ($p = 10$ atm, $\tau = 700$ ms, $\chi_{0,\text{fuel}} = 1000$ ppm).

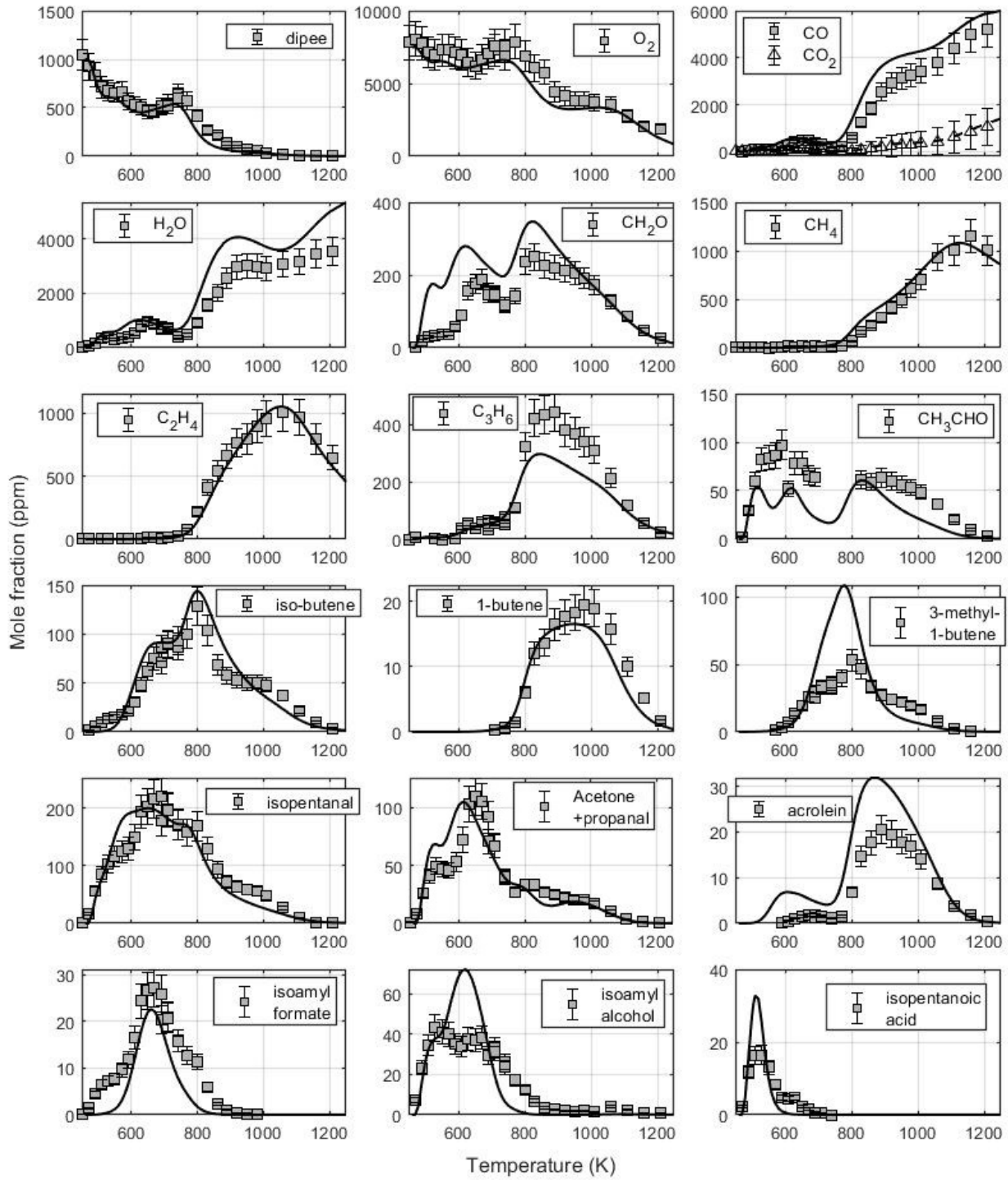


Figure 5.5: Mole fractions of the fuel and the main products and intermediates during the oxidation of DIPEE in the JSR for $\phi = 2$ ($p = 10$ atm, $\tau = 700$ ms, $\chi_{0,\text{fuel}} = 1000$ ppm).

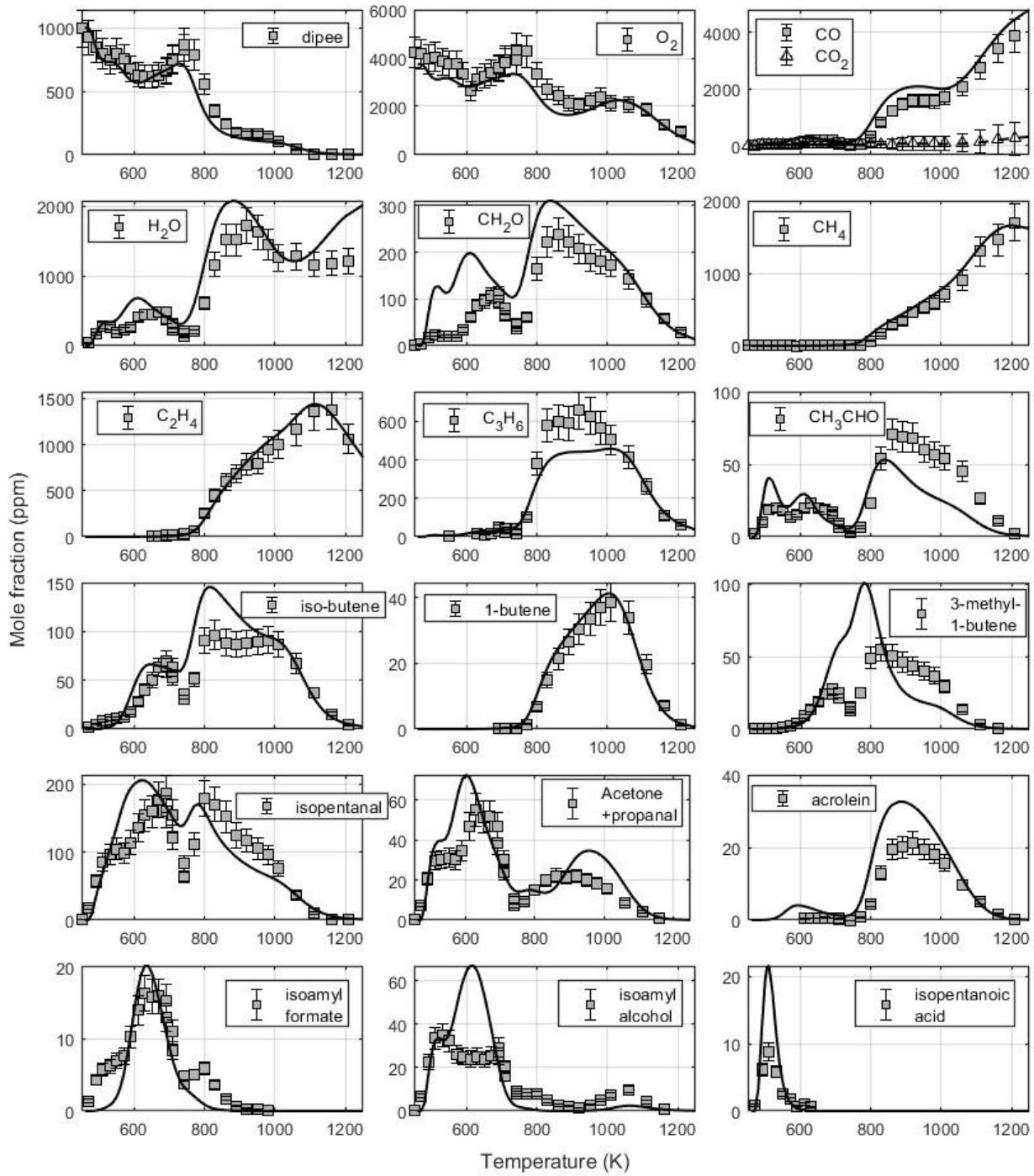


Figure 5.6: Mole fractions of the fuel and the main products and intermediates during the oxidation of DIPEE in the JSR for $\phi = 4$ ($p = 10$ atm, $\tau = 700$ ms, $\chi_{0,\text{fuel}} = 1000$ ppm).

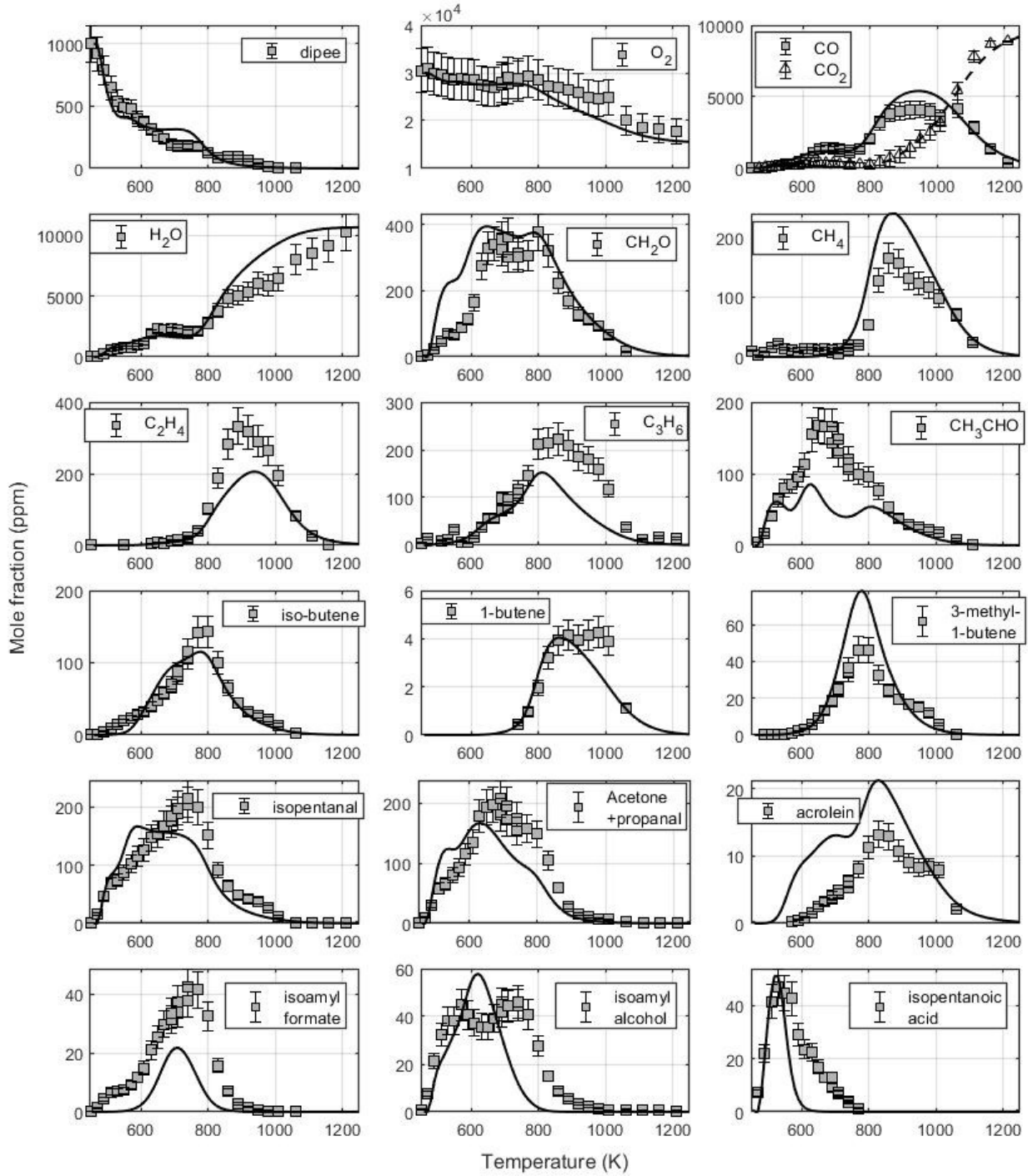


Figure 5.7: Mole fractions of the fuel and the main products and intermediates during the oxidation of DIPEE in the JSR for $\phi = 0.5$ ($p = 10$ atm, $\tau = 700$ ms, $\chi_{0, \text{fuel}} = 1000$ ppm).

Similar to the previously studied ethers, including DEE, DPE and DBE, between the main intermediates several aldehydes can be found, with mole fractions up to 300–400 ppm. The mechanism is in reasonable agreement with these values, but not for all the conditions. For example, considering formaldehyde, it is possible to see that under lean conditions the maximum measured mole fractions is 377 ppm at 800 K, where the mechanism predicts around 372 ppm, hence with a very good accuracy. At lower temperature, for the same conditions, the mechanism overpredicts the mole fraction of formaldehyde, with an overestimation of almost 170% at 600 K while it is in very good agreement at intermediate and high temperatures. Similar results can be seen for the stoichiometric and rich conditions: the mechanism is capable of well representing the mole fraction of formaldehyde at high temperature (generally above 800 K), but largely overpredicts the experimental mole fractions at low temperatures. Nevertheless, the general trend of the curve is reasonably captured by the mechanism and the position of the peaks is generally simulated well. Another aldehyde which is produced in important quantities is acetaldehyde, which was measured up to around 170 ppm under lean conditions. In this case, the simulation underpredicts the mole fraction of this species by a factor of two and it seems unable to retrace the evolution of the production of acetaldehyde over the temperature range, as shown in Figure 5.7. The mechanism predicts a peak mole fraction of 85 ppm, which is half the measured value and even the temperature at which this maximum is reached is not perfectly captured. Nevertheless, for the other conditions (both rich and stoichiometric), the mechanism is performing slightly better, following the trend of the curve quite well and getting closer to the measured values of mole fractions. Finally, a very important aldehyde which is produced specifically during the oxidation of di-*iso*-pentyl ether is isopentanal. In the oxidation of DEE, DPE and DBE, a similar role was covered by acetaldehyde, propanal and butanal, respectively. Isopentanal is very important for the reactivity of DIPEE. It is produced in quite large quantities (around 200 ppm for all conditions) and takes part in the low-intermediate temperature chemistry thanks to its own low-temperature reactivity. It is therefore important to focus on its way of production during the oxidation of DIPEE. To this aim, a reaction pathway analysis has been performed and the main paths leading to the formation of this species are shown in Figure 5.8. The main reactions leading to isopentanal are identified by colors and numbers from 1 to 5 and are summarized in Table 5.3 for clarity. The rates of production of isopentanal for each of these reactions over the temperature range are then plotted in Figure 5.9, in order to have a better understanding of what reactions are important in the different temperature ranges. One of the five reactions considered in Figure 5.9 is not shown in the reaction pathways of Figure 5.8, but it will be discussed as well. As can be seen from Figure 5.8, the main two reaction pathways leading to the formation of isopentanal both start from the α -radical of the fuel. The first pathway involves the direct β -scission of this radical (which is indicated with **R2**), forming an isopentyl radical, which in turn leads to the formation of isopentanal, which will be discussed later. The second pathway starting from the α -radical requires a first addition to molecular oxygen, followed by internal isomerisation through

a six-membered transition state and then either direct decomposition (indicated as **R1**) giving two molecules of isopentanal, or a sequence of reaction leading to the formation of a carbonyl-hydroperoxide, which then decomposes and forms isopentanal (**R5**).

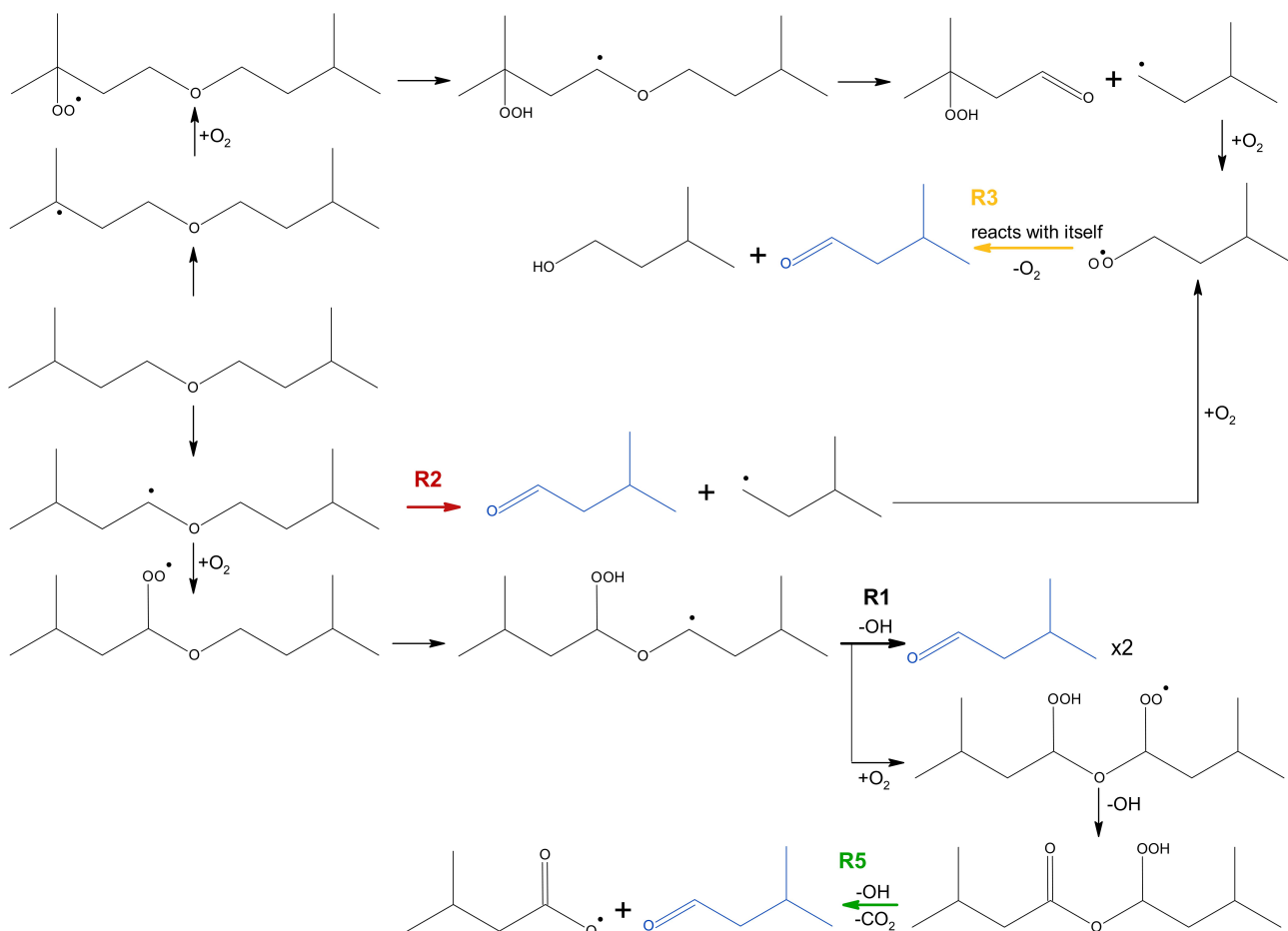
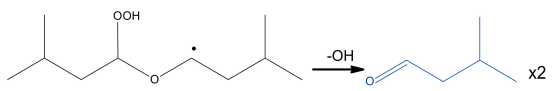
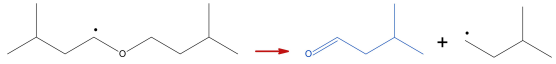
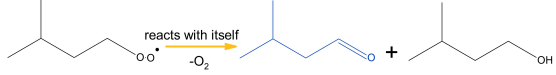
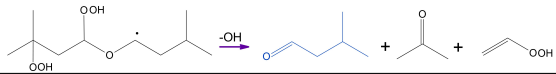
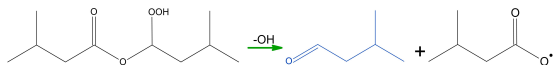


Figure 5.8: Main reaction pathways leading to the formation of isopentanal during the oxidation of DIPEE in the jet-stirred reactor.

In Figure 5.9, it can be seen that the two most important reactions, **R1** and **R2** reach their maximum contribution in the formation of isopentanal at very different temperatures, for all the conditions considered. This is important, because it means that isopentanal is being produced over the whole temperature range thanks to different reactions that are important at both low and high temperatures. The fact that isopentanal can be produced at all temperatures and that it can produce radicals with their own low-temperature chemistry makes it essential for the overall reactivity. From Figure 5.9, it is also interesting to see how the relative position and shape of the peaks of the two main reactions influences the shape of the predicted mole fractions of isopentanal: for $\phi = 0.5$ and 1, the two reactions have quite similar maximum ROP and their peaks are quite close to each other, when one starts decreasing, the other increases enough to counterbalance, leading to a unique large peak for isopentanal mole fraction, with a quasi plateau on the top. On the other

side, for the two rich conditions ($\phi = 2$ and 4), the maximum ROP of **R1** and **R2** start being quite different and the shape of the second peak start being less defined, with even a small plateau in the ascending part at $\phi = 4$, leading to a clearer separation of two peaks on the mole fraction profile (especially for $\phi = 4$). It is also interesting to note that these two peaks are also visible in the experimental mole fractions of the richest condition.

Table 5.3: Main reactions leading to the formation of isopentanal during the oxidation of DIPEE in the JSR.

Label	Reaction scheme	Mechanism expression
R1		$\text{dipee-aooH1} \Rightarrow \text{butal3m} + \text{butal3m} + \text{oh}$
R2		$\text{dipee-a} \Rightarrow \text{butal3m} + \text{but2m-4}$
R3		$\text{but2m-4oo} + \text{but2m-4oo} \Rightarrow \text{butoh3m} + \text{butal3m} + \text{o2}$
R4		$\text{dipee-aooHtooh1} \Rightarrow \text{butal3m} + \text{ch2chooh} + \text{ch3coch3} + \text{oh}$
R5		$\text{dipee-1oohketa} \Rightarrow \text{butal3m} + \text{ic4h9co2} + \text{oh}$

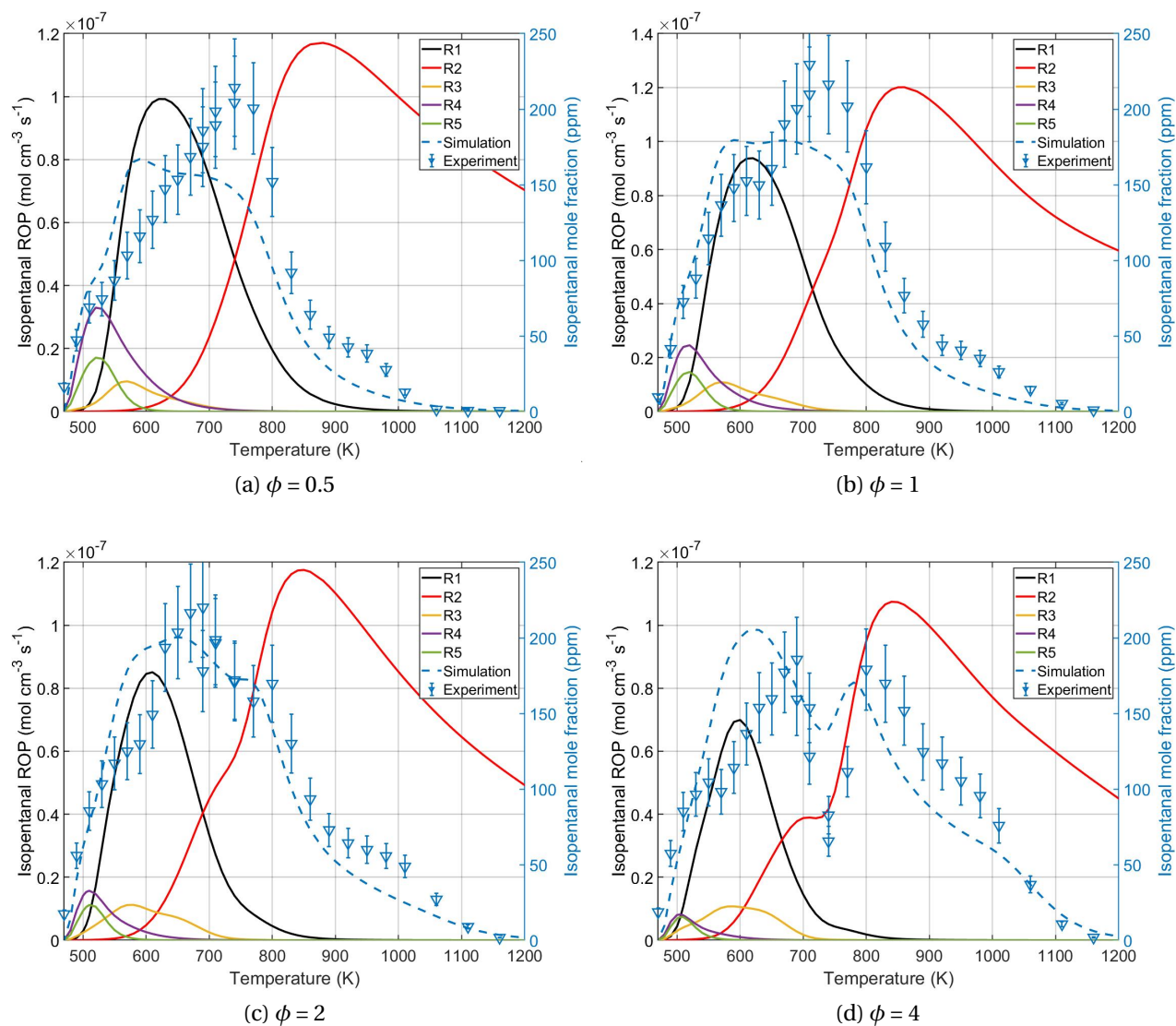
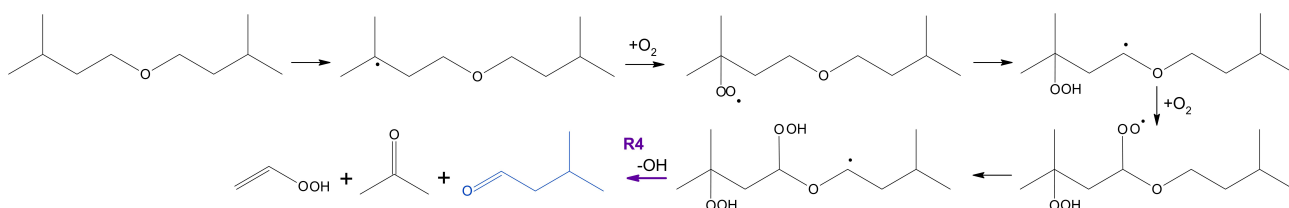


Figure 5.9: Rate of production of isopentanal from the five most important reactions in its production path and isopentanal mole fractions (symbols: experiments, lines: simulations) for the all equivalence ratios. R1: decomposition of QOOH radical from the α -radical of the fuel; R2: β -scission of the α -radical of the fuel; R3: reaction of two RO $_2$ radicals obtained from the isopentyl radical; R5: decomposition of the carbonylhydroperoxide obtained from the α -radical of the fuel. (All the reactions are summarised in Table 5.3).

The other reaction already mentioned, **R5**, only contributes at very low temperature and to a lower extent compared to the main two reactions just discussed. Similarly to **R5**, two other reactions contribute to the formation of isopentanal at low temperature. The first one, also included in Figure 5.8, involves the isopentyl radical, which can be obtained as already explained from the scission of the α -radical of the fuel or it can be formed from the tertiary radical, as shown in the reaction pathway analysis. The isopentyl radical undergoes addition to molecular oxygen and the RO $_2$ formed reacts with another RO $_2$ radical (**R3**) to give isopentanal, isopentyl alcohol and O $_2$.

Once again, this path is less important than the first two, but it can still contribute to the formation of isopentanal at lowest temperatures of interest.

The last important reaction path that leads to the formation of isopentanal is not shown in the previous scheme, but reported below. This path starts from the gamma radical of the fuel, following the typical low-temperature path undergoing a first addition to molecular oxygen, isomerisation, then a second addition to O₂. At this point, for this specific OOQOOH radical it is not possible to form a carbonyl-hydroperoxide; it therefore undergoes another isomerisation via a 6-membered transition state and then decomposes (**R4**), forming isopentanal. It appears that this path can be important at very low temperature and especially for lean conditions.



Going back to the main products and intermediates of DIPEE oxidation, it is also interesting to note the formation isopentanoic acid. In fact, the formation of carboxylic acids, observed only at low temperature, is also typical of the oxidation of ethers. In the previous studies performed in the same JSR, acetic acid was identified among the oxidation intermediates of DEE, as well as propanoic acid for DPE and butanoic acid for DBE (butanoic acid was not quantified). In all cases, the mechanism was not able to simulate the mole fractions of these species accurately. In the case of isopentanoic acid, the mechanism reproduces quite well the position of the peak, but it captures its maximum value only for stoichiometric and lean conditions. Nevertheless, for these two conditions, there is an underestimation of the mole fraction on the end of the peak, towards the intermediate temperature range. For the fuel-rich conditions, on the other hand, the maximum mole fraction is largely overestimated, even if its position is quite well captured. The fact that this species is produced only at low temperature is explained through its formation pathway analysis. In fact, isopentanoic acid is only produced from the decomposition of one of the main ketohydroperoxides obtained from the α -radical of the fuel, via the Korcek mechanism [132].

Other products that were identified and quantified are reported in Figures 5.4–5.7, as oxygen, CO, CO₂, water, methane, ethylene, propene, isobutene, 1-butene, acetone, acrolein, isopentyl formate and isopentyl alcohol. The mechanism shows in general a reasonable agreement with the experimental data, even if a factor of 1.5–2 of difference can still be found for the mole fractions of some species. Nevertheless, the mechanism is well capable of simulating the double-cool flame behaviour of this fuel, which is one of its most interesting features during its oxidation.

5.1.1 Reaction pathways

A complete reaction pathway analysis for fuel oxidation is performed at two temperatures, 500 K (Fig. 5.10) and 1000 K (Fig. 5.11) for the stoichiometric condition, in order to see the most important reactions consuming the fuel in two very different temperature regimes. In both figures, the pathways followed by the largest flux are indicated by thicker arrows, in order to have more clarity in the reading.

Considering the analysis performed at low temperature (shown in Figure 5.10), it is possible to see that the four possible primary radicals obtained from the fuel are formed, but the most abundant one is the α -radical. In fact, the presence of the ether function weakens the adjacent C-H bond, as it was already observed for the other ethers [12, 49, 57, 58, 68, 76, 79, 80]. The most common path followed by all primary radicals is the typical path of low temperature reactivity, with a first addition to O_2 , an internal isomerisation, a second addition to molecular oxygen and then the formation of carbonyl-hydroperoxides, which then decompose. Smaller fluxes follow other paths, for example 2% of the most abundant OOQOOH radical coming from the α -radical of the fuel forms two molecules of isopentanal. Also, it has to be noted that the tertiary radicals cannot form carbonyl-hydroperoxides; therefore, even if they can get to form OOQOOH radicals, they would then just decompose directly after an internal H-transfer.

Considering the pathway analysis performed at 1000 K, shown in Figure 5.11, reaction pathways are different. The α -radical is still the most abundant and in this case, even the δ -radical can isomerise into the α -radical (63% of the flux follows this path). As expected at high temperatures, the most common reactions for radicals are β -scission reactions. Most of the fluxes of the primary fuel radicals follow these pathways. Nevertheless, it can be seen that a small flux (25%) of the β -radical (which is also the least abundant) still adds to molecular oxygen, before either eliminating an HO_2 radical and forming an unsaturated compound or isomerising and then decomposing. Nonetheless, these fluxes are almost negligible and are therefore expected to have low to none influence on the overall reactivity.

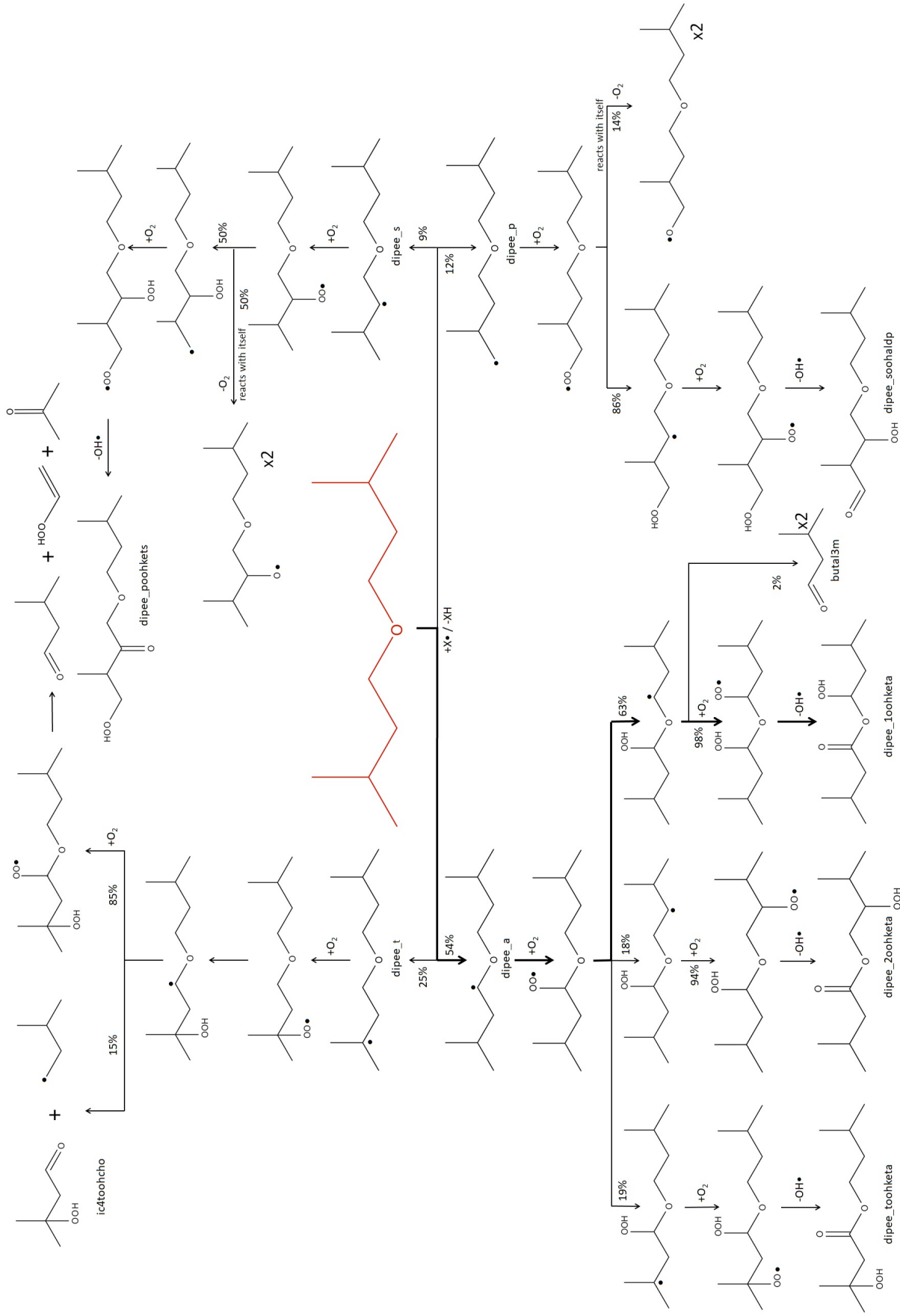


Figure 5.10: Reaction pathways in di-iso-pentyl ether oxidation in the jet-stirred reactor ($\phi = 1$, $p = 10$ atm, 500 K, $\chi_{0,\text{fuel}} = 1000$ ppm).

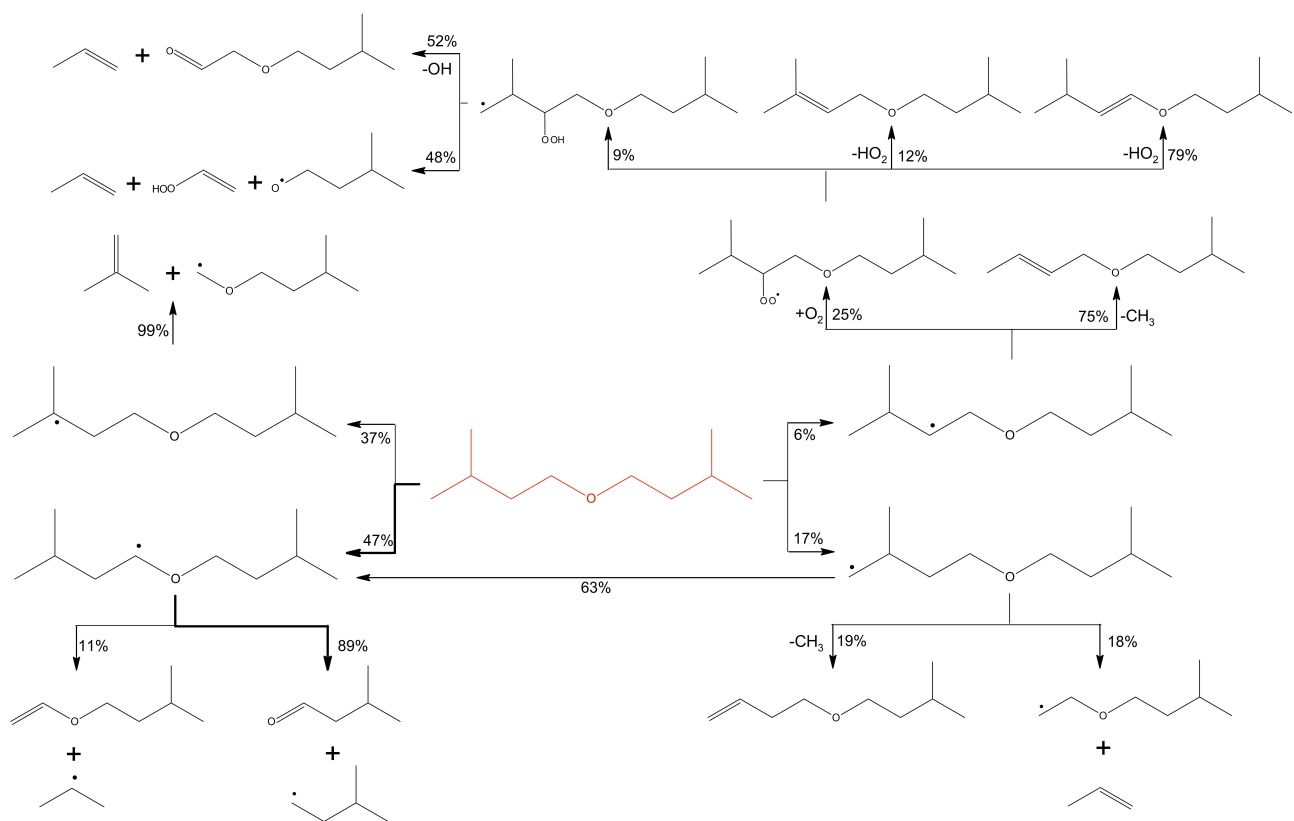


Figure 5.11: Reaction pathways in di-*iso*-pentyl ether oxidation in the jet-stirred reactor ($\phi = 1$, $p = 10$ atm, 1000 K, $\chi_{0,\text{fuel}} = 1000$ ppm).

5.2 DNPEE

Similarly, the oxidation of di-*n*-pentyl ether is studied in the jet-stirred reactor at 10 atm and with a residence time of 700 ms. Four different equivalence ratios (0.5, 1, 2 and 4) were considered and the resulting fuel conversions are reported in Figure 5.12. Several intermediates have been identified and quantified during DNPEE oxidation, but first it may be interesting to discuss fuel reactivity at different equivalence ratios.

In Figure 5.12, the fuel conversions for all conditions can be seen. The rich mixtures show a double-cool flame behaviour, which is more pronounced at $\phi = 4$. The stoichiometric condition clearly shows different levels of reactivity in different temperature ranges, but considering the experimental uncertainty, a double-cool flame is arguable. In the case of the lean mixture, there is no clear temperature zone where the fuel displays an NTC behaviour. Nevertheless, it seems that the reactivity still decreases in the temperature range where the rich mixtures have the second NTC zone, even if the fuel conversion is over 90%. For the lean mixture, the fuel is already completely converted at 1010 K, while for the stoichiometric ones this is happening around 1060 K and for the two rich mixtures it is necessary to reach around 1100 K.

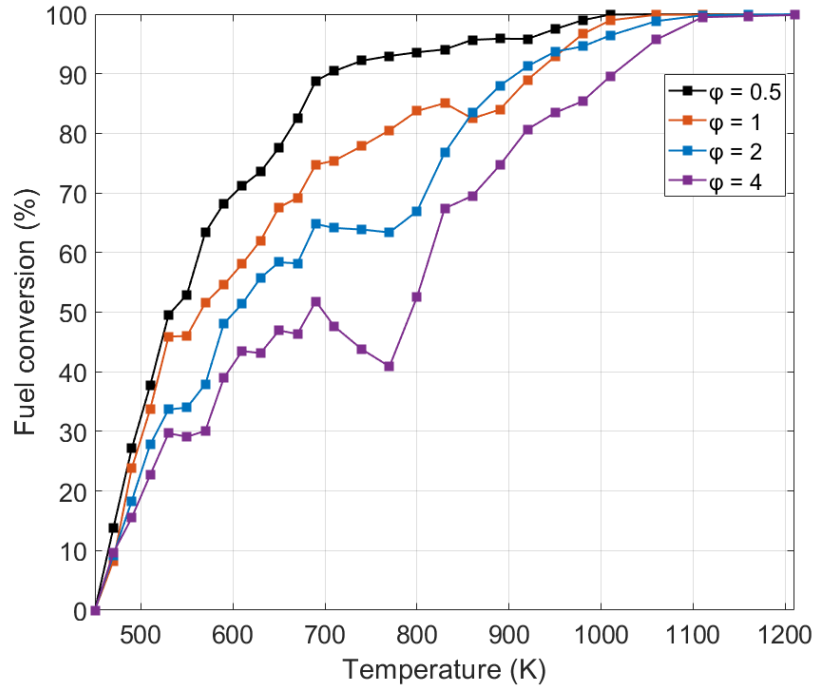


Figure 5.12: Fuel conversion of di-*n*-pentyl ether over the temperature range studied in the jet-stirred reactor for the four equivalence ratios at $p = 10$ atm, $\tau = 700$ ms, $\chi_{0,\text{fuel}} = 1000$ ppm (lines are only added to represent the trend).

In order to have a clearer vision, the mole fraction of the fuel for one of the conditions ($\phi = 2$) has been plotted and is shown in Figure 5.13. As for di-*iso*-pentyl ether, it is possible to see that di-*n*-pentyl ether oxidation shows different zones of reactivity and the temperature range can be divided in 5 sections. DNPEE is already quite reactive at low temperature and its conversion starts at 470 K. The first zone extends up to 530 K and in this zone the reactivity rapidly increases with temperature. At 530 K, the first cool flame zone starts, and it continues up to 550 K. In this zone the reactivity reaches a small plateau and the fuel conversion stagnates at around 34%. Above 550 K, the reactivity starts increasing again, up to around 690 K, where the second cool flame zone is reached. This zone, which extends up to 770 K, sees the reactivity reaching a plateau again, this time with the fuel conversion being constant at around 64%. After this zone, the reactivity starts increasing again with the temperature, up to around 1100 K, where all the fuel is consumed.

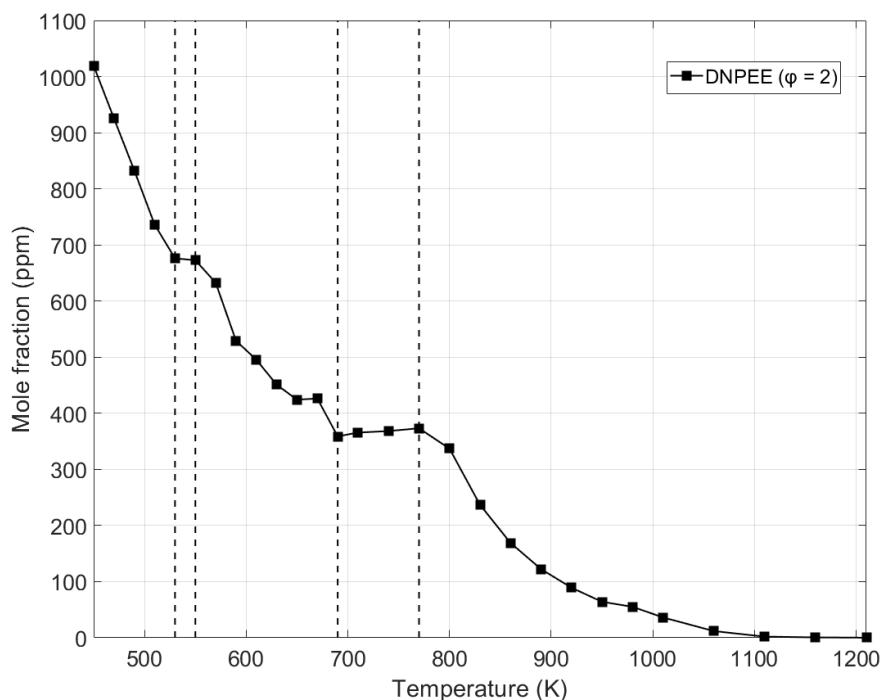


Figure 5.13: Mole fraction of di-*n*-pentyl ether over the temperature range studied in the jet-stirred reactor ($\phi = 2$, $p = 10$ atm, $\tau = 700$ ms, $\chi_{0,\text{fuel}} = 1000$ ppm).

The double cool flame behaviour is common for DIPEE and DNPEE; nevertheless, the temperature at which the different regimes are situated are slightly different. Also, it is important to note that for DIPEE, in the second cool flame zone, the fuel conversion was decreasing for both rich mixtures. For DNPEE, in the $\phi = 2$ mixture, the fuel conversion only reaches a plateau and does not decrease, as opposed to DIPEE. For $\phi = 4$, on the other hand, the second cool flame zone is more important (Fig. 5.12) and the fuel conversion decreases from 52% at 690 K to 41% at 770 K, but also in this case it is not getting close to the values of the first cool flame zone, while for DIPEE it was getting to even lower values than the plateau of the first cool flame. A deeper investigation on the comparison of DIPEE and DNPEE and also the other ethers will be presented in Section 5.3. Figures 5.14–5.17 illustrate the mole fractions of some of the identified and quantified products and intermediates of the oxidation of DNPEE. In this case, no simulations are available, since the mechanism is still under development.

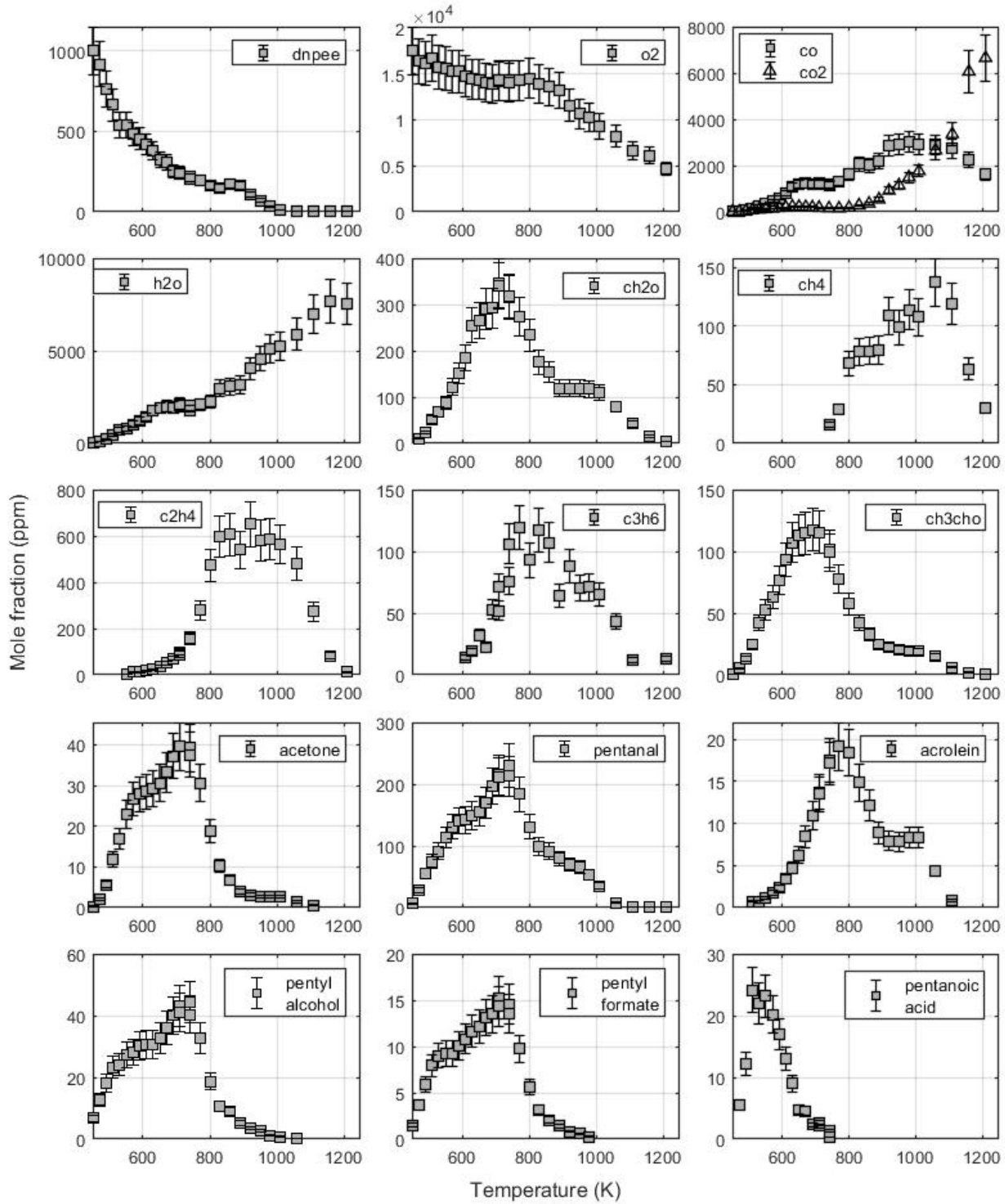


Figure 5.14: Mole fractions of the fuel and the main products and intermediates during the oxidation of DNPEE in the JSR for $\phi = 1$ ($p = 10$ atm, $\tau = 700$ ms, $\chi_{0,\text{fuel}} = 1000$ ppm).

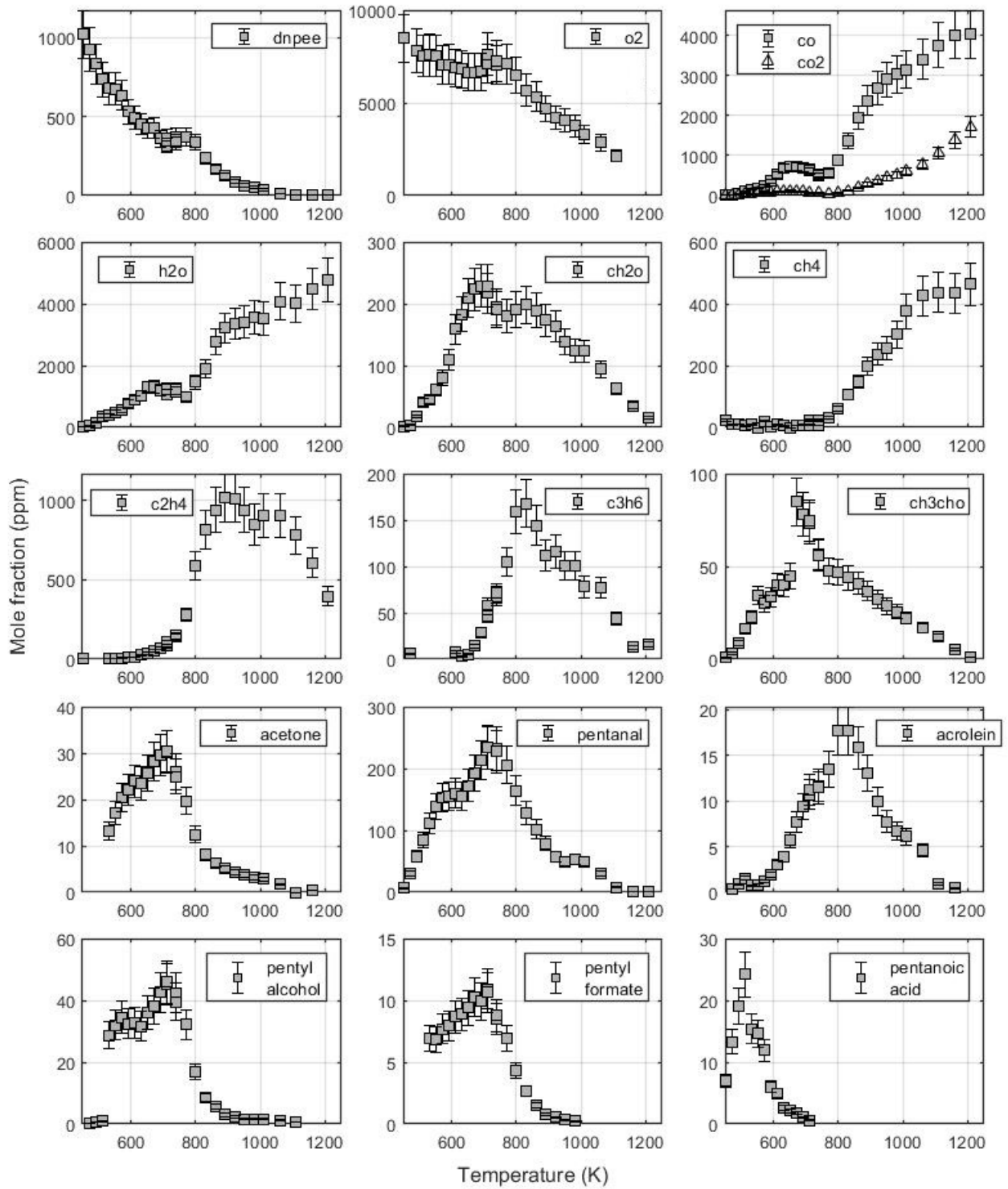


Figure 5.15: Mole fractions of the fuel and the main products and intermediates during the oxidation of DNPEE in the JSR for $\phi = 2$ ($p = 10$ atm, $\tau = 700$ ms, $\chi_{0,\text{fuel}} = 1000$ ppm).

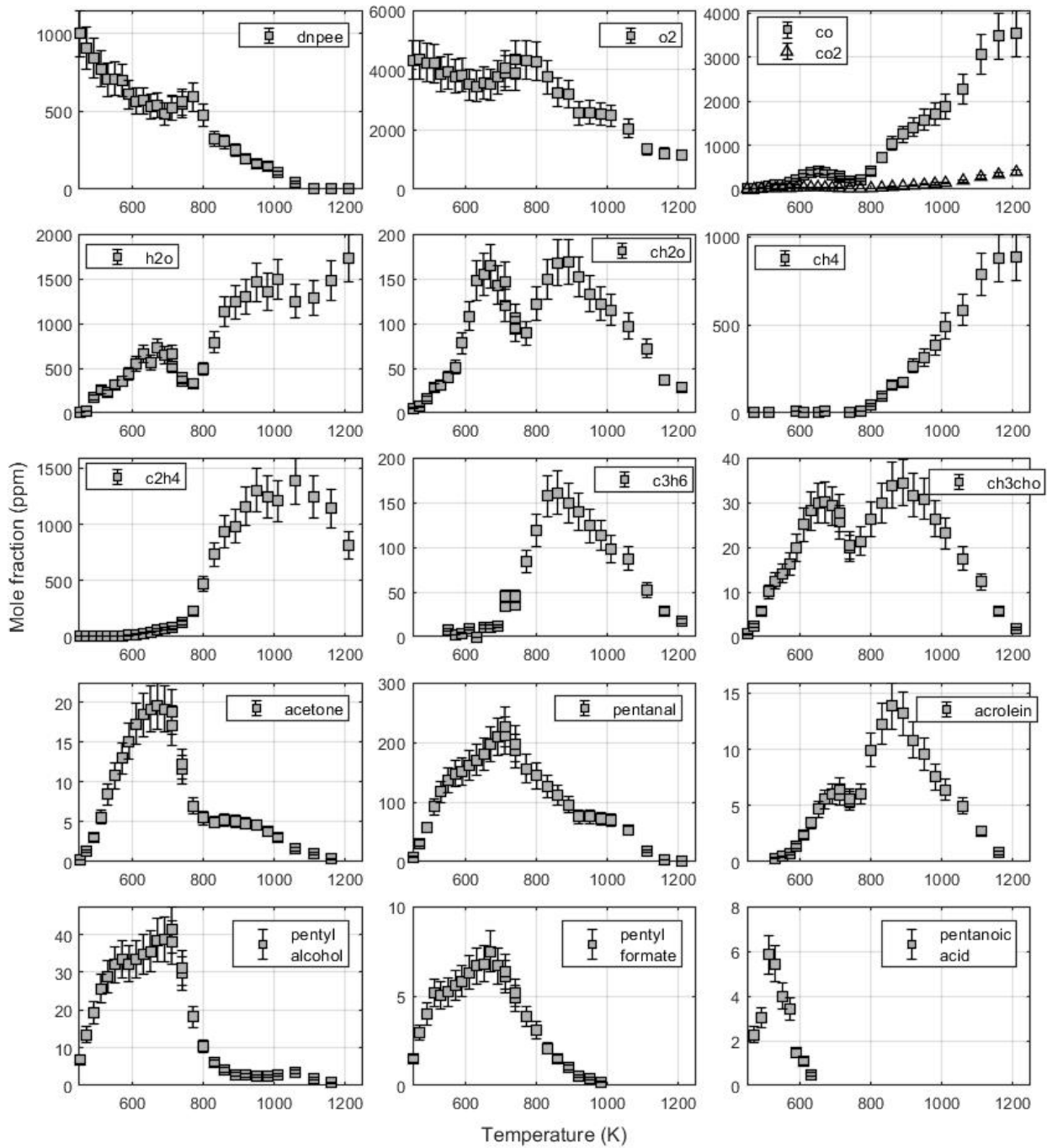


Figure 5.16: Mole fractions of the fuel and the main products and intermediates during the oxidation of DNPEE in the JSR for $\phi = 4$ ($p = 10$ atm, $\tau = 700$ ms, $\chi_{0,\text{fuel}} = 1000$ ppm).

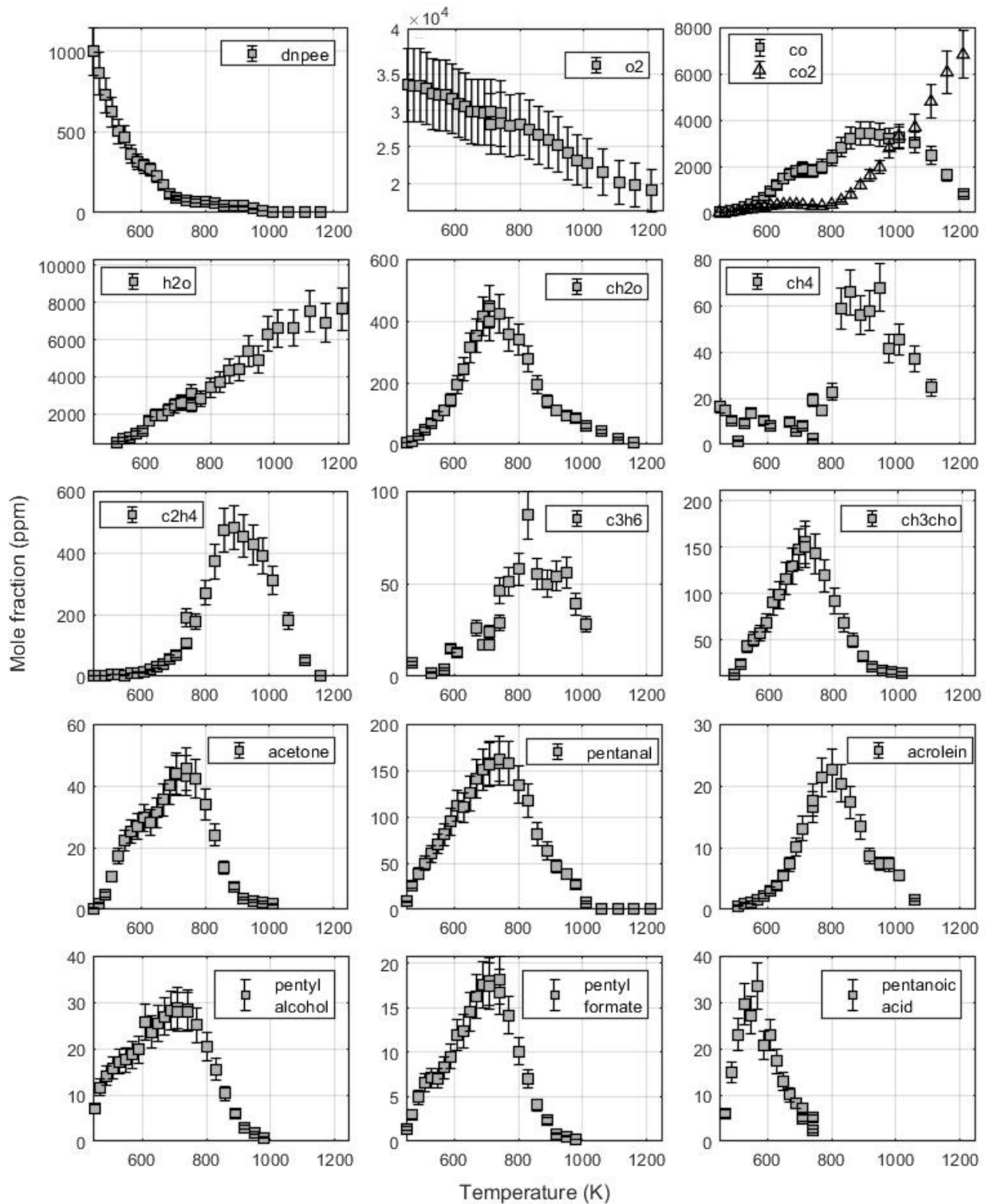


Figure 5.17: Mole fractions of the fuel and the main products and intermediates during the oxidation of DNPEE in the JSR for $\phi = 0.5$ ($p = 10$ atm, $\tau = 700$ ms, $\chi_{0,\text{fuel}} = 1000$ ppm).

As for DIPEE and the other ethers, among the main species formed, several aldehydes can be found. First of all, formaldehyde is produced in important quantities at all conditions. It is a marker of low temperature reactivity and it is produced in large amounts also during DNPEE oxidation. Figure 5.18a shows its mole fraction profiles for all equivalence ratios and in Figure 5.18b mole fractions of the fuel and formaldehyde are plotted together at $\phi = 4$. It is interesting to observe the difference in formaldehyde profiles between lean and rich mixtures. In fact, for lean and stoichiometric mixtures, only one peak of formaldehyde mole fraction can be seen and this is coherent with the almost absence of the "first NTC" zone. On the other hand, for the two rich mixtures, two peaks could be identified, separated by the second NTC. This can be clearly seen also in Figure 5.18b, where the zone between the two peaks (690–770 K) corresponds exactly to the second stronger negative temperature coefficient zone.

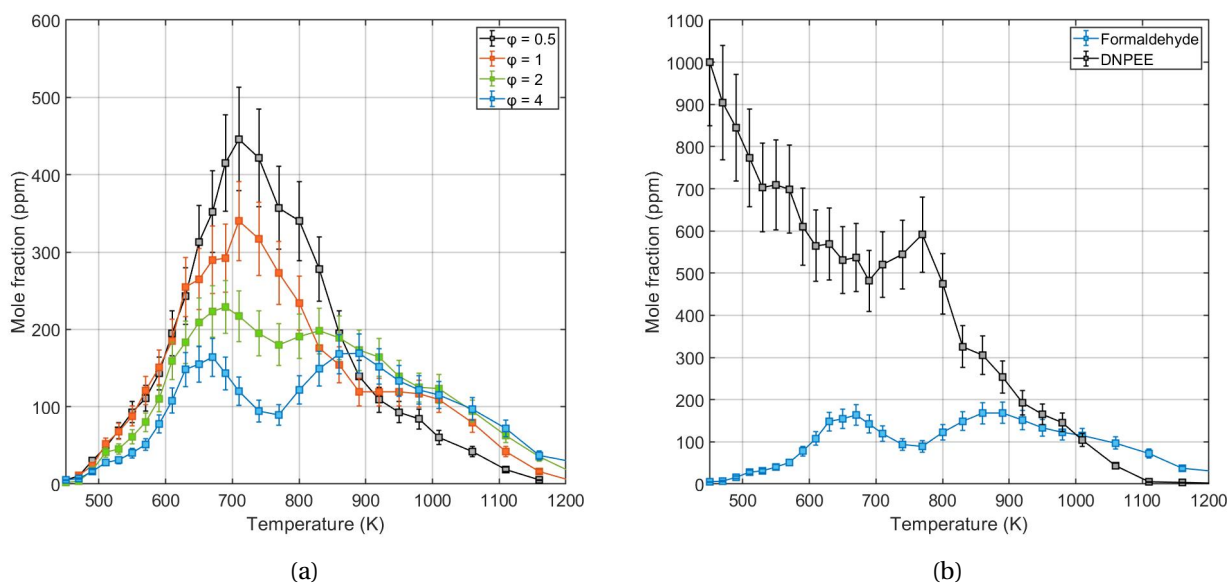


Figure 5.18: **a)** Formaldehyde mole fractions for all conditions; **b)** Formaldehyde and DNPEE mole fractions at $\phi = 4$, $p = 10$ atm, $\tau = 700$ ms, $\chi_{0,\text{fuel}} = 1000$ ppm.

Another aldehyde which is produced at all equivalence ratios is acetaldehyde. Although it is produced in smaller amounts than formaldehyde, it reaches a peak of 156 ppm for the lean condition and of 34 ppm for the richest one. Only for the condition with $\phi = 4$ it is possible to find two peaks, in the same temperature ranges as the ones for formaldehyde in the same condition. The C_5 aldehyde produced as a typical product of di-*n*-pentyl ether oxidation is *n*-pentanal (such as isopentanal during the oxidation of di-*iso*-pentyl ether). This aldehyde is produced in considerable quantities for all conditions, from 162 ppm for $\phi = 0.5$, to 235 ppm at $\phi = 2$. In Figure 5.19, its mole fraction profiles for all conditions are shown. The profiles have similar shapes and similar values. This species is certainly very important in DNPEE oxidation, as was the case for isopentanal in DIPEE oxidation, because it can be produced at all temperatures through differ-

ent pathways and it can influence the overall reactivity, especially due to its own low-temperature chemistry. It is therefore interesting to discuss the probable pathways that can lead to the formation of *n*-pentanal.

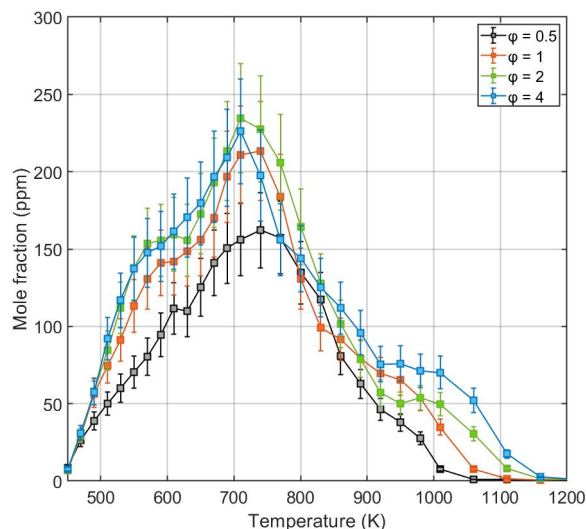


Figure 5.19: Mole fraction profiles of *n*-pentanal at all conditions during DNPEE oxidation.

The most probable reaction pathways leading to the formation of *n*-pentanal are shown in Fig. 5.20, where the *n*-pentanal is highlighted in green. The reaction pathways are quite similar to the ones producing isopentanal in DIPEE oxidation. The formation of *n*-pentanal originates from the α -radical of DNPEE. Especially at high temperature, this radical can directly undergo β -scission, which leads to the formation of *n*-pentanal and *n*-pentyl radicals. These radicals follow their own low temperature oxidation pathways, which may lead to the formation of another *n*-pentanal molecule and *n*-pentanol, as shown in Figures 5.14–5.17. Another possible pathway leading to *n*-pentanal is via the decomposition of the carbonyl-hydroperoxide formed as a result of a series of low-temperature reactions starting with the addition of the α -radical to O_2 . The QOOH radical so formed can also yield *n*-pentanal by β -scission.

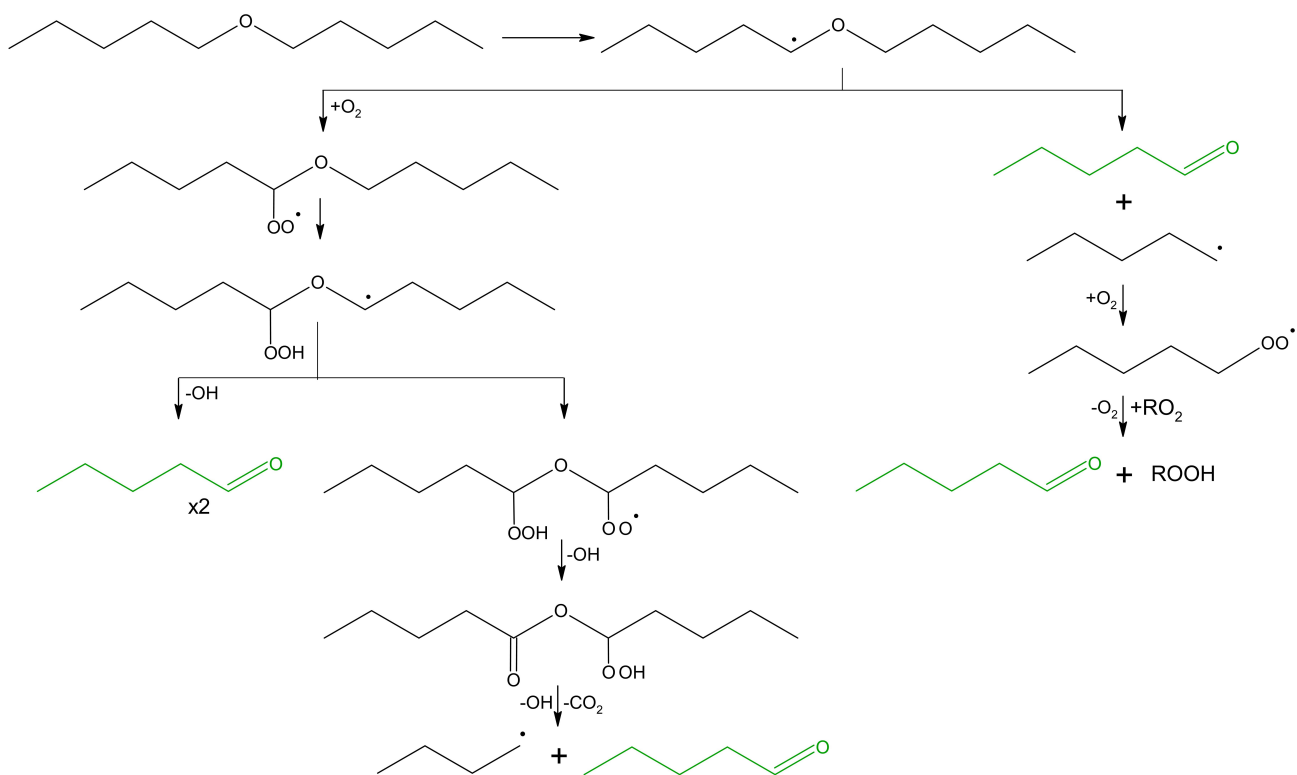


Figure 5.20: *N*-pentanal most probable formation pathways.

As already seen for DIPEE, carboxylic acids are typical intermediates during the low-temperature oxidation of ethers. In the case of DNPEE oxidation, the acid produced is *n*-pentanoic acid and, as can be seen in Figures 5.14–5.17, it is only observed at low temperatures for all conditions. It is expected to be produced from the decomposition of a carbonyl-hydroperoxide (Korcek mechanism [132]), which is coherent with the temperature range where it is measured, since those pathways are typical of low-temperature oxidation.

Among the other products, also *n*-pentanol and pentyl formate are produced in small quantities and at low-intermediate temperatures. When analysing the reaction paths leading to *n*-pentanal, it was possible to see that one of its formation pathways also leads to the formation of *n*-pentanol. This pathway involved the low-temperature chemistry of the pentyl radical, it has to be expected therefore that the zone where this alcohol is produced corresponds to the temperature range of the low-temperature reactivity of this radical.

Pentyl formate is formed in smaller quantities compared to *n*-pentanol; its way of formation depends on the α -radical of the fuel, which adds to molecular oxygen and then isomerises, taking a hydrogen from the γ -site. The decomposition of this QOOH radical can then form pentyl formate and 1-butene. This is not expected to be the most followed pathway for fuel consumption, which is coherent with the low mole fraction measured for this formate.

5.2.1 Expected reaction pathways

Figure 5.21 shows the most probable reaction pathways, starting from the α -radical of DNPEE. If all the primary radicals are expected to be formed, similar to DIPEE and the other ethers, the α -radical is expected to be the most abundant, since the C–H bond neighbouring the ether function is the weakest one. This radical can either decompose to *n*-pentanal and an *n*-pentyl radical (probably more important at intermediate/high temperature) or add to molecular oxygen at lower temperatures. The RO₂ radical so produced can then internally isomerise through two different six-membered transition states. Since the six-membered transition state is the most favoured, both of the QOOH radicals shown in Figure 5.21 are expected to be formed. Both these radicals can then follow the typical chain branching path of low-temperature oxidation. The carbonyl-hydroperoxides so formed produce *n*-butyl radicals as illustrated in Figure 5.21, which are expected to follow their own low-temperature reaction pathways. Similarly, the radicals of *n*-pentanal will follow their own low-temperature paths and the same can be expected from the *n*-pentyl radical, formed for example from the β -scission of the primary fuel radical.

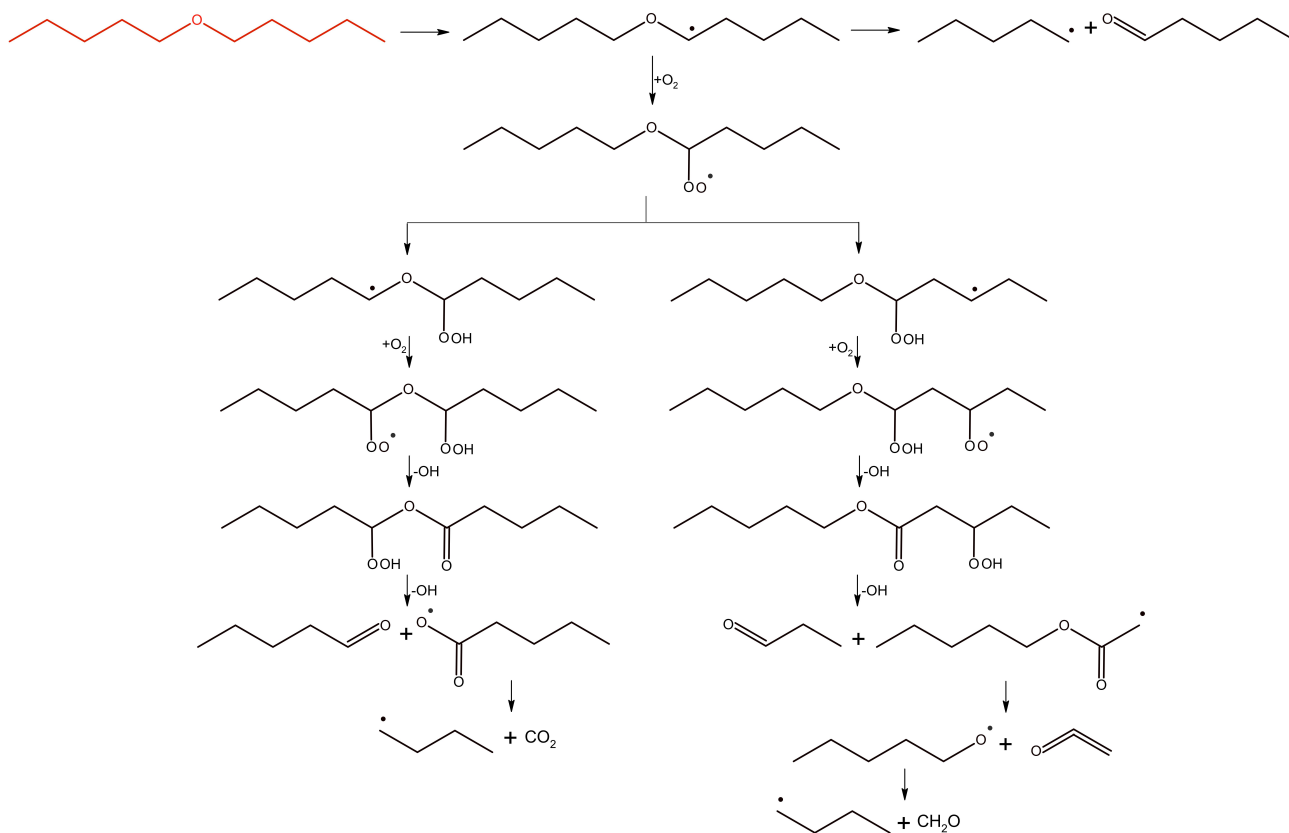


Figure 5.21: Most probable reaction pathways of the α -radical of DNPEE.

5.3 Comparison to the other ethers

Seven different ethers have been studied so far in the same jet-stirred reactor, two of which were investigated in this study. The same oxidation conditions were conserved: initial fuel concentration of 1000 ppm, a pressure of 10 atm, a residence time of 700 ms and equivalence ratios ranging from 0.5 to 2 (or even 4). The aim of keeping the same conditions was to be able to compare and analyse the reactivity of the different structures of these molecules belonging to the same family. Figure 5.22 collects three plots of the fuel conversion of the seven ethers for three equivalence ratios (0.5, 1 and 2). First of all, it is possible to observe that all ethers, except DIPE, start to react at very low temperature (< 500 K). DIPE, the smallest branched symmetrical ether, starts reacting above 700 K, showing no low-temperature reactivity at all, unlike all the other members of the family. This has been explained by the fact that the most easily formed radical cannot follow the path leading to the formation of the carbonyl-hydroperoxide and therefore the reactivity at low-temperature cannot be properly sustained [68].

The smallest symmetrical ether considered here, DEE, shows a conventional NTC behaviour, with the reactivity strongly increasing in the first zone, reaching a fuel conversion between 50% (at $\phi = 2$) and 75% (at $\phi = 0.5$). Then, in the NTC zone, the reactivity strongly decreases, with the fuel conversion going down to less than 10% for all conditions. A similar behaviour is seen for DPE, even if the increase in the length of the chain allows to start seeing a first double-cool flame regime, however not certain, given the uncertainty on the measurements. Increasing the chain length and keeping the symmetry, DBE shows a very clear double-cool flame regime, especially for the fuel-rich condition. This is also the case for DNPEE, which is nevertheless more reactive than DBE and even in the cool flame region, the fuel conversion remains very high. This is due to the fact that the longer chain allows for the formation of more radicals, that can in turn be very reactive and follow their own low-temperature chemistry.

If other modifications to the structure, as for example the branching or the asymmetry are to be considered, the first fuel it may be worth looking at is DIPE. As already anticipated, DIPE is the only ether studied in this JSR under these conditions that did not show any reactivity at low temperatures. The ramification close to the ether function reduces the possibility of the formation of carbonyl-hydroperoxides, which lead to chain branching at low temperature. If the primary radical considered is the tertiary one (α -radical), there is no additional hydrogen available to be abstracted during the second isomerisation ($\text{OOQOOH} \rightleftharpoons \text{HOOQ'OOH}$), thus preventing the elimination of an OH radical and the formation of the carbonyl-hydroperoxide. There are other ways of forming carbonyl-hydroperoxides, but they depend on the less favourable primary radical (β -radical). DIPEE is a branched, symmetrical ether as well, however with a longer chain compared to DIPE and the ramification is further from the ether function. That allows this ether to be very reactive and the long chain allows the formation of radicals and molecules (as for example isopentyl radical or isopentanal) that can follow a low temperature chain branching pathway thus contribut-

ing to the double NTC, but also keeping the reactivity to a higher level also within the cool flame region.

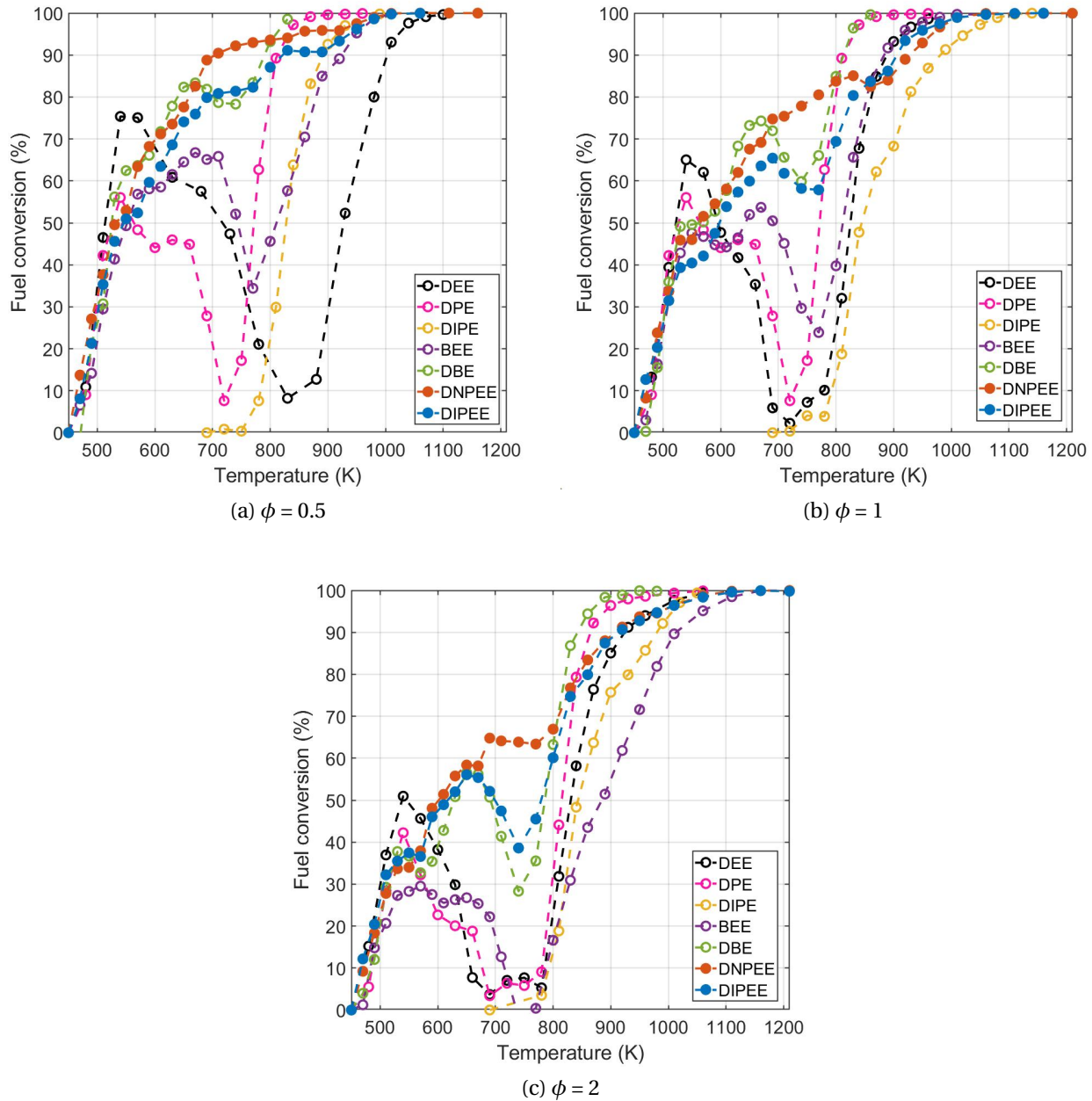


Figure 5.22: Comparison of fuel conversion for three different equivalence ratios (0.5, 1, 2) for seven different ethers (DEE, DPE, DIPE, BEE, DBE, DNPEE, DIPEE), $p = 10$ atm.

The final variation is the asymmetry. To this aim, butyl ethyl ether has been considered. This ether structure is situated between DEE and DBE and it is an isomer of DPE and DIPE. Observing the fuel conversion, its oxidation behaviour also appears to be between DEE and DBE. As DBE, it

presents a double-cool flame regime, but more similarly to DEE (and unlike DBE), at the end of the NTC region its fuel conversion goes back to very low values (almost 0% for fuel-the rich condition). Considering a direct comparison between DIPEE and DNPEE, it is interesting to notice how their long chain places these two fuels among the most reactive ones, but the branching of DIPEE moves it back closer to DBE behaviour, thus apparently leveling out the influence of the longer chain. DNPEE appears to be the most reactive, especially in the cool flame regions, showing how the length of the chain, allowing the formation of more radicals and products, is very important for the overall reactivity. The double cool flame regime seems to be more important for the ethers presenting a chain of intermediate length, as DBE, or a long chain with branching, as DIPEE, while it becomes less clear for the shorter chain (DPE), where there are not enough intermediates with their own low-temperature chemistry, or for the very long chain (DNPEE), where reactivity is always very high.

5.4 Conclusions

To sum up, this chapter presented the main results obtained for the oxidation of two isomers, di-*iso*-pentyl and di-*n*-pentyl ether, in a jet-stirred reactor. Both these fuels showed a double-cool flame regime, which was more pronounced for DIPEE, while DNPEE shows a stronger reactivity over the whole temperature range. For most conditions (except $\phi = 4$), DNPEE does not show a zone where reactivity decreases, but only some temperature ranges where the reactivity reaches a plateau. For both fuels, a large number of products and intermediates has been identified and quantified. Some products as CO, CO₂, water, CH₄, C₂H₄, C₃H₆, acetone are in common, as well as the smaller aldehydes (acetaldehyde and formaldehyde), which were also formed during the oxidation of other ethers. The two specific aldehydes, isopentanal and *n*-pentanal respectively for DIPEE and DNPEE, are produced in considerable amounts (around 200 ppm) and have a very important role in the reactivity of these two ethers. Other specific products include the carboxylic acids (isopentanoic and *n*-pentanoic acids, respectively), that are produced only at low temperatures and the specific formates and alcohols (isopentyl and *n*-pentyl), that are also produced at low-intermediate temperatures.

For DIPEE, a detailed kinetic mechanism was developed, which proved to be in reasonable agreement with the experimental results and helped to understand the reactivity thanks to the reaction pathway analysis and the analysis of the rate of production of OH and isopentanal.

A final comparison between all the ethers showed how the length of the chain seems to increase the reactivity, by helping the formation of more radicals and products that can in turn have their own chemistry, which helps the reactivity. On the other hand, the ramification seems to reduce the reactivity, even if its influence is lower when the chain is longer and the methyl group is far from the ether function.

Chapter 6

Results and discussion: oxidation of ethers in the RCM

In this chapter, the results obtained from the rapid compression machine are presented. For each ether, a first section introduces the measured ignition delay times and the comparison to the simulations (when available), followed by a reaction pathway analysis. A heat release rate analysis is also presented for each fuel. Finally, the results for the different ethers are compared and the last part of the chapter will focus on the results for ethyl lactate.

Contents

6.1 DEE	86
6.1.1 Reaction pathways	88
6.1.2 HRR	89
6.2 DPE	91
6.2.1 Reaction pathways	95
6.2.2 HRR	98
6.3 DIPE	99
6.3.1 Reaction pathways	102
6.3.2 HRR	105
6.4 BEE	107
6.4.1 Reaction pathways	109
6.4.2 HRR	111
6.5 DBE	113
6.5.1 Reaction pathways	116
6.5.2 HRR	118

6.6	DIPEE	120
6.6.1	Reaction pathways	123
6.6.2	HRR	126
6.7	DNPEE	128
6.7.1	HRR	130
6.8	Comparison	132
6.8.1	DPE vs DIPE	132
6.8.2	DNPEE vs DIPEE	135
6.8.3	BEE vs DEE/DBE/DPE	136
6.8.4	Final comparison	138
6.9	Ethyl lactate	142
6.9.1	Reaction pathways	143
6.9.2	Comparison to ethanol	145
6.9.3	Comparison to DIPE	146
6.10	Conclusion	147

Introduction

The following sections present the experimental results obtained for each fuel in the rapid compression machine (as well as in the facilities of the University of Galway for DPE and DIPE). When possible, the tests have been performed under the same conditions ($p_c = 15$ bar, dilution = $[\text{inert gases}]/[\text{O}_2] = 10$, $\phi = 2$, $T_c = \sim 510\text{--}660$ K) in order to be able to compare the reactivity of the different ethers. This was not always possible, due to the different reactivity of the studied molecules, nevertheless at least one condition (dilution 10, $\phi = 2$) is in common between all the ethers and allows a direct comparison of the ignition delay times. For the heat release rate analysis, on the other hand, the results for DIPE are in different conditions with respect to the other ethers (due to its low reactivity) and it will therefore not be directly comparable.

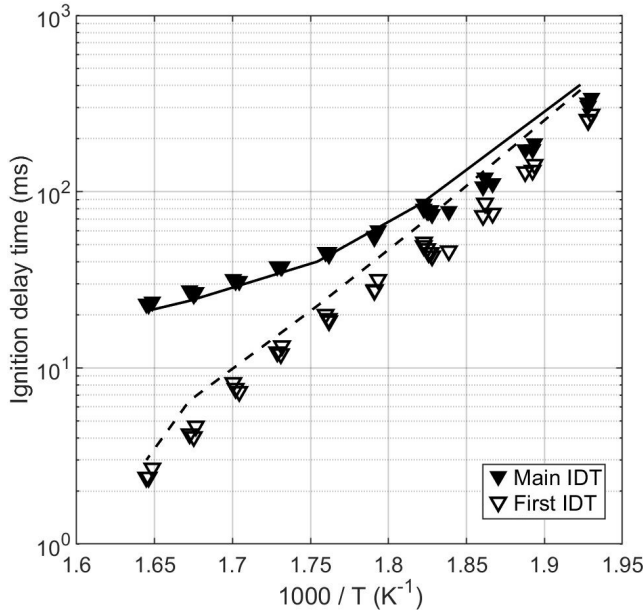
The experimental uncertainty for the ignition delay times measured in the RCM was discussed in section 3.4.2. Two choices were therefore possible for the figures in this chapter: computing a mean value for the IDT at each temperature, with the related error bars, or including all the ignition delay times measured several times for each condition. This last option was chosen, so that the repeatability of the tests can clearly be seen from the plots. Nevertheless, it should be noted that the experimental uncertainty is assessed around 10%.

6.1 DEE

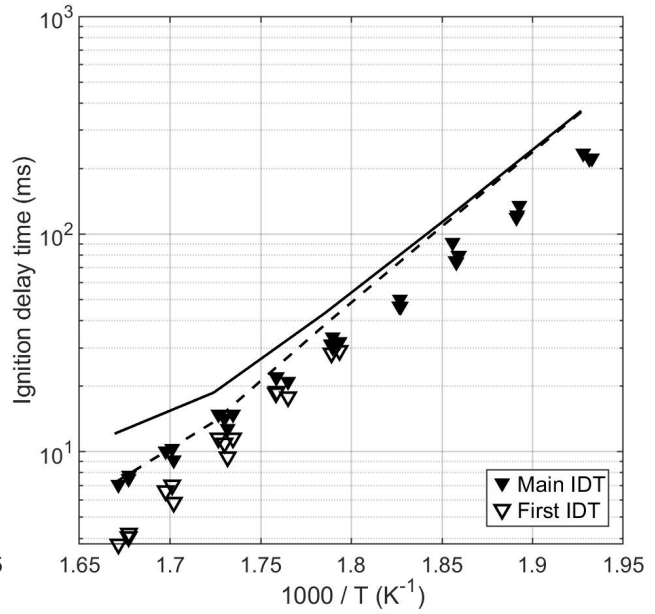
The first fuel that was studied in the rapid compression machine is the smallest ether included in this study, diethyl ether. In Figure 6.1, the measured ignition delay times are plotted, together with the simulated ones. The Figure 6.1a shows the ignition delay times for the stoichiometric mixture with a dilution of 10, at 15 bar. The ignition happens in two stages over the studied temperature range (520-610 K), as can be also seen in the pressure profiles in appendix B.1.1. The ignition delay times of the first stage seem to follow a linear trend (on a logarithmic scale), while the IDTs of the main ignition seem to reach a plateau towards the higher temperatures of the considered range. The mechanism is capable of simulating this behaviour properly, even if there is a slight overestimation of the IDTs (both of the first and main stages) at lower temperatures. The same overprediction can be seen for the rich mixture (6.1b) over the whole temperature range. Also in this case, it is possible to see a two-stage ignition, as for the stoichiometric mixture, but only at higher temperatures. At the lowest temperatures, the model also predicts two stages, but the ignition delay times are very close to one another. It is possible to suppose that it is the same in the experimental results, but the time difference is so small and the two slopes in the pressure so similar that it is impossible to distinguish the first and main ignition delay times at very low temperatures. Nevertheless, the distance between the first and the main stage IDTs increases as the temperature increases and it is then possible to distinguish them. The mechanism predicts the same behavior, even if it simulates longer ignition delays both for the first and the main ignition events.

The Figure 6.1c shows the measurements and simulations of two different lean mixtures, one with dilution of 5 and one with dilution of 10. For the mixture with dilution of 5 (red points and lines), two stages in the ignition were recorded, similar to what was seen for the stoichiometric one. The mixture with dilution 10 showed only one stage ignition, which appears to be a first-stage ignition and not one single main ignition. An example of the pressure profiles (both experimental and simulated) from the two mixtures with different dilutions at a similar temperature (608-609 K) is shown in Figure 6.2 and others can be seen in the appendix B.1.1. The hypothesis of the more dilute mixture having only a first stage ignition comes from the small pressure increase, which seems to be related to a low-temperature heat release. In addition, if the simulated pressure profiles are considered, it is possible to see that the sharp pressure increase of the first stage is in very good agreement, while the pressure in the simulation keeps increasing and shows another stage much less steep. The third reason that corroborates this hypothesis is the comparison of the IDTs of the two mixtures, as shown in Figure 6.1c: the single delays measured for the more dilute mixture superpose to the first stage delays of the mixture with dilution 5, while the main delays of this last mixture are longer. If the single stage of the more diluted mixture was a main stage, it would be expected to be longer than the one of the less diluted mixture. Regardless, for both mixtures the agreement of the simulations with the experimental results is quite good, even if also in this case

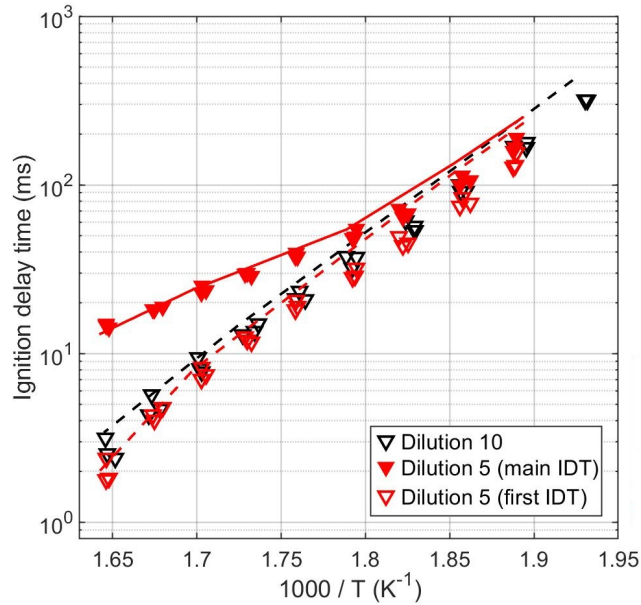
there is a slight overprediction of the delays at lower temperatures.



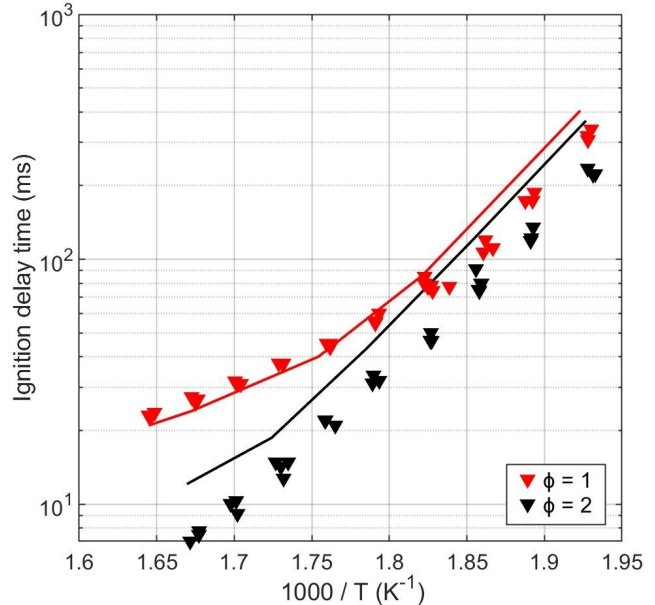
(a) $\phi = 1$, $p_c = 15$ bar, dilution = 10, DEE = 1.5%



(b) $\phi = 2$, $p_c = 15$ bar, dilution = 10, DEE = 2.9%



(c) $\phi = 0.5$, $p_c = 15$ bar, dilution = 5 (red), 10 (black), DEE = 1.37% (red), 0.8% (black)



(d) Comparison of main IDTs, $p_c = 15$ bar, dilution = 10

Figure 6.1: Ignition delay times of diethyl ether in the RCM (points: experimental data, lines: simulations (solid: main IDT, dashed: first IDT)), $p_c = 15$ bar.

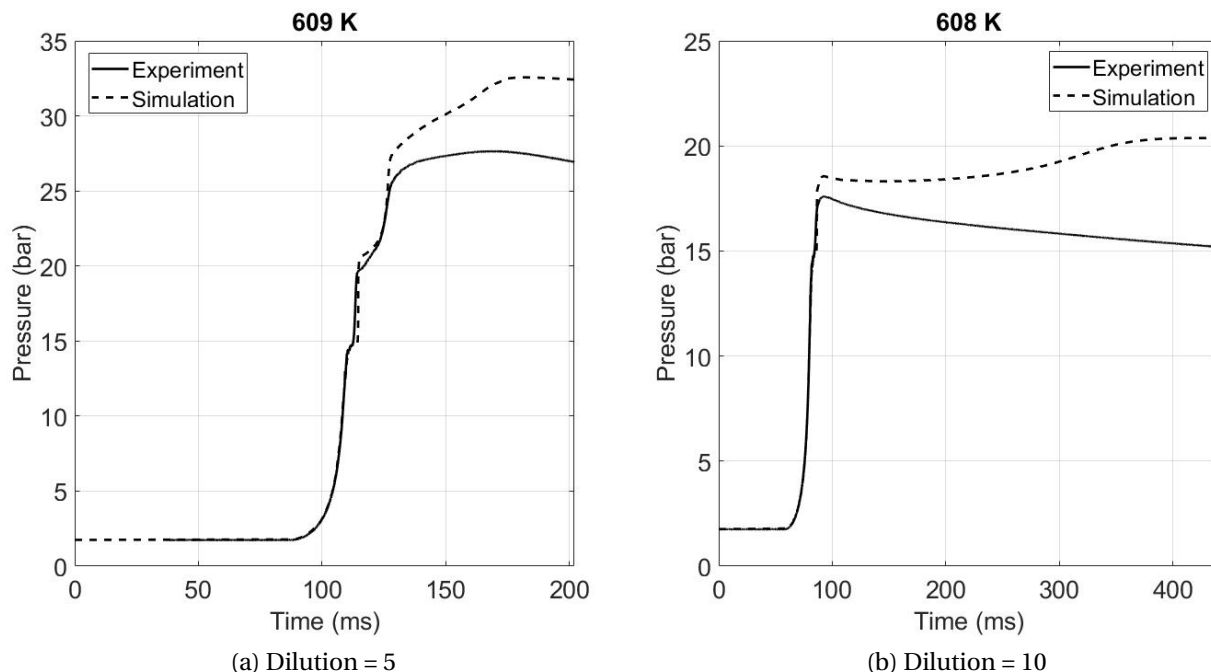


Figure 6.2: Experimental and simulated pressure profiles for diethyl ether mixtures at $\phi = 0.5$, $p_c = 15$ bar.

6.1.1 Reaction pathways

A reaction pathway analysis was also performed, in order to see which reactions were driving the reactivity during the ignition in the rapid compression machine. In figure 6.3, the results of this analysis are shown for a stoichiometric mixture at two temperatures, 549 and 608 K. These two temperatures, even if they are at the extremities of the studied range, are not that far from each other, therefore the percentages are quite similar, but some small differences can be seen. The most abundant radical is the one formed from the H-abstraction on the α -site, as expected. This radical mainly follows the typical low-temperature reaction path.

A very small flux forms the β -radical (2-3%). This radical adds to molecular oxygen and then the RO_2 isomerises to the QOOH radical. At the lower temperature, 88% of this radical then adds to O_2 for a second time, but at the higher temperature this percentage decreases to 60% and a small flux (11%) forms a cyclic ether, while another flux (29%) decomposes through β -scission. This is interesting, because it shows how the increase of temperature leads to the appearance of pathways, such as the one leading to the cyclic ether formation, that were not favoured at low temperature. Nevertheless, in this case, this flux is so small that it is negligible on the overall reactivity.

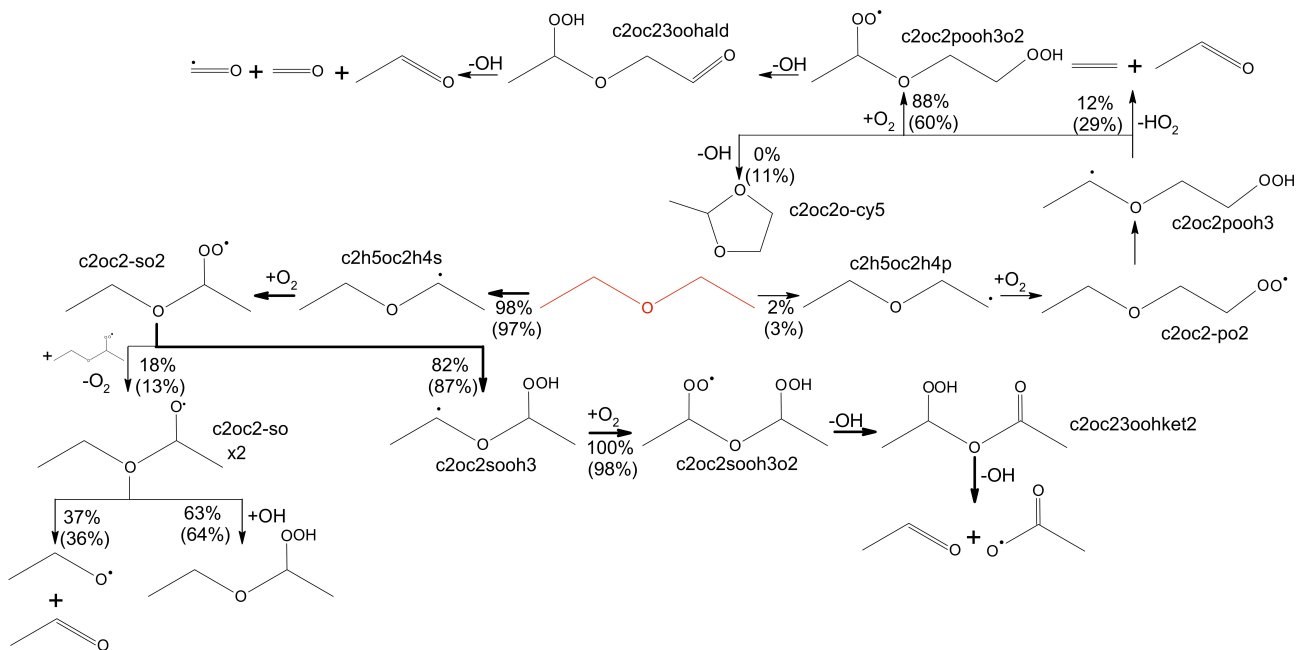
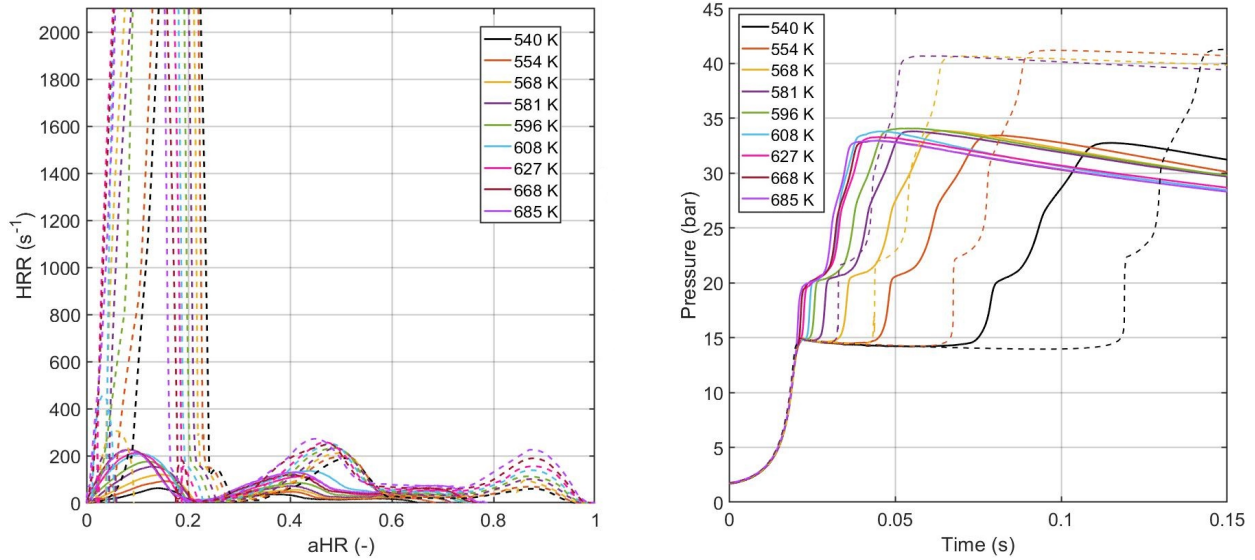


Figure 6.3: Reaction pathways in diethyl ether oxidation ($\phi = 1$, DEE = 1.5%, $p_c = 15$ bar, 549 K and 608 K (in parenthesis), at 20% fuel consumption).

6.1.2 HRR

More tests were performed for the stoichiometric mixture, with dilution equal to 10, in order to perform an analysis on the heat release during the ignition process in the rapid compression machine. The computed heat release rate over the accumulated heat release, both from the experiments and from the simulations are shown in figure 6.4a. From this figure, it is possible to see that the ignition appears to be happening in three stages, with the first stage being the one where the highest heat release rate is reached. The second and third stages have lower heat release rate, around half or less than the first one. The simulations predict similar accumulated heat release, especially for the first stage, but the predicted maximum heat release rate is very different. This can be seen also by comparing the pressure profiles, as shown in figure 6.4b. In fact, the mechanism predicts a very sharp pressure increase, especially for the first stage ignition. When computing the HRR, the first derivative of the pressure is used and this value is expected to be different between experiments and simulations if the slope of the pressure increase is different. It is also possible to see that the mechanism overpredicts the ignition delay at the lowest temperatures, but it gets quite close to the experimental value as the temperature increases, while the heat release is still very different, since the shape of the predicted pressure profile is also very different.



(a) Heat release rate vs accumulated heat release (both normalised by the mixture LHV) (b) Pressure profiles (only some simulations for clarity of the plot)

Figure 6.4: Experiments (solid) vs simulations (dashed): **a)** HRR vs aHR, **b)** pressure profiles. Mixture: DEE, $\phi = 1$, dilution = 10 (inert gases: 50% CO_2 / 50% N_2), DEE = 1.5%, $p_c = 15$ bar.

As explained in section 4.3, it is possible to determine the low-temperature heat release and the maximum accumulated heat release from the plot in figure 6.4a. In figure 6.5, these values are compared between the experiments and the simulations. The LTHR was selected as the first inflection point and the second inflection points were not compared, because these were hard to be accurately identified in the experiments, where the inflection point is not clearly discernible. From Figure 6.5, it is possible to see that the LTHR is reasonably well simulated by the mechanism (even if it must be remembered that the heat release rate was largely overpredicted), while the maximum accumulated heat release is very different, with the model reaching a value of 1, while the experiments showed a maximum of around 0.8. This is partially caused by facility effects, as for example the flow going into the crevice, that cannot be accounted for [97]. Nevertheless, these effects can usually explain a difference around 10%, which implies that there is also some discrepancy linked to the mechanism that cannot correctly predict the heat released during the combustion. Both in the experiments and in the simulations, it is possible to see that, as the temperature increases, the maximum accumulated heat release also slightly increases. On the other hand, the low-temperature heat release slightly decreases with increasing temperature, which is expected, since the cool flame tends to disappear at higher temperatures. Nevertheless, all the tests performed are in the low-temperature range for DEE, therefore it is not possible to really see the cool flame disappearance.

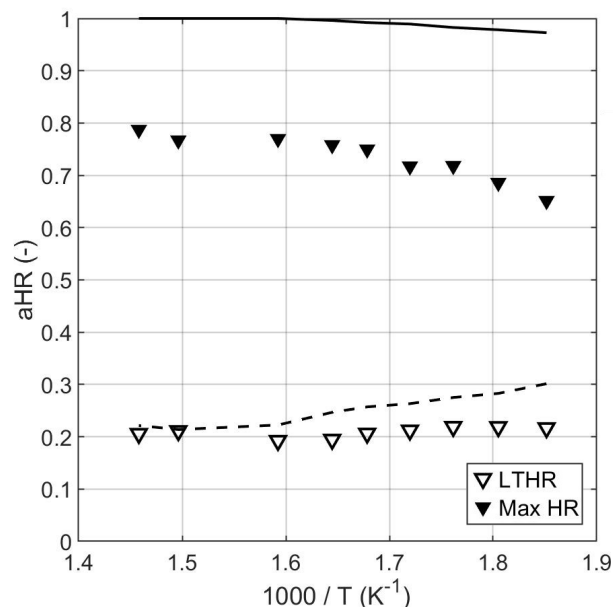


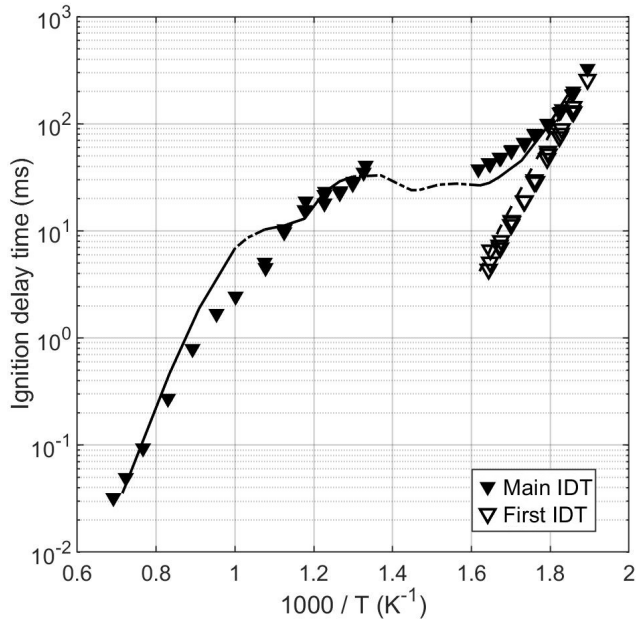
Figure 6.5: Low-temperature heat release and maximum accumulated heat release (normalised by the mixture LHV): comparison between experiments (points) and simulations (lines). Mixture: DEE, $\phi = 1$, dilution = 10 (inert gases: 50% CO₂ / 50% N₂), DEE = 1.5%, $p_c = 15$ bar.

6.2 DPE

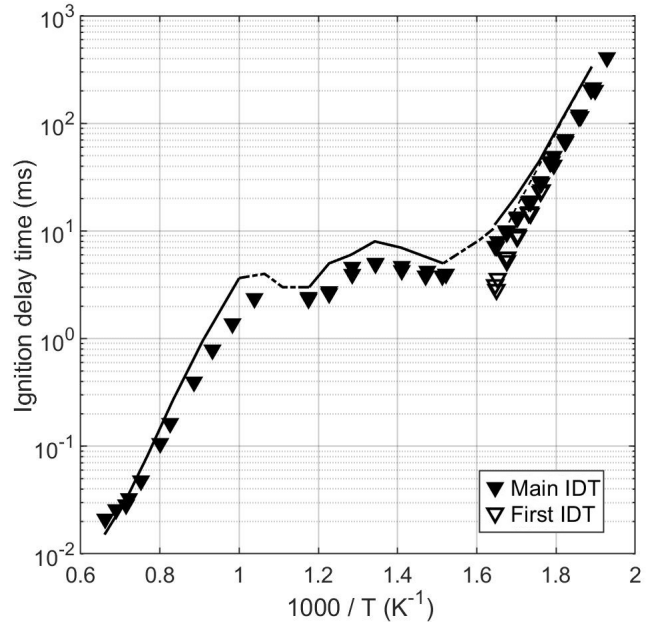
Di-*n*-propyl ether was one of the two ethers that have been studied both in the RCM of Orléans and in the RCM and ST of Galway. The measured ignition delay times in all set-ups and the simulations are shown in Figure 6.6. The IDTs at low temperature were measured in the PRISME RCM, while the ones at intermediate temperatures for the rich and stoichiometric mixtures were measured in the Galway RCM. The ignition delay times at high temperature were measured in the shock tube of the University of Galway for all the mixtures. The lines represent the simulated values: the solid lines represent simulation performed using the corresponding volume profile from the non-reactive mixtures for the RCM and constant volume for the ST. The dotted lines between the temperature ranges where the experiments were performed represent simulations performed using the closest volume profile, changing the initial conditions in order to obtain the missing temperatures. This was done after comparing the volume profiles obtained for similar temperatures and seeing that the pressure decay was quite similar if the temperature was not too different (± 25 K) and it was only to have a continuous line in the temperatures where none of the used set-ups could be exploited.

Figure 6.6a shows the ignition delay times of the stoichiometric mixture. At low temperatures, ignition happens in two stages, as shown by the presence of the measured first ignition delay times and as can be seen from the pressure profiles in Figure 6.7 and in the appendix B.1.2. The mechanism is in quite good agreement with the first ignition delay times, while it slightly underpredicts

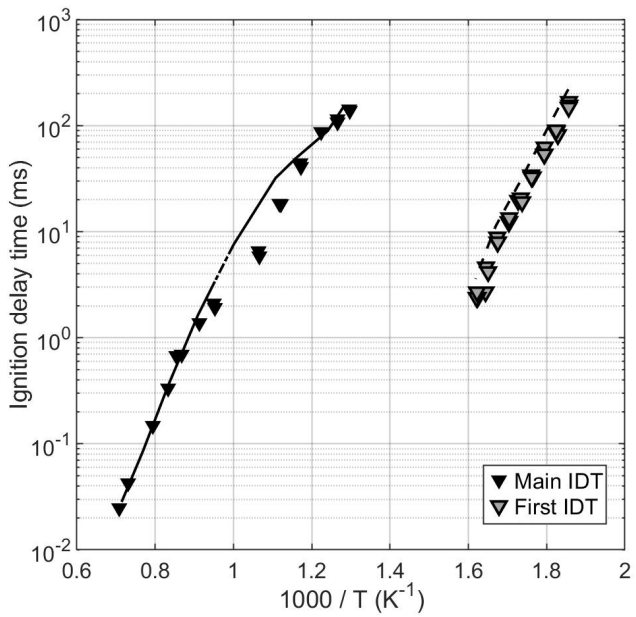
the main IDTs, especially when the temperature starts increasing. The trend of the last experimental points in this low-temperature range and the first ones that could be measured with the second RCM seems to hint that there is an NTC zone, where the ignition delay times reach a plateau and the reactivity is not increasing. In agreement, the simulations show a plateau in the main ignition delay times between 625 and 720 K. They are also in good agreement with the IDTs measured in Galway RCM (760-910 K), except for the higher temperatures, where the mechanism starts overpredicting the delay. This is also the case for the ignition delays at the lowest temperature in the shock tube, while it gets closer to the experimental points for temperatures higher than 1150 K. A similar situation is found for the rich mixture, for which the IDTs are shown in Figure 6.6b. At low temperatures, a two-stage ignition is seen, but in this case, similar to what was seen for DEE (section 6.1), at very low temperatures it is impossible to distinguish the two stages in the experimental pressure profiles and also the simulations predict first and main ignition delays to be very similar, as shown in Figure 6.8a. As the temperature increases, the two IDTs distance from each other, both in the experiments and in the simulations, as shown in Figure 6.8b. Over the whole temperature range, with the exception of high temperatures over 1150 K, the mechanism slightly overpredicts the main ignition delay times. Unlike $\phi = 1$, where the NTC zone was outside the range of temperature where the IDTs are measured, for the rich mixture it is possible to see that there is a zone between 660 and 760 K where the ignition delay times reach a plateau value or even slightly increase with increasing temperature. The mechanism is also in good agreement with this trend, even if it overpredicts the IDTs. The predicted values between the RCM and the ST range show another small plateau or even increase in the simulation, but this could be caused by the difference in the set-ups and their relative facility effects, therefore it is not really possible to assume the fuel having a double NTC. It would be necessary to perform tests in a single set-up over that temperature range in order to assess with greater certainty if a second NTC is present or not. Finally, Figure 6.6c shows the IDTs of the lean mixture. Similarly to DEE, in the lowest temperature range only the ignition delay times of the first stage could be measured and the mechanism predicts these values quite well (some pressure profiles, both experimental and simulated, are included in the appendix B.1.2). In the intermediate temperature range, it was not possible to measure the ignition delay times, since they were outside the reliability range of both RCMs. The IDTs between 770 and 940 K were then measured in the RCM of the University of Galway and between 1050 and 1410 K in the ST (Galway). The mechanism is in good agreement with the measured values, with a slight overprediction in the highest temperature reached with the RCM. From these experimental data, it is impossible to predict if the lean mixture would show an NTC zone as it was the case for the other two mixtures. Nevertheless, it is clear that the lean mixture is the least reactive, except at very high temperature (over 1350 K), where the typical crossover of the IDTs of the mixtures at different equivalence ratios happens and the lean mixture shows the shortest delays.



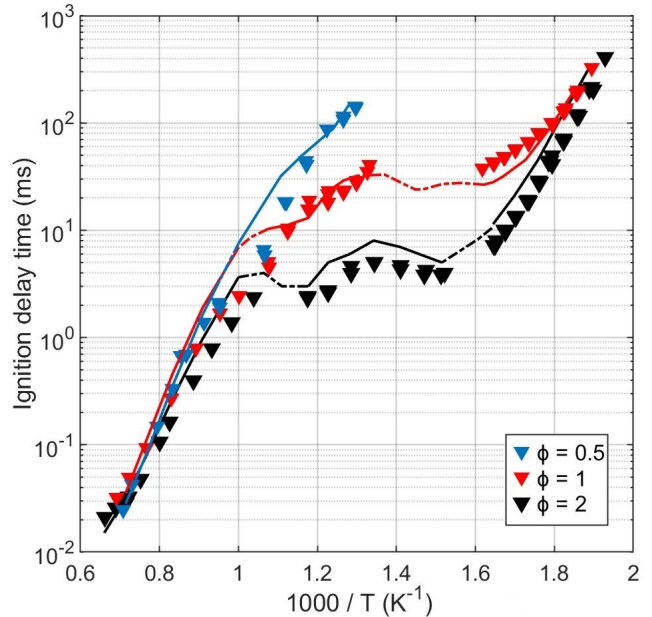
(a) $\phi = 1$, $p_c = 15$ bar, dilution = 10, DPE = 1.0%



(b) $\phi = 2$, $p_c = 15$ bar, dilution = 10, DPE = 2.0%



(c) $\phi = 0.5$, $p_c = 15$ bar, dilution = 10, DPE = 0.5%



(d) Comparison of main IDTs, $p_c = 15$ bar, dilution = 10

Figure 6.6: Ignition delay times of di-*n*-propyl ether in the RCM and ST (points: experimental data, lines: simulations (solid: main IDT, dashed: first IDT), $p_c = 15$ bar.

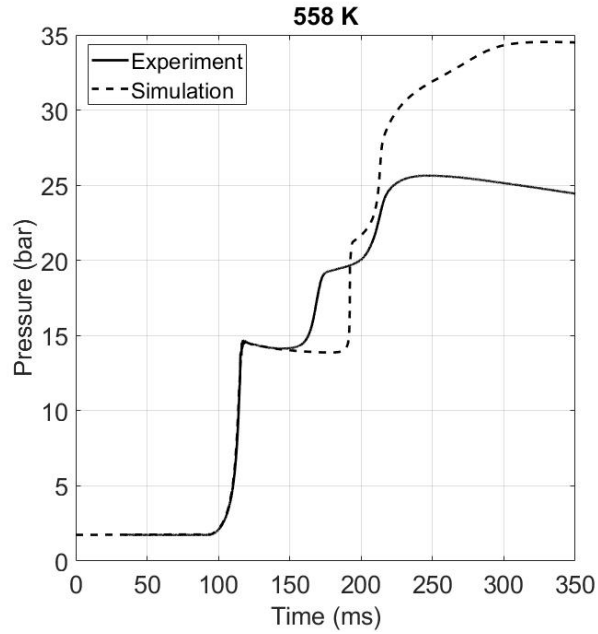


Figure 6.7: Experimental and simulated pressure profiles for a mixture of DPE at $\phi = 1$, dilution = 10 (inert gas: 100% CO₂), DPE = 1.0%, $p_c = 15$ bar, $T_c = 558$ K.

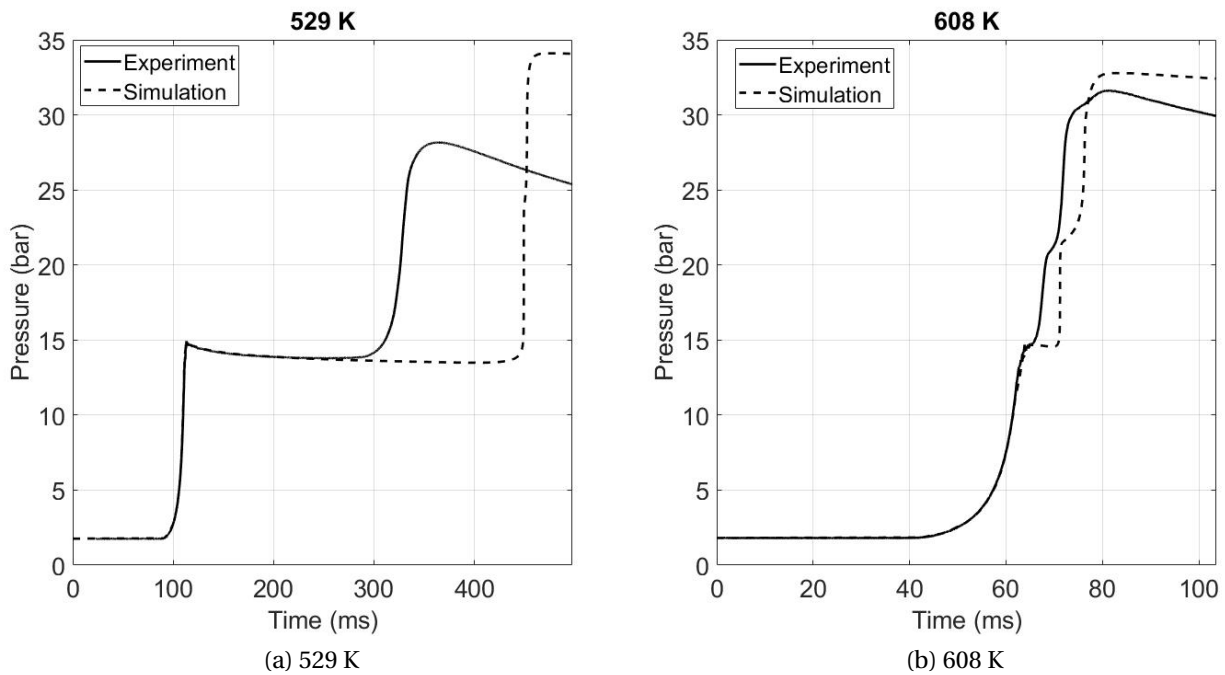


Figure 6.8: Experimental and simulated pressure profiles for a mixture of DPE at $\phi = 2$, dilution = 10 (inert gas: 100% CO₂), DPE = 2.0%, $p_c = 15$ bar, $T_c = 529$ K (a), 608 K (b).

6.2.1 Reaction pathways

A reaction pathway analysis has been performed at low and intermediate temperatures (610 and 789 K) and at higher temperatures (1000 and 1200 K) for the stoichiometric mixture. The results of this analysis are shown respectively in figures 6.9 and 6.10.

At 610 K, the typical pathways of low-temperature reactivity are followed. The most abundant fuel radical is the α -radical (77%), followed by the β - (13%) and γ - (10%) radicals. All these fuel radicals add to molecular oxygen and then isomerise to form QOOH radicals. More than 90% of the QOOH radicals go through a second addition to O₂, followed by the formation of ketohydroperoxides, which then decompose, forming smaller products and radicals. These pathways are very similar to the ones that were predicted in the jet-stirred reactor at 500 K in the work of Serinyel et al. [57]; this shows how the main oxidation pathways at very low temperature seem to be similar under different conditions and set-ups.

When the temperature increases to around 800 K (Fig. 6.9), the β -scission reactions and the formation of cyclic ethers become more important pathways. The cyclic ether formations from the QOOH radicals remain mostly negligible, while the β -scission becomes the main pathway followed by these radicals (for example, the flux from the radical `dpe1ooh1` increases to 73%, with respect to the 9% at 610 K).

The reaction pathway analysis performed at high temperatures shows quite different results compared to low temperature. The main pathways are shown in figure 6.10. At 1000 K, the fuel still undergoes H-abstraction, with the α -radical being the most abundant one (77%). At 1200 K, this percentage decreases to 52% and 27% of the fuel undergoes unimolecular decomposition. This reaction was not important at low temperature and at 1000 K, but it becomes more and more important as the temperature increases. The fuel radicals obtained by H-abstraction either directly undergo β -scission reactions or can still add to molecular oxygen (mainly at 1000 K, while the fluxes following these pathways at 1200 K become negligible). Nevertheless, the low-temperature pathways are no longer followed after the addition to oxygen: RO₂ radicals undergo isomerisation to QOOH radicals, but these either decompose by β -scission or form unsaturated compounds.

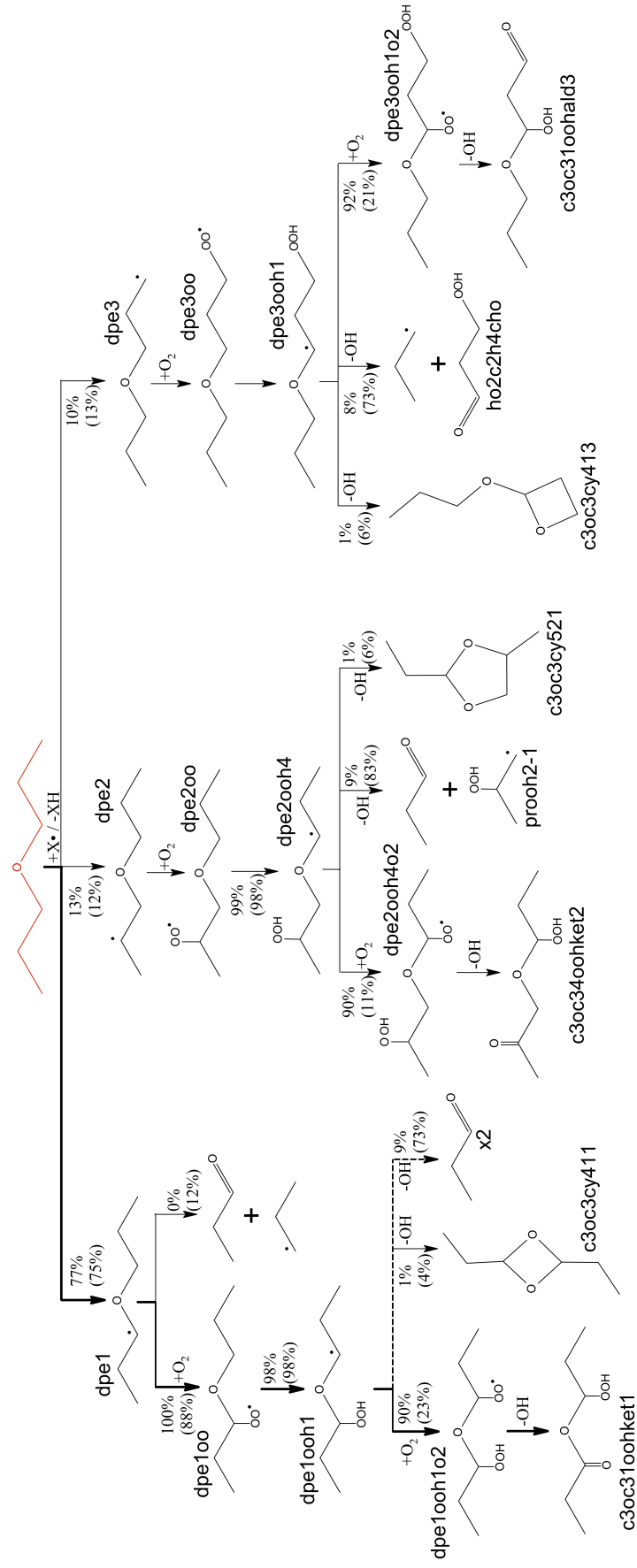


Figure 6.9: Reaction pathways in di-*n*-propyl ether oxidation ($\phi = 1$, DPE = 1.0%, $p_c = 15$ bar, 610 K and 789 K (in parenthesis), at 20% fuel consumption).

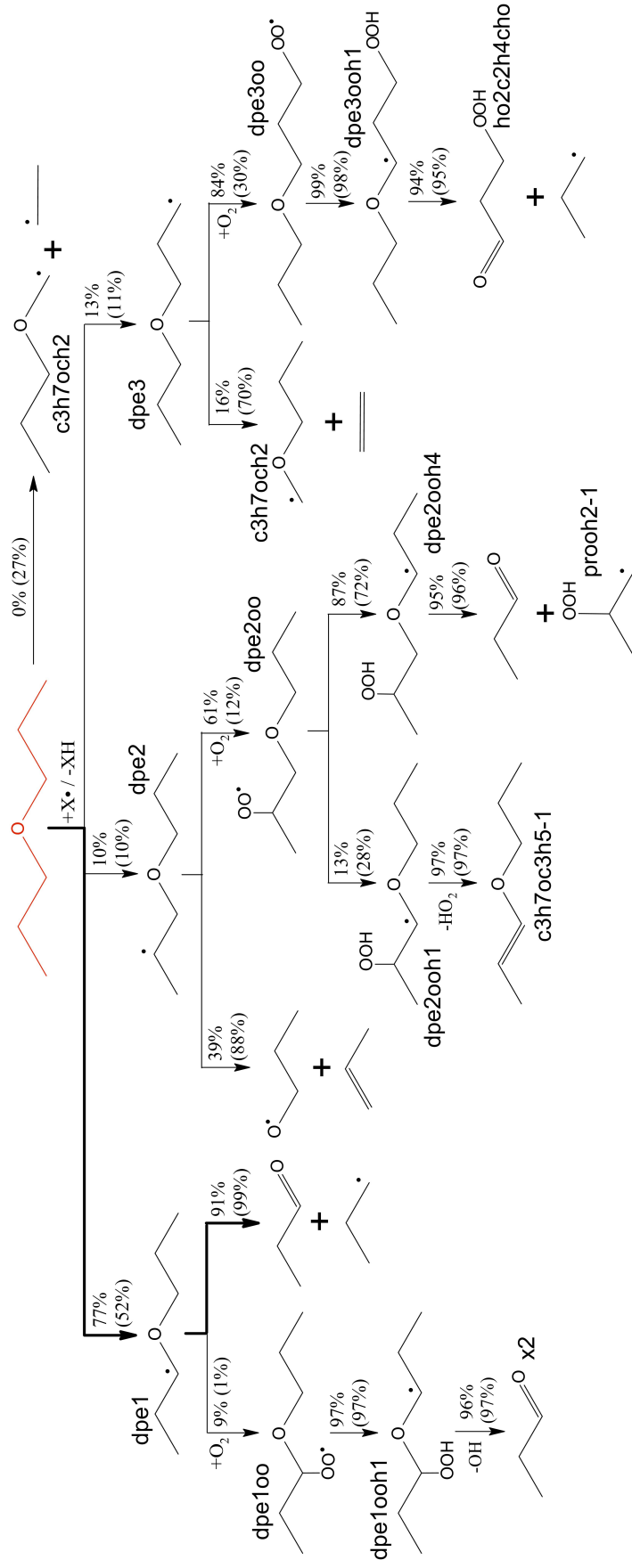
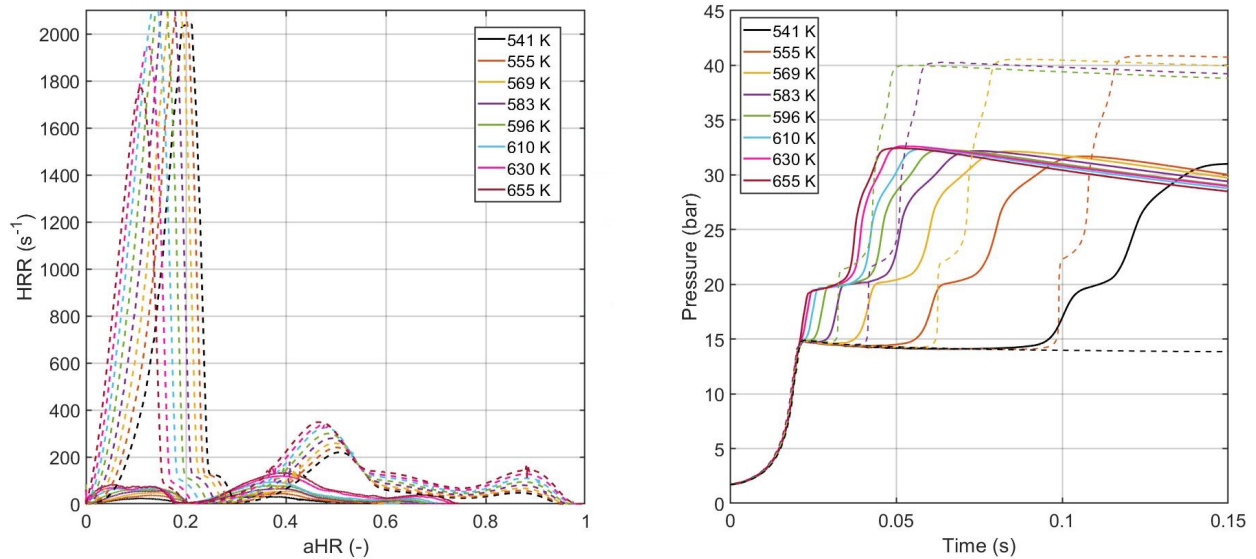


Figure 6.10: Reaction pathways in di-*n*-propyl ether oxidation in the HPST ($\phi = 1$, DPE = 1.0%, $p_c = 15$ bar, 1000 K and 1200 K (in parenthesis), at 20% fuel consumption).

6.2.2 HRR

Similarly to what was done for DEE, a heat release rate analysis has been performed for the stoichiometric condition and a dilution of 10.



(a) Heat release rate vs accumulated heat release (both normalised by the mixture LHV)

(b) Pressure profiles (only some simulations for clarity of the plot)

Figure 6.11: Experiments (solid) vs simulations (dashed): **a)** HRR vs aHR, **b)** pressure profiles. Mixture: DPE, $\phi = 1$, dilution = 10 (inert gases: 50% CO_2 + 50% N_2), DPE = 1.0%, $p_c = 15$ bar.

Figure 6.11 shows the heat release rate plotted against the accumulated heat release and the pressure profiles, both experimental (solid lines) and simulated (dashed). Also in this case, it is possible to see that there are actually three distinct heat releases, with the third one being almost impossible to distinguish in the experiments. Once again, the mechanism, even if it was in reasonable agreement concerning the ignition delay times, is unable to correctly predict the heat release rate. In fact, in the experiments the HRR reaches its maximum during the main ignition, while the model predicts a higher heat release rate for the first stage. In any case, the model overpredicts the HRR for all stages and this is evident also from the comparison of some of the simulated pressure profiles shown in figure 6.11b. The simulated profiles show very steep pressure increase, especially for the cool flame. Also, the overall pressure increase is largely overpredicted for all temperatures. Figure 6.12 shows the comparison of simulations and experiments concerning the low-temperature heat release and the maximum accumulated heat release. Once again, as it was for DEE, the values predicted by the model for the LTHR are not that far from the experimental values, even if there is an overprediction also in this case. On the other hand, the maximum accumulated heat release is still largely overpredicted. A part of this overprediction can be caused by physical effects (as for example the flow of reacting mixture that is trapped in the crevice of the piston), but the difference

is big enough to imply that also the model has to be improved in order to better represent the heat release during combustion.

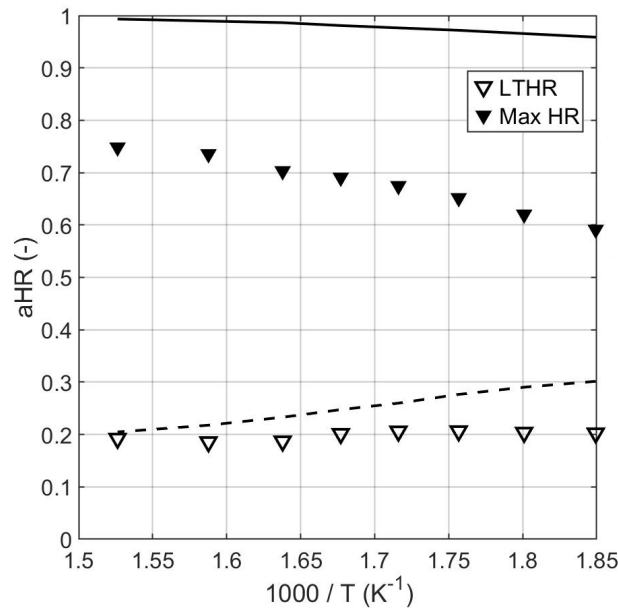


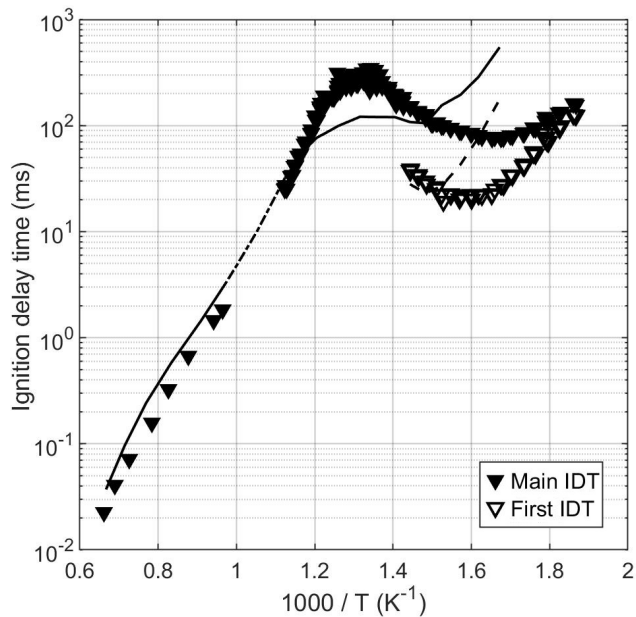
Figure 6.12: Low-temperature heat release and maximum accumulated heat release (normalised by the mixture LHV): comparison between experiments (points) and simulations (lines). Mixture: DPE, $\phi = 1$, dilution = 10 (inert gases: 50% CO₂ + 50% N₂), DPE = 1.0%, $p_c = 15$ bar.

6.3 DIPE

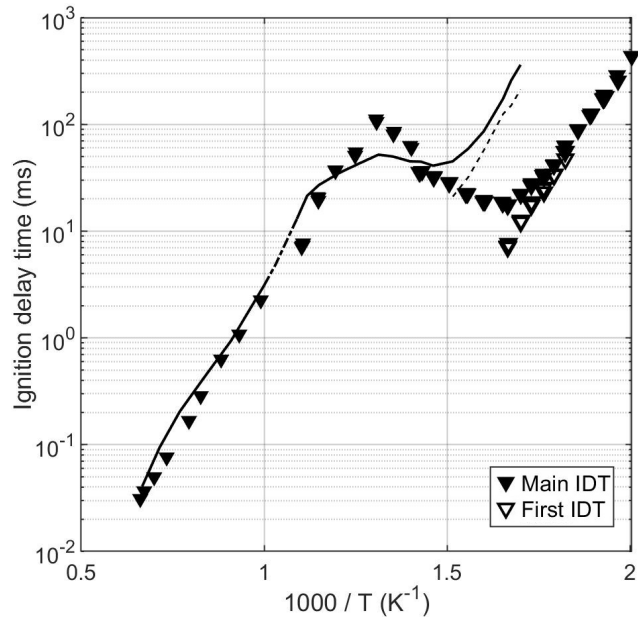
Di-*iso*-propyl ether (DIPE), isomer of DPE, has less oxidative reactivity than di-*n*-propyl ether. If it showed no reactivity at low temperatures in the jet-stirred reactor, as shown in [67] and [68], in the experiments performed in the rapid compression machine of PRISME, a low temperature reactivity followed by an NTC region has been observed, even if it appears to be weaker than the ones observed with the previously presented ethers. The measured ignition delay times and the corresponding simulated values are shown in figure 6.13. It has to be noted that the dilution in this case is 5, while it was 10 for DPE. A mixture with common characteristics was also tested for both isomers, but it will be presented in a later section (6.8.1), where the comparison between the reactivity of DPE and DIPE will be discussed.

The Figure 6.13a shows the ignition delay times for the stoichiometric mixture. As for DPE, DIPE was also tested in the facilities of the University of Galway, for this specific mixture (in RCM and shock tube for the higher temperature range). At low temperature, DIPE shows a two-stage ignition and at intermediate temperatures, a negative temperature coefficient zone can be observed. It can be seen from Figure 6.13a that a large number of tests was performed in this temperature range and the scatter of the results appears more important than in the low and high temperature

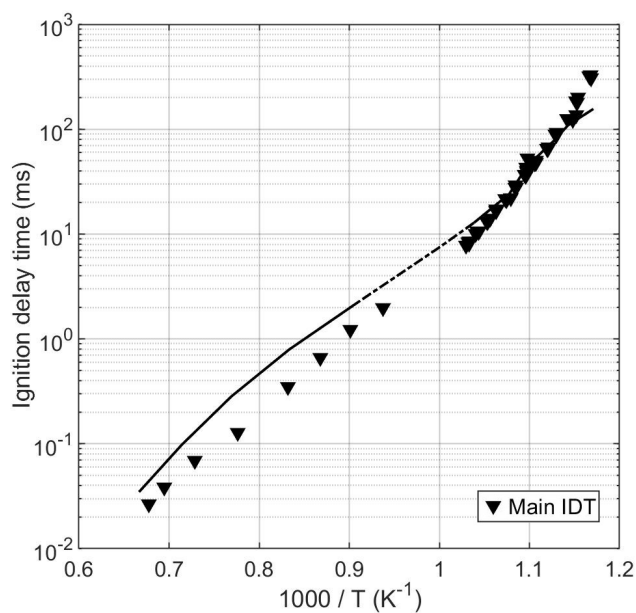
zone. This is due to the fact that these ignition delay times are actually outside the usual reliability limit of the rapid compression machine. In fact, the maximum acceptable measured delay in our facility is considered to be 200 ms. Over this time, the heat losses become too important, as well as the related decrease in the pressure before the ignition. Nevertheless, these points are included in the plot, since they follow a coherent trend with the ones in the reliable operating range and they allow to see the complete NTC zone. Considering the performance of the mechanism, it is possible to see that at low temperature it is still far from the experimental results, with the lowest temperatures where no reactivity is expected from the simulations. The low-temperature sub-mechanism of DIPE has been developed specifically after these experiments were performed. The literature lacks other data that could allow a further improvement, nor there are direct calculations on the main reactions involved. Nevertheless, it is possible to see that the mechanism can still predict the NTC zone and also the trend of the delay of the first stage seems to have some similarities to the experiments (it has to be noted that towards the intermediate temperature, the increase in pressure due to the cool flame starts to be very small, up to when it becomes almost negligible and impossible to be categorised as an ignition. An example is shown in Figure 6.14, while other pressure profiles are included in the appendix B.1.3). At high temperature, the mechanism seems to be in better agreement with the experimental results, with only a slight overprediction of the delays.



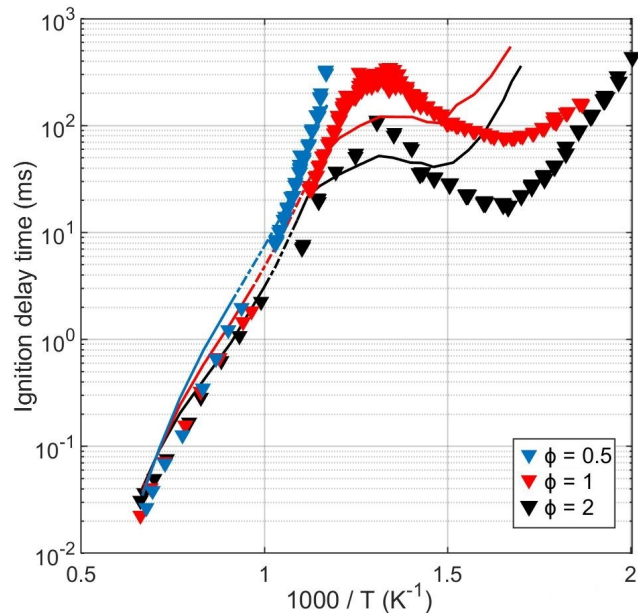
(a) $\phi = 1$, $p_c = 15$ bar, dilution = 5, DIPE = 1.8%



(b) $\phi = 2$, $p_c = 15$ bar, dilution = 5, DIPE = 3.6%



(c) $\phi = 0.5$, $p_c = 15$ bar, dilution = 5, DIPE = 0.9%



(d) Comparison of main IDTs, $p_c = 15$ bar, dilution = 5

Figure 6.13: Ignition delay times of di-*iso*-propyl ether in the RCM (points: experimental data, lines: simulations (solid: main IDT, dashed: first IDT), $p_c = 15$ bar.

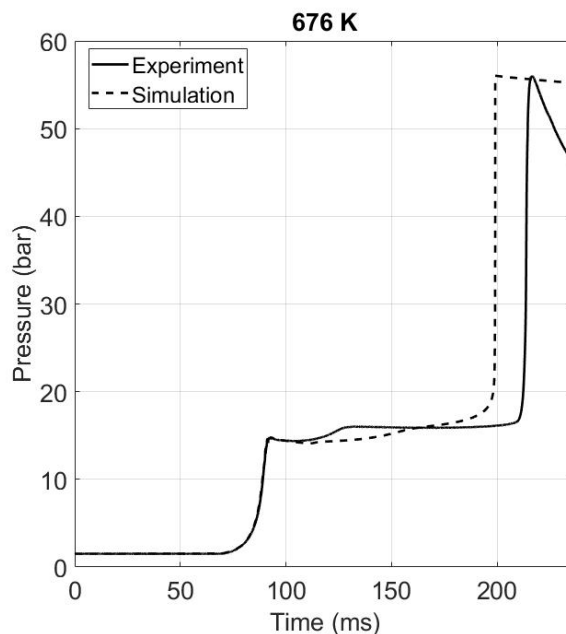


Figure 6.14: Experimental and simulated pressure profiles for a mixture of DIPE at $\phi = 1$, dilution = 5 (inert gas: 100% N_2), DIPE = 1.8%, $p_c = 15$ bar, $T_c = 676$ K.

The Figure 6.13b shows the IDTs for the rich mixture. The trend is similar to that of the stoichiometric mixture, but the delays are shorter, as shown in the comparison in Figure 6.13d. Also in this case, at low temperature the ignition happens in two stages and a negative temperature coefficient zone is present at intermediate temperatures. For this mixture, the ignition delays are in the operating range of the RCM (Galway). Also for this mixture, the mechanism underpredicts the reactivity at low and intermediate temperatures, while it is reasonably close to the data at high temperatures. It is interesting to note that, even if it is shifted with respect to the experiments, the trend of the first stage ignition delays in relation to the main ignition appears to be well captured by the simulations.

The Figure 6.13c shows the ignition delay times of the lean mixture. In this case, no IDTs could be measured at low temperatures, probably because they were too long. Reactivity started to be visible after around 830 K and, since this is already in the higher temperature zone, the simulations are in reasonable agreement with the measured delays. As can be shown from the comparison in figure 6.13d, the IDTs of the lean mixture are the slowest ones, up to the crossover temperature, which is around 1250 K.

6.3.1 Reaction pathways

A reaction pathway analysis has been performed, both at low-intermediate temperature (600 and 792 K) and at high temperature (1000 and 1200 K) for the stoichiometric mixture.

In Figure 6.15, the main reaction pathways at low and intermediate temperature are shown. As expected, the most abundant fuel radical (77%) is the tertiary radical, indicated with "dipe1" in Fig. 6.15. At 600 K, this radical then adds to oxygen, as typical of low-temperature chemistry and the RO₂ isomerises through a six-membered transition state. The typical step after this QOOH radical is formed would be a second addition to O₂ followed by the formation of a ketohydroperoxide. Nevertheless, due to the branched structure of DIPE, this is not possible, leading to a weak low-temperature reactivity (or actually absent, under other conditions, as in the JSR or for lean mixtures). In this case, the QOOH radical mainly decomposes to form two molecules of acetone and an OH radical. A smaller flux of the fuel (23% at 600 K) forms the primary radical (dipe2 in Fig. 6.15), which then mainly follows the typical low-temperature chain branching path. At intermediate temperature (around 800 K), dipe1 mainly decomposes forming two molecules of acetone and an OH radical (55%), while the rest of the flux follows the same path of the lower temperature. Similarly, dipe2 mostly undergoes β -scission, and the smaller flux adding to O₂ also undergoes β -scission, after isomerising to QOOH radicals.

The reaction pathway analysis performed at higher temperatures is shown in Figure 6.16. The most important paths that can be seen here start being more similar to what was seen in the JSR at similar temperature in [68], suggesting that, once again, the oxidation in these two different setups happens in similar ways. The most abundant radical deriving from the fuel is still the tertiary one, but the flux is smaller compared to what was predicted at low temperature. The main path followed by this radical is β -scission, which gives as products acetone and an isopropyl radical. A small flux (4%) at 1000 K can still add to oxygen and isomerise, then decompose forming two molecules of acetone and an OH radical. On the other hand, dipe2 is less abundant and it mainly decomposes through β -scission, with 24% of the flux forming unsaturated compounds. The unimolecular decomposition of the fuel becomes more important as the temperature increases, with its percentage increasing from 0 to 14% when moving from 1000 to 1200 K. As in the JSR, this path is more important for the rich mixture and at high temperature.

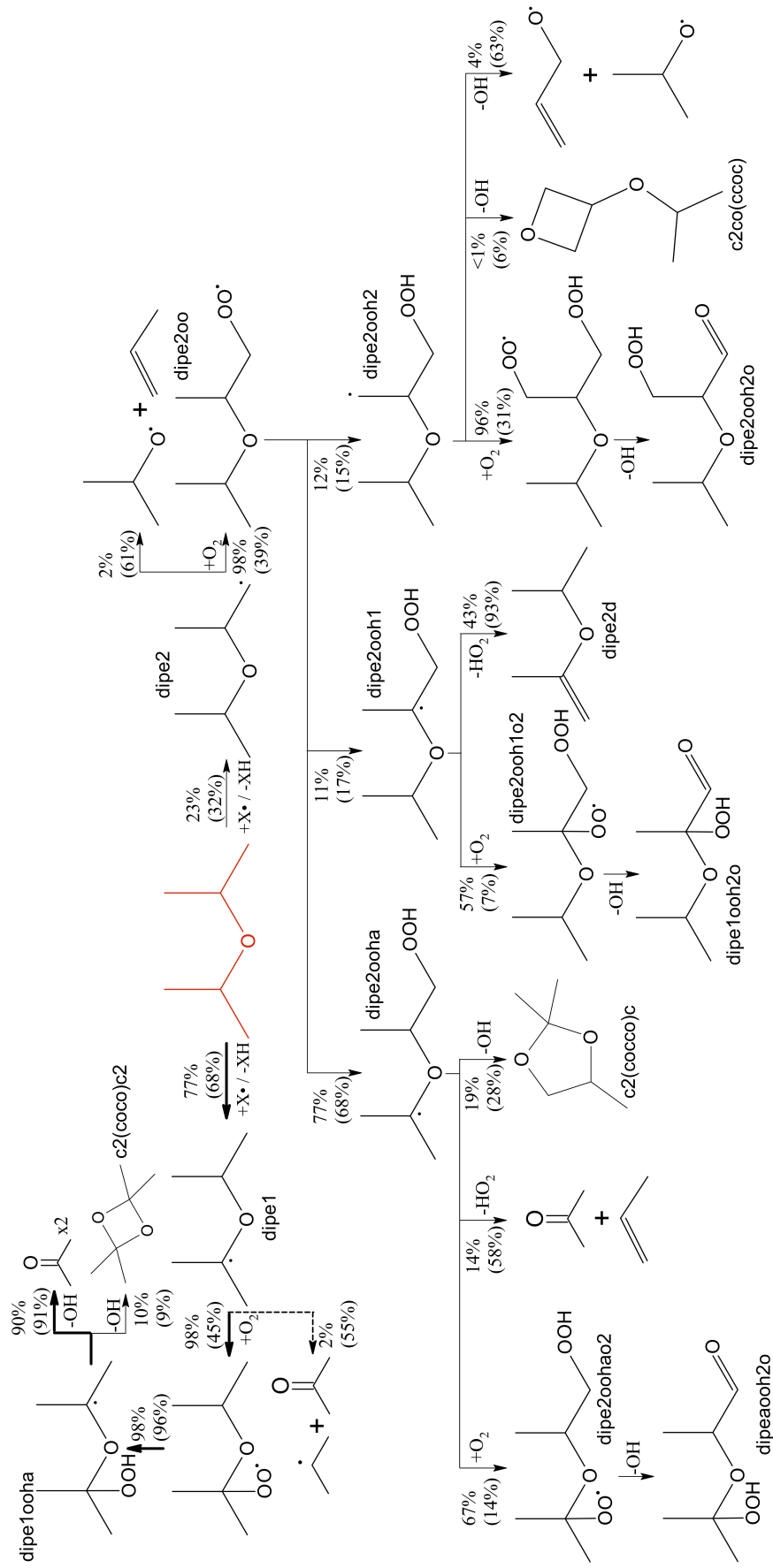


Figure 6.15: Reaction pathways in di-isopropyl ether oxidation ($\phi = 1$, DIPE = 1.8%, $p_c = 15$ bar, 600 K and 792 K (in parenthesis), at 20% fuel consumption).

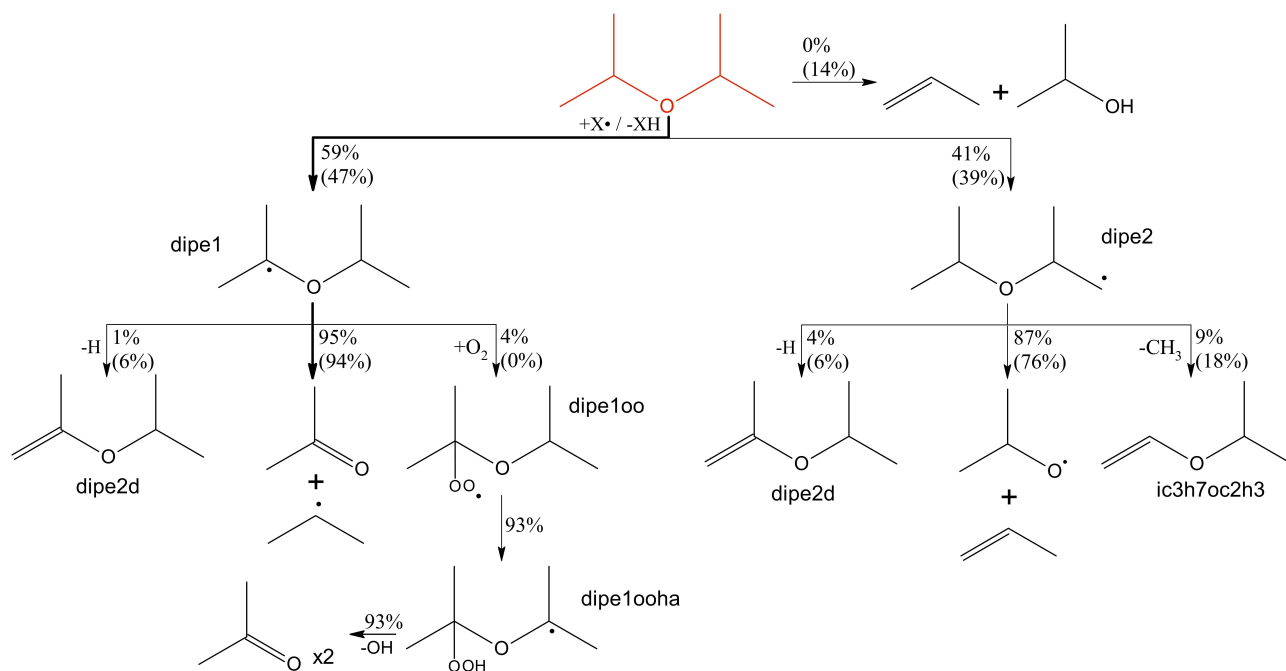


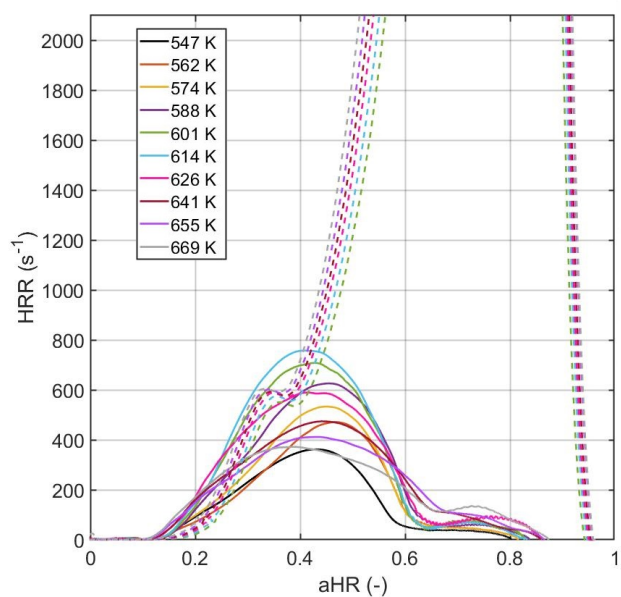
Figure 6.16: Reaction pathways in di-*iso*-propyl ether oxidation in the HPST ($\phi = 1$, DIPE = 1.8%, $p_c = 15$ bar, 1000 K and 1200 K (in parenthesis), at 20% fuel consumption).

6.3.2 HRR

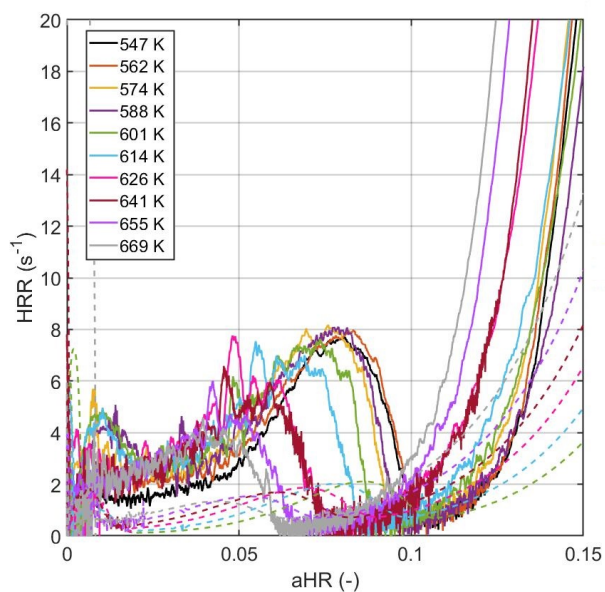
A heat release rate analysis was performed for some points of the stoichiometric mixture, with dilution equal to 5. Some tests were tried with a higher dilution, in order to be able to compare all the ethers, but DIPE was not reactive enough and no ignition was observed under these conditions and in the same temperature range considered for the other ethers.

Figure 6.17 shows a comparison of the heat release computed from the experiments and the one computed from the simulations. It has to be noted that at temperatures lower than 600 K, the pressure profiles obtained from the simulations did not show a clear ignition event, therefore it was not possible to perform the HRR analysis on those tests. Nevertheless, the heat release computed from the experiments is reported for all the temperatures that were tested.

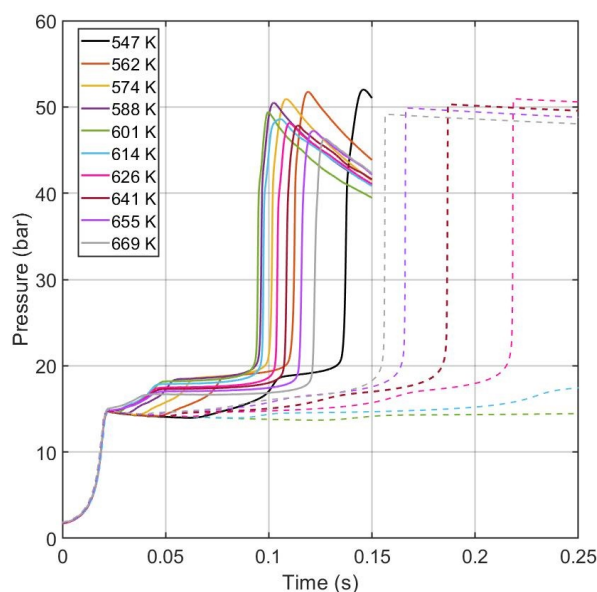
The Figure 6.17a shows the heat release rate as a function of the accumulated heat release. The simulations largely overpredict the maximum heat release rate of the main stage of the ignition (with a peak value around 10000 s^{-1} , which is not shown in the plot, in order to keep the visibility of the experimental results). It is also interesting to note how the simulations predict a second small heat release (after the one of the first stage), right before the main ignition, which can also be seen from the simulated pressure profiles in Figure 6.17c. In the experiments, on the other hand, this heat release right before the main ignition is inexistent, while there is a slight change in the slope of the pressure increase, which determines the small peak towards the maximum of the accumulated heat release.



(a) Heat release rate vs accumulated heat release (both normalised by the mixture LHV)



(b) Zoom on the LTHR



(c) Pressure profiles

Figure 6.17: Experiments (solid) vs simulations (dashed): **a)** HRR vs aHR, **b)** pressure profiles. Mixture: DIPE, $\phi = 1$, dilution = 5 (inert gases: 50% CO_2 + 50% N_2), DIPE = 1.8%, $p_c = 15$ bar.

Figure 6.17b allows to have a better look at the low-temperature heat release, which is almost two orders of magnitude smaller than the main ignition heat release in the experiments and it is even almost negligible in the simulations. It is interesting to see how this heat release decreases, as temperature increases, which can also be seen from the pressure profiles, with the pressure in-

crease due to the cool flame decreasing as the temperature increases.

Figure 6.18 compares the low-temperature heat release and the maximum accumulated heat release as computed from the experiments (points) and from the simulations (lines). The simulations predict well the low-temperature heat release (even if it was underpredicting its rate), while it slightly overpredicts the maximum heat release. Nevertheless, this overprediction is in a range of 10-15%, which can be mainly related to physical effects that cannot be properly accounted for in the simulations. It is also possible to see, especially from the experimental results which extend over a range of around 120 K, how the low-temperature heat release decreases when the temperature increases, while the maximum heat release increases.

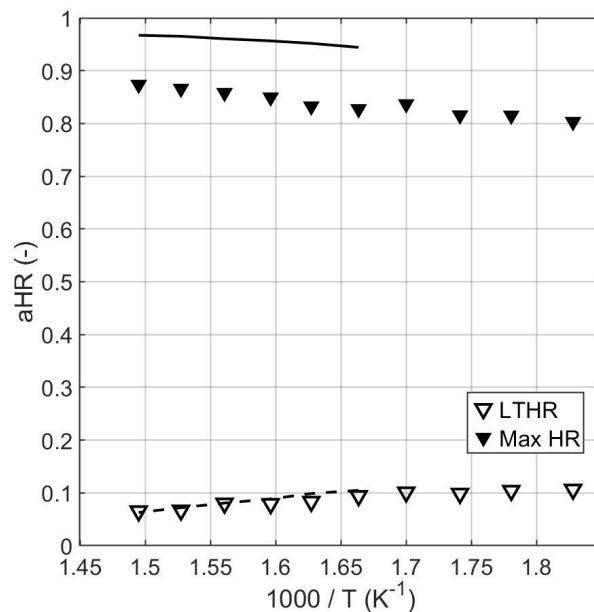
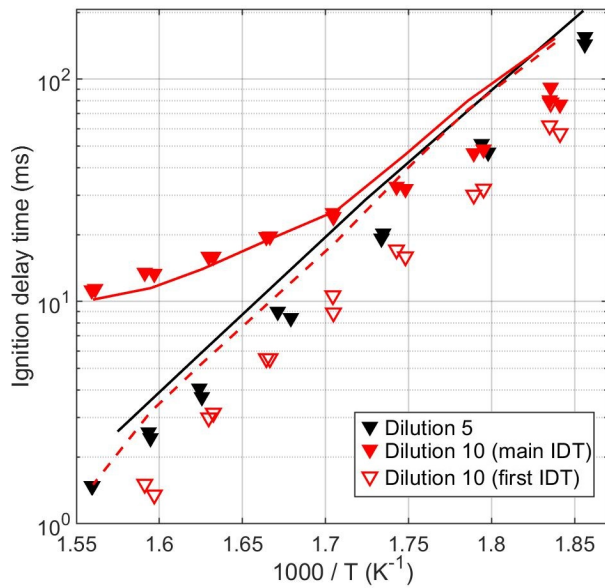


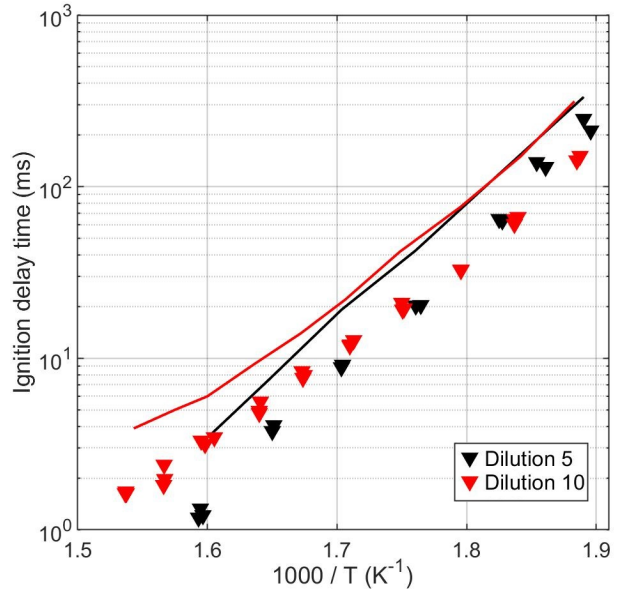
Figure 6.18: Low-temperature heat release and maximum accumulated heat release (normalised by the mixture LHV): comparison between experiments (points) and simulations (lines). Mixture: DIPE, $\phi = 1$, dilution = 5 (inert gases: 50% CO₂ + 50% N₂), DIPE = 1.8%, $p_c = 15$ bar.

6.4 BEE

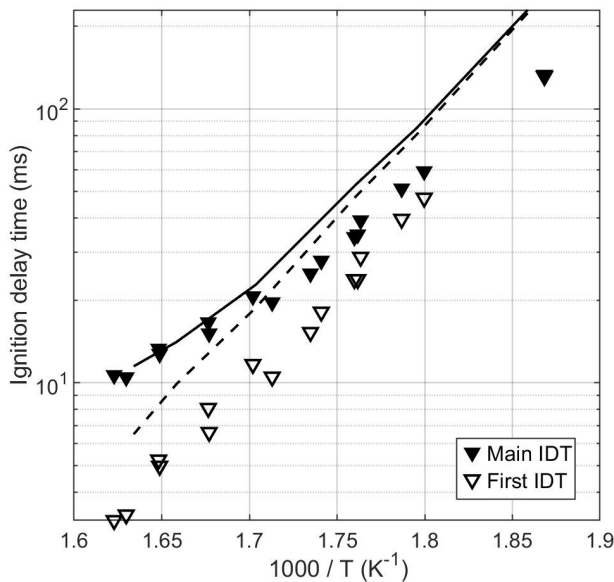
Butyl ethyl ether was studied in the rapid compression machine at both dilutions 5 and 10 for the stoichiometric (BEE = 1.8% and 1% respectively) and rich (BEE = 3.6% and 1.98% respectively) mixtures and at dilution 5 for the lean mixture (BEE = 0.9%). The measured ignition delay times (points), along with the simulations (lines) obtained from the mechanism, are shown in Figure 6.19.



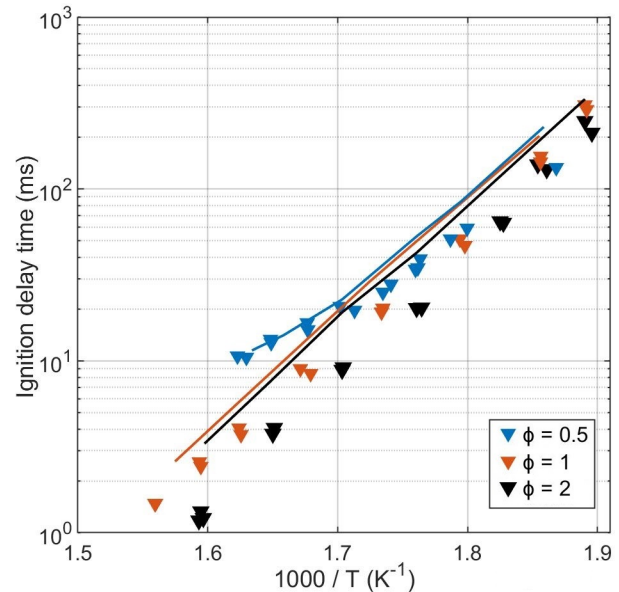
(a) $\phi = 1$, $p_c = 15$ bar, dilution = 5 (black), 10 (red), BEE = 1.8% (black), 1.0% (red)



(b) $\phi = 2$, $p_c = 15$ bar, dilution = 5 (black), 10 (red), BEE = 3.6% (black), 1.98% (red)



(c) $\phi = 0.5$, $p_c = 15$ bar, dilution = 5, BEE = 0.9%



(d) Comparison of main IDTs, $p_c = 15$ bar, dilution = 5

Figure 6.19: Ignition delay times of butyl ethyl ether in the RCM (points: experimental data, lines: simulations (solid: main IDT, dashed: first IDT)), $p_c = 15$ bar.

The Figure 6.19a shows the IDTs of the two stoichiometric mixtures with different dilution. Considering the ignition delay times of the main stage, the ones for the mixture with higher dilution are longer, even if there is an overlap at the lowest temperature. It is also interesting to note that for the mixture with dilution 10 it is possible to identify a two-stage ignition, while for the mixture with dilution 5 the ignition seems to happen in a single stage. If the pressure profiles are

compared (appendix B.1.4) both for the experiments and the simulations, it is possible to see that in the simulated profile a two-stage event seems to be present also for the less diluted mixture, but they are so close that it is almost impossible to distinguish them. On the other hand, this is hardly the case if the experiments are considered, where a single stage is clearly recognisable. As far as the simulations of the ignition delay times are concerned, there is an overprediction of the IDTs, at the lowest temperature for the main ignition of the more dilute mixture and over the whole temperature range for the less dilute one. Nevertheless, the trends are quite well captured and if the lower temperature range is considered, it is possible to see that the model predicts the overlap that appears to happen for the main ignition delay times.

The Figure 6.19b shows the ignition delay times (measured and simulated) for the two rich mixtures. At both dilutions, ignition was observed to happen in a single stage. At very low temperature, the ignition delay times of the mixture with dilution 5 and the one with dilution 10 are very close and this tendency is well represented by the simulations even if there is an overall overprediction. As the temperature increases, the ignition delays of the mixture with dilution of 10 are slower compared to the mixture with dilution 5. Simulations show the same tendency even if the mechanism appears to be still less reactive than the experimental results.

The Figure 6.19c shows the ignition delay times for the lean mixture with dilution 5. In this case, a two-stage ignition was recorded as predicted by the simulations. At low temperature, the simulations overpredict the measured delays, but they get closer to the experimental values at higher temperatures, at least for the main ignition event. From the slope of the simulations and the trend of the experimental results, it may be speculated that the ignition delays start reaching a plateau towards intermediate temperatures. Nevertheless, the delays of the cool flame are linearly decreasing, and the reactions start happening before the end of the compression at higher temperatures. The Figure 6.42 shows a comparison of the main ignition delay times for different equivalence ratios at dilution 5. It is possible to see that only the lean mixture seems to show the beginning of a possible NTC region, while the rich and stoichiometric mixture show a typical Arrhenius trend.

6.4.1 Reaction pathways

A reaction path analysis has been performed for the stoichiometric mixture at 538 K and the results are shown in Figure 6.20. In order to identify the radicals, numbers are used on the ethyl side and letters are used on the butyl side (starting from the carbon neighbouring the ether function in both cases, as can be seen from the Figure 6.42).

The other ethers presented so far were symmetrical and had therefore one most abundant radical. BEE, on the other hand, has an asymmetrical structure and two primary radicals (bee-1 and bee-a) are equally favored. The first radical (bee-1) follows the low-temperature chain branching pathway. The second radical (bee-a) also adds to molecular oxygen, but it can then isomerise

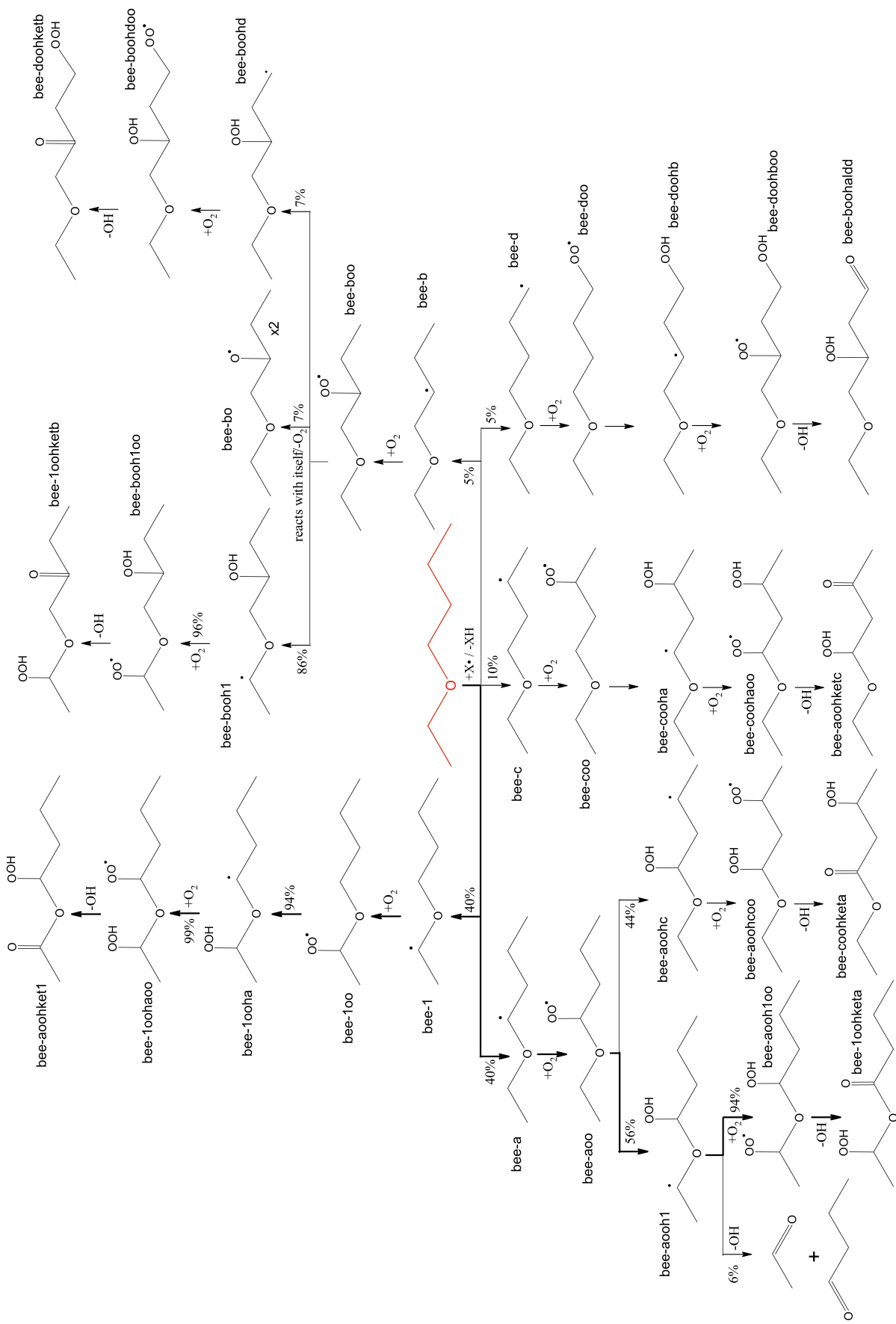


Figure 6.20: Reaction pathways in butyl ether oxidation ($\phi = 1$, dilution = 5, BEE = 1.8%, $p_c = 15$ bar, 538 K, at 20% fuel consumption).

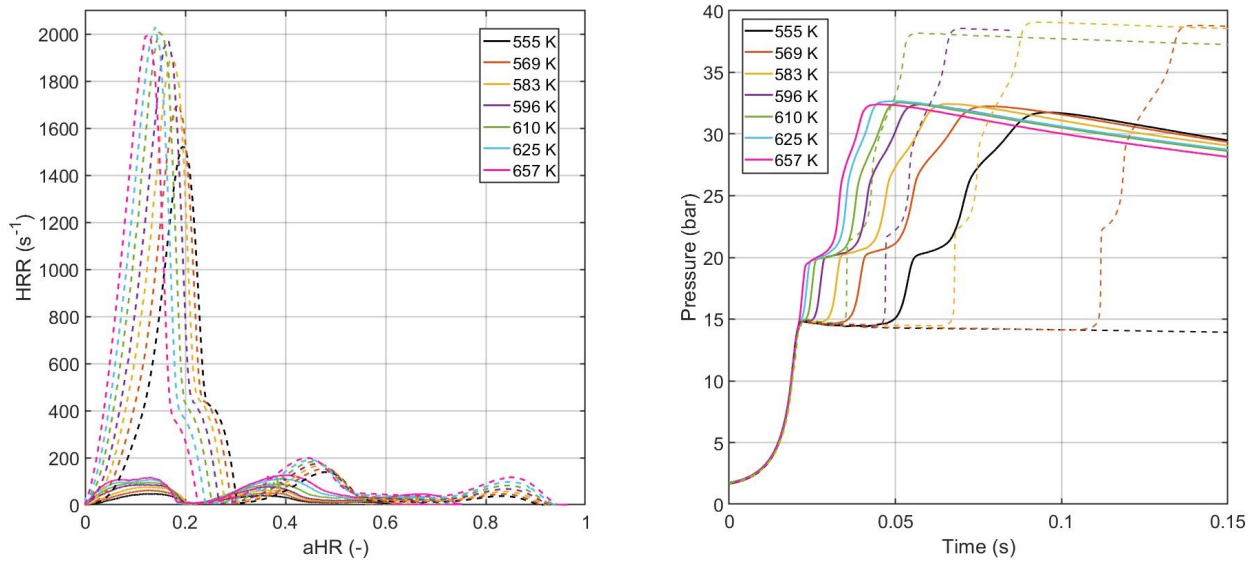
through a 6-membered transition state to give two different QOOH radicals. The more abundant QOOH (56%) is the one including the ether function in the cycle of the transition state (bee-aooH1), but the other one is also quite important. Both QOOH radicals then go through second O₂ addition thereby forming the corresponding ketohydroperoxide. A small flux (6%) of the radical bee-aooH1 undergoes β -scission.

The three other possible fuel radicals are also formed, but with smaller fluxes and mostly follow the typical chain branching paths which are controlling the low-temperature reactivity, through the formation and decomposition of ketohydroperoxides.

6.4.2 HRR

An analysis on the heat release during the ignition in the RCM was also performed, for the stoichiometric mixture with a dilution of 10. Figure 6.21 shows the comparison of the heat release rate plotted as function of the accumulated heat release (6.21a) as computed from both the experimental and simulated pressure profiles, which are shown in the right panel (Fig. 6.21b).

As it was the case for DEE and DPE, the heat release rate computed from the simulations is much higher than what is observed in the experiments, especially for the first stage of the ignition. This can be seen also from the pressure profiles, where the pressure increase of the first stage in the simulated profiles appears to be much sharper than in the experimental profiles. This is the case for all temperatures, even when the ignition delay times are in agreement between experiments and simulations. The main ignition appears to have two heat releases happening quite close to each other, which can be seen as the change of slope in the pressure increase in the plot 6.21b. This behaviour could be seen as an actual three-stage ignition, instead of two, which was already seen in diluted mixtures also for the other ethers. For these two heat releases, the computed rates from experiments and simulations are closer than the ones for the first stage, even if the mechanism still overpredicts the values.



(a) Heat release rate vs accumulated heat release (both normalised by the mixture LHV) (b) Pressure profiles (only some simulations for clarity of the plot)

Figure 6.21: Experiments (solid) vs simulations (dashed): **a)** HRR vs aHR, **b)** pressure profiles. Mixture: BEE, $\phi = 1$, dilution = 10 (inert gases: 50% CO_2 + 50% N_2), BEE = 1.0%, $p_c = 15$ bar.

Figure 6.22 compares experimental results and simulations of the low-temperature heat release and the maximum accumulated heat release. If the overprediction of the heat release rates for the first stage was quite important, the simulated low-temperature heat release is actually quite close to the experimental results and in both cases, it is possible to see a slightly decreasing trend as the temperature increases. On the other hand, the maximum accumulated heat release simulated with the mechanism is quite higher than the one obtained from the experiments; even if a part of this overestimation can be caused by physical effects, there is surely some discrepancy linked to the kinetic mechanism or the thermodynamical properties of the key species. Nevertheless, both experiments and simulations show an increasing trend on the maximum accumulated heat release as the temperature is increased, which seems to be slightly more pronounced in the experiments.

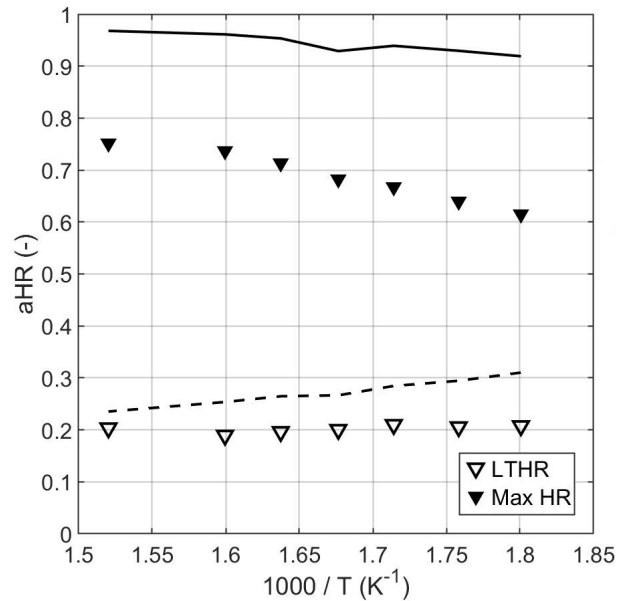
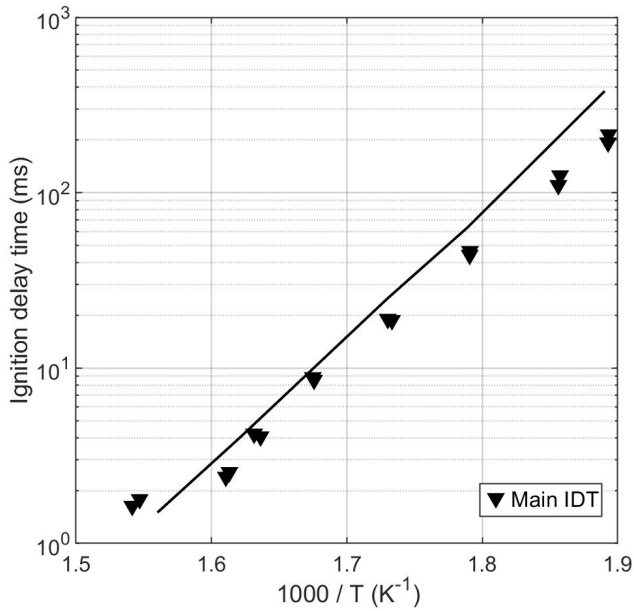


Figure 6.22: Low-temperature heat release and maximum accumulated heat release (normalised by the mixture LHV): comparison between experiments (points) and simulations (lines). Mixture: BEE, $\phi = 1$, dilution = 10 (inert gases: 50% CO₂ + 50% N₂), BEE = 1.0%, $p_c = 15$ bar.

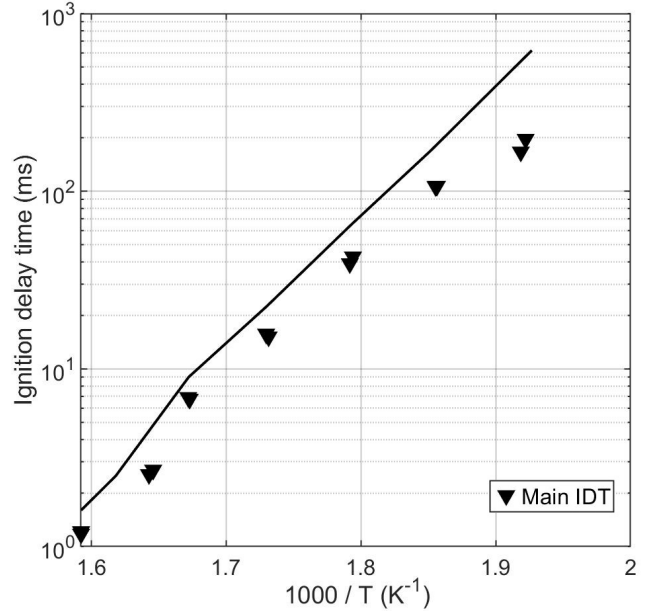
6.5 DBE

Di-butyl ether ignition delay times were measured under several conditions: for the mixtures with dilution 5 (results in Figure 6.23) three different equivalence ratios were tested, all at a pressure of 15 bar; for the mixtures with dilution 10 (results in Figure 6.24), only stoichiometric and rich conditions were considered, finally the stoichiometric conditions were tested at both 15 and 20 bar. Considering the experimental results for the less dilute mixtures, from Figure 6.23a and 6.23b it is possible to see that for stoichiometric and rich mixtures the ignition happens in a single stage. If the simulations are considered, it is possible to see that their agreement to the experimental data is quite good, but looking at the pressure profiles (appendix B.1.5), an actual two-stage ignition can be seen, with the two stages being at around 1 ms from each other for the stoichiometric mixture and almost indistinguishable for the rich mixture, where they appear as a small change in slope in the very steep pressure increase.

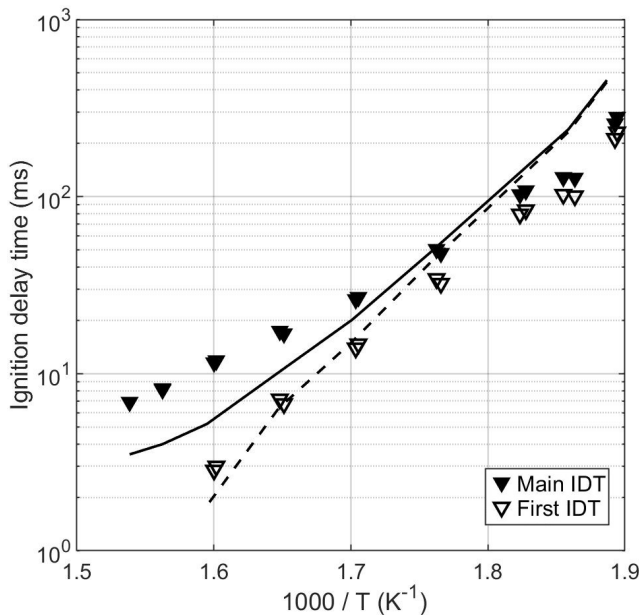
The lean mixture, for which the ignition delay times are shown in Figure 6.23c, a two-stage ignition can be seen both in the experiments and in the simulations. For the first stage, the simulations slightly overpredict the delay at lower temperatures, but they get in better agreement as the temperature increases. For the main ignition, on the other hand, the simulations overpredict the ignition delays at lower temperatures and underpredict them at the higher temperatures.



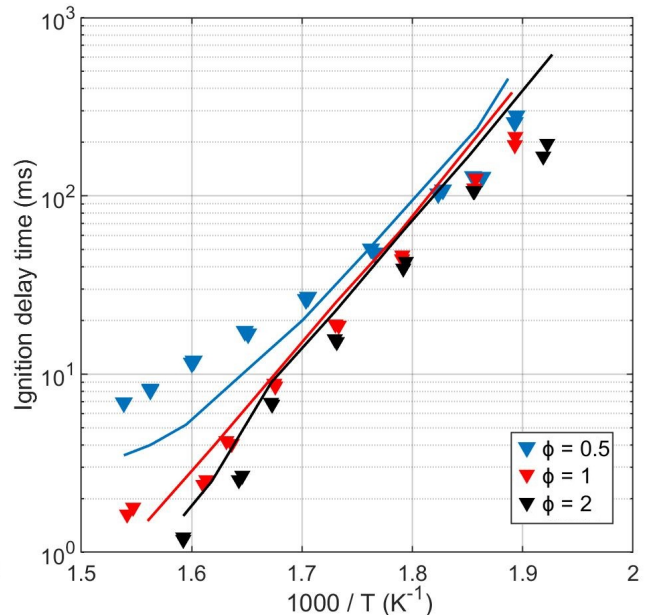
(a) $\phi = 1$, $p_c = 15$ bar, dilution = 5, DBE = 1.4%



(b) $\phi = 2$, $p_c = 15$ bar, dilution = 5, DBE = 2.7%



(c) $\phi = 0.5$, $p_c = 15$ bar, dilution = 5, DBE = 0.7%



(d) Comparison of main IDTs, $p_c = 15$ bar, dilution = 5

Figure 6.23: Ignition delay times of dibutyl ether in the RCM (points: experimental data, lines: simulations (solid: main IDT, dashed: first IDT)), $p_c = 15$ bar.

Looking at the comparison of the main ignition delay times for the three equivalence ratios, shown in Figure 6.23d, it is possible to see that rich and stoichiometric mixtures have quite similar ignition delays, while the lean mixture is considerably slower especially as the temperature increases. This trend is captured by the simulations, which also predicts very similar delays for all three mixtures at low temperature and the delays of the lean mixture become slower as the tem-

perature increases.

In Figure 6.24, the ignition delay times for the two mixtures with higher dilution are shown. In the first plot (6.24a), the results for the stoichiometric mixture at two different pressures are shown. If Hakimov et al. [82] found a negligible pressure dependence of the IDTs for their stoichiometric mixture in air, it appears that with higher dilution even a difference of only 5 bar in the compressed gas pressure can mark a non-negligible difference in the main ignition delay times, which becomes more evident as the temperature is increased. On the other hand, the first-stage ignition delay times appear to be pressure independent over the whole temperature range considered. The simulations show a similar behaviour, with the first ignition delay times at both pressures being superposed and the main ignition delay times growing apart as the temperature increases. It is also possible to see that at both pressures it seems that a plateau could be reached for the main ignition delay time at slightly higher temperatures than the ones that have been tested.

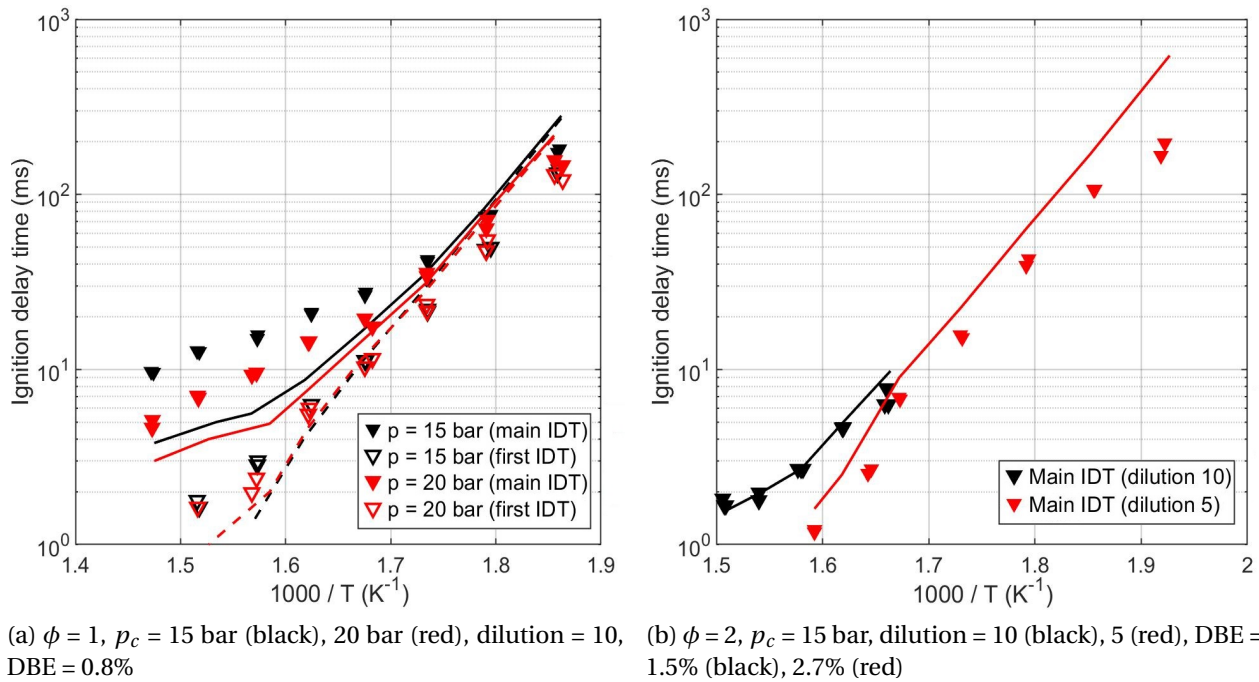


Figure 6.24: Ignition delay times of dibutyl ether in the RCM (points: experimental data, lines: simulations (solid: main IDT, dashed: first IDT)).

The Figure 6.24b shows some points for the rich mixture with higher dilution and the IDTs of the mixture with dilution 5 were included as comparison. Even if only a few temperatures were tested for the more dilute mixture, it is possible to see a trend similar to what is reported for the previously presented ethers, with the ignition delay distancing as the temperature increases. The simulations seem to be in good agreement, concerning the ignition delay times of this dilute rich mixture and a beginning of an NTC region seems to be appearing on the higher temperature side.

6.5.1 Reaction pathways

A reaction pathway analysis was also performed using Thion et al. [76] mechanism for a stoichiometric mixture at 560 K and it is reported in Figure 6.25. All the four possible radicals that can be formed from the fuel through H-abstraction are produced, the most abundant one (37%) being the α -radical. This radical follows a typical low-temperature chain branching pathway. All the other fuel radicals also follow this same path. Even if it is not reported in the figure, similar percentages were found when the analysis was performed at 640 K. If these results are compared to the analysis done by Zhong et al. [83], which used a tuned version of the mechanism proposed by Thion et al. [76], it is possible to see that the expected pathways at lower temperatures are quite similar even if the percentages are slightly different. On the other hand, at higher temperatures, in Zhong's analysis the flux of QOOH adding to O₂ starts becoming smaller while β -scissions and cyclic ether formation reactions become more important. Their analysis was performed at a lower pressure (7 bar), but since the mechanism used here underestimates the IDTs at that temperature, it might be necessary to further investigate the rate constants of these reactions, since a bigger flux going into β -scission or cyclic ether formation may decrease the overall reactivity, in order to better represent the measured ignition delay times at these conditions.

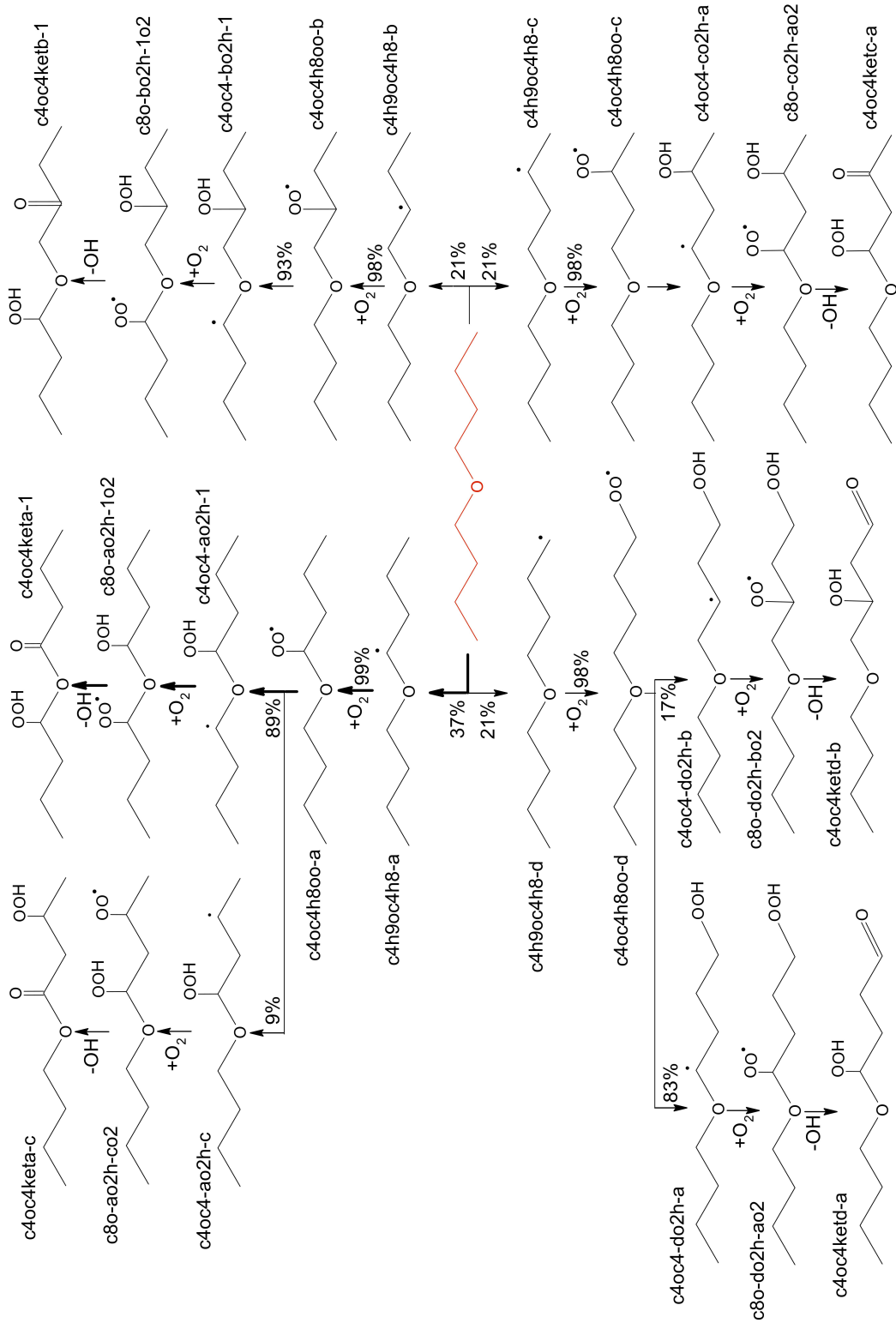
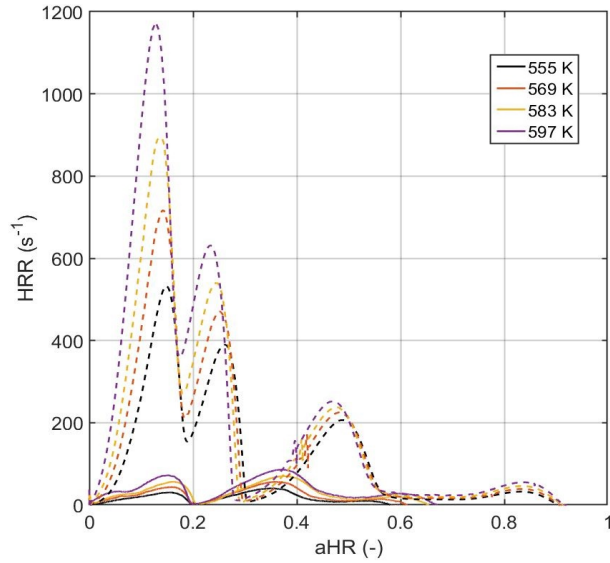
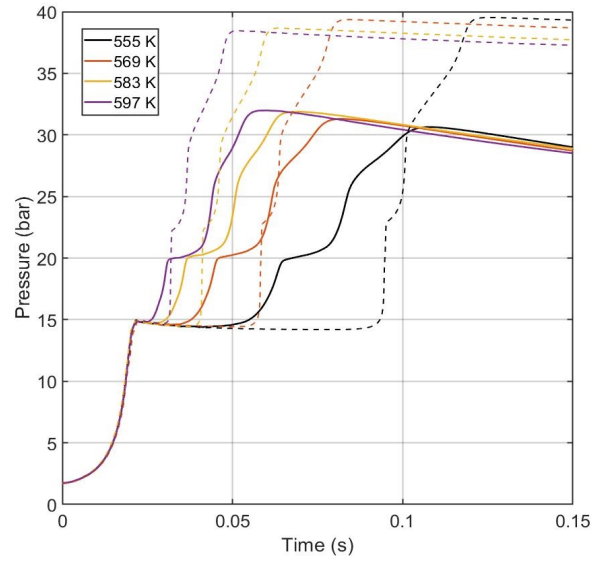


Figure 6.25: Reaction pathways in dibutyl ether oxidation in the rapid compression machine ($\phi = 1$, dilution = 5, DBE = 1.4%, $p_c = 15$ bar, 560 K, 20% fuel consumption).

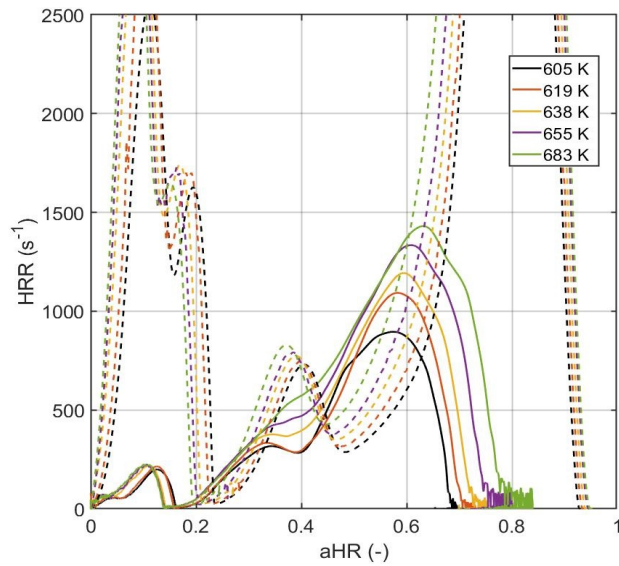
6.5.2 HRR



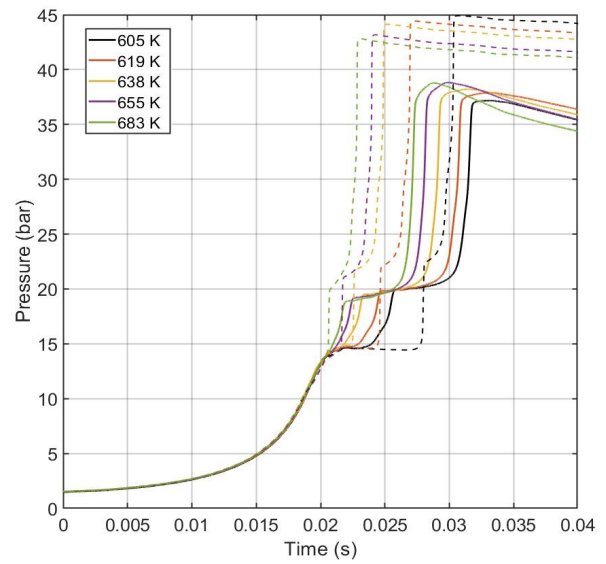
(a) Heat release rate vs accumulated heat release (both normalised by the mixture LHV)



(b) Pressure profiles



(c) Heat release rate vs accumulated heat release (both normalised by the mixture LHV)



(d) Pressure profiles

Figure 6.26: Experiments (solid) vs simulations (dashed): **a), c)** HRR vs aHR, **b), d)** pressure profiles. Mixture: DBE, $\phi = 1$, dilution = 10 (inert gases: **a)-b)**: 50% CO_2 + 50% N_2 , **c)-d)**: 100% N_2), DBE = 0.8%.

A heat release rate analysis was performed for a stoichiometric mixture with dilution equal to 10, with two different inert gas composition: at low temperatures, 50% CO_2 and 50% N_2 was used,

while at higher temperatures only N_2 was used. Even if the temperature ranges are not overlapping, this allows to have an idea of the effect of the different inert gases in the mixture on the heat release during the ignition in the RCM.

Figure 6.26 shows the results of this analysis: on the left panel (Figs. 6.26a and 6.26c) the heat release rate is represented against the accumulated heat release, while on the right panel the pressure profiles are shown. Once again, these plots compare the experimental results (solid lines) to the simulations (dashed).

First, if the influence of the inert gases in the mixture is considered, it is possible to see that the presence of CO_2 lowers the heat release rate considerably. For example, considering the main ignition (last peak) in the experimental results, taking the higher temperature from the mixture with CO_2 and the lowest one for the mixture with only N_2 (8 K of difference), it is possible to see that the heat release rate is lowered by a factor of 10 when CO_2 is used. An influence seems to be present also on the low-temperature heat release, although to a lesser extent, while it seems to be completely negligible on the maximum heat release.

Comparing the simulations to the experiments, for both mixtures it is possible to see that the mechanism largely overpredicts the heat release rates, for all the stages of the ignition. Also, the heat release calculated from the simulations shows two clearly distinct peaks in the first stage of the ignition for both mixtures, while in the experiments it is unclear. A first peak seems to be present for some temperatures, but it is almost indistinguishable from the main peak. A similar trend can be seen for the mixture with only N_2 in Figure 6.26c, with the main ignition having two clear peaks in the heat release from the simulations, while it is barely distinguishable in the experiments and the first peak completely smoothens out as the temperature increases. For the mixture with CO_2 (Fig. 6.26a), it is also possible to see that there is a very small peak after the main ignition, which is also possible to see in the pressure profiles as a change in the slope of the main pressure increase. This is also present in the simulations and the magnitude of the heat release rates in this case is almost comparable.

Figure 6.27 compares the low-temperature heat release (LTHR) and the maximum accumulated heat release as computed from experiments and simulations for both mixtures. As already discussed, the maximum heat release seems to be independent on the inert gases in the mixture, while the LTHR seems to be slightly dependent. Nevertheless, it is possible to see that the maximum heat release increases as the temperature increases, while the LTHR seems to be constant for the mixture with CO_2 and starts to slightly decrease for the mixture with only N_2 . The simulations show a similar trend, even if the increase in the maximum heat release is less than what was seen with the experimental values. In general, the simulations overpredict both values for both mixtures and over the whole range of temperature. This shows, once again, that even if the mechanism appears to be in reasonable agreement considering the ignition delay times, when the heat release is considered the performance is sensibly worse and a further improvement would be needed.

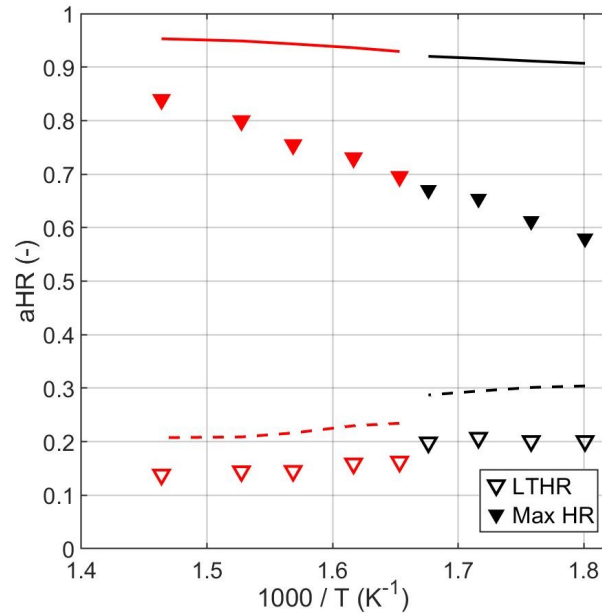


Figure 6.27: Low-temperature heat release and maximum accumulated heat release (normalised by the mixture LHV): comparison between experiments (points) and simulations (lines). Mixture: DBE, $\phi = 1$, dilution = 10 (inert gases: black 50% CO₂ + 50% N₂, red 100% N₂), DBE = 0.8%, $p_c = 15$ bar.

6.6 DIPEE

The ignition delay times of di-*iso*-pentyl ether (DIPEE) were also measured in the rapid compression machine, for different mixtures. Figure 6.28 shows the results for the mixtures with dilution 5 and three different equivalence ratios, 0.5, 1 and 2. As it was the case in the jet-stirred reactor experiments, DIPEE seems to have a behaviour similar to di-butyl ether. As can be seen from Figures 6.28a and 6.28b, for the stoichiometric and rich mixtures, only one stage could be identified for the ignition in the rapid compression machine. The IDTs seem to follow a typical Arrhenius trend and the mechanism, even if it largely overpredicts the delays for both conditions, seems to be at least capturing the slope of the stoichiometric points. Nevertheless, the simulations predict a two-stage ignition, which is particularly evident for the stoichiometric condition, while in the case of the rich mixture the two delays are almost indistinguishable and only visible as a small change in slope in the pressure increase.

The Figure 6.28c shows the first and main ignition delay times of the lean mixture. In this case, as it was for DBE, ignition happens in two stages in the experiments and the simulations show the same behaviour. Also in this case, the simulation overpredicts the ignition delay times, both of the first and main stage, but captures reasonably well the relative trend of both stages.

Figure 6.28d shows a comparison of the ignition delay times of the main stage of the three condi-

tions. At low temperatures, the IDTs are quite similar for all conditions, while they show differences as temperature increases (when $T_c > \sim 550$ K), especially for the lean condition which is the slowest within this temperature window. For all three mixtures in this range of temperature, the IDTs show a typical Arrhenius trend.

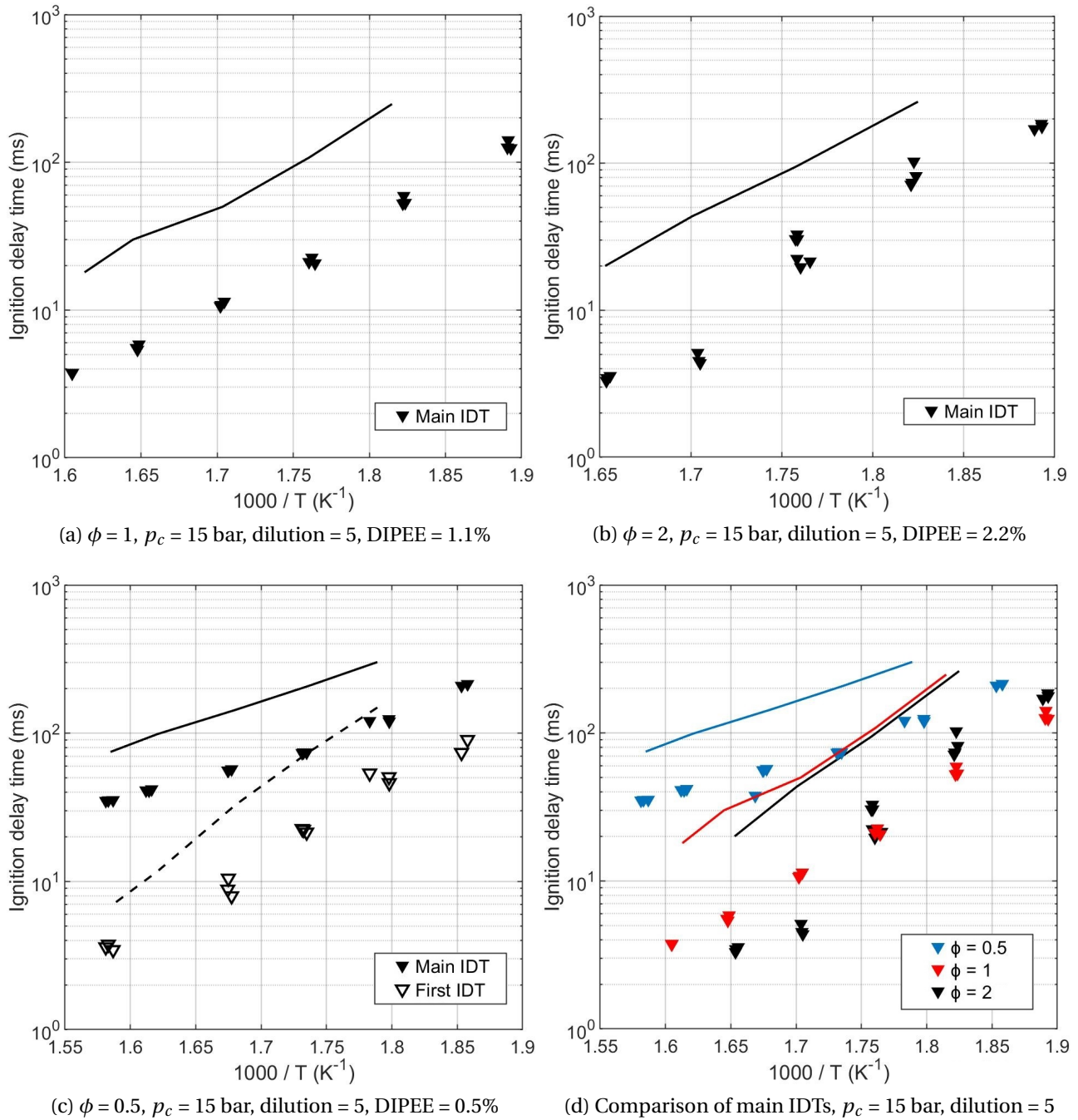
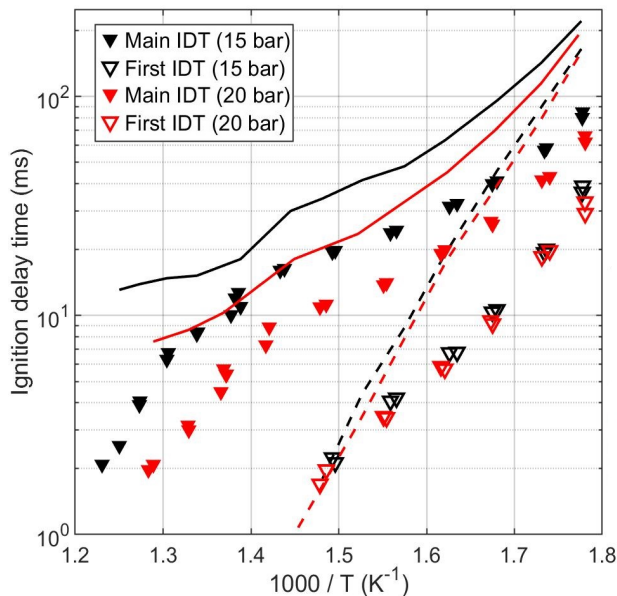


Figure 6.28: Ignition delay times of di-iso-pentyl ether in the RCM (points: experimental data, lines: simulations (solid: main IDT, dashed: first IDT), $p_c = 15$ bar.

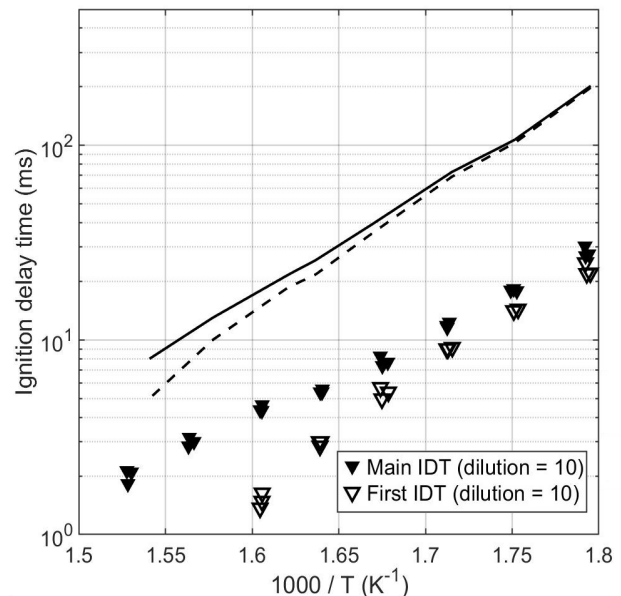
The Figure 6.29 shows the ignition delay times for the mixtures with dilution 10. In this case, as for DBE, only stoichiometric and rich mixtures were considered, with the stoichiometric mixture tested at both 15 and 20 bar.

The Figure 6.29a shows the ignition delay times of the stoichiometric mixture at two different pressures and compares the experimental results to the simulations, as shown by the pressure profiles in appendix B.1.6. It is possible to see that for both conditions ignition happens in two stages at low temperatures. The delays of the first stage seem to be almost independent of the pressure, while the main delays are longer at lower pressure. The same trend can be seen in the simulations, that correctly predict very similar first IDTs and faster delays for the main ignition at 20 bar. Nonetheless, the simulations are still overpredicting both the first and main ignition delay times over the whole temperature range. It is also interesting to note that even if there is not a clear negative temperature coefficient zone, there are some clearly visible changes in the slope of the trending line of the points, which is also visible in the simulations.

The Figure 6.29b, on the other hand, shows the IDTs of the rich mixture. Also in this case, for this mixture with dilution of 10, ignition happens in two-stages in the experiments and this is represented by the simulations. Both in the experiments and in the simulations, the first and main ignition delays are very similar at low temperature and they distance from each other as the temperature increase. Nevertheless, the mechanism overpredicts both first and second stage ignition delay times at all temperatures.



(a) $\phi = 1$, $p_c = 15$ bar (black), 20 bar (red), dilution = 10, DIPEE = 0.6%



(b) $\phi = 2$, $p_c = 15$ bar, dilution = 10, DIPEE = 1.2%

Figure 6.29: Ignition delay times of di-*iso*-pentyl ether in the RCM, dilution = 10, $\phi = 1$ and 2 (points: experimental data, lines: simulations (solid: main IDT, dashed: first IDT)).

6.6.1 Reaction pathways

A reaction pathway analysis was performed for a stoichiometric mixture, at 560 and 800 K, in order to identify the most important reactions happening in different temperature regions, and the results are shown in Figure 6.30.

At both temperatures the fuel is consumed by H-abstraction and the most abundant radical is the α -radical in both cases. At low temperature, this radical only adds to molecular oxygen, while at 800 K a part of the flux (36%) undergoes β -scission, forming isopentanal and an isopentyl radical, which have been shown to be very important for the reactivity in the jet-stirred reactor as well. The ROO radical can then isomerise to three different QOOH radicals (only two at 800 K) and the most abundant one is the one formed via a six-membered transition state which include the ether function in the cycle (dipee-aooht). At 800 K, more than 90% of this QOOH radical is expected to decompose into two isopentanal, with release of an OH radical. At 560 K, on the other hand, a second addition to O₂ is the main path followed (66%), followed by the formation and then decomposition of the corresponding ketohydroperoxide. The other QOOH formed at both temperatures (dipee-aooht) follows similar reaction paths, with the β -decomposition being more important at higher temperature and the ketohydroperoxide formation path being the most common path at low temperature. The third QOOH which is only formed at low temperature only follows the typical chain branching path.

The second most abundant radical obtained from the fuel from H-abstraction is the tertiary radical (dipee-t). The pathways followed by this radical are slightly different from what was explained for the α -radical, since this radical cannot lead to a ketohydroperoxide. At 560 K, the whole flux adds to molecular oxygen, while at 800 K a small flux (8%) undergoes β -scission. The RO₂ radical then isomerises to QOOH, through a six-membered transition state. At 560 K, the second addition to O₂ follows, while at 800 K this does not happen. After the addition to O₂, since no ketohydroperoxide can be formed, another isomerisation happens, followed by β -decomposition, giving products which include an OH radical and isopentanal. At 800 K, more than 90% of the flux from the QOOH radical goes through β -scission, which also leads to the formation of an isopentyl radical.

The third radical (in order of abundance) is the primary radical (dipee-p), which is slightly more important at higher temperature (21% against 15%). At 800 K, 14% of this flux isomerises to α -radical. This primary fuel radical (dipee-p) is therefore almost negligible and it mostly follows the typical low-temperature chain branching pathway.

The β -radical (dipee-s) is also formed, but a very small flux of the fuel actually follows this path (less than 10% at both temperatures). After addition to O₂, at 560 K the bigger flux (63%) undergoes a reaction of type RO₂ + RO₂ → RO + RO + O₂. At high temperatures, most of the flux (58%) still follows the typical low-temperature branching pathway, leading to the ketohydroperoxide. The other part of the flux (42%) at high temperature forms the associated unsaturated compound, by elimination of an HO₂ radical.

Since from the results in the jet-stirred reactor it appeared that isopentanal was very important in

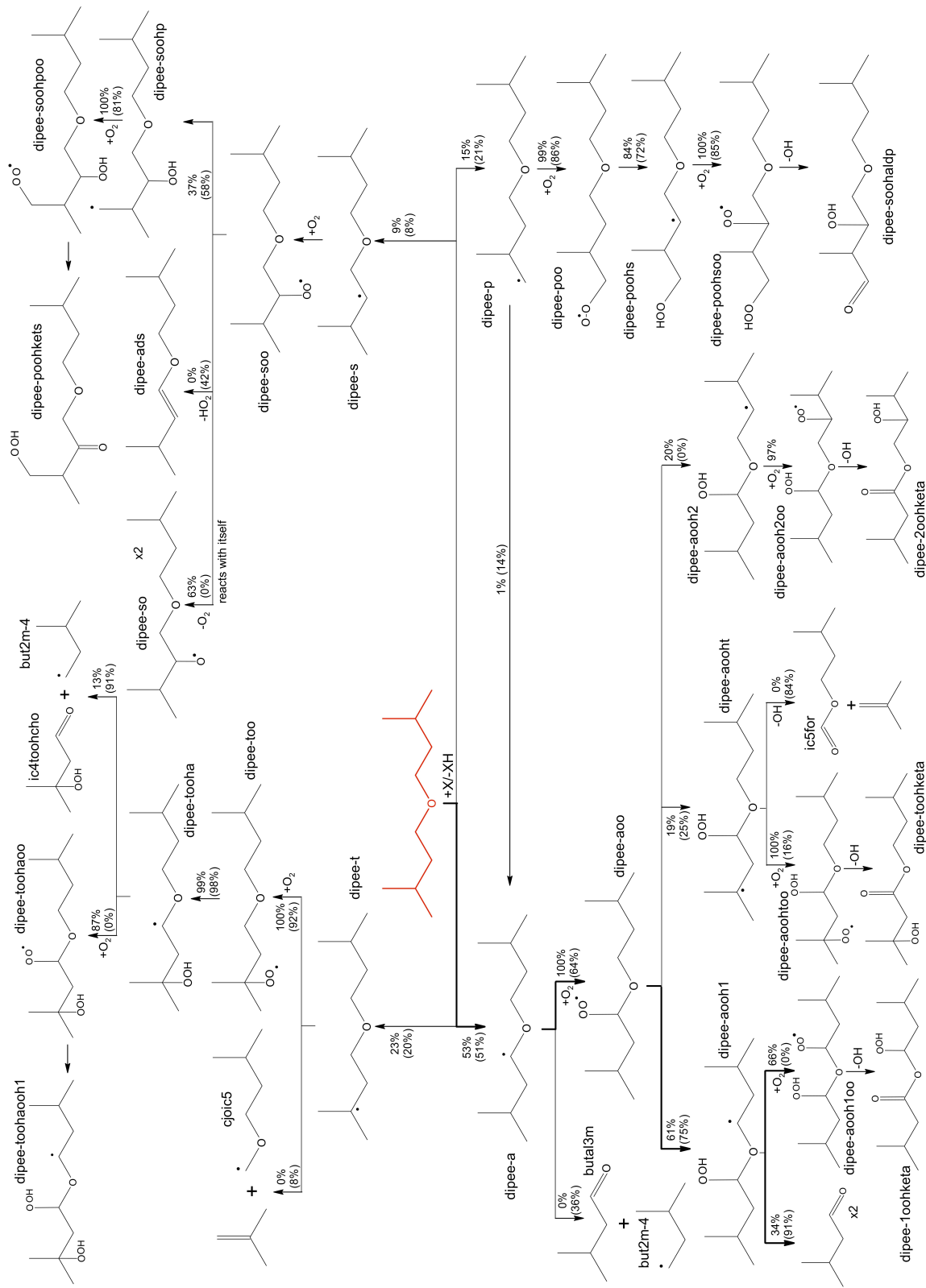
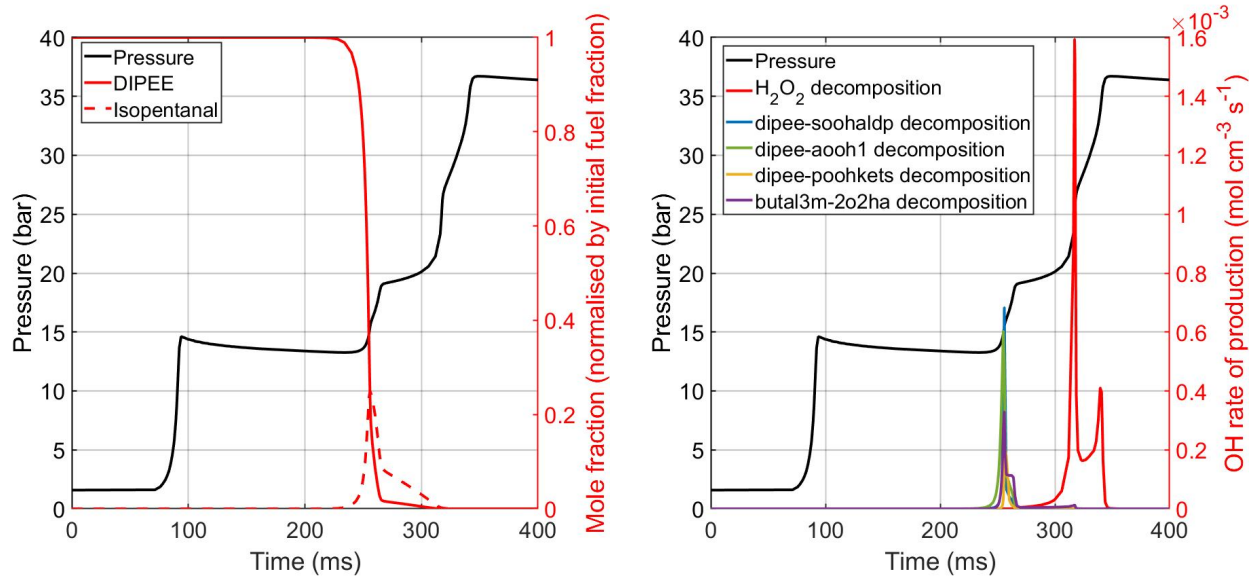


Figure 6.30: Reaction pathways in di-iso-pentyl ether oxidation in the RCM ($\phi = 1$, $p_c = 15$ bar, 560 K and 800 K (in parenthesis), dilution = 10, DIPEE = 0.6%, at 20% fuel consumption).

the overall reactivity of the fuel, it might be interesting to have a look at the reaction pathways in the rapid compression machine as far as this product is concerned. To this aim, in Figure 6.31, a first plot shows the mole fraction of DIPEE and isopentanal (both normalised by the initial mole fraction of DIPEE), along with the pressure profile obtained for a test at 560 K, for the stoichiometric mixture with dilution of 10. The Figure 6.31b shows the rate of production of OH from some reactions: the most important during the main stage ignition (where reactions involving DIPEE or isopentanal are no longer found) and the four most important reactions for the first stage (where the fuel is being consumed and isopentanal is produced and consumed).



(a) Molar fraction of DIPEE and isopentanal (normalised by DIPEE initial mole fraction)

(b) OH rate of production from the most important reactions

Figure 6.31: Isopentanal production during the ignition of DIPEE in the RCM: **a)** mole fraction of the fuel and of isopentanal over the test time (both normalised by the initial mole fraction of DIPEE), **b)** OH rate of production from the most important reactions during the first stage and the most important one during the main stage for comparison. Conditions: $\phi = 1$, dilution = 10, DIPEE = 0.6%, $p_c = 15$ bar, $T_c = 560$ K.

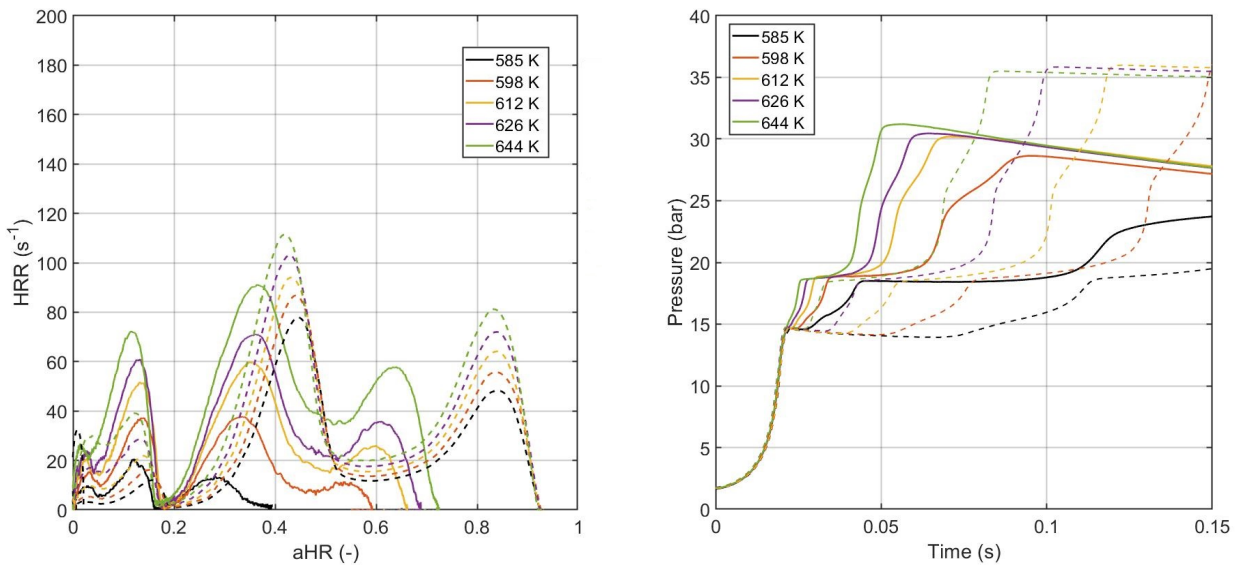
As can be seen from Figure 6.31a, also in the rapid compression machine isopentanal appears to be an important intermediate during DIPEE oxidation. It is possible to see that it reaches around 25% of the initial mole fraction of DIPEE, which is comparable to the 200 ppm produced in the JSR from 1000 ppm of initial fuel mole fraction. Isopentanal is produced during the first stage of the ignition, where also fuel is consumed. It is possible to see that then isopentanal is reacting and being rapidly consumed during the second part of the first stage, while a smaller part is being consumed between the end of the first stage and the beginning of the main stage of the combustion. In order to have an idea of the influence of isopentanal on the reactivity, it is possible to analyse the most important reactions producing OH radicals. In Figure 6.31b, these reactions are plot-

ted along the time scale of the experimental run, together with the pressure profile to be able to identify the ignition stages. The OH ROP from the high temperature H_2O_2 decomposition was also included in order to have a comparison of the relative magnitude of the rate of production from these reactions. It has to be noted that all the ROP, except this last one (decomposition of H_2O_2), have been multiplied by 10 for a better clarity of the plot. During the first stage, the most important reactions in the production of OH radicals appear to be the one linked to the decomposition of ketohydroperoxides. Among these, the decomposition of the QOOH previously discussed (dipee-aooH1), which gives two molecules of isopentanal and one OH radical, is found. Isopentanal itself appears to be important in the first stage: in fact, the decomposition reaction of one of its QOOH radicals is between the reactions that are mostly producing OH radical in the first part of the ignition. Unlike the decomposition of DIPEE ketohydroperoxides or QOOH, this reaction still produces some OH radicals in the time space between the first and the main stages, even if the magnitude of the ROP is negligible compared to the H_2O_2 decomposition.

6.6.2 HRR

An analysis on the heat release rate during the tests in the rapid compression machine was carried out for DIPEE, considering the stoichiometric mixture with dilution of 10. The results are shown in Figure 6.32, where two comparisons are shown: the first one between the HRR computed from the experiments and from the simulations and the second one between the pressure profiles from which the HRR is obtained.

The Figure 6.32a shows that unlike all the other ethers, the heat release rates from the experiments and the simulations have comparable values. The shapes of the profiles representing the heat release rate as a function of the accumulated heat release are also very similar, excluding the first point at 585 K. Both the experiments and the simulations show that the first stage of the ignition induces two peaks of heat release and the same happens for the main stage of ignition. This can be seen also in the Figure 6.32b where there is a change in the slope for both the first and the main stages. The simulations still slightly overpredict the maximum heat release rate of the main stage of the ignition, but the difference here is much smaller than what was shown for the ethers previously presented. On the other hand, the simulations underpredict the heat release rates of the first stage.



(a) Heat release rate vs accumulated heat release (both normalised by the mixture LHV) (b) Pressure profiles (only some simulations for clarity of the plot)

Figure 6.32: Experiments (solid) vs simulations (dashed): **a)** HRR vs aHR, **b)** pressure profiles. Mixture: DIPEE, $\phi = 1$, dilution = 10 (inert gases: 50% CO_2 + 50% N_2), DIPEE = 0.6%, $p_c = 15$ bar.

Figure 6.33 completes the heat release rate analysis by showing the comparison between low-temperature heat release and maximum accumulated heat release from the experiments and from the simulations. The agreement is almost perfect concerning the low-temperature heat release (as can be seen also from the comparison of the pressure profiles, where it can be seen that the increase in pressure due to the first stage is the same between experiments and simulations). On the other hand, the maximum accumulated heat release is overpredicted by the simulations and even if the fact that facility effects can be present is taken into account, the difference is still quite important. Also, there is a clear increasing trend in the maximum accumulated heat release as the temperature increases in the experiments, which is not well captured by the mechanism, which predicts an almost constant value.

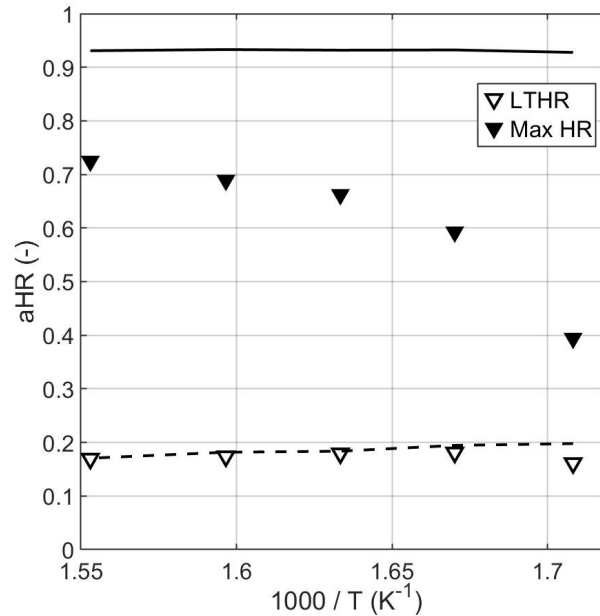


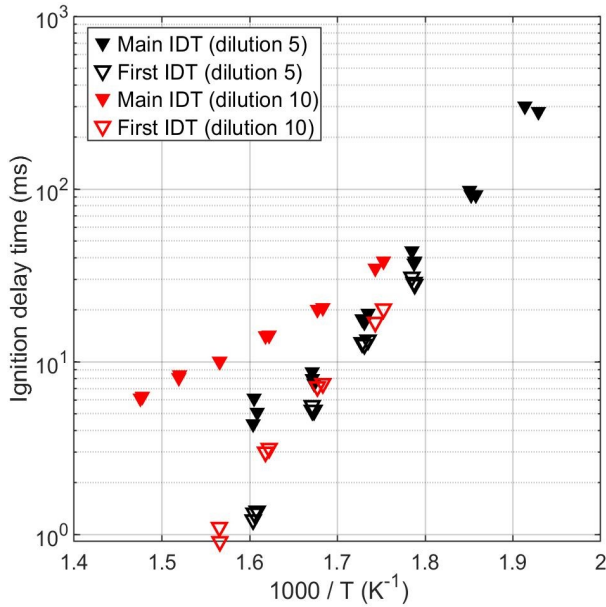
Figure 6.33: Low-temperature heat release and maximum accumulated heat release (normalised by the mixture LHV): comparison between experiments (points) and simulations (lines). Mixture: DIPEE, $\phi = 1$, dilution = 10 (inert gases: 50% CO₂ + 50% N₂), DIPEE = 0.6%, $p_c = 15$ bar.

6.7 DNPEE

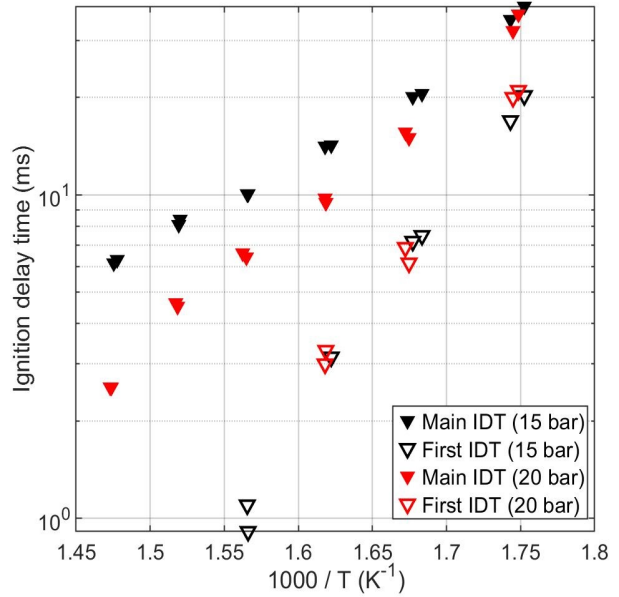
Di-*n*-pentyl ether was also tested in the RCM under different conditions: equivalence ratios (0.5, 1, 2), dilution (5, 10) and pressures (15, 20 bar). Figure 6.34 shows the ignition delay times for the different mixtures that were tested, while figure 6.35 displays a comparison of the IDTs for the three equivalence ratios for mixtures with dilution of 5.

The Figures 6.34a and 6.34b show the experimental results for the stoichiometric mixtures: in the first one (Fig. 6.34a), two mixtures with different dilution are compared, while in the second one (Fig. 6.34b) two different pressures are tested, with the same mixture with dilution of 10. In both cases, the first ignition delay times are quite similar, showing little to none dependence on the dilution or on the pressure. The main ignition delay times, on the other hand, are dependent on both factors. From the first plot, it can be seen that increasing the dilution is sensibly increasing the ignition delay times, while it is also changing the trend. In fact, as the temperature increases, the delays of the more diluted mixture decrease with a smaller pace, almost hinting a possible plateau at intermediate temperatures. On the other hand, if the influence of the pressure is considered, it can be seen that increasing the pressure at the end of the compression decreases the ignition delay times, by a more important extent at higher temperatures. Even if also in this case it appears that the pressure changes the slope of the IDTs, it does not seem as if it is determining the beginning of an NTC region. It seems that at both pressures the delays are still following a typical Arrhenius

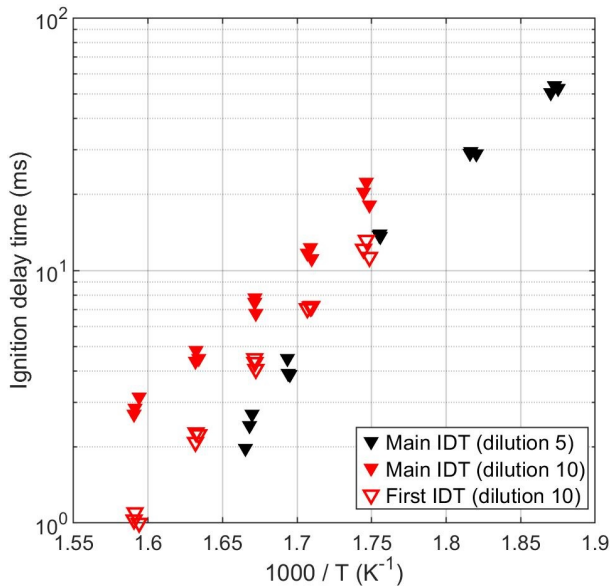
trend, just with different slopes.



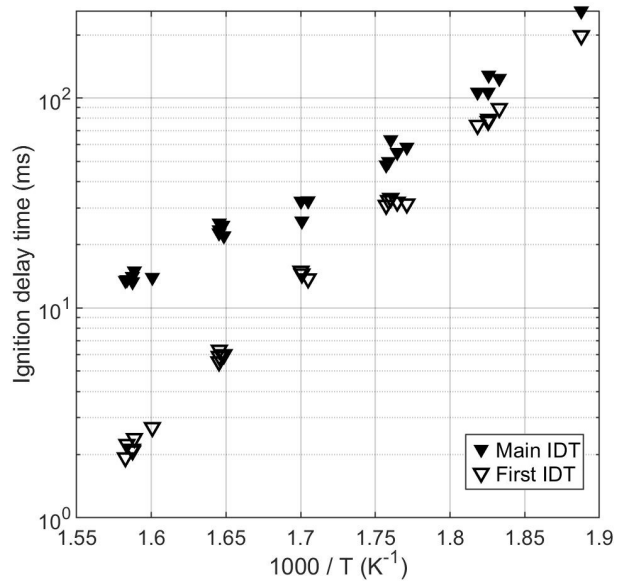
(a) $\phi = 1$, $p_c = 15$ bar, dilution = 5 (black), 10 (red), DNPEE = 1.1% (black), 0.6% (red)



(b) $\phi = 1$, $p_c = 15$ bar (black), 20 bar (red), dilution = 10, DNPEE = 0.6%



(c) $\phi = 2$, $p_c = 15$ bar, dilution = 5 (black), 10 (red), DNPEE = 2.2% (black), 1.2% (red)



(d) $\phi = 0.5$, $p_c = 15$ bar, dilution = 5, DNPEE = 0.5%

Figure 6.34: Ignition delay times of di-*n*-pentyl ether in the RCM.

The Figure 6.34c shows again the influence of the dilution, this time for two rich mixtures ($\phi = 2$). The main difference that can be seen is the presence of a two-stage ignition for the mixture with dilution of 10, while the one with dilution of 5 appears to have only one stage, as shown by the pressure profiles in appendix B.1.7. Both first and main IDTs of the more diluted mixture appear

longer than the main ignition delays for the less diluted one. In this case, the slopes of the main IDTs in the two cases appear more similar than what was seen for the stoichiometric mixtures.

The Figure 6.34d shows the ignition delay times for a lean mixture with dilution 5. IDTs of the mixture with higher dilution could not be determined due to a too weak increase in the pressure that could hardly be identified as ignition. The ignition in these conditions (dilution of 5) happens in two stages, with the first ignition delays decreasing faster than the main ones as the temperature increases.

Figure 6.35 shows the influence of the equivalence ratio on the main ignition delay times. As expected, as the equivalence ratio increases, the IDTs decrease, over the whole temperature range. The influence of the equivalence ratio is less important at very low temperature, where all IDTs are quite similar, while a bigger difference can be seen as the temperature increases. The slopes are quite different, but the three conditions seem to have a typical Arrhenius trend, with no NTC zone that can be identified or even hinted, at least within this temperature range.

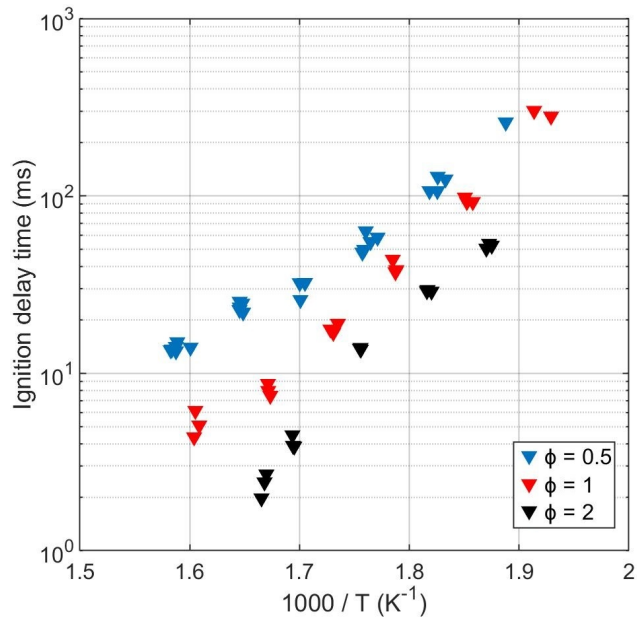


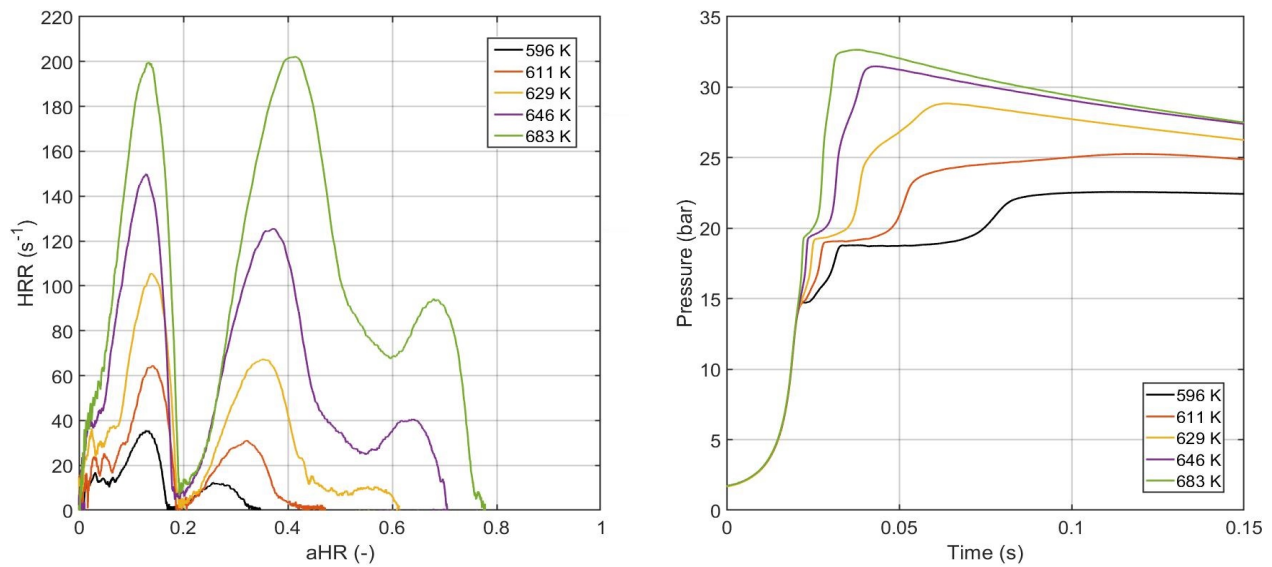
Figure 6.35: Comparison of the main ignition delay times of di-*n*-pentyl ether in the RCM for different equivalence ratios (0.5, 1 and 2), with dilution = 5 and $p_c = 15$ bar.

6.7.1 HRR

Similarly to the other ethers, an analysis on the heat release rate was performed also for DNPEE, however only on the experimental results. The computed heat release rate as a function of the accumulated heat release is shown in Figure 6.36a, side by side with the pressure profiles from which it was computed in Figure 6.36b. It can be seen that the heat release rate of the first stage is very important and at low temperature it is higher than the rate of the main stage ignition. Also, the first stage seems to have a change in slope in the pressure increase, especially at low temperature, while

the main ignition is showing only one peak in the heat release rate for lower temperatures and two peaks appear as the temperature increases. This can be seen also in the pressure profiles, where a change in slope appears in the increase of pressure due to the main ignition as temperature is increased.

Figure 6.37 completes the analysis on the heat release rate by showing the low-temperature heat release and the maximum accumulated heat release over the temperature range. The low-temperature heat release seems to be constant as the temperature is increased. In fact, the studied temperature range is quite narrow and therefore all the points can be considered to be in the low-temperature regime. If the maximum accumulated heat release is considered, it is possible to see that it strongly increases as the temperature increases and this increase can be expected to slow down at higher temperature.



(a) Heat release rate vs accumulated heat release (both normalised by the mixture LHV)

(b) Pressure profiles

Figure 6.36: Experimental results for the heat release rate analysis: **a)** HRR vs aHR, **b)** pressure profiles. Mixture: DNPEE, $\phi = 1$, dilution = 10 (inert gases: 50% CO_2 + 50% N_2), DNPEE = 0.6%, $p_c = 15$ bar.

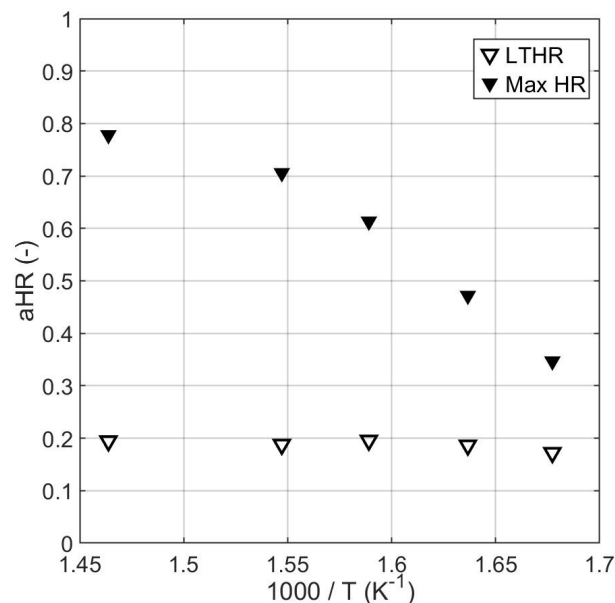


Figure 6.37: Experimental low-temperature heat release and maximum accumulated heat release (normalised by the mixture LHV). Mixture: DNPEE, $\phi = 1$, dilution = 10 (inert gases: 50% CO₂ + 50% N₂), DNPEE = 0.6%, $p_c = 15$ bar.

6.8 Comparison

The results presented so far have explored the ignition behaviour of several molecules of the ether family in the rapid compression machine. The simulations performed through the developed mechanism were compared to the experimental results, showing different levels of agreement for the different ethers. With the goal of understanding how the structure of these molecules is influencing their reactivity, it is vital to compare the experimental results that could be performed in the same conditions. The following subsections will present these comparisons, starting from direct comparison between two or three fuels sharing some characteristics (isomers, branching, symmetry/asymmetry), and will conclude with a comparison of all the ethers together.

6.8.1 DPE vs DIPE

The first comparison is between di-*n*-propyl and di-*iso*-propyl ethers, which were studied both in Orléans and in Galway. The ignition delay times reported in Figure 6.38 are for a mixture with $\phi = 2$ and a dilution of 10. For DIPE, the low temperature IDTs were measured in the RCM in PRISME and only the high temperature delays were measured in the shock tube in Galway. For DPE, together with the high temperature shock tube data, also the intermediate temperature IDTs were measured in Galway, in the twin-piston RCM. It is possible to see that there is a gap in the measurements of the delay of DIPE in the NTC region: in fact, the delays become so long that they

could not be measured in the rapid compression machine in a reliable manner.

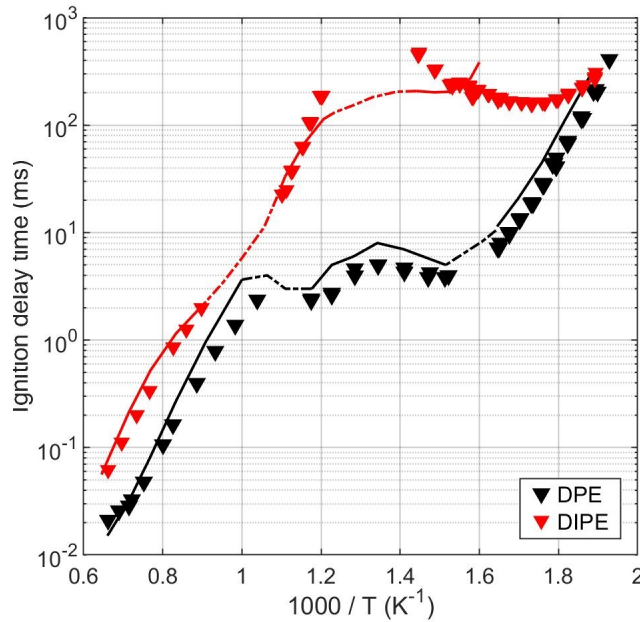


Figure 6.38: Comparison of the main ignition delay times of di-*n*-propyl and di-*iso*-propyl ethers at $\phi = 2$, dilution = 10, $p_c = 15$ bar, DPE = 2.0%, DIPE = 2.0%.

It has to be noted that this condition for DIPE was not presented in section 6.3, therefore a quick comparison between experiments and simulations may be interesting. As for the other conditions, the simulations do not show any reactivity at very low temperature and they underestimate the delays in the peak at the end of the NTC region (even if the experimental results have a gap there, it is clear that the experimental values would be much higher than the simulated ones). As temperature increases, the simulations become in better agreement with the experiments, with very good accuracy for the shock tube results.

If the reactivity of these two fuels has to be compared, the first obvious observation is that DPE is more reactive than DIPE over the whole temperature range, with lower ignition delay times. Only at very low temperatures, at the beginning of the studied temperature range (around 520 K), the ignition delays of DPE and DIPE are actually quite similar. Under these conditions, it is possible to see that both fuels show an NTC region, which is situated in a similar temperature range. Nevertheless, the trend of the delays in this region is very different between the two isomers: IDTs of DPE reach what appears as a plateau, with a very small increase in the delays as the temperature increases from around 3.8 to 4.9 ms (which can probably be in the uncertainty interval). DIPE, on the other hand, shows a real increase in the ignition delay times, which change from ~150 ms at 575 K (beginning of NTC) to ~450 ms at 690 K (last measurement possible, even if already outside the reliability interval of the RCM). The measurements of ignition delay times are possible again starting from around 830 K, where the delay decreases back to around 190 ms.

In the higher temperature zone, DIPE still shows longer ignition delay times than DPE, but the

values are closer than in the low-intermediate temperatures. Also, the slope of the experimental results appear quite similar between the two isomers and the simulations are quite in good agreement for both fuels.

A third fuel can be compared to this two, i.e. diethyl ether, since it is the symmetrical ether just before DPE for its chain length. Figure 6.39 therefore shows the ignition delay times at low temperature for the same conditions as in figure 6.38 ($\phi = 2$, dilution = 10, $p_c = 15$ bar), including DEE in the comparison. It is possible to see that diethyl ether has ignition delay times similar to di-*n*-propyl ether, but slightly shorter (by a factor of around 1.5) over the whole temperature range. It appears therefore that increasing the length of the chain slightly increases the ignition delay times, while the addition of a branching increases them by a considerable larger amount and it also influences the trend, increasing the importance of the NTC behaviour. The decrease in reactivity due to the branching was shown also in the JSR results, while increasing the length of the chain increased the reactivity, due to the possibility of producing more radicals and products that were also having their own reactivity. To have a better idea of the possible influence of the structure on the IDTs measured in the RCM, it is noted that the same relations between these three ethers (DEE, DPE and DIPE) is shared by another three, DBE, DNPEE and DIPEE, which will be presented in the next section.

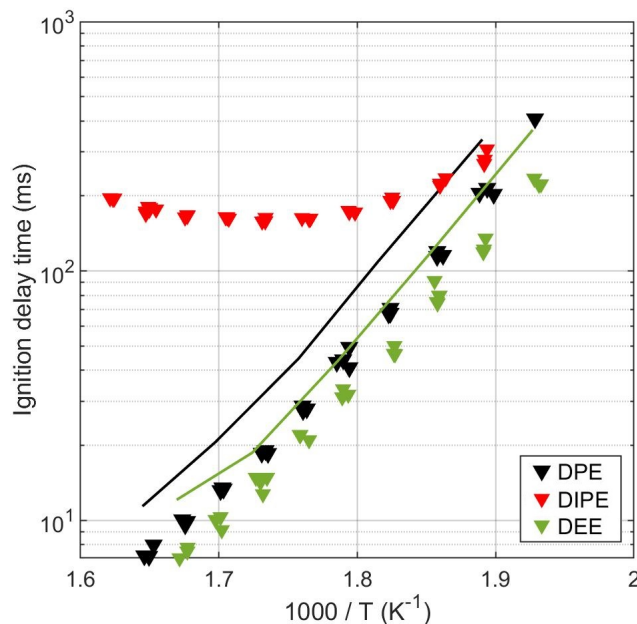


Figure 6.39: Comparison of the main ignition delay times of di-*n*-propyl, di-*iso*-propyl and diethyl ethers at low temperatures, with $\phi = 2$, dilution = 10 (DEE = 2.9%, DPE = 2.0%, DIPE = 2.0%), $p_c = 15$ bar.

6.8.2 DNPEE vs DIPEE

Similar to DPE and DIPE, di-*n*-pentyl and di-*iso*-pentyl ethers are symmetrical isomers, with one being linear and the other branched. The comparison of their ignition delay times for two stoichiometric mixtures (one with dilution 5 and one with dilution 10) are shown in figure 6.40. From the first plot, it is possible to see that for the mixtures with dilution 5 the ignition delay times of the two ethers are quite similar. Nevertheless, DNPEE shows a two-stage ignition, while DIPEE shows only one stage. It is possible that also DIPEE has a two-stage ignition, but they are so close to each other that they are indistinguishable. Nevertheless, it is only a speculation, since from the simple experimental pressure profiles (visible in Appendix B.1.6) no conclusions could be drawn.

The Figure 6.40b shows the two mixtures with dilution of 10. In this case, both fuels show a clear two-stage ignition. The first ignition delay times appear comparable at low temperatures, while the ones for DNPEE become faster when the temperature increases. Considering the main ignition delay times, over the whole temperature range DNPEE ignites faster than DIPEE, showing that, as for DIPE and DPE, the branched structure decreases the reactivity of the fuel. If the trends are considered, it can be seen that DIPEE has a change of slope, that even if it cannot really be identified as an NTC, it can identify a change in the reactivity linked to the different temperature zones. This is hardly arguable for DNPEE from the experimental data that could be collected; in fact, higher temperature measurements were not possible in this RCM, due to the strong first stage ignition that was starting to happen before the end of the compression.

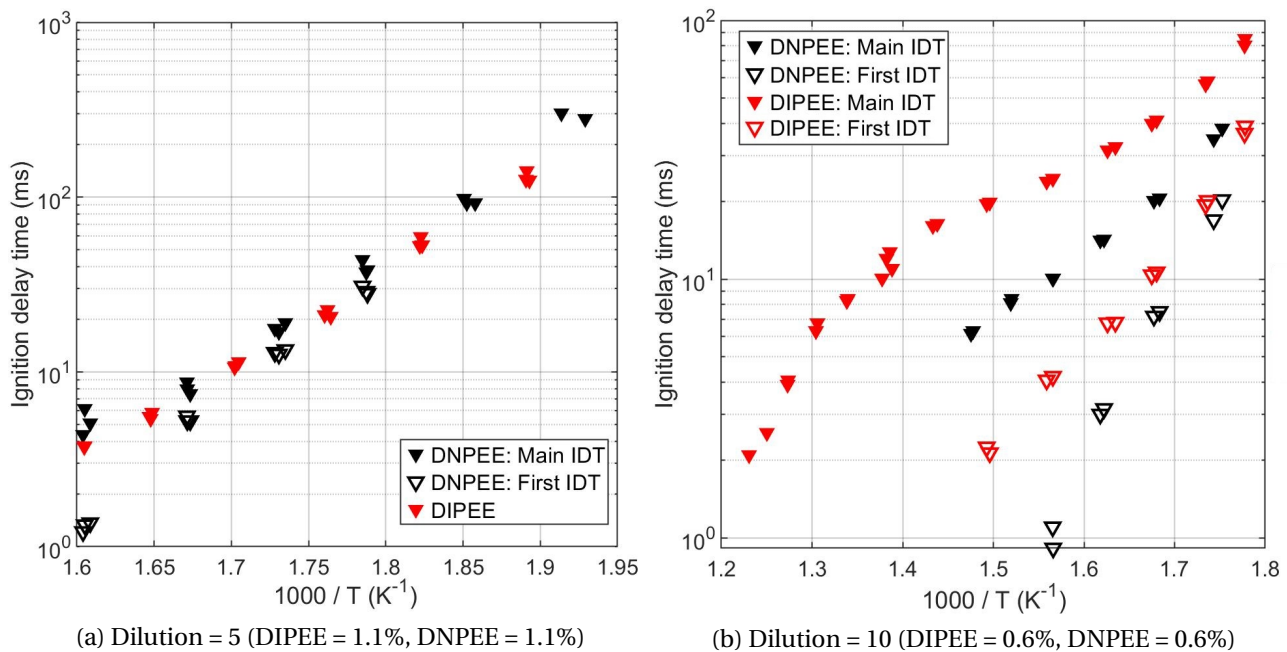


Figure 6.40: Comparison of the experimental results of di-*n*-pentyl and di-*iso*-pentyl ethers, at $\phi = 1$, dilution = 5 (a), 10 (b), $p_c = 15$ bar.

As previously done with DPE, DIPE and DEE, it may be interesting to add also dibutyl ether to the comparison. Figure 6.41 shows the main ignition delay times of the two pentyl ethers and dibutyl ether, for a stoichiometric mixture, with dilution of 10.

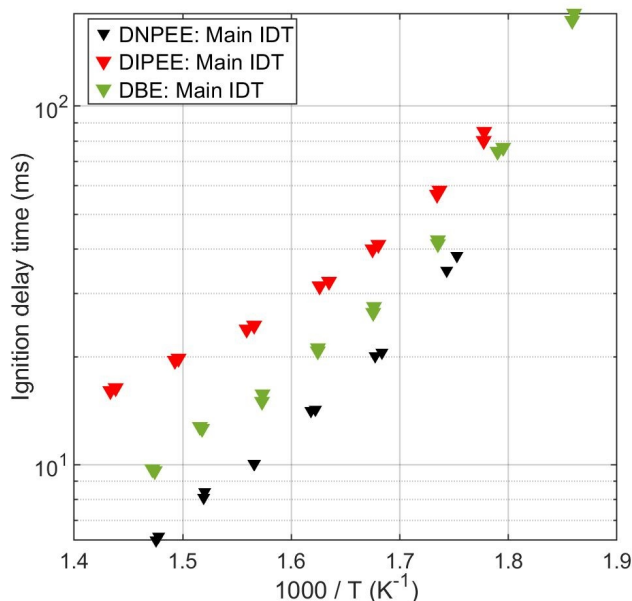


Figure 6.41: Comparison of the main ignition delay times of di-*n*-pentyl, di-*iso*-pentyl and dibutyl ethers at low temperatures, with $\phi = 1$, dilution = 10 (DBE = 0.8%, DIPEE = 0.6%, DNPEE = 0.6%), $p_c = 15$ bar.

The branched di-*iso*-pentyl ether has the longest ignition delay times and it is also the only one that seems to have a trend not completely linear. Di-*n*-pentyl ether and dibutyl ether, on the other hand, are quite close to each other, regarding their main ignition delay times, with DNPEE having shorter IDTs over the whole temperature range, by a factor of around 1.5. This is the opposite of what observed for DEE and DPE and in this case it is not possible to observe if the simulations are predicting the same trend or not. Some further considerations will therefore be presented on the possible influence of the length of the carbon chain on the ignition delay times in a later section, where all the ethers will be compared.

6.8.3 BEE vs DEE/DBE/DPE

Butyl ethyl ether is the only asymmetrical ether that was included in this work and it shares one side with diethyl ether and one with dibutyl ether. For this reason, its ignition delay times have been compared to these two other ethers as the first comparison.

Figure 6.42 shows this comparison for two different mixtures, a lean mixture with dilution of 5 and a stoichiometric mixture with dilution of 10. In the case of the stoichiometric mixture, the main ignition delay times for the three ethers at low temperatures have very similar values. As the temperature increases, their value starts to be slightly different, with butyl ethyl ether having the

shortest IDTs, while the other two are still very close to each other. The first ignition delay times, on the other hand, are longer for dibutyl ether, followed by butyl ethyl ether, while it seems that diethyl ether has the shortest delay for the first stage.

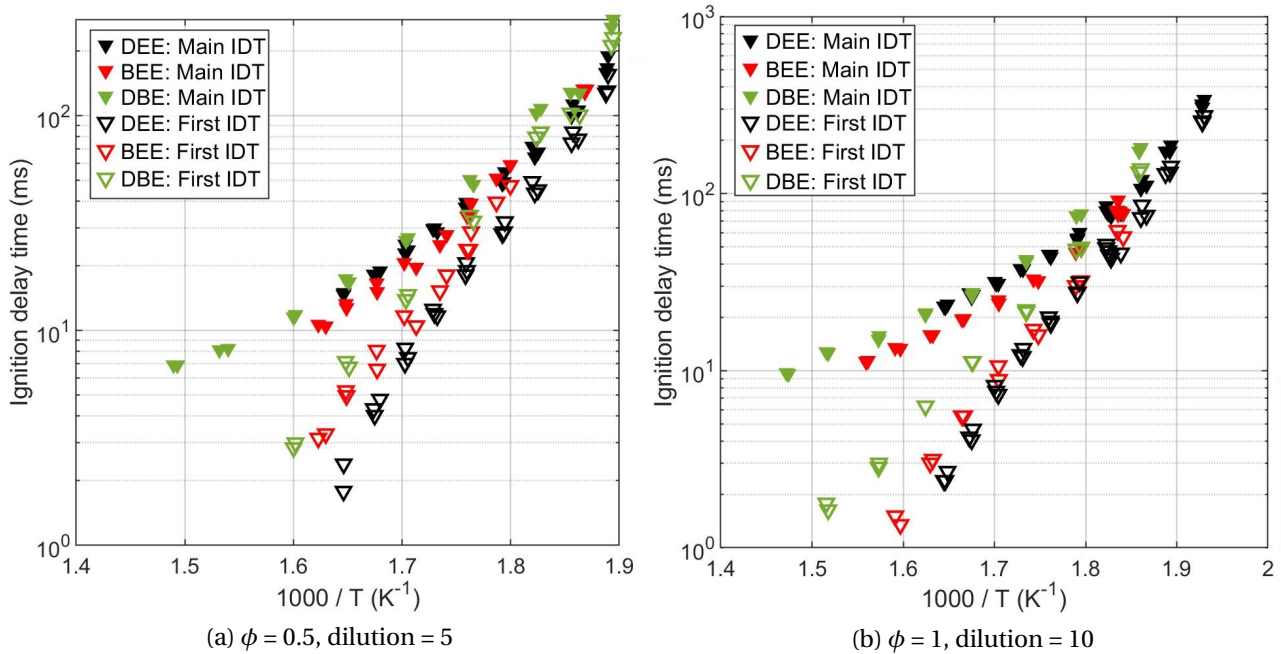


Figure 6.42: Comparison of the experimental results of butyl ethyl ether and diethyl and dibutyl ethers, at $\phi = 0.5$, dilution = 5, BEE = 0.9%, DEE = 1.37%, DBE = 0.7% (a) and $\phi = 1$, dilution = 10, BEE = 1.0%, DEE = 1.5%, DBE = 0.8% (b), $p_c = 15$ bar.

The results for the lean mixtures, with lower dilution, are quite similar to what was just presented. The main ignition delay times are very similar at low temperature, with also the first delays being in the same range or even indistinguishable from the main stage for butyl ethyl ether. As the temperature increases, a slight difference can be seen, but in this case the delays are closer to each other than for the stoichiometric mixtures. A bigger difference seems to be present for the first stage ignition delays, which have the same behaviour as the ones for the stoichiometric case. Nevertheless, it has to be kept in mind that, even if some difference is visible, the main delays are still quite similar and this will be further discussed in the section comparing all ethers.

A second comparison is possible between BEE and DPE, since they are isomers. The comparison is shown in Figure 6.43, for two different mixtures ($\phi = 1$ and 2) with a dilution of 10. The two stoichiometric mixtures, shown in Figure 6.43a, show very similar ignition delay for the first stage, while the main IDTs appear slightly longer for DPE. DPE shows longer main ignition delay also for the rich mixture (shown in Figure 6.43b) and a two-stage ignition could be identified for DPE, while only one stage was found for BEE. It appears therefore that the asymmetry of BEE leads to slightly shorter ignition delays, compared to its symmetrical, linear isomer. Nevertheless, once again the

ignition delays appear quite similar under these conditions.

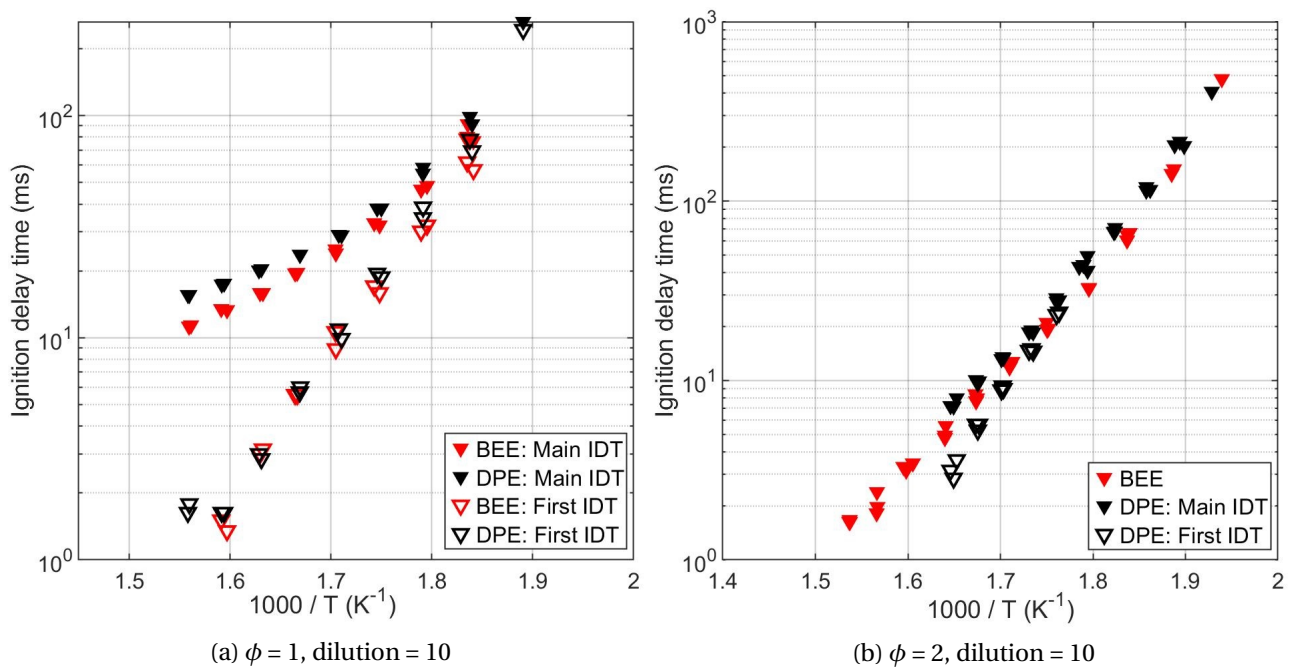


Figure 6.43: Comparison of the experimental results of butyl ethyl ether and diethyl and dibutyl ethers, at $\phi = 1$, dilution = 10, BEE = 1.0%, DPE = 1.0% (a) and $\phi = 2$, dilution = 10, BEE = 1.98%, DPE = 2.0% (b), $p_c = 15$ bar.

6.8.4 Final comparison

As previously done with the experimental results obtained in the jet-stirred reactor, it is also interesting to compare the ignition delay times for all the ethers that could be studied under the same conditions in the rapid compression machine. Only one condition could be common between all the ethers, a rich mixture ($\phi = 2$), with dilution of 10 and performing the experiments at 15 bar. These results can be seen in Figure 6.44b). The Figure 6.44a, on the other hand, shows another condition (stoichiometric mixtures, with dilution of 10), but DIPE is missing, since it was not enough reactive.

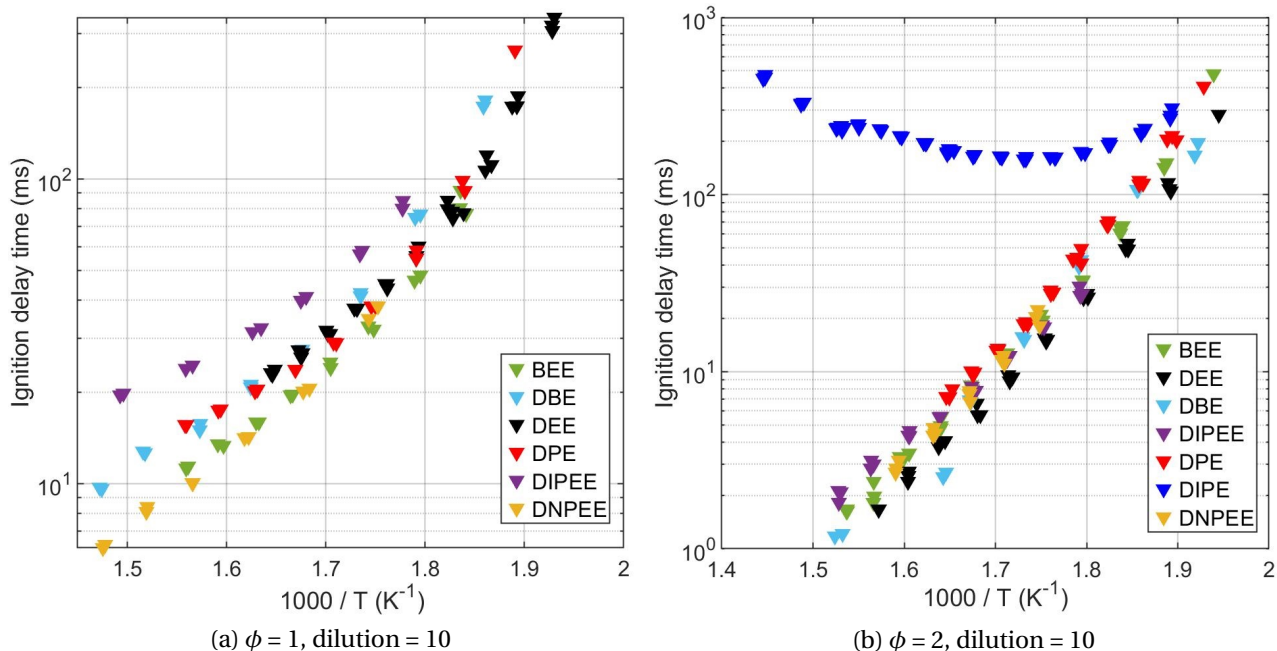


Figure 6.44: Comparison of the experimental results for all the ethers studied in the RCM, at $\phi = 1$, dilution = 10 (a) and $\phi = 2$, dilution = 10 (b), $p_c = 15$ bar.

Starting from the Figure 6.44b, where all the ethers are compared, it is possible to see that, except DIPE, all the other ethers have quite similar main ignition delay times (the first ignition delay times are not plotted, to avoid confusion in the plot). Di-*iso*-propyl ether, which was the least reactive also in the JSR, with no fuel conversion happening before 700 K, is igniting in the RCM in the same temperature range as the other ethers, but its ignition delay times are longer by a factor of 2 at 530 K, which increases up to around 140 at 650 K, where DIPE shows an NTC region which none of the other ethers under these conditions do. All these rich mixtures for the other ethers show a typical Arrhenius trend, with very similar slopes and very similar values.

In order to see if under different conditions, the main ignition delay times were different for the different ethers, the Figure 6.44a shows the comparison of the stoichiometric mixtures, still with a dilution of 10. In this case, even if the ignition delays are still quite similar at low temperatures, some differences can be seen as temperature increases. Unluckily, due to the constraint of the RCM and to the very strong first stage ignition, it was not possible to cover higher temperatures without the issue of the reactions starting to happen during the compression. From what is shown in the figure, it seems that di-*iso*-pentyl ether is the least reactive, while DNPEE, BEE, DEE and DBE have shorter main ignition delay times, all quite similar to each other. It appears that the ether with shorter ignition delay times in these conditions is di-*n*-pentyl ether, which would be reasonable, since its longer chain would help the formation of small, reactive radicals, but it should be remembered that it was the opposite way for the comparison DEE/DPE for rich conditions and high dilution. Nevertheless, considering the high dilution and the very low temperature range, the

main ignition delay times are all quite similar to each other, which is actually also quite similar to what was seen for the fuel conversion in the jet-stirred reactor at very low temperatures. Therefore, concluding on the order of the magnitude of the ignition delay times and the influence of the length of the chain from only these results would be tricky. The only conclusion is the fact that, adding a branching in the structure, especially for small ethers, is strongly decreasing the reactivity and enhancing the NTC.

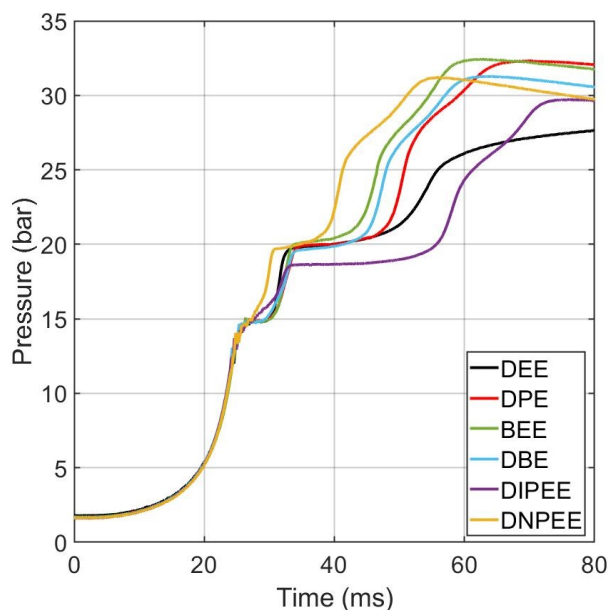


Figure 6.45: Comparison of the experimental pressure traces for all the ethers studied in the RCM (except DIPEE), with $\phi = 1$, dilution = 10, $T_c = 615$ K, $p_c = 15$ bar.

As part of this final comparison, also the pressure traces at 615 K for the different ethers, except DIPEE, are plotted in Figure 6.45. It can be seen that the first ignition delays are very similar, except for DNPEE, which is slightly faster. The pressure increase is also quite similar between the ethers, except for DIPEE, which is sensibly lower. The main ignition delay times are slightly more different, with DIPEE (the only branched ether in this comparison) being the one with a longer delay and DNPEE (the one with the longest chain) having the shortest delay. It has to be remembered that, at the same dilution, the percentage of fuel in the mixture is different. It might therefore be interesting to compare also the results for the heat release, since in that case all the results are also normalised by the lower heating value of the mixtures.

The maximum accumulated heat release for all the ethers tested in the RCM are shown in Figure 6.46a. For the sake of completeness, di-*iso*-propyl ether has been included, even if its results are obtained for a mixture with dilution 5, instead of 10. It can be seen that the less diluted mixture leads to a higher maximum accumulated heat release, which gets close to 90% of the lower heating value of the mixture. For the other ethers, for which the dilution is 10, the accumulated heat release hardly reaches around 80% of the lower heating value, with only dibutyl ether getting to

almost 85% with a mixture containing only nitrogen. For all the ethers, a more or less pronounced increasing trend can be seen as the temperature increases. From these results, it seems that longer chain fuels are less efficient (i.e. having lower maximum accumulated heat release with respect to their lower heating value) in the heat release under these conditions in the rapid compression machine. This can be caused by the fact that bigger products that may be formed could be storing more energy compared to the smaller products that can be obtained from ethers with shorter chain.

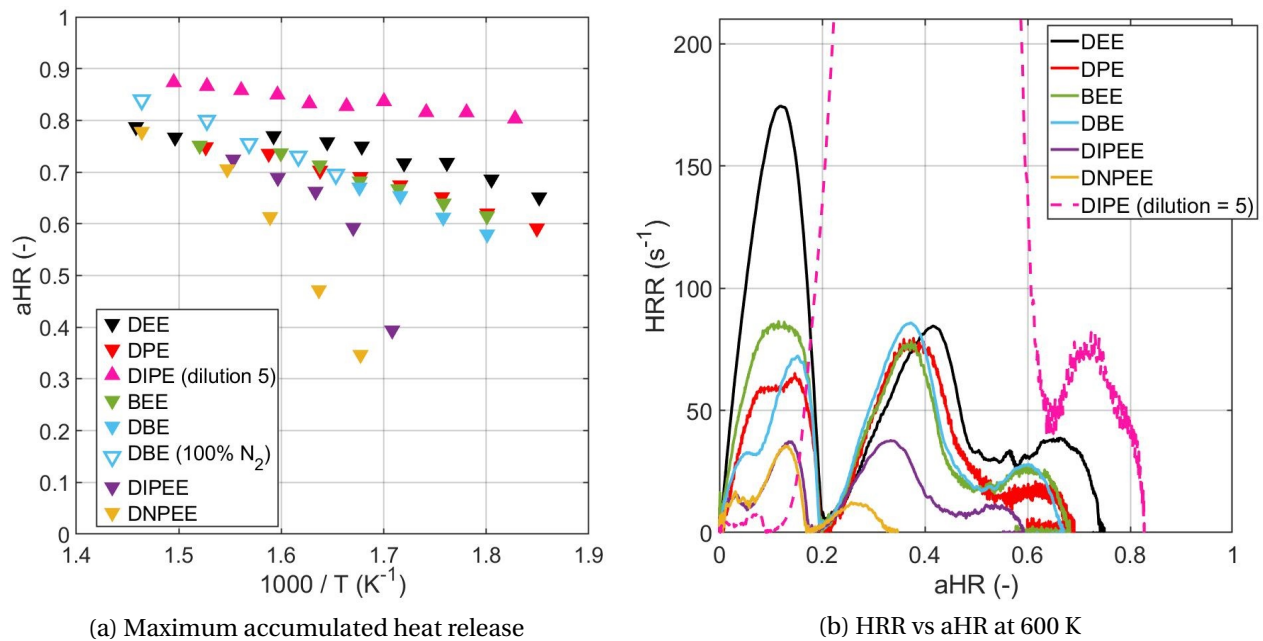


Figure 6.46: Comparison of the experimental results from the heat release analysis for all the ethers studied in the RCM (it must be noted that DIPE has a different dilution), with $\phi = 1$, dilution = 10 (except for DIPE, for which the dilution is 10), $p_c = 15$ bar, inert gases: 50% CO₂ + 50% N₂ (unless differently specified).

In Figure 6.46b the heat release rate as function of the accumulated heat release for the tests performed at 600 K is shown for all the ethers. Once again, DIPE has been tested with a mixture with dilution of 5, while it was 10 for all the other fuels, which explains why the heat release rate peak of DIPE is so much higher. It was included just to show how, on the other hand, even with such a lower dilution, the heat release rate of the first stage is much lower than the ones of the other ethers, which is coherent with the weak low-temperature reactivity shown by DIPE under all conditions. Considering the other ethers, DEE seems to have the fastest heat release of in the first stage, while BEE, DPE and DBE are quite similar to each other. Also, DIPEE and DNPEE seems to be perfectly identical in the heat release rate of the first stage at this temperature, even if the ignition delay times are quite different. Considering the main ignition, the values and the shapes

of the heat release rates of DEE, DPE, BEE and DBE appear quite similar. DIPEE and DNPEE, on the other hand, have much lower heat release rates, which might be in line with the idea of the bigger products formed during the combustion that can store part of the energy that would otherwise be released in a faster way.

6.9 Ethyl lactate

Ignition delay times of ethyl lactate were measured at different equivalence ratios (0.5, 1, 1.5) and two different pressures (20 and 30 bar) for the stoichiometric mixture. At all conditions, the ignition delay times decrease with increasing temperature. Unlike the ethers presented in the previous sections, ethyl lactate shows no NTC zone or cool flame, proving that ethyl lactate does not present a significant low temperature reactivity, at least under the considered conditions.

As Figure 6.47 shows, increasing the equivalence ratio decreases the ignition delay times at all temperatures, but it also slightly changes the slope of the tendency lines of the data. A small remark has to be done on why the rich mixture here considered has an equivalence ratio of 1.5 and not of 2 like for all the other fuels. In fact, ethyl lactate has a quite high boiling point and in order to be sure that it was vaporised at all the stages of the experiments, the saturation temperature was verified using Antoine's equation and the heating system of the RCM did not allow temperatures high enough to study a mixture with equivalence ratio equal to 2.

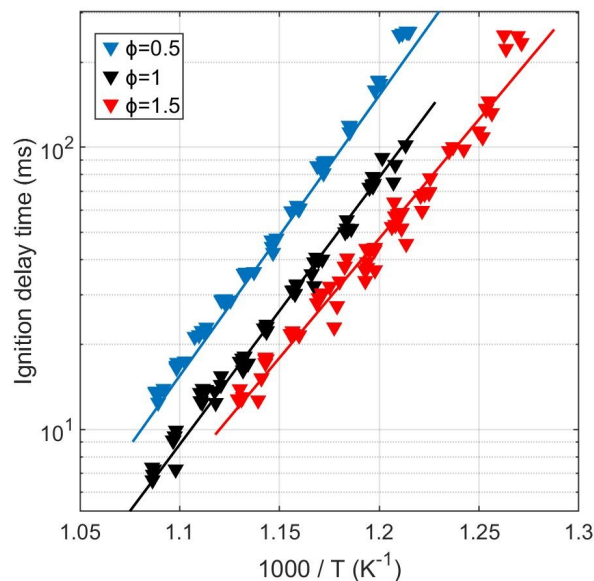


Figure 6.47: Ethyl lactate ignition delay times, for three different equivalence ratios at a compressed pressure of 20 bar (points: experiments, lines: simulations).

Figure 6.48 shows the ignition delay times of a stoichiometric mixture at compressed pressure of 20 and 30 bar. It is possible to see that, as expected, increasing the pressure leads to an increased

reactivity and therefore shorter ignition delay times at all temperatures. In this case though, the slope of the trendline of the data seems to be the same.

The lines reported in the two figures (Figs. 6.47 and 6.48) are the ignition delay times obtained by the simulations using the developed mechanism. In general, there is a good agreement between the experimental results and the simulations. The model is capable of predicting the tendency of the data under all conditions and the values are well captured, with a maximum deviation of 28% at stoichiometric conditions, for the compressed pressure of 30 bar, at high temperature.

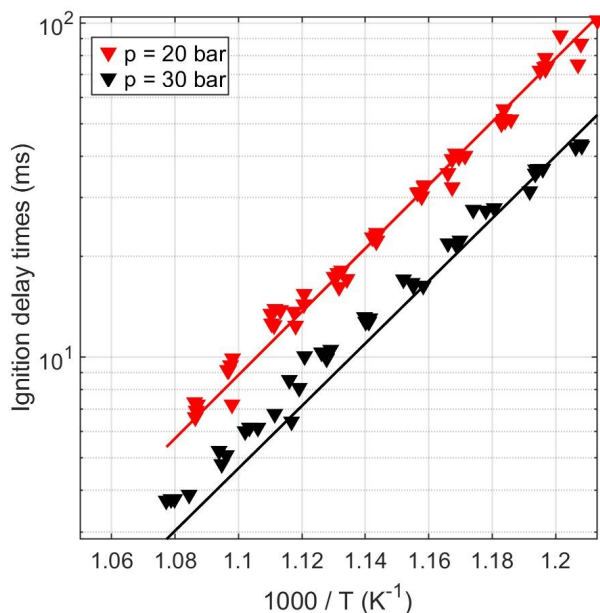


Figure 6.48: Ethyl lactate ignition delay times, for two different pressures at $\phi = 1$, EtLac = 3.38% (points: experiments, lines: simulations).

6.9.1 Reaction pathways

In order to have a better understanding of the reactions predicted by the model during the combustion under these conditions, a reaction pathway analysis has been performed. Figure 6.49 shows the resulting path for a stoichiometric mixture at two different temperatures, 830 and 915 K. The analysis has been performed for both cases at around 20% of fuel consumption, as usually done in the literature. At both temperatures, the paths followed are the same and only their relative importance is slightly changed.

The fuel is mainly consumed by H-abstraction by OH and HO₂ radicals, on the tertiary C-H bond (50% at the lowest temperature) forming the EtLac2j radical, and on carbon neighbouring the ether function (more than 40% at the lowest temperature), forming EtLacej. A smaller flux is undergoing the molecular reaction leading to the formation of lactic acid (LacAc) and ethylene. This unimolecular reaction account for only 7% at 830 K, but the percentage increases to 23% at 915 K. At lean

and rich conditions, the fuel is consumed by similar reactions. It is interesting to note that at high temperatures, the unimolecular reaction accounts for 31% of the flux at lean conditions (920 K), while this percentage decreases to 12% at rich conditions (at 880 K). Therefore, it appears that this unimolecular decomposition can have a non-negligible effect on the fuel consumption, especially at high temperatures.

A small flux of the radical EtLac2j leads to the formation of ethyl pyruvate (EtPyr), which is interestingly completely consumed by unimolecular decomposition, similar to the molecular reaction of ethyl lactate. On the other hand, the biggest percentage of this fuel radical forms the conjugate unsaturated compound (EtLac2d) and then decomposes or isomerises to ethyl pyruvate.

The second most abundant fuel radical (EtLacej) undergoes β -scission and no other pathways were predicted by the mechanism.

Finally, lactic acid produced through the unimolecular decomposition can either undergo H-abstraction, followed by two possible decomposition paths, or directly decomposes through a unimolecular reaction leading to acetaldehyde, CO and water.

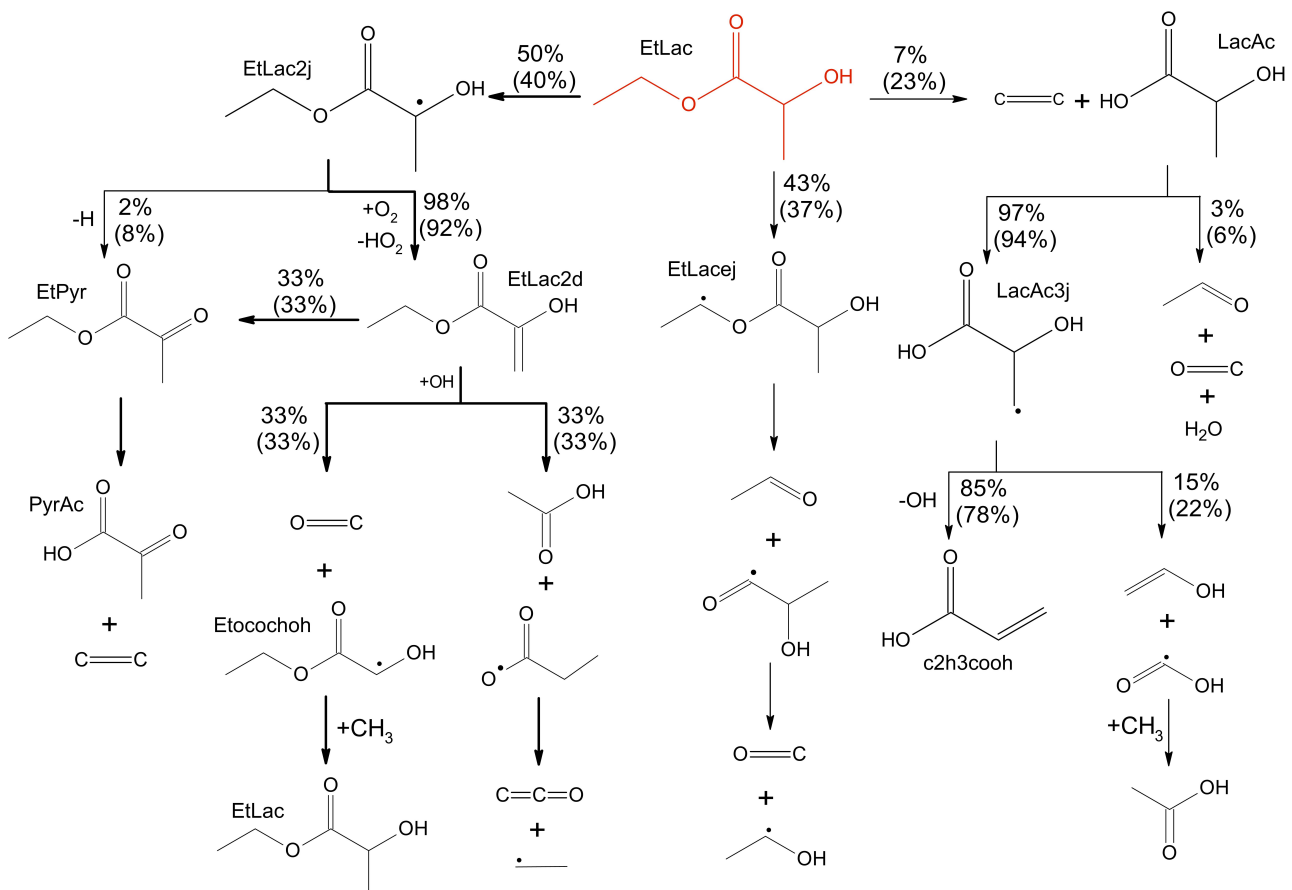


Figure 6.49: Reaction pathways in ethyl lactate oxidation ($\phi = 1$, EtLac = 3.38%, $p_c = 20$ bar, 830 K and 915 K (in parenthesis)).

6.9.2 Comparison to ethanol

Ethyl lactate presents an ether function as the other molecules studied in this work. Nevertheless, it is clear from the experimental results so far presented that its behaviour is very different from all the other fuels. In fact, even if experiments have been tried at lower temperatures than what is presented in Figure 6.47, no reactivity was shown in the lowest range of temperature, where the ethers were already very reactive. Therefore, a comparison has been envisaged with ethanol. In fact, ethyl lactate has a very low reactivity, like ethanol, thus qualifying as a possible octane booster for spark ignition engines. If this application has to be considered, it is interesting to compare the characteristics of ethyl lactate to the ones of ethanol, as presented in table 6.1, where also gasoline mean values have been included.

Table 6.1: Comparison of ethyl lactate characteristics with ethanol and gasoline.

	Ethyl lactate	Ethanol	Gasoline
Molecular formula	$C_5H_{10}O_3$	C_2H_6O	$\sim C_{7.4}H_{13.8}$
Density ($kg\ L^{-1}$)	1.031	0.784	~ 0.75
Molar mass ($kg\ mol^{-1}$)	0.118	0.046	~ 0.100
Heat of vaporization ($kJ\ kg^{-1}$)	416.95	918.20	335
Flash point ($^{\circ}C$)	46	14	-40
Boiling point ($^{\circ}C$)	154	78.35	30–190

It is interesting to consider for example the heat of vaporisation: ethyl lactate shows a value that is less than a half that of ethanol, which might be undesired for the envisaged application, but it is very close to the one of common gasoline, which means that this molecule could be used as an additive without the need of major modifications to the engines already in the market. Another important physical property for this kind of additive is the boiling point. As already stated, ethyl lactate has a quite high boiling temperature, but this is nevertheless in the admissible range ($T_b < 165^{\circ}C$), as suggested in [133].

Having assessed that the physical properties of ethyl lactate are suitable for an octane booster, it is then interesting to compare the ignition delay times of this molecule to the ones of ethanol. To this aim, ethanol has been tested under the same conditions presented for ethyl lactate and the ignition delay times of the two are shown in figure 6.50 (stoichiometric mixture, pressure of 20 bar, temperature range between 815 and 890 K).

As can be seen, ethyl lactate has slightly longer ignition delay times at all temperatures, even if the difference seems to be slightly larger at high temperature. These results may show that a smaller quantity of ethyl lactate used as an additive for gasoline can lead to the same results concerning the knock resistance as ethanol. Nevertheless, it is important to remember that these are only preliminary results and wider studies would be needed for a real life application in engines, since for

example the octane number of the mixture might be different than expected if there is a synergistic or antagonistic blending.

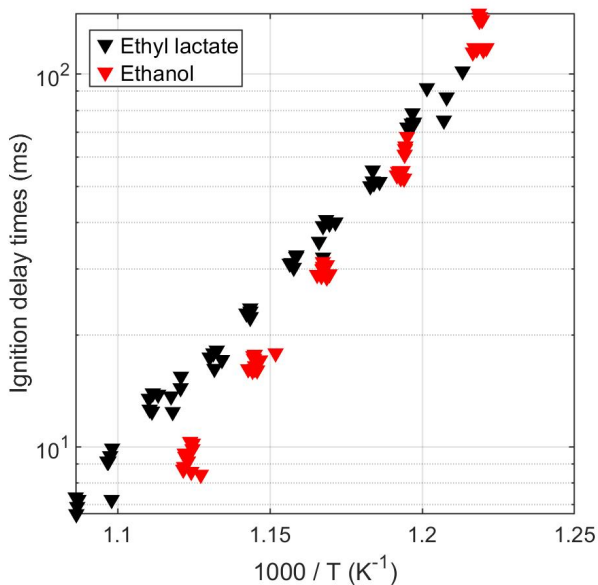


Figure 6.50: Comparison between the ignition delay times of ethyl lactate and ethanol ($\phi = 1$, $p_c = 20$ bar, in "air", EtOH = 6.5%, EtLac = 3.38%).

6.9.3 Comparison to DIPE

Di-*iso*-propyl ether showed to be the least reactive of all the ethers studied in the rapid compression machine, reason for which it has been considered as an anti-knock agent for spark-ignition engines, similarly to ethyl lactate. A comparison between the two would therefore be interesting; nevertheless, all the experiments for DIPE were performed at 15 bar for comparison to the other ethers, while the ones for ethyl lactate were performed at minimum 20 bar, due to its low reactivity. Nevertheless, it may be interesting to compare some results, and to this aim, figure 6.51 shows the ignition delay times for both fuels under lean conditions ($\phi = 0.5$), in "air" (dilution = 3.76), at slightly different pressures (15 and 20 bar).

The first thing to note is the fact that di-*iso*-propyl ether is already reactive at low temperature, even at lower pressure than ethyl lactate and it shows a two-stage ignition in this range. It also shows a strong NTC region, which makes the ignition delay times too long to be measured between 715 and 830 K. Ethyl lactate, on the other hand, starts being reactive only at high temperature. The ignition delay times of ethyl lactate are slightly shorter than the one of DIPE, but it has to be remembered that the pressure is also higher. If the considered pressure was the same, it might be expected to have comparable or longer delays for ethyl lactate, based on the pressure dependence seen from the results in Figure 6.48.

Therefore, even if ethyl lactate presents an ether function in its structure, its reactivity appears

quite different from all the other ethers, since it has no low temperature reactivity nor cool flame or NTC regions. Its global reactivity might appear similar, at high temperature, to the one of DIPE, which was shown to be the least reactive and having much longer ignition delay times compared to all the other ethers.

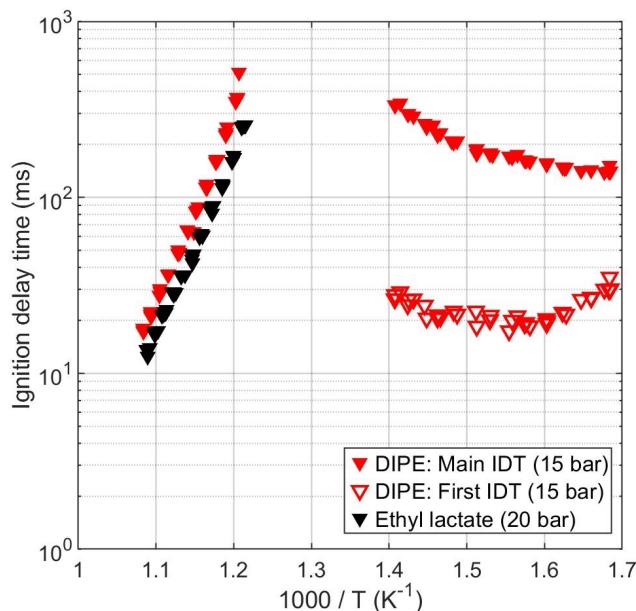


Figure 6.51: Comparison between the ignition delay times of ethyl lactate and di-*iso*-propyl ether ($\phi = 0.5$, $p_c = 20$ bar (ethyl lactate), 15 bar (DIPE), in "air" (EtLac = 1.72%, DIPE = 1.15%)).

6.10 Conclusion

In this chapter, the results obtained from the rapid compression machine for the oxidation of several ethers were presented. These experimental results have been compared for the different ethers, in order to gain a deeper insight on the influence of the structure of these molecules on their reactivity, but also to the simulations obtained from the kinetic mechanism that was developed, in order to improve and validate it. In general, most of the results were reasonably simulated, even if for some ethers, as for example the two branched ones (di-*iso*-propyl and di-*iso*-pentyl), the results were still not completely satisfactory. It can be therefore concluded that the developed mechanism is still not perfectly capable of capturing the influence of the branched structure on the global reactivity of these fuels.

Considering the comparison of the experimental results, it can be stated that at these very low temperatures and for dilute mixtures, the different ethers have quite similar ignition delay times, especially for the first stage ignition. Nevertheless, it was noted that the presence of the branching in the structure is decreasing the overall reactivity, as it was already suggested by the experimental results in the jet-stirred reactor. In fact, di-*iso*-propyl ether was shown to be the least reactive, with very long ignition delay times when compare to its isomer, di-*n*-propyl ether and a much more

pronounced NTC zone. DIPE had such a different reactivity compared to the other ethers that its experiments had to be performed using less dilute mixtures and only the rich mixture could be tested in the same conditions as the other ethers and still, in the NTC region the ignition delays were so long that they could not be recorded. The same influence of the branched structure increasing the ignition delay times could be seen from the comparison of the two pentyl isomers, but to a much lower extent. In fact, the presence of the longer chain surely helped increasing the reactivity, as it was the case in the JSR. Nevertheless, especially for the more diluted mixture, it is clear that the branching decreases the reactivity and enhances the NTC behaviour.

The heat release rate analysis is a quite innovative approach concerning the study of ethers in the rapid compression machine. If some analysis of this kind has been performed on the simulations, to our knowledge this is the first study applying this analysis to the experimental results of different ethers. Even if the simulations are not able to capture the heat release obtained from the experiments, there is still a quite important interest in the analysis of the experimental results, as for example the multi-stage heat release that seems to be typical of these complex oxygenated compounds. In fact, if the main stage ignition is showing a two-stage heat release already for diethyl ether, this behaviour starts appearing for the longer chain ethers also in the first stage. Therefore, as can be seen from the comparison in section 6.8.4, BEE still shows only one heat release peak in the first stage, while two small peaks, almost undistinguishable, can already be seen for DPE and DIPE and starting from DBE, the two peaks become clearly distinct and even more pronounced for DIPEE and DNPEE. This shows how the kinetics of the reactions governing the combustion can be very varied and complex and even if sometimes the mechanism is able to correctly simulate the ignition delay times, it does not mean that it is able to capture the whole phenomenon.

Finally, the last part of the chapter focused on a complex molecule which also presents an ether function, ethyl lactate. In this case, the reactivity of this fuel was completely different than the one showed by the ethers previously presented. No low temperature reactivity was detected and the global reactivity was quite low, thus allowing the experiments to be performed in "air" and at higher pressures (20, 30 bar). The only ether that appeared to have a comparable reactivity was DIPE, which is also considered for similar engine applications as ethyl lactate. Nevertheless, ethyl lactate is not showing low-temperature reactivity, while DIPE did in the rapid compression machine conditions.

Overall, these results showed how there is still need of more experimental results in order to have a complete understanding of the influence of the different structures and functions. For some of these ethers, the results here presented are the first one concerning the global reactivity and the mechanism developed considering the analogy to the previously studied ethers or to other molecules is performing fairly well.

Chapter 7

Conclusions and perspectives

This work is the result of three years of research on the combustion fundamentals of several ethers. The present context requires new solutions for the transportation sector. If these needs can be partially covered by electric vehicles, some categories, such as heavy duty vehicles, appear incompatible and a fair share of the vehicles used today will still be on the roads in thirty years. Oxygenated compounds, as ethers, are therefore being considered as interesting solutions which can reduce the emissions, improve the combustion (in some applications) and, most importantly, are compatible with the actual engine technology.

The understanding of the combustion behaviour of potential biofuels is of paramount importance. To this aim, this study focuses on the experimental and kinetic modelling of several ethers, with the aim of finding a correlation between their structure and their oxidation characteristics. For the experimental part, two complementary set-ups were used: a jet-stirred reactor, which allows the measurements of reaction intermediates and products, and a rapid compression machine, which allows the determination of the ignition delay times. A kinetic mechanism was developed and compared to the experimental results, for validation and improvement.

In the jet-stirred reactor, two ethers were studied in this work, di-iso-pentyl and di-n-pentyl ethers. Both showed very high reactivity, which started at very low temperatures (lower than 500 K). Di-iso-pentyl ether showed a very clear double-NTC behaviour, very similar to dibutyl ether. Di-n-pentyl ether also showed a double-NTC behaviour to some extent, but only under rich conditions. For the stoichiometric and poor mixtures, the reactivity was always very high and not even a plateau could be clearly identified. Between the intermediates for these two ethers, some common smaller products were identified (as CO, CO₂, water, CH₄, C₂H₄, ...) as well as smaller aldehydes (acetaldehyde and formaldehyde). Bigger aldehydes are typical of the oxidation of ethers and in this case, isopentanal and n-pentanal were found for DIPEE and DNPEE, respectively. The mechanism developed for DIPEE shows reasonable agreement with the experimental data and can represent well the double-NTC behaviour. The measurements performed for these two ethers were compared to the ones already collected for other ethers under the same conditions, in order to analyse the influence of the different features of the structure on the reactivity in the jet-stirred reactor. By

comparing linear ethers with different chain lengths (DEE, DPE, DBE, DNPEE), it appears that the length of the chain increases the reactivity. Also, as the size increases, two distinct NTC regions appear, as identified for DBE and DNPEE. This double-NTC behaviour was explained through the fact that the longer chain allows the formation of numerous radicals, which can in turn have their own low-temperature chain branching in a different temperature range than the fuel. Nevertheless, in the case of DNPEE, this ether appears to be so reactive that even the NTC regions tend to disappear due to the very high reactivity of the intermediates and radicals produced. Moving to the influence of the branching, two ethers are compared to their isomers or to linear ethers of the same length: DIPE shows a very different behaviour, with no reactivity under 700 K. DIPEE, on the other hand, has a reactivity comparable to DBE, as well as the same double-NTC behaviour. It seems therefore that adding a branching lowers the reactivity compared to its isomer DNPEE and make the behaviour close to the linear ether with the same chain length, DBE. Finally, if the asymmetry is considered, butyl ethyl ether shares its structure on one side with DEE and on the other with DBE and its behaviour mirrors this characteristic, with a reactivity which appears intermediate between the two.

The rapid compression machine was used to measure the ignition delay times of all the ethers. Considering the high reactivity of these fuels, the conditions for the experiments had to be carefully chosen and, in order to avoid reactions during the compression phase, dilute mixtures were studied. Under these conditions, all ethers except DIPE showed quite similar reactivities, making it difficult to find a correlation between their ignition delays and their structures. The branching seems to still decrease the reactivity, especially for DIPE, which was the least reactive. DIPE is also the one showing the strongest NTC behaviour. All ethers showed a multi-stage ignition under some conditions. A heat release rate analysis was also performed, showing a multi-stage heat release for all ethers in the studied conditions. The simulations generally show an acceptable agreement with the ignition delay times, while the results appear quite different for the HRR. This shows that the mechanism can be capable of capturing the overall phenomenon, while still being inaccurate on some parts of the thermochemistry involved.

A final part of the study focused on ethyl lactate, which is a fuel with different functional groups, among which an ether function. The ignition delay times of ethyl lactate were measured in the same rapid compression machine, showing a very different behaviour from all the other ethers. In fact, this fuel does not show any low-temperature reactivity. Also, its ignition delays were quite long, only comparable to the least reactive of ethers, i.e. DIPE. Nevertheless, it has to be remembered that DIPE shows low-temperature reactivity and an NTC region, while it is not the case for ethyl lactate. A mechanism was developed also for ethyl lactate, with good results.

This study provides a vast dataset on the oxidation characteristics of seven ethers, some of which have never been studied before. It also enriches the measurements performed in the rapid compression machine, thanks to the analysis on the heat release, which is not often done in the studies performed through this kind of set-up. The kinetic mechanisms here presented were partially al-

ready published, while some modifications and additions were required in the light of the new measurements. Nevertheless, there is still room for improvement and for further studies.

In the perspective of characterizing the combustion properties of the whole family of ethers based on their structures, it is of paramount importance to improve the accuracy of the mechanism developed so far and to include the last ether that we studied, DNPEE, for which the mechanism is still being developed. If the rates determined by analogies seem to be reasonable, direct calculations are surely needed in order to improve the simulations under all conditions. Therefore, considering the future development of this study, from a modelling point of view, the possible steps would be:

- complete the available mechanisms by adding the mechanism for DNPEE and compare the simulations to the collected experimental data;
- perform direct calculations on the rate constants of the main reactions, starting from the smallest ethers;
- calculations on the thermodynamics properties of the ethers, their radicals and the main intermediates would surely improve the performance of the mechanisms and should therefore be considered in the next steps of this work.

On the other hand, considering the experimental part, other further developments can be envisaged, as:

- for the ethers studied here for the first time in the JSR, atmospheric pressure experiments could be performed;
- for the RCM, a larger temperature range could be envisaged if the compression time could be reduced, trying to avoid reactions during the compression phase;
- different mixtures could be tested in the RCM, for example changing the dilution;
- since some of these ethers are considered as additives to Diesel or gasoline (depending on their characteristics), it would be interesting to study their behaviour in such mixtures;
- different conditions for the heat release rate analysis could be considered, in order to assess the influence of different parameters, as dilution, pressure, inert gases composition, etc.
- finally, other ethers can be studied under the same conditions, in order to analyse other variations to the structure (asymmetry, cyclic ethers).

In the light of the results here presented, it appears that ethers, among other oxygenated compounds, have very promising characteristics for a wide range of applications. Moreover, from a fundamental point of view, it is very interesting to understand how different features can contribute to different oxidation behaviour. The mechanisms developed so far can be a starting point

for further improvements and, together with the experimental data collected, they represent a step towards a better understanding of the combustion of quite complex oxygenated fuels with a great potential.

Résumé

Introduction

Contexte

Dans les dernières décennies, la globalisation des échanges commerciaux a provoqué une croissance importante du secteur du transport. La plupart de moyens de transport actuels reposent sur les moteurs à combustion interne (99.8%) et le 95% de l'énergie demandée dans ce secteur est produite à partir de carburants fossiles.

Récemment, plusieurs régulations ont été mises en place pour réduire l'impact sur l'environnement. Le secteur du transport est responsable d'environ 25% du total des émissions à effet serre à niveau global. En plus, les carburants fossiles produisent d'autres émissions, comme le monoxyde de carbone (CO), les oxydes d'azote (NOx), des particules (PM) et des hydrocarbures imbrulés, qui peuvent être nocives pour les humains.

La recherche de solutions pour réduire les émissions et éviter les pires conséquences de l'impact environnemental est donc très actuelle. Selon les prévisions, le seul moyen pour réussir dans cet objectif c'est d'avoir zéro émission de gaz à effet de serre avant 2050. Si l'électrification peut sembler une solution (au moins pour les véhicules légers), il faut aussi considérer qu'une bonne partie des nouveaux véhicules actuellement en circulation va encore être présente en 2050. Donc, sauf si un gros investissement est prévu niveau global pour le renouvellement complet du parc, il semble aussi nécessaire de trouver des solutions compatibles avec les moteurs actuels. La seule possibilité pour avoir zéro émission en 2050 sera donc la coexistence des véhicules électriques et des véhicules avec des carburants à bas contenu de carbone.

Même si les biocarburants ne sont pas classés dans les carburants à bas contenu de carbone, ils peuvent être considérés comme « carbon-neutral » si tout le biomatériau utilisé dans leur production est après régénéré sur un cycle court. En plus, le contenu d'oxygène a été prouvé comme bénéfique pour les émissions et pour les performances.

Dans ce cadre, il devient important d'acquérir davantage de connaissances fondamentales sur la combustion de ces molécules, pour pouvoir prédire leur performance dans un moteur, mais aussi pour connaître les possibles produits formés pendant la combustion et potentiellement relâchés dans l'atmosphère.

Objectifs

Le but de cette thèse est donc l'étude expérimentale et la modélisation de l'oxydation de plusieurs éthers, une famille de potentiels biocarburants. Un des objectifs principaux est de relier le comportement pendant l'oxydation à la structure des éthers étudiés. Dans ce but, plusieurs variations de structures différentes ont été considérées :

- Longueur de la chaîne : plusieurs éthers symétriques et linéaires ont été étudiés pour évaluer l'influence de la longueur de la chaîne (éther diéthylique, éther dipropylique, éther dibutylique, éther dipentylique) ;
- Ramification : deux types de comparaison sont possible si la ramification dans la structure est considérée. La première comparaison est entre deux isomères, un linéaire et un ramifié. La deuxième comparaison est entre des éthers avec une structure similaire, où on rajoute une ramification. Donc deux groupes de trois éthers peuvent être considérés pour cette analyse : éther diéthylique, éther dipropylique et éther diisopropylique dans le premier, éther dibutylique, éther dipentylique et éther diisopentylique dans le deuxième.
- Asymétrie : pour évaluer l'influence de l'asymétrie, le butyl ethyl ether a été inclus dans cet étude. Il partage sa structure avec l'éther diéthylique d'une côté et l'éther dibutylique de l'autre, mais il est aussi un isomère des éthers dipropylique et diisopropylique.
- Autres groupes fonctionnels : le dernier carburant qui a été considéré est le lactate d'éthyle. C'est une molécule qui présente différents groupes fonctionnels, dont un groupe éther, et permet d'illustrer les interactions entre différents groupes fonctionnels dans la même molécule.

Les mesures expérimentales ont été effectuées dans deux dispositifs complémentaires : un réacteur auto-agité par jets gazeux (jet-stirred reactor, JSR), pour déterminer les profils des espèces intermédiaires, et une machine à compression rapide (rapid compression machine, RCM), pour mesurer les délais d'auto-inflammation. Les données expérimentales sont utilisées pour développer et valider un modèle de cinétique chimique. Un des objectifs principaux est donc de pouvoir modéliser le comportement de tous les éthers pendant l'oxydation, à partir de leur structure.

Etat de l'art

Les biocarburants issus de la biomasse peuvent être obtenus selon différentes procédures, ce qui détermine l'existence de biocarburants de première, deuxième, troisième et quatrième génération. Différemment des carburants traditionnels, les biocarburants contiennent un pourcentage d'oxygène entre 10 et 45%, mais l'oxydation suit le même type de réactions. En particulier, c'est possible de distinguer différentes régions de réactivité, selon la température considérée. A basse

température, des classes de réactions spécifiques pour ce régime peuvent être trouvées, comme par exemple les peroxydations et les isomérisations. Dans le régime de température intermédiaire, les équilibres de certaines réactions changent et déterminent ce qui est appelé une zone à coefficient négatif de température, où la réactivité décroît quand la température augmente. A la suite, la zone de haute température est atteinte et les réactions les plus importantes deviennent les réactions de β -scission.

Parmi les éthers considérés dans cette étude, certains (comme pour exemple l'éther diéthylique ou l'éther dibutylique) ont été largement étudiés dans les dernières décennies, d'autres (comme l'éther dipentylique ou le butyl éthyl éther) n'ont jamais été analysés pour leur comportement sous des conditions de combustion.

L'**éther diéthylique** a été considéré comme possible additif ou même alternative pour les moteurs Diesel [42] et il a donc été largement étudié, déjà à partir de 1959, quand Waddington [43] a présenté la première étude sur les produits de l'oxydation en phase gazeuse. Plusieurs études ont été publiées sur l'oxydation de l'éther diéthylique, dans différents JSR et avec des conditions différentes [12, 46, 47] et, selon les conditions, une ou deux zones à coefficient négatif de température ont été détectées. L'étude la plus récente sur l'oxydation en JSR a été présentée par Belhadj et al. [49], avec un focus sur les produits de la flamme froide et les espèces hautement oxygénées. Pour cet éther, plusieurs études peuvent être trouvées dans la littérature sur les délais d'auto-inflammation, plus souvent dans des tubes à choc ([50, 52]), mais parfois aussi dans des machines à compression rapide ([51, 53]). Dans plusieurs de ces études, une zone à coefficient négatif de température a été détectée et dans certaines conditions (notamment pour des mélanges pauvres) les profils de pressions montraient une inflammation en trois étages.

L'**éther dipropylique** a été récemment étudié, mais les études sont moins nombreuses que pour l'éther diéthylique. Cet éther n'est actuellement pas considéré comme un potentiel biocarburant, mais sa structure intermédiaire entre les éthers diéthylique et dibutylique le rend intéressant à étudier. La première étude publiée en 2020 par Serinyel et al. [57] examine l'oxydation de ce carburant dans un JSR et développe un premier mécanisme cinétique. La même équipe a aussi étudié la pyrolyse dans le même JSR [48] et a analysé les produits spécifiques de la flamme froide [58]. D'autres études sur les produits et les intermédiaires ont été publiées entre 2021 et 2022 [59–61], avec aussi des mesures de vitesse de flamme.

L'**éther diisopropylique** a reçu un peu plus d'intérêt de la part de la communauté de combustion, avec la première étude en JSR publiée en 1998 [65]. En effet, cet éther est considéré comme un possible additif dans de moteur à allumage commandé [62–64]. Des travaux plus récents ont aussi été proposés [48, 67, 68], en considérant la pyrolyse et l'oxydation dans des JSR. Les deux études sur l'oxydation ont montré que cet éther, différemment des autres, ne montre aucune réactivité à basse température (dans les conditions considérées).

L'**éther dibutylique**, comme l'éther diéthylique, a été largement étudié, vu ses possibles applications en moteur Diesel [71–75]. Plusieurs études sont disponibles sur l'oxydation ([76, 77, 79, 80]) et

la pyrolyse ([48]) dans un JSR. L'éther dibutylique montre, dans certaines conditions, deux zones à coefficient négatif de température, à cause de la formation des radicaux qui ont leur propre réactivité à basse température dans une zone différente de celle du carburant. Différentes études ont aussi été publiées sur les délais d'auto-inflammation [81–83], dans des RCM et dans des tubes à choc. Certains de ces résultats montrent même une auto-inflammation qui se passe en trois ou quatre étapes.

La combustion des **autres** éthers inclus dans cette étude (butyl éthyl éther et les éthers dipentylique et diisopentylique) n'a pas encore été étudiée. Seul l'éther dipentylique a été testé dans des mélanges pour des applications en moteur ([85, 86], mais aucune étude n'est disponible sur ce carburant pur.

Le dernier carburant considéré, le **lactate d'éthyle**, a été considéré comme un additif alimentaire ou comme un solvant [87, 88], mais l'étude issue de notre travail [89] est la première qui considère l'oxydation de cette molécule, en mesurant les délais d'auto-inflammation et des vitesses de flamme laminaire.

Dispositifs expérimentaux

Deux dispositifs expérimentaux ont été principalement utilisés dans cette thèse, le réacteur auto-agité par jets gazeux à ICARE (CNRS) et la machine à compression rapide à PRISME (Université d'Orléans). En complément, les éthers dipropylique et diisopropylique ont aussi été étudiés dans le tube à choc et la machine à compression rapide de University of Galway.

Le **réacteur auto-agité** par jets gazeux (ou réacteur auto-agité, JSR) consiste en une sphère en silice fondue (volume : 42 cm^3), dans lequel quatre injecteurs sont positionnés de façon pyramidale pour obtenir une agitation uniforme. Le carburant et l'oxygène sont introduits séparément dans le réacteur, pour éviter toute réaction avant l'introduction dans le réacteur. Le mélange est hautement dilué pour éviter de dégagements de chaleur qui pourraient modifier la température et endommager le réacteur. Le réacteur est chauffé par deux systèmes de chauffage et une enceinte en acier permet la pressurisation du réacteur. Une sonde de prélèvement et un thermocouple sont introduits dans le réacteur, ce qui permet de récupérer des échantillons et vérifier la température. Les gaz prélevés par la sonde sont acheminés par une ligne chauffée, jusqu'à un spectromètre InfraRouge à Transformée de Fourier (FTIR) ou stockés dans des ballons en Pyrex pour des analyses hors-ligne par chromatographie en phase gazeuse (GC). Différents détecteurs et différentes colonnes ont été utilisés pour les analyses par GC, pour identifier et quantifier différentes espèces. Les éthers dont l'oxydation a été étudiée dans le réacteur auto-agité sont les éthers dipentylique et diisopentylique, dans les mêmes conditions que les études précédentes menées par notre équipe (pression : 10 atm, temps de passage : 0.7 s, fraction molaire initiale du carburant : 1000 ppm, température : 450-1210 K).

La **machine à compression rapide** consiste en une chambre de combustion de forme cylindrique,

où le mélange air/carburant est comprimé par un piston. Le piston est mis en route par un système à air comprimé, alors que la régulation de la vitesse et le freinage sont contrôlés par un système hydraulique. La pression dans la chambre de combustion est mesurée par un transducteur de pression piézoélectrique AVL QC34C. Dans le même temps, la position du piston est enregistrée, pour pouvoir déterminer exactement le moment où le point mort haut est atteint. Les températures de la machine et du réservoir sont mesurées par des thermocouples de type K. Le mélange carburant/oxygène/gaz inertes est préparé dans un réservoir chauffé pour éviter la condensation et agité mécaniquement en continu afin d'assurer l'homogénéité. Deux types de tests sont effectués dans la machine pour chaque condition : un test avec un mélange réactif (généralement répété trois fois par température pour vérifier la répétabilité) et un test avec un mélange non réactif, où l'oxygène est remplacé par la même fraction d'azote (généralement, deux tirs/température). Les tests avec le mélange réactif sont utilisés pour calculer les délais d'auto-inflammation à partir de la dérivée du premier ordre de la pression. Les tests avec le mélange non réactif, par contre, sont utilisés pour déterminer un profil de volume qui sera implémenté dans les simulations pour prendre en considération les pertes de chaleur comme une expansion du cœur isentropique. Les sept éthers présentés et le lactate d'éthyle ont été étudiés dans la machine à compression rapide. Pour certaines conditions, des analyses supplémentaires sur le dégagement de chaleur ont été effectuées. Les dispositifs expérimentaux de l'University of Galway ont été utilisés, en complément, pour effectuer des mesures des délais d'auto-inflammation à des températures plus élevées. Seulement deux éthers ont été étudiés dans ces dispositifs, les éthers dipropylique et diisopropylique.

Le **tube à choc haute-pression** a été utilisé pour la mesure des délais à partir de 950 K. L'enceinte amont a une longueur de 3 mètres, alors que celle aval est longue de 5.7 mètres. Les deux ont un diamètre interne de 63.5 mm et sont séparées par une section de 3 cm dotée d'un système de doubles diaphragmes. Les diaphragmes en aluminium ont une épaisseur entre 0.8 ou 2 mm et sont pré-marqués pour faciliter leur rupture. Six capteurs de pression (PCB; 113A24) sur la paroi latérale et un sur le fond du tube (Kistler; 603B) sont utilisés pour déterminer la vitesse de l'onde de choc. En utilisant cette vitesse dans le programme Gaseq, la température du mélange après l'onde peut être déterminée. Les délais d'auto-inflammation sont déterminés à partir de la mesure de OH*, qui est mesurée par un photomultiplicateur sur la paroi d'extrémité, équipée d'un filtre OH*, FBH300-10. Le tube à choc est chauffé pour éviter toute condensation et le mélange carburant/oxygène/gaz inertes est préparé dans un réservoir chauffé et agité.

La **machine à compression rapide** de l'University of Galway a été utilisée pour compléter les mesures de délais des éthers dipropylique et diisopropylique dans les conditions de température que la machine à compression rapide d'Orléans ne pouvait pas atteindre ou bien quand la première inflammation était trop proche du point mort haut. La machine à compression rapide de Galway fonctionne de manière similaire à celle d'Orléans, mais elle a deux pistons, qui se déplacent de façon synchronisée. Ça permet d'avoir un temps de compression plus court (environ 16 ms) par rapport à celui de la machine d'Orléans. La position des deux pistons est enregistrée, pour

identifier la fin de la compression, mais aussi pour assurer la synchronisation du mouvement. La pression dans la chambre de combustion est mesurée par un capteur de pression Kistler 603B. Le post-traitement des résultats est similaire à ce qui a été présenté pour la RCM d'Orléans. De même, les tests avec des mélanges non réactifs sont utilisés pour déterminer des profils de volume à utiliser dans les simulations pour prendre en compte les pertes de chaleur.

Mécanisme, simulations et autres analyses

Construction du mécanisme

Un des objectifs de cette thèse était d'avoir un mécanisme détaillé capable de représenter toutes les données expérimentales obtenues dans le réacteur auto-agité et dans la machine à compression rapide. Pour certains éthers (diéthylique, dipropylique, diisopropylique et dibutylique) des mécanismes détaillés étaient déjà disponibles à partir des études précédemment publiées par notre équipe [12, 57, 68, 76]. Pour les autres, le mécanisme a été développé pendant cette étude, à partir des études précédentes ou en utilisant des analogies avec des molécules similaires. Le mécanisme de base était le même pour tous les carburants, c'est-à-dire un sous-mécanisme pour l'éthanol et les autres petites espèces (C_0 - C_2) qui a été développé à ICARE.

Les mécanismes déjà disponibles pour les éthers diéthylique et dibutylique n'ont pas subi de modifications majeures et les nouvelles données obtenues dans la machine à compression rapide ont été utilisées comme cibles de validation supplémentaire. Des petites modifications ont été effectuées pour le mécanisme de l'éther dipropylique, pour obtenir un meilleur accord avec les nouvelles données expérimentales. Le cas de l'éther diisopropylique est légèrement différent : dans [68], aucune réactivité à basse température n'avait été enregistrée. Donc, vu que le mécanisme avait été développé à partir de ces données, aucune classe de réaction de basse température n'avait été incluse. Dans les tests effectués dans la machine à compression rapide, par contre, une première étape de l'auto-inflammation, liée à la flamme froide, a été observée. Ce mécanisme a donc été mis à jour en incluant les réactions liées à la chimie de basse température.

Le premier mécanisme développé dans cette thèse concerne le butyl éthyl éther, qui a été principalement construit à partir des mécanismes des éthers diéthylique et dibutylique, vu que ce carburant a une structure partiellement partagée avec les deux.

Pour l'éther diisopentylique, aucun calcul direct sur les constantes de vitesse pour les réactions les plus importantes n'était disponible dans la littérature. Le mécanisme a donc été développé à partir des études précédentes sur les autres éthers ou en comparant la structure de DIPEE avec d'autres espèces déjà étudiées.

Finalement, pour le lactate d'éthyle, aucun mécanisme était déjà présent dans la littérature. Les vitesses de certaines réactions avaient été calculées par Wurmel [88]. Toutes les autres vitesses de réaction ont été obtenues par analogie avec des espèces avec des structures similaires.

Simulations

Les simulations incluses dans cette thèse ont été effectuées en utilisant ChemkinPRO, développé par Ansys. Le réacteur auto-agité est modélisé par le modèle « Perfectly Stirred Reactor ». Ce modèle permet de simuler un réacteur adiabatique, avec un volume constant, avec un écoulement stationnaire qui est introduit dans le réacteur et réagit pendant un temps donné. Différents paramètres doivent être fournis (température, pression, volume du réacteur, temps de passage, concentration des réactifs). A travers la résolution des équations de conservation de la masse et de l'énergie, Chemkin calcule les fractions molaires de toutes les espèces incluses dans le mécanisme.

Le deuxième modèle, qui est utilisé pour simuler la machine à compression rapide et le tube à choc, est le modèle « Closed Homogeneous Reactor ». Ce modèle a différentes options et dans ce cas l'option utilisée est celle où le volume est fixé et l'équation de la conservation de l'énergie doit être résolue. La différence principale entre la machine à compression rapide et le tube à choc sera donc donnée par le choix du volume imposé : dans le cas du tube à choc, le volume sera, en général, constant, alors que dans le cas de la machine à compression rapide, le volume sera imposé à partir du profil mesuré lors de tests avec les mélanges non réactifs. Comme pour le modèle précédent, il faut donner la composition du mélange initial et en sortie, le code fournit la pression, la température et les fractions molaires des espèces déclarées dans le mécanisme.

Résultats et discussion : l'oxydation de DIPEE et DNPEE dans le JSR

Dans cette partie, les résultats sur l'oxydation des éthers diisopentylique et dipentylique sont présentés. Pour le premier éther, un mécanisme détaillé a été développé et les résultats expérimentaux sont comparés avec les simulations. Pour le deuxième éther, le mécanisme est encore en phase de développement, donc les résultats expérimentaux sont présentés et des hypothèses sur les principales voies réactionnelles seront incluses. Une comparaison avec les autres éthers est aussi présentée.

DIPEE

La Figure 5.1 montre la conversion de l'éther diisopentylique pour les quatre conditions de richesse étudiées et la Figure suivante (Fig. 5.2) montre la fraction molaire du DIPEE à $\phi = 2$, en identifiant les différentes zones de température en fonction de la réactivité. Dans les deux Figures, c'est possible de voir que pour des mélanges riches, il est possible d'identifier très clairement deux zones à coefficient négatif de température. En particulier, si on considère le mélange avec $\phi = 2$, la première zone NTC se situe entre 530 et 570 K, avec un plateau de la réactivité, et la deuxième apparaît entre 650 et 740 K, où la réactivité diminue fortement quand la température augmente. Le

même comportement est présenté par le mélange encore plus riche ($\phi = 4$), avec la réactivité qui semble diminuer un peu aussi dans la première zone NTC et le taux de conversion du carburant qui descend jusqu'à presque 10% dans la deuxième zone. Dans des conditions stœchiométriques, par contre, la première zone NTC semble disparaître, même si on retrouve une différence dans la pente du taux de conversion, mais on a encore une claire diminution de la réactivité dans la deuxième zone de NTC. Dans des conditions de mélange pauvre, il est difficile de distinguer une vraie diminution de réactivité quand la température augmente, mais une petite zone de plateau peut être identifiée, bien que pas très clairement.

Une analyse sur les réactions les plus importantes dans la formation de radicaux OH est montrée dans la Figure 5.3 et les réactions considérées sont détaillées dans le Tableau 5.2. Les différentes zones de réactivité sont proposées dans les Figures et ça permet d'identifier l'influence de chaque réaction à différentes températures. Dans la première zone, où la réactivité est déjà importante à basse température, la formation et la décomposition de cétohydroperoxydes sont très importantes. Quand la température augmente, ces réactions, spécialement pour le cétohydroperoxyde principal provenant du radical α du carburant, deviennent plus lentes et produisent moins de radicaux OH. Par ailleurs, d'autres réactions commencent à montrer des taux de réaction plus importants, mais pas encore suffisants pour compenser les pertes sur les voies de branchement dégénéré, ce qui détermine le plateau de la réactivité dans la deuxième zone. Quand la troisième zone est atteinte, les réactions liées aux cétohydroperoxydes d'autres radicaux ou intermédiaire (comme celles montrées dans le tableau) produisent beaucoup de radicaux OH et la réactivité augmente à nouveau. Une fois passé cette zone, la réactivité diminue de nouveau dans la deuxième zone de NTC, quand la réactivité de basse température de ces radicaux n'est plus suffisante. Dans la dernière zone, les radicaux OH sont produits pour la plupart par la décomposition de H_2O_2 .

Les Figures 5.4-5.7 montrent les fractions molaires du carburant et des intermédiaires principaux pour toutes les conditions étudiées. Les simulations sont aussi incluses sous forme de traits. En général, le mécanisme semble capable de bien reproduire les résultats expérimentaux, même si parfois il y a encore de légers désaccords.

Parmi ces intermédiaires, on trouve plusieurs aldéhydes, comme le formaldéhyde (qui est considéré comme un marqueur de réactivité à basse température) et l'acétaldéhyde. L'aldéhyde spécifique produit pendant l'oxydation de DIPEE est l'isopentanal, qui est produit en grande quantité pour toutes les conditions et qui participe à la réactivité à basse et intermédiaire température à travers la formation d'autres radicaux qui ont leur propre chimie d'oxydation à basse température. La Figure 5.8 montre les voies principales qui amènent à la formation de l'isopentanal et les réactions analysées sont aussi listées dans le Tableau 5.3. La figure 5.9 montre la fraction molaire de l'isopentanal pour les quatre conditions étudiées, avec les ROP liées aux différentes réactions. A partir de cette figure, on peut voir comme des réactions différentes règlent la production de l'isopentanal dans les différentes zones de température. A très basse température, on trouve des réactions liées à la formation des cétohydroperoxydes ou de décomposition des radicaux QOOH, lorsque à

des températures plus hautes, la réaction la plus importante est celle de β -scission du radical α du carburant.

DNPEE

L'oxydation du DNPEE a été étudiée dans le JSR dans les mêmes conditions que le DIPEE. La Figure 5.12 montre la conversion du carburant pour les quatre conditions de richesse, alors que la Figure 5.13 montre la fraction molaire du carburant pour $\phi = 2$, en identifiant les différentes régions de réactivité. Dans la première figure on peut voir que les zones de NTC sont beaucoup moins marquées que pour DIPEE et on voit une vraie diminution de la réactivité seulement pour le mélange le plus riche dans la deuxième zone de NTC. Pour le mélange à $\phi = 2$, on a plutôt deux plateaux lors des zones de NTC et pour les mélanges stœchiométrique et pauvre il est difficile de bien identifier ces zones, puisque la réactivité reste importante sur tout l'intervalle de température étudié. Dans la Figure 5.13 on voit plus clairement les deux zones de NTC pour le mélange à $\phi = 2$, avec les deux plateaux de la fraction molaire du carburant.

Les Figures 5.14-5.17 montrent les fractions molaires du carburant et des intermédiaires dans toutes les conditions étudiées. Dans ce cas, seulement les données expérimentales sont incluses, vu que le mécanisme est encore en phase de développement.

Comme pour DIPEE, on voit que les aldéhydes sont parmi les intermédiaires majoritaires. Les fractions molaires du formaldéhyde sont montrées dans la Figure 5.18. Si on regarde en particulier le cas pour $\phi = 4$, on peut voir que le profil du formaldéhyde montre deux pics, qui sont séparés par la zone de NTC où la réactivité diminue. Pour les cas des mélanges stœchiométrique et pauvre un seul pic peut être identifié et ça semble en accord avec le fait qu'il est presque impossible de distinguer des zones de NTC et donc la réactivité ne diminue vraiment dans aucune zone.

L'aldéhyde typique de l'oxydation de DNPEE est le n-pentanal, dont on peut voir les fractions molaires en Figure 5.19. Même si le mécanisme n'est pas encore développé, on peut faire des hypothèses sur les voies de production de cet intermédiaire et les réactions les plus probables sont montrées en Figure 5.20. De façon similaire au DIPEE, on suppose que la formation du n-pentanal dépend des voies réactionnelles des cétohydroperoxydes ou de décomposition des radicaux QOOH à basse température et que la décomposition par β -scission du radical α du carburant qui devient bien plus importante à haute température.

En général, on s'attend à ce que le radical α du carburant soit le plus produit et les voies les plus probables pour ce radical sont montrées dans la figure 5.21. A haute température, la réaction de β -scission va sûrement être majoritaire. A basse température, les radicaux RO_2 vont pouvoir s'isomériser par réarrangements internes en formant deux radicaux QOOH différents (les deux à travers un état de transition avec un cycle à 6 membres), et on s'attend donc la présence des deux cétohydroperoxydes majoritaires.

Comparaison

Tous les éthers inclus dans cette thèse ont été étudiés dans le JSR dans les mêmes conditions (soit pendant le développement de cette étude ou dans des études précédentes), ce qui permet de comparer directement les profils de conversion de carburant. Cette comparaison est montrée dans la Figure 5.22, pour trois différentes richesses, $\phi = 0.5, 1$ et 2 .

La première chose qu'on remarque c'est le fait que tous les éthers, sauf l'éther diisopropylique, sont réactifs basse température (moins de 500 K). L'éther diisopropylique est un cas spécial, avec aucune réactivité au-dessous de 700 K dans les conditions étudiées. La cause de ce comportement est à retrouver dans le fait que le radical du carburant le plus facile à former (donc celui produit par arrachement d'un atome H sur le site à côté de la fonction éther) ne peut pas suivre la voie typique de la basse température qui amène à la formation d'un cétohydroperoxyde, ce qui diminue donc fortement la réactivité à basse température.

Si on considère la présence des zones de NTC, on voit que pour les éthers avec une chaîne plus courte (DEE, DPE), on a clairement une seule zone NTC, alors que pour les éthers avec une chaîne plus longue (DBE, DIPEE, DNPEE), on voit plutôt l'apparition de deux zones NTC. Le BEE est un cas un peu particulier, avec sa structure entre le DEE et le DBE : cet éther semble aussi avoir une double zone de NTC, mais sa réactivité est inférieure à celle du DBE, avec la conversion qui descend à 0 dans la deuxième zone de NTC.

Les deux éthers avec la chaîne la plus longue, DIPEE et DNPEE, semblent aussi être les plus réactifs, à cause de la formation plus facile de radicaux qui peuvent suivre leurs mêmes voies réactionnelles. La présence de la fonction de ramification dans l'éther diisopentylique diminue sa réactivité par rapport à son isomère, l'éther dipentylique, et présente une forte similarité avec l'éther dibutylique. On avait vu que la présence de ramifications cause une diminution de la réactivité déjà dans le cas de l'éther diisopropylique, mais cette réduction est moins importante pour le DIPEE grâce à sa longue chaîne.

Conclusion

En conclusion, dans cette partie on a présenté les résultats expérimentaux du DIPEE et DNPEE dans le JSR, avec la modélisation du mécanisme d'oxydation pour le DIPEE. Les résultats expérimentaux montrent, pour les deux isomères, un comportement très intéressant de double NTC, avec le DNPEE beaucoup plus réactif que le DIPEE sur toute la plage de température. Le mécanisme développé pour le DIPEE montre des résultats acceptables, même s'il y a encore des améliorations possibles.

La comparaison avec les autres éthers nous aide à comprendre comment les différentes structures peuvent influencer la réactivité : la longueur de la chaîne favorise la réactivité grâce à la formation plus facile des radicaux qui peuvent après avoir leur propre réactivité, alors que la présence de ramification diminue la réactivité et peut fortement influencer le comportement surtout dans le

cas d'une ramification sur le site adjacent à la fonction éther. Le seul cas d'asymétrie considéré a montré un comportement intermédiaire entre les deux éthers avec lesquels il partage sa structure.

Résultats et discussion : l'oxydation des éthers dans la RCM

Tous les éthers ont été étudiés pendant cette étude dans la machine à compression rapide, dans des conditions similaires dans la mesure du possible. Pour certaines conditions, une analyse sur le dégagement de chaleur a été effectuée. Cette partie présente les résultats expérimentaux, comparés avec les simulations possibles, et se termine par une comparaison entre les différents éthers.

DEE

Les délais mesurés et simulés de l'éther diéthylique sont montrés dans la Figure 6.1. Pour toutes les richesses, un mélange avec une dilution de 10 a été testé, avec une auto-inflammation en deux étapes pour les mélanges stoechiométrique et riche. Pour le mélange pauvre, seul un délai a pu être mesuré pour le mélange dilué, mais deux étapes de l'auto-inflammation ont été identifiées pour un mélange à dilution 5. En regardant les profils de pressions, on suppose que les seuls délais pour le mélange à haute dilution sont en réalité des délais de première étape. Les simulations semblent plutôt en accord avec les résultats expérimentaux, même s'il y a une tendance à surestimer les délais surtout pour le mélange riche.

L'analyse des voies réactionnelles incluse en Figure 6.3 montre surtout des réactions typiques de la basse température. Le radical le plus formé est le radical α , qui représente 97-98% du flux. Le flux majoritaire partant de ce radical forme (après addition sur O_2 , isomérisation et une deuxième addition sur O_2) un cétohydroperoxyde. Le radical β , par contre, forme aussi un éther cyclique (11%) à la température la plus haute.

L'analyse de dégagement de chaleur est montrée dans les Figures 6.4 et 6.5, pour un mélange stoechiométrique avec une dilution de 10. Le taux de dégagement de chaleur est plus élevé pour la première étape de l'auto-inflammation, soit expérimentalement, soit numériquement. Toutefois, les valeurs calculées par les simulations sont beaucoup plus élevées. Aussi pour le deuxième et le troisième dégagement de chaleur les simulations ont un taux plus élevé que les résultats expérimentaux, mais la différence est beaucoup moins importante. Si on considère la chaleur dégagée dans l'étape à basse température et la maximale, on peut voir que les simulations surestiment largement ces valeurs, surtout pour le dégagement accumulé maximum.

DPE

Les délais d'auto-inflammation de l'éther dipropylique sont montrés en Figure 6.6. Dans ce cas, les tests ont été effectués dans la RCM de l'Université d'Orléans, mais aussi dans le tube à choc et la

machine à compression rapide de University of Galway. Les trois mélanges considérés ont tous une dilution de 10. Pour les mélanges stœchiométrique et riche on peut voir que l'auto-inflammation se passe en deux étapes à basse température, lorsque pour le mélange pauvre, comme dans le cas du DEE, à basse température une seule étape peut être mesurée et ce sera plutôt liée à la flamme froide. Pour le mélange riche, on peut trouver une zone de NTC, entre environ 660 et 760 K. Les délais du mélange stœchiométrique présentent une zone de plateau dans une zone de température qui ne peut être atteinte ni avec la RCM d'Orléans, ni avec celle de Galway. Le mécanisme semble plutôt en accord avec les données expérimentales, même s'il y a une légère surestimation des délais, surtout pour le mélange riche dans les températures intermédiaires.

Les voies réactionnelles déterminées à partir des simulations à 610, 1000 et 1200 K sont montrées dans les Figures 6.9 et 6.10. A 610 K, tous les radicaux primaires du carburant sont formés, avec le radical α qui est le plus abondant. La totalité du flux de ces radicaux suit les voies réactionnelles de basse température, qui amènent à la formation et décomposition de cétohydroperoxydes. A 1000 et 1200 K, les réactions de β -scission deviennent prédominantes, même si des petits flux peuvent encore suivre partiellement des voies typiques de la basse température, comme par exemple l'addition sur O_2 , suivie par l'isomérisation à radical QOOH, qui va après subir une réaction de β -scission. On trouve aussi la réaction de décomposition unimoléculaire du carburant, qui à 1200 K représente presque 30% du flux.

Si on considère l'analyse de dégagement de chaleur, les résultats pour un mélange stœchiométrique avec dilution de 10 sont montrés dans les Figures 6.11 et 6.12. Les résultats expérimentaux montrent que le taux de dégagement de chaleur atteint son maximum dans l'étape principale de l'auto-inflammation, lors que les simulations prévoient le maximum dans la première étape. Les taux de dégagement de chaleur sont surestimés par le mécanisme dans toutes les conditions. La même chose peut être vue pour le dégagement de chaleur accumulé maximal et lié aux réactions de basse température.

DIPE

Les délais d'auto-inflammation du DIPE sont montrés dans la Figure 6.13. Comme pour le DPE, l'éther diisopropylique a été étudié soit dans la machine à compression rapide d'Orléans, soit dans les deux installations de Galway. C'est important de considérer que la dilution des mélanges pour lesquels les résultats sont montrés dans la figure est de 5. On peut voir que à basse température les mélanges stœchiométrique et riche montrent une auto-inflammation en deux étapes. Par contre, les délais du mélange pauvre étaient trop longs pour être mesurés à des températures basses ou intermédiaires. De même, les délais du mélange stœchiométrique dans la zone de NTC sont au dehors de l'intervalle de confiance de la RCM (200 ms max), mais ils ont été inclus dans la figure pour montrer la tendance, vu qu'ils semblent cohérents. Les mélanges stœchiométrique et riche montrent une très claire zone de NTC, avec une augmentation des délais quand la température

augmente. Le même comportement est simulé par le mécanisme, mais les valeurs simulées sont plutôt loin des mesures expérimentales pour toutes les conditions. Seulement à haute température le mécanisme semble capable de reproduire les délais correctement.

Les voies réactionnelles à 600, 1000 et 1200 K sont montrées dans les Figures 6.15 et 6.16. A 600 K, on peut voir que le radical le plus produit est le radical α , qui ne peut pas former de cétohydroperoxydes et qui donc ne peut pas accélérer la réactivité. On peut voir qu'on retrouve une plus grande variété de réactions par rapport aux deux éthers déjà présentés, avec des petits flux qui forment des éthers cycliques ou des composés insaturés. A haute température, on trouve plutôt des réactions de β -scission et, comme pour le DPE, la décomposition unimoléculaire du carburant devient plus importante à 1200 K (14%).

L'analyse du dégagement de chaleur pour un mélange stœchiométrique avec dilution de 5 est montrée dans les Figures 6.11 et 6.18. Comme pour les éthers précédents, les taux du délai principal sont largement surestimés pour toutes les températures. Par contre, le taux de dégagement de chaleur de la flamme froide, qui est vraiment faible pour le DIPE, est sous-estimé par le mécanisme. Si on considère la chaleur dégagée accumulée maximale et de la flamme froide, on peut voir que le mécanisme capture bien la deuxième, alors qu'il y a une surestimation pour la première.

BEE

Les délais d'auto-inflammation du BEE sont montrés en Figure 6.19. Deux dilutions différentes ont été utilisées pour les mélanges stœchiométrique et riche, alors que le mélange pauvre a été testé seulement avec une dilution de 5. Les mélanges stœchiométrique et pauvre avec dilution de 5 montrent une inflammation en deux étapes, tandis que les deux mélanges riches et le mélange stœchiométrique moins dilué montrent un seul délai. Le mécanisme semble surestimer les délais pour toutes les conditions et sur toute la plage de températures.

Une analyse des voies réactionnelles à environ 540 K pour un mélange stœchiométrique est montrée en Figure 6.20. Les deux radicaux obtenus avec l'arrachement d'un atome H sur le site à côté de la fonction éther sont les plus produits. Les deux suivent après les voies réactionnelles typiques de l'oxydation à basse température, avec la formation et décomposition des cétohydroperoxydes associés.

L'analyse de dégagement de chaleur est montrée dans les Figures 6.21 et 6.22. Comme pour les éthers précédents (sauf DIPE), cette analyse est effectuée pour un mélange stœchiométrique avec dilution 10. Encore une fois, on voit que le mécanisme surestime largement le taux de dégagement de chaleur, surtout pour le premier délai. Si on considère la chaleur dégagée accumulée maximale et celle liée à la réactivité à basse température, on voit que le mécanisme surestime ces valeurs, surtout pour la maximale.

DBE

Les délais de l'éther dibutylique ont été mesurés pour des mélanges avec dilution 5 (Figure 6.23) et avec dilution 10 (Figure 6.24). Pour les mélanges moins dilués, on voit que l'auto-inflammation dans des conditions stœchiométrique et riche se passe en une seule étape, tandis que pour le mélange pauvre on mesure deux délais. Si on considère les mélanges plus dilués, pour la condition stœchiométrique on mesure deux délais, à 15 bar comme à 20 bar, avec les délais de la première étape qui sont presque identiques, tandis que les délais de l'inflammation principale sont plus courts à plus haute pression. Les simulations sont plutôt en accord avec les données expérimentales, même s'il y a une sous-estimation des délais pour le mélange stœchiométrique plus dilué et pour le mélange pauvre vers les températures intermédiaires.

La figure 6.25 montre une analyse des voies réactionnelles pour un mélange stœchiométrique à 560 K. Les quatre radicaux primaires du carburant sont formés, avec le radical α qui est le majoritaire. Sans aucune surprise, tous les flux suivent les réactions typiques des basses températures, avec une addition sur O_2 , une isomérisation interne, une deuxième addition sur O_2 et la formation et décomposition des cétohydroperoxydes.

L'analyse sur le dégagement de chaleur est montrée dans les Figures 6.26 et 6.27. Dans ce cas, deux mélanges différents ont été considérés, les deux stœchiométriques et avec dilution de 10, mais avec deux compositions des gaz inertes différentes : le premier 50% CO_2 et 50% N_2 et le deuxième avec 100% N_2 . Les taux de dégagement de chaleur sont beaucoup plus élevés pour le deuxième mélange, soit dans les tests, soit dans les simulations. Si on considère la comparaison entre les résultats expérimentaux et les simulations, on voit que comme pour les autres éthers, le mécanisme semble surestimer les taux de dégagement de chaleur pour toutes les étapes de l'inflammation, mais surtout pour la flamme froide. En regardant la chaleur dégagée accumulée maximale et liée à la basse température, on trouve une surestimation des simulations pour toutes les températures, pour les deux mélanges.

DIPEE

Comme pour l'éther dibutylique, des mélanges avec dilution 5 et 10 ont été testés pour le DIPEE et les délais sont montrés dans les Figures 6.28 et 6.29. Dans ce cas, les simulations surestiment largement les délais dans toutes les conditions. Pour les mélanges stœchiométrique et riche, on trouve une auto-inflammation en deux étapes seulement pour une dilution de 10, alors que pour les mélanges avec dilution de 5, seulement la condition pauvre montre une inflammation en deux étapes. Pour le mélange stœchiométrique avec dilution de 10, deux pressions différentes ont été testées : 15 et 20 bar. Les délais de la première étape de l'inflammation semblent être indépendants de la pression, alors que les délais principaux diminuent quand la pression augmente.

La Figure 6.30 montre une analyse des voies réactionnelles à 560 et 800 K. Le radical le plus produit est le même dans les deux cas, mais les voies suivies après sont légèrement différentes, avec les ré-

actions de β -scission des radicaux qui deviennent importantes à haute température. Une analyse des réactions qui forment les radicaux OH est montrée dans la Figure 6.31, pour comprendre le rôle de l'isopentanal dans l'oxydation dans la machine à compression rapide. Cette espèce est formée en quantité non-négligeable et sa réactivité de basse température semble avoir une influence possible sur la réactivité totale.

Les résultats de l'analyse sur le dégagement de chaleur sont montrés dans les Figures 6.32 et 6.33. Le mécanisme montre des résultats comparables aux résultats expérimentaux, surtout pour les taux de dégagement de chaleur. Par contre, il y a une surestimation de la chaleur dégagée accumulée maximale.

DNPEE

Les délais d'auto-inflammation de l'éther dipentylique ont été mesurés dans les mêmes conditions que pour le DIPEE, donc pour trois richesses différentes, deux dilutions (pour les mélanges stœchiométrique et riche) et deux pressions (pour le mélange stœchiométrique avec dilution de 10). Les résultats sont montrés dans les Figures 6.34 et 6.35. Comme pour le DIPEE, le mélange riche avec dilution de 10 montre une ignition en deux étapes, alors que celui avec dilution de 5 montre un seul délai. Par contre, pour les mélanges stœchiométriques on retrouve une inflammation en deux étapes indépendamment de la dilution. Augmenter la dilution du mélange détermine des délais plus longs et semble favoriser l'apparition d'un plateau. La pression montre le même effet présenté pour le DIPEE.

L'analyse sur le dégagement de chaleur est montrée dans les Figures 6.36 et 6.37. Pour la chaleur dégagée accumulée maximale on trouve un comportement similaire du DIPEE, avec une augmentation lorsque la température augmente. Les taux de dégagement de chaleur semblent plus importants que pour le DIPEE et dans l'étape principale de l'inflammation on voit l'apparition d'un deuxième pic de dégagement de chaleur, lié au changement de pente de l'augmentation de pression, visible dans les profils.

Comparaison

Différentes comparaisons sont possibles, entre les éthers qui partagent au moins une caractéristique dans leur structure. Les Figures 6.38–6.42 montrent ces comparaisons, alors que la Figure 6.44 montre la comparaison des délais d'auto-inflammation entre tous les éthers. En général, il semble que la présence d'une ramification diminue la réactivité globale et intensifie la présence des zones de NTC. Par contre, la longueur de la chaîne ne semble pas déterminer un effet précis dans ces conditions. Les délais d'auto-inflammation de ces mélanges très dilués semblent plutôt similaires dans cet intervalle de température. La Figure 6.46 montre la comparaison des dégagements de chaleur. Dans ce cas, il semble que les éthers avec une chaîne plus longue ont des taux

de dégagement de chaleur plus petits. Tous les éthers montrent un dégagement de chaleur en plusieurs étapes, ce qui prouve une chimie d'oxydation très complexe pour ces carburants.

Lactate d'éthyle

La dernière partie de ce chapitre est dédiée aux délais d'auto-inflammation du lactate d'éthyle, qui sont montrés dans les Figures 6.47 et 6.48. Le lactate d'éthyle ne montre pas de la réactivité à basse température, ni des zones de NTC. On trouve un comportement très standard, avec les délais qui suivent une tendance typique d'Arrhenius. Si la pression ou la richesse est augmentée, les délais diminuent. Les simulations sont plutôt en accord avec les données expérimentales.

Une analyse des voies réactionnelles est montrée en Figure 6.49 pour un mélange stœchiométrique à deux températures, 830 et 915 K. Dans les deux cas, on trouve des voies plutôt similaires, même s'il y a des changements dans les pourcentages. On peut voir que la réaction unimoléculaire du carburant devient plus importante à haute température.

Une comparaison avec l'éthanol (Fig. 6.50) et avec le DIPE (Fig. 6.51) montre que le lactate d'éthyle n'est pas très réactif et son comportement est plutôt similaire à l'éthanol. Même si les délais sont proches des délais du DIPE, le comportement de ces deux carburants est assez différent, avec le DIPE qui montre une réactivité de basse température et une zone de NTC, tandis que le lactate d'éthyle réagit seulement à haute température.

Conclusion

En conclusion, ce chapitre montre les résultats obtenus pour les différents éthers dans la machine à compression rapide. Les mécanismes utilisés pour les simulations montrent des niveaux de précision différents, mais en général les performances sont acceptables en ce qui concerne les délais. En considérant les taux des dégagements de chaleur, par contre, une amélioration est sûrement nécessaire. En comparant les délais des différents éthers, on voit que la présence d'une ramification dans la structure induit des délais plus longs, alors que la longueur de la chaîne a une influence plus difficile à déterminer. Les éthers plus longs, par contre, ont des taux de dégagement de chaleur plus faibles en général.

Conclusions et perspectives

Ce travail est le résultat de trois années de recherche sur la compréhension fondamentale de la combustion de plusieurs éthers. Le contexte actuel conduit à la nécessité de trouver de nouvelles solutions pour le secteur des transports : bien que certains de ses besoins puissent être partiellement couverts par les véhicules électriques, certaines catégories semblent incompatibles, et une part importante des véhicules utilisés aujourd'hui sera encore sur les routes dans trente ans. Les

composés oxygénés, tels que les éthers, sont donc considérés comme des solutions intéressantes susceptibles de réduire les émissions, d'améliorer la combustion et, surtout, de s'adapter à la technologie actuelle des moteurs.

La compréhension du comportement de combustion des biocarburants potentiels revêt une importance capitale. Dans ce but, cette étude se concentre sur la modélisation cinétique et expérimentale de plusieurs éthers, pour faire apparaître une relation entre la structure et les caractéristiques d'oxydation. Pour la partie expérimentale, deux dispositifs complémentaires ont principalement été utilisés : un réacteur auto-agité par jets gazeux, permettant la mesure des intermédiaires et des produits, et une machine à compression rapide, permettant la détermination des temps de délai d'inflammation. Un mécanisme cinétique a été développé et comparé aux résultats expérimentaux.

Dans le réacteur auto-agité, deux éthers ont été étudiés dans ce travail, les éthers dipentylique et di-iso-pentylique. Ces deux éthers présentent une réactivité très élevée, qui démarre à des températures très basses (inférieures à 500 K). Le DIPEE présente un comportement de double NTC très clair, très similaire à celui de l'éther dibutylique. Le DNPEE montre également un comportement de double NTC dans une certaine mesure, mais seulement dans des conditions riches. Pour les mélanges stœchiométrique et pauvre, la réactivité est toujours très élevée, et il n'a même pas été possible d'identifier un plateau. Parmi les intermédiaires pour ces deux éthers, certains produits plus courants ont été identifiés (comme CO, CO₂, l'eau, CH₄, C₂H₄, ...) ainsi que des aldéhydes plus petits (acétaldéhyde et formaldéhyde). Les aldéhydes plus grands sont caractéristiques de l'oxydation des éthers, et dans ce cas, l'isopentanal et le n-pentanal ont été trouvés pour le DIPEE et le DNPEE respectivement. Le mécanisme développé pour le DIPEE montre un accord raisonnable avec les données expérimentales et peut bien représenter le comportement de double NTC. Les mesures effectuées pour ces deux éthers ont été comparées à celles déjà recueillies pour d'autres éthers dans les mêmes conditions, afin d'analyser l'influence des différentes caractéristiques de la structure sur la réactivité dans le réacteur agité par jet gazeux. En comparant les éthers linéaires de différentes longueurs de chaîne (DEE, DPE, DBE, DNPEE), il apparaît que la longueur de la chaîne augmente la réactivité. En outre, à mesure que la longueur de chaîne augmente, le NTC devient un comportement de double NTC, comme identifié pour le DBE et le DNPEE. Ce comportement de double NTC a été expliqué par le fait que la chaîne plus longue permet la formation de nombreux radicaux, qui peuvent à leur tour avoir leur propre réactivité à basse température dans une plage de température différente de celle du carburant. Néanmoins, dans le cas du DNPEE, cet éther semble être tellement réactif que même les régions de NTC tendent à disparaître en raison de la très grande réactivité des intermédiaires et des radicaux produits. En ce qui concerne l'influence de la ramification, deux éthers sont comparés à leurs isomères ou à des éthers linéaires de même longueur : le DIPEE montre un comportement très différent, avec aucune réactivité en dessous de 700 K. Le DIPEE, en revanche, a une réactivité comparable à celle du DBE, ainsi qu'un comportement de double NTC similaire. Il semble donc que l'ajout d'une ramification réduise la réactivité

par rapport à son isomère DNPEE et rende le comportement proche de celui de l'éther linéaire de même longueur, le DBE. Enfin, en ce qui concerne l'asymétrie, le BEE partage sa structure d'un côté avec le DEE et de l'autre avec le DBE, et son comportement reflète ces caractéristiques, avec une réactivité qui semble intermédiaire entre les deux.

La machine à compression rapide a été utilisée pour recueillir des mesures sur les délais d'auto-inflammation de tous les éthers. Compte tenu de la grande réactivité de ces carburants, les conditions des expériences ont dû être soigneusement choisies, et afin d'éviter les réactions pendant la phase de compression, des mélanges dilués ont été étudiés. Dans ces conditions, tous les éthers, à l'exception du DIPE, ont montré des réactivités assez similaires, ce qui rend difficile de trouver une corrélation entre les délais d'auto-inflammation et leurs structures. La ramification semble toujours diminuer la réactivité, en particulier pour le DIPE, qui était le moins réactif et le seul qui a dû être étudié avec des mélanges moins dilués. Le DIPE est également celui qui présente le NTC le plus prononcé. Tous les éthers ont montré une inflammation en plusieurs étapes dans certaines conditions. Une analyse du taux de dégagement de chaleur a également été réalisée, montrant un taux de dégagement de chaleur en plusieurs étapes pour tous les éthers dans les conditions étudiées. Les simulations montrent généralement un accord acceptable avec les délais d'auto-inflammation, tandis que les résultats sont assez différents pour le taux de dégagement de chaleur. Cela montre que le mécanisme est capable de capturer le phénomène global, tout en étant imprécis sur certaines parties de la thermochimie impliquée.

Une partie finale de l'étude s'est concentrée sur le lactate d'éthyle, un carburant avec différents groupes fonctionnels, dont une fonction éther. Les délais d'auto-inflammation du lactate d'éthyle ont été mesurés dans la même machine à compression rapide, montrant un comportement très différent de tous les autres éthers. En fait, ce carburant ne montre aucune réactivité à basse température, ce qui semblait être commun à tous les éthers. De plus, les délais d'inflammation étaient assez longs, comparables seulement à ceux du moins réactif des éthers, c'est-à-dire le DIPE. Cependant, il faut se rappeler que le DIPE montre une réactivité à basse température et un NTC, ce qui n'est pas le cas pour le lactate d'éthyle. Un mécanisme a également été développé pour le lactate d'éthyle, avec de bons résultats.

Cette étude fournit un vaste ensemble de données sur les caractéristiques d'oxydation de sept éthers, dont certains n'avaient jamais été étudiés auparavant. Elle enrichit également les mesures effectuées dans la machine à compression rapide, grâce à l'analyse du taux de dégagement de chaleur, qui est généralement négligée dans les études réalisées avec ce type d'appareil. Les mécanismes cinétiques ici présentés ont déjà été partiellement publiés, mais des modifications et des ajouts étaient nécessaires à la lumière des nouvelles mesures. Néanmoins, il reste de la place pour des améliorations et des études ultérieures.

Dans l'optique de pouvoir caractériser les propriétés de combustion de toute la famille des éthers en fonction de leur structure, il est d'une importance capitale d'améliorer la précision du mécanisme développé jusqu'à présent et d'inclure le dernier éther que nous avons étudié, le DNPEE,

pour lequel le mécanisme est encore en cours de développement. Si les vitesses de réaction déterminées par analogie semblent raisonnables, des calculs directs sont certainement nécessaires pour améliorer les simulations dans toutes les conditions. Par conséquent, en envisageant le développement futur de cette étude, d'un point de vue de la modélisation, les étapes possibles pourraient être les suivantes :

- compléter les mécanismes disponibles en ajoutant le mécanisme pour le DNPEE et comparer les simulations aux données expérimentales recueillies ;
- effectuer des calculs directs sur les vitesses des réactions principales, en commençant par les plus petits éthers, pour lesquels la littérature fournit déjà une quantité considérable de données auxquelles nos mesures peuvent être ajoutées ;
- des calculs sur les propriétés thermodynamiques des éthers, de leurs radicaux et des principaux intermédiaires amélioreraient sûrement la performance des mécanismes et devraient donc être pris en compte dans les prochaines étapes de ce travail.

D'autre part, en ce qui concerne la partie expérimentale, d'autres développements ultérieurs peuvent être envisagés, tels que :

- pour les éthers étudiés ici pour la première fois dans le JSR, des expériences à pression atmosphérique pour mettre en avant les réactions unimoléculaires ;
- pour la RCM, une plage de température plus large pourrait être envisagée si le temps de compression pouvait être réduit, afin d'éviter les réactions pendant la phase de compression ;
- différents mélanges pourraient être testés dans la RCM, en modifiant par exemple la dilution ;
- étant donné que certains de ces éthers sont considérés comme des additifs au diesel ou à l'essence (selon leurs caractéristiques), il serait intéressant d'étudier leur comportement dans de tels mélanges ;
- il serait possible de considérer différentes conditions pour l'analyse du taux de dégagement de chaleur, afin d'évaluer l'influence de différents paramètres, tels que la dilution, la pression, la composition des gaz inertes, etc.
- enfin, d'autres éthers pourraient être testés, pour analyser l'effet d'autres variations de la structure (asymétrie, éthers cycliques)

À la lumière des résultats présentés ici, il apparaît que les éthers, parmi d'autres composés oxygénés, présentent des caractéristiques très intéressantes pour un large éventail d'applications. De plus, d'un point de vue fondamental, il est très intéressant de comprendre comment différentes

caractéristiques peuvent contribuer à différents comportements d'oxydation. Les mécanismes développés jusqu'à présent peuvent servir de point de départ pour des améliorations ultérieures, et, conjointement avec les données expérimentales recueillies, ils représentent une étape vers une meilleure compréhension de la combustion de carburants oxygénés assez complexes, ayant un grand potentiel.

Bibliography

- [1] S. Gross, “The challenge of decarbonizing heavy transport,” report, Brookings Institution, 2020.
- [2] F. Leach, G. Kalghatgi, R. Stone, and P. Miles, “The scope for improving the efficiency and environmental impact of internal combustion engines,” *Transportation Engineering*, vol. 1, p. 100005, 2020.
- [3] P. Senecal and F. Leach, “Diversity in transportation: Why a mix of propulsion technologies is the way forward for the future fleet,” *Results in Engineering*, vol. 4, p. 100060, 2019.
- [4] M. Z. A. Khan, H. A. Khan, S. S. Ravi, J. W. Turner, and M. Aziz, “Potential of clean liquid fuels in decarbonizing transportation – an overlooked net- zero pathway?,” *Renewable and Sustainable Energy Reviews*, vol. 183, p. 113483, 2023.
- [5] “Global Warming of 1.5 °C,” 2018.
- [6] N. Powell, N. Hill, J. Bates, N. Bottrell, M. Biedka, B. White, T. Pine, S. Carter, J. Patterson, and S. Yucel, “Impact analysis of mass ev adoption and low carbon intensity fuels scenarios,” *Ricardo Eng Concauwe*, vol. 15713, p. 166, 2018.
- [7] T. Mendiara, F. García-Labiano, A. Abad, P. Gayán, L. F. d. Diego, M. T. Izquierdo, and J. Adánez, “Negative CO₂ emissions through the use of biofuels in chemical looping technology: A review,” *Applied Energy*, vol. 232, pp. 657–684, 2018.
- [8] P. Friedlingstein, M. O’Sullivan, M. W. Jones, R. M. Andrew, L. Gregor, J. Hauck, C. Le Quéré, I. T. Lujckx, A. Olsen, G. P. Peters, W. Peters, J. Pongratz, C. Schwingshackl, S. Sitch, J. G. Canadell, P. Ciais, R. B. Jackson, S. R. Alin, R. Alkama, A. Arneeth, V. K. Arora, N. R. Bates, M. Becker, N. Bellouin, H. C. Bittig, L. Bopp, F. Chevallier, L. P. Chini, M. Cronin, W. Evans, S. Falk, R. A. Feely, T. Gasser, M. Gehlen, T. Gkritzalis, L. Gloege, G. Grassi, N. Gruber, O. Gürses, I. Harris, M. Hefner, R. A. Houghton, G. C. Hurtt, Y. Iida, T. Ilyina, A. K. Jain, A. Jersild, K. Kadono, E. Kato, D. Kennedy, K. Klein Goldewijk, J. Knauer, J. I. Korsbakken, P. Landschützer, N. Lefèvre, K. Lindsay, J. Liu, Z. Liu, G. Marland, N. Mayot, M. J. McGrath, N. Metz, N. M. Monacci, D. R. Munro, S.-I. Nakaoka, Y. Niwa, K. O’Brien, T. Ono, P. I. Palmer,

- N. Pan, D. Pierrot, K. Pocock, B. Poulter, L. Resplandy, E. Robertson, C. Rödenbeck, C. Rodriguez, T. M. Rosan, J. Schwinger, R. Séférian, J. D. Shutler, I. Skjelvan, T. Steinhoff, Q. Sun, A. J. Sutton, C. Sweeney, S. Takao, T. Tanhua, P. P. Tans, X. Tian, H. Tian, B. Tilbrook, H. Tsjino, F. Tubiello, G. R. van der Werf, A. P. Walker, R. Wanninkhof, C. Whitehead, A. Willstrand Wranne, R. Wright, W. Yuan, C. Yue, X. Yue, S. Zaehle, J. Zeng, and B. Zheng, “Global carbon budget 2022,” *Earth System Science Data*, vol. 14, no. 11, pp. 4811–4900, 2022.
- [9] “Our World in Data.” <https://ourworldindata.org>.
- [10] B. Rotavera and C. A. Taatjes, “Influence of functional groups on low-temperature combustion chemistry of biofuels,” *Progress in Energy and Combustion Science*, vol. 86, p. 100925, 2021.
- [11] A. Demirbas, “Combustion efficiency impacts of biofuels,” *Energy Sources, Part A: Recovery, Utilization, and Environmental Effects*, vol. 31, no. 7, pp. 602–609, 2009.
- [12] Z. Serinyel, M. Lailliau, S. Thion, G. Dayma, and P. Dagaut, “An experimental chemical kinetic study of the oxidation of diethyl ether in a jet-stirred reactor and comprehensive modeling,” *Combustion and Flame*, vol. 193, pp. 453–462, 2018.
- [13] S. W. Benson, “The kinetics and thermochemistry of chemical oxidation with application to combustion and flames,” *Progress in Energy and Combustion Science*, vol. 7, no. 2, pp. 125–134, 1981.
- [14] F. Battin-Leclerc, “Detailed chemical kinetic models for the low-temperature combustion of hydrocarbons with application to gasoline and diesel fuel surrogates,” *Progress in Energy and Combustion Science*, vol. 34, no. 4, pp. 440–498, 2008.
- [15] J. Zádor, C. A. Taatjes, and R. X. Fernandes, “Kinetics of elementary reactions in low-temperature autoignition chemistry,” *Progress in Energy and Combustion Science*, vol. 37, no. 4, pp. 371–421, 2011.
- [16] L. S. Tran, B. Sirjean, P.-A. Glaude, R. Fournet, and F. Battin-Leclerc, “Progress in detailed kinetic modeling of the combustion of oxygenated components of biofuels,” *Energy*, vol. 43, no. 1, pp. 4–18, 2012.
- [17] Z. Huang, H. Miao, L. Zhou, and D. Jiang, “Technical Note: Combustion characteristics and hydrocarbon emissions of a spark ignition engine fuelled with gasoline-oxygenate blends,” *Proceedings of the Institution of Mechanical Engineers, Part D: Journal of Automobile Engineering*, vol. 214, no. 3, pp. 341–346, 2000.

- [18] R. Suerz, K. Eränen, N. Kumar, J. Wärnä, V. Russo, M. Peurla, A. Aho, D. Yu. Murzin, and T. Salmi, "Application of microreactor technology to dehydration of bio-ethanol," *Chemical Engineering Science*, vol. 229, p. 116030, 2021.
- [19] E. Chaichana, N. Boonsinvarothai, N. Chitpong, and B. Jongsomjit, "Catalytic dehydration of ethanol to ethylene and diethyl ether over alumina catalysts containing different phases with boron modification," *Journal of Porous Materials*, vol. 26, no. 2, pp. 599–610, 2019.
- [20] T. Kamsuwan, P. Praserttham, and B. Jongsomjit, "Diethyl Ether Production during Catalytic Dehydration of Ethanol over Ru- and Pt- modified H-beta Zeolite Catalysts," *Journal of Oleo Science*, vol. 66, no. 2, pp. 199–207, 2017.
- [21] T. K. Phung and G. Busca, "Diethyl ether cracking and ethanol dehydration: Acid catalysis and reaction paths," *Chemical Engineering Journal*, vol. 272, pp. 92–101, 2015.
- [22] A. Rahmanian and H. S. Ghaziaskar, "Continuous dehydration of ethanol to diethyl ether over aluminum phosphate–hydroxyapatite catalyst under sub and supercritical condition," *The Journal of Supercritical Fluids*, vol. 78, pp. 34–41, 2013.
- [23] F. P. Heese, M. E. Dry, and K. P. Möller, "Single stage synthesis of diisopropyl ether – an alternative octane enhancer for lead-free petrol," *Catalysis Today*, vol. 49, no. 1, pp. 327–335, 1999.
- [24] F. P. Heese, M. E. Dry, and K. P. Möller, "The mechanism of diisopropyl ether synthesis from a feed of propylene and isopropanol over ion exchange resin," in *Studies in Surface Science and Catalysis* (A. Corma, F. V. Melo, S. Mendioroz, and J. L. G. Fierro, eds.), vol. 130 of *12th International Congress on Catalysis*, pp. 2597–2602, 2000.
- [25] Z. Li, H. Li, J. Wang, and X. Gao, "Novel intensified process for di-isopropyl ether production from isopropanol etherification using reactive distillation technology," *Separation and Purification Technology*, vol. 322, p. 124243, 2023.
- [26] M. A. Perez-Macia, R. Bringue, M. Iborra, J. Tejero, and F. Cunill, "Kinetic study of 1-butanol dehydration to di-n-butyl ether over amberlyst 70," *AIChE Journal*, vol. 62, no. 1, pp. 180–194, 2016.
- [27] M. A. Pérez, R. Bingué, M. Iborra, J. Tejero, and F. Cunill, "Ion exchange resins as catalysts for the liquid-phase dehydration of 1-butanol to di-n-butyl ether," *Applied Catalysis A: General*, vol. 482, pp. 38–48, 2014.
- [28] J. K. Kim, J. H. Choi, D. R. Park, and I. K. Song, "Etherification of n-butanol to di-n-butyl ether over Keggin-, Wells-Dawson-, and Preyssler-type heteropolyacid catalysts," *Journal of Nanoscience and Nanotechnology*, vol. 13, no. 12, pp. 8121–8126, 2013.

- [29] J. Tejero, F. Cunill, M. Iborra, J. F. Izquierdo, and C. Fité, "Dehydration of 1-pentanol to di-n-pentyl ether over ion-exchange resin catalysts," *Journal of Molecular Catalysis A: Chemical*, vol. 182-183, pp. 541–554, 2002.
- [30] J. Tejero, C. Fité, M. Iborra, J. F. Izquierdo, R. Bringué, and F. Cunill, "Dehydration of 1-pentanol to di-n-pentyl ether catalyzed by a microporous ion-exchange resin with simultaneous water removal," *Applied Catalysis A: General*, vol. 308, pp. 223–230, 2006.
- [31] J. Tejero, C. Fité, M. Iborra, J. F. Izquierdo, F. Cunill, and R. Bringué, "Liquid-phase dehydrocondensation of 1-pentanol to di-n-pentyl ether (DNPE) over medium and large pore acidic zeolites," *Microporous and Mesoporous Materials*, vol. 117, no. 3, pp. 650–660, 2009.
- [32] C. S. Bildea, R. György, E. Sánchez-Ramírez, J. J. Quiroz-Ramírez, J. G. Segovia-Hernandez, and A. A. Kiss, "Optimal design and plantwide control of novel processes for di-n-pentyl ether production," *Journal of Chemical Technology & Biotechnology*, vol. 90, no. 6, pp. 992–1001, 2015.
- [33] J. E. Rorrer, A. T. Bell, and F. D. Toste, "Synthesis of biomass-derived ethers for use as fuels and lubricants," *ChemSusChem*, vol. 12, no. 13, pp. 2835–2858, 2019.
- [34] P. Dagaut, J.-C. Boettner, and M. Cathonnet, "Chemical kinetic study of dimethylether oxidation in a jet stirred reactor from 1 to 10 ATM: Experiments and kinetic modeling," *Symposium (International) on Combustion*, vol. 26, no. 1, pp. 627–632, 1996.
- [35] X. Qin and Y. Ju, "Measurements of burning velocities of dimethyl ether and air premixed flames at elevated pressures," *Proceedings of the Combustion Institute*, vol. 30, no. 1, pp. 233–240, 2005.
- [36] G. Mittal, M. Chaos, C.-J. Sung, and F. L. Dryer, "Dimethyl ether autoignition in a rapid compression machine: Experiments and chemical kinetic modeling," *Fuel Processing Technology*, vol. 89, no. 12, pp. 1244–1254, 2008.
- [37] R. D. Cook, D. F. Davidson, and R. K. Hanson, "Shock tube measurements of ignition delay times and OH time-histories in dimethyl ether oxidation," *Proceedings of the Combustion Institute*, vol. 32, no. 1, pp. 189–196, 2009.
- [38] Y. L. Wang, A. T. Holley, C. Ji, F. N. Egolfopoulos, T. T. Tsotsis, and H. J. Curran, "Propagation and extinction of premixed dimethyl-ether/air flames," *Proceedings of the Combustion Institute*, vol. 32, no. 1, pp. 1035–1042, 2009.
- [39] N. Kurimoto, B. Brumfield, X. Yang, T. Wada, P. Diévar, G. Wysocki, and Y. Ju, "Quantitative measurements of HO₂/H₂O₂ and intermediate species in low and intermediate tem-

- perature oxidation of dimethyl ether,” *Proceedings of the Combustion Institute*, vol. 35, no. 1, pp. 457–464, 2015.
- [40] K. Moshhammer, A. W. Jasper, D. M. Popolan-Vaida, A. Lucassen, P. Diévert, H. Selim, A. J. Eskola, C. A. Taatjes, S. R. Leone, S. M. Sarathy, Y. Ju, P. Dagaut, K. Kohse-Höinghaus, and N. Hansen, “Detection and Identification of the Keto-Hydroperoxide (HOOCH₂OCHO) and Other Intermediates during Low-Temperature Oxidation of Dimethyl Ether,” *The Journal of Physical Chemistry A*, vol. 119, no. 28, pp. 7361–7374, 2015.
- [41] Z. Wang, C. Yan, Y. Lin, M. Zhou, B. Jiang, N. Liu, H. Zhong, and Y. Ju, “Kinetics and extinction of non-premixed cool and warm flames of dimethyl ether at elevated pressure,” *Proceedings of the Combustion Institute*, vol. 39, no. 2, pp. 1871–1879, 2023.
- [42] I. Sezer, “A review study on using diethyl ether in diesel engines: Effects on fuel properties, injection, and combustion characteristics,” *Energy & Environment*, vol. 31, no. 2, pp. 179–214, 2020.
- [43] D. J. Waddington and A. C. Egerton, “The gaseous oxidation of diethyl ether,” *Proceedings of the Royal Society of London. Series A. Mathematical and Physical Sciences*, vol. 252, no. 1269, pp. 260–272, 1959.
- [44] W. G. Agnew and J. T. Agnew, “Composition profiles of the diethyl ether-air two-stage reaction stabilized in a flat-flame burner,” *Symposium (International) on Combustion*, vol. 10, no. 1, pp. 123–138, 1965.
- [45] N. Vin, O. Herbinet, and F. Battin-Leclerc, “Diethyl ether pyrolysis study in a jet-stirred reactor,” *Journal of Analytical and Applied Pyrolysis*, vol. 121, pp. 173–176, 2016.
- [46] L.-S. Tran, O. Herbinet, Y. Li, J. Wullenkord, M. Zeng, E. Bräuer, F. Qi, K. Kohse-Höinghaus, and F. Battin-Leclerc, “Low-temperature gas-phase oxidation of diethyl ether: Fuel reactivity and fuel-specific products,” *Proceedings of the Combustion Institute*, vol. 37, no. 1, pp. 511–519, 2019.
- [47] L.-S. Tran, Y. Li, M. Zeng, J. Pieper, F. Qi, F. Battin-Leclerc, K. Kohse-Höinghaus, and O. Herbinet, “Elevated pressure low-temperature oxidation of linear five-heavy-atom fuels: diethyl ether, n-pentane, and their mixture,” *Zeitschrift für Physikalische Chemie*, vol. 234, no. 7-9, pp. 1269–1293, 2020.
- [48] Z. Serinyel, G. Dayma, V. Glasziou, M. Lailliau, and P. Dagaut, “A pyrolysis study on C₄–C₈ symmetric ethers,” *Proceedings of the Combustion Institute*, vol. 38, no. 1, pp. 329–336, 2021.

- [49] N. Belhadj, R. Benoit, M. Lailliau, V. Glasziou, and P. Dagaut, "Oxidation of diethyl ether: Extensive characterization of products formed at low temperature using high resolution mass spectrometry," *Combustion and Flame*, vol. 228, pp. 340–350, 2021.
- [50] K. Yasunaga, F. Gillespie, J. M. Simmie, H. J. Curran, Y. Kuraguchi, H. Hoshikawa, M. Yamane, and Y. Hidaka, "A Multiple Shock Tube and Chemical Kinetic Modeling Study of Diethyl Ether Pyrolysis and Oxidation," *The Journal of Physical Chemistry A*, vol. 114, no. 34, pp. 9098–9109, 2010.
- [51] M. Werler, L. R. Cancino, R. Schiessl, U. Maas, C. Schulz, and M. Fikri, "Ignition delay times of diethyl ether measured in a high-pressure shock tube and a rapid compression machine," *Proceedings of the Combustion Institute*, vol. 35, no. 1, pp. 259–266, 2015.
- [52] Y. Uygun, "Ignition studies of undiluted diethyl ether in a high-pressure shock tube," *Combustion and Flame*, vol. 194, pp. 396–409, 2018.
- [53] G. Issayev, S. Mani Sarathy, and A. Farooq, "Autoignition of diethyl ether and a diethyl ether/ethanol blend," *Fuel*, vol. 279, p. 118553, 2020.
- [54] N. Zhang, Y. Di, Z. Huang, B. Zheng, and Z. Zhang, "Experimental Study on Combustion Characteristics of N₂-Diluted Diethyl Ether-Air Mixtures," 2009.
- [55] F. Gillespie, W. K. Metcalfe, P. Dirrenberger, O. Herbinet, P.-A. Glaude, F. Battin-Leclerc, and H. J. Curran, "Measurements of flat-flame velocities of diethyl ether in air," *Energy*, vol. 43, no. 1, pp. 140–145, 2012.
- [56] L.-S. Tran, J. Pieper, H.-H. Carstensen, H. Zhao, I. Graf, Y. Ju, F. Qi, and K. Kohse-Höinghaus, "Experimental and kinetic modeling study of diethyl ether flames," *Proceedings of the Combustion Institute*, vol. 36, no. 1, pp. 1165–1173, 2017.
- [57] Z. Serinyel, M. Lailliau, G. Dayma, and P. Dagaut, "A high pressure oxidation study of di-n-propyl ether," *Fuel*, vol. 263, p. 116554, 2020.
- [58] N. Belhadj, R. Benoit, P. Dagaut, M. Lailliau, Z. Serinyel, and G. Dayma, "Oxidation of di-n-propyl ether: Characterization of low-temperature products," *Proceedings of the Combustion Institute*, vol. 38, no. 1, pp. 337–344, 2021.
- [59] X. Fan, W. Sun, Y. Gao, N. Hansen, B. Chen, H. Pitsch, and B. Yang, "Chemical insights into the multi-regime low-temperature oxidation of di-n-propyl ether: Jet-stirred reactor experiments and kinetic modeling," *Combustion and Flame*, vol. 233, p. 111592, 2021.
- [60] Z. Cheng, H. Wang, W. Yin, J. Wang, W. Li, Z. Wang, L. Xing, X. Gao, B. Mei, Y. Zhang, J. Yang, L. Wei, X. Zhong, H. Wang, Y. Li, B. Yan, and G. Chen, "Experimental and kinetic modeling

study of di-n-propyl ether and diisopropyl ether combustion: Pyrolysis and laminar flame propagation velocity,” *Combustion and Flame*, vol. 237, p. 111809, 2022.

- [61] Z. Cheng, W. Yin, J. Tian, W. He, J. Wang, J. Yang, L. Xing, B. Yan, and G. Chen, “Experimental and kinetic modeling studies of di-n-propyl ether pyrolysis at low and atmospheric pressures,” *Fuel*, vol. 298, p. 120797, 2021.
- [62] G. Dhamodaran, G. S. Esakkimuthu, and Y. K. Pochareddy, “Experimental study on performance, combustion, and emission behaviour of diisopropyl ether blends in MPFI SI engine,” *Fuel*, vol. 173, pp. 37–44, 2016.
- [63] A. Uyumaz, B. Aydođan, A. Calam, F. Aksoy, and E. Yılmaz, “The effects of diisopropyl ether on combustion, performance, emissions and operating range in a HCCI engine,” *Fuel*, vol. 265, p. 116919, 2020.
- [64] A. V. Kale and A. Krishnasamy, “Investigations on load range extension of a homogeneous charge compression ignited light-duty diesel engine operated with diisopropyl ether and gasoline blends,” *Fuel*, vol. 314, p. 122856, 2022.
- [65] A. Goldaniga, T. Faravelli, E. Ranzi, P. Dagaut, and M. Cathonnet, “Oxidation of oxygenated octane improvers: MTBE, ETBE, DIPE, and TAME,” *Symposium (International) on Combustion*, vol. 27, no. 1, pp. 353–360, 1998.
- [66] E. Ranzi, T. Faravelli, P. Gaffuri, A. Sogaro, A. D’Anna, and A. Ciajolo, “A wide-range modeling study of iso-octane oxidation,” *Combustion and Flame*, vol. 108, no. 1, pp. 24–42, 1997.
- [67] X. Fan, W. Sun, Z. Liu, Y. Gao, J. Yang, B. Yang, and C. K. Law, “Exploring the oxidation chemistry of diisopropyl ether: Jet-stirred reactor experiments and kinetic modeling,” *Proceedings of the Combustion Institute*, vol. 38, no. 1, pp. 321–328, 2021.
- [68] Z. Serinyel, M. Lailliau, G. Dayma, and P. Dagaut, “A detailed high-pressure oxidation study of di-isopropyl ether,” *Proceedings of the Combustion Institute*, 2022.
- [69] X. Liu, Q. Zhang, S. Ito, and Y. Wada, “Oxidation characteristics and products of five ethers at low temperature,” *Fuel*, vol. 165, pp. 513–525, 2016.
- [70] J. Hashimoto, J. Hosono, K. Shimizu, R. Urakawa, and K. Tanoue, “Extinction limits and flame structures of ETBE, DIPE and TAME non-premixed flames,” *Proceedings of the Combustion Institute*, vol. 36, no. 1, pp. 1439–1446, 2017.
- [71] A. García, J. Monsalve-Serrano, D. Villalta, M. Zubel, and S. Pischinger, “Potential of 1-octanol and di-n-butyl ether (DNBE) to improve the performance and reduce the emissions of a direct injected compression ignition diesel engine,” *Energy Conversion and Management*, vol. 177, pp. 563–571, 2018.

- [72] Z. Gao, L. Zhu, X. Zou, C. Liu, B. Tian, and Z. Huang, "Soot reduction effects of dibutyl ether (DBE) addition to a biodiesel surrogate in laminar coflow diffusion flames," *Proceedings of the Combustion Institute*, vol. 37, no. 1, pp. 1265–1272, 2019.
- [73] Q. Wang, S. Yin, and J. Ni, "The effects of n-pentanol, di-n-butyl ether (DBE) and exhaust gas recirculation on performance and emissions in a compression ignition engine," *Fuel*, vol. 284, p. 118961, 2021.
- [74] C. Wu, Y. Wang, H. Sang, H. Huang, Q. Wang, and M. Pan, "Potential of Di-n-Butyl Ether as an Alternative Fuel for Compression Ignition Engines with Different EGR Rates and Injection Pressure," *Journal of Energy Engineering*, vol. 147, no. 6, p. 04021042, 2021.
- [75] M. Kalil Rahiman, S. Santhoshkumar, D. Subramaniam, A. Avinash, and A. Pugazhendhi, "Effects of oxygenated fuel pertaining to fuel analysis on diesel engine combustion and emission characteristics," *Energy*, vol. 239, p. 122373, 2022.
- [76] S. Thion, C. Togbé, Z. Serinyel, G. Dayma, and P. Dagaut, "A chemical kinetic study of the oxidation of dibutyl-ether in a jet-stirred reactor," *Combustion and Flame*, vol. 185, pp. 4–15, 2017.
- [77] L.-S. Tran, J. Wullenkord, Y. Li, O. Herbinet, M. Zeng, F. Qi, K. Kohse-Höinghaus, and F. Battin-Leclerc, "Probing the low-temperature chemistry of di-n-butyl ether: Detection of previously unobserved intermediates," *Combustion and Flame*, vol. 210, pp. 9–24, 2019.
- [78] L. Cai, A. Sudholt, D. J. Lee, F. N. Egolfopoulos, H. Pitsch, C. K. Westbrook, and S. M. Sarathy, "Chemical kinetic study of a novel lignocellulosic biofuel: Di-n-butyl ether oxidation in a laminar flow reactor and flames," *Combustion and Flame*, vol. 161, no. 3, pp. 798–809, 2014.
- [79] N. Belhadj, R. Benoit, P. Dagaut, M. Lailliau, Z. Serinyel, G. Dayma, F. Khaled, B. Moreau, and F. Foucher, "Oxidation of di-n-butyl ether: Experimental characterization of low-temperature products in JSR and RCM," *Combustion and Flame*, vol. 222, pp. 133–144, 2020.
- [80] N. Belhadj, M. Lailliau, R. Benoit, and P. Dagaut, "Towards a comprehensive characterization of the low-temperature autoxidation of di-n-butyl ether," *Molecules*, vol. 26, no. 23, 2021.
- [81] L. Guan, C. Tang, K. Yang, J. Mo, and Z. Huang, "Experimental and Kinetic Study on Ignition Delay Times of Di-n-butyl Ether at High Temperatures," *Energy & Fuels*, vol. 28, no. 8, pp. 5489–5496, 2014.
- [82] K. Hakimov, F. Arafin, K. Aljohani, K. Djebbi, E. Ninnemann, S. S. Vasu, and A. Farooq, "Ignition delay time and speciation of dibutyl ether at high pressures," *Combustion and Flame*, vol. 223, pp. 98–109, 2021.

- [83] A. Zhong and D. Han, "Experimental and kinetic modelling studies on di-n-butyl ether (DBE) low temperature auto-ignition," *Combustion and Flame*, vol. 237, p. 111882, 2022.
- [84] X. Fan, Z. Liu, J. Yang, and B. Yang, "Pyrolysis of Lignocellulosic Biofuel Di-n-butyl Ether (DBE): Flow Reactor Experiments and Kinetic Modeling," *Energy & Fuels*, vol. 35, no. 17, pp. 14077–14086, 2021.
- [85] E. Koivisto, N. Ladommatos, and M. Gold, "Compression ignition and exhaust gas emissions of fuel molecules which can be produced from lignocellulosic biomass: Levulinates, valeric esters, and ketones," *Energy & Fuels*, vol. 29, no. 9, pp. 5875–5884, 2015.
- [86] P. T. Aakko-Saksa, M. Westerholm, R. Pettinen, C. Söderström, P. Roslund, P. Piimäkorpi, P. Koponen, T. Murtonen, M. Niinistö, M. Tunér, and J. Ellis, "Renewable methanol with ignition improver additive for diesel engines," *Energy & Fuels*, vol. 34, no. 1, pp. 379–388, 2020.
- [87] C. S. M. Pereira, V. M. T. M. Silva, and A. E. Rodrigues, "Ethyl lactate as a solvent: Properties, applications and production processes – a review," *Green Chemistry*, vol. 13, no. 10, pp. 2658–2671, 2011.
- [88] J. Würmel, K. P. Somers, and J. M. Simmie, "Ethyl lactate: a sinister molecule exhibiting high chemical diversity with potential as a "green" solvent," *International Journal of Chemical Kinetics*, vol. 53, no. 3, pp. 457–464, 2021.
- [89] G. Cenedese, Z. Serinyel, F. Halter, F. Foucher, and G. Dayma, "An experimental and kinetic modeling study of auto-ignition and flame propagation of ethyl lactate/air mixtures, a potential octane booster," *Proceedings of the Combustion Institute*, vol. 39, no. 1, pp. 285–293, 2023.
- [90] M. Koutinas, M. Menelaou, and E. N. Nicolaou, "Development of a hybrid fermentation-enzymatic bioprocess for the production of ethyl lactate from dairy waste," *Bioresource Technology*, vol. 165, pp. 343–349, 2014.
- [91] X. Li, X. Zhang, H. Jian, X. Xu, and Y. Xi, "Biocycle Fermentation Based on Lactic Acid Bacteria and Yeast for the Production of Natural Ethyl Lactate," *ACS Omega*, vol. 4, no. 14, pp. 16009–16015, 2019.
- [92] P. Dagaut, M. Cathonnet, J. P. Rouan, R. Foulatier, A. Quilgars, J. C. Boettner, F. Gaillard, and H. James, "A jet-stirred reactor for kinetic studies of homogeneous gas-phase reactions at pressures up to ten atmospheres (≈ 1 MPa)," *Journal of Physics E: Scientific Instruments*, vol. 19, no. 3, p. 207, 1986.

- [93] J. T. Scanlon and D. E. Willis, "Calculation of Flame Ionization Detector Relative Response Factors Using the Effective Carbon Number Concept," *Journal of Chromatographic Science*, vol. 23, no. 8, pp. 333–340, 1985.
- [94] S. S. Goldsborough, S. Hochgreb, G. Vanhove, M. S. Wooldridge, H. J. Curran, and C.-J. Sung, "Advances in rapid compression machine studies of low- and intermediate-temperature autoignition phenomena," *Progress in Energy and Combustion Science*, vol. 63, pp. 1–78, 2017.
- [95] G. Mittal, M. P. Raju, and C.-J. Sung, "CFD modeling of two-stage ignition in a rapid compression machine: Assessment of zero-dimensional approach," *Combustion and Flame*, vol. 157, no. 7, pp. 1316–1324, 2010.
- [96] M. Pochet, V. Dias, B. Moreau, F. Foucher, H. Jeanmart, and F. Contino, "Experimental and numerical study, under LTC conditions, of ammonia ignition delay with and without hydrogen addition," *Proceedings of the Combustion Institute*, vol. 37, no. 1, pp. 621–629, 2019.
- [97] S. S. Goldsborough, J. Santner, D. Kang, A. Fridlyand, T. Rockstroh, and M. C. Jespersen, "Heat release analysis for rapid compression machines: Challenges and opportunities," *Proceedings of the Combustion Institute*, vol. 37, no. 1, pp. 603–611, 2019.
- [98] G. Mittal, M. P. Raju, and C.-J. Sung, "Vortex formation in a rapid compression machine: Influence of physical and operating parameters," *Fuel*, vol. 94, pp. 409–417, 2012.
- [99] H. Nakamura, D. Darcy, M. Mehl, C. J. Tobin, W. K. Metcalfe, W. J. Pitz, C. K. Westbrook, and H. J. Curran, "An experimental and modeling study of shock tube and rapid compression machine ignition of n-butylbenzene/air mixtures," *Combustion and Flame*, vol. 161, no. 1, pp. 49–64, 2014.
- [100] K. Zhang, C. Banyon, U. Burke, G. Kukkadapu, S. W. Wagnon, M. Mehl, H. J. Curran, C. K. Westbrook, and W. J. Pitz, "An experimental and kinetic modeling study of the oxidation of hexane isomers: Developing consistent reaction rate rules for alkanes," *Combustion and Flame*, vol. 206, pp. 123–137, 2019.
- [101] C. Morley, "Gaseq: a chemical equilibrium program for windows," *Ver. 0.79*, 2005. <http://www.gaseq.co.uk>.
- [102] W. S. Affleck and A. Thomas, "An Opposed Piston Rapid Compression Machine for Pre-flame Reaction Studies," *Proceedings of the Institution of Mechanical Engineers*, vol. 183, no. 1, pp. 365–387, 1968.
- [103] S. M. Gallagher, H. J. Curran, W. K. Metcalfe, D. Healy, J. M. Simmie, and G. Bourque, "A rapid compression machine study of the oxidation of propane in the negative temperature coefficient regime," *Combustion and Flame*, vol. 153, no. 1, pp. 316–333, 2008.

- [104] C.-W. Zhou, J. M. Simmie, and H. J. Curran, "An ab initio/Rice-Ramsperger-Kassel-Marcus study of the hydrogen-abstraction reactions of methyl ethers, $\text{H}_3\text{COCH}_3\text{-x}(\text{CH}_3)_x$, $x = 0-2$, by $\cdot\text{OH}$; mechanism and kinetics," *Physical Chemistry Chemical Physics*, vol. 12, no. 26, pp. 7221–7233, 2010.
- [105] R. D. Cook, D. F. Davidson, and R. K. Hanson, "High-Temperature Shock Tube Measurements of Dimethyl Ether Decomposition and the Reaction of Dimethyl Ether with OH," *The Journal of Physical Chemistry A*, vol. 113, no. 37, pp. 9974–9980, 2009.
- [106] J.-C. Lizardo-Huerta, B. Sirjean, P.-A. Glaude, and R. Fournet, "Pericyclic reactions in ether biofuels," *Proceedings of the Combustion Institute*, vol. 36, no. 1, pp. 569–576, 2017.
- [107] C. F. Goldsmith, W. H. Green, and S. J. Klippenstein, "Role of $\text{O}_2 + \text{QOOH}$ in Low-Temperature Ignition of Propane. 1. Temperature and Pressure Dependent Rate Coefficients," *The Journal of Physical Chemistry A*, vol. 116, no. 13, pp. 3325–3346, 2012.
- [108] Y. Sakai, H. Ando, H. K. Chakravarty, H. Pitsch, and R. X. Fernandes, "A computational study on the kinetics of unimolecular reactions of ethoxyethylperoxy radicals employing CTST and VTST," *Proceedings of the Combustion Institute*, vol. 35, no. 1, pp. 161–169, 2015.
- [109] S. M. Villano, L. K. Huynh, H.-H. Carstensen, and A. M. Dean, "High-Pressure Rate Rules for Alkyl + O_2 Reactions. 2. The Isomerization, Cyclic Ether Formation, and β -Scission Reactions of Hydroperoxy Alkyl Radicals," *The Journal of Physical Chemistry A*, vol. 116, no. 21, pp. 5068–5089, 2012.
- [110] K. Y. Choo, D. M. Golden, and S. W. Benson, "Very low-pressure pyrolysis (vlpp) of t-butylmethyl ether," *International Journal of Chemical Kinetics*, vol. 6, no. 5, pp. 631–641, 1974.
- [111] J. Zador and J. Miller, "Hydrogen abstraction from n-, i-propanol and n-butanol: A systematic theoretical approach," in *Combustion Institute, JOINT MEETING US SECTIONS OF THE COMBUSTION INSTITUTE*, vol. 1, pp. 483–488, 2011.
- [112] C.-W. Zhou, J. M. Simmie, and H. J. Curran, "Rate constants for hydrogen abstraction by HO_2 from n-butanol," *International Journal of Chemical Kinetics*, vol. 44, no. 3, pp. 155–164, 2012.
- [113] P. Seal, E. Papajak, and D. G. Truhlar, "Kinetics of the Hydrogen Abstraction from Carbon-3 of 1-Butanol by Hydroperoxyl Radical: Multi-Structural Variational Transition-State Calculations of a Reaction with 262 Conformations of the Transition State," *The Journal of Physical Chemistry Letters*, vol. 3, no. 2, pp. 264–271, 2012.
- [114] A. T. Droege and F. P. Tully, "Hydrogen atom abstraction from alkanes by hydroxyl. 5. n-Butane," *The Journal of Physical Chemistry*, vol. 90, no. 22, pp. 5937–5941, 1986.

- [115] J. Mendes, C.-W. Zhou, and H. J. Curran, "Rate Constant Calculations of H-Atom Abstraction Reactions from Ethers by HO₂ Radicals," *The Journal of Physical Chemistry A*, vol. 118, no. 8, pp. 1300–1308, 2014.
- [116] P. Seal, G. Oyedepo, and D. G. Truhlar, "Kinetics of the Hydrogen Atom Abstraction Reactions from 1-Butanol by Hydroxyl Radical: Theory Matches Experiment and More," *The Journal of Physical Chemistry A*, vol. 117, no. 2, pp. 275–282, 2013.
- [117] N. Cohen, "The use of transition-state theory to extrapolate rate coefficients for reactions of h atoms with alkanes," *International Journal of Chemical Kinetics*, vol. 23, no. 8, pp. 683–700, 1991.
- [118] T. Ogura, A. Miyoshi, and M. Koshi, "Rate coefficients of H-atom abstraction from ethers and isomerization of alkoxyalkylperoxy radicals," *Physical Chemistry Chemical Physics*, vol. 9, no. 37, pp. 5133–5142, 2007.
- [119] J. Aguilera-Iparraguirre, H. J. Curran, W. Klopper, and J. M. Simmie, "Accurate Benchmark Calculation of the Reaction Barrier Height for Hydrogen Abstraction by the Hydroperoxyl Radical from Methane. Implications for C_nH_{2n+2} where n = 2 → 4," *The Journal of Physical Chemistry A*, vol. 112, no. 30, pp. 7047–7054, 2008.
- [120] Z. F. Xu, J. Park, and M. C. Lin, "Thermal decomposition of ethanol. III. A computational study of the kinetics and mechanism for the CH₃+C₂H₅OH reaction," *The Journal of Chemical Physics*, vol. 120, no. 14, pp. 6593–6599, 2004.
- [121] S. M. Sarathy, P. Oßwald, N. Hansen, and K. Kohse-Höinghaus, "Alcohol combustion chemistry," *Progress in Energy and Combustion Science*, vol. 44, pp. 40–102, 2014.
- [122] J. Mendes, C.-W. Zhou, and H. J. Curran, "Theoretical Chemical Kinetic Study of the H-Atom Abstraction Reactions from Aldehydes and Acids by \dot{H} Atoms and $\dot{O}H$, $H\dot{O}2$, and $\dot{C}H_3$ Radicals," *The Journal of Physical Chemistry A*, vol. 118, no. 51, pp. 12089–12104, 2014.
- [123] G. Dayma, S. Thion, M. Lailliau, Z. Serinyel, P. Dagaut, B. Sirjean, and R. Fournet, "Kinetics of propyl acetate oxidation: Experiments in a jet-stirred reactor, ab initio calculations, and rate constant determination," *Proceedings of the Combustion Institute*, vol. 37, no. 1, pp. 429–436, 2019.
- [124] R. Van de Vijver, K. M. Van Geem, G. B. Marin, and J. Zádor, "Decomposition and isomerization of 1-pentanol radicals and the pyrolysis of 1-pentanol," *Combustion and Flame*, vol. 196, pp. 500–514, 2018.
- [125] W. Sun, T. Tao, R. Zhang, H. Liao, C. Huang, F. Zhang, X. Zhang, Y. Zhang, and B. Yang, "Experimental and modeling efforts towards a better understanding of the high-temperature

- combustion kinetics of C3C5 ethyl esters,” *Combustion and Flame*, vol. 185, pp. 173–187, 2017.
- [126] A. Zaras, M. Szóri, S. Thion, P. Van Cauwenberghe, F. Deguillaume, Z. Serinyel, G. Dayma, and P. Dagaut, “A Chemical Kinetic Investigation on Butyl Formate Oxidation: Ab Initio Calculations and Experiments in a Jet-Stirred Reactor | Energy & Fuels,” *Energy fuels*, vol. 31, no. 6, pp. 6194–6205, 2017.
- [127] N. Cohen and S. W. Benson, “Estimation of heats of formation of organic compounds by additivity methods,” *Chemical Reviews*, vol. 93, no. 7, pp. 2419–2438, 1993.
- [128] ANSYS, “Chemkin-pro 2022 r2.”
- [129] R. G. Gilbert, K. Luther, and J. Troe, “Theory of thermal unimolecular reactions in the fall-off range. ii. weak collision rate constants,” *Berichte der Bunsengesellschaft für physikalische Chemie*, vol. 87, no. 2, pp. 169–177, 1983.
- [130] Reaction Design: San Diego, *ANSYS Chemkin Theory Manual 17.0 (15151)*.
- [131] S. Gordon and B. J. McBride, *Computer program for calculation of complex chemical equilibrium compositions, rocket performance, incident and reflected shocks and Chapman-Jouguet detonations*. NASA.
- [132] R. K. Jensen, S. Korcek, L. R. Mahoney, and M. Zinbo, “Liquid-phase autoxidation of organic compounds at elevated temperatures. 2. kinetics and mechanisms of the formation of cleavage products in n-hexadecane autoxidation,” *Journal of the American Chemical Society*, vol. 103, no. 7, pp. 1742–1749, 1981.
- [133] R. L. McCormick, G. Fioroni, L. Fouts, E. Christensen, J. Yanowitz, E. Polikarpov, K. Albrecht, D. J. Gaspar, J. Gladden, and A. George, “Selection criteria and screening of potential biomass-derived streams as fuel blendstocks for advanced spark-ignition engines,” *SAE International Journal of Fuels and Lubricants*, vol. 10, no. 2, pp. 442–460, 2017.
- [134] F. Halter, Z. Chen, G. Dayma, C. Bariki, Y. Wang, P. Dagaut, and C. Chauveau, “Development of an optically accessible apparatus to characterize the evolution of spherically expanding flames under constant volume conditions,” *Combustion and Flame*, vol. 212, pp. 165–176, 2020.
- [135] F. Halter, G. Dayma, Z. Serinyel, P. Dagaut, and C. Chauveau, “Laminar flame speed determination at high pressure and temperature conditions for kinetic schemes assessment,” *Proceedings of the Combustion Institute*, vol. 38, no. 2, pp. 2449–2457, 2021.

- [136] A. Stagni, C. Cavallotti, S. Arunthanayothin, Y. Song, O. Herbinet, F. Battin-Leclerc, and T. Faravelli, "An experimental, theoretical and kinetic-modeling study of the gas-phase oxidation of ammonia," *React. Chem. Eng.*, vol. 5, pp. 696–711, 2020.
- [137] A. Karan, G. Dayma, C. Chauveau, and F. Halter, "Experimental study and numerical validation of oxy-ammonia combustion at elevated temperatures and pressures," *Combustion and Flame*, vol. 236, p. 111819, 2022.
- [138] Y. Wu, S. Panigrahy, A. B. Sahu, C. Bariki, J. Beeckmann, J. Liang, A. A. Mohamed, S. Dong, C. Tang, H. Pitsch, Z. Huang, and H. J. Curran, "Understanding the antagonistic effect of methanol as a component in surrogate fuel models: A case study of methanol/n-heptane mixtures," *Combustion and Flame*, vol. 226, pp. 229–242, 2021.

Appendix A

JSR: additional results

In this appendix, some additional results from the jet-stirred reactor are presented. First, some species that were identified during the oxidation of DIPEE and their simulated profiles (when available) are included, for all the equivalence ratios that were studied. These species were not presented in chapter 5 since most of them are produced in trace or negligible amounts compared to the other species that were plotted in figures 5.4-5.7 or they were not possible to identify with full accuracy and only reasonable hypothesis could lead to their identification. In the second part, some species that were identified and quantified during the oxidation of DNPEE are also shown. As for DIPEE, these species are produced in smaller quantities or are less interesting from the point of view of the analysis of the reactivity and the reaction pathways.

A final part of this appendix presents some results on the oxidation of butyl ethyl ether in the jet-stirred reactor. These experiments were not performed during this study, but they were used to test the mechanism for butyl ethyl ether, which is not available in the literature.

A.1 DIPEE: additional species

Figures A.1-A.4 show the mole fraction (measured and, when available, simulated) for some additional species that were identified and quantified in the jet-stirred reactor, for all equivalence ratios already introduced in chapter 5 (0.5, 1, 2 and 4). Most of these species are produced in small quantities (less than 10-20 ppm); nevertheless, for most of them the mechanism is still able to simulate the mole fraction profiles reasonably well.

Among the species presented in this appendix, some cyclic ethers can be found. These species are supposed to be cyclic ethers based on the fragments present in the mass spectrometry spectra. Nevertheless, they could not be individually identified and are included here in order to see that, even if they cannot be identified, the range of temperature where they are produced validate this hypothesis.

Isobutanal is produced in smaller quantities compared for example to isopentanal, but it still reaches a peak of around 40 ppm for the stoichiometric condition. The simulations are quite close to the experimental results for the stoichiometric conditions, while the accuracy is lower for the other conditions. Nevertheless, for the rich conditions both the experiments and the simulations show three different peaks, even if in slightly different positions. The first peak is well captured by the mechanism, while in the intermediate-high temperature the discrepancy grows bigger.

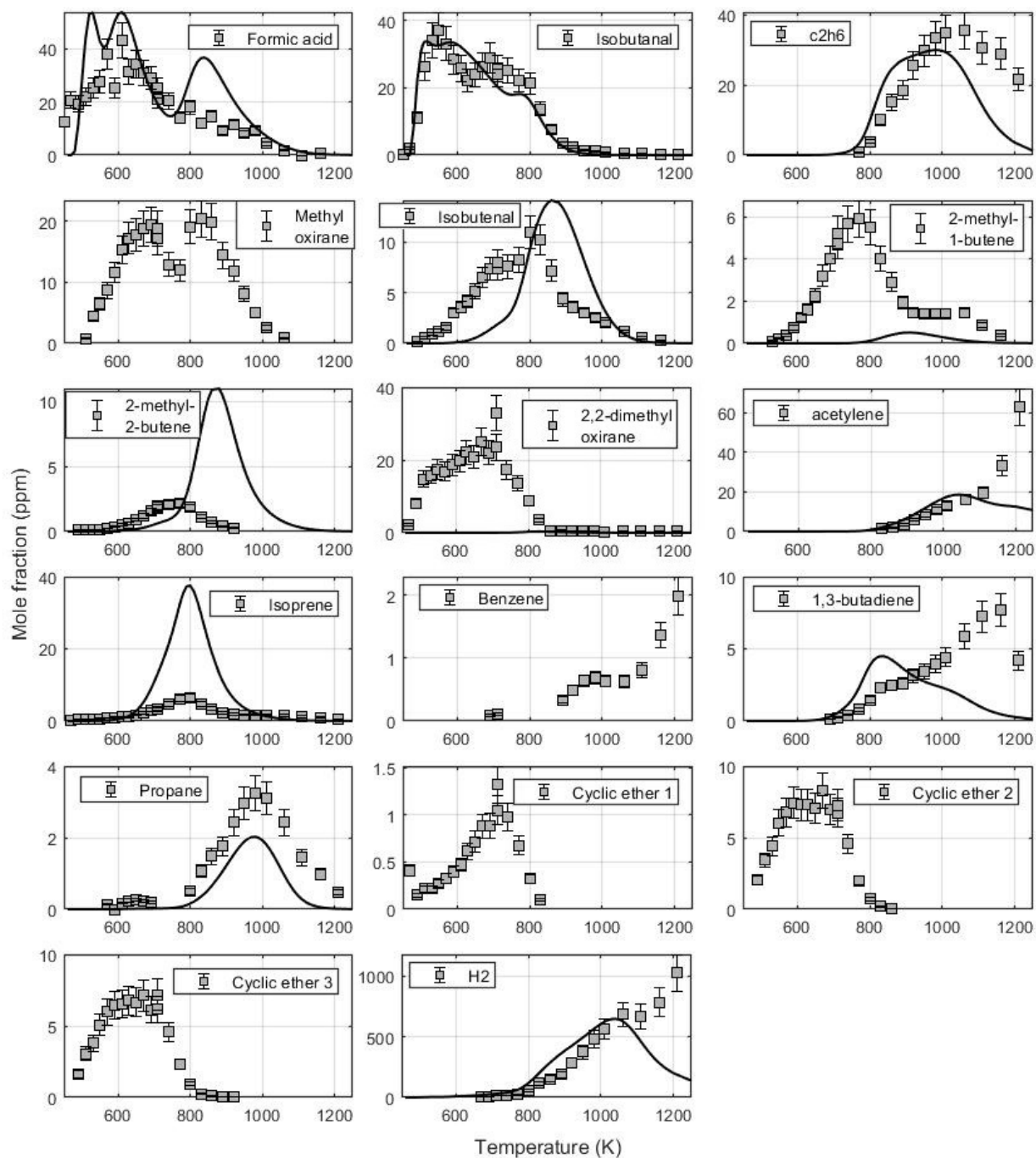


Figure A.1: Mole fractions of some products and intermediates during the oxidation of DIPEE in the JSR $\phi = 1$, $p = 10$ atm, $\tau = 700$ ms, $\chi_{0,\text{fuel}} = 1000$ ppm (in addition to the ones included in chapter 5).

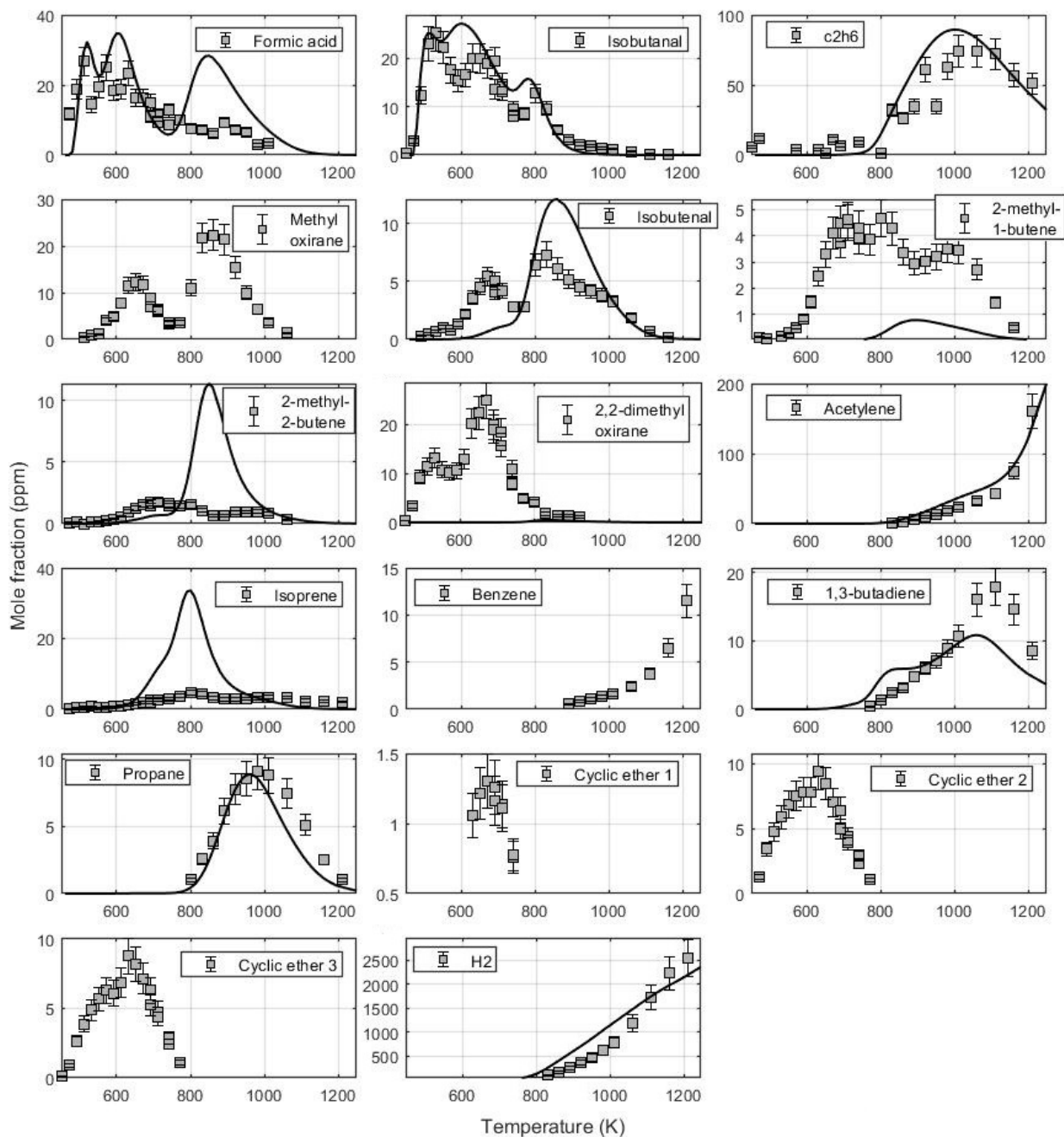


Figure A.2: Mole fractions of some products and intermediates during the oxidation of DIPEE in the JSR $\phi = 2$, $p = 10$ atm, $\tau = 700$ ms, $\chi_{0,\text{fuel}} = 1000$ ppm (in addition to the ones included in chapter 5).

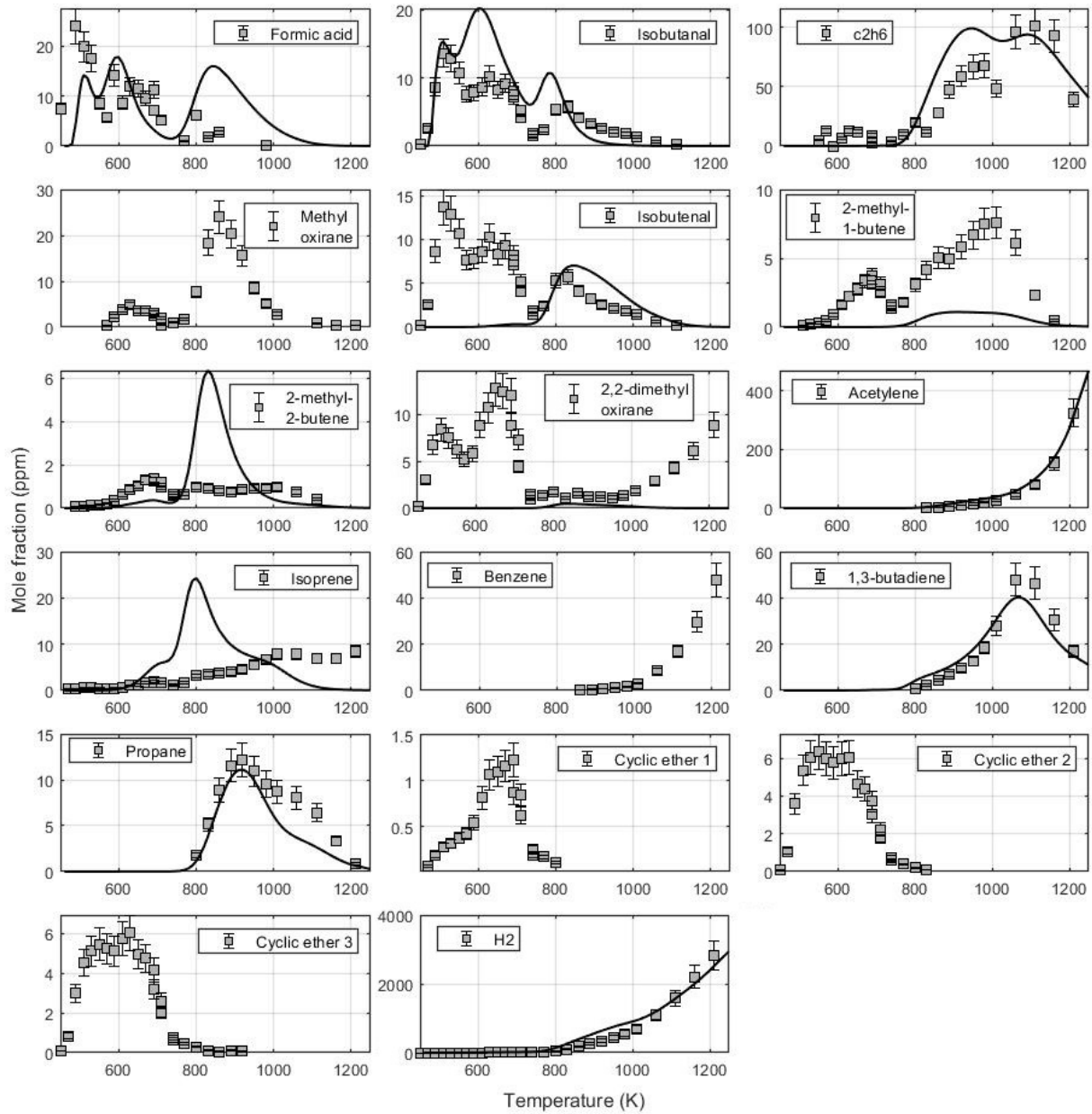


Figure A.3: Mole fractions of some products and intermediates during the oxidation of DIPEE in the JSR $\phi = 4$, $p = 10$ atm, $\tau = 700$ ms, $\chi_{0,\text{fuel}} = 1000$ ppm (in addition to the ones included in chapter 5).

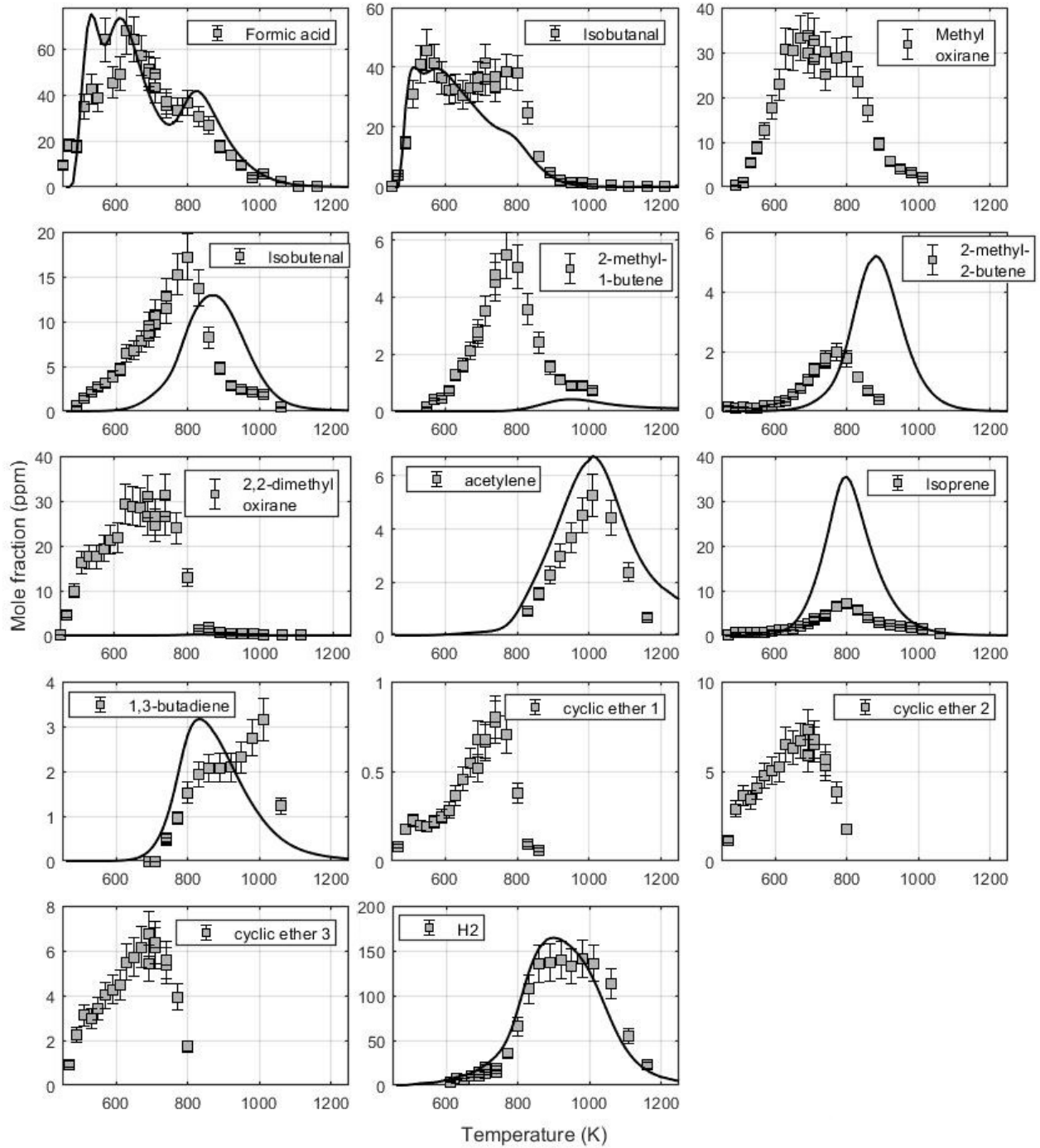


Figure A.4: Mole fractions of some products and intermediates during the oxidation of DIPEE in the JSR $\phi = 0.5$, $p = 10$ atm, $\tau = 700$ ms, $\chi_{0,\text{fuel}} = 1000$ ppm (in addition to the ones included in chapter 5).

A.2 DNPEE: additional species

As for DIPEE, some additional species that were identified and quantified are shown in figures A.5-A.8, for all equivalence ratios (0.5, 1, 2 and 4).

Also in this case, it is possible to find another aldehyde which is formed, i.e. n-butanal. Similarly to isobutanal in the case of DIPEE, this species is formed up to around 30 ppm for the stoichiometric condition. If for isobutanal it was possible to identify two or even three peaks, which were a sign of the double-NTC of DIPEE, for n-butanal it is possible to see one clear peak, followed by a small plateau (for example around 620-700 K for the stoichiometric conditions), which can be seen as logical considering the weak NTC of DNPEE, which also appeared more like a plateau than a real decrease in the reactivity.

As for the other species, similar to what explained for DIPEE, three cyclic ethers supposedly formed from the QOOH radicals of the fuel were found. Once again, it is not possible to individually identify them. Nevertheless, from the position of the peaks after the fuel in the GC spectra and from the analysis of the fragments in the MS spectrum, it is a valid hypothesis.

As previously explained, the mechanism for DNPEE is still under development; nevertheless, it is important to have a set of data as important as possible in order to be able to validate and improve it.

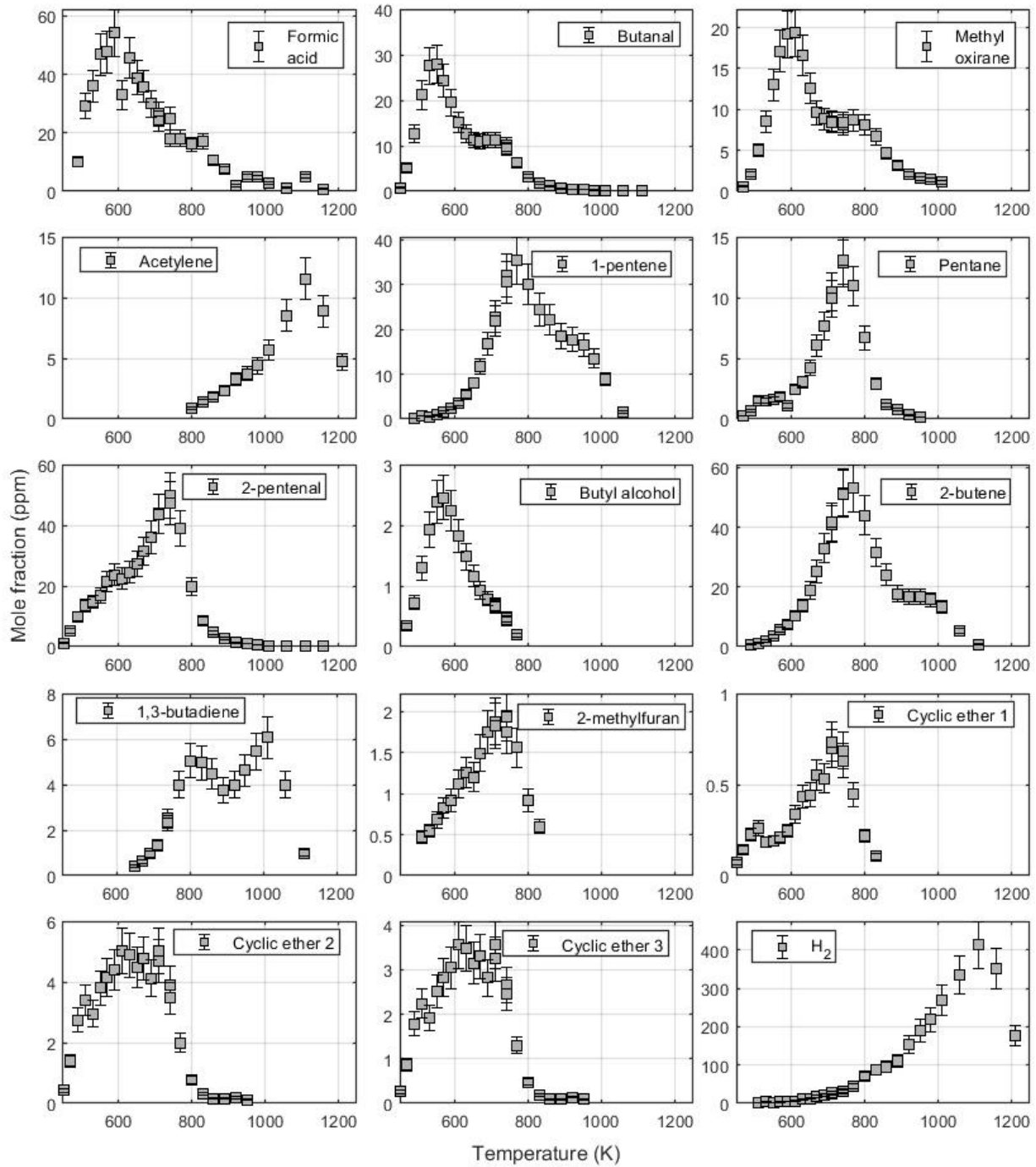


Figure A.5: Mole fractions of some products and intermediates during the oxidation of DNPEE in the JSR $\phi = 1$, $p = 10$ atm, $\tau = 700$ ms, $\chi_{0,\text{fuel}} = 1000$ ppm (in addition to the ones included in chapter 5).

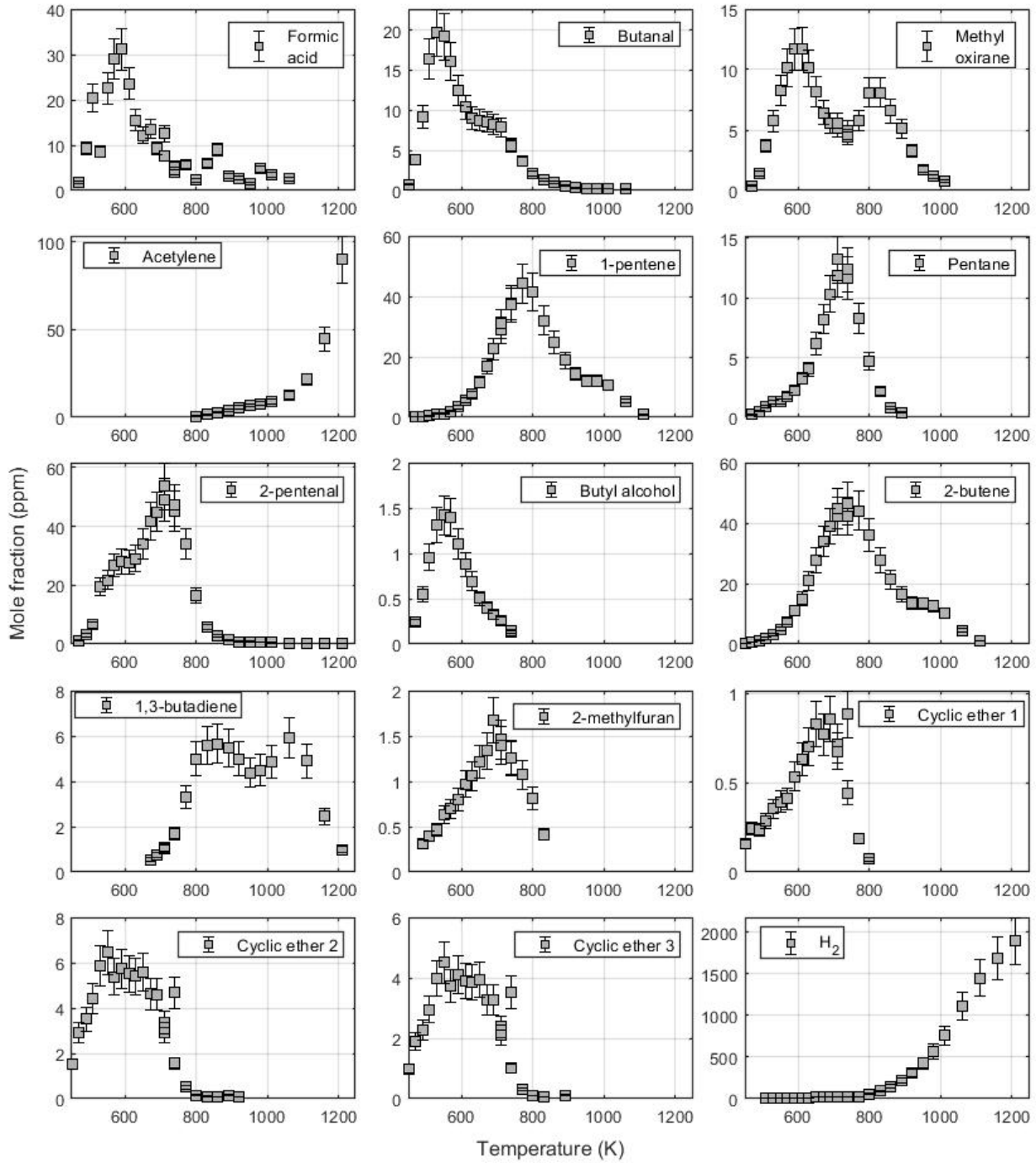


Figure A.6: Mole fractions of some products and intermediates during the oxidation of DNPEE in the JSR $\phi = 2$, $p = 10$ atm, $\tau = 700$ ms, $\chi_{0,\text{fuel}} = 1000$ ppm (in addition to the ones included in chapter 5).

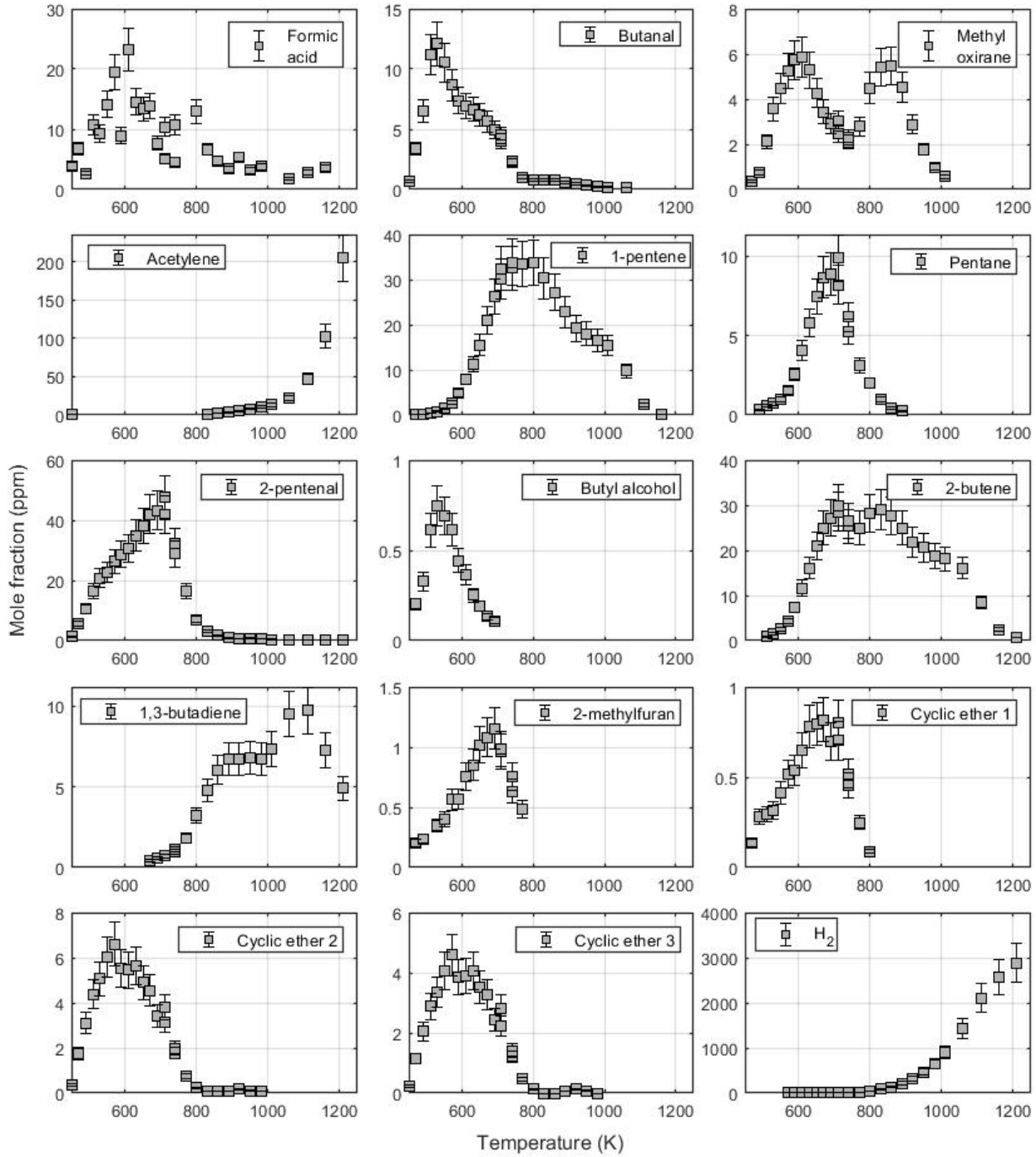


Figure A.7: Mole fractions of some products and intermediates during the oxidation of DNPEE in the JSR $\phi = 4$, $p = 10$ atm, $\tau = 700$ ms, $\chi_{0,\text{fuel}} = 1000$ ppm (in addition to the ones included in chapter 5).

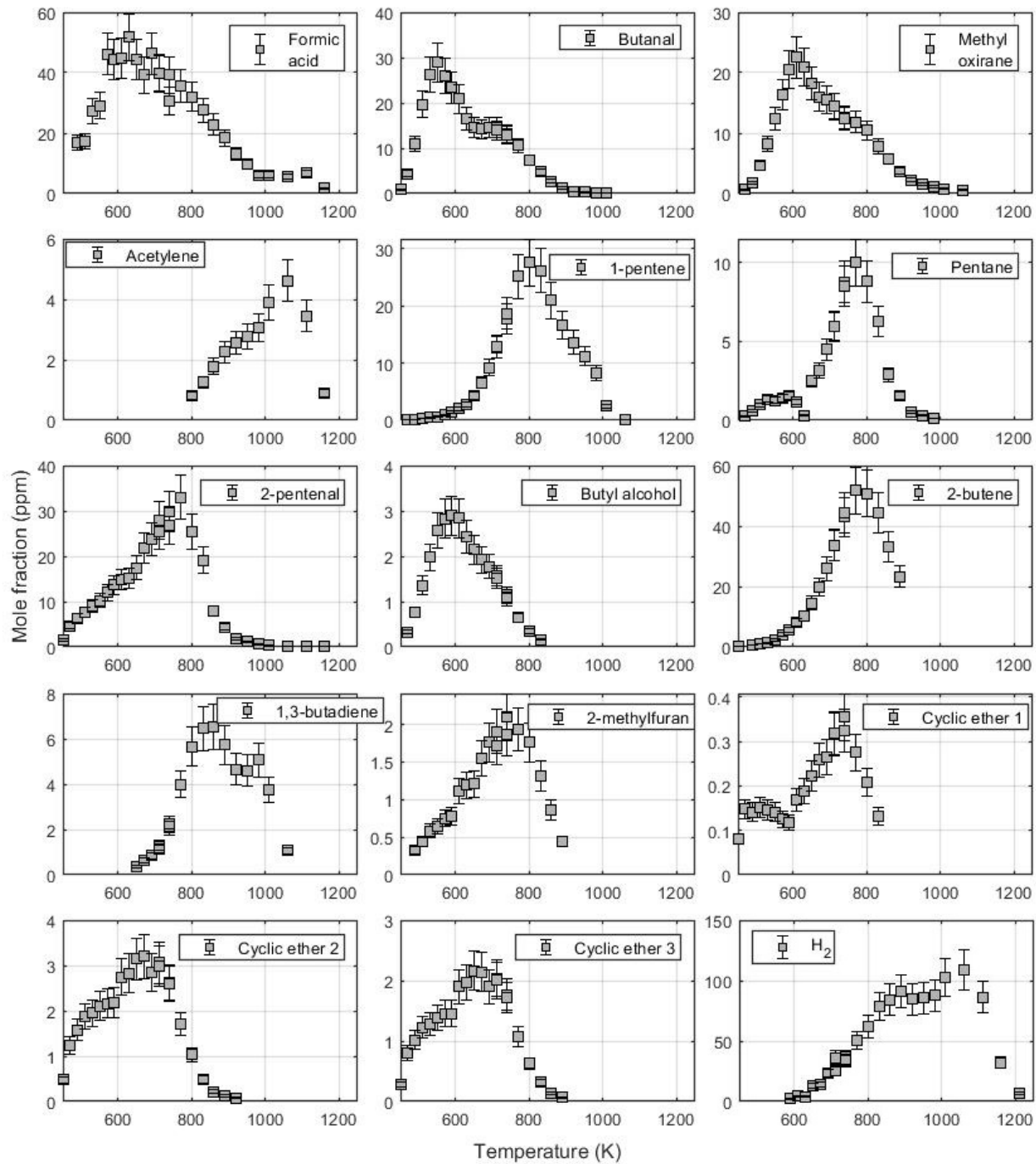


Figure A.8: Mole fractions of some products and intermediates during the oxidation of DNPEE in the JSR $\phi = 0.5$, $p = 10$ atm, $\tau = 700$ ms, $\chi_{0,\text{fuel}} = 1000$ ppm (in addition to the ones included in chapter 5).

A.3 BEE: further validation

This final section of this appendix is dedicated to the further validation of butyl ethyl ether thanks to the experimental data on its oxidation in the jet-stirred reactor. As previously explained, these experiments were not performed during this PhD work and they are still being analysed. Nevertheless, considering that no other data is available on the fundamentals of BEE combustion, this data set represents the only possible validation target other than the ignition delay times presented in chapter 6.

The experiments were performed in the same jet-stirred reactor presented in chapter 3, under the same conditions considered for the other ethers: $p = 10$ atm, $\tau = 0.7$ s, initial fuel mole fraction = 1000 ppm, $\phi = 0.5, 1, 2$ and 4. The experimental mole fractions of the fuel and some species, as well as the simulations, are shown in Figures A.9-A.12. Before considering the performance of the mechanism, which is the main focus of this section, a few remarks on the experimental results may be interesting.

First of all, it can be seen that this fuel shows a behaviour different to some extent from the other ethers: looking for example at the mole fraction of the fuel for the stoichiometric condition, it can be seen that there is a first zone at low temperature where the reactivity rapidly increases as the temperature increases. Then, at around 550 K a plateau is reached and the mole fraction of the fuel seems to be constant at around 600 ppm until 690 K. At this temperature, the reactivity starts decreasing when the temperature increases, up to 770 K, where the mole fraction is back to 916 ppm. After this point, the high temperature zone is reached and the reactivity starts increasing again, up to around 1100 K., where all the fuel is consumed. A similar behaviour can be seen for the rich mixture, with the mole fraction going back to the initial value at 740-770 K; on the other hand, for the lean mixture the reactivity seems to be stronger overall, with the plateau covering a smaller range (around 650-710 K, while before the reactivity slows down, but does not stagnate) and the mole fraction never goes back to more than 670 ppm. This trend is interesting, since it seems to be almost an intermediate between the single NTC of DEE and the double-NTC shown by DBE.

First, it has to be noted that there was an impurity in the fuel: in the first point of all the experiments, around 10 ppm of butanol were measured and its trend shows its own oxidation, with a small NTC zone. It was included in the simulations, adding it to the reactants, and the results are included in the figures, showing a reasonable agreement with the experimental measurements.

Similar to all the other ethers, some aldehydes are found among the products of butyl ethyl ether. The smallest one, formaldehyde, which is considered as a marker of low-temperature reactivity, is produced under all conditions, with mole fraction as high as 300 ppm for the lean condition. For the three conditions, the experiments show two peaks, more pronounced for the rich condition. Acetaldehyde is also produced in large quantities for all conditions and it reaches a peak of more than 300 ppm for the lean mixture. For this species, there are clearly two peaks for the rich condi-

tion, while they appear less distinct for the stoichiometric one and for the lean condition only one peak is seen. This is also quite well reproduced by the mechanism, even if the maximum mole fraction is underestimated for $\phi = 0.5$ and slightly overestimated for $\phi = 2$. Another aldehyde, which was typical also for DBE, is n-butanal. For all conditions, n-butanal shows a trend very similar to acetaldehyde, with two clear peaks for the rich condition, two less distinct peaks for the stoichiometric one and one single peak under lean conditions. The maximum mole fractions are slightly lower than acetaldehyde for all conditions. The mechanism can reproduce these results quite well, even if there is an overestimation of the mole fractions for the stoichiometric and rich conditions. Considering the production of acids, typical of ether oxidation, it is possible to see that both acetic and butanoic acid are produced. Acetic acid was identified among the products of diethyl ether, while butanoic acid was the typical acid produced during the oxidation of dibutyl ether. Both these acids are produced at low temperature, with the peak mole fraction of acetic acid which is around three times that of butanoic acid. The simulation is quite close to correctly represent the mole fraction of acetic acid, even if there is a slight underprediction of the peak value and a small production at high temperature, which was not measured in the experiments. The mole fraction of butanoic acid, on the other hand, is largely underpredicted, especially for lean and stoichiometric conditions.

In general, the simulations are in reasonable agreement with the experimental data. There is a slight overprediction on the reactivity of the fuel, for all the conditions, but the mechanism is capable of predicting the trend quite well, with the initial decrease of the mole fraction, followed by the plateau and by the increase, until the reactivity increases again in the higher temperature zone. The simulations are also overall in fairly good agreement with the measured mole fractions of the main products of butyl ethyl ether, even if some discrepancies can still be found.

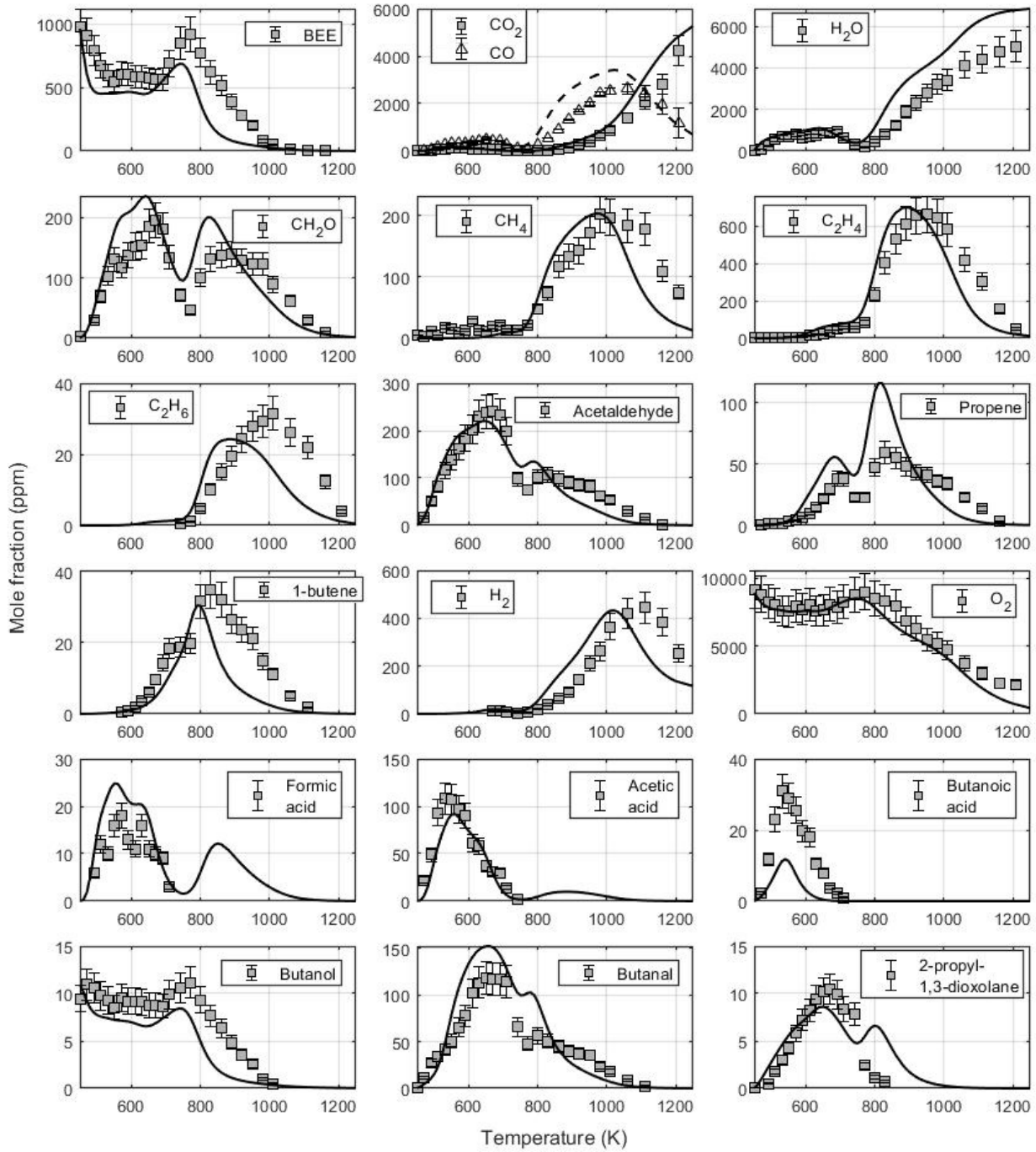


Figure A.9: Mole fractions of some products and intermediates during the oxidation of BEE in the JSR $\phi = 1$, $p = 10$ atm, $\tau = 700$ ms, $\chi_{0,\text{fuel}} = 1000$ ppm.

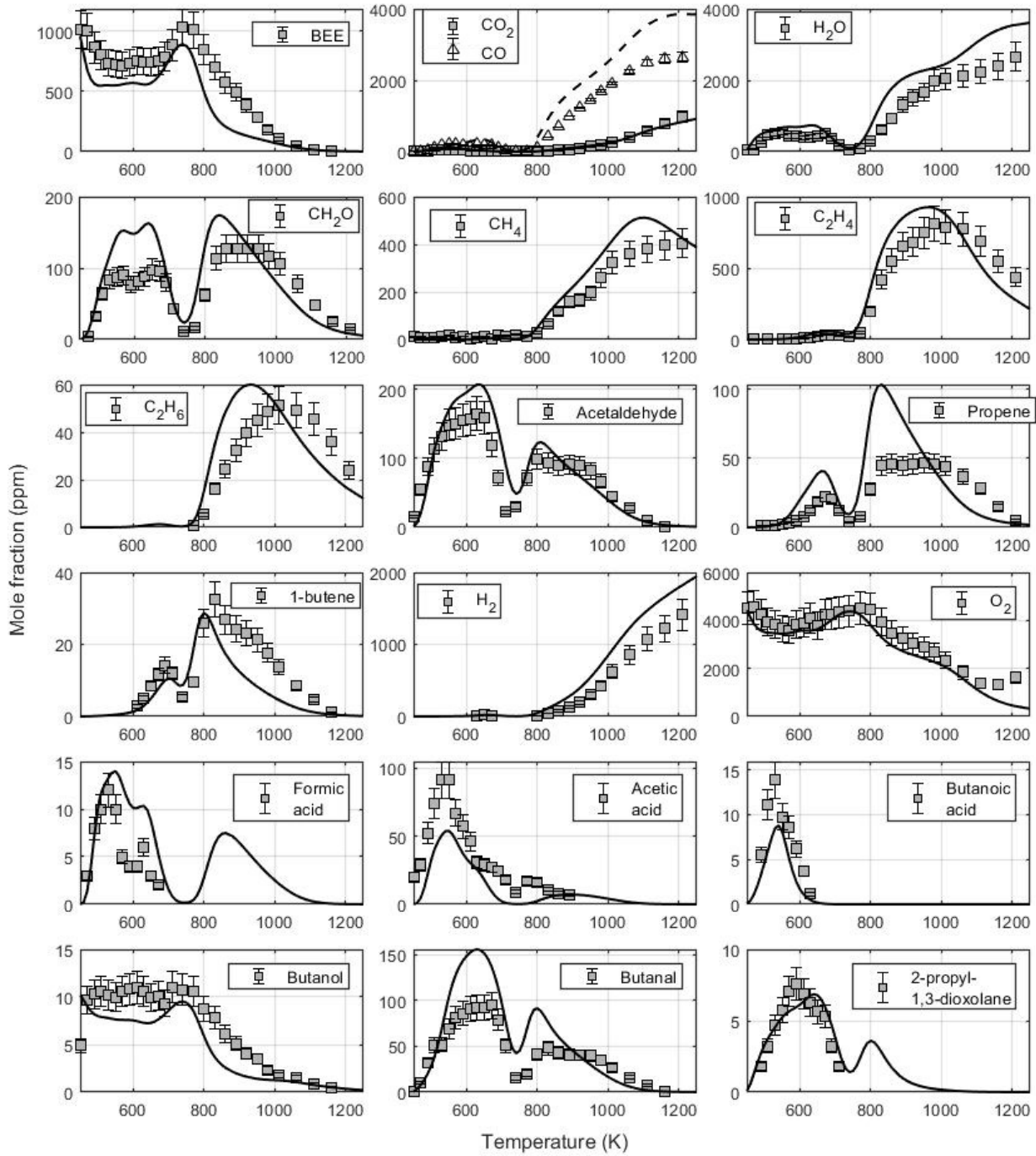


Figure A.10: Mole fractions of some products and intermediates during the oxidation of BEE in the JSR $\phi = 2$, $p = 10$ atm, $\tau = 700$ ms, $\chi_{0,\text{fuel}} = 1000$ ppm.

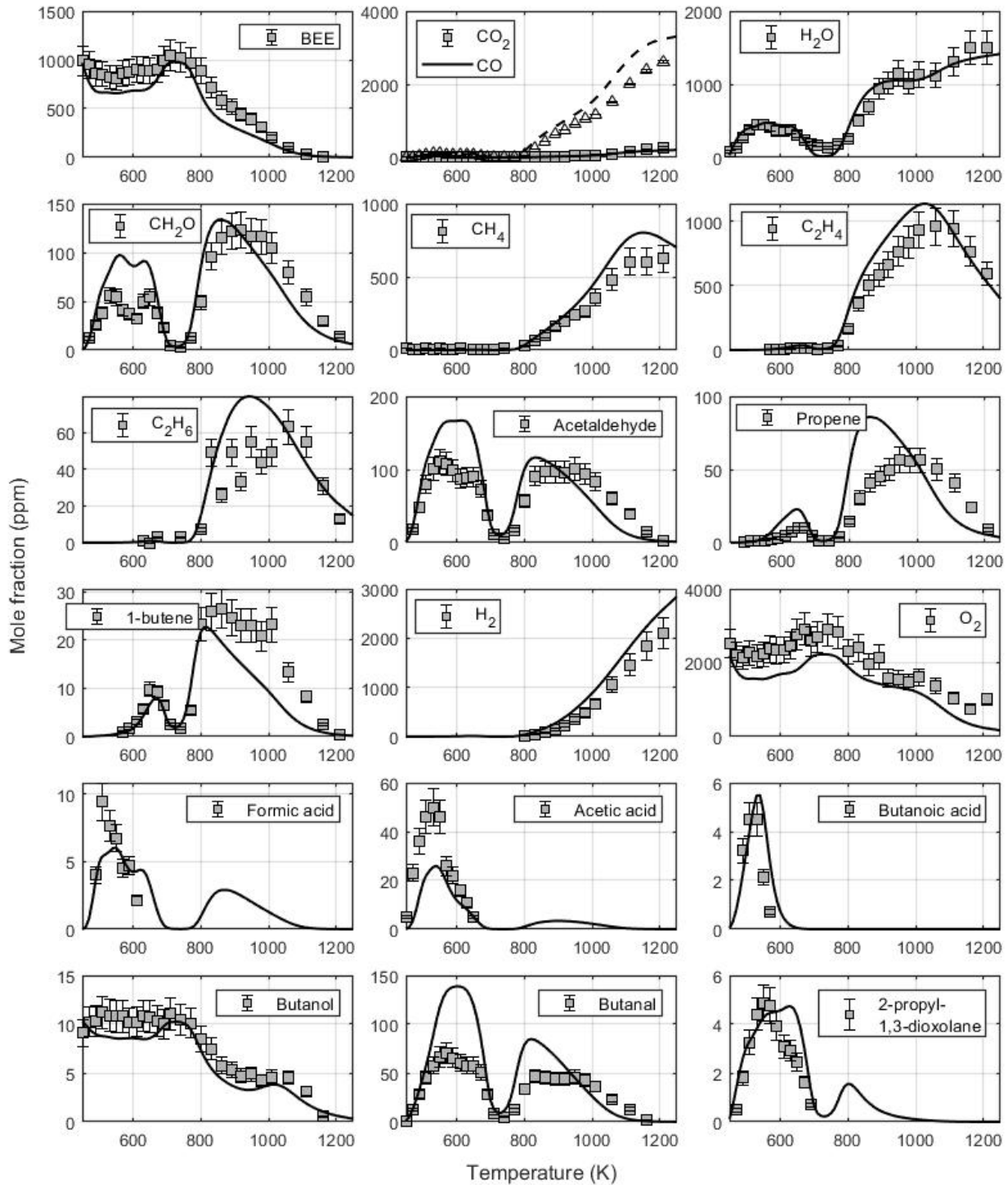


Figure A.11: Mole fractions of some products and intermediates during the oxidation of BEE in the JSR $\phi = 4$, $p = 10$ atm, $\tau = 700$ ms, $\chi_{0,\text{fuel}} = 1000$ ppm.

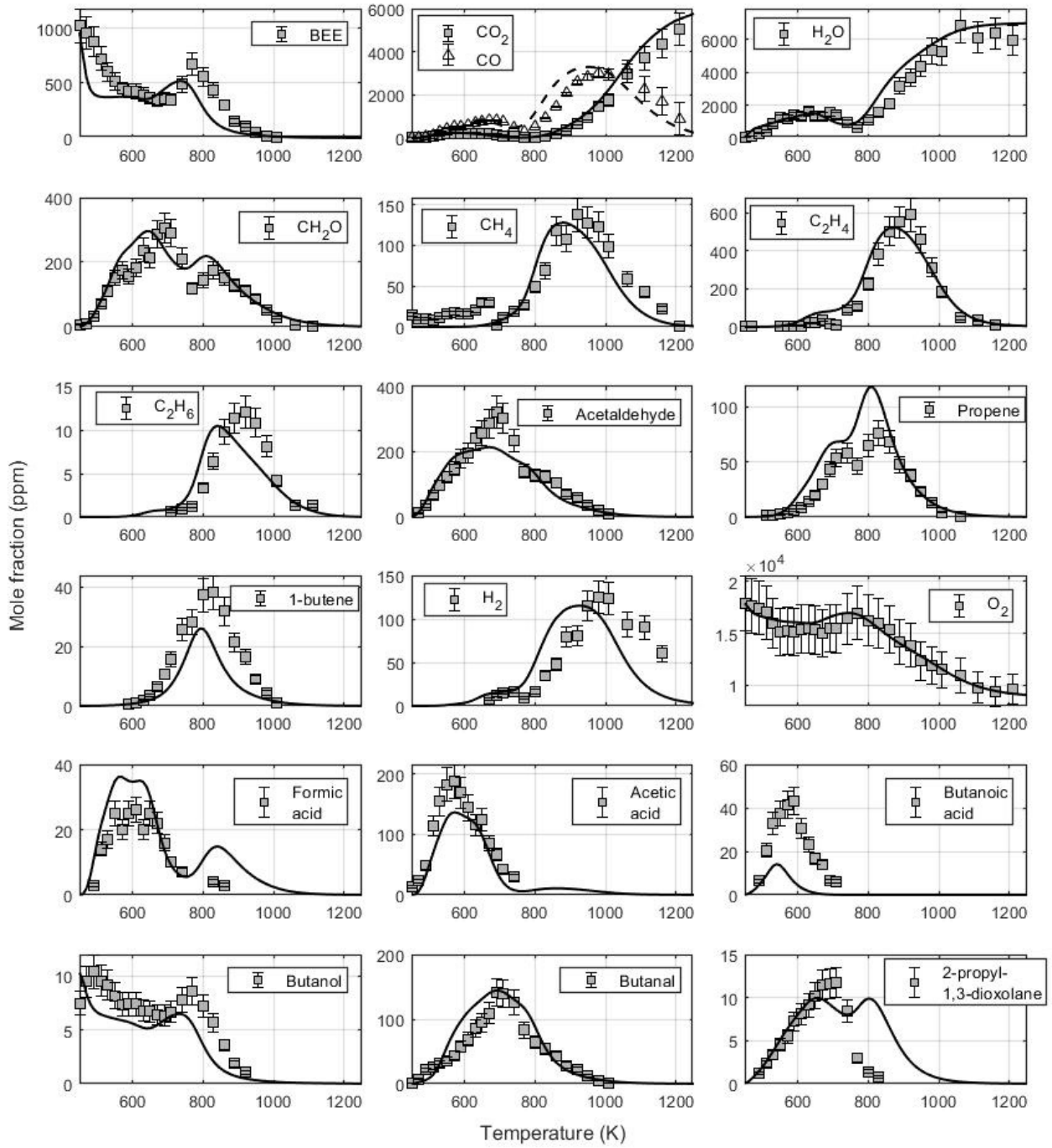


Figure A.12: Mole fractions of some products and intermediates during the oxidation of BEE in the JSR $\phi = 0.5$, $p = 10$ atm, $\tau = 700$ ms, $\chi_{0,\text{fuel}} = 1000$ ppm.

Appendix B

RCM: pressure profiles and additional results

B.1 Pressure profiles

B.1.1 Diethyl ether

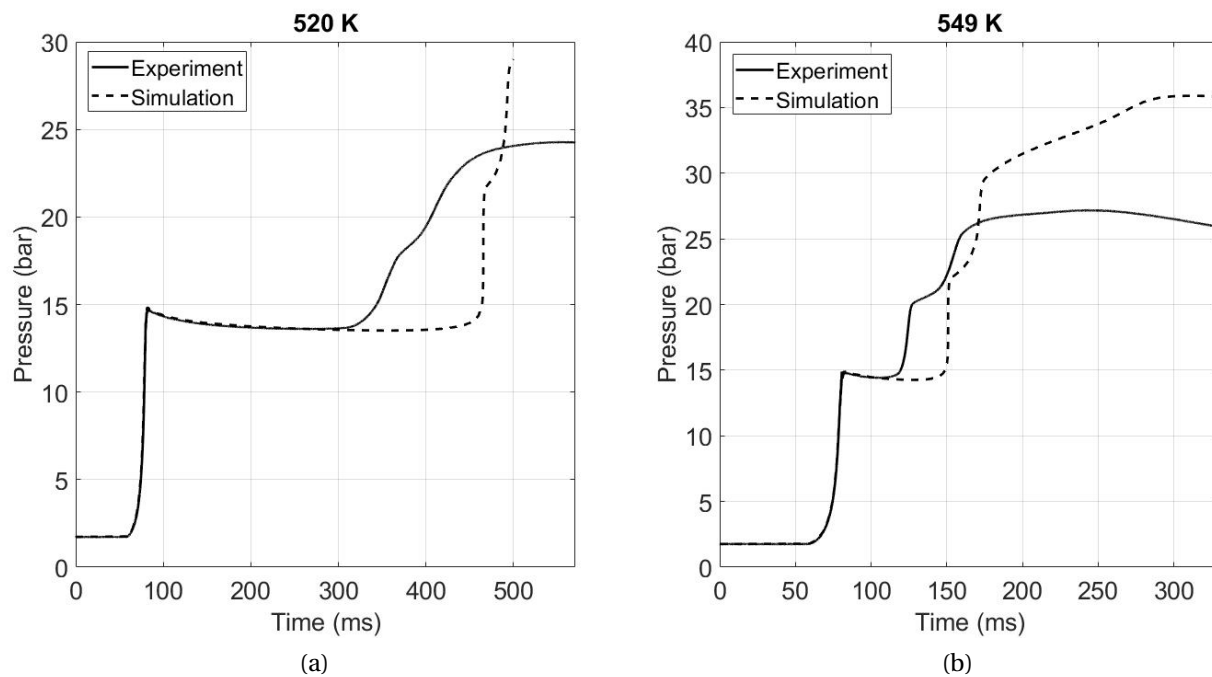


Figure B.1: Diethyl ether: $\phi = 1$, dilution = 10 (inert gas: 100% CO₂), $p_c = 15$ bar, DEE = 1.5%.

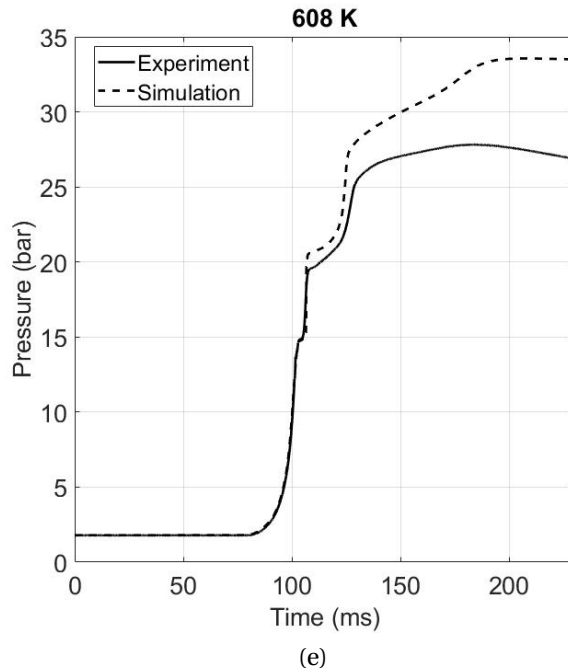
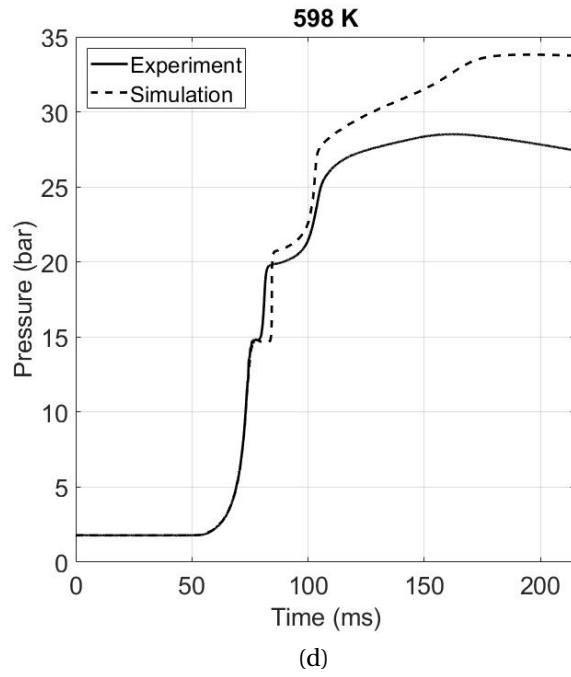
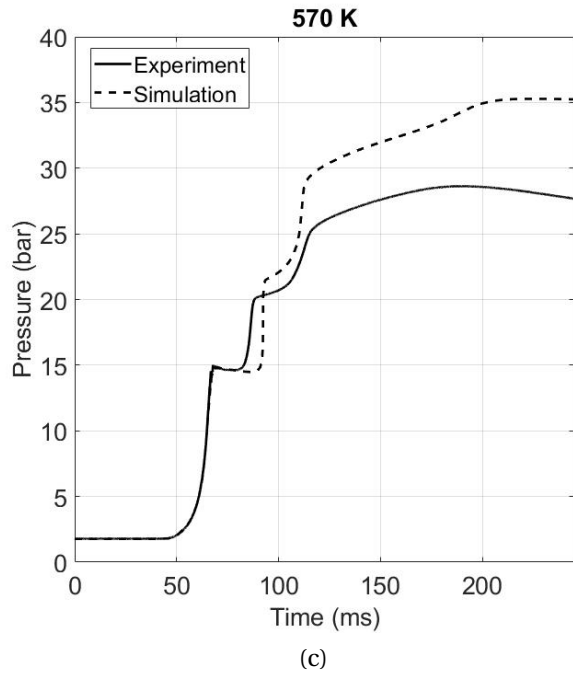


Figure B.1: Diethyl ether: $\phi = 1$, dilution = 10 (inert gas: 100% CO₂), $p_c = 15$ bar, DEE = 1.5%.

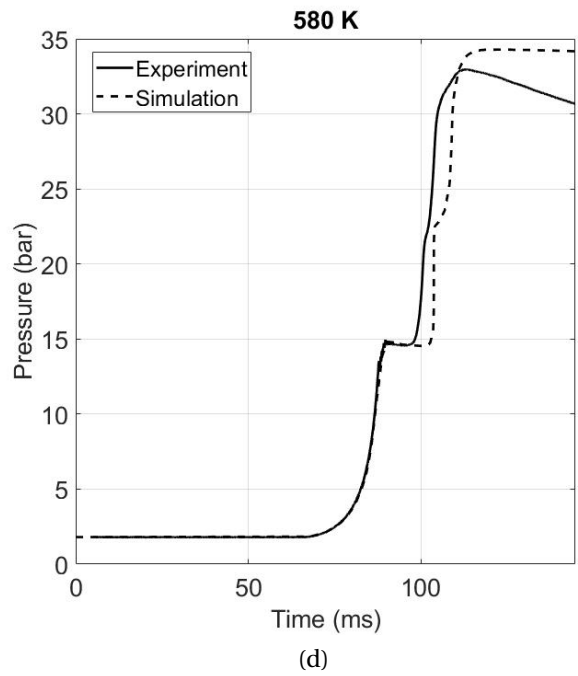
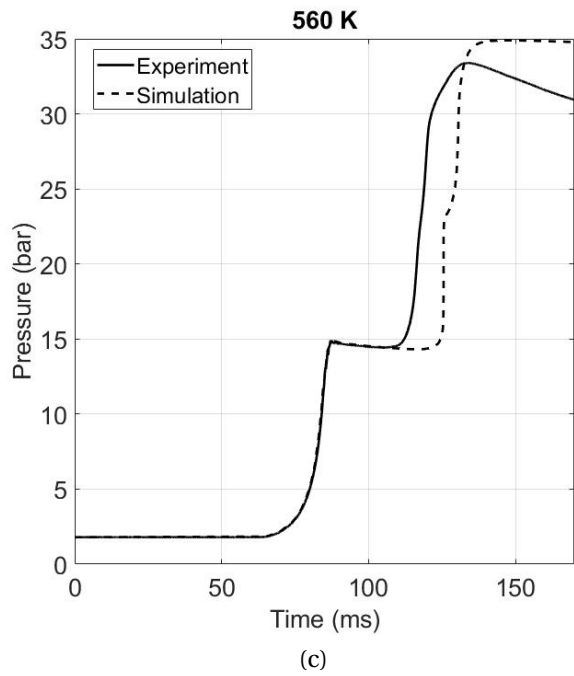
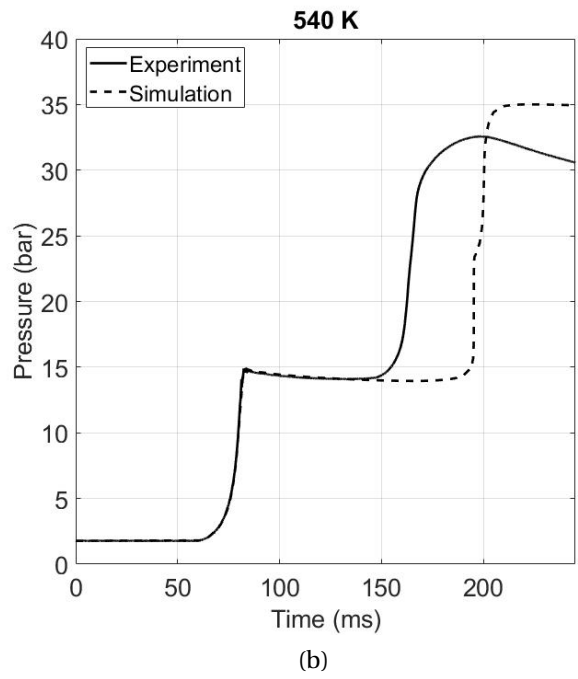
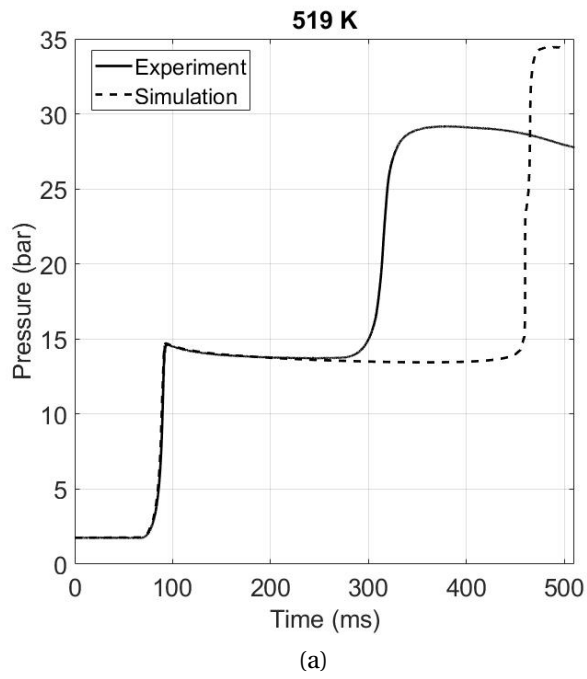


Figure B.2: Diethyl ether: $\phi = 2$, dilution = 10 (inert gas: 100% CO₂), $p_c = 15$ bar, DEE = 2.9%.

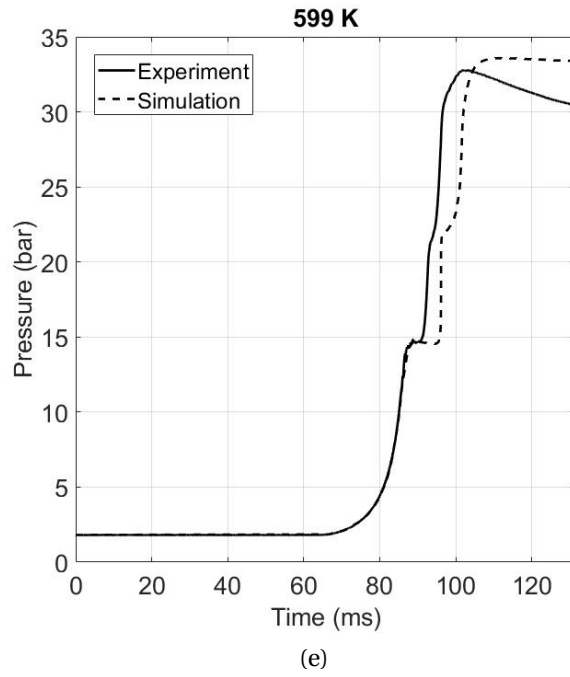


Figure B.2: Diethyl ether: $\phi = 2$, dilution = 10 (inert gas: 100% CO₂), $p_c = 15$ bar, DEE = 2.9%.

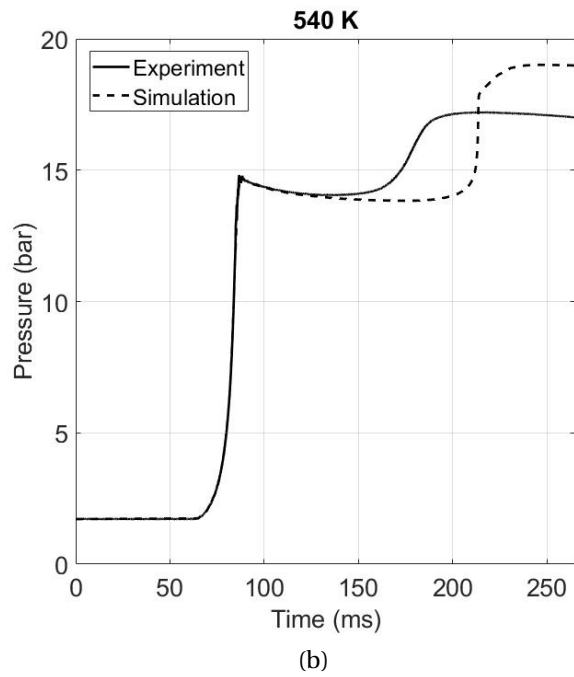
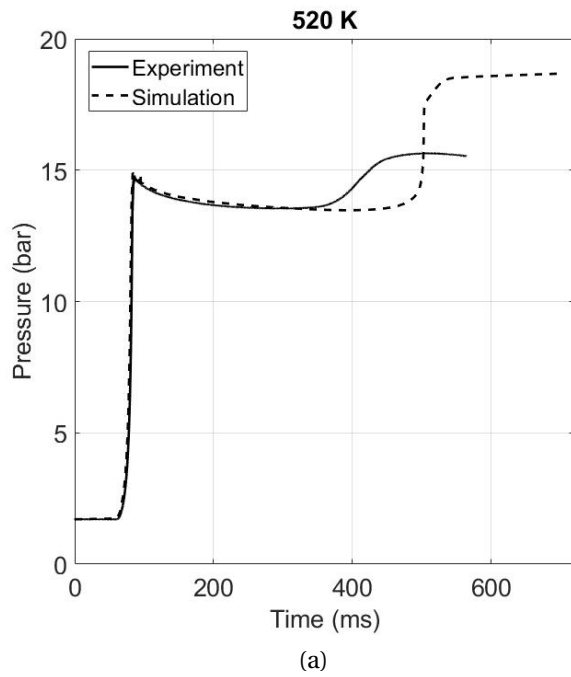
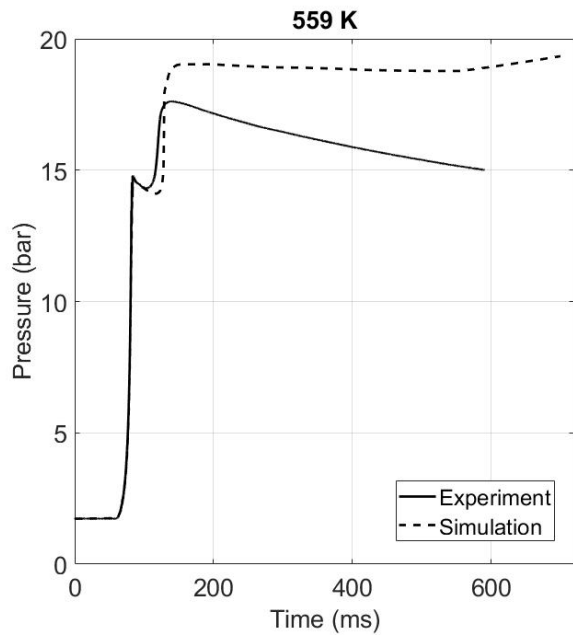
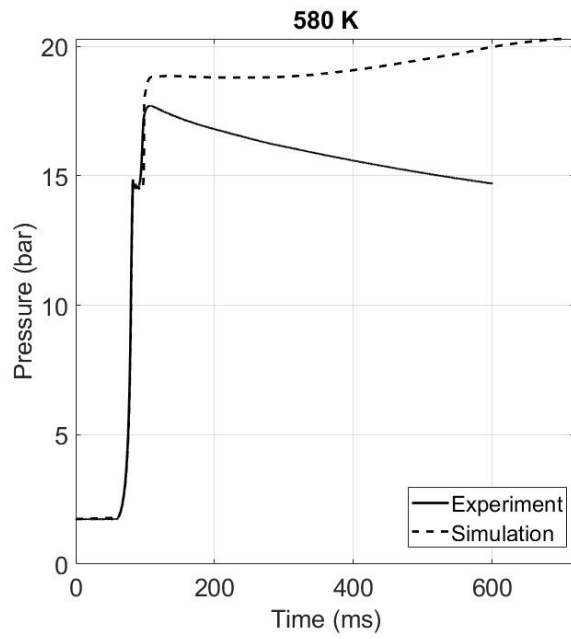


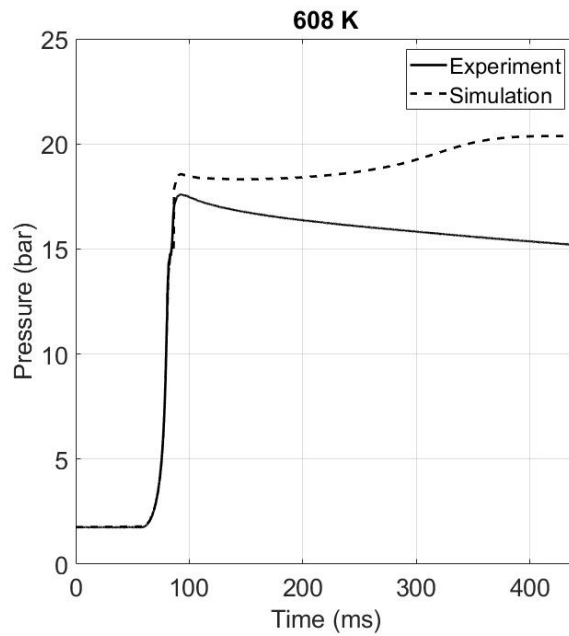
Figure B.3: Diethyl ether: $\phi = 0.5$, dilution = 10 (inert gas: 100% CO₂), $p_c = 15$ bar, DEE = 0.8%.



(c)



(d)



(e)

Figure B.3: Diethyl ether: $\phi = 0.5$, dilution = 10 (inert gas: 100% CO₂), $p_c = 15$ bar, DEE = 0.8%.

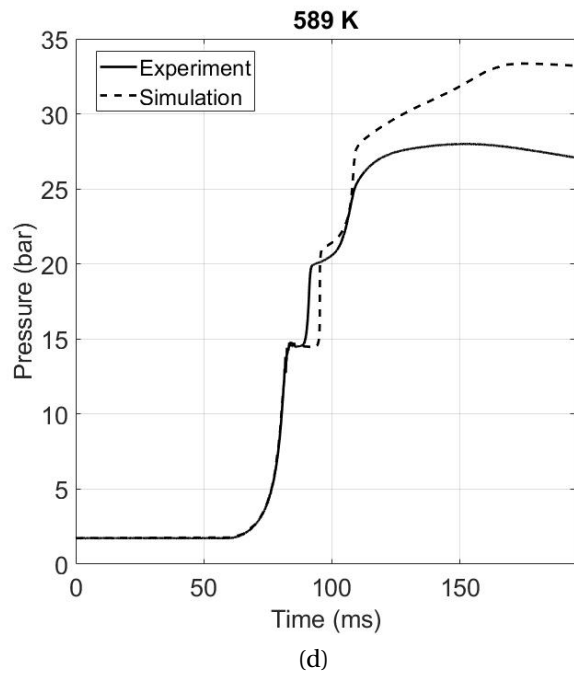
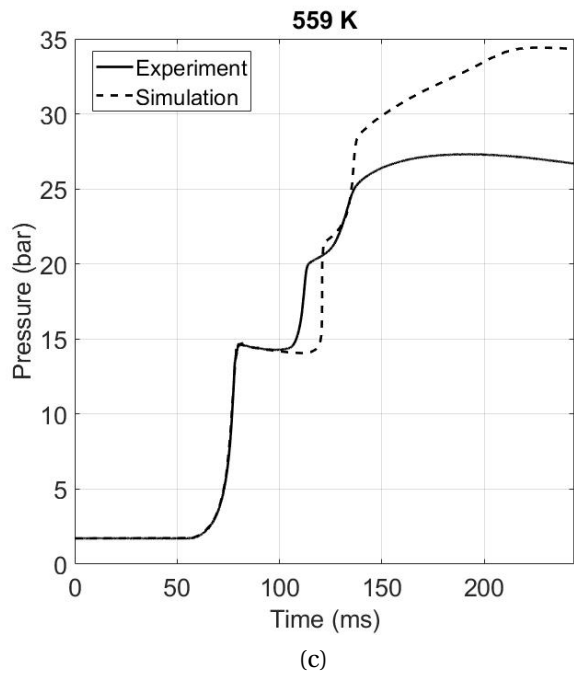
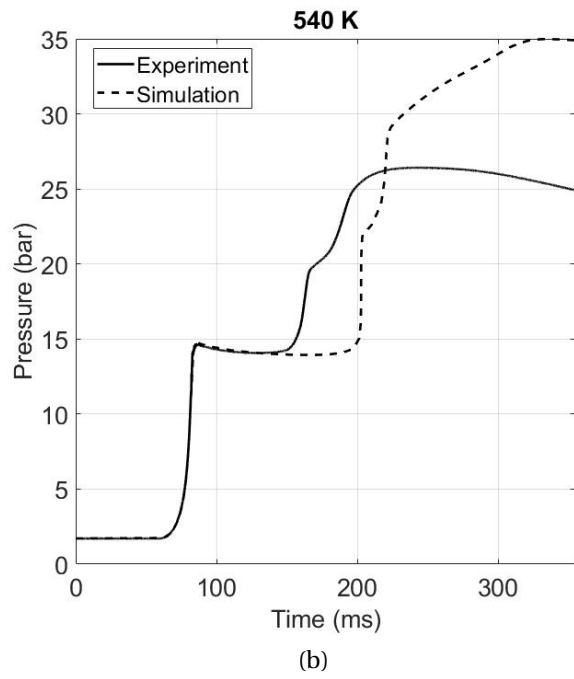
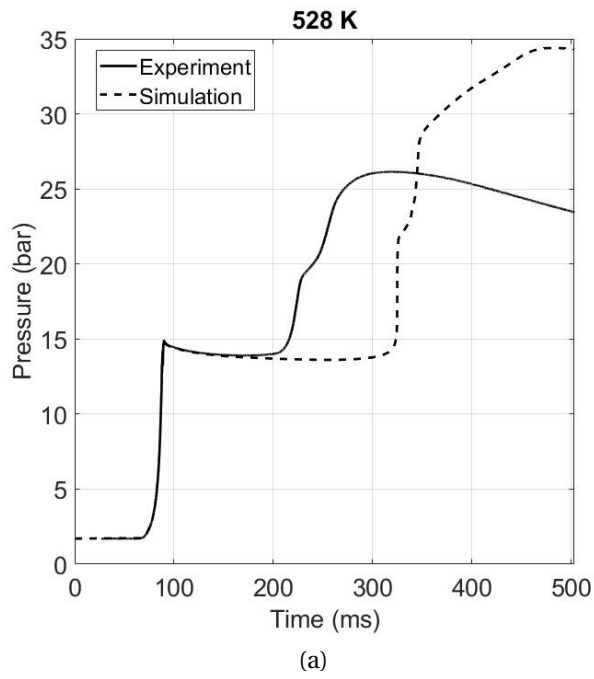


Figure B.4: Diethyl ether: $\phi = 0.5$, dilution = 5 (inert gas: 100% CO₂), $p_c = 15$ bar, DEE = 1.37%.

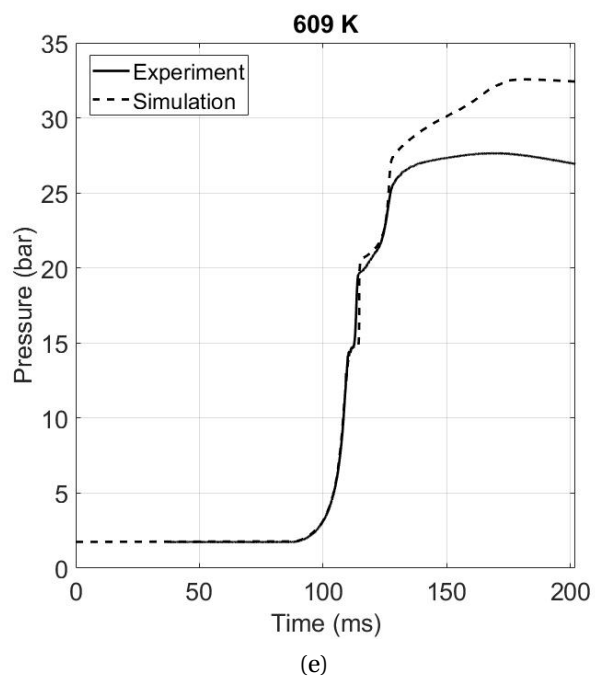


Figure B.4: Diethyl ether: $\phi = 0.5$, dilution = 5 (inert gas: 100% CO₂), $p_c = 15$ bar, DEE = 1.37%.

B.1.2 Di-n-propyl ether

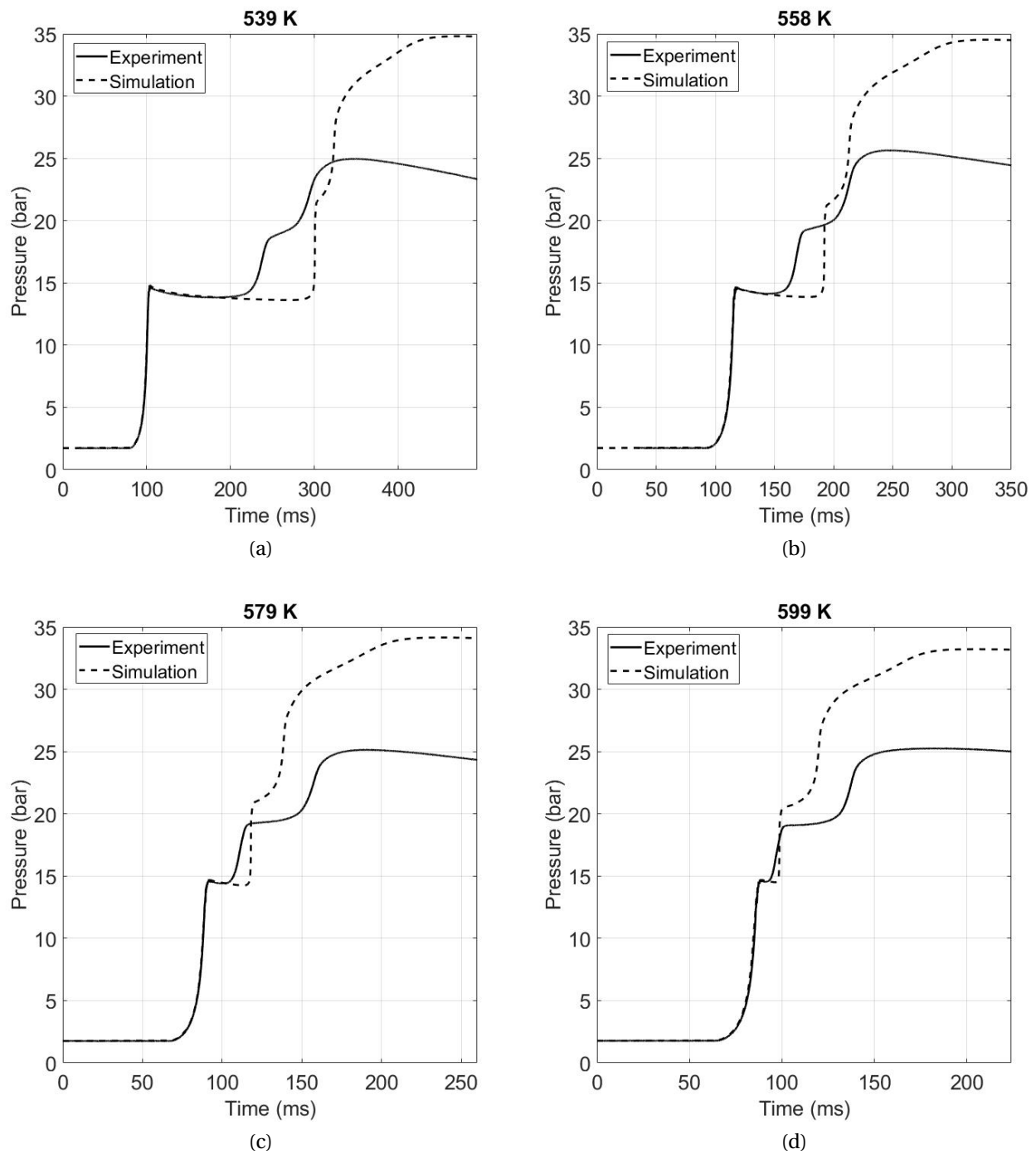


Figure B.5: Di-n-propyl ether: $\phi = 1$, dilution = 10 (inert gas: 100% CO₂), $p_c = 15$ bar, DPE = 1.0%.

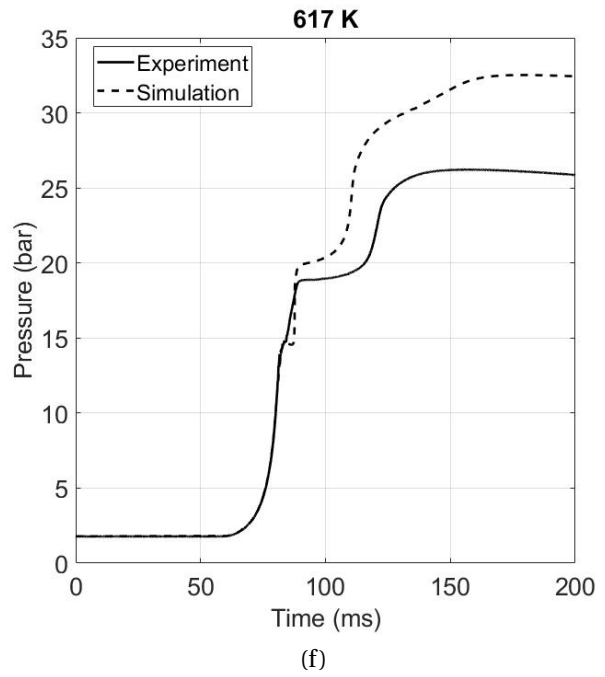
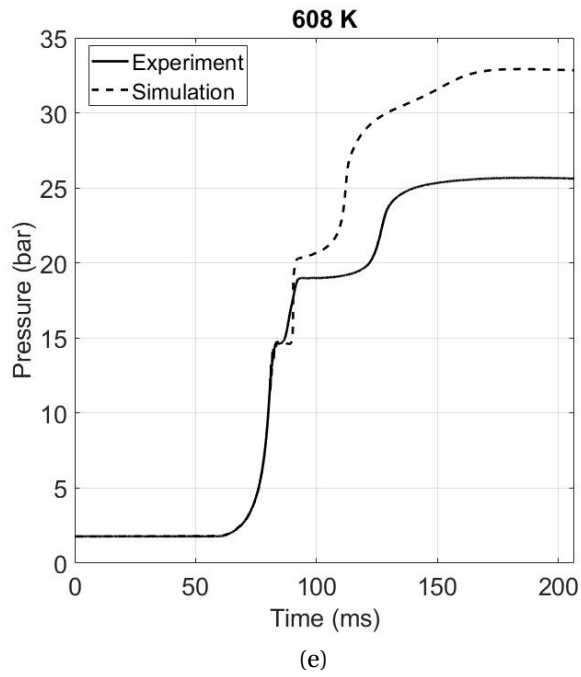


Figure B.5: Di-n-propyl ether: $\phi = 1$, dilution = 10 (inert gas: 100% CO₂), $p_c = 15$ bar, DPE = 1.0%.

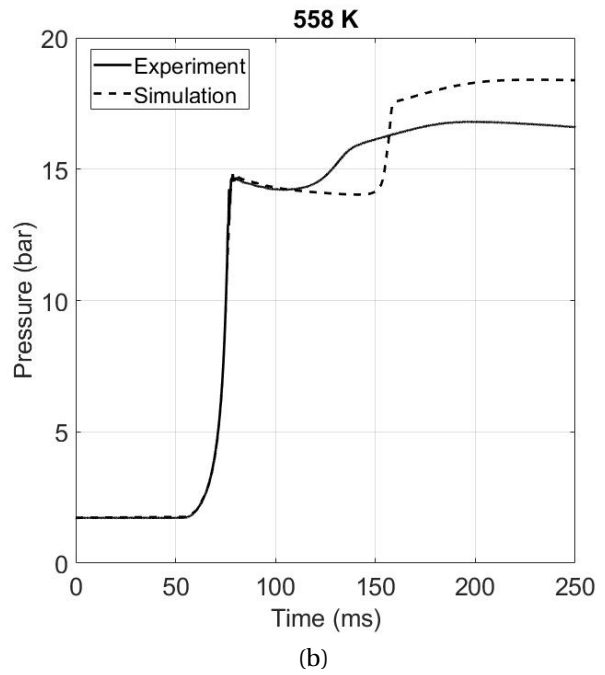
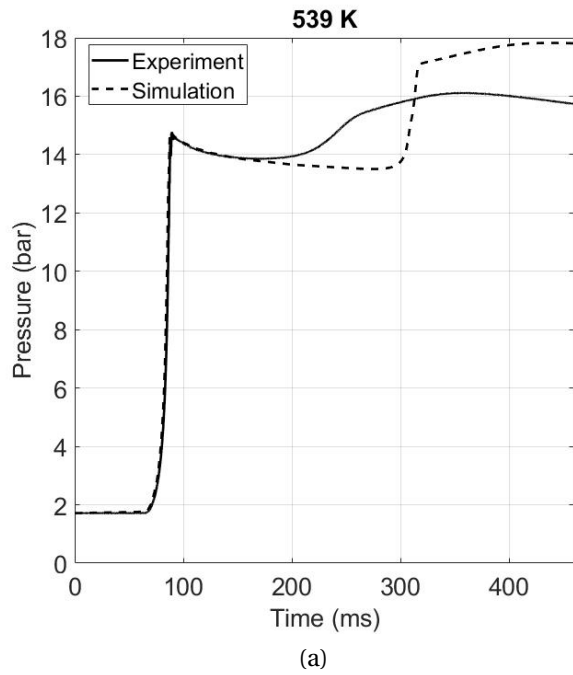


Figure B.6: Di-n-propyl ether: $\phi = 0.5$, dilution = 10 (inert gas: 100% CO₂), $p_c = 15$ bar, DPE = 0.5%.

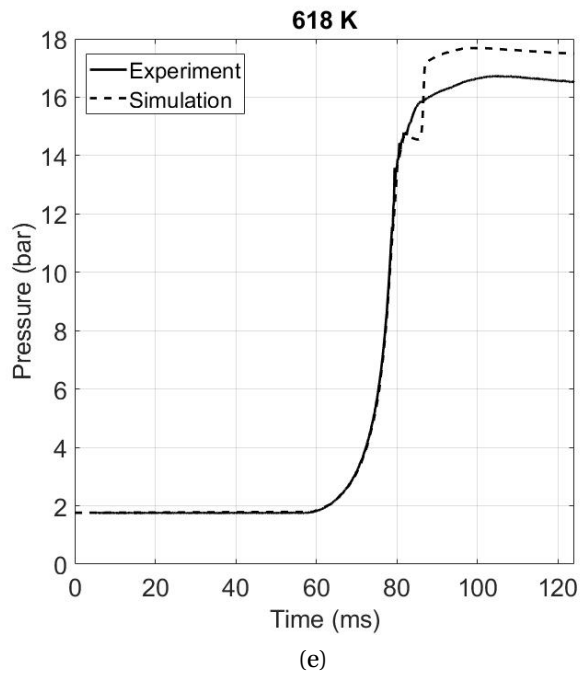
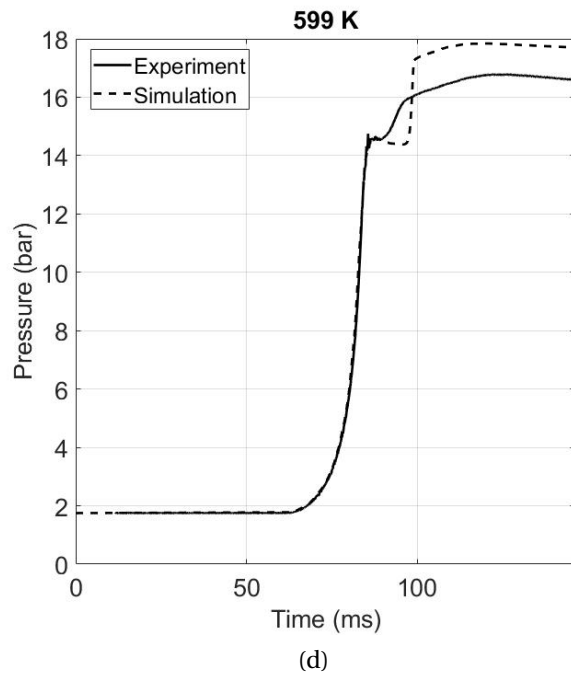
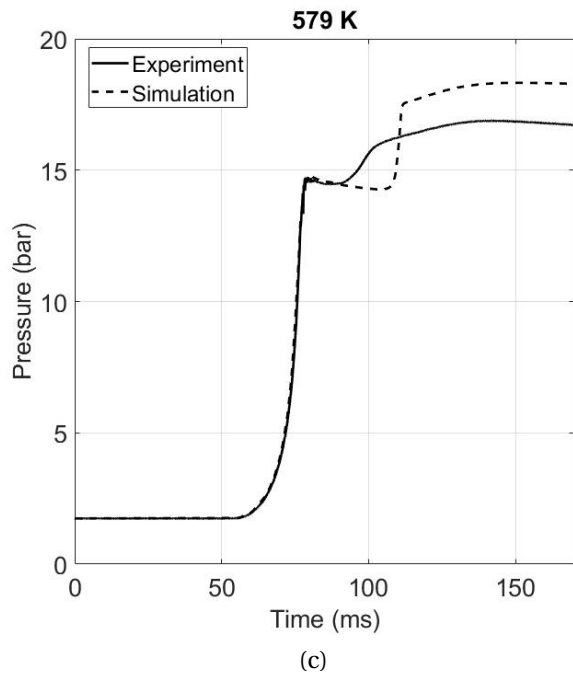
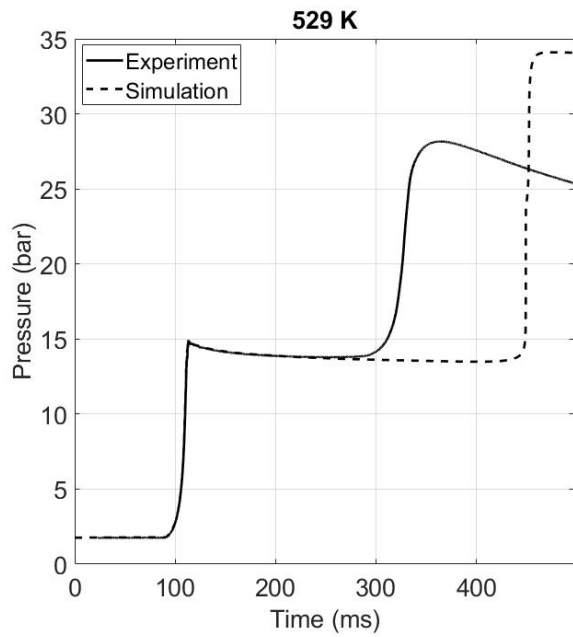
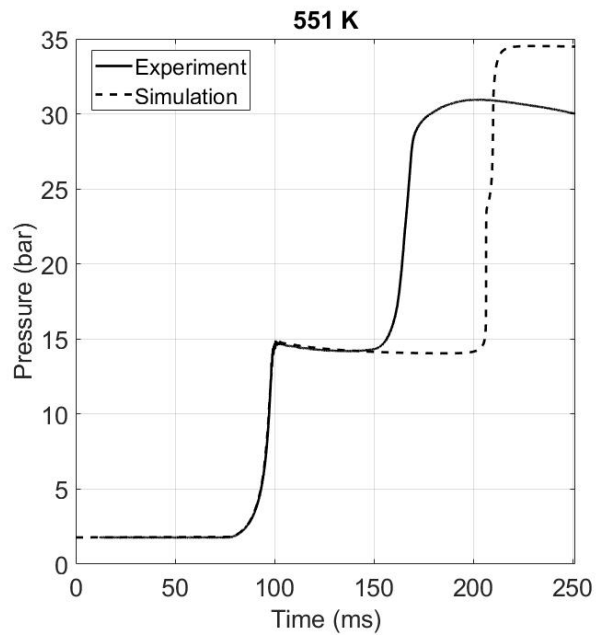


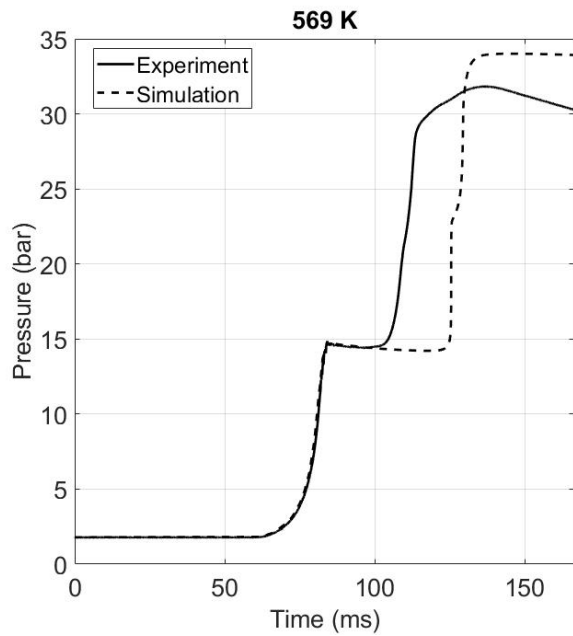
Figure B.6: Di-n-propyl ether: $\phi = 0.5$, dilution = 10 (inert gas: 100% CO₂), $p_c = 15$ bar, DPE = 0.5%.



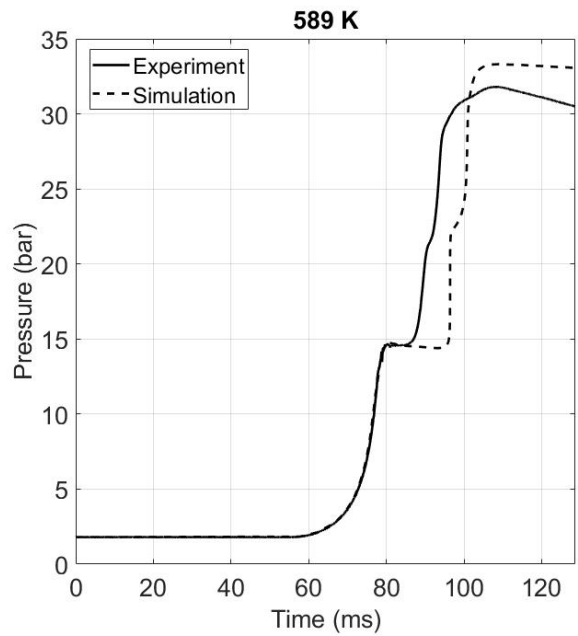
(a)



(b)



(c)



(d)

Figure B.7: Di-n-propyl ether: $\phi = 2$, dilution = 10 (inert gas: 100% CO₂), $p_c = 15$ bar, DPE = 2.0%.

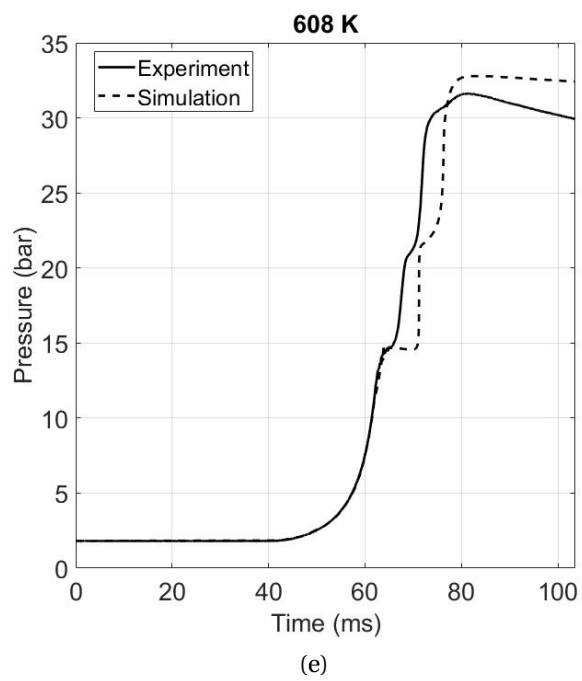


Figure B.7: Di-n-propyl ether: $\phi = 2$, dilution = 10 (inert gas: 100% CO₂), $p_c = 15$ bar, DPE = 2.0%.

B.1.3 Di-iso-propyl ether

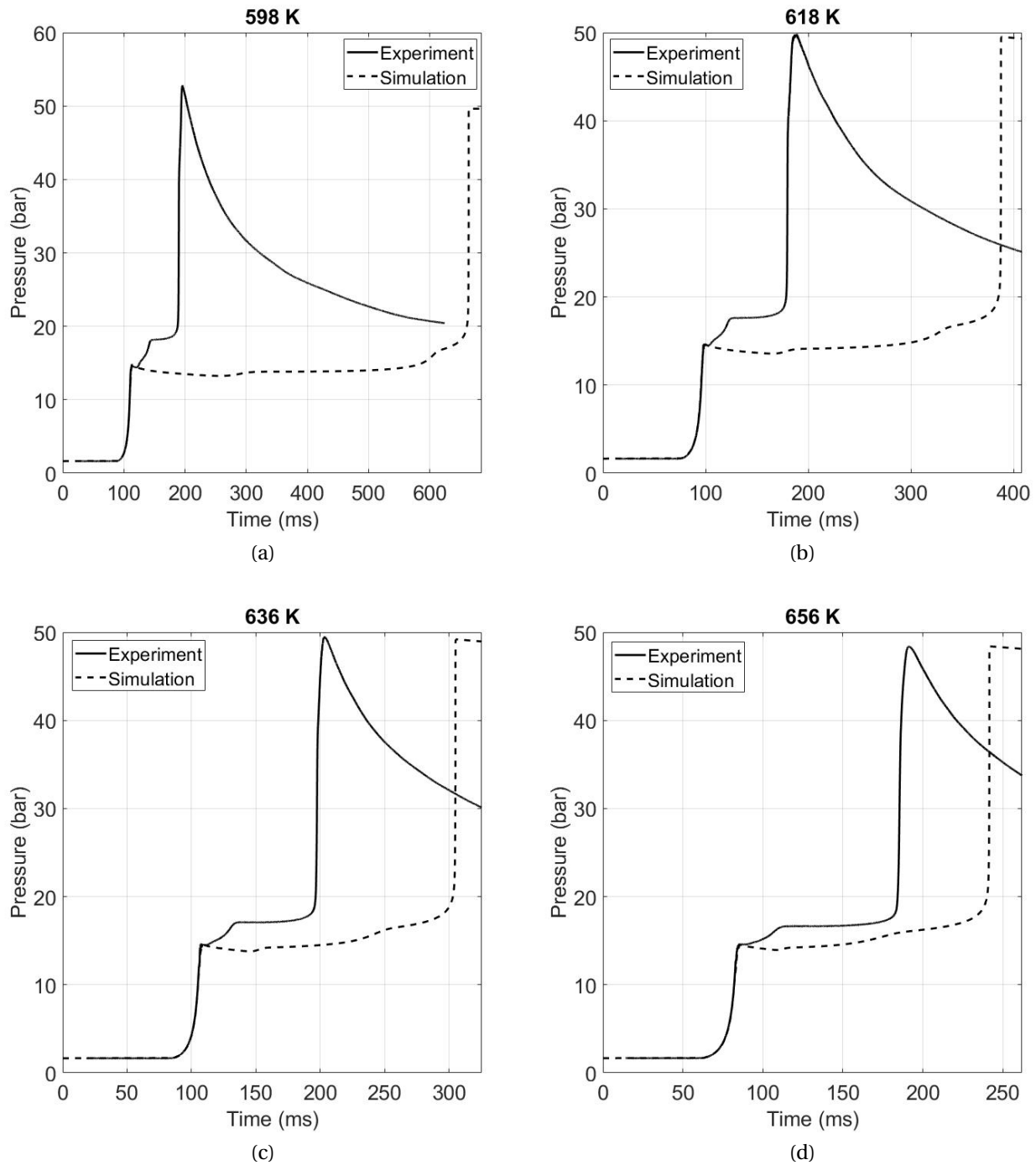


Figure B.8: Di-iso-propyl ether: $\phi = 1$, dilution = 5, $p_c = 15$ bar (a)-d) inert gases 50% CO₂ + 50% N₂, DIPE = 1.8%.

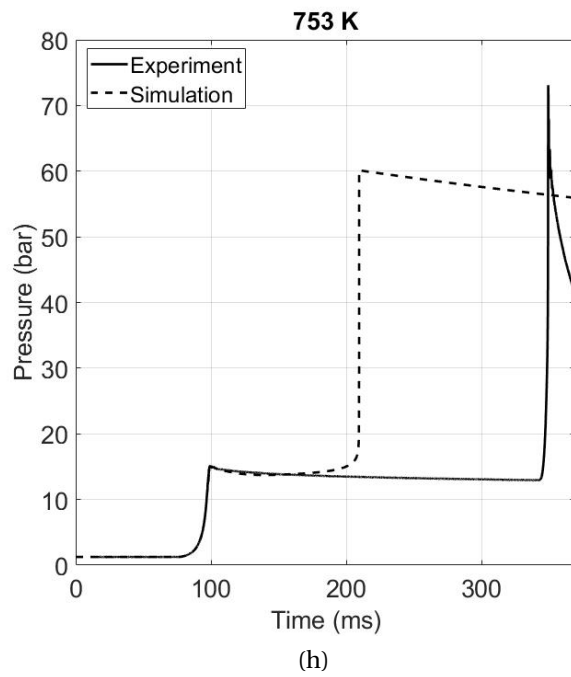
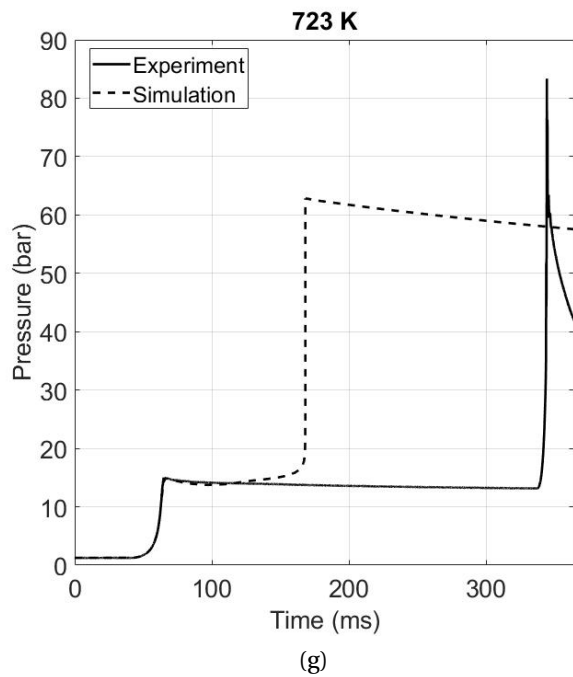
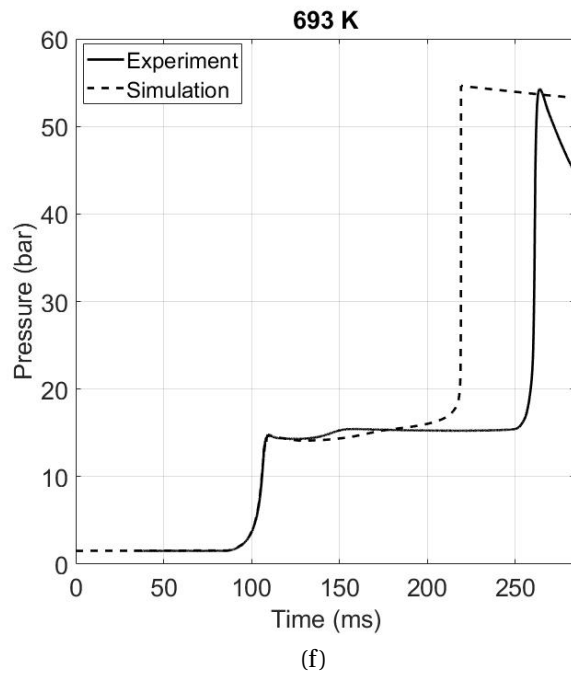
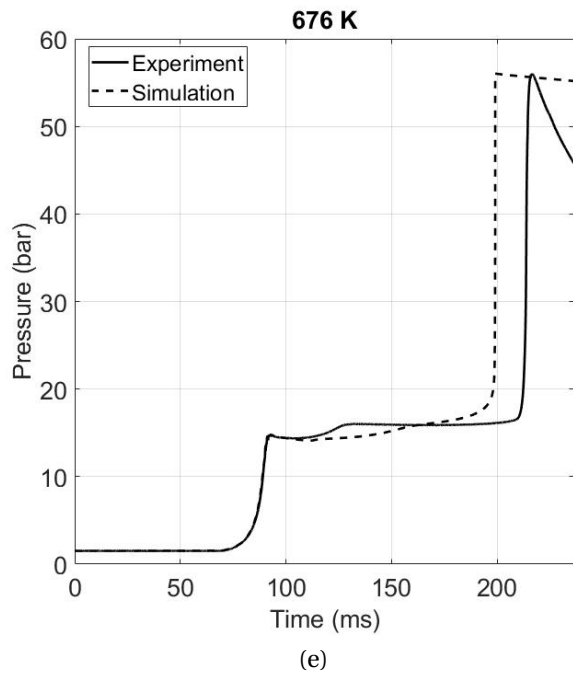
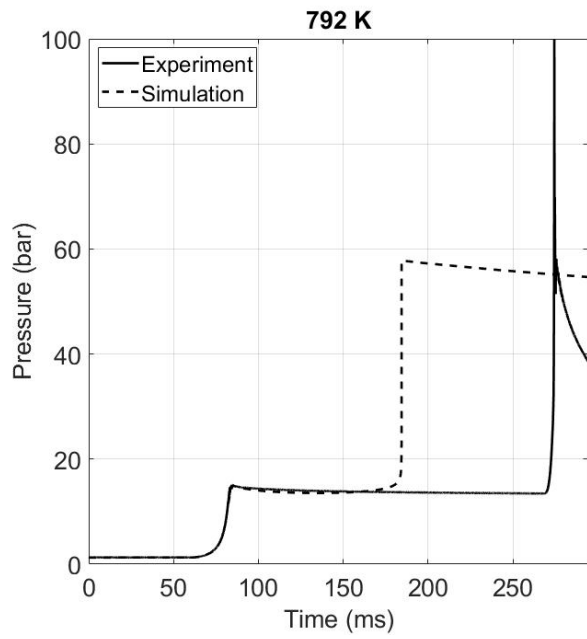
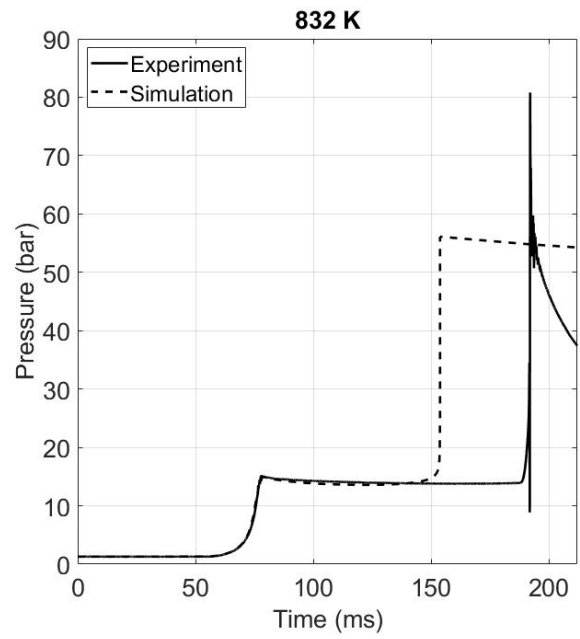


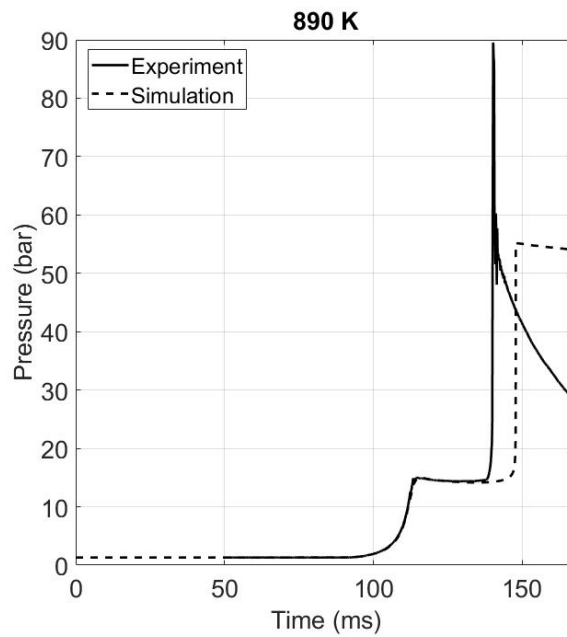
Figure B.8: Di-iso-propyl ether: $\phi = 1$, dilution = 5, $p_c = 15$ bar (e)-f) inert gases 100% N_2 , g)-h) 100% Ar, DIPE = 1.8%.



(i)



(j)



(k)

Figure B.8: Di-iso-propyl ether: $\phi = 1$, dilution = 5, $p_c = 15$ bar (i-k) inert gases 100% Ar), DIPE = 1.8%.

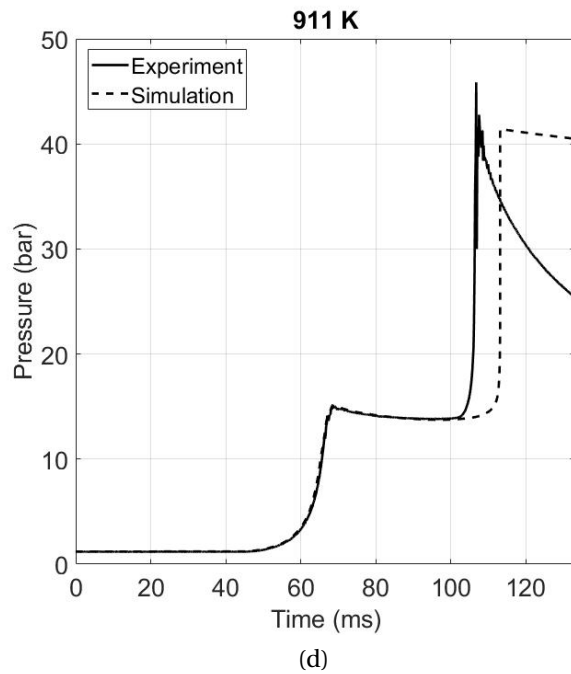
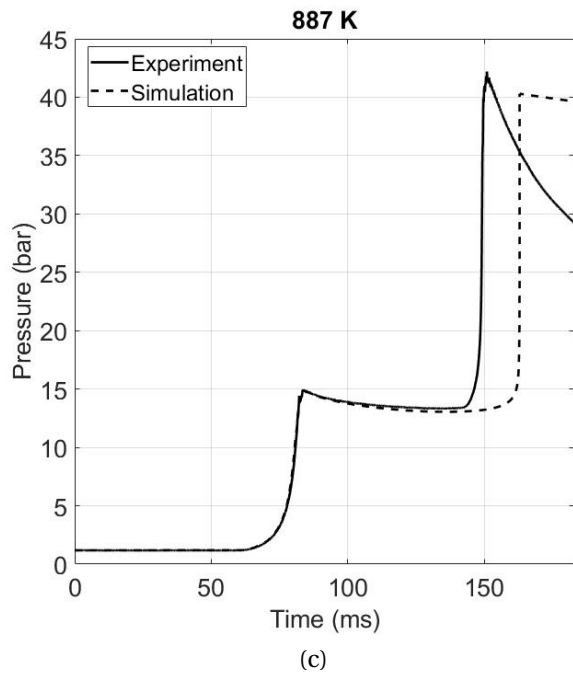
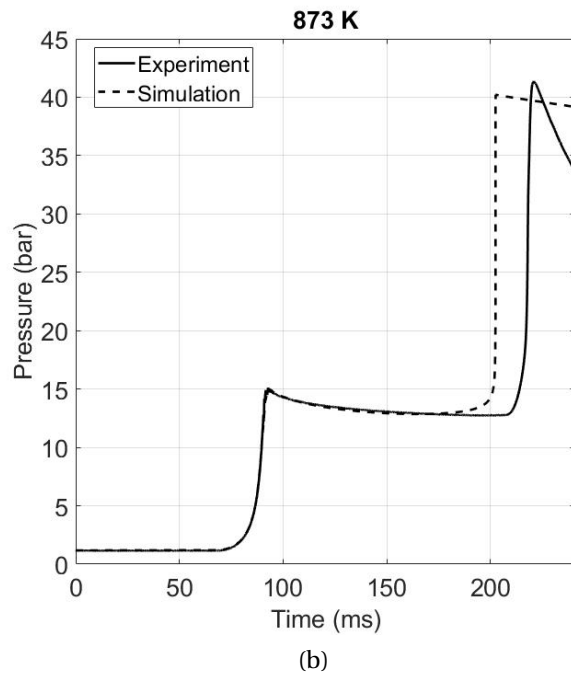
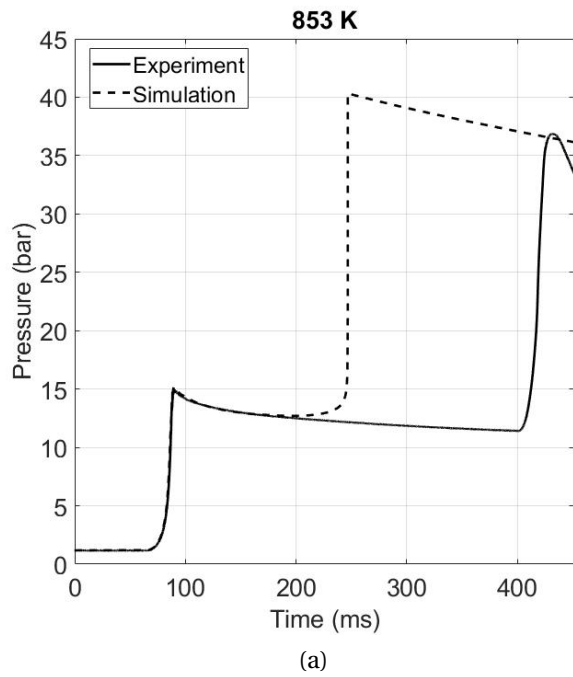


Figure B.9: Di-iso-propyl ether: $\phi = 0.5$, dilution = 5 (inert gas: 100% Ar), $p_c = 15$ bar, DIPE = 0.9%.

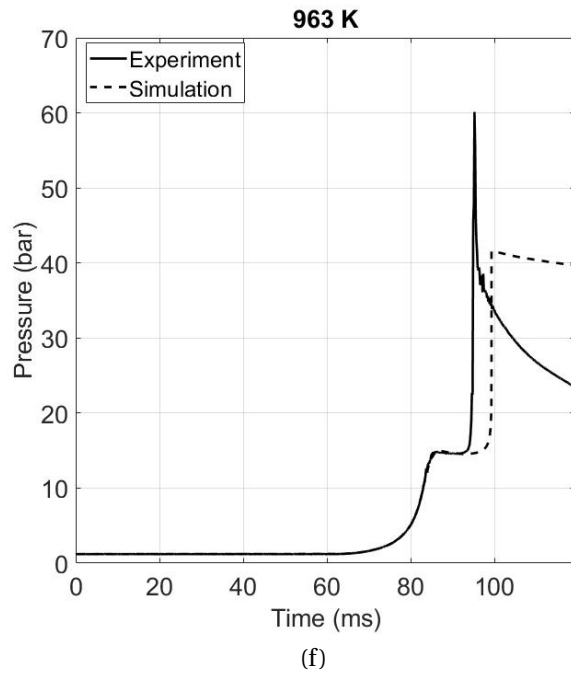
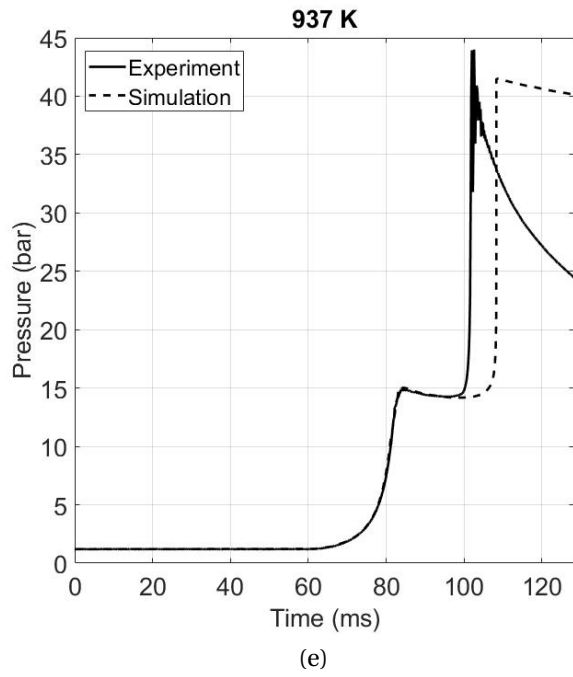


Figure B.9: Di-iso-propyl ether: $\phi = 0.5$, dilution = 5 (inert gas: 100% Ar), $p_c = 15$ bar, DIPE = 0.9%.

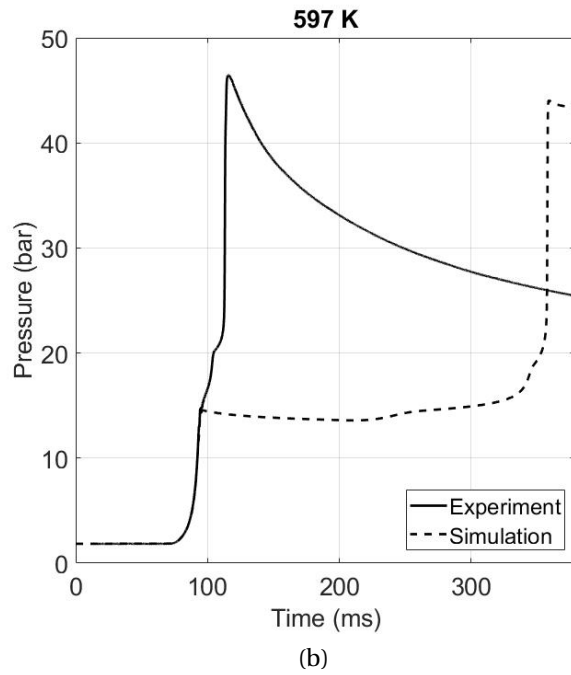
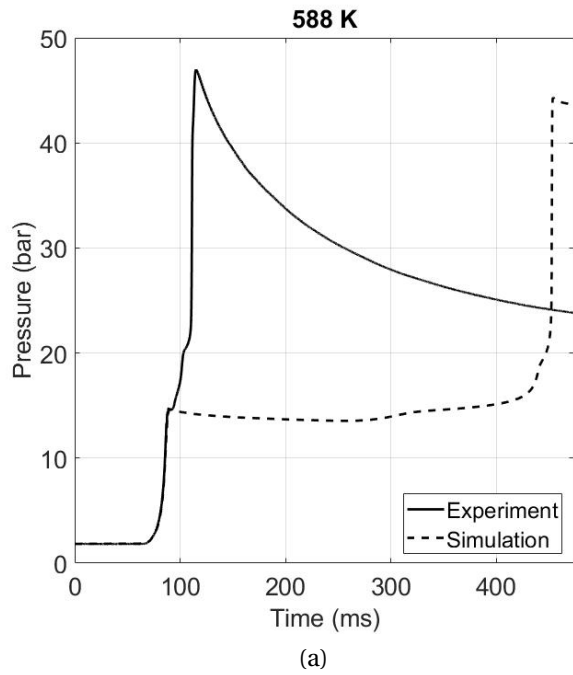
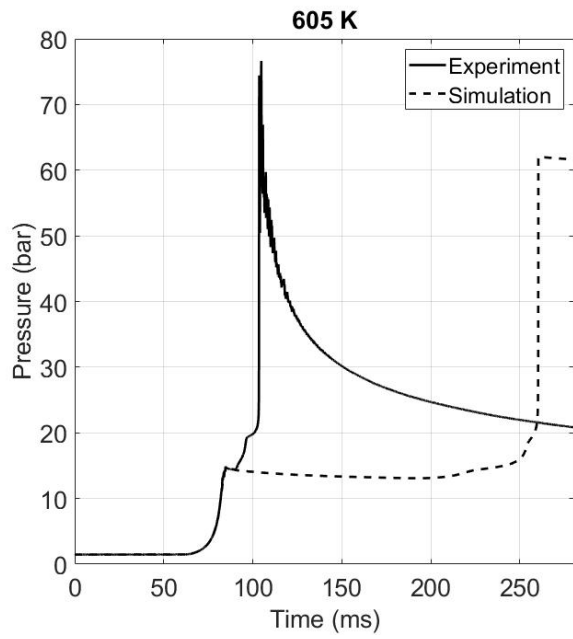
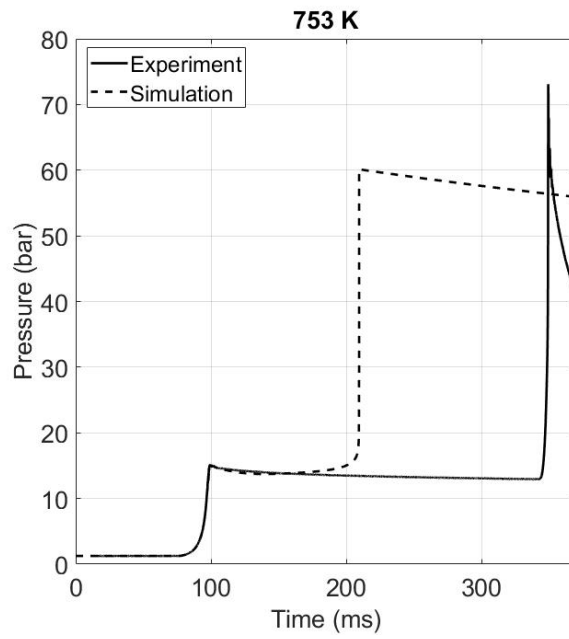


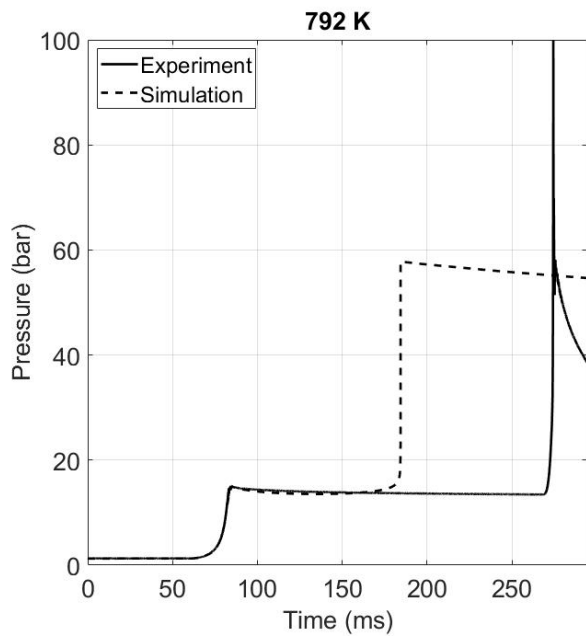
Figure B.10: Di-iso-propyl ether: $\phi = 2$, dilution = 5, $p_c = 15$ bar (a)-b) inert gases 50% CO₂ + 50% N₂, DIPE = 3.6%.



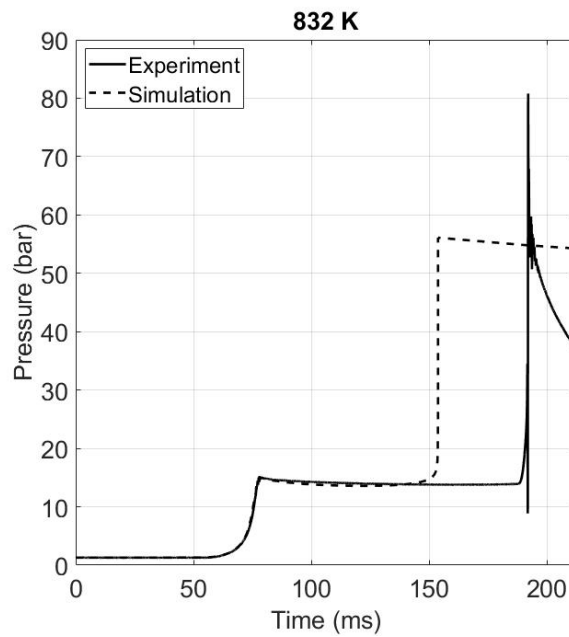
(c)



(d)



(e)



(f)

Figure B.10: Di-iso-propyl ether: $\phi = 2$, dilution = 5, $p_c = 15$ bar (c)-f) inert gases 50% $N_2 + 50\%$ Ar), DIPE = 3.6%.

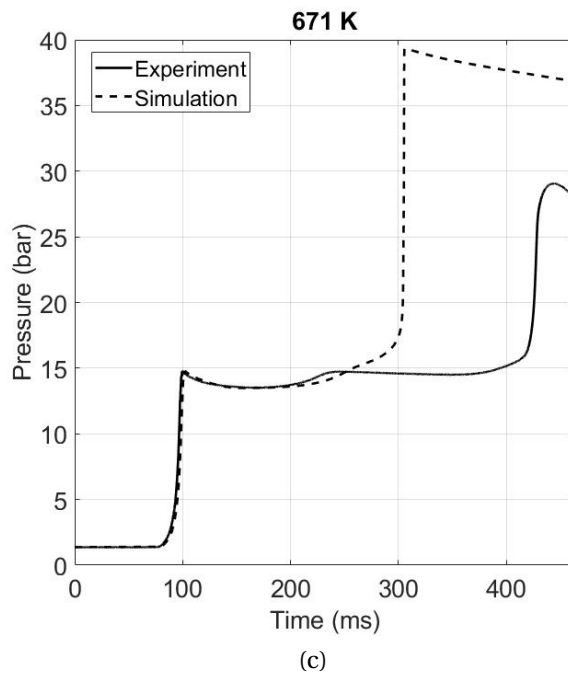
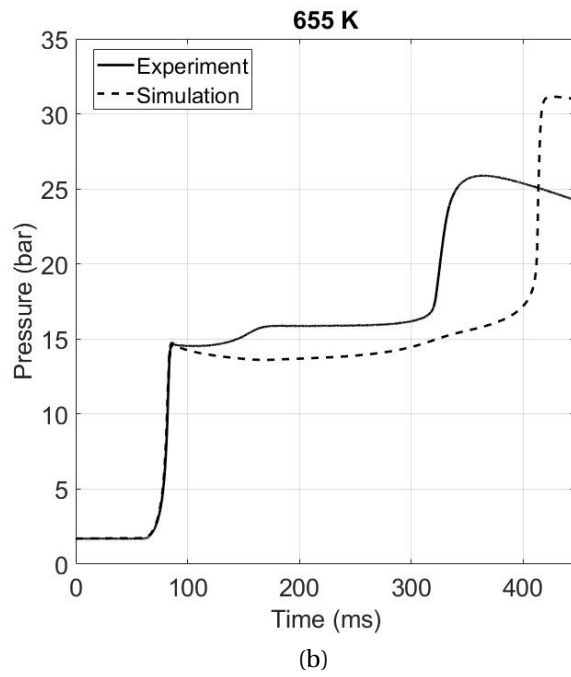
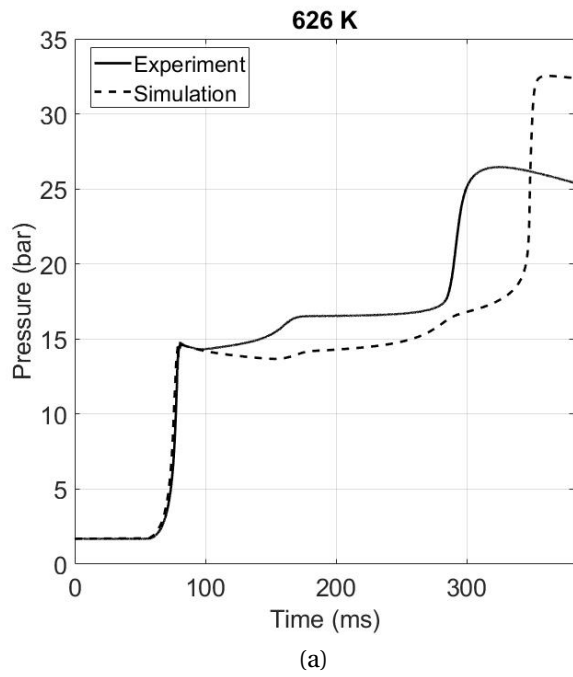


Figure B.11: Di-iso-propyl ether: $\phi = 2$, dilution = 10, $p_c = 15$ bar (a)-b) inert gases 50% CO_2 + 50% N_2 , c) 50% N_2 + 50% Ar), DIPE = 2.0%.

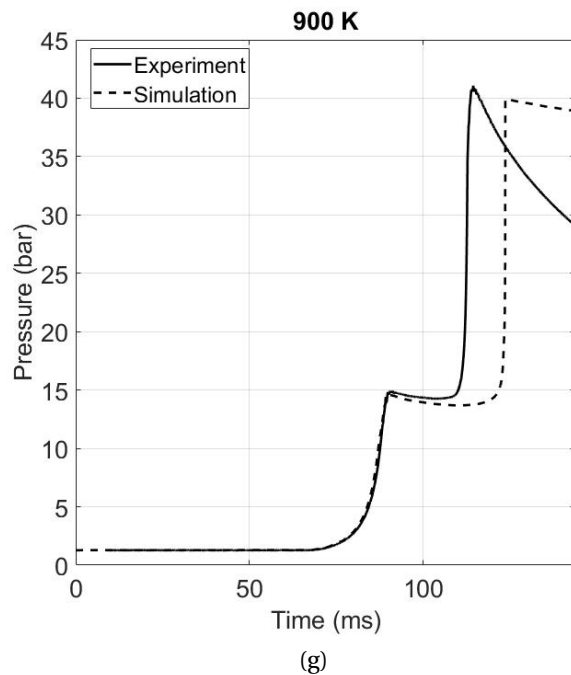
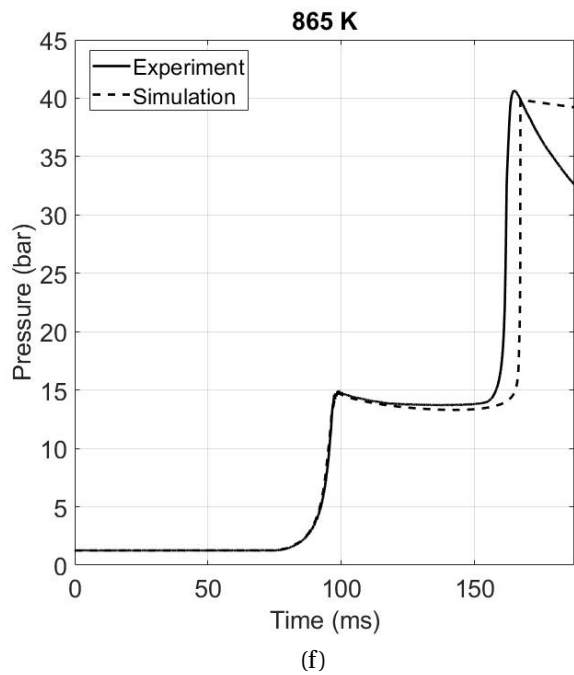
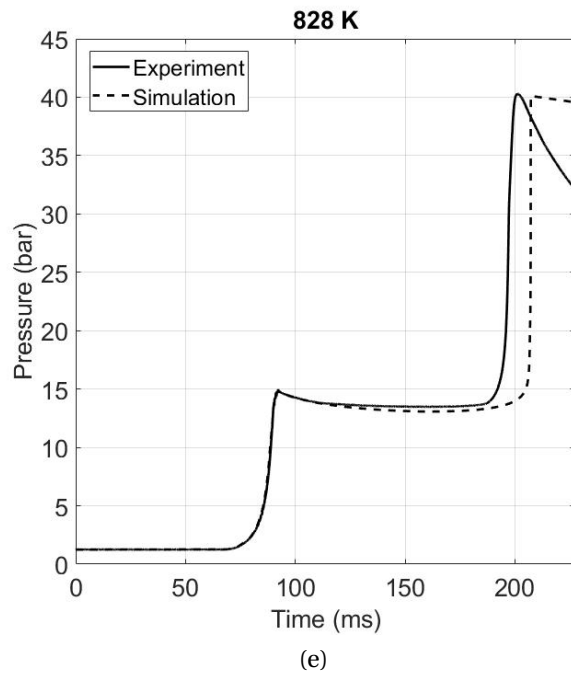
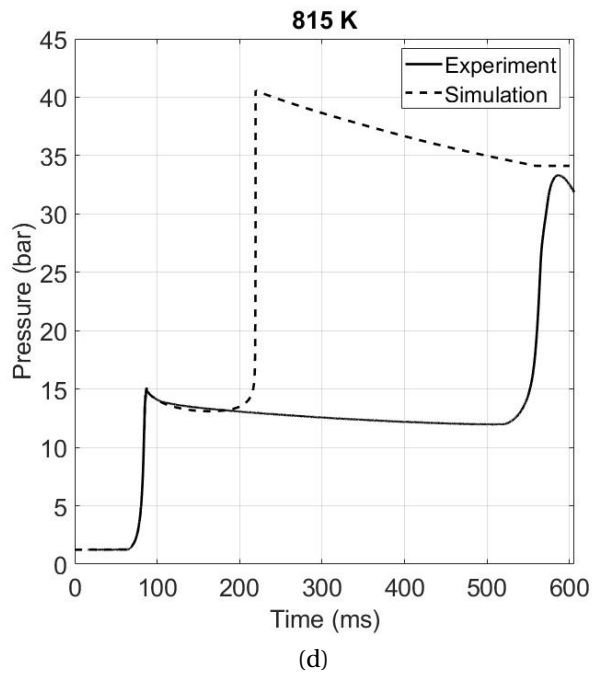


Figure B.11: Di-iso-propyl ether: $\phi = 2$, dilution = 10, $p_c = 15$ bar (d-g) inert gases 100% Ar, DIPE = 2.0%.

B.1.4 Butyl ethyl ether

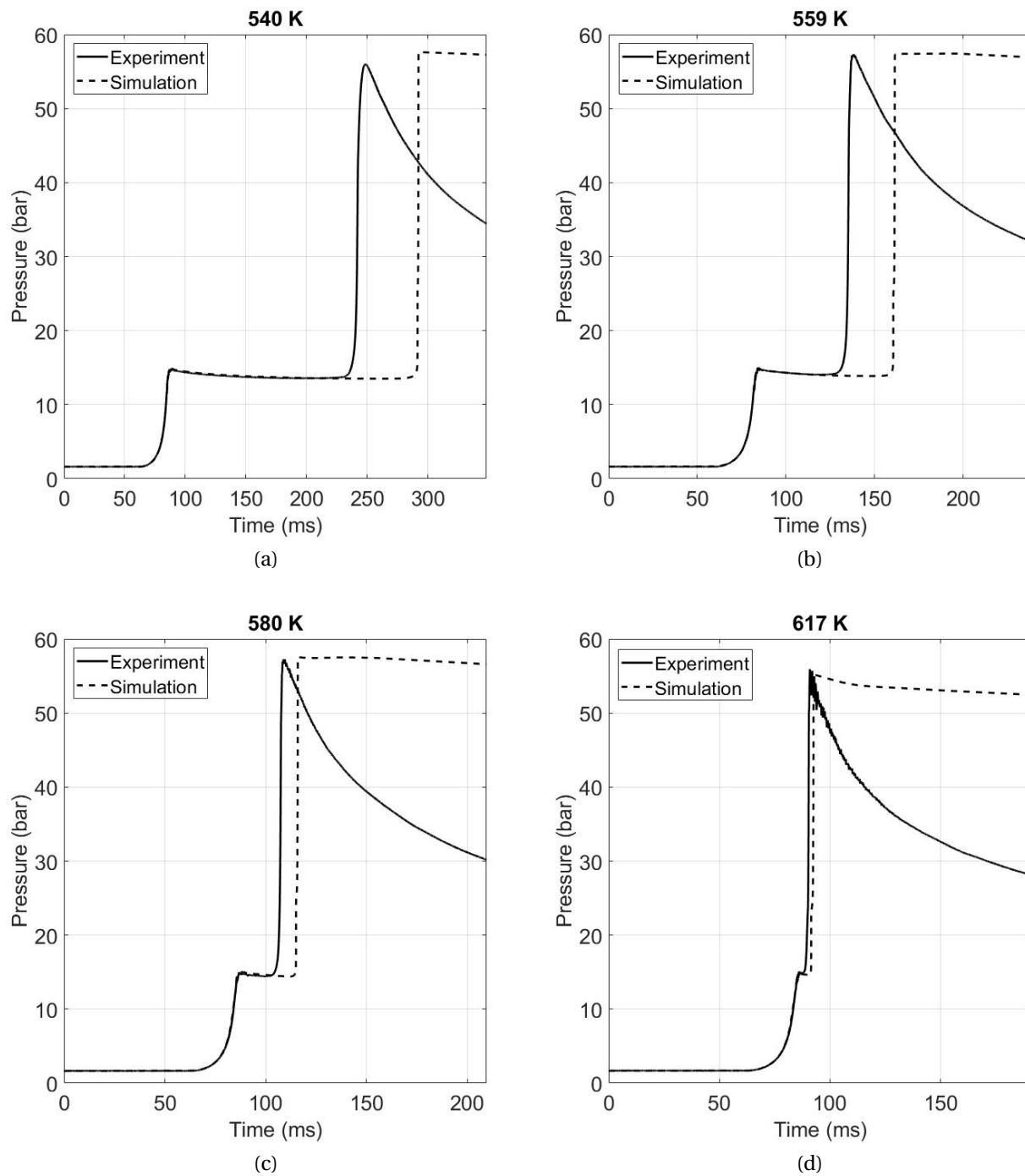


Figure B.12: Butyl ethyl ether: $\phi = 1$, dilution = 5 (inert gases: 50% CO₂ + 50% N₂), $p_c = 15$ bar, BEE = 1.8%.

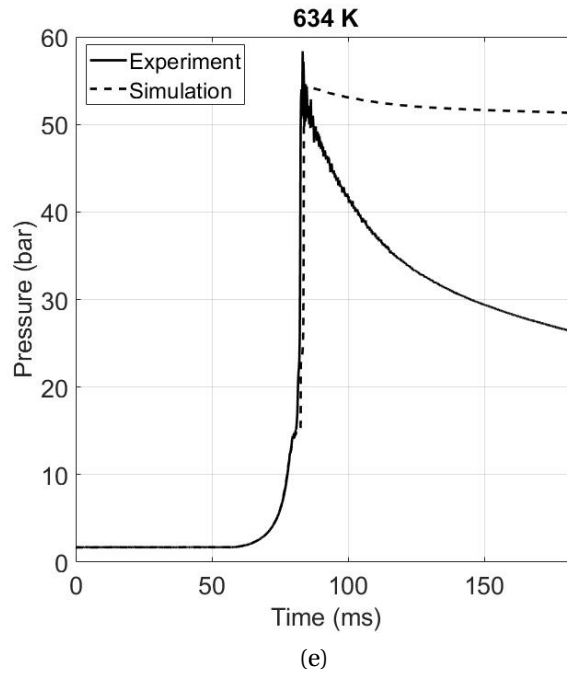


Figure B.12: Butyl ethyl ether: $\phi = 1$, dilution = 5 (inert gases: 50% CO₂ + 50% N₂), $p_c = 15$ bar, BEE = 1.8%.

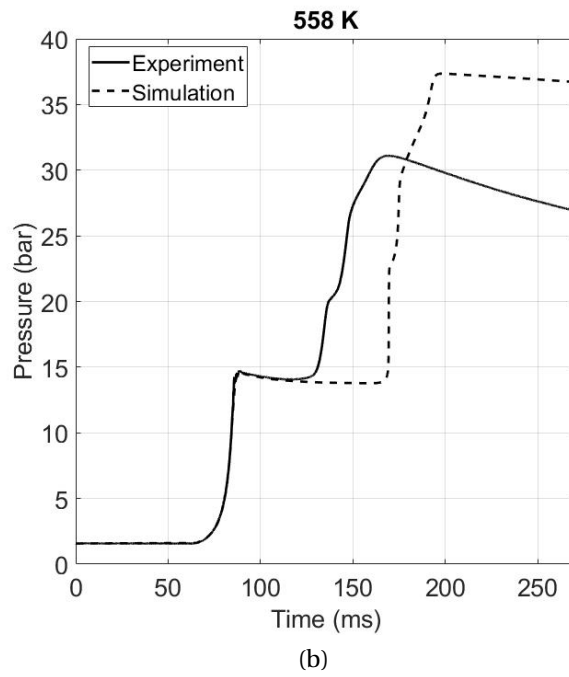
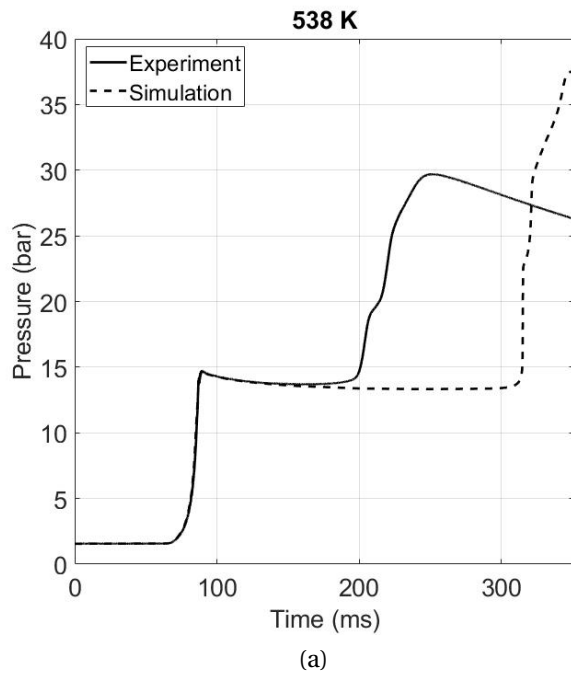


Figure B.13: Butyl ethyl ether: $\phi = 0.5$, dilution = 5 (inert gases: 50% CO₂ + 50% N₂), $p_c = 15$ bar, BEE = 0.9%.

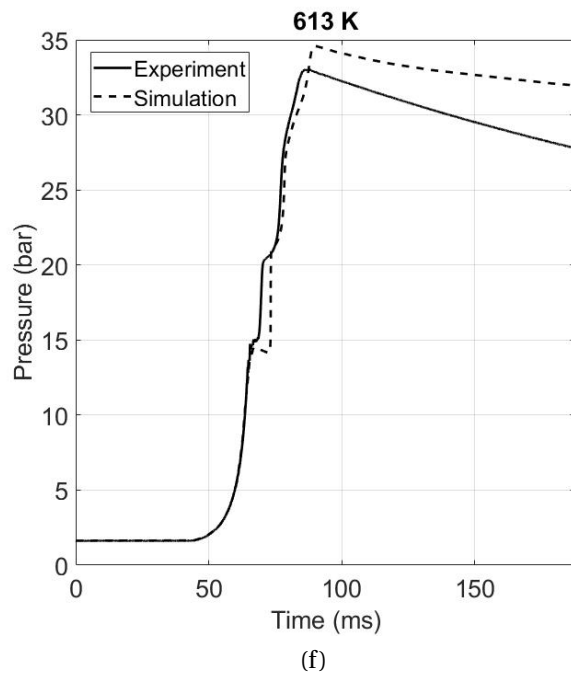
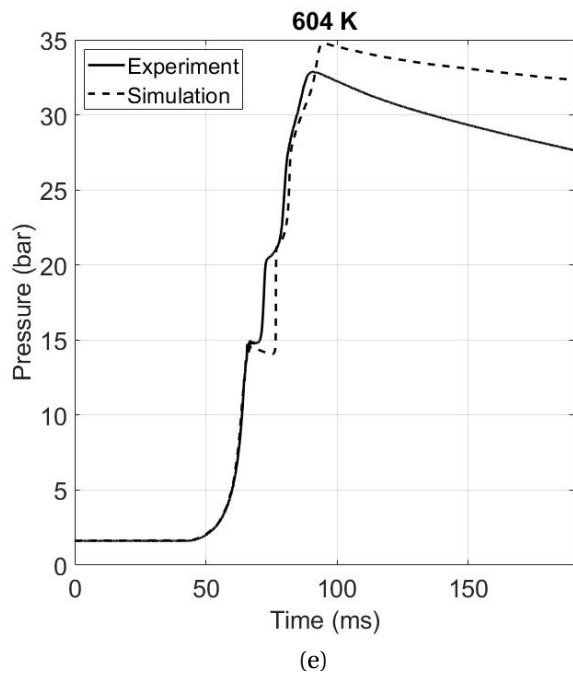
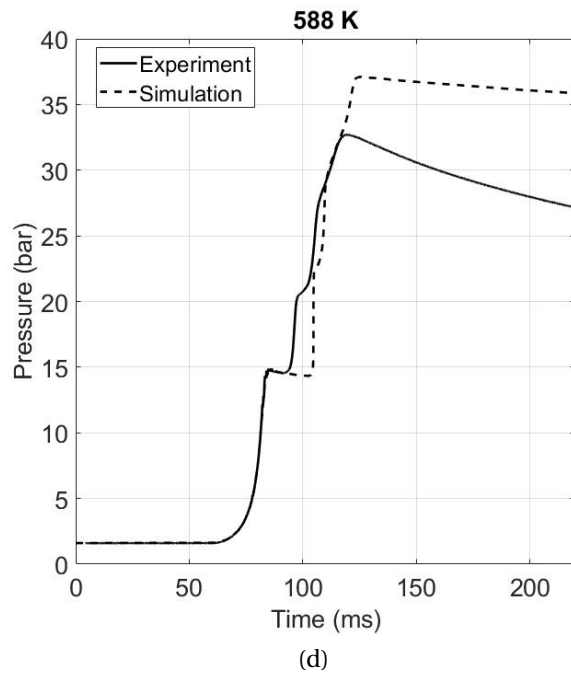
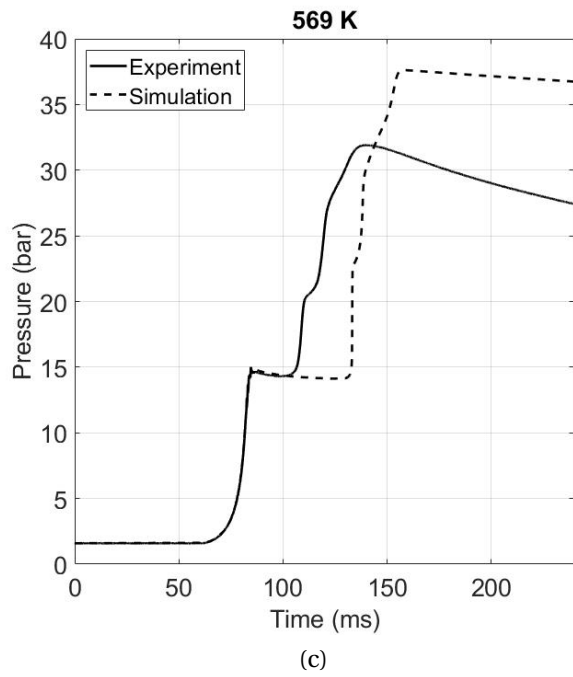
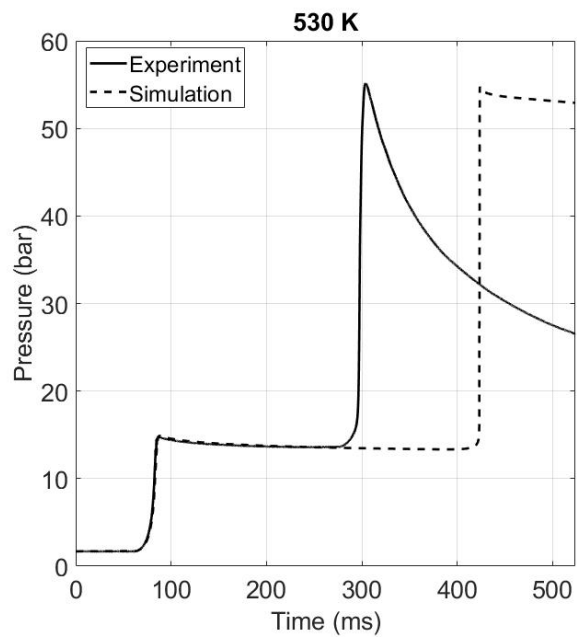
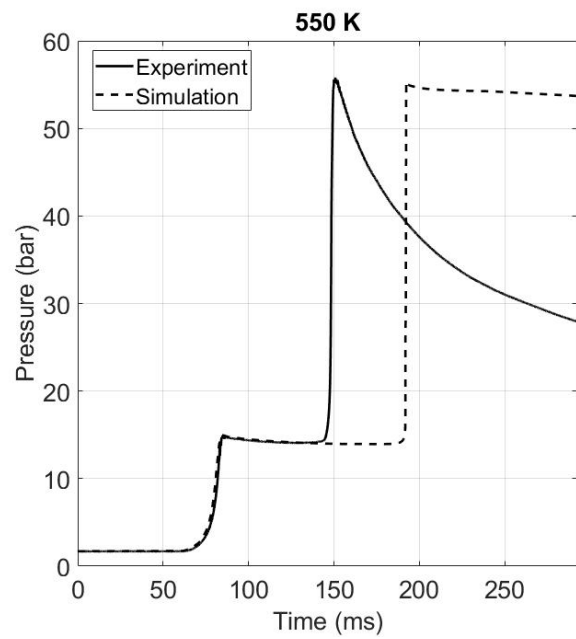


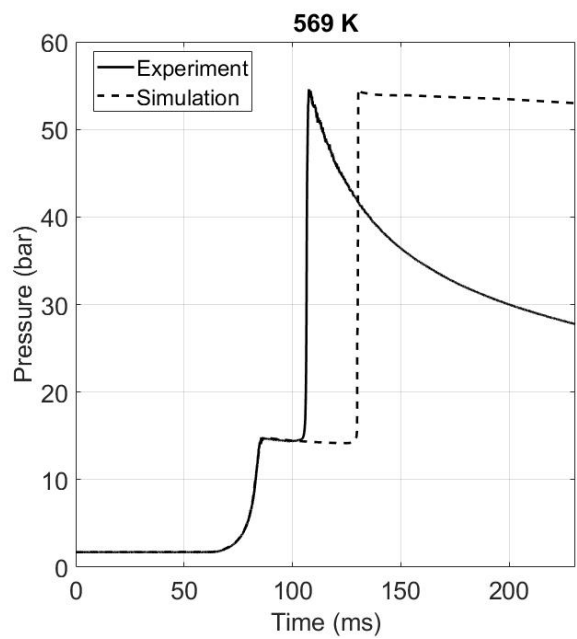
Figure B.13: Butyl ethyl ether: $\phi = 0.5$, dilution = 5 (inert gases: 50% CO₂ + 50% N₂), $p_c = 15$ bar, BEE = 0.9%.



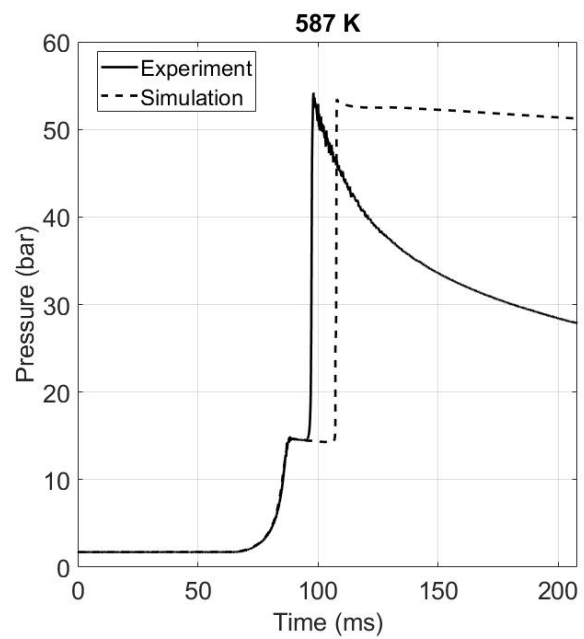
(a)



(b)



(c)



(d)

Figure B.14: Butyl ethyl ether: $\phi = 2$, dilution = 5 (inert gases: 50% CO_2 + 50% N_2), $p_c = 15$ bar, BEE = 3.6%.

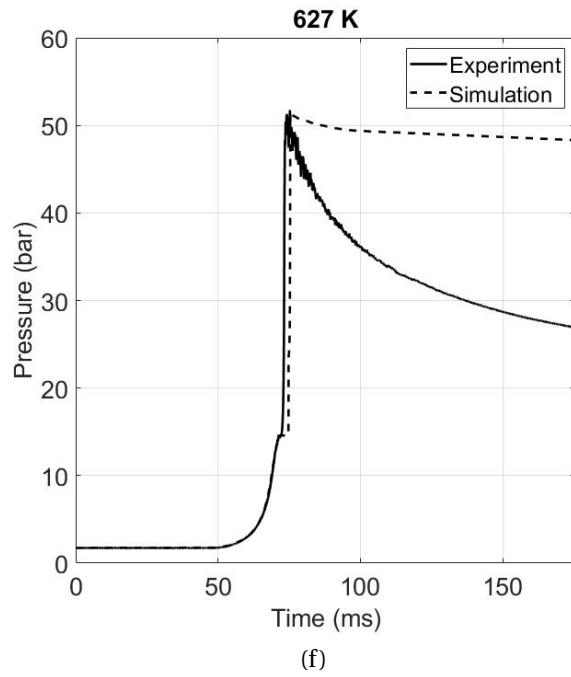
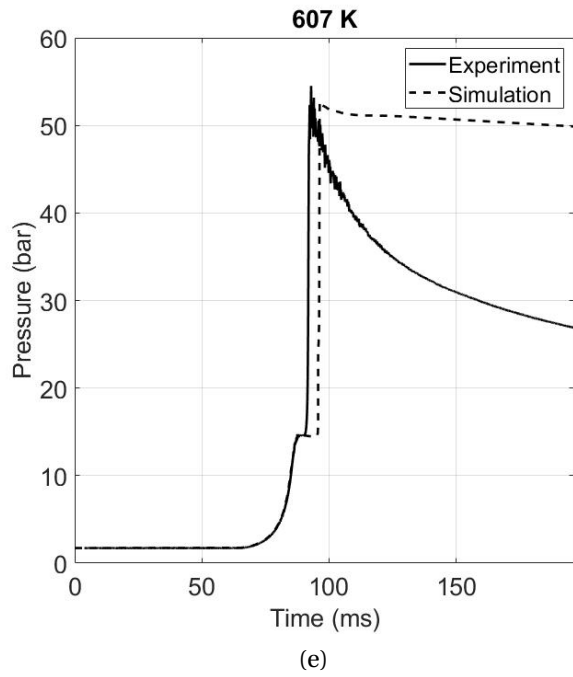


Figure B.14: Butyl ethyl ether: $\phi = 2$, dilution = 5 (inert gases: 50% CO₂ + 50% N₂), $p_c = 15$ bar, BEE = 3.6%.

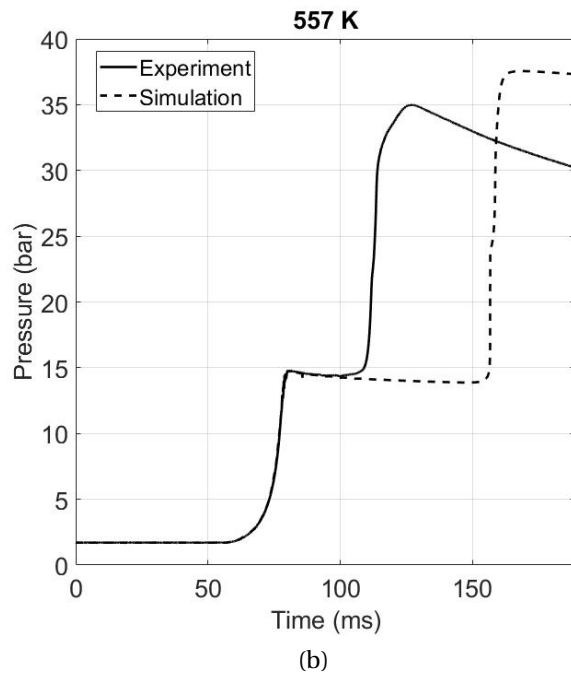
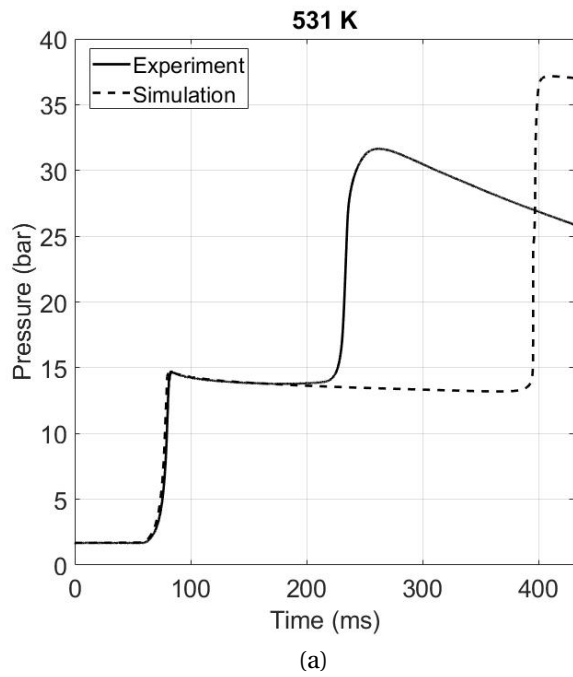
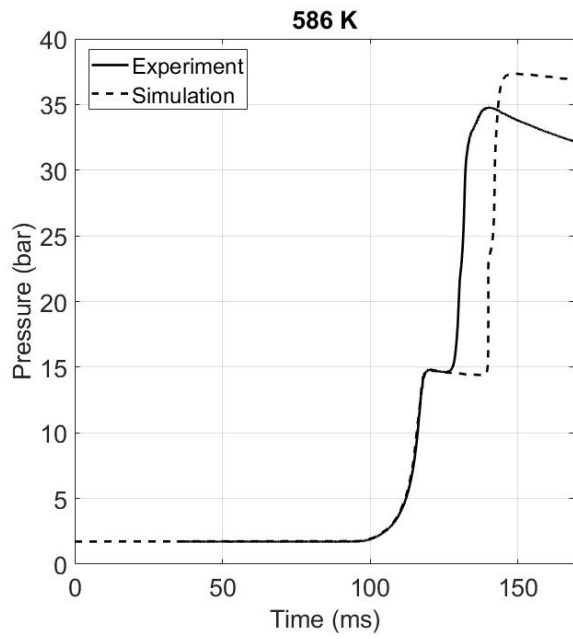
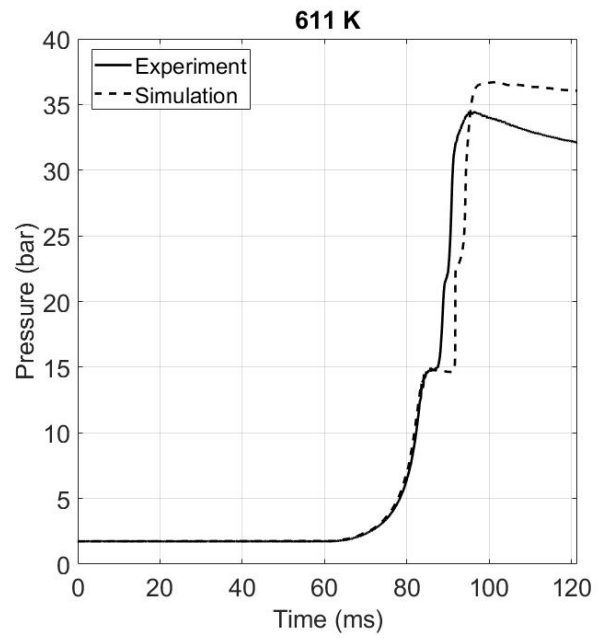


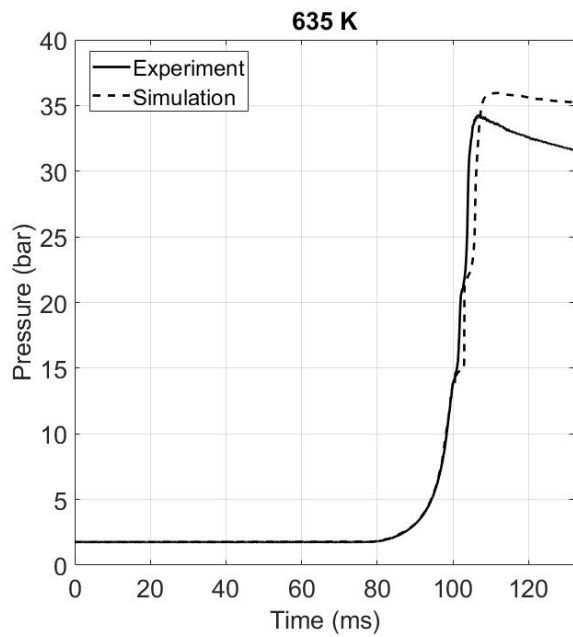
Figure B.15: Butyl ethyl ether: $\phi = 2$, dilution = 10 (inert gases: 50% CO₂ + 50% N₂), $p_c = 15$ bar, BEE = 1.98%.



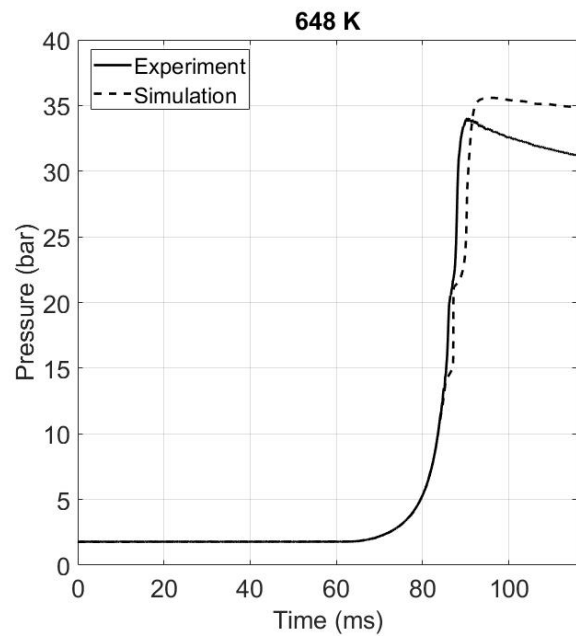
(c)



(d)



(e)



(f)

Figure B.15: Butyl ethyl ether: $\phi = 2$, dilution = 10 (inert gases: 50% CO_2 + 50% N_2), $p_c = 15$ bar, BEE = 1.98%.

B.1.5 Dibutyl ether

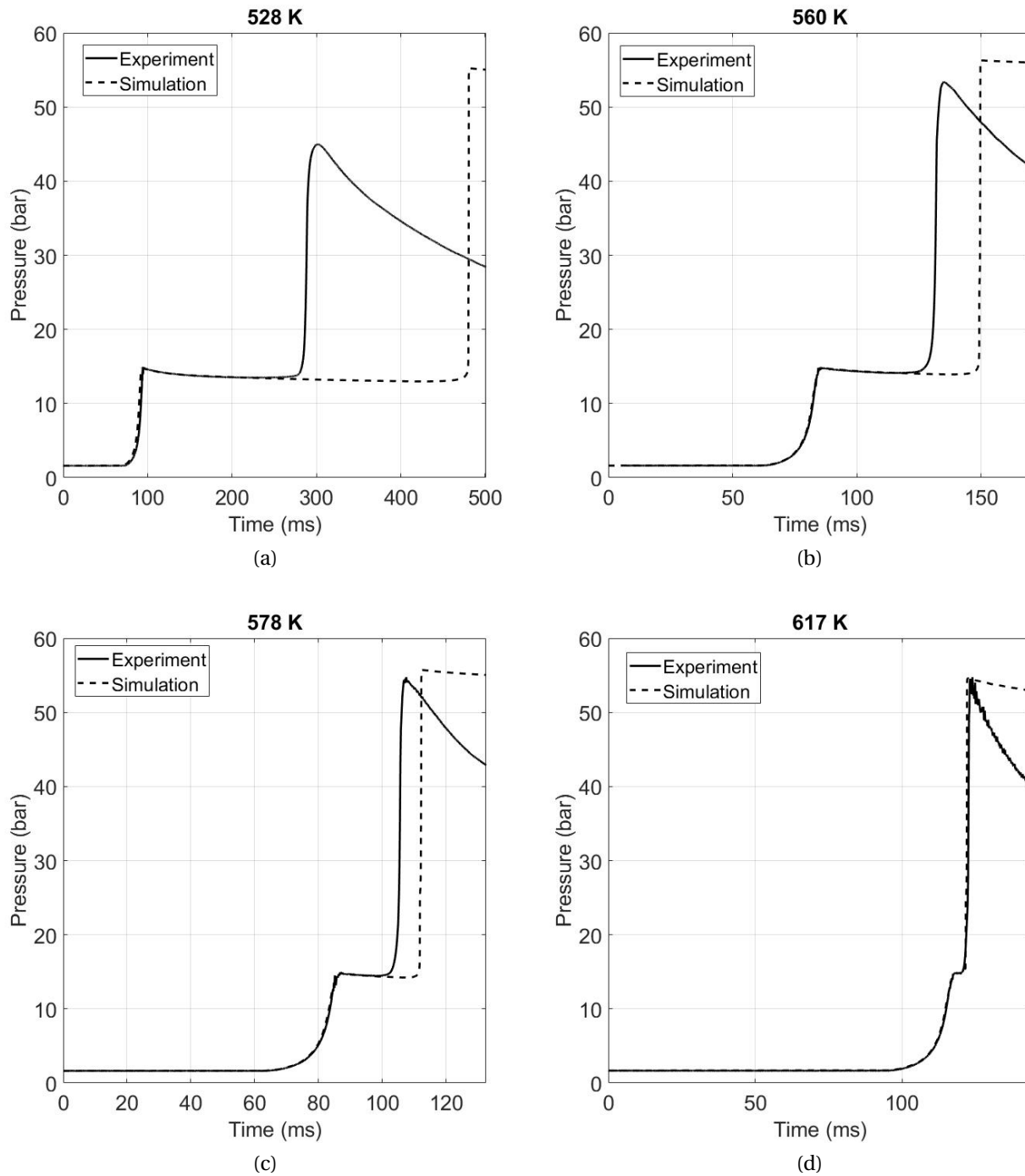


Figure B.16: Dibutyl ether: $\phi = 1$, dilution = 5 (inert gases: 50% CO₂ + 50% N₂), $p_c = 15$ bar, DBE = 1.4%.

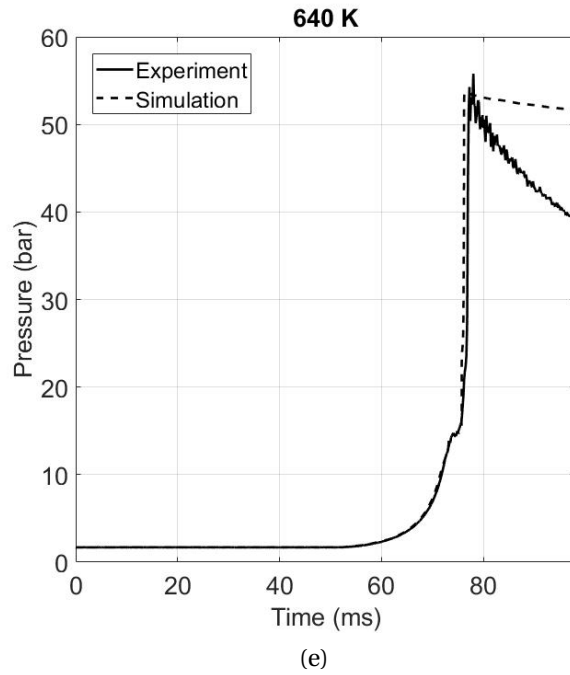


Figure B.16: Dibutyl ether: $\phi = 1$, dilution = 5 (inert gases: 50% CO₂ + 50% N₂), $p_c = 15$ bar, DBE = 1.4%.

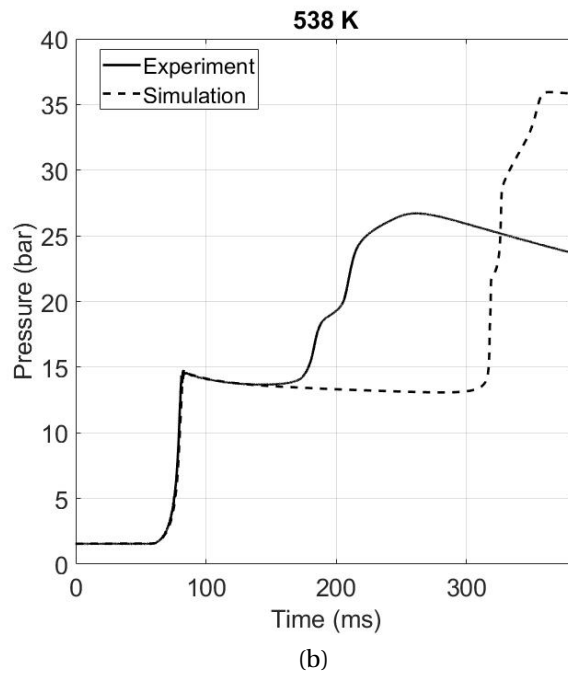
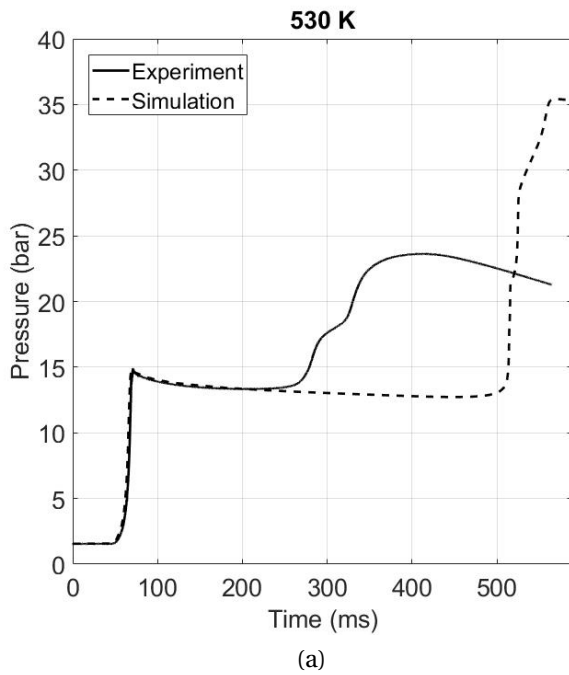


Figure B.17: Dibutyl ether: $\phi = 0.5$, dilution = 5 (inert gases: 50% CO₂ + 50% N₂), $p_c = 15$ bar, DBE = 0.7%.

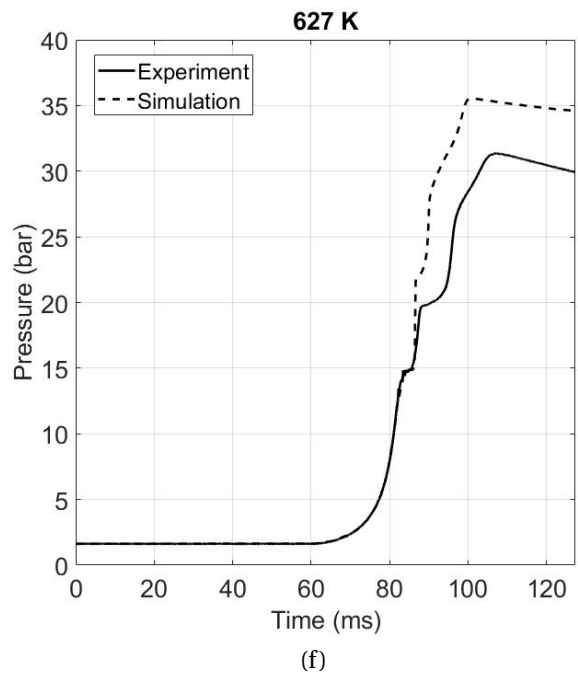
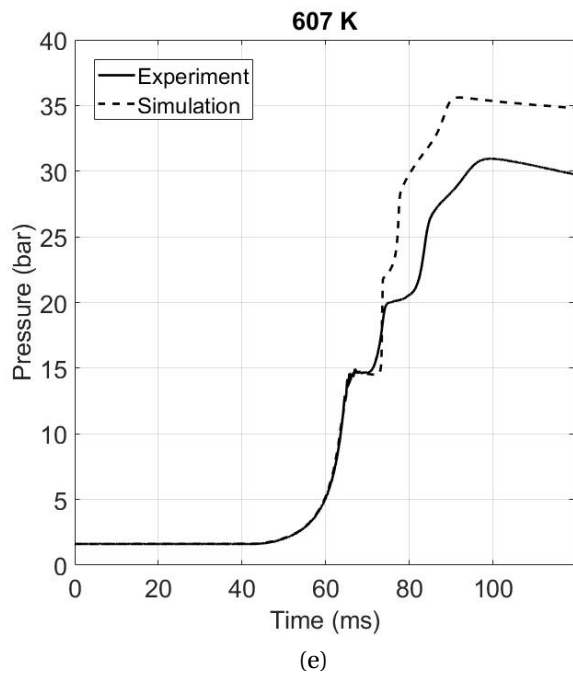
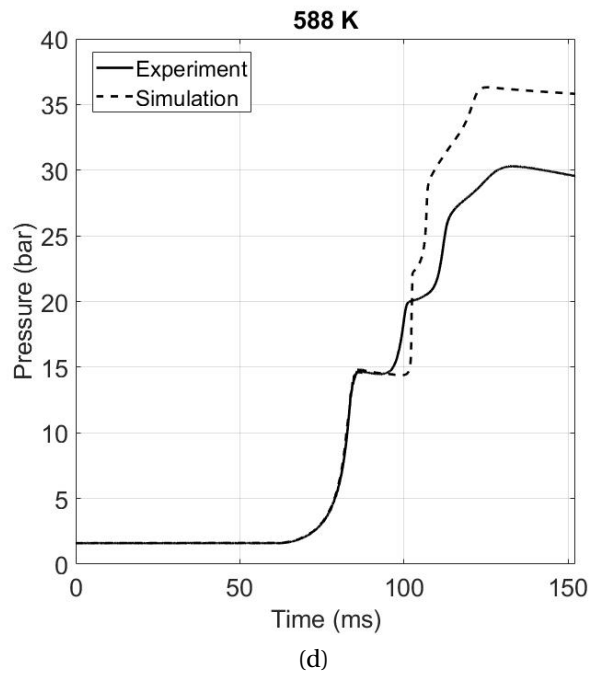
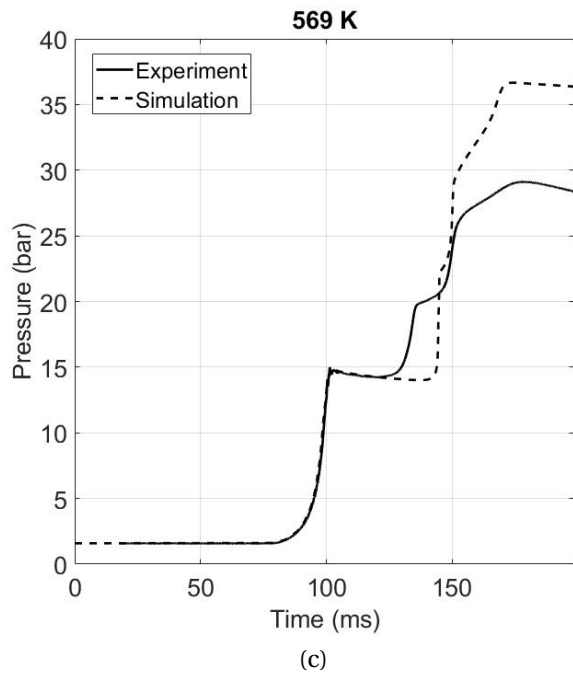


Figure B.17: Dibutyl ether: $\phi = 0.5$, dilution = 5 (inert gases: 50% CO₂ + 50% N₂), $p_c = 15$ bar, DBE = 0.7%.

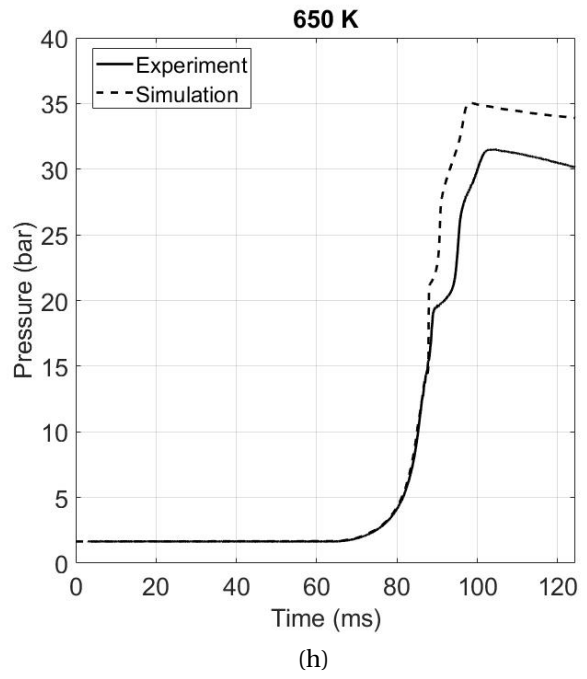
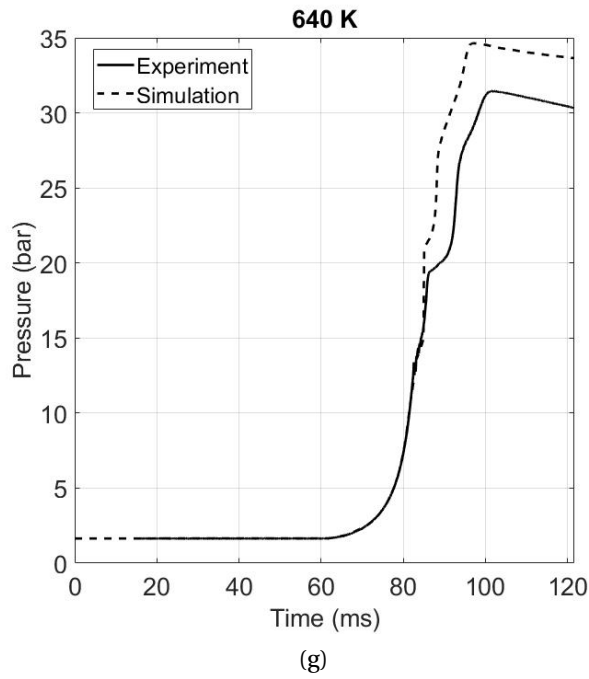


Figure B.17: Dibutyl ether: $\phi = 0.5$, dilution = 5 (inert gases: 50% CO₂ + 50% N₂), $p_c = 15$ bar, DBE = 0.7%.

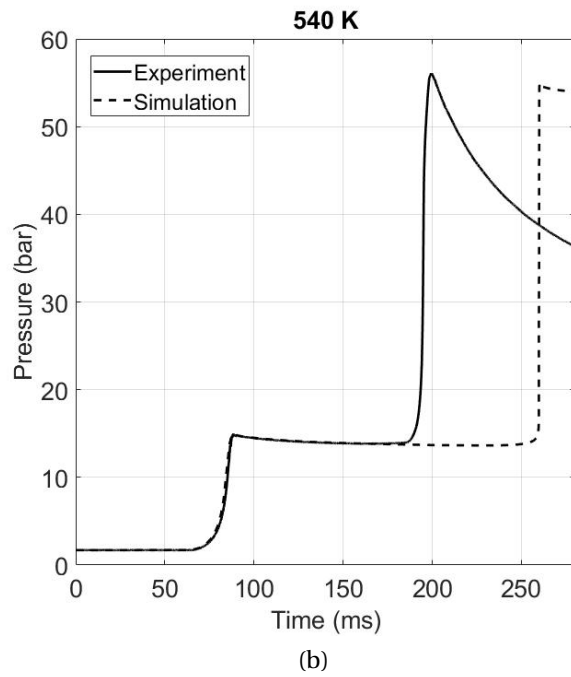
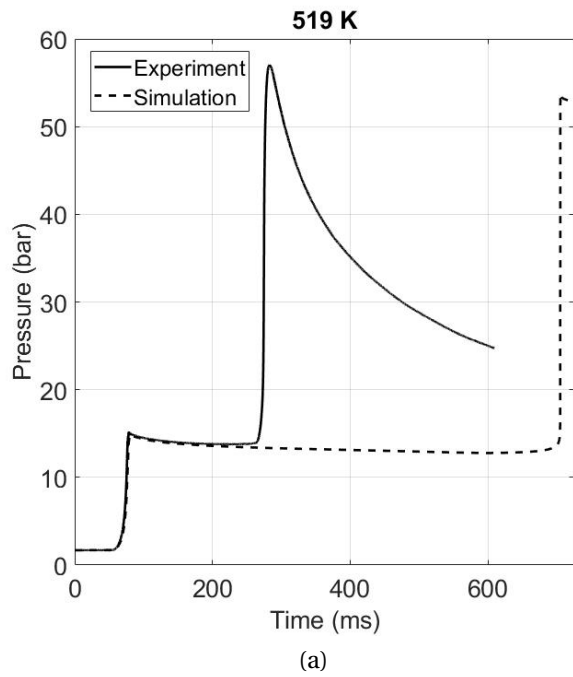
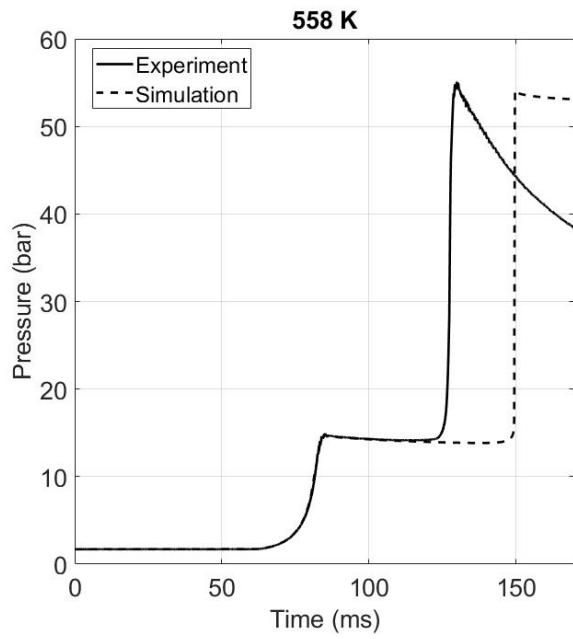
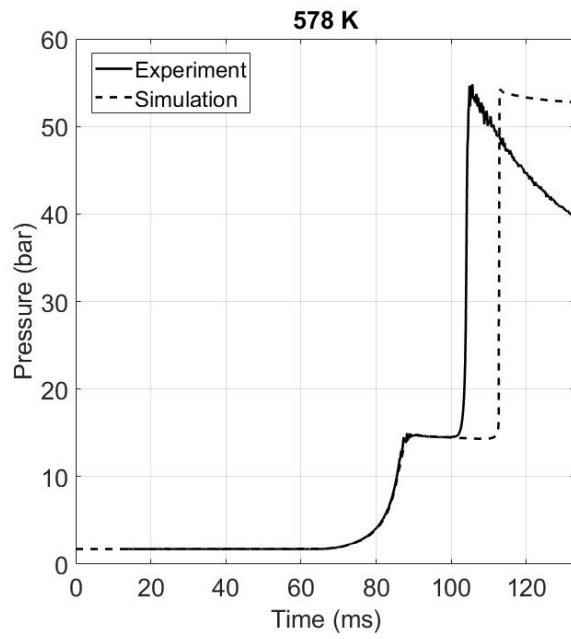


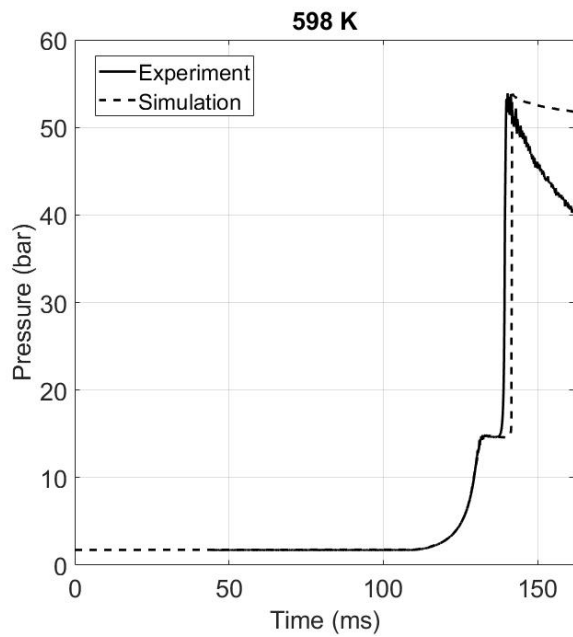
Figure B.18: Dibutyl ether: $\phi = 2$, dilution = 5 (inert gases: 50% CO₂ + 50% N₂), $p_c = 15$ bar, DBE = 2.7%.



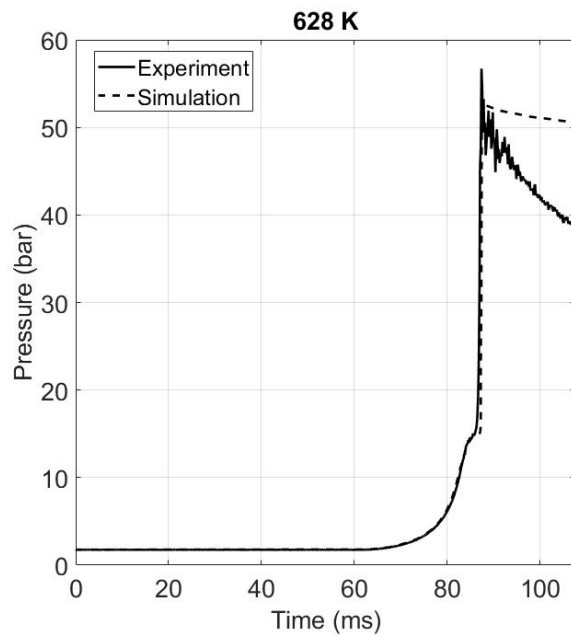
(c)



(d)



(e)



(f)

Figure B.18: Dibutyl ether: $\phi = 2$, dilution = 5 (inert gases: 50% CO_2 + 50% N_2), $p_c = 15$ bar, DBE = 2.7%.

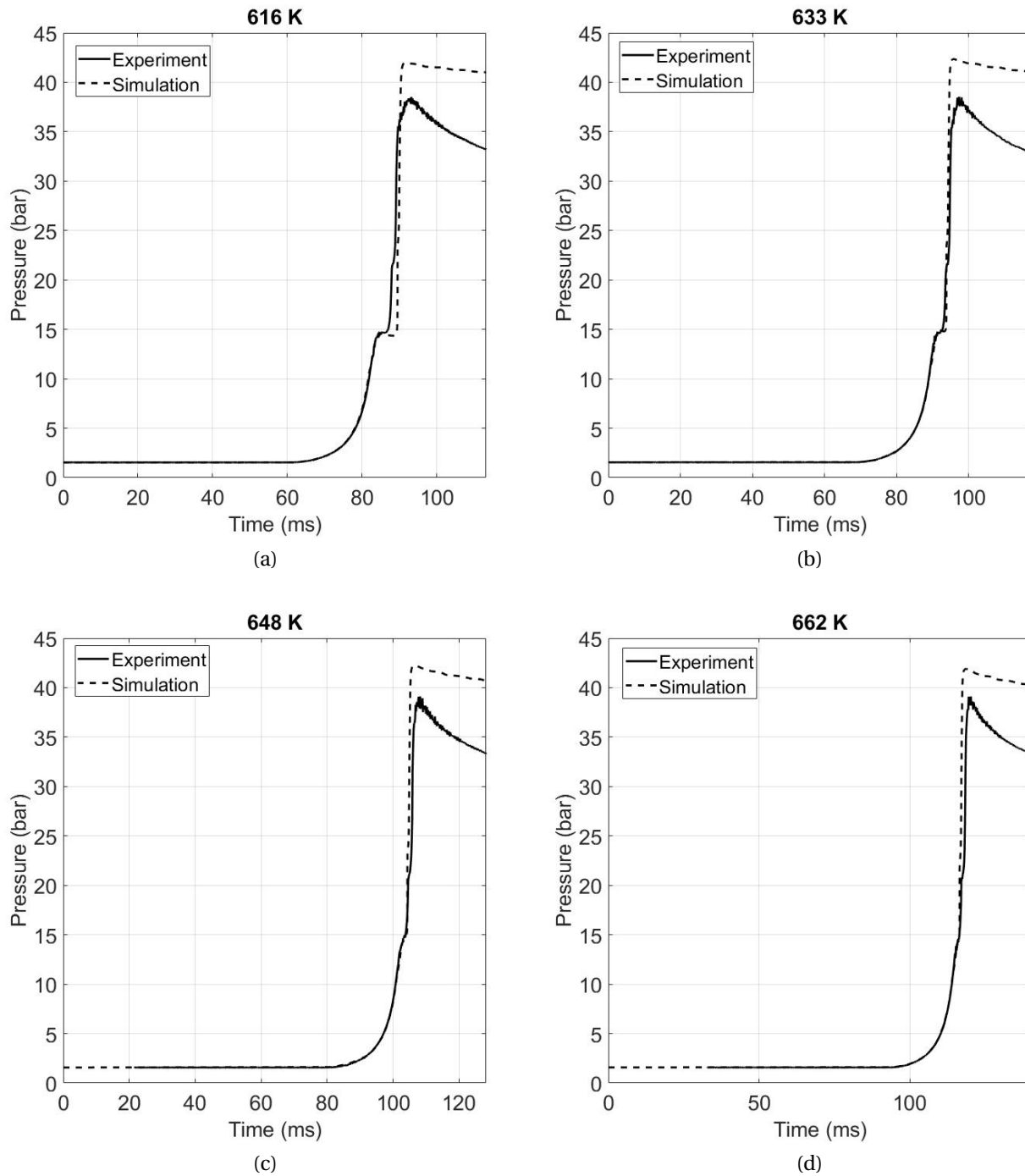


Figure B.19: Dibutyl ether: $\phi = 2$, dilution = 10 (inert gases: 100% N_2), $p_c = 15$ bar, DBE = 1.5%.

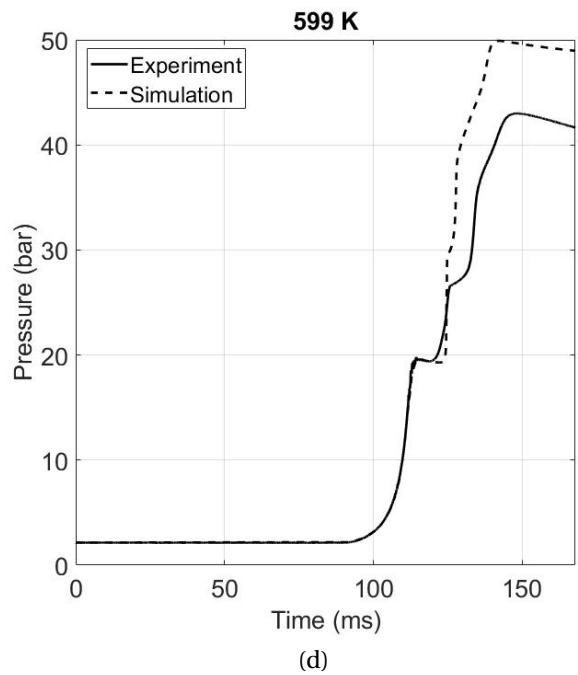
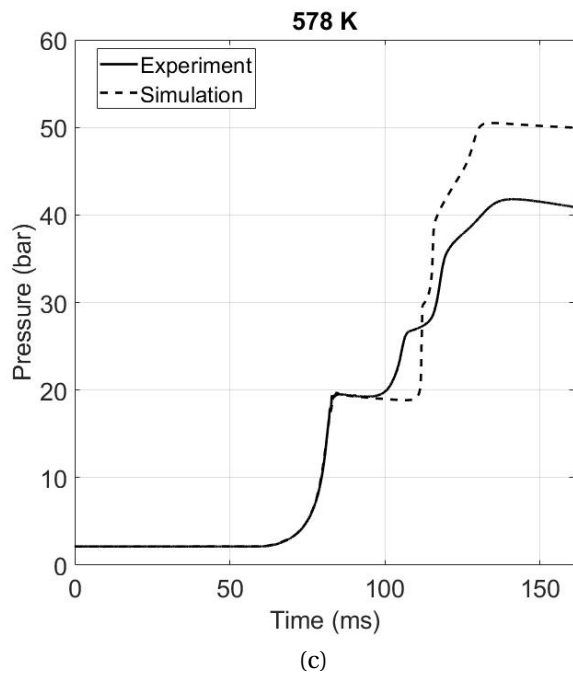
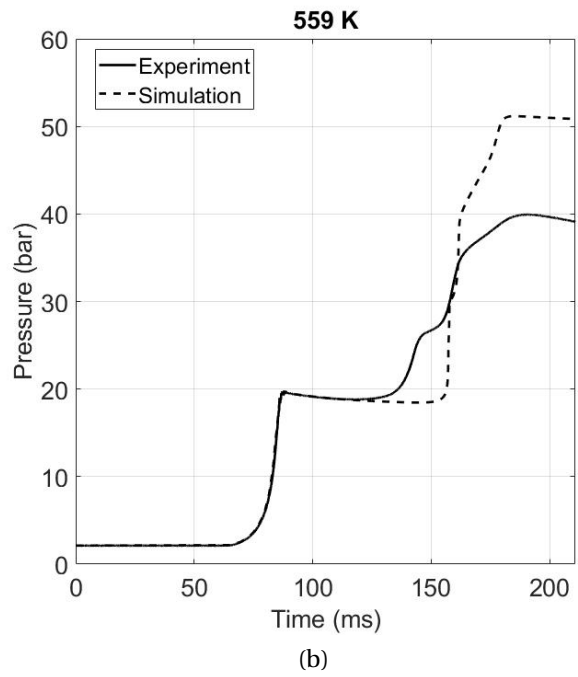
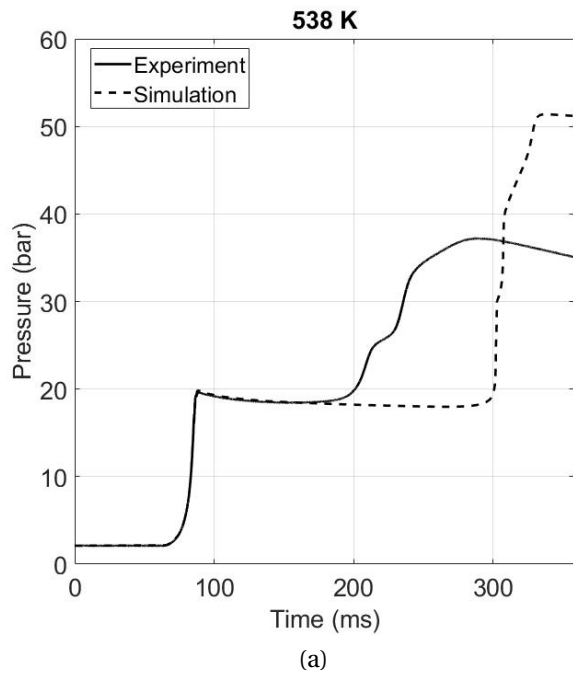
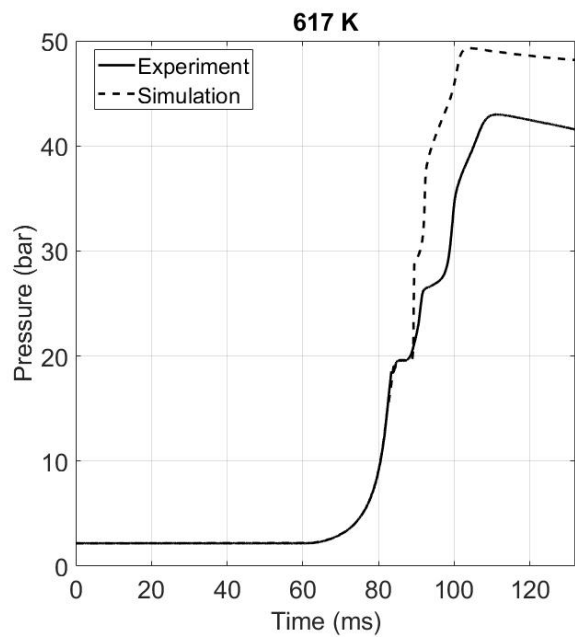
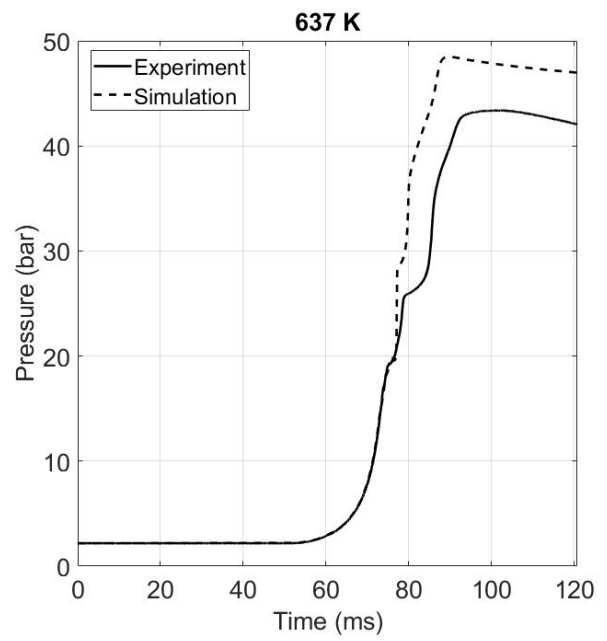


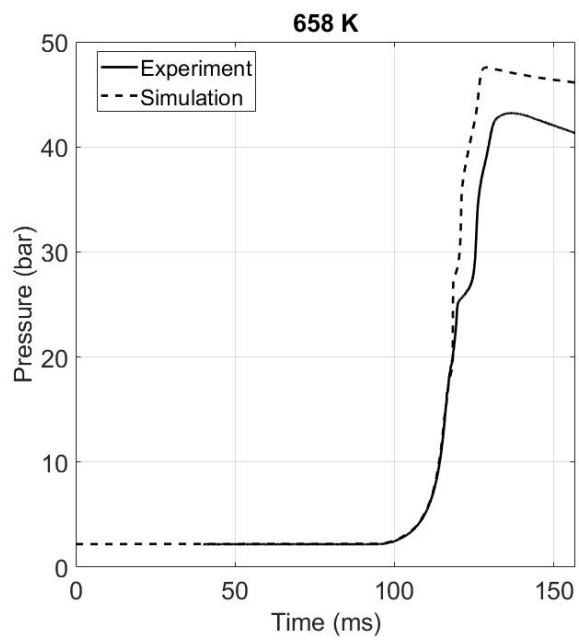
Figure B.20: Dibutyl ether: $\phi = 1$, dilution = 10 (inert gases: 50% CO_2 + 50% N_2), $p_c = 20$ bar, DBE = 0.8%.



(e)



(f)



(g)

Figure B.20: Dibutyl ether: $\phi = 1$, dilution = 10 (inert gases: 50% CO_2 + 50% N_2), $p_c = 20$ bar, DBE = 0.8%.

B.1.6 Di-iso-pentyl ether

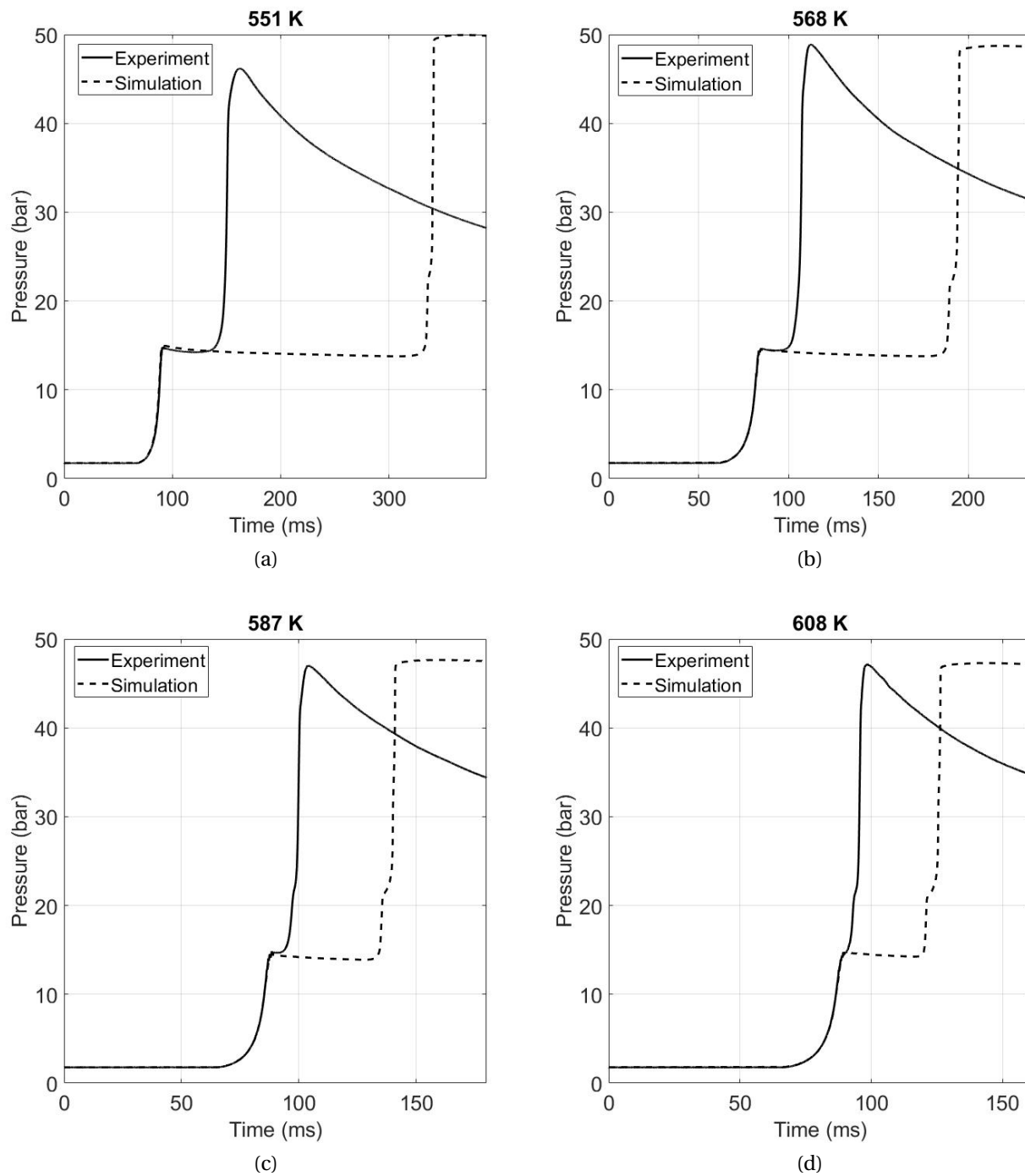
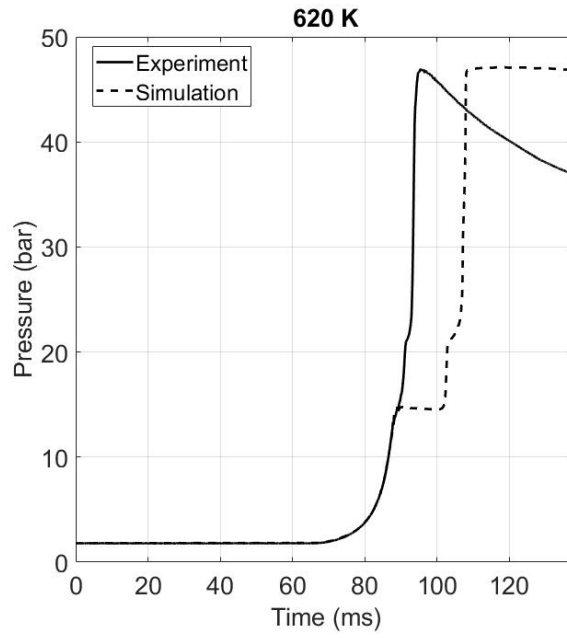
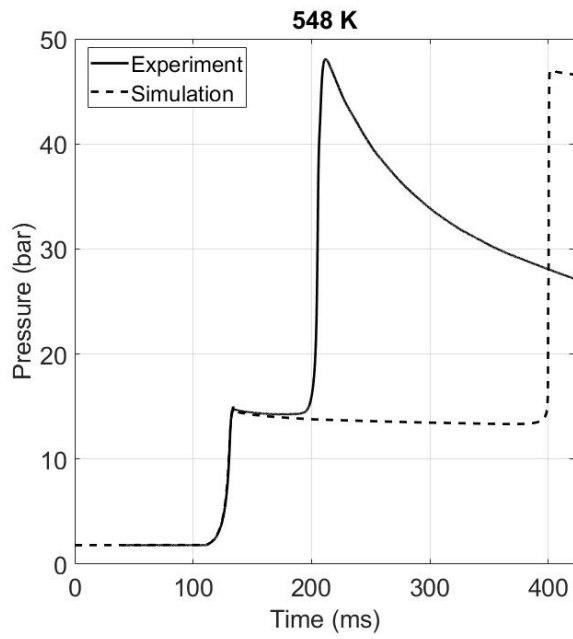


Figure B.21: Di-iso-pentyl ether: $\phi = 1$, dilution = 5 (inert gas: 100% CO₂), $p_c = 15$ bar, DIPEE = 1.1%.

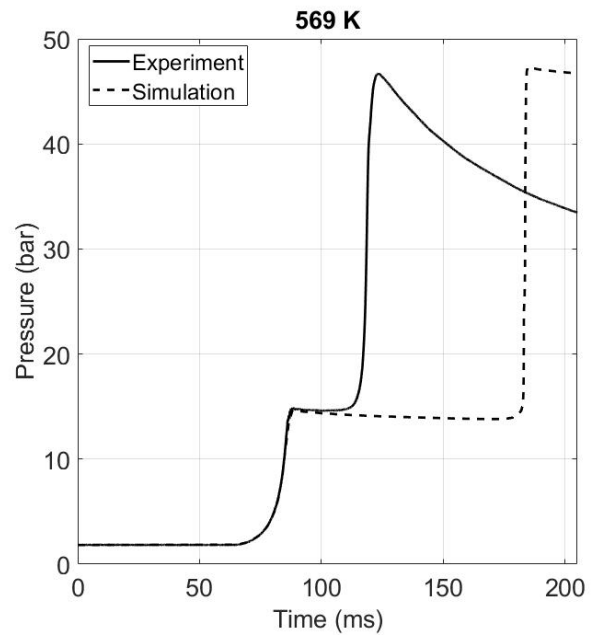


(e)

Figure B.21: Di-iso-pentyl ether: $\phi = 1$, dilution = 5 (inert gas: 100% CO₂), $p_c = 15$ bar, DIPEE = 1.1%.



(a)



(b)

Figure B.22: Di-iso-pentyl ether: $\phi = 2$, dilution = 5 (inert gas: 100% CO₂), $p_c = 15$ bar, DIPEE = 2.2%.

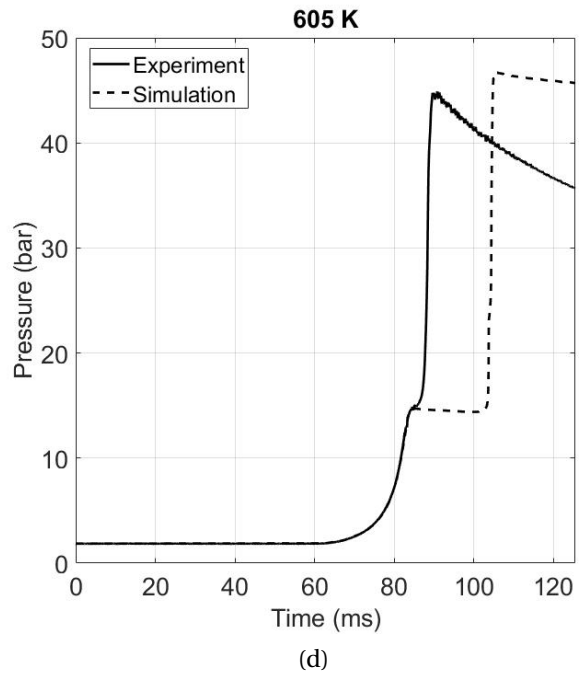
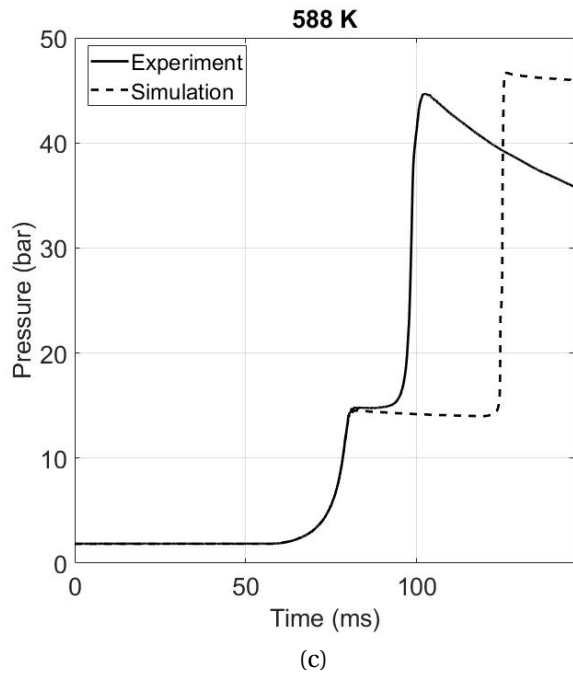


Figure B.22: Di-iso-pentyl ether: $\phi = 2$, dilution = 5 (inert gas: 100% CO₂), $p_c = 15$ bar, DIPEE = 2.2%.

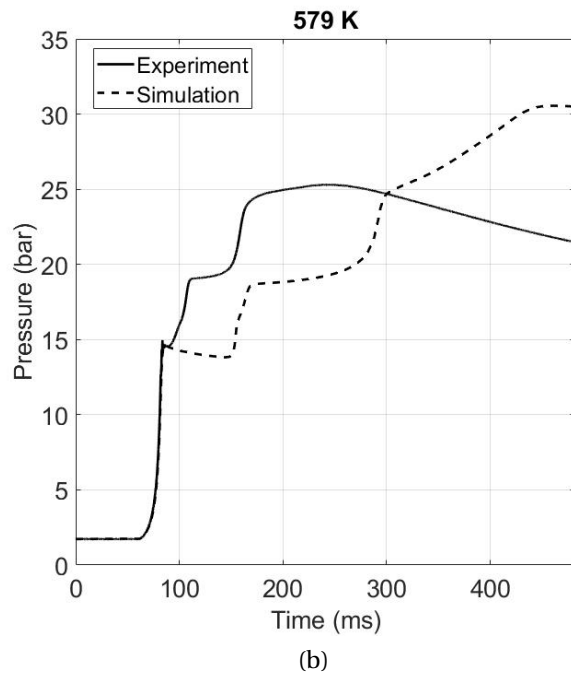
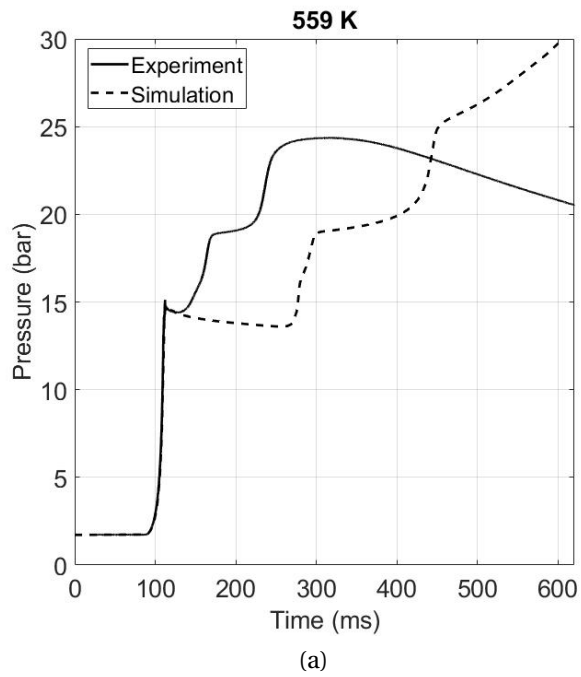


Figure B.23: Di-iso-pentyl ether: $\phi = 0.5$, dilution = 5 (inert gas: 100% CO₂), $p_c = 15$ bar, DIPEE = 0.5%.

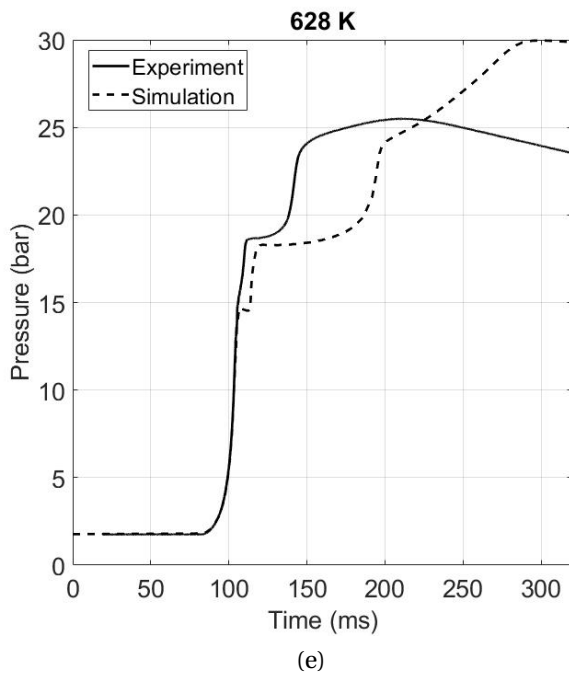
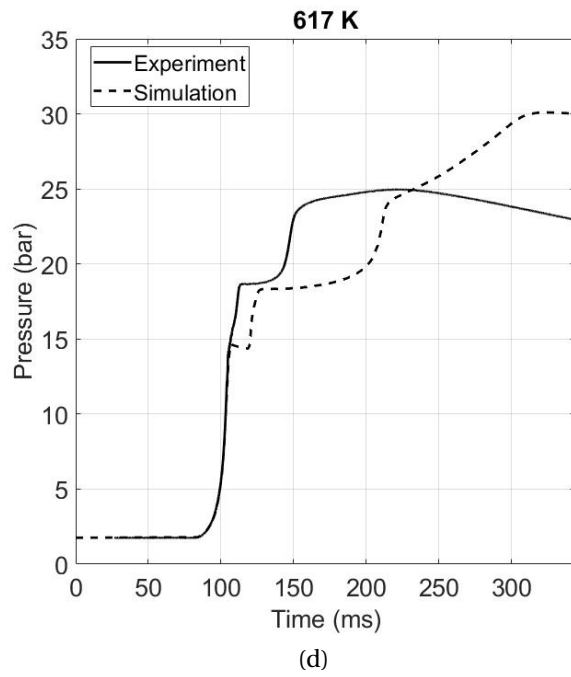
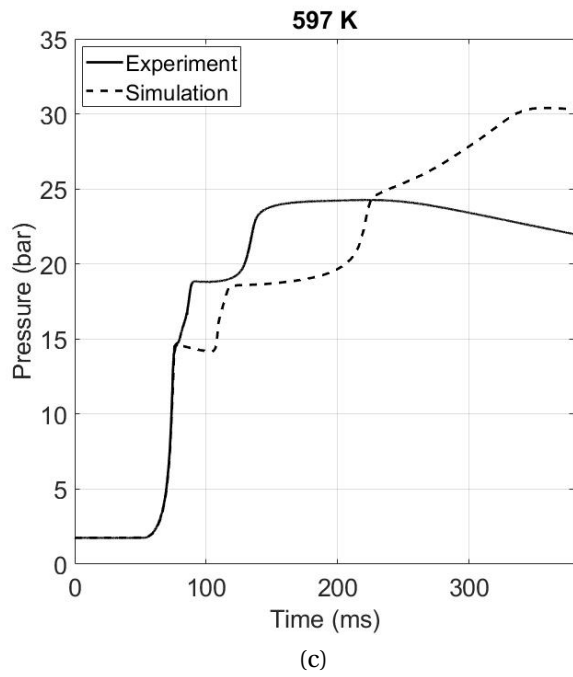
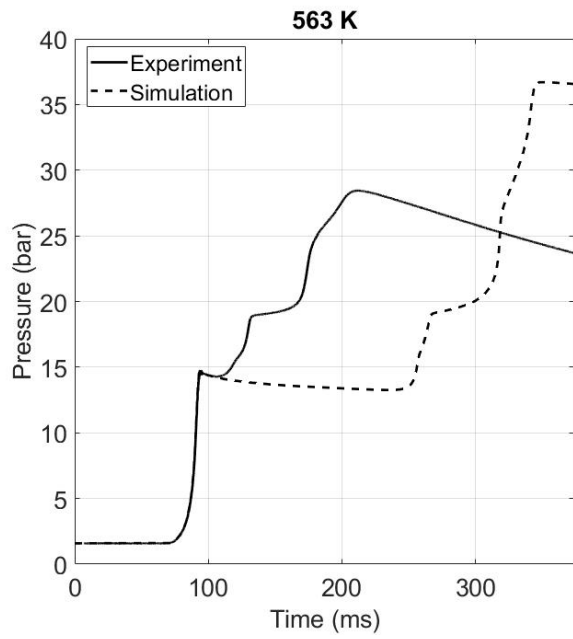
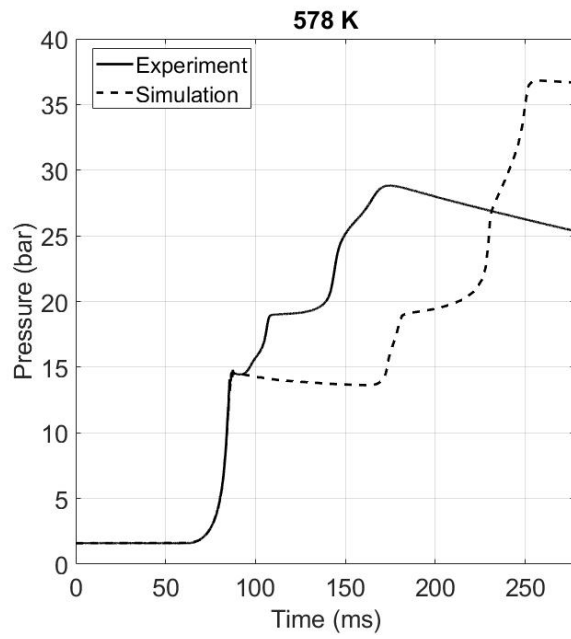


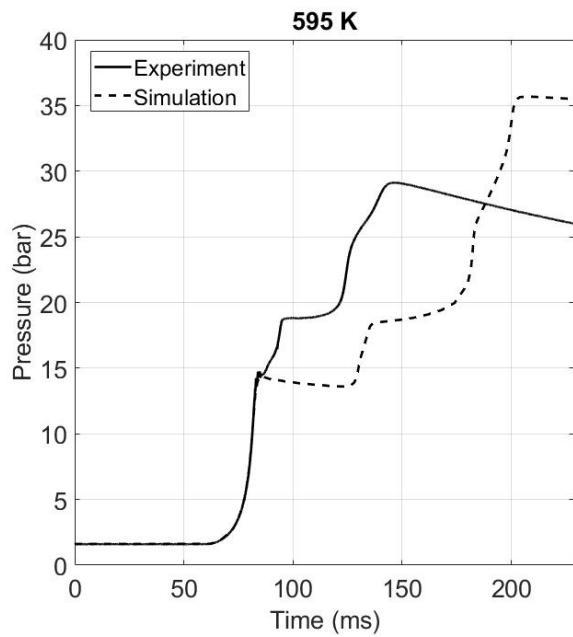
Figure B.23: Di-iso-pentyl ether: $\phi = 0.5$, dilution = 5 (inert gas: 100% CO₂), $p_c = 15$ bar, DIPEE = 0.5%.



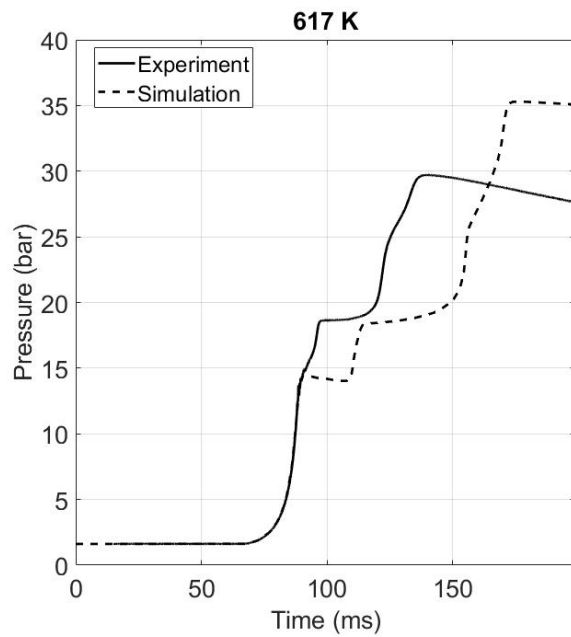
(a)



(b)



(c)



(d)

Figure B.24: Di-iso-pentyl ether: $\phi = 1$, dilution = 10 (inert gases: 50% CO₂ + 50% N₂), $p_c = 15$ bar, DIPEE = 0.6%.

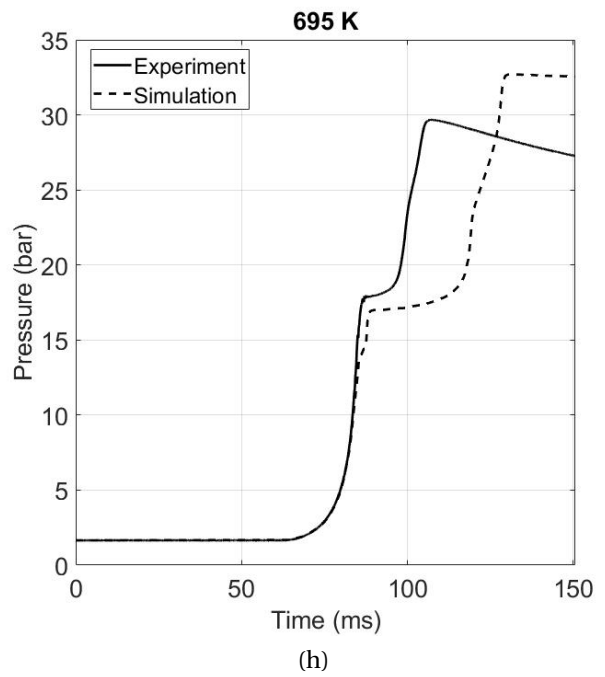
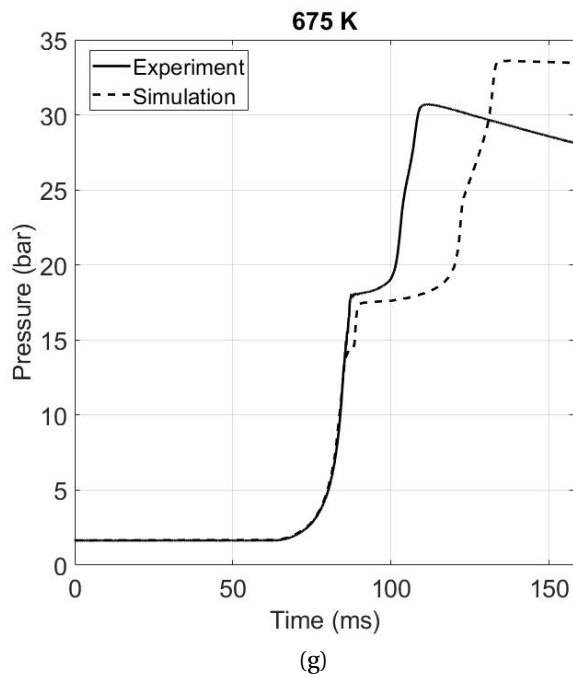
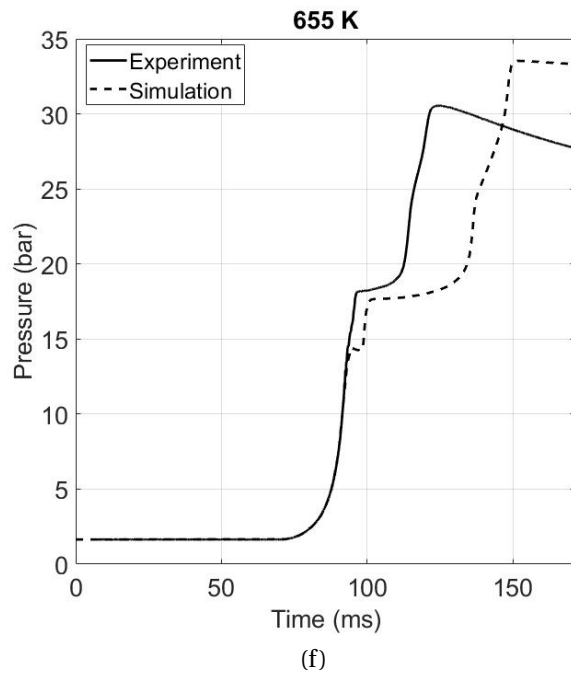
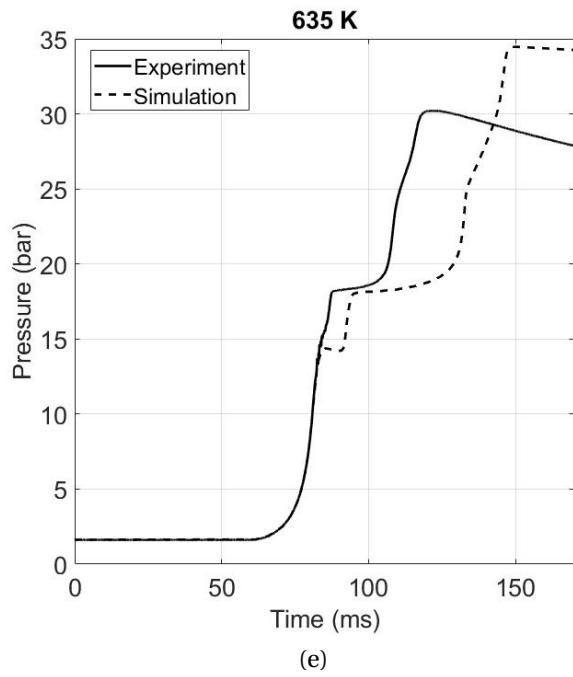
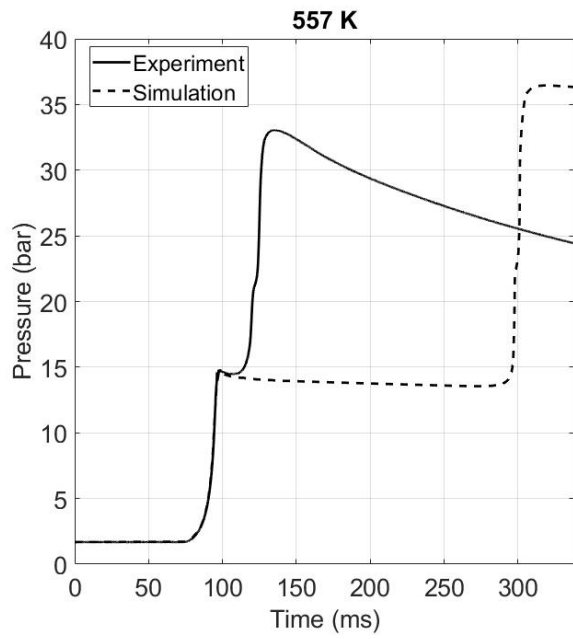
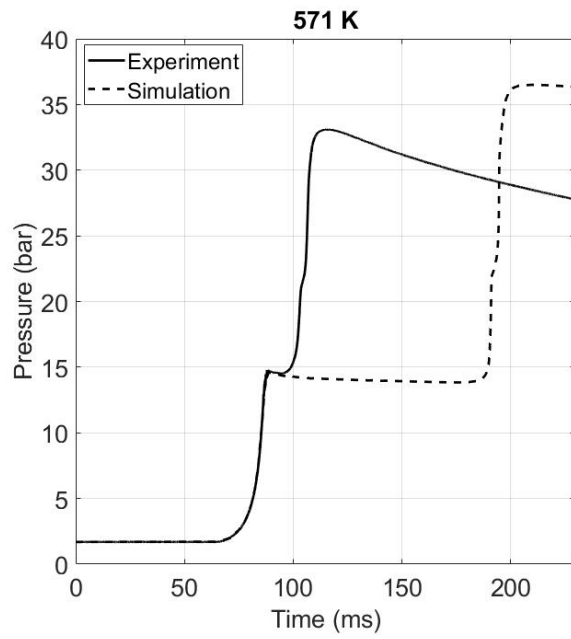


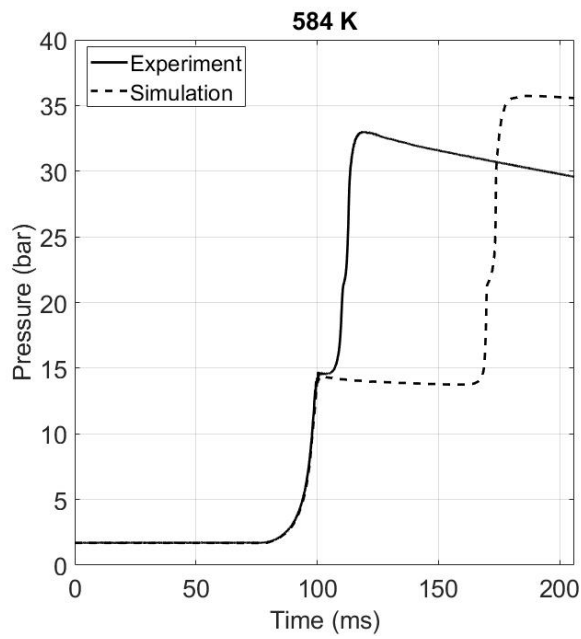
Figure B.24: Di-iso-pentyl ether: $\phi = 1$, dilution = 10 (inert gases: 50% CO₂ + 50% N₂), $p_c = 15$ bar, DIPEE = 0.6%.



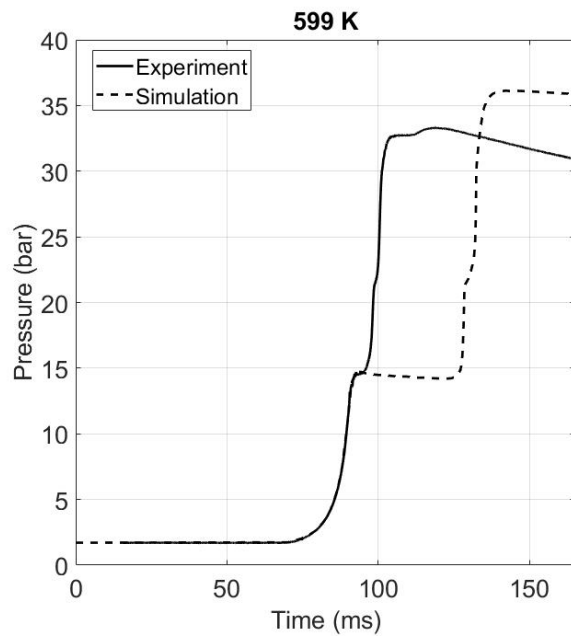
(a)



(b)



(c)



(d)

Figure B.25: Di-iso-pentyl ether: $\phi = 2$, dilution = 10 (inert gases: 50% CO₂ + 50% N₂), $p_c = 15$ bar, DIPEE = 1.2%.

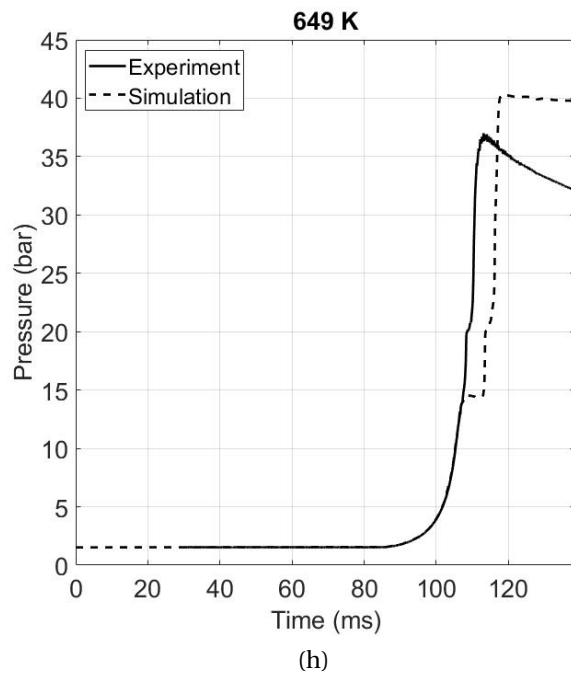
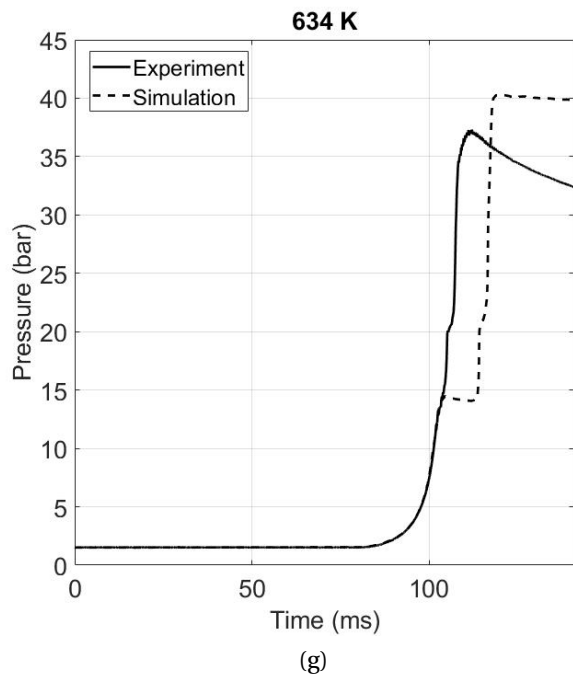
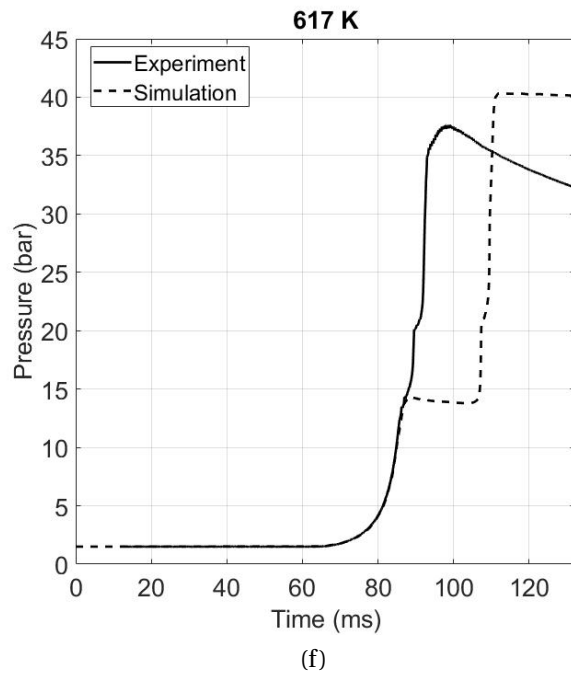
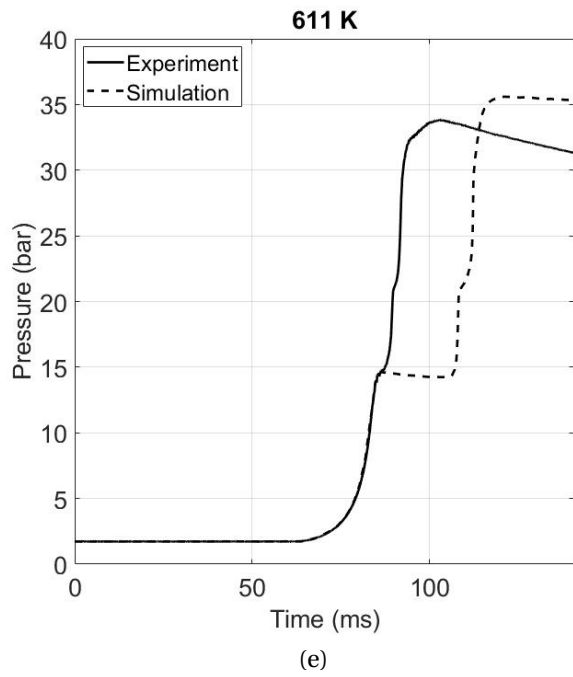
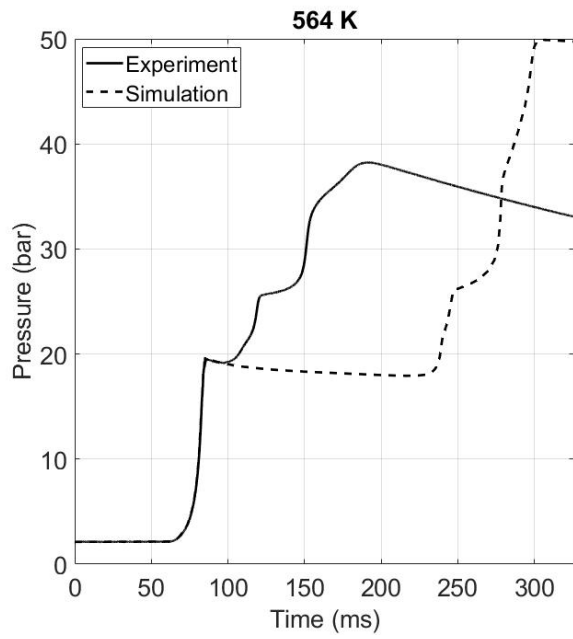
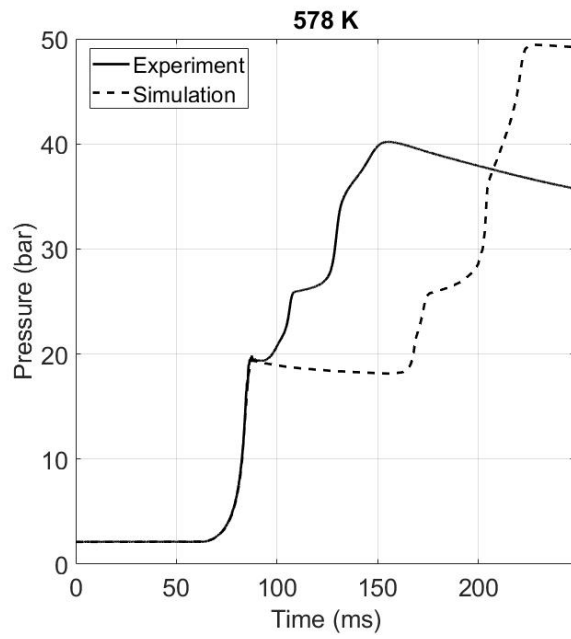


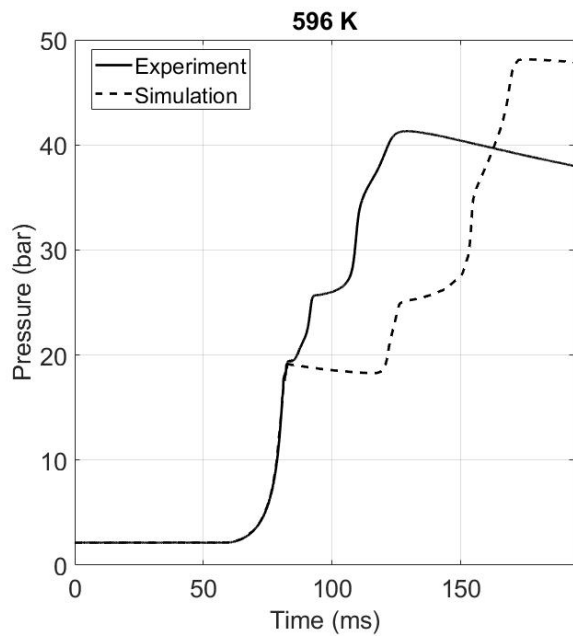
Figure B.25: Di-iso-pentyl ether: $\phi = 2$, dilution = 10, $p_c = 15$ bar (f), (g) and (h): inert gas 100% N_2 , the others 50% CO_2 + 50% N_2 , DIPEE = 1.2%.



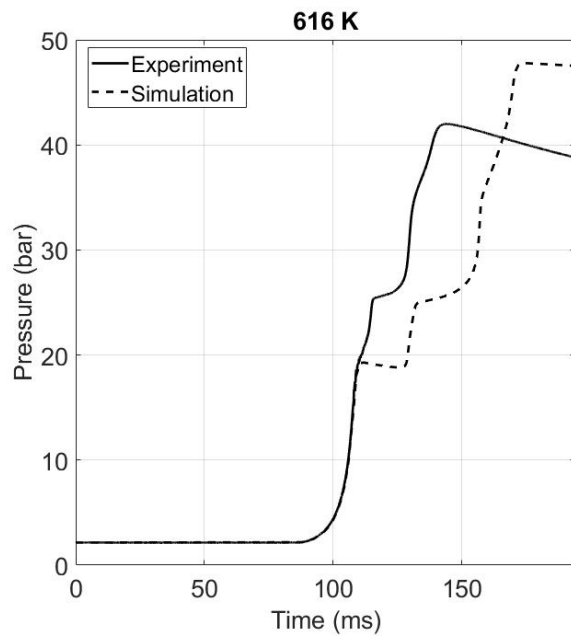
(a)



(b)



(c)



(d)

Figure B.26: Di-iso-pentyl ether: $\phi = 1$, dilution = 10 (inert gases: 50% CO₂ + 50% N₂), $p_c = 20$ bar, DIPEE = 0.6%.

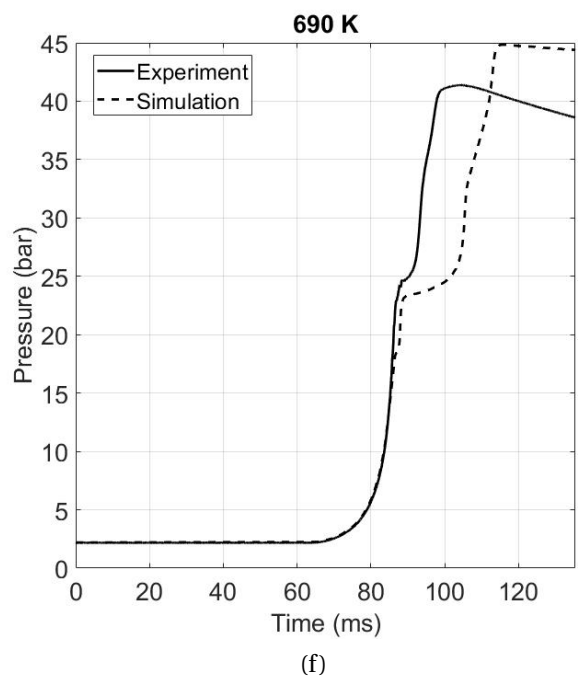
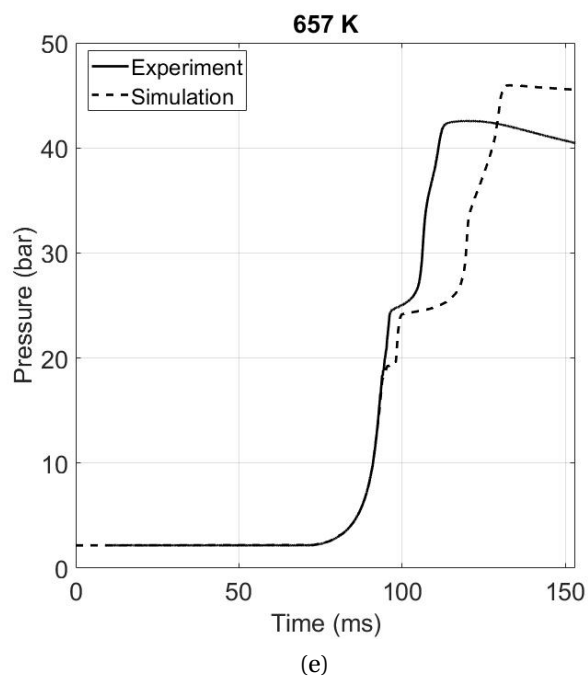


Figure B.26: Di-iso-pentyl ether: $\phi = 1$, dilution = 10 (inert gases: 50% CO₂ + 50% N₂), $p_c = 20$ bar, DIPEE = 0.6%.

B.1.7 Di-n-pentyl ether

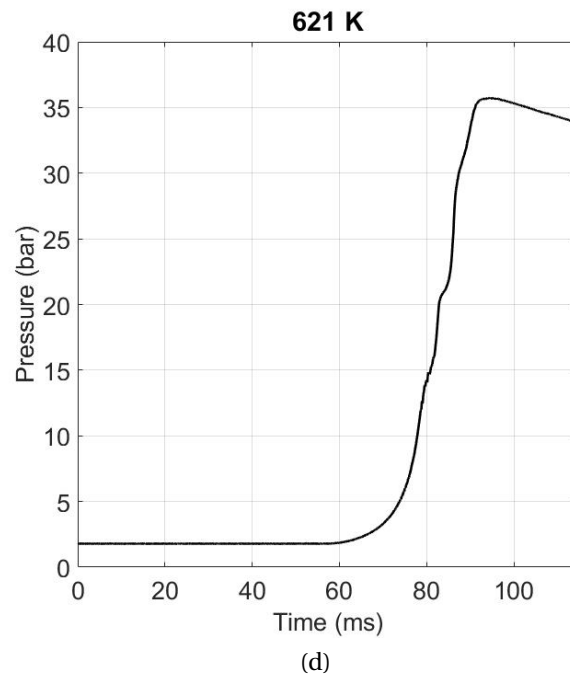
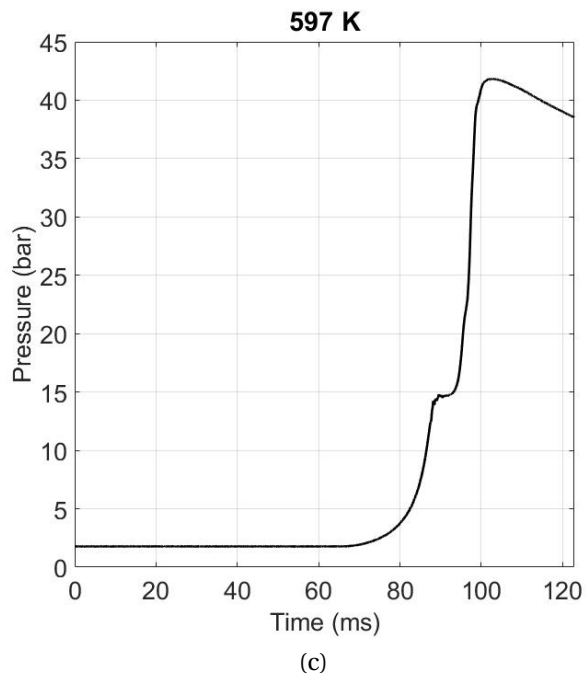
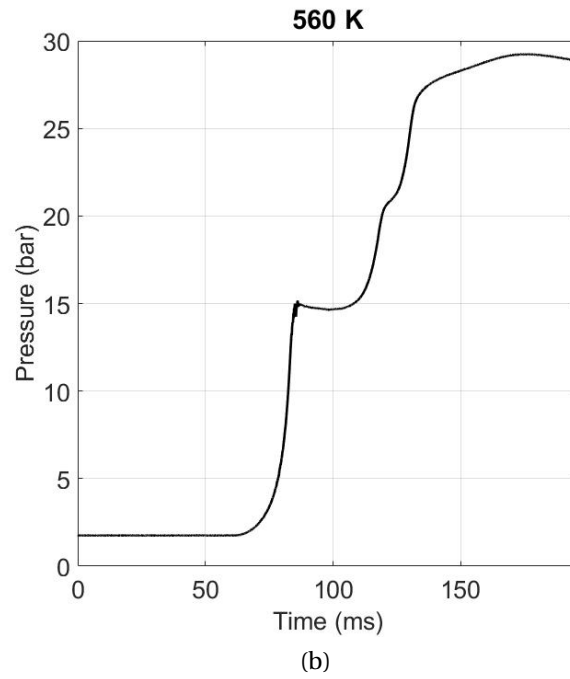
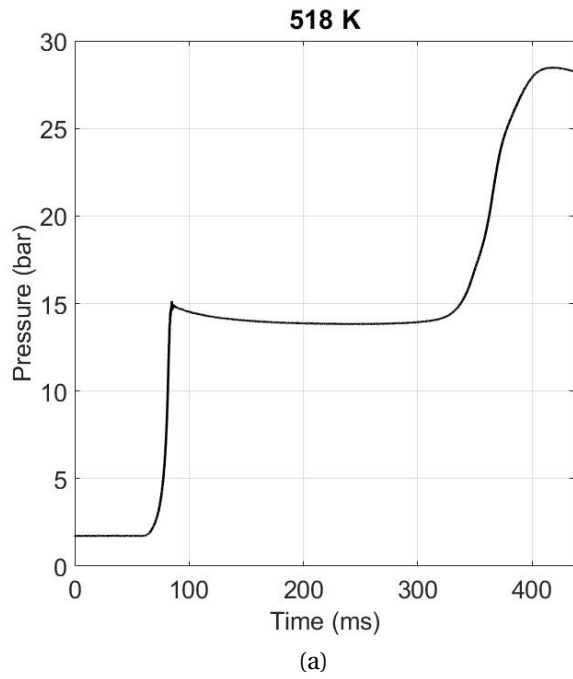


Figure B.27: Di-n-pentyl ether: $\phi = 1$, dilution = 5 (inert gas: 100% CO_2), $p_c = 15$ bar, DNPEE = 1.1%.

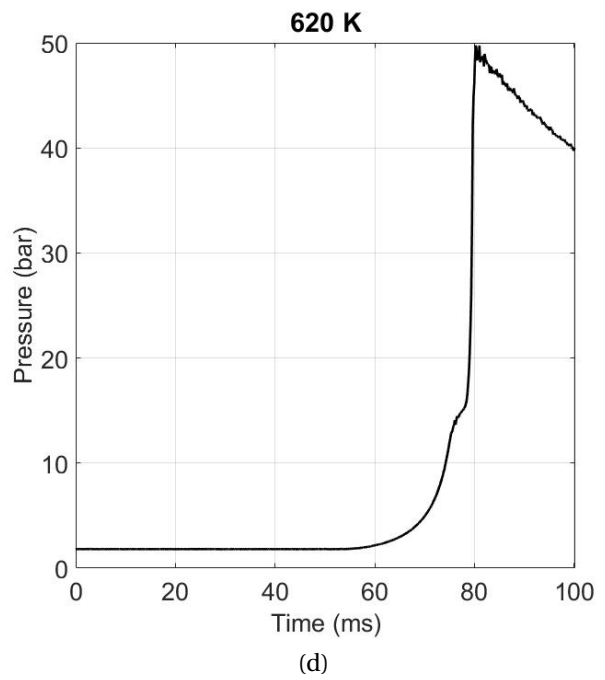
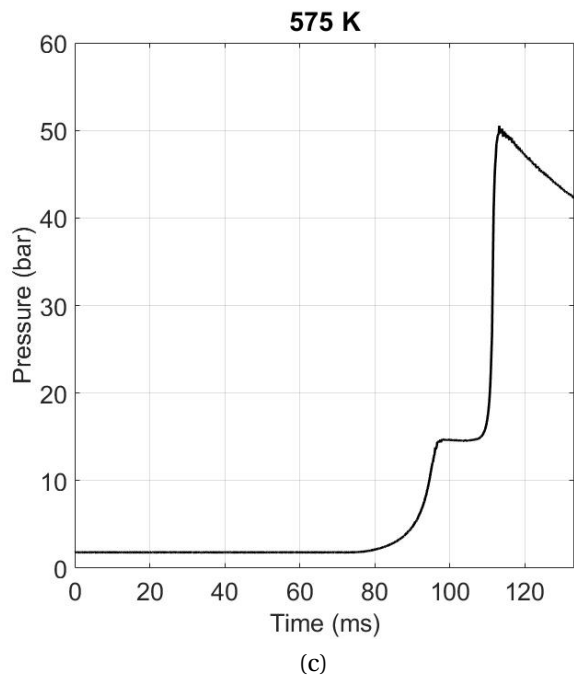
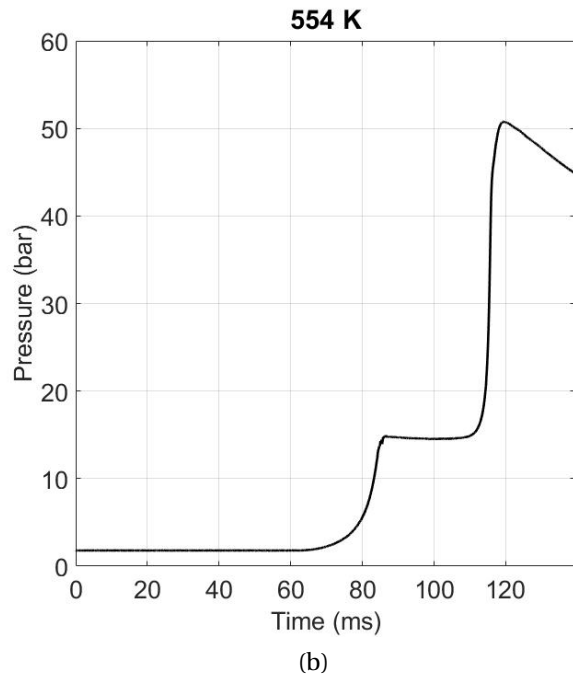
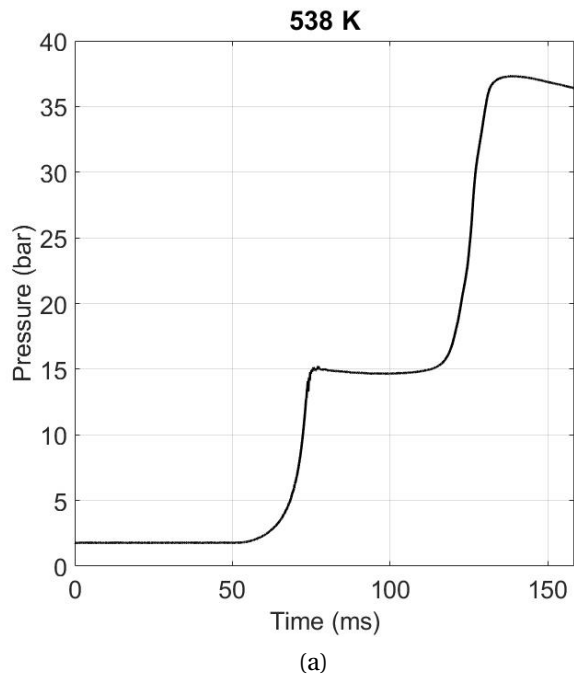


Figure B.28: Di-n-pentyl ether: $\phi = 2$, dilution = 5 (inert gas: 100% CO₂), $p_c = 15$ bar, DNPEE = 2.2%.

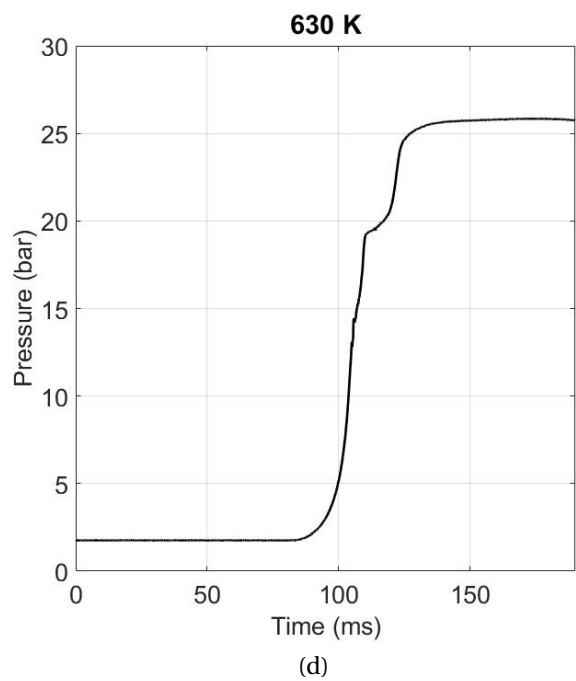
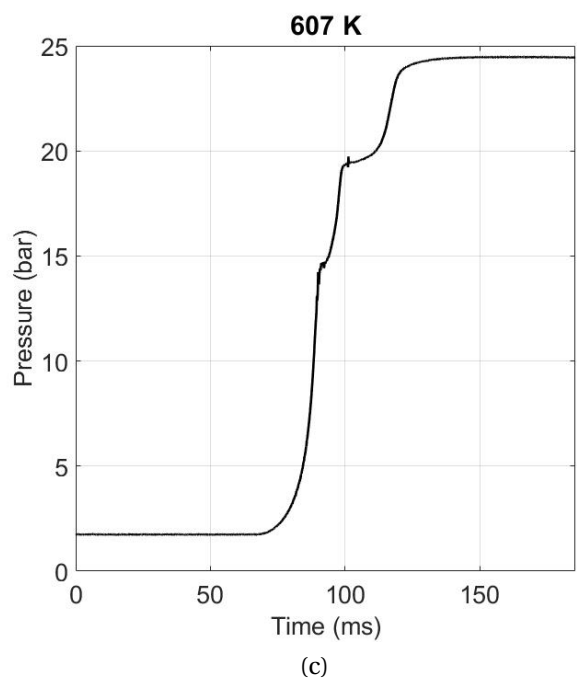
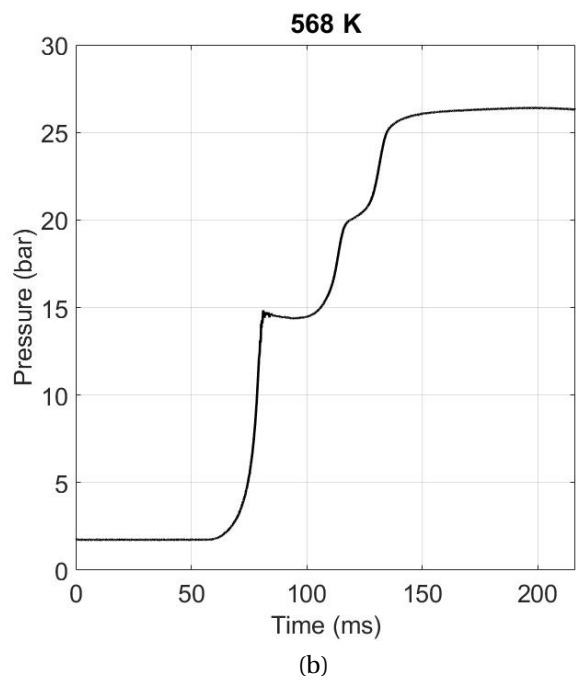
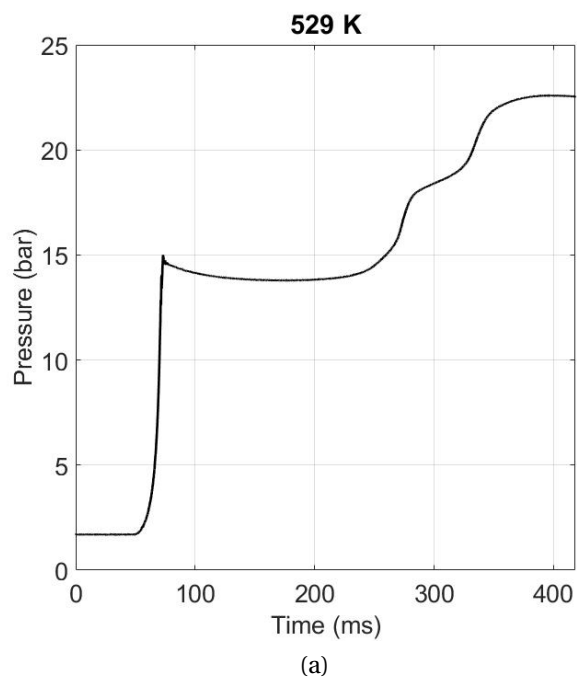


Figure B.29: Di-n-pentyl ether: $\phi = 0.5$, dilution = 5 (inert gas: 100% CO₂), $p_c = 15$ bar, DNPEE = 0.5%.

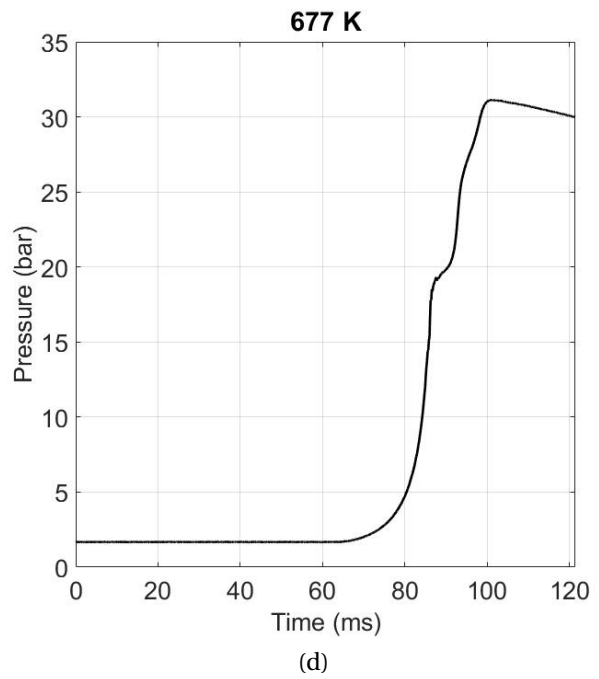
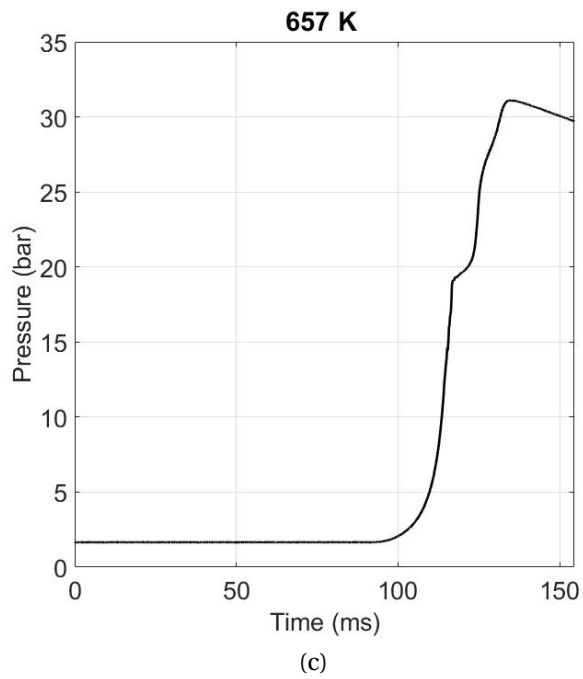
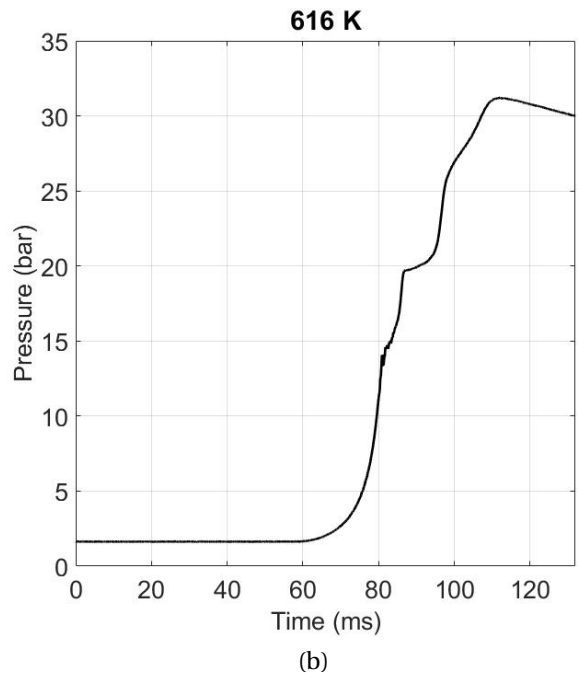
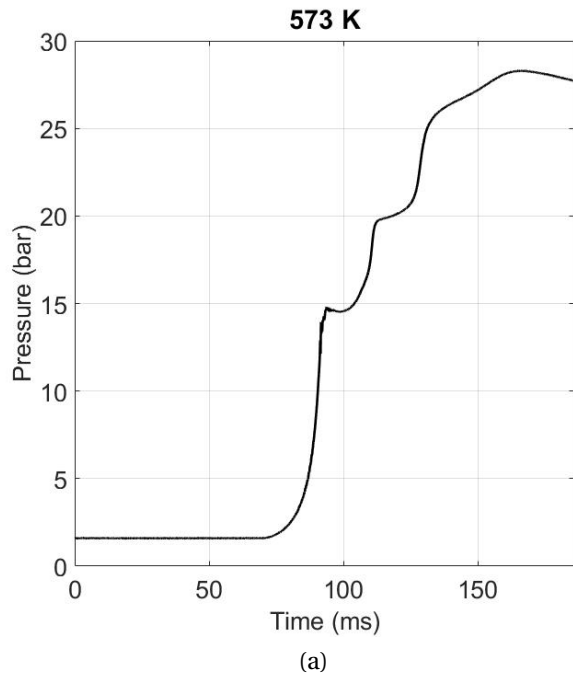


Figure B.30: Di-n-pentyl ether: $\phi = 1$, dilution = 10 (inert gases: 50% CO₂ + 50% N₂), $p_c = 15$ bar, DNPEE = 0.6%.

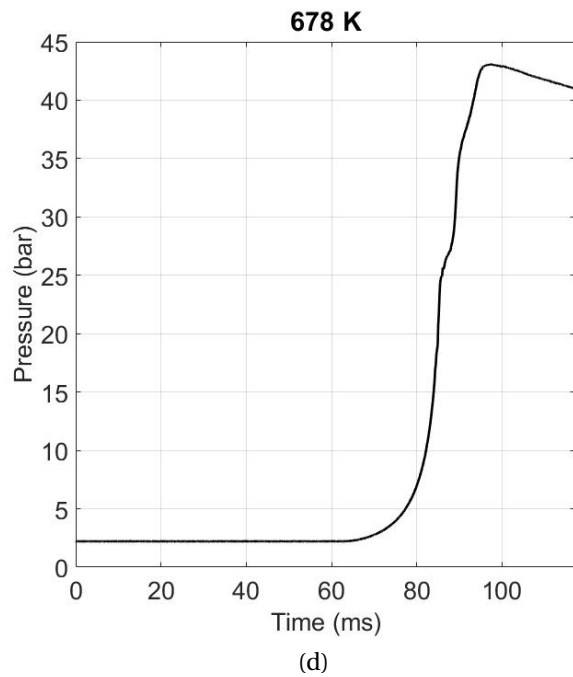
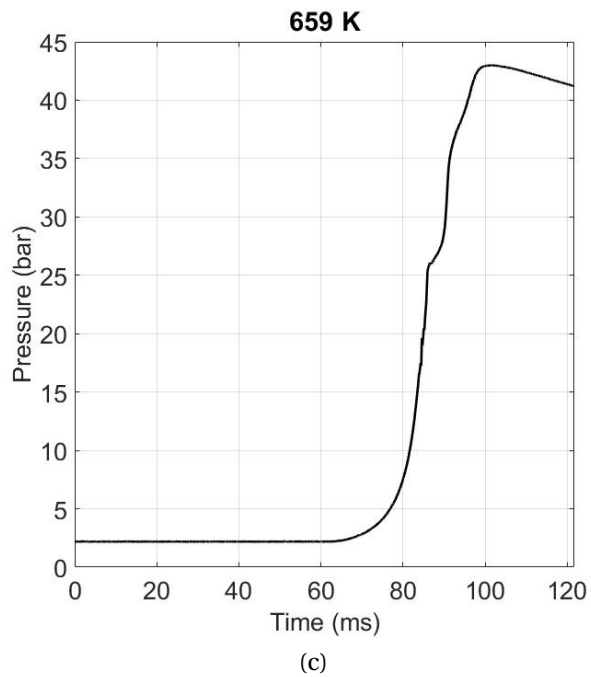
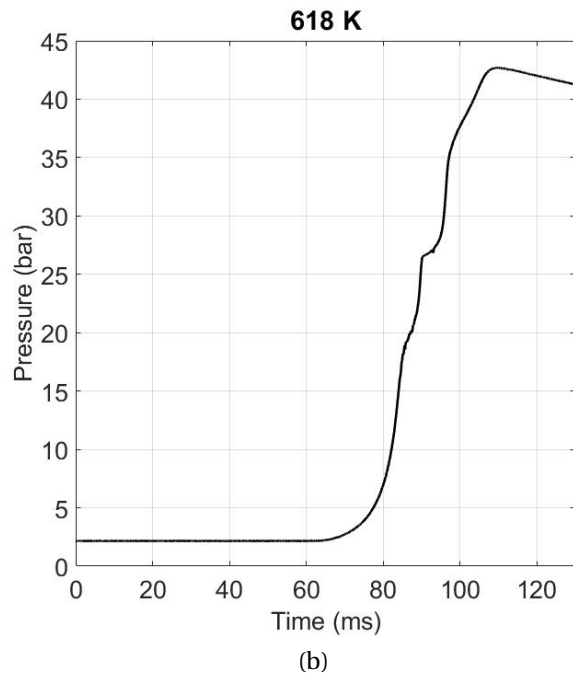
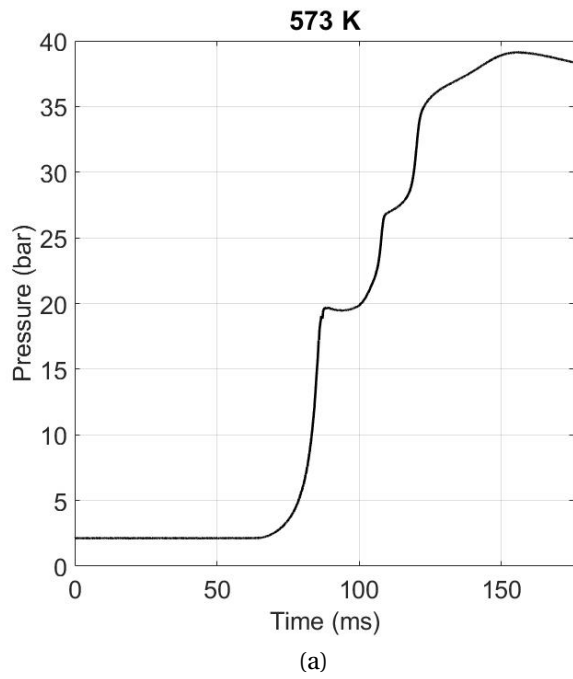
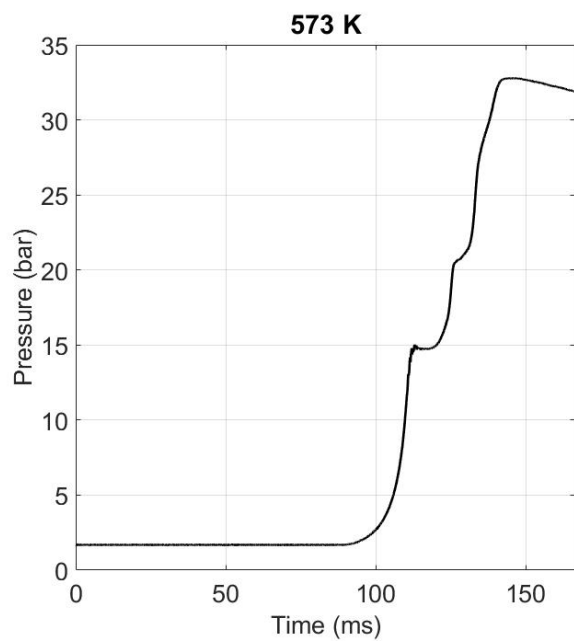
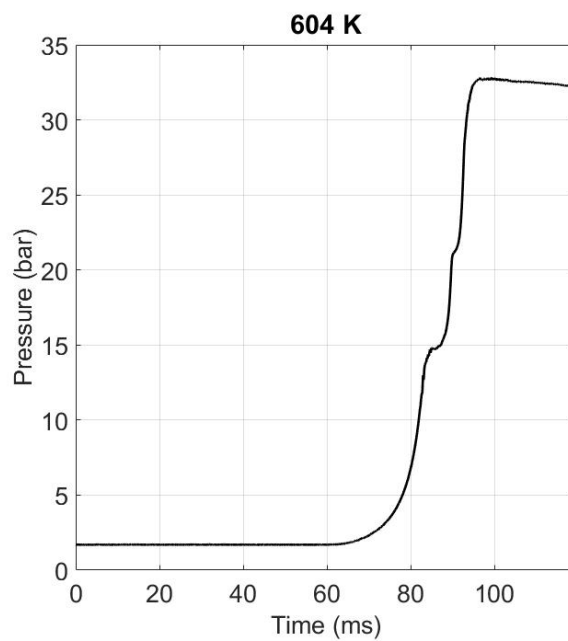


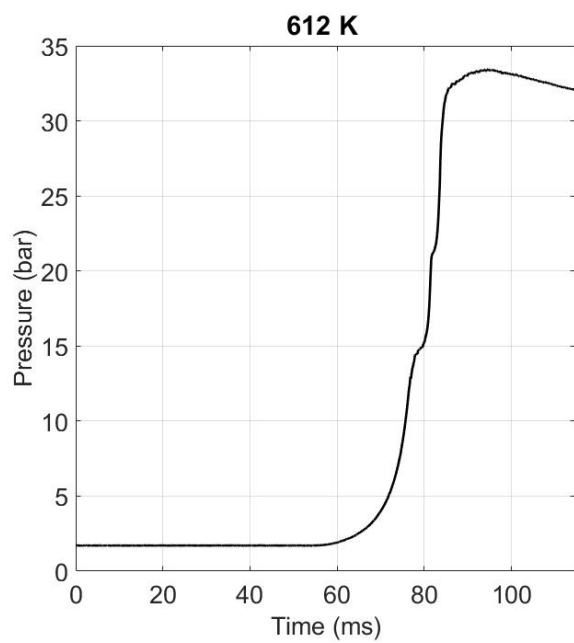
Figure B.31: Di-n-pentyl ether: $\phi = 1$, dilution = 10 (inert gases: 50% CO₂ + 50% N₂), $p_c = 20$ bar, DNPEE = 0.6%.



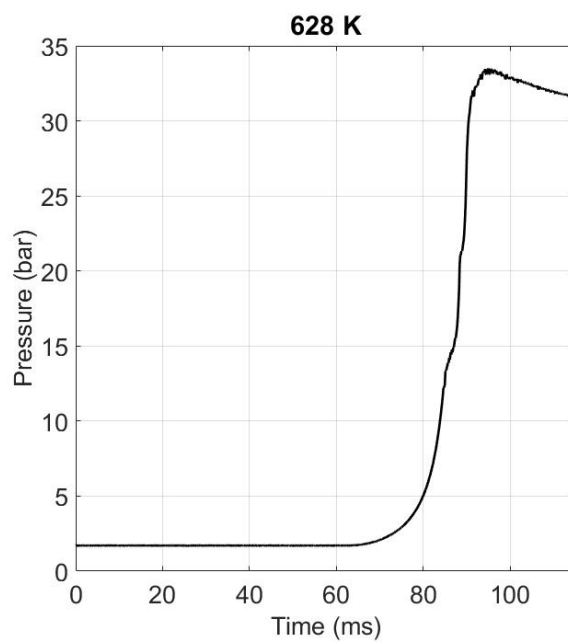
(a)



(b)



(c)



(d)

Figure B.32: Di-n-pentyl ether: $\phi = 2$, dilution = 10 (inert gases: 50% CO₂ + 50% N₂), $p_c = 15$ bar, DNPEE = 1.2%.

B.1.8 Ethyl lactate

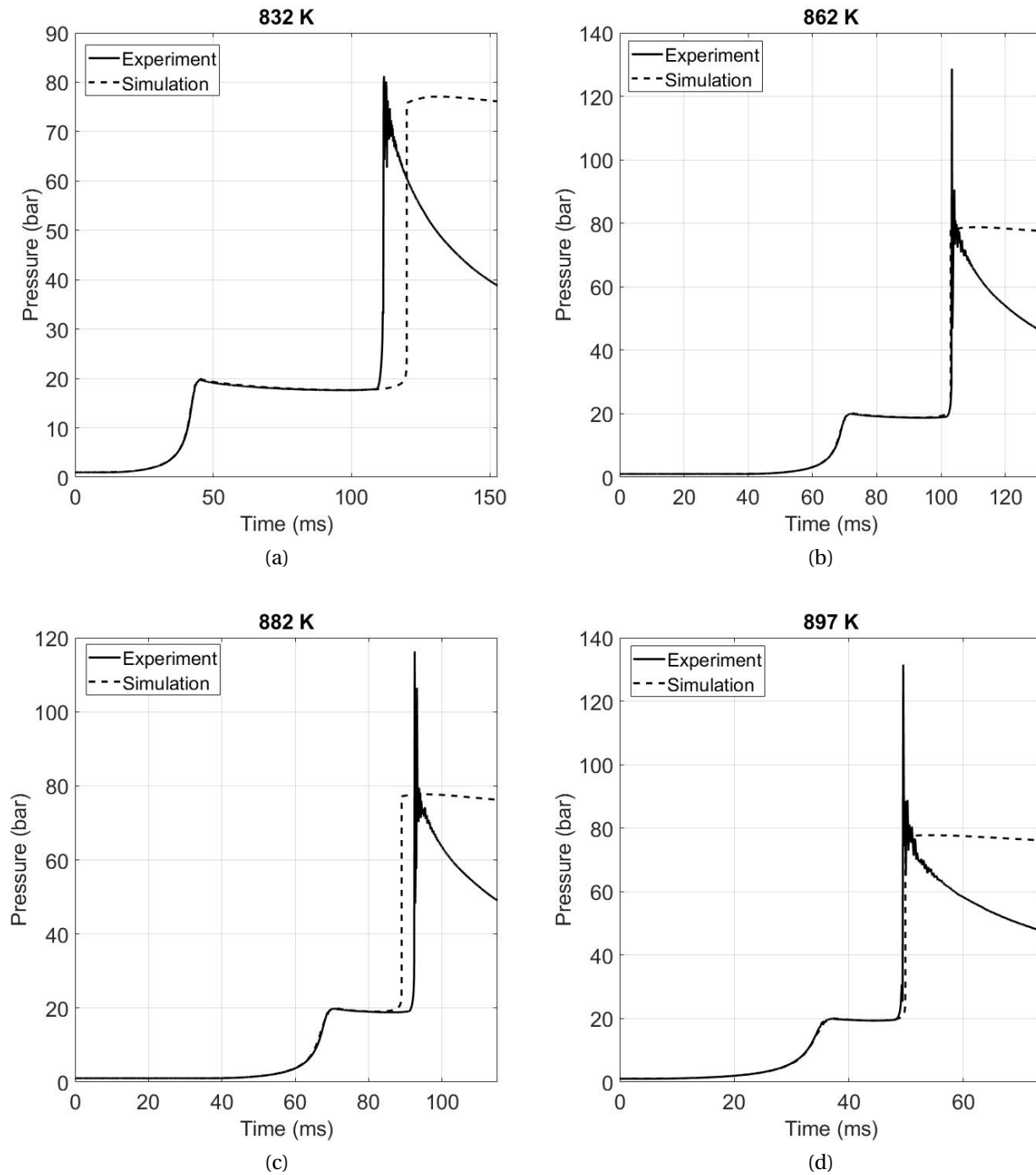
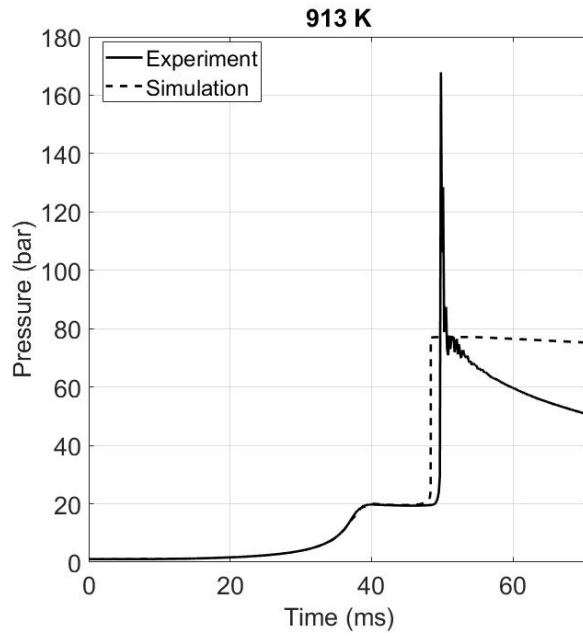
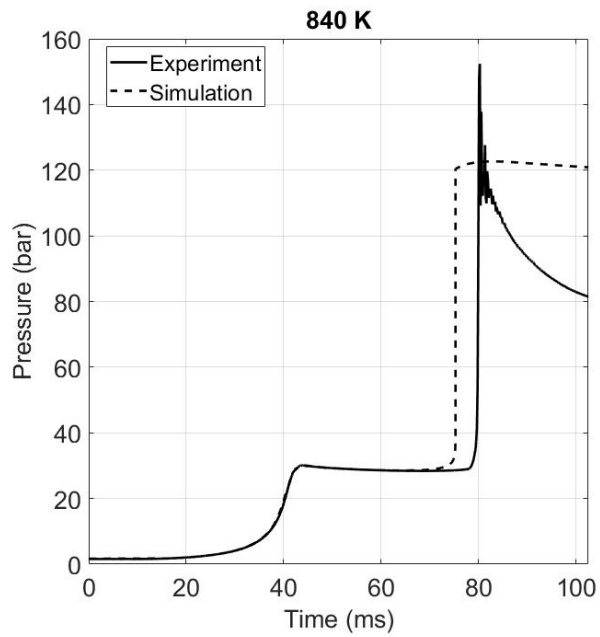


Figure B.33: Ethyl lactate: $\phi = 1$, dilution: "air", $p_c = 20$ bar, EtLac = 3.38%.

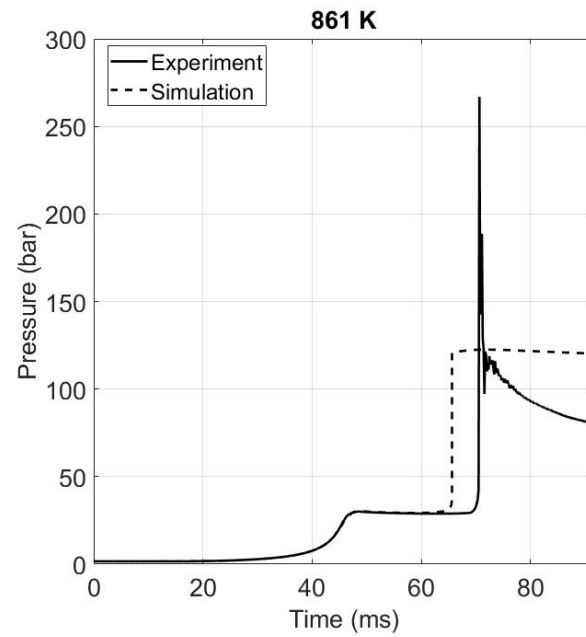


(e)

Figure B.33: Ethyl lactate: $\phi = 1$, dilution: "air", $p_c = 20$ bar, EtLac = 3.38%.



(a)



(b)

Figure B.34: Ethyl lactate: $\phi = 1$, dilution: "air", $p_c = 30$ bar, EtLac = 3.38%.

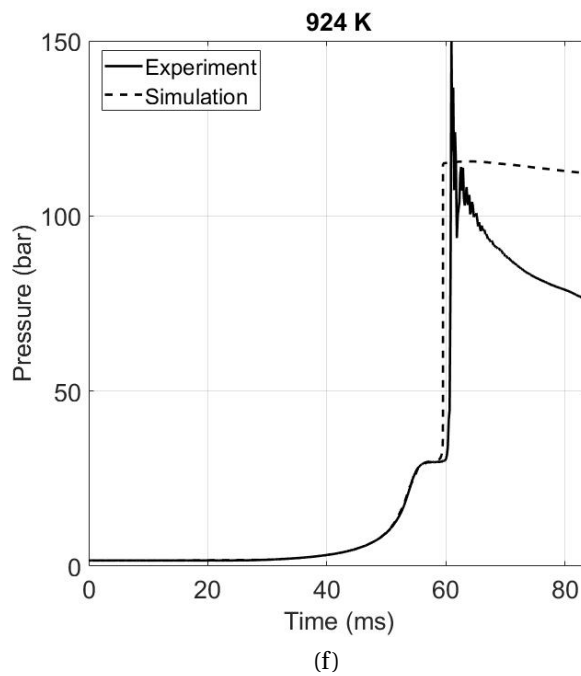
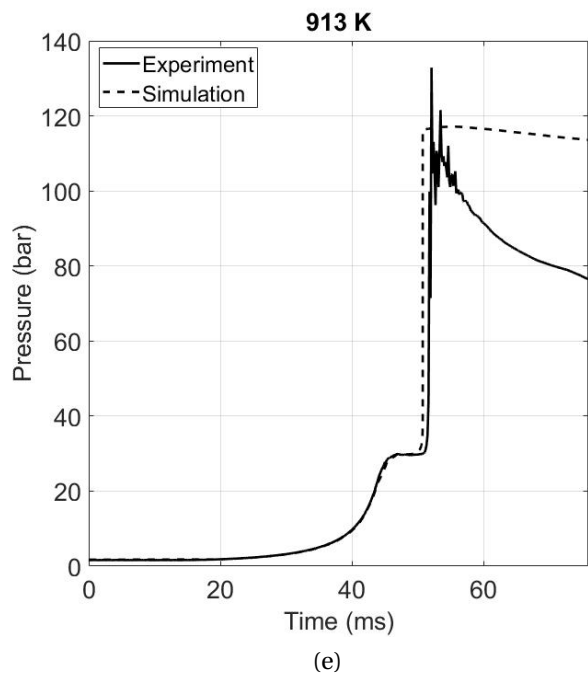
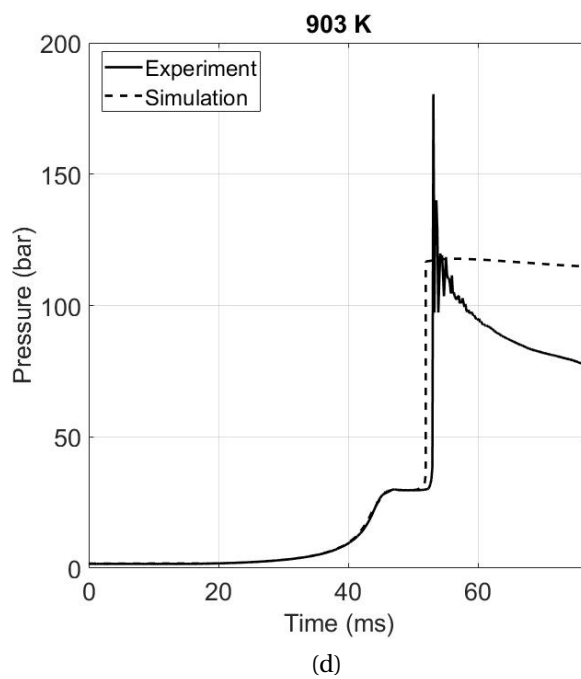
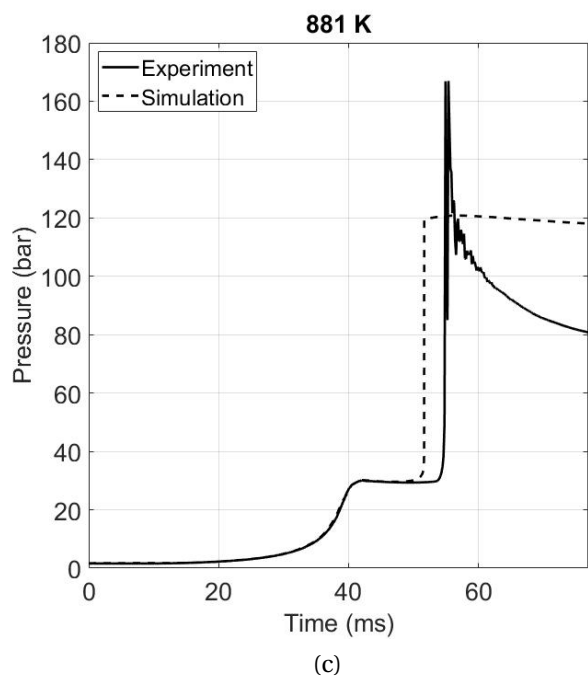
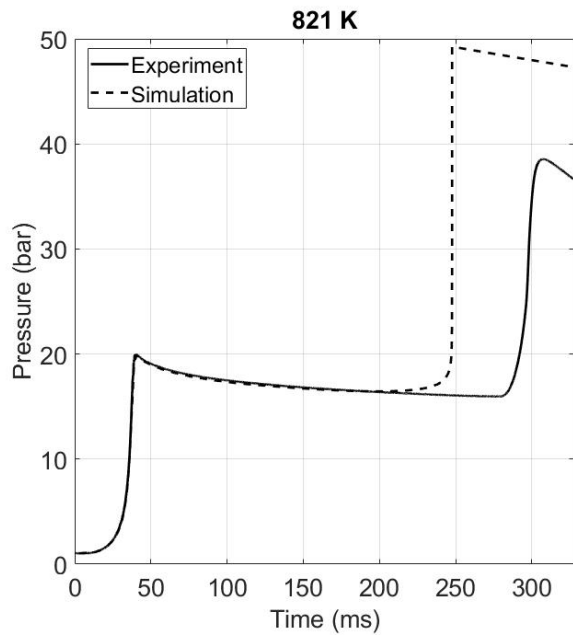
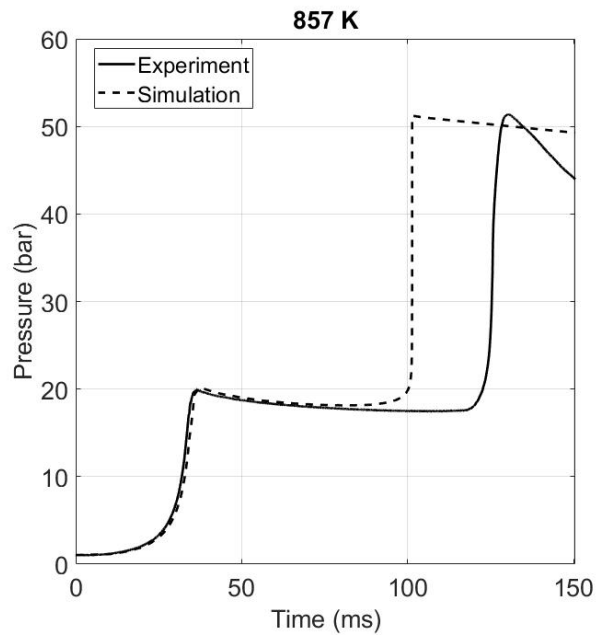


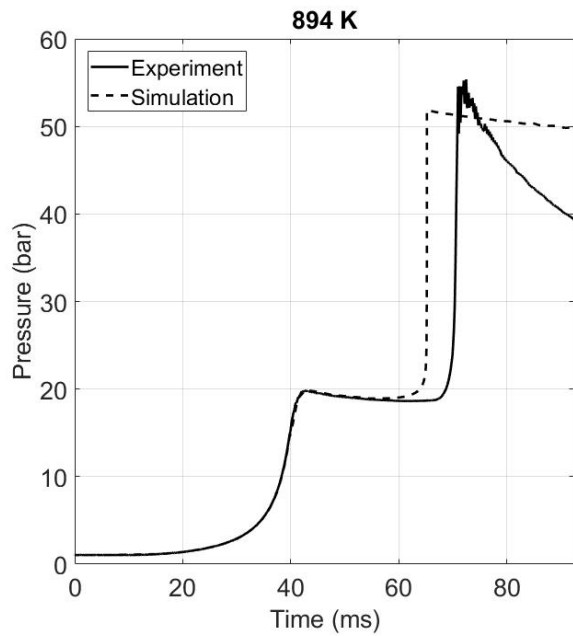
Figure B.34: Ethyl lactate: $\phi = 1$, dilution: "air", $p_c = 30$ bar, EtLac = 3.38%.



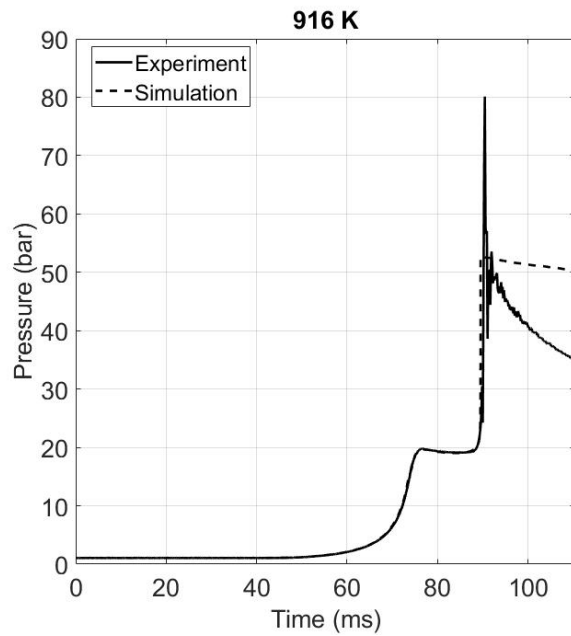
(a)



(b)

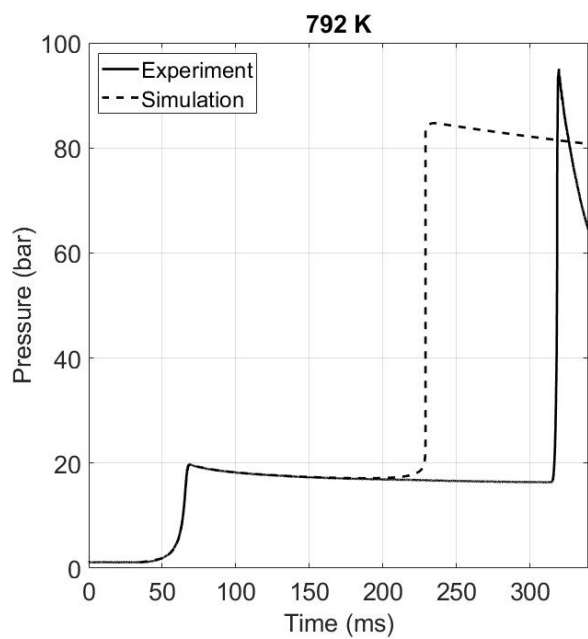


(c)

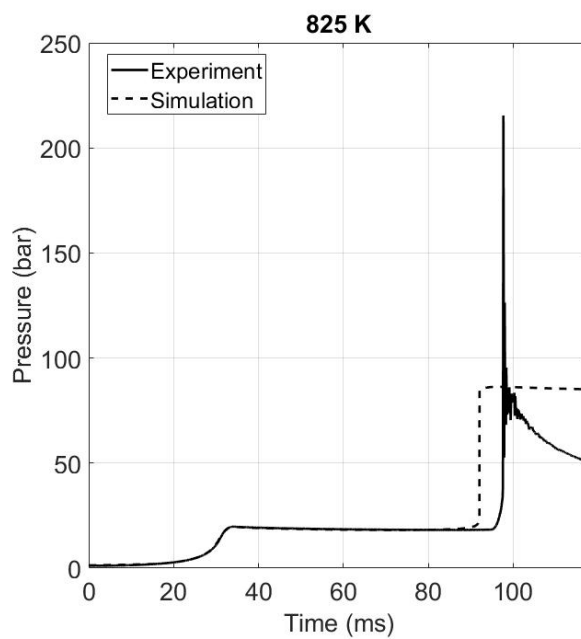


(d)

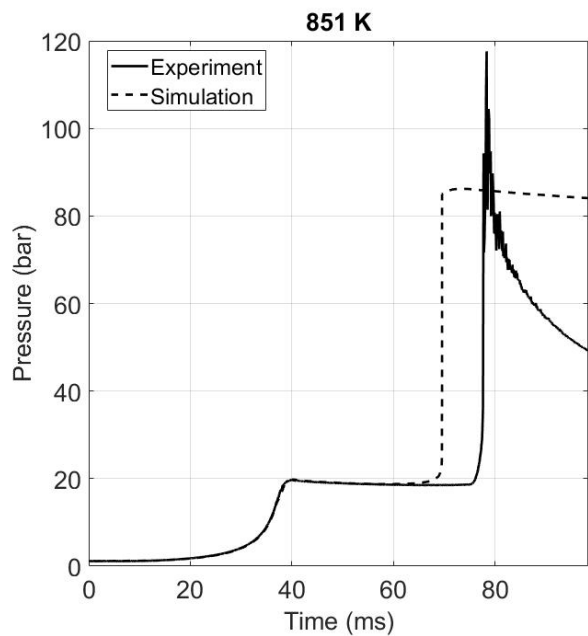
Figure B.35: Ethyl lactate: $\phi = 0.5$, dilution: "air", $p_c = 20$ bar, EtLac = 1.72%.



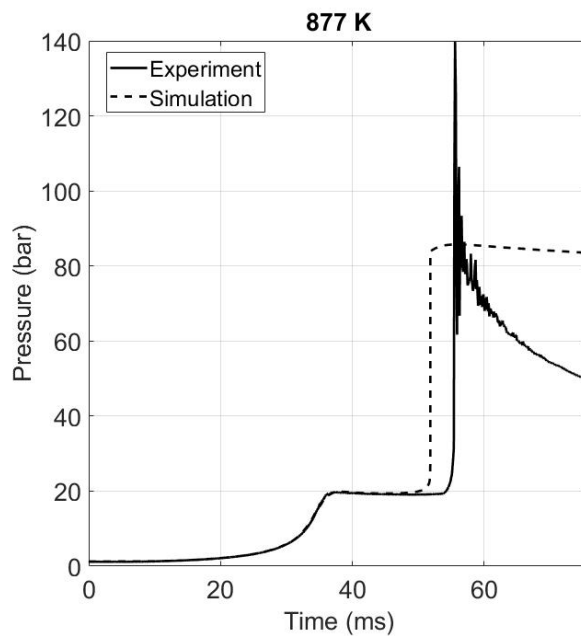
(a)



(b)



(c)



(d)

Figure B.36: Ethyl lactate: $\phi = 1.5$, dilution: "air", $p_c = 20$ bar, EtLac = 4.99%.

B.2 HRR

For some ethers, the heat release rate analysis was performed also for a rich mixture. This allows two comparisons: the first one, similar to what was done for $\phi = 1$, between experimental and simulation results, the second between the pressure profiles and heat release at the same temperature for the two different equivalence ratios (stoichiometric and rich).

The first thing to be noted is that the lower heating value is very different for the two mixtures, since the fuel percentage changes, while the heat release is not so different. Therefore, both plots of normalised and not normalised HRR vs aHR are provided.

Table B.1 shows the conditions that were considered for the heat release rate analysis of rich mixtures.

Table B.1: Tested fuels and experimental conditions for the heat release rate analysis of rich mixtures

Fuel	Dilution	ϕ	% Fuel	P (bar)	T (K)
DEE	10	2.0	2.9	15	528–655
DIPE	5	2.0	3.6	15	528–654
BEE	10	2.0	1.98	15	543–696
DIPEE	10	2.0	1.2	15	557–698

DEE

Figure B.37 shows the comparison of experiments and simulations for the heat release rate of the rich mixture of diethyl ether. It is possible to see that the low-temperature heat release and the maximum accumulated heat release are quite similar between experiments and simulation, showing a reasonably good performance of the mechanism. Nevertheless, the heat release rate, especially for the first stage, is largely overpredicted by the simulations at all temperatures. For the main stage heat release, the simulated rate gets quite close to the experimental one at higher temperatures, while it is still overpredicted for the lower temperatures.

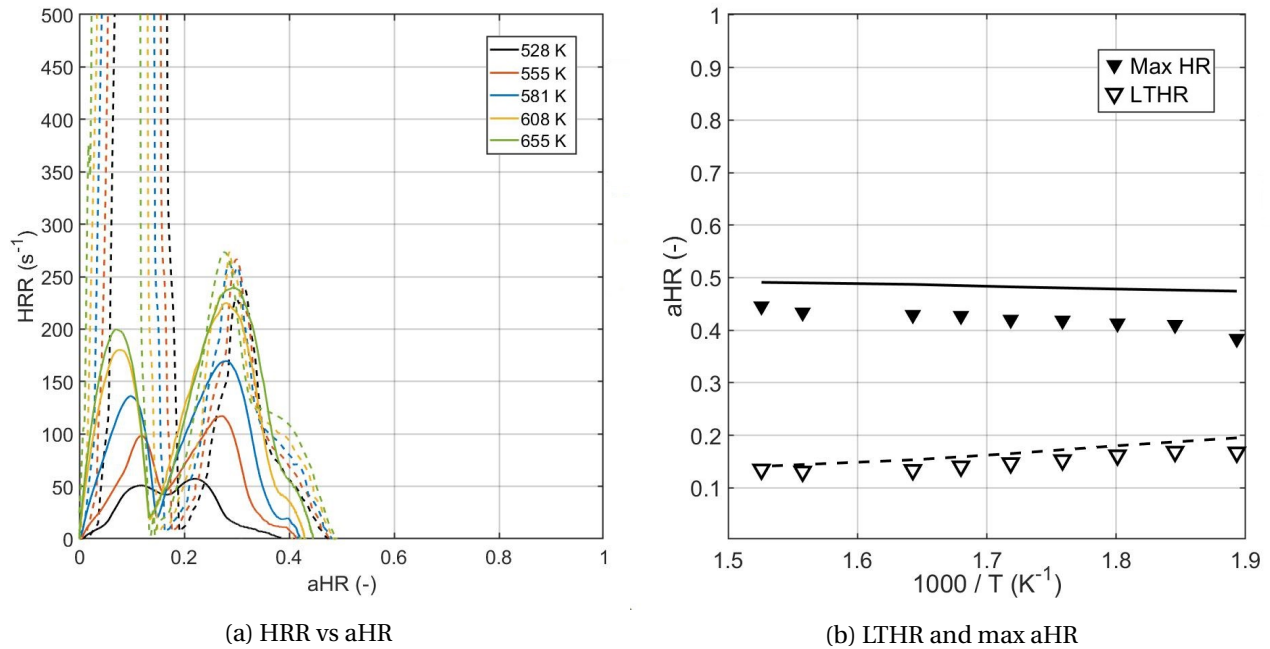
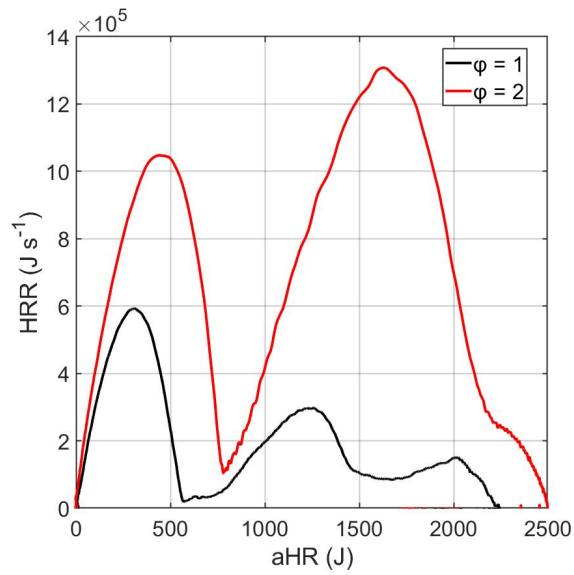


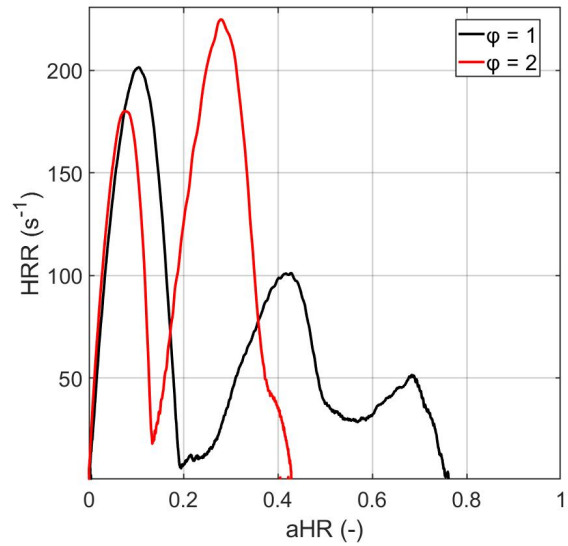
Figure B.37: Heat release rate analysis for DEE: $\phi = 2$, $p_c = 15$ bar, dilution = 10 (50% CO₂ + 50% N₂), DEE = 2.9%.

Figure B.38 shows the comparison between the stoichiometric and rich mixture at the same temperature of 608 K. The Figure B.38a shows the heat release rate against the accumulated heat release for the two conditions, without normalising them. It can be seen that, for similar temperature and pressure, the maximum accumulated heat release has quite similar values, while the heat release rates are higher for the rich conditions both for the first and the main stage. The second plot (Fig. B.38b) shows the same profiles, but this time normalised by the LHV of each mixture ($LHV_{\phi=1} = 2.9417 \cdot 10^3$ J, $LHV_{\phi=2} = 5.8156 \cdot 10^3$ J). It appears therefore that the rich conditions are expected to release more heat, since the fuel content and therefore the LHV is higher. Nevertheless, the quantity of oxygen is not ideal for the combustion and the maximum accumulated heat release reaches less than half the LHV value of the mixture.

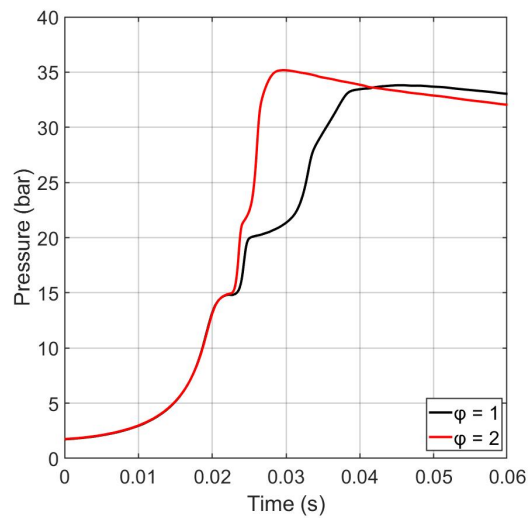
In the Figure B.38c the pressure profiles are also compared. The pressure increase is only slightly higher for the rich mixture, but the ignition delays are shorter and the slope of the increase is steeper, which translates in the higher heat release rates.



(a) HRR vs aHR



(b) HRR vs aHR (normalised by mixture LHV)



(c) Pressure profiles

Figure B.38: Heat release rate analysis for DEE: comparison between stoichiometric and rich mixture, $T_c = 608$ K, $p_c = 15$ bar, dilution = 10 (50% CO_2 + 50% N_2).

DIPE

A heat release rate analysis was performed for the rich mixture of DIPE with a dilution of 5 (the same used for $\phi = 1$). Figure B.39 shows the comparison between experimental results and simulations. Similar to what is already seen for the other conditions for DIPE, at low temperature the mechanism does not show any reactivity. For the temperatures where the simulations start to show an ignition, it is possible to see that the low-temperature heat release and the maximum accumulated heat release are in a quite good agreement. The low-temperature heat release is almost impossible to see in the first plot, since the associated HRR is very small compared to the one of the main stage. Also, in the simulations it seems that the main heat release is actually happening in two stages, as shown by the two peaks in the profile, while only one peak is visible in the experiments. In general, the simulations overpredict the heat release rates by a factor of around 2-3.

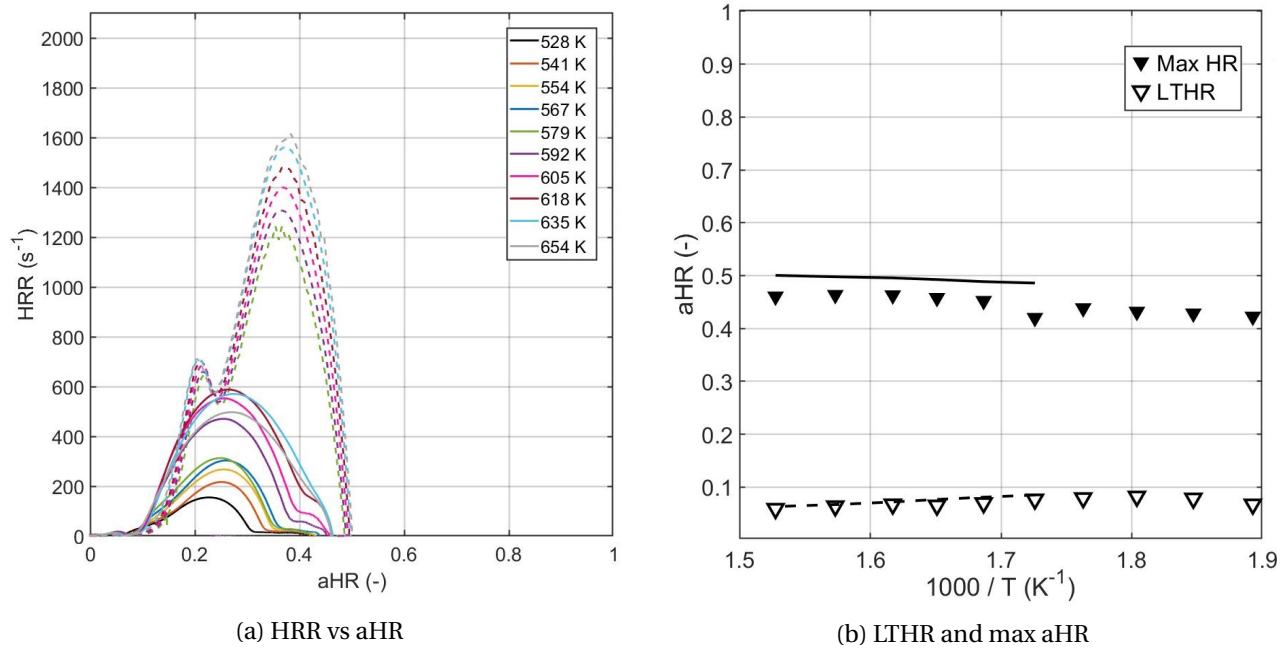


Figure B.39: Heat release rate analysis for DIPE: $\phi = 2$, $p_c = 15$ bar, dilution = 5 (50% CO_2 + 50% N_2), DIPE = 3.6%.

Figure B.40 on the other hand shows the comparison of the HRR analysis for stoichiometric and rich mixtures at a temperature of 615 K. The first plot shows the computed values for HRR and aHR, without any normalisation: it is possible to note that the maximum accumulated heat release are quite similar for the two mixtures, while the heat release rate is higher for the rich mixture, both for the first and main stage heat release. If the results are normalised by the lower heating values of the two mixtures, respectively ($\text{LHV}_{\phi=1} = 5.2151 \cdot 10^3$ J, $\text{LHV}_{\phi=2} = 1.0315 \cdot 10^4$ J), the maximum accumulated heat release of the rich mixture appears to be around 0.46, while the

one of the stoichiometric one is slightly higher than 0.8. As suggested for DEE, this is probably due to the fact that the combustion happening in non-stoichiometric conditions is less “efficient”, resulting in a lower heat release compared to what expected from the quantity of fuel contained in the mixture. The Figure B.40c shows the comparison between the pressure profiles: the pressure increase is slightly higher for the rich mixture, both for the first and main stages. The steepness of the increase is higher for the rich mixture and it is possible to see that for the stoichiometric mixture there is a slight change in slope towards the end of the main ignition.

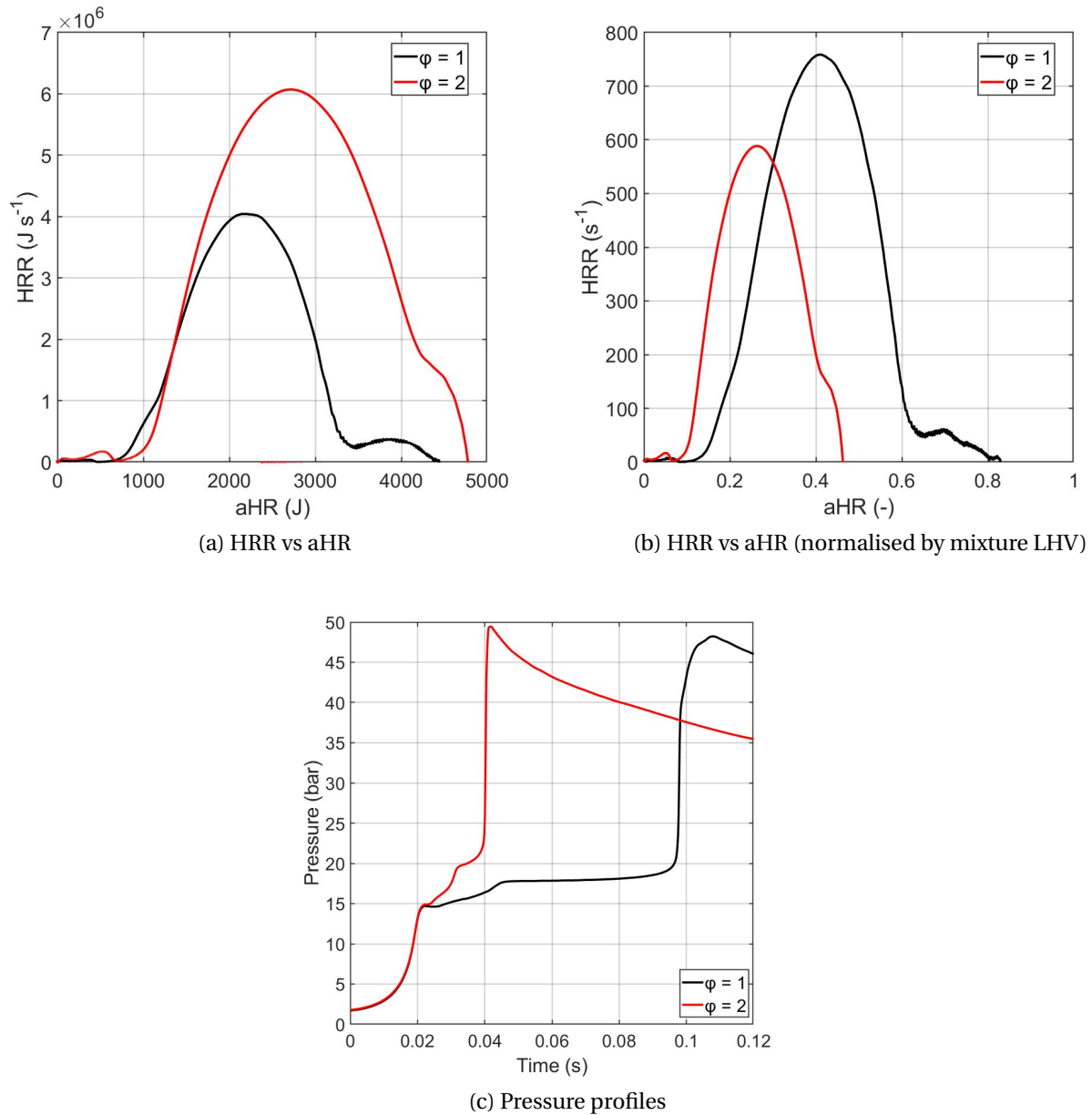


Figure B.40: Heat release rate analysis for DIPE: comparison between stoichiometric and rich mixture, $T_c = 615$ K, $p_c = 15$ bar, dilution = 5 (50% CO_2 + 50% N_2).

BEE

Figure B.41 shows the experimental results against the simulations for the rich mixture of butyl ethyl ether. From Figure B.41a, it is possible to see that the heat release rates of the main stage are in reasonable agreement between experiments and simulations, while the mechanism largely overpredicts the heat release rate of the first stage ignition. In the main ignition, both the simulations and the experiments show a small secondary “bump” toward the end, which is more evident in the simulations, with a higher heat release rate. The Fig. B.41b shows the low-temperature heat release and the maximum accumulated heat release, which are slightly overpredicted by the simulations, but still in quite good agreement. For the low-temperature heat release, it is possible to see that both simulations and experiments show a decrease in this value as the temperature increases, which is coherent with the expected disappearance of the cool flame at higher temperatures.

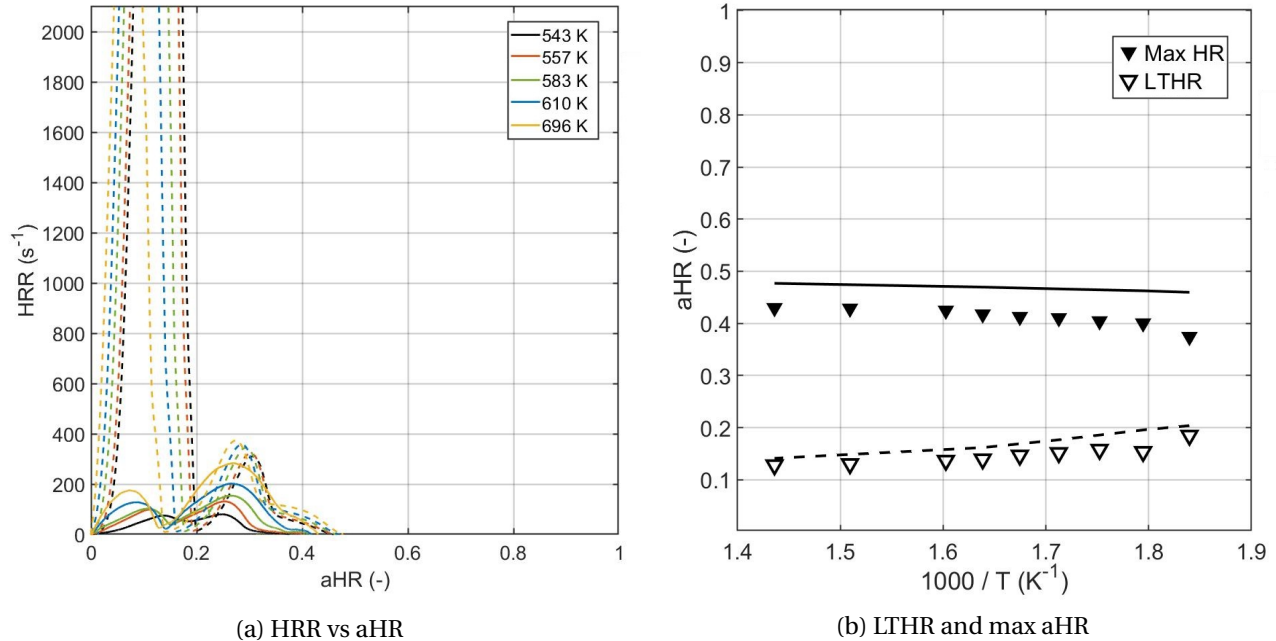


Figure B.41: Heat release rate analysis for BEE: $\phi = 2$, $p_c = 15$ bar, dilution = 10 (50% CO_2 + 50% N_2), BEE = 1.98%.

If the comparison between stoichiometric and rich mixtures is considered, Figure B.42 shows a comparison at 610 K. The Fig. B.42a shows the HRR vs aHR, both of them not normalised. Both the low-temperature heat release and the maximum accumulated heat release are slightly higher for the rich mixture, but not by a large amount. On the other hand, the heat release rates are quite higher for the rich mixture. If both HRR and aHR are normalised by the LHV of each mixture ($LHV_{\phi=1} = 2.9290 \cdot 10^3$ J, $LHV_{\phi=2} = 5.7854 \cdot 10^3$ J), the Figure B.42b is obtained and it can be seen that the maximum accumulated heat release of the $\phi = 2$ mixture is slightly over 0.4, while for the stoichiometric mixture it is around 0.7. Nevertheless, even when normalised, the heat release rate

of the rich mixture appears substantially larger. The Figure B.42c the comparison between the pressure profiles of the tests with the two mixtures: in this case, the first ignition delay times are comparable, while the main ignition is clearly faster for the rich mixture. The pressure increase is more important for the rich mixture and the slope is steeper. The stoichiometric mixture shows a more distinguishable change in slope for the main pressure increase.

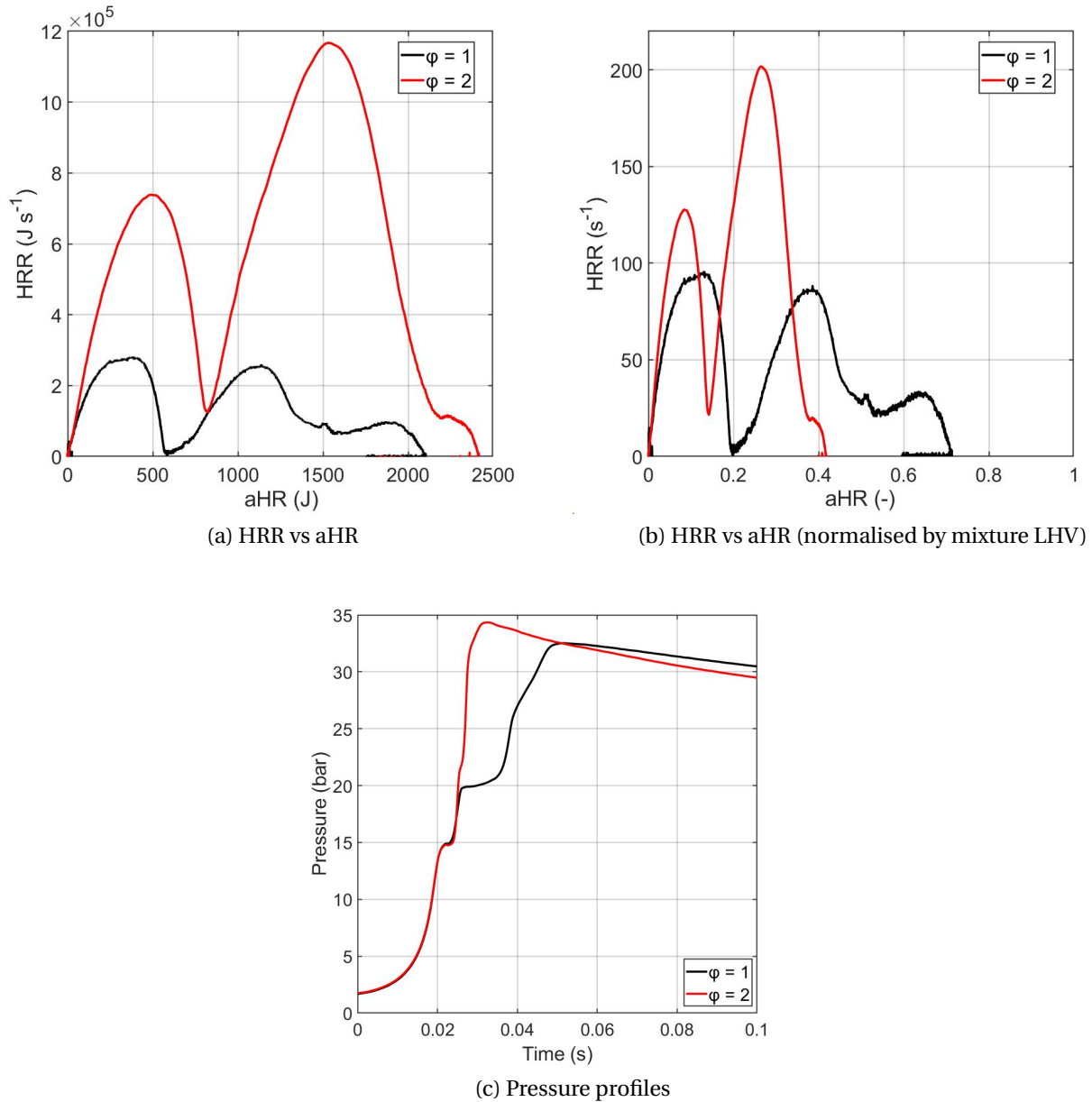
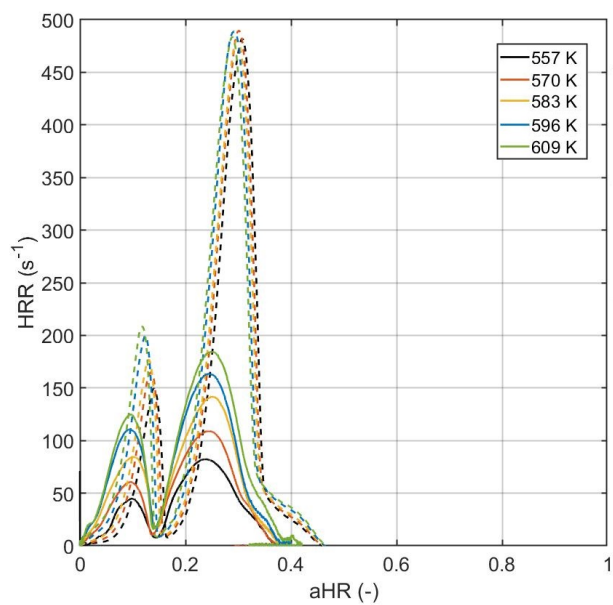


Figure B.42: Heat release rate analysis for BEE: comparison between stoichiometric and rich mixture, $T_c = 610$ K, $p_c = 15$ bar, dilution = 10 (50% CO_2 + 50% N_2).

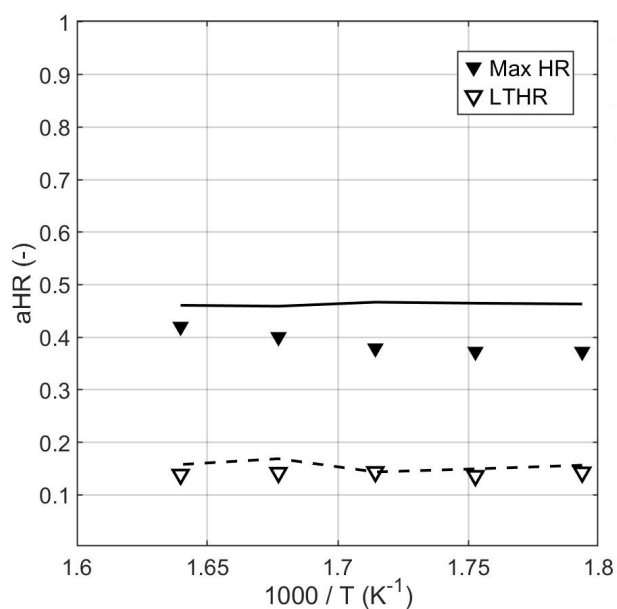
DIPEE

For di-iso-pentyl ether, two rich mixtures were analysed from the heat release rate point of view, one with 50% CO₂ and 50% N₂ and one with 100% N₂ as inert gas. The comparison between experiments and simulations for the two mixtures are shown in Figure B.43. The heat release rates are slightly higher for the mixture containing only N₂, both for the first and the main stage. The simulations show the same tendency, but they overestimate the heat release rates for both mixtures, at all temperatures. Also, the simulations show a third smaller peak for the mixture with only N₂, which cannot really be identified in the experiments. If the low-temperature heat release and maximum accumulated heat release are considered, the agreement between experiments and simulations is sensibly better, for both mixtures. In particular, the low-temperature heat release is almost perfectly captured by the mechanism, while there is a slight overprediction of the maximum accumulated heat release.

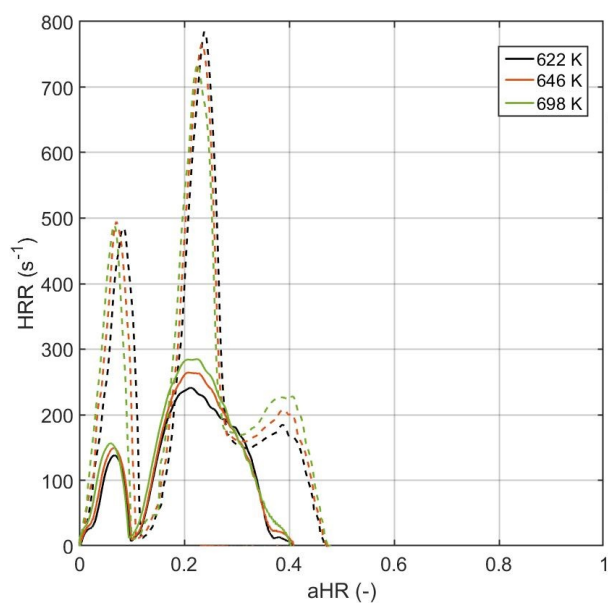
Figure B.44 shows the comparison of stoichiometric and rich mixtures (both with the same inert gases composition) at a temperature of 610 K. The Fig. B.44a shows the heat release rate versus accumulated heat released for both mixtures, without normalisation. If the maximum accumulated heat releases are quite similar, the heat release rates for the rich mixture are at least three times higher. The stoichiometric mixture shows a third peak in the heat release rate, after the main one, which can also be seen from the clear slope change in the pressure profile shown in the Fig. B.44c. If HRR and aHR are normalised by each mixture lower heating value ($LHV_{\phi=1} = 2.8755 \cdot 10^3$ J, $LHV_{\phi=2} = 5.7078 \cdot 10^3$ J), the Fig. B.44b is obtained. The heat release rates are still more important for the rich mixture, but if the maximum accumulated heat release is considered, the value reached for the rich mixture is only slightly more than 0.4, while the value for the stoichiometric mixture is close to 0.7. Once again, this shows how the fuel content of the mixture is not completely exploited when a rich mixture is considered, since the oxygen content is lower than the “optimal” stoichiometric condition. The Fig. B.44c shows the comparison of the two pressure profiles. The pressure increases (both for the first and main stages) are higher for the rich mixture. The slope of these increases for the rich mixture is sensibly steeper, which determines the higher heat release rates that were computed. It can also be seen that the stoichiometric mixture shows a clear change in slope both in the first and main stage pressure increases, while the rich one shows only a slight change in slope at the end of the main ignition, which translate to a very small “bump” in the HRR vs aHR profile.



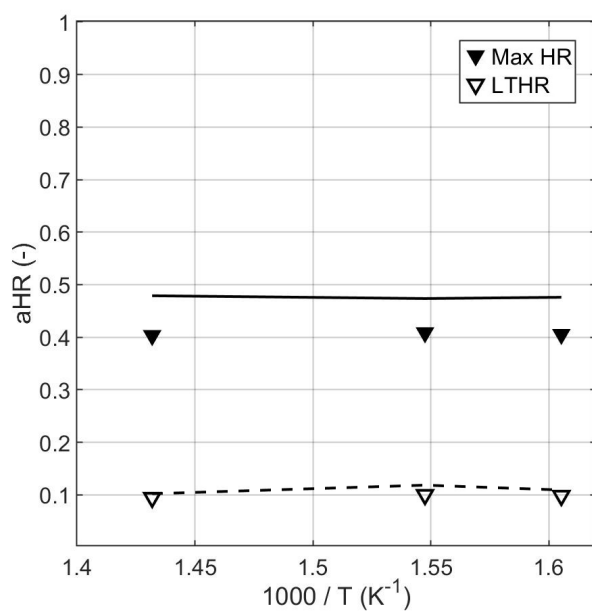
(a) HRR vs aHR



(b) LTHR and max aHR



(c) HRR vs aHR



(d) LTHR and max aHR

Figure B.43: Heat release rate analysis for DIPEE: $\phi = 2$, $p_c = 15$ bar, dilution = 10 (a), b): 50% CO_2 + 50% N_2 , c), d): 100% N_2), DIPEE = 1.2%.

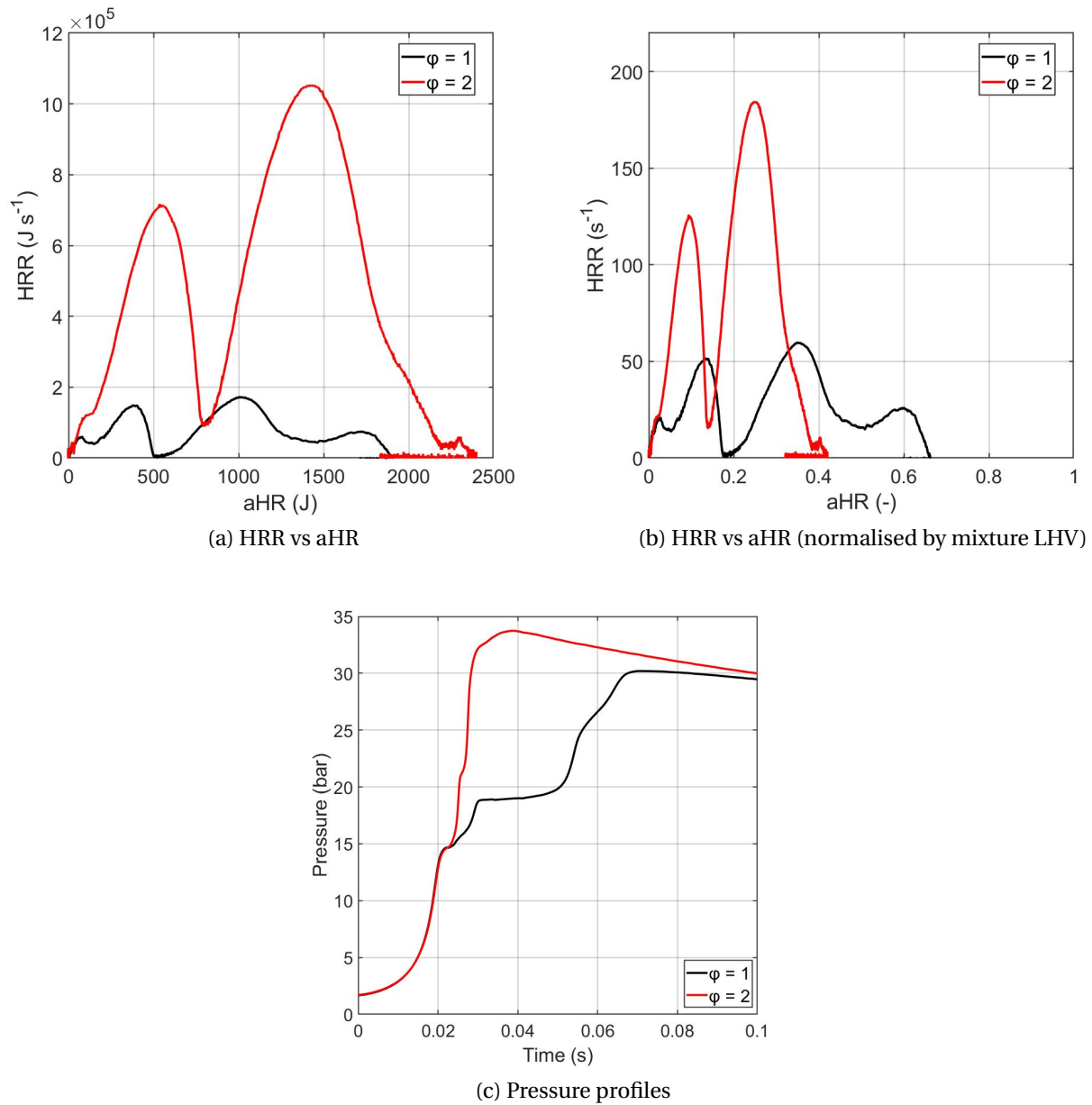


Figure B.44: Heat release rate analysis for DIPEE: comparison between stoichiometric and rich mixture, $T_c = 610$ K, $p_c = 15$ bar, dilution = 10 (50% CO_2 + 50% N_2).

Appendix C

Ethyl lactate: additional data

The sub-mechanism for ethyl lactate was developed from scratch in this work and no previous mechanism from the literature was available. In order to make it more accurate, it was also validated against other experimental data, which will be presented in this appendix. These experimental measures of laminar flame speeds were also collected in the laboratory of ICARE (CNRS - Orléans), using an innovative set-up called OPTIPRIME, which will be shortly presented in the following section. Then, the comparison of measured and simulated flame speeds will be shown.

C.1 OPTIPRIME

OPTIPRIME is a spherical bomb set-up, which is designed to measure laminar flame speeds under isochoric conditions. This set-up was completely developed in ICARE and a thorough description can be found in [134].

This set-up is a perfect spherical isochoric combustion chamber, made by two stainless steel half shells, with a 360° fused silica ring. This allows a full optical access, making possible to record simultaneously the pressure and the flame radius from the ignition point until the wall. The quartz thickness is 11 mm, ensuring resistance to pressure greater than 100 bar. The total volume of the chamber is 0.943 L; this small volume allows an easier homogeneous pre-mixture and reduces the effects of radiation and hydrodynamic instabilities.

Two pressure sensors with high sensitivity and frequency are used to record the pressure during the tests. A type K thermocouple is introduced in the sphere to check the initial temperature. The whole sphere is placed inside a furnace (temperature range: 10-200°C), in order to avoid inhomogeneity in the temperature. The test mixture is prepared in a separate tank; ethyl lactate is directly injected in the sphere, using a high-precision syringe, in order to avoid condensation in the buffer tank, which is not heated.

The mixture in the bomb is ignited thanks to an electric discharge between two ultra-fine electrodes. Images are recorded using a PHANTOM V1611, which operates between 8000 and 15000

fps. A calibration of the system is performed before the tests, in order to limit optical deformations. The experimental conditions tested in OPTIPRIME and used to validate the mechanism for ethyl lactate are reported in table C.1.

Table C.1: Experimental conditions for the measurements of laminar flame speeds of ethyl lactate in OPTIPRIME

Dilution	ϕ	p_0 (bar)	T_0 (°C)
Air (21% O ₂ / 79% N ₂)	0.7	1, 2, 3	135
	1	1, 2	135
	1.2	1	135

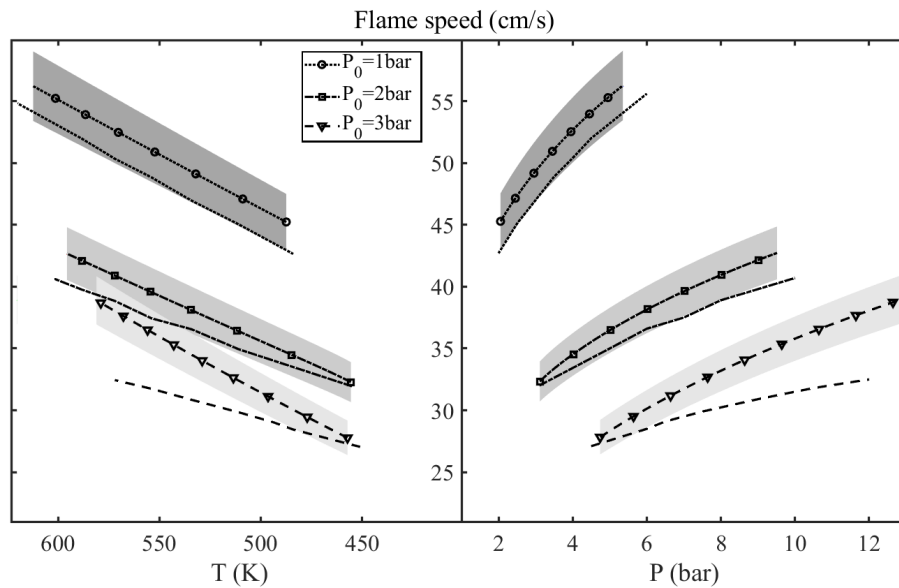
C.2 Laminar flame speeds

The experimental measurements and the simulations of the laminar flame speeds of ethyl lactate are shown in Figure C.1. The lines with symbols, with the shadowed area, represent the experimental results and their uncertainty ($\pm 5\%$) [135]. On the other hand, the simple dashed or pointed lines (without symbols) represent the simulations obtained with the newly developed mechanism. First of all, it is important to remember that the measurements obtained from OPTIPRIME are in isochoric conditions. Therefore, during the experimental run, pressure and temperature increase together, as the flame expands. The resulting flame speeds are consequently associated to a pair of temperature and pressure in every point along the development of the experimental run. It is not surprising then to see the laminar flame speeds increasing with the increasing pressure, because at the same time also the temperature increases.

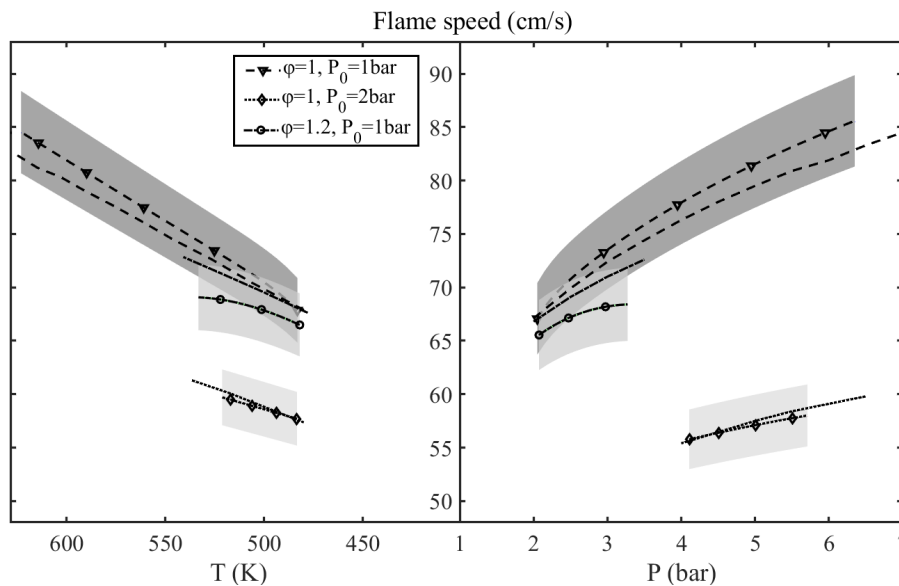
Looking at the experimental results shown in Figure C.1a, where the three tested conditions for the lean mixture are plotted, it is possible to see that a higher initial pressure leads to lower flame speeds over the whole isentropic evolution of the flame. A different initial pressure seems to also determine a different slope in the evolution of the flame speeds over the temperature/pressure. If the simulations are considered, it is possible to see that for the lower initial pressure the mechanism fairly predicts the laminar flame speeds and the simulated values are in the uncertainty range over the whole range. Moreover, the simulated slope retraces the experimental slope very well. On the other hand, if the initial pressure is increased, the simulations start deviating from the experimental results, with the simulated values that are sensibly lower at high pressures and temperatures, reaching a maximum error around 15%. It can be noted that actually the simulations are quite accurate at the beginning of the experimental run (low temperature and pressure), but since the slope of the simulated flame speeds is different from the one of the experiments, at high temperature and pressure the values are quite different.

Figure C.1b on the other hand shows the results for the stoichiometric and rich mixtures. The first remark on the experimental results is that the rich mixture has lower flame speeds over the

whole temperature/pressure range, compared to the stoichiometric mixture. Also, as noticed for the lean mixture, increasing the initial pressure for the same stoichiometric mixture leads to lower flame speeds over the whole isentropic evolution. It has to be noted that for the rich mixture there are less experimental data; this is caused by the fact that at higher pressures, the flames showed instabilities.



(a) $\phi = 0.7$, $p_0 = 1, 2, 3$ bar



(b) $\phi = 1$, $p_0 = 1, 2$ bar and $\phi = 1.2$, $p_0 = 1$ bar

Figure C.1: Laminar flame speeds of ethyl lactate.

The simulations perform fairly well for the stoichiometric and rich mixtures, with the simulated

flame speeds overall falling inside the uncertainty range of the experimental results. Nevertheless, the slopes are not perfectly captured, especially for the stoichiometric conditions. In fact, for the lower initial pressure (1 bar), flame speeds are underpredicted at higher temperature and pressure, while for the higher initial pressure (2 bar) the opposite trend can be seen. For the rich mixture, there is a slight overprediction of the flame speed at the higher pressure and temperature. Overall, the mechanism shows fairly good performances concerning the laminar flame speeds under the considered conditions, making this mechanism, first in the literature, reasonably good for representing the behaviour of ethyl lactate under combustion conditions.

C.2.1 Sensitivity analysis

To complete the analysis on the mechanism performance concerning the laminar flame speeds, a sensitivity analysis on the flow rate was performed for two conditions, one for which the mechanism performs well ($\phi = 1$, $p_0 = 1$ bar) and one for which the simulations are the furthest from the experiments ($\phi = 0.7$, $p_0 = 3$ bar). The results are shown in Figure C.2.

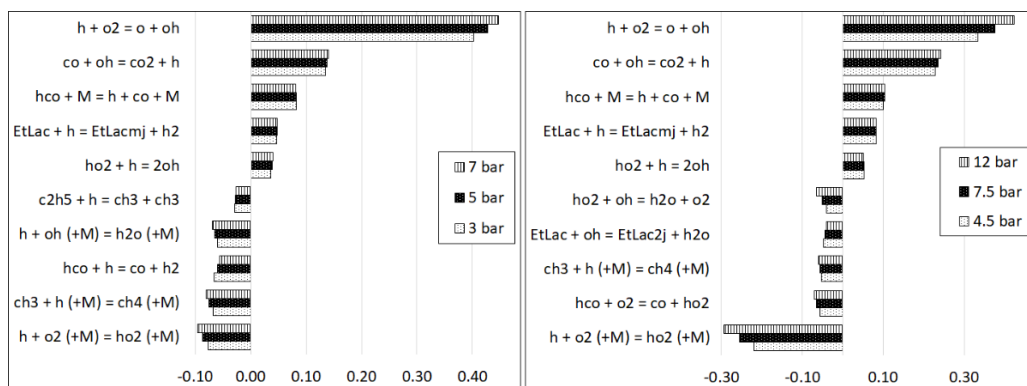


Figure C.2: Laminar flame speed analysis for two conditions: left panel: $\phi = 1$, $p_0 = 1$ bar, right panel: $\phi = 0.7$, $p_0 = 3$ bar.

For both conditions, the competition between the reaction $\text{H} + \text{O}_2 \rightleftharpoons \text{O} + \text{OH}$ and $\text{H} + \text{O}_2(+\text{M}) \rightleftharpoons \text{HO}_2(+\text{M})$ is important, as expected, for laminar flame speeds. The rate constants of these reactions have been taken from Stagni et al. [136], since they seem to properly describe this competition [137]. Another important reaction that appears in this analysis is $\text{HCO} + \text{H} \rightleftharpoons \text{CO} + \text{H}_2$, for which the rate constant (+M) was adopted from NUIG 1.1 mechanism [138]. This reaction can be interesting, since it appears to have an inhibiting effect on rich and stoichiometric conditions, while it does not show a great sensitivity for the lean conditions, where the flame speeds are already underpredicting.

To conclude, it might be interesting to have a look at the reactions directly involving ethyl lactate. The H-abstraction on the primary site (on the ethyl side of the ether function) by H atoms is enhancing the flame speeds for all conditions. On the other hand, the H-abstraction from the site

neighbouring the OH function by OH radicals has an inhibiting effect for the lean mixture, while it seems unimportant for the rich and stoichiometric conditions.